SOFT-SEDIMENT DEFORMATION PROCESSES AND PRODUCTS IN SHELF TO BASE SLOPE SETTINGS

UNIVERSITY OF LIVERPOOL

Thesis submitted in accordance with the requirements of the University of Liverpool for the degree of Doctor in Philosophy

by

Carlos Mauricio Monnerat de Oliveira

August 2008

Abstract

Soft-sediment deformation structures (SSDS) can be divided into *in situ* and detached structures. The latter include slides, slumps, and debrites (mass transport deposits) and dominate the literature compared to processes and products of deformation that takes place *in situ*. This thesis addresses in detail the origin and development of *in situ* SSDS and their stratigraphic and depositional context in well exposed shelf edge and upper to lower slope successions of the Karoo and the Neuquén basins.

In the study areas, *in situ* SSDS occur preferentially in shelf-edge/upper-slope settings, but can also develop in middle and lower slope settings in association with detached structures. Flame and load structures are the most common *in situ* features and a systematic quantitative study of flame structures shows that they are elongated and have preferential orientation. The relationship between morphometric parameters, such as height, width and spacing, is statistically proven to be independent of the scale of occurrence and depositional environment in the majority of the cases. This indicates that similar physical and rheological conditions occurred during their formation in both shallow and deepwater environments. Divergence in the trends can indicate changes in the boundary conditions. Comparison of statistical results from Karoo and Neuquén datasets indicates a grain size influence on the dimension of structures; the greater the grain size the shorter the flame structures.

Fine-grained sediment was commonly debouched through the flames onto the palaeo-sea floor resulting in subtle sea bed topography. This observation confirms the near-to-seabed setting of *in situ* SSDS formation. Liquidization was the main deformational process in the formation of *in situ* SSDS and was triggered by loading caused by rapid deformation of sand packages, driven by Rayleigh-Taylor instabilities and vertical shear stress due to fluidization. The downslope component of body force was an additional driving force that controlled the orientation of the *in situ* SSDS. This was the main force acting during the formation of detached SSDS permitting deformation without the requirement of liquidization. Detached SSDS were triggered by the association of local steeper gradient and loading due to sediment deposition. *In situ* SSDS (foundering and water escape structures) can occur as a final stage in the evolution of detached SSDS, caused by loading during deposition of overlying beds. This complex interaction of SSDS types has led to examples of *in* situ products being mistaken for detached types, which can lead to incorrect interpretation of depositional environment.

Synthesis of the outcrop data from the two basins has resulted in a new classification scheme for SSDS, based on the combination of distance of movement and dominant stress, which provides a link between types of structures that were formed in a process continuum. This study shows that major, widespread SSDS can occur aseismically and that these processes are important in, and integral to, the shaping of the shelf-edge/slope during basin filling.

Acknowledgements

I would like to thank Petrobras for the opportunity to stop my day-by-day work and to come to the academic environment in a unique opportunity; for the sponsorship of the full project and the permission to use laboratory facilities.

The guidance, enthusiasm, knowledge and incredible energy of my supervisors Steve Flint and Dave Hodgson during my research were essential. Thank you very much for everything. Also, I would like to thanks the University of Liverpool for the good academic environment and material resources.

In a project based on field work, I thank John Kav, Dave, Steve and Jose Luis for accompanying and the valuable discussions in the field. Thanks John Hakes for the fundamental help in the GPR acquisition. Also, DeVille Wickens and Willem gave valuable logistical support in the Karoo Basin.

During this project I had the opportunity to test different methodologies. I thank Paradigm Geophysical Brazil for providing a free licence for the Software VoxelGeo for use in this research. Also, I thank the technical support and friendship of Elisabete Campos for the acquisition of tomographic data; Eldues and Mundin for fundamental help in the seismic modelling; Amilson during the GPR reprocessing; John Kav for sample preparation; Fernando, Rosa, Lilian and Leandro for their support in VoxelGeo and Gocad, and Grahame Settle and Olinto for statistical review.

For all people that I met in the Strat Group for the very good environment of work and good beer-time (and chips) we had after hard days work (in the field or office).

A special thanks to my friends Jorge, Gilvan and their families that gave to me (and to my family) the friendship and all support during the time spent in Liverpool (and the opportunity to have a real Brazilian barbecue).

Finally I thank and dedicate all this work to my family Michelle, Gabriel and Clara, and my mother Anna and my father Ivanyr. Without your support, dedication and love I am sure I would not be here.

Table of contents

List of figures and tables

Chapter 1

Chapter 5

Chapter 6

Chapter 1 - Introduction

1.1 Aims of the thesis

1.1.1 The geological environment

The submarine slope plays a fundamental role in the transfer of sediment from continent to deep ocean basins through a range of erosional, depositional and post-depositional processes and products. Among them, resedimentation processes (rock falls, sediment creep, slides and slumps, debris flows, liquefaction and fluidization of sediment, turbidity currents; Stow *et al.*, 1996) play a crucial role in the development of soft-sediment deformation structures (SSDS).

Soft-sediment deformation structures comprise a wide range of features formed non-tectonically before the sediment is lithified, either during deposition or shallow burial. Structures can be formed *in situ* or be the result of transportation, at scales varying from few millimetres to several kilometres (Allen, 1982). They are commonly found in submarine slope setting, which provides ideal pre-requisite conditions for their development: (1) large volumes and alternating packages of mud and fine-grained sand; (2) aqueous system; (3) common occurrence of instabilities and types of loading to trigger the deformation and (4) a gradient favourable for development of gravity flows that drive the deformation.

For decades, the recognition of soft-sediment structures in the deep water environment was restricted to the identification of occurrences in outcrops of ancient deposits that furnished the basis for understanding of the gravitational flow processes (Kuenen & Migliorini, 1950), of the deformational processes and classification of structures (Potter & Pettijohn, 1963), supported by a new generation of laboratory experiments (Kuenen, 1958). In parallel, engineering studies on the stability of modern slopes provided new insights in the understanding and classification of mass movement (Vernes, 1958). This background, together with the pioneering advent of reflection seismic acquisition and oceanographic expeditions during the 1960s to 1980s, supported the classical models that considered the submarine slope as comprising two regions: one of bypass (upper and middle slope) and another of

accumulation (lower slope and basin; e. g. Walker, 1978; Bouma, 1979; Galloway, 1998). More recently, improvements in acquisition, processing and display of seismic reflection datasets have brought new advances in the understanding of the slope sedimentary processes and deposits (e.g. Prather, 2000; Prather, 2003; Saller *et al.* 2004). In this context, the slope is recognized now as a complex system that consists of a series of erosional, sediment bypass and depositional sites that evolve temporally and spatially, resulting in a wide range of deposits, with a wide range of intercalated soft-sediment deformation structures (Figure 1.1).

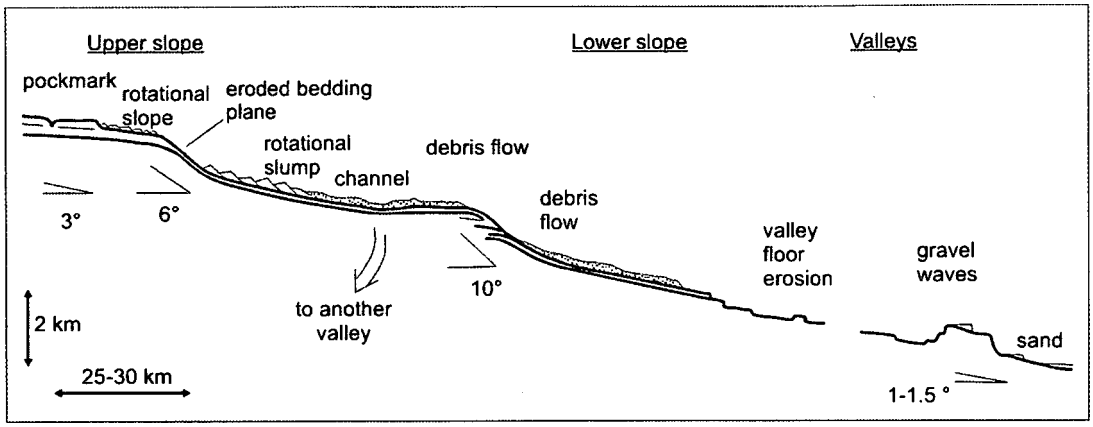

Figure 1.1: Interpretative figure from Piper et al. (1999) with the sequence of sedimentary and associated deformational facies developed down the present day slope of the Grand Banks, Canada. Notice the distinct angles of the slope creating local sections of bypass and deposition.

Large scale mass movement deposits were initially identified in geo-hazard studies at continental margins and partially observable in ancient deposits. Recently, these detached deposits have been detailed with the use of high resolution geophysical data, which helped to elucidate deformational processes on the slope (e. g. Trincard & Field, 1992; Piper *et al.*, 1999; Canals *et al.*, 2004; Moscardelli *et al.*, 2006). Deformation of unlithified sediments can occur without significant down-slope remobilisation (Lowe, 1975; Allen, 1982); however, *in situ* soft-sediment deformation structures are not recognized in high resolution geophysical data. Thus the knowledge of *in situ* SSDS has been limited to outcrop studies of small structures, commonly carried out in isolation from larger-scale analysis of slope evolution (e.g. Postma, 1983; Mount, 1993; Stromberg & Bluck, 1998; Moretti *et al.*, 2001, Hildebrandt & Egenhoff, 2007). From this background arise a number of questions that led to the research presented herein.

1.1.2 – Objectives and key question to be addressed

The main objective of this thesis is to investigate the conditions, processes and drivers of soft-sediment deformation in shelf-edge to submarine slope settings through the geometric and morphological analyses of the resultant structures, with emphasis on *in situ* soft-sediment deformation.

To address these objectives a series of questions were posed and discussed:

A – About the process:

1. What are the most common types of SSDS found between the shelf-edge and the lower slope?
2. What criteria can be used to differentiate detached vs. *in situ* structures?
3. What are the pre-requisite conditions and trigger mechanisms that govern the initiation of deformation that forms distinct soft-sediment deformation structures?
4. What processes and stress conditions acted during the deformation?
5. What type of force could amplify or conduct the deformation?

B – About the distribution:

1. What is the preferential stratigraphic and profile position for the occurrence of SSDS?
2. Are *in situ* and detached structures associated? If so, what is the spatio-temporal nature of this relationship?
3. Do SSDS follow a preferential orientation?

C – About the scale of occurrence:

1. Are the large scale *in situ* soft-sediment deformation features observable on seismic sections? Can these structures be misidentified as detached (mass transport deposits) in seismic sections?
2. What methods could be used to the study of features below and above the average outcrop scale?
3. Are the *in situ* structures predictable at different scales?

1.1.3 Methods and techniques

Two basins were selected to carry out the studies: the Permian SW Karoo Basin, in South Africa, and the Jurassic Neuquén Basin, in Argentina. These basins were chosen based on extensive previous regional stratigraphic studies at the University of Liverpool (Burgess & Flint, 1998; Burgess *et al.*, 2000; Flint *et al.*, 2004; King, 2005; Wild, 2005; Wild *et al*, 2005; Hodgson *et al.*, 2006) that provided a good large-scale context for the study and allowed the analysis of features in deposits that range from shelf to lower slope (Figure 1.2). The most common studied structures were vertical fluid escape structures, due their abundance and different scales of occurrence (from a few centimetres to five metres high in the study areas).

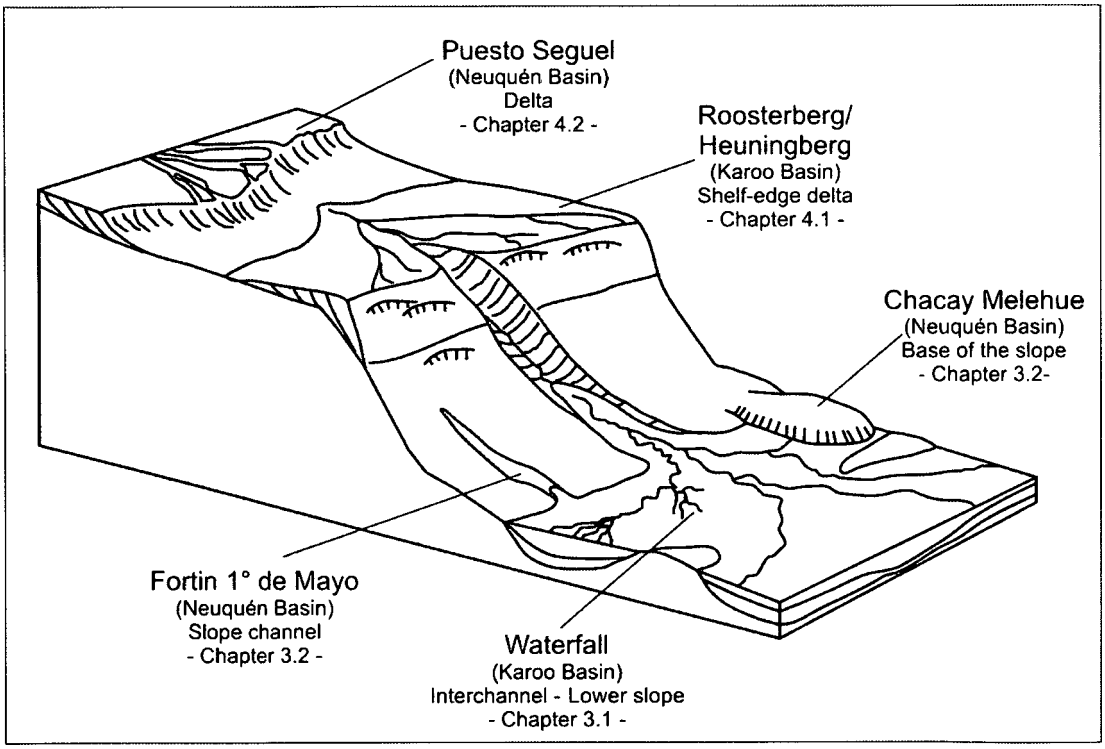

Figure 1.2: Block diagram (from Posamentier and Walker, 2006) providing a schematic view of the shelf to slope to basin floor profile. The outcrops studied in this research are located in their interpreted profile positions.

The bulk of the data were obtained through extensive field work that resulted in 1500 m of sedimentological logs collected at centimetre scale, tens of geological panels with detailed mapping of the deformation features between the logs; 300 measurements of geometrical multi-attributes and orientations of flame structures and around 400 palaeocurrent indicators. This study was complemented by the

acquisition, processing and interpretation of 600m^2 (200 m linear) of high resolution ground penetrating radar (GPR) data. Laboratory work involved computed tomography analyses and serial slice interpretation of hand specimens. Finally, one synthetic reflection seismic model was built considering the parameters from one deformed interval (Figure 1.3). A summary description of these methodologies is presented in Chapter 5.

1.1.4 Thesis layout

Chapter 1 summarises current knowledge of the shelf-edge to base of slope evolution, focusing on slope instabilities and readjustments and their influence on the generation of soft-sediment deformation structures. The basis for the origin of soft-sediment deformation structures, the deformational processes involved, the conditions and drivers, and the previously published classifications are synthesised in this chapter. This is accompanied by a literature review on the occurrence of soft-sediment deformation structures in these environments. Chapter 2 briefly describes the SW Karoo and Neuquén basins and the characteristics of the Permian and Jurassic lithostratigraphic formations studied. Chapters 3 and 4 present the main outcrop data from lower slope and upper slope/shelf settings respectively. Chapter 3.1 is presented in the format of a paper that is now in press and therefore contains some general information that complements Chapters 1 and 2.

Chapter 5 focuses on the application of additional methodologies (computer tomography, serial rock slices, GPR profiles and seismic modelling) for the analyses of soft-sediment deformation structures at a range of scales that complement the core outcrop work. All of the information above is integrated in Chapter 6, with a new scheme for the classification SSDS and the comparison of the triggers, deformational processes and drivers considering the distinct depositional/deformational settings. The results of the statistical analyses are compared in order to verify the similarities and differences between the *in situ* soft-sediment deformation structures and their predictability at different scales in different settings. Finally, Chapter 7 provides the main conclusions and recommendations from this research.

Appendixes with log coordinates (Appendix 1), acquisition methodology (Appendix 2), raw data for statistical studies (Appendix 3) and regression analyses for each bed (Appendix 4) are at the end of this volume.

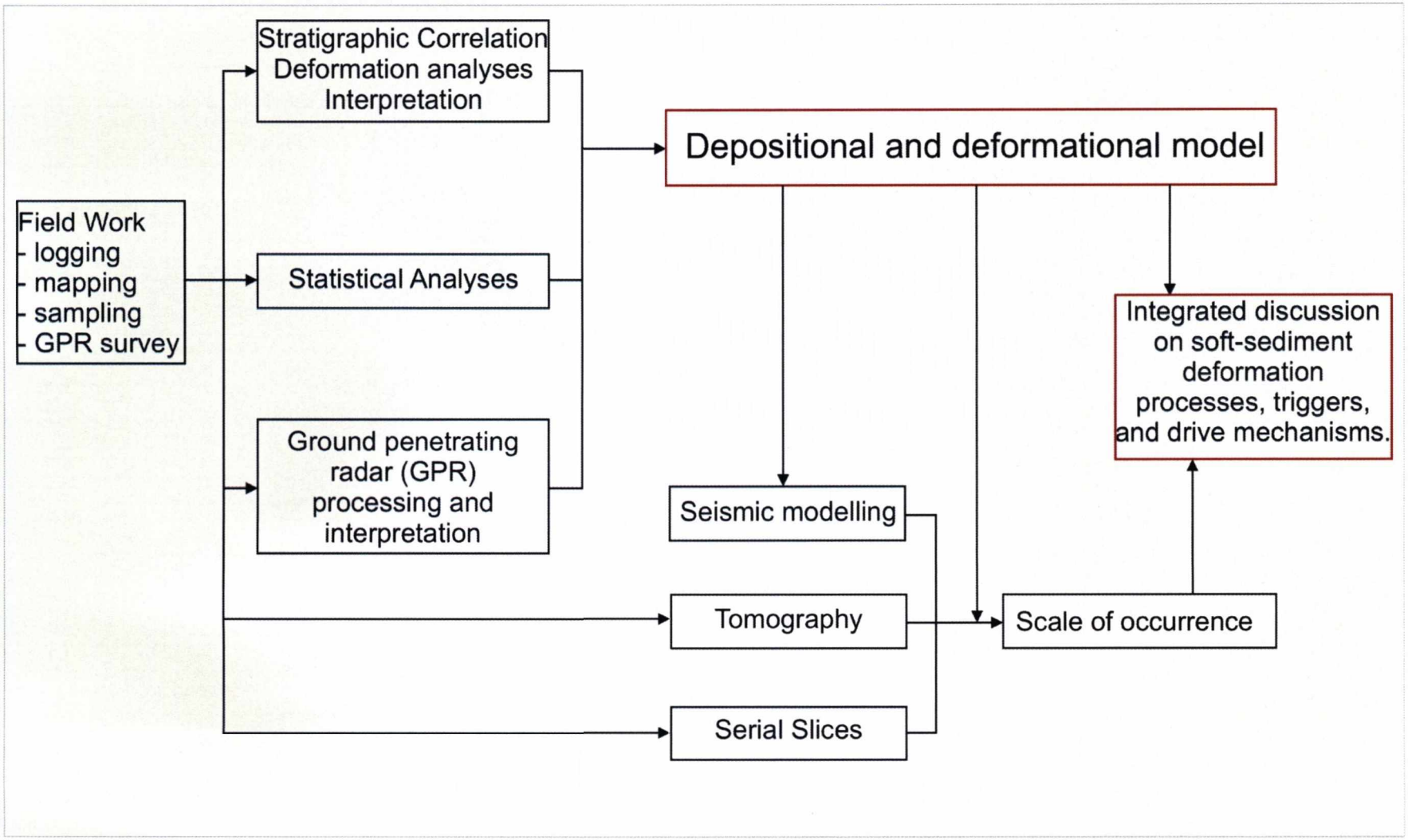

Figure 1.3: Summary diagram of the integrated methodology of this study.

1.2 – Soft-sediment deformation

1.2.1 – General aspects

Soft-sediment deformation structures are those structures developed as a result of deformation either soon after and/or during deposition, or when some compaction and/or diagenesis has initiated (Potter & Pettijohn, 1963; Collinson, 1994). Soft-sediment deformation structures (SSDS) may form over time scales from instantaneous, through hours or days to centuries. The force acting to form deformation can cease, generating an 'unfinished' structure (Allen, 1982, van Loon & Brodzikowski, 1987). For near surface sediments, the dominant factor is the amount of water involved in deformation (this can be judged by the form of the structure produced), which will make sediment ductile (Maltman, 1984). Another fundamental controlling factor is the load acting on the unconsolidated sediment that imparts an increase in pore pressure leading to deformation, normally by liquefaction or fluidization (cf. Chapter 3.1.1).

Soft-sediment deformation was first demonstrated by mid-nineteenth century observations of glaciogenic structures and clastic dykes, but it was only at the turn of that century that the concept was applied to other structures. Around the 1950s three new approaches contributed to the knowledge of SSD: (i) the turbidite concept, (ii) the soil mechanics approach, and (iii) the identification of mass wasting processes at modern continental margins (Woodcock, 1978). From the 1960s, van Loon & Brodzikowski (1987) identify three phases of development in the studies of SSDS: (1) during the early 1960s attempts were made to classify and explain the origin of the deformation; (2) during the late 1970s SSDS were used for the reconstruction of depositional environment and (3) from the middle 1980s interest was renewed with the publication of a series of papers, but difficulties arose due to the confusing terminology.

Two problems in the field of SSDS study are related to: (i) the use of inappropriate terminology and classification, and (ii) the criteria to distinguish structures created by tectonic processes vs. non-tectonic (SSD) processes. The proliferation of names for the same feature or the use of the same name to describe structures formed by different processes and the misunderstanding of the deformational process led to the generation of inadequate and inconsistent

classification schemes (Lowe, 1975; Allen, 1982; Mills, 1983; Owen, 1985; van Loon & Brodzikowiski; 1987).

Criteria for distinguishing structures produced by soft-sediment deformation vs. tectonic processes were proposed since the first half of the twentieth century (Rettger, 1935) but many of them are not exclusive to one or other process. Features found in both types of deformation include: (i) angular discordance at the upper bed contact; (ii) lack of associated cleavage; (iii) small size of the structures; (iv) soft-structures not related (kinematically) to local tectonic structures; and (v) occurrence of SSD between non-deformed beds (Potter & Pettijohn, 1963; Owen, 1985; van Loon & Brodzikowski, 1987). However, features like folds cut by burrows (Kleist, 1974) and association with sand volcanoes (Gill & Kuenen, 1957) are suggestive that soft-sediment deformation has occurred.

Apparently identical structures may be due to completely different processes, whereas one single process may result in entirely different structures (Allen, 1982; van Loon & Brodzikowski, 1987). Mills (1983) reinforced this concept affirming that "deformation structures are not invariable indicators of specific environments of deposition, because the hydraulic conditions responsible for their development can be established in a variety of depositional settings".

1.2.2 Mechanical background of soft-sediment deformation

Fundamental concepts: Stress, strain and strength

From the moment of deposition sediments are subject to body forces mainly due to the action of gravity. Response to these forces depends on (i) the physical properties of the sediments, (ii) the magnitude of the forces and (iii) the physical location (e.g., if deposited on the shelf or on the slope). After deposition sediments develop coexisting states of stress and strain (Jones, 1994). Strain is the change in size and shape of a body due to the applied force per unit area (stress). Two end members for stress are normal stress and shear stress, if the component of the stress acting in a plane is normal or parallel to the plane, respectively. The shear stress is particularly important because it is responsible for down-slope movement and can produce many of the fabrics associated with mass movement (landslides, slumps, debris flows and turbidity currents). The yield stress is the critical shear stress above

which ductile deformation begins. Also important is the effective stress, defined as the stress state where the applied normal stress is reduced by the pore fluid pressure.

When a body of sediment/rock is stressed, the individual particles are displaced (displacement field = deformation) to new positions by translation or by rotation and distortion. The deformation can be homogeneous, if the displacement is a constant; otherwise it is inhomogeneous (Hobbs et al, 1976) (Figure 1.4a). Two particular types of homogeneous deformation, pure shear and simple shear, are constantly cited as products of the stress involving rocks and sediment (Figure 1.4b).

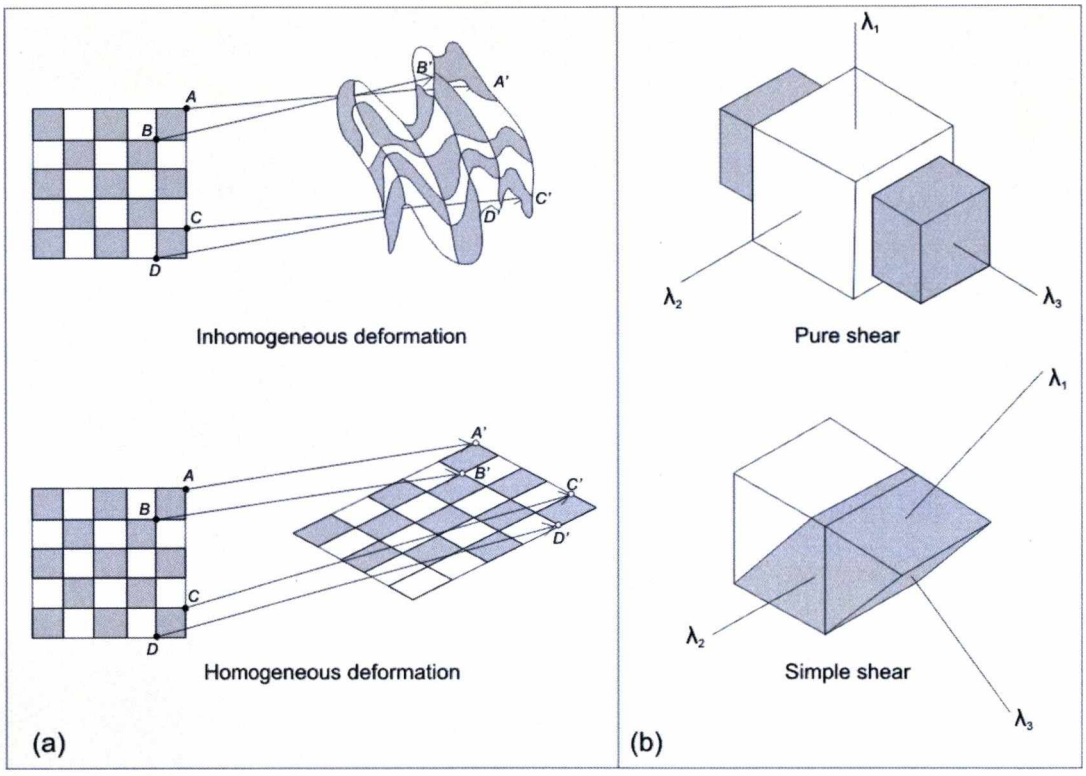

Figure 1.4: (a) Homogeneous and inhomogeneous deformation and examples of displacement vectors; (b) Simple types of homogeneous deformation: pure shear, when the deformation occurs parallel to one or more of the principal axes (λ_1, λ_2 or λ_3 in the figure) of the strain ellipsoid; simple shear, when the deformation occur with the rotation around one of the principal axes (from Hobbs *et al.*, 1976).

The strength of a material is defined as the stress at which failure will occur (Twiss & Moores, 2007); in other words it is the measure of the resistance of a material to failure. By analogy the maximum shear stress that sediment can sustain without failure is the shear strength. Sediments like dense sands and overconsolidated clays (e.g., due to erosion removing overlying sediment) when submitted to stress develop a stress-strain curve where the highest point is called peak strength, normally equivalent to the shear strength. It is followed by a strain

softening that results in a drop in strength to a value called residual strength (Matman, 1994) (Figure 1.5). Changes in the values of the applied stress and/or in the sediment strength are fundamental for the occurrence of deformation in sediments.

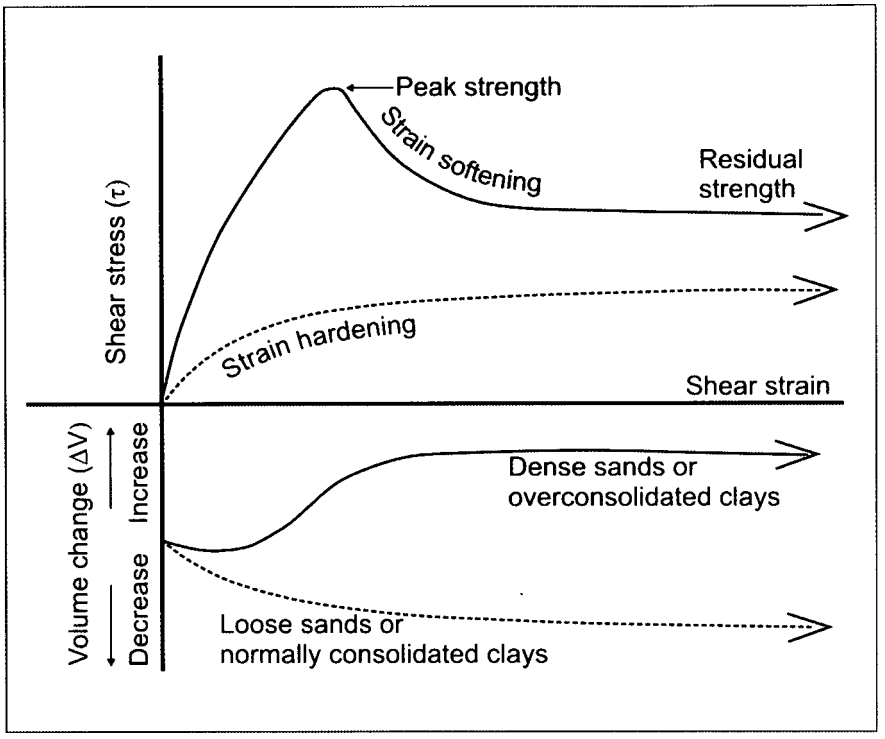

Figure 1.5: Stress-strain curve with the behaviour of a densely packed or loose sand when subjected to shear. Observe the positions of peak strength and of residual strength. For comparison the responses of a normally and overconsolidated clay and the respective changes in volume are included (from Maltman, 1994).

Elements of rheology

Different materials behave differently under the same state of stress. Soft-sediment deformation structures are formed under conditions that imply distinct rheological behaviour during deformation. The three basic classes of material behaviour are: (1) elastic; (2) viscous; and (3) plastic (Figure 1.6). The concepts described below follow Twiss & Moores (2007). Elastic materials deform by an amount proportional to the applied stress. When the stress is released, the material returns to the original undeformed state; deformation in this case is said to be recoverable (Figure, 1.6a). Viscous materials behave as a liquid, i.e., if a deviatoric stress (a state of stress for which the normal stress on the plane of maximum shear stress is zero) on the plane of maximum shear stress is zero, is applied the material

begins to flow, in a relationship where the greater the applied stress, the faster the material will deform. If the relationship between the applied stress and the strain rate is linear it is called as a Newtonian material. When the stress is removed, the flow stops but the fluid does not return to the original condition and in this case is called non-recoverable because the deformation is permanent (Figure 1.6b). Plastic materials do not suffer permanent deformation if the applied stress is less than the yield stress, but they flow readily and deform permanently if the stress reaches or exceeds the yield stress (Figure 1.6c). The idealized material that suffers no deformation below the yield stress is called perfectly plastic material or a rigid-plastic material.

The models above do not describe all types of material behaviour. Among others, the following are important in sediment deformation: (a) visco-elastic materials (Maxwell material) are characterized by displaying both viscous and elastic properties; for high viscosities, loads of short duration will result in elastic behaviour while during loads of long duration they will behave like a viscous material. This is the response of the Earth's crust to the loading-unloading by seismic waves (Figure 1.6d); (b) visco-plastic materials (Bingham material) display linear viscous behaviour only above the yield stress (Figure 1.6e); (c) elastic plastic materials (Prandtl material) show a combination of elastic strain and plastic deformation. Release of the stress results in the disappearance (recovery) of the elastic deformation while the plastic part of deformation is permanent (non-recoverable) (Figure 1.6f).

Maltman (1994) discusses briefly some of the concepts above applied to the deformation in sediments. Settling sediments are commonly regarded as approximately Newtonian fluids. As the settling approaches completion, the aggregate acquires significant strength and begins to show a liner response to the shear stress as a Bingham fluid after the yield stress is exceeded. Many sediments exhibit an elastic-plastic rheology. In this case the elastic behaviour is considered to be minimal in poorly lithified sediments. Realistic models of geological sediments may combine several models of geological behaviour in a non linear manner governed by complex power-laws (i.e., laws for deformation of non linear behaviours) (Figure 1.7).

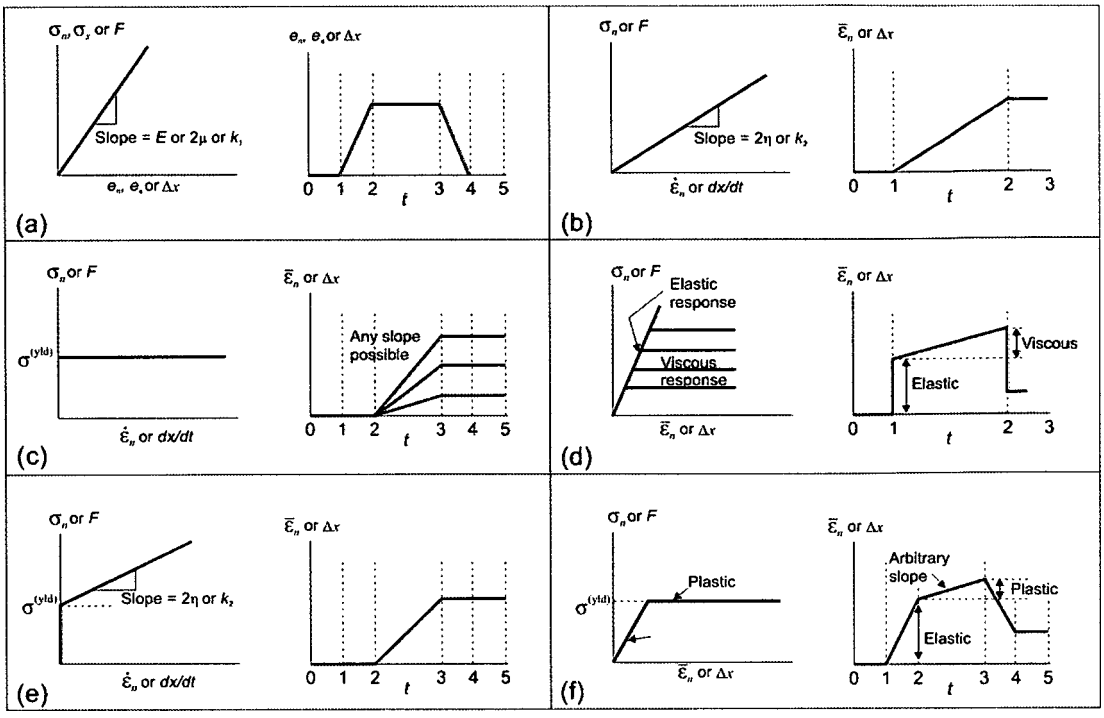

Figure 1.6: Distinct rheological behaviour during deformation: (a) elastic; (b) viscous; (c) plastic; (d) visco-elastic; (e) visco-plastic and (f) elastic-plastic. At the left side is stress (σ) or force (*F*) as a function of the extension (*e*) (or displacement, Δx), or strain rate (ε_n) (or displacement rate, $^{dx}/_{dt}$). At the right side is natural strain vs. time history resulting from the imposed stress (adapted from Twiss and Moores, 2007).

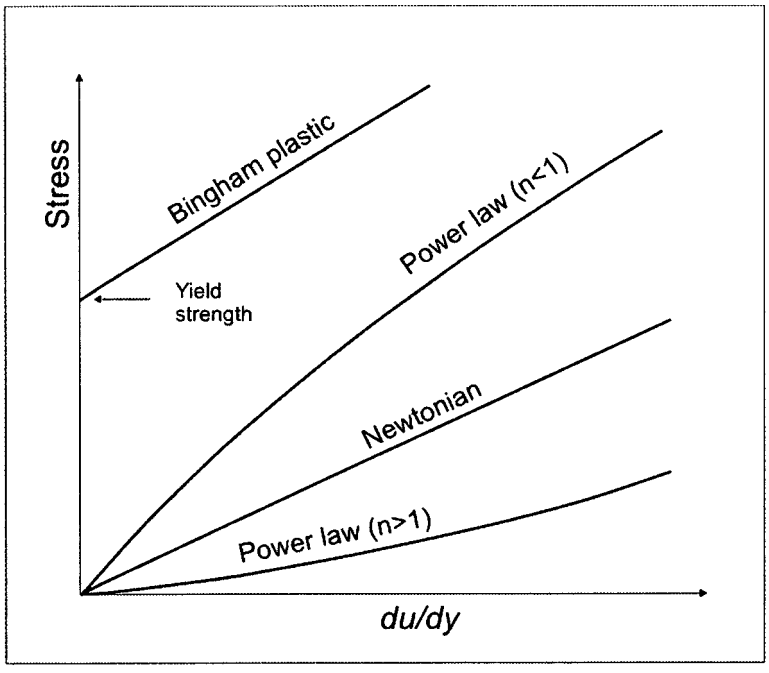

Figure 1.7: Stress vs. shear rate ($^{du}/_{dy}$) variations for Newtonian (linear) and a variety of non-Newtonian fluids controlled by specific power law (from Allen, 1994).

1.2.3 Consolidation processes and pore pressure

Sediment lithification is marked by mechanical (consolidation and frictional strength) and diagenetic processes (not analysed here). Consolidation results in a progressive densification of the sediment in the presence of increasing stress (loading), and typically accompanies sediment burial, normally with loss of pore volume, implying fluid drainage (Jones, 1994; Maltman & Bolton, 2003). During burial, if sediment is unable to drain adequately the lithostatic load becomes proportionally added to the pore-fluid pressure and reduction of frictional strength occurs. If it evolves to the situation where the entire load is sustained by the pore-fluid, the sediment loses its frictional strength and then becomes liquidized. In many types of sediment consolidation this is the major mechanism responsible for pore-volume changes, development of stress and pore pressure regimes, and development of early fabric (Jones, 1994; Bitzer *et al.*, 2000).

Excess pore fluid pressure normally develops in near-surface sediment as the result of initial high porosity that is maintained during burial, mainly if the sediment has low permeability that retards fluid escape. This is most likely to occur in fine-grained sediment (silts and clays) particularly after rapid deposition (Collinson, 1994). In the case of coarser grained sediment, the pore pressure of loosely packed sediments will increase after the action of an external trigger (Owen, 1987). Maltman (1994) lists a series of implications of overpressure in sediment mechanics; the most important is that the sediment becomes weak. Because the fluid is sustaining an extra part of the stress acting across the aggregate framework, the effective stress decreases, the internal friction is reduced and so is the sediment strength. These effects are crucial in all settings of sediment deformation. Also, overpressured horizons are commonly sites of shear failure and overpressured sediments are likely to become involved in intrusion and diapirism (Abbott *et al.*, 1985; Lash, 1985; Jolly & Lonergan, 2002).

The permeability controls the pore fluid dissipation in response to applied loading. In general, sediments with high permeability tend to become mobilized by overpressuring due to external fluids entering and rapidly passing through the system, while lower permeability material become weakened by overpressure in trapped fluids. Consolidation is inhibited during sediment burial by low permeabilities because it retards the dissipation of excess pore fluid pressures. On

the other hand, active deformation affects the permeability behaviour especially where the confining pressure is low (Maltman & Bolton, 2003).

1.2.4 Deformational process

The deformational process can involve three important components: (1) presence of a trigger or trigger mechanism; (2) onset of the deformation mechanism and (3) the presence of a driving force (Allen, 1982; Owen, 1987). Weakening of the sediment due to the action of some type of load (trigger) is followed by sediment mobilization under the action of a deformation mechanism. The driving force controls and/or amplifies the effects of the deformation mechanisms.

Trigger mechanism

Weakening of sediment is caused by some load that precludes pore-fluid dissipation. These loadings act as a trigger that creates the condition for deformation (Lowe, 1975; Allen, 1982; Owen, 1987; Maltman, 1994; Maltman & Bolton, 2003). Owen (1987) indicated that triggers can be generated by: (i) pore fluid pressure; (ii) impulsive stress; and (iii) cyclic stress. Maltman & Bolton (2003) assigned triggers to three classes: (1) external or dynamic; (2) internal or static; and (3) fluids movement or hydraulic (Figure 1.8). Dynamic loading is mechanical loading that arises from a source external to the sediment and is the main trigger mechanism for soft-sediment deformation. Static loading is the process that operates within the evolving sediment rather than those imposed externally. It tends to act directly on the pore fluid, reducing the yield strength and is a process likely to become important at greater depths, during lithification. Hydraulic loading is a localized process associated with vigorous fluid movement resulting in osmotic and capillary forces that tend to weaken intergranular friction and promote the sediment to deform.

A great advance in the study of trigger mechanisms occurred after the 1970s with the appreciation of slope along the continental margins (Locat & Lee, 2002; Canals *et* al., 2004) which provide the following triggers: (1) high sedimentation rates leading to excess pore pressure (overpressure) and underconsolidation (weak layers), (2) loading and flexing by a static weight such as a grounded ice sheet, (3) fast loading by a dynamic weight such as a landslide mass released from upslope, (4)

destabilization of gas hydrates, (5) fluid seepage including seepage of shallow methane gas, (6) bubble-phase gas charging, (7) presence of diagenetic fronts, (8) oversteepening of the margin, (9) erosion at the base of the slope, (10) seismic loading due to earthquakes, (11) low tides, (12) storm-wave loading, (13) sea-level change, (14) volcanic growth and dyke injection, (15) faulting, (16) tectonic compression, (17) diapir and mound formation, (18) biologic processes and (19) human activities on or affecting the seafloor.

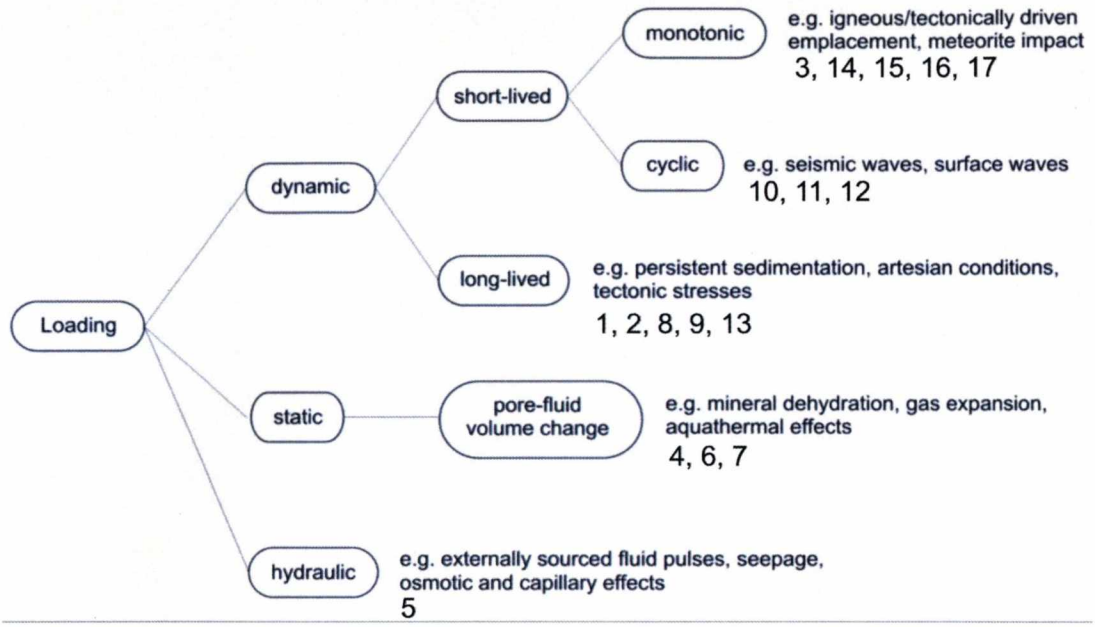

Figure 1.8: Representation of the range of loading processes that may affect sediments in addition to progressive burial due to continued sedimentation (from Maltman & Bolton, 2003). These processes may act as triggers for deformation. Numbers refer to trigger mechanisms listed above from Locat & Lee (2000) and Canals et al. (2004). Maltman and Bolton (2003) do not quantify short- and long-lived loading, so the trigger mechanisms will change depending on the timescale that is being observed.

In ancient depositional systems such discrimination is not easy; although a range of trigger mechanisms are identified. The most common association is with earthquakes and seismicity, but others also are described including: rapid sediment deposition, differential loading, groundwater movements, steep depositional slope and oversteepening due to erosion. The challenge is identification of what type of trigger mechanism caused deformation present in ancient deposits. The lack of clear evidence implies in some interpretation during the identification of triggers. Earthquakes or deposition of large amount of sediment (e.g., channel complexes or thick lobes) are easily identified due to the dimension of the events and the distinct

register in the geological record. Thus, subtle triggers (e.g., small tide variations) or instantaneous and isolated events (e.g., a single storm) can result in deformation which origin will be hardly identified. Some literature citations from these examples are found in Chapter 3.1.5.

Many authors consider earthquakes the most potent trigger to initiate soft-sediment deformation (Allen, 1982), supported by measurements of the intensity and observation of the products of modern earthquakes (Obermeier, 1996; Tuttle & Barstow, 1996; Piper *et al.*, 1999) as well as by laboratory experiments (e.g. Owen, 1996b, Moretti *et al.*, 1999). During the cyclic loading, the oscillatory transmission of seismic waves causes the stress to rise to a value much less than commonly produced by a monotonic event, but if each fluid pressure response is not completely dissipated before the next pulse, the incremental accumulation of overpressure can be large, and can lead to major sediment mobilization (Seed, 1979, Seed & Idriss, 1982). The distance affected by liquefaction during an earthquake is directly proportional to the magnitude of the earthquake (Kuribayashi & Tatsuoka, 1975; Youd, 1977) (Figure 1.9). Some authors have attributed SSDS to earthquakes with no additional evidence for seismicity. The potential overuse/misuse of seismicity in explaining the formation of SSDS is discussed further in Chapter 3.1.5.

Deformation mechanism

Under the action of a deformation mechanism the sediment, initially behaving like a solid, begins to behave like a liquid and deform by ductile processes. Owen (1987) separated the deformation mechanisms capable of causing ductile deformation as: (1) exceed yield strength; (2) reduce yield strength and (3) liquidize. Exceed and reduction in yield strength are slow processes associated with processes of lithification or tectonics. Liquidization causes the deformation of unconsolidated sediment that temporally behaves like a fluid and deforms as a viscous fluid or a plastic substance of negligible yield strength under the action of weak stress (Allen, 1977, 1982). Four types of liquidization can be considered: (1) thixotrophy, (2) sensitivity, (3) liquefaction and (4) fluidization. Among them, liquefaction and fluidization generate the greatest amount of soft-sediment structures. Seepage, which involves the slow upward movement of pore fluid, is irrelevant for deformation.

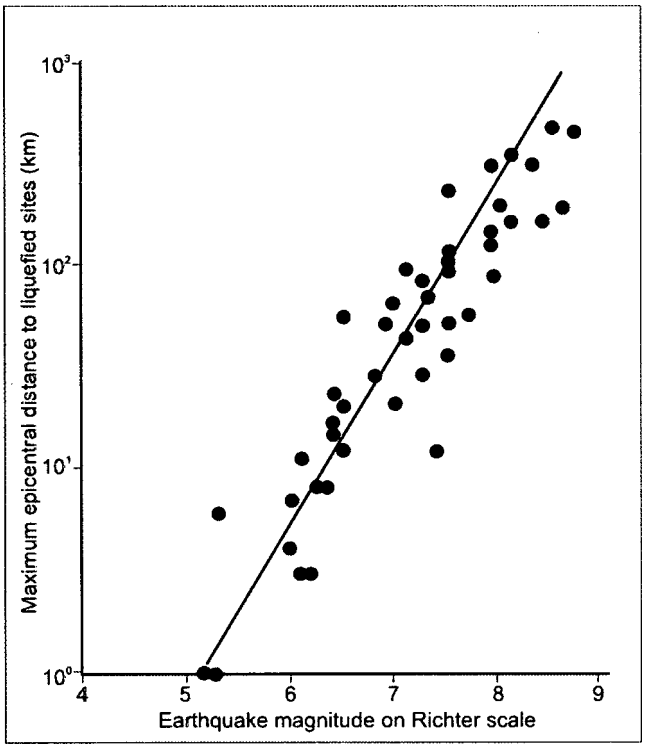

Figure 1.9: Liquefaction distance as a function of earthquake magnitude (Richter) (from Allen, 1985, after original data of Kuribayashi & Tatsuoka, 1975, and Youd, 1977).

Thixotrophy and sensitivity materials, normally cohesive and including some clays, temporarily lose their strength when disturbance disrupts their flocculate structure. Thixotropic materials have their strength restored as the flocculated structure re-forms, while sensitivity materials (quick clays) only regain strength if they lose fluid (Owen, 1987).

Liquefaction is marked by sudden breakdown of a metastable, loosely packed grain framework, the grains becoming temporally suspended in the pore fluid and settling rapidly through the fluid until a grain-supported structure is re-established by settling of the particles. During this process, a sedimentation front passes toward the upper border of the perturbed bed, separating the solid-like sand with restored contacts from the liquid-like liquefied dispersion above (Owen, 1987) (Figure 1.10). Liquefaction can occur rapidly and within a closed system without net loss or gain of pore fluid.

Fluidization occurs when the drag exerted by upward moving pore fluids exceeds the effective weight of the grains; the particles are lifted, the grain framework destroyed, and the sediment strength reduced to nearly zero. The minimum fluidization velocity is reached when the upward component of fluid drag

balances the particle weight and in this case the system behaves like a viscous fluid (Owen, 1987). With an increase of fluidization velocity, grain separation increases (with bed expansion) and the apparent viscosity decreases. Fluidization occurs in an open system, requiring a continuous flow of fluid through the sediment and can be accompanied by the destruction of the original sediment fabric. Lowe (1975) in an original approach emphasized the importance of water escape associated with all deformational processes described above. This view helps to understand and classify important features observed in this research.

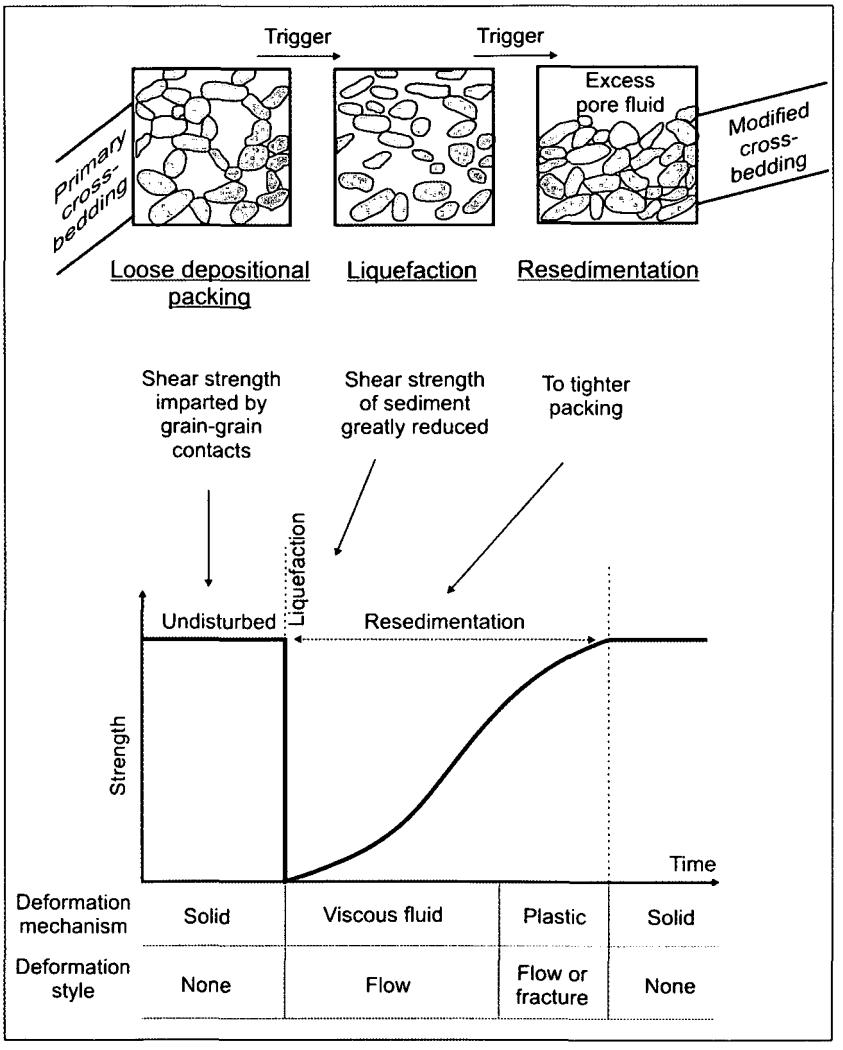

Figure 1.10: Top: schematic view of the rearrangement of sediment fabric during the processes of liquefaction and resedimentation. See text for details. Bottom: changes in strength, deformation mechanism and deformation style associated with sedimentation from a liquefied state (from Owen, 1985; 1987, modified by Collinson, 1994).

Driving force

Liquefaction and fluidization relate to the state of the sediment and in themselves are not sufficient to drive bulk movement of the sediment (Allen, 1982; Maltman & Bolton, 2003). In general, the description of soft-sediment deformation structures is accompanied by additional information about the process (driving force) that acted on the liquidized sediment in order to give the final configuration of the structures (cf. Chapter 1.2.6). Precaution must be taken in order to avoid mismatching driving force with deformation mechanism (Mills, 1983). Until late 1970s and early 1980s, driving forces were listed without a systematic classification. Lowe (1975), Allen (1982), and latterly Owen (1987) systematized the most important driving forces into 4 groups: (1) a downward component of body force (gravity) associated with depositional slope, which is associated with all features associated with gravitational mass movement; (2) non-uniform distribution of the confining load, created where a sediment surface possesses relief or where there is variation in the thickness of the upper layer, imposing distinct stress conditions along the body; (3) gravitationally unstable density gradient, normally associated with structures generated by upward and downward movement (*in situ* deformation) and under the action of Rayleigh-Taylor instabilities, i.e., that allows the formation of load casts of the higher density sediment in the lower density sediment and/or diapirs of lower density sediment in the higher density sediment (Hindmarsh & Rijsdijk, 2000); and (4) shear stress (tangential or vertical) acting within or at the surface, such as the effect of currents or internal shear intrinsic to fluidization phenomena. Many soft-sediment deformation structures can be generated by the association of two or more of these driving forces. Lowe (1975) emphasized the importance of the driving forces, affirming that they create a second cycle of transport, deposition and consolidation. Features associated with each one of these classes are presented in the Allen (1982) classification in Chapter 1.2.6.

1.2.5 Soft-sediment deformation structures

Two groups of soft-sediment structures can be distinguished, the first related to gravitational down-slope movement, also called mass movement (Varnes, 1958) or mass transport (Stow, 1994) and the second not necessary related to gravitational down-slope movement. These two groups broadly coincide with the initial classification of (1) detached and (2) *in situ* deformation structures, respectively; or the categories of flow and load structures proposed by Dżulyński & Walton (1965).

From the first group (Figure 1.11); slide, slumps and debris flows deposits are particularly important in this research. Slides and slumps describe down-slope displacement of a semi-consolidated sediment mass along a basal shear plane. Sliding emphasizes the lateral displacement along translational or rotational shear planes, while slumping emphasizes the internal disturbance and folded shear planes. Debris flows are highly concentrated, highly viscous, sediment dispersions that possess yield strength and display plastic flow behaviour. Commonly, debrites (the deposits of debris flow) contain rafts supported by a matrix and a chaotic internal structures.

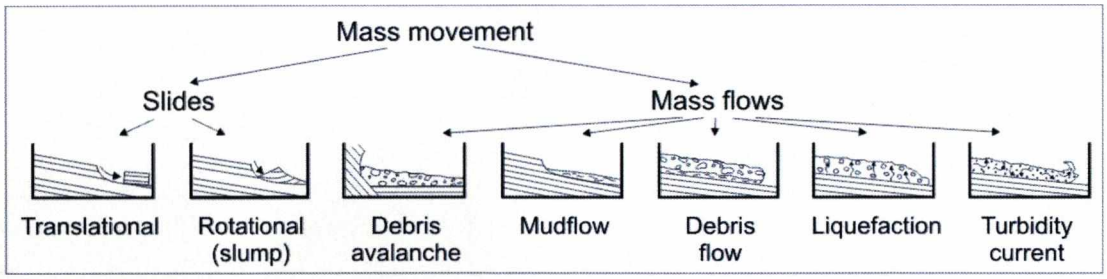

Figure 1.11: General landslide classification (from Varnes, 1958, modified by Lee et al., 2007).

The second group includes load structures, water escape structures and convolute lamination. Load structure is the general name for a group of structures comprising synforms and antiforms at an interface between sediments with distinct density differences and formed by Rayleigh -Taylor instabilities. They include load casts, pseudonodules and ball-and-pillow structures, classified as a function of their attachment to the original bedding (Figure 1.12a). The second class of structures in this group includes water escape structures (sensu Lowe, 1975); pillar, dish and flame structures, formed due to the upward escape of fluids while sediment is liquidized (Lowe & LoPiccolo, 1974) (Figure 1.12b). Convolute lamination

corresponds to laterally extensive series of more or less regular folds developed throughout or confined to the upper part of a single depositional unit (Figure 1.12c). Convolute lamination originates when sediment is liquidized or hydroplastic and is considered to be formed by vertical movement of the particles (Allen, 1982), but other origins (e.g. localized expulsion of pore water, down-slope slip of an overlying sedimentary layer, effect of fluid drag on rapidly accumulating sediment) are still a subject of discussion among sedimentologists.

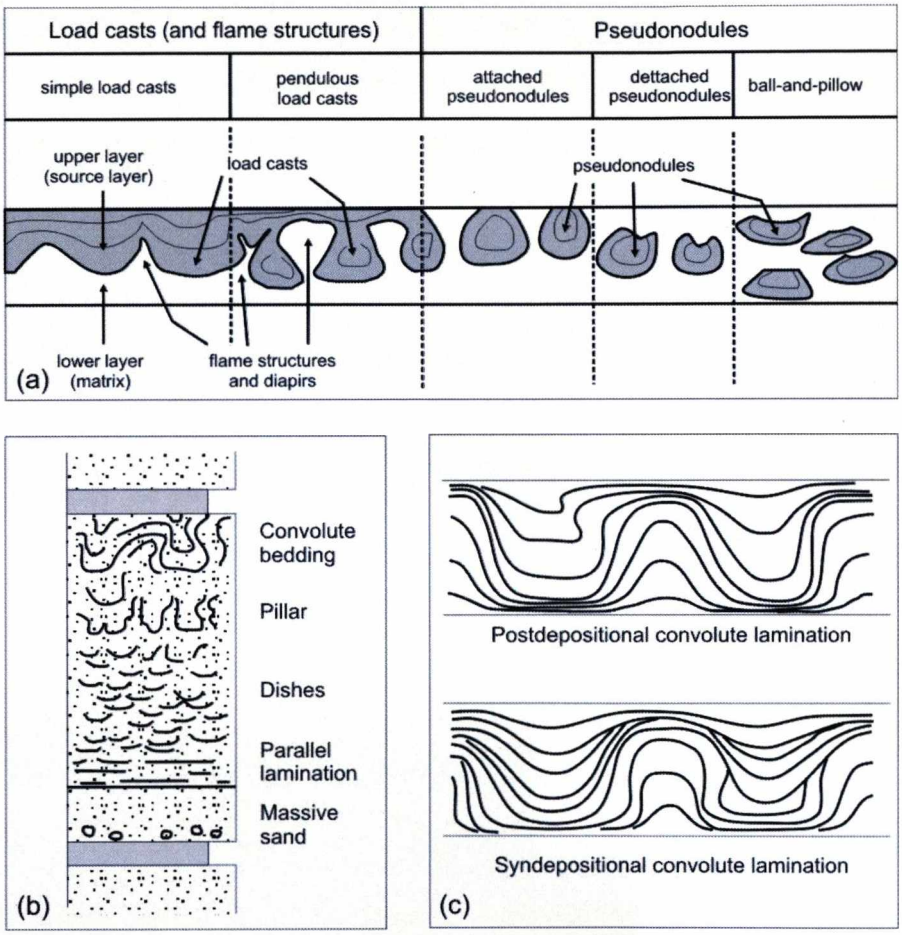

Figure 1.12: (a) Load structure evolution, from weakly deformed simple load casts to the most deformed ball-and-pillow structures (from Owen, 2003). (b) Distribution of structures formed by upward fluid escape (Lowe & LoPiccolo, 1974). (c) Schematic view of convolute lamination (from Allen, 1982). Not to scale.

1.2.6 Soft-sediment structures classifications

As mentioned in the introduction to this chapter, the lack of uniform terminology and the sometimes poorly defined criteria to classify structures are reflected in the current classifications of soft-sediment deformation structures.

Elliot (1965) considered rheological and kinematic parameters; Nagtegaal (1965) based his classification on space and time (syn-, meta- or post-depositional, involving depositional and deformational structures); Lowe (1975) considered the structures as originated by water escape and considered geometry, kinematics and processes to create a inclusive but confused classification; Brenchley & Newall (1977) considered the sense of movement (vertical or horizontal) and the origin of the deformation with focus on contorted beds; Allen (1982) defined four categories based on the causative stress; Owen (1987) used deformation mechanism and driving forces in order to discriminate between classes of structures. Figure 1.13 illustrates the classifications of Elliot (1965), Allen (1982) and Owen (1987), considered the most embracing classification considering only deformational structures. In this research, three basic groups of soft-sediment deformation structures were considered: *in situ*, detached and injected, similarly to the grouping proposed by Dżulyński & Walton (1965) (cf. Chapter 3.1).

<table>
<tr><th rowspan="2">Nature of operation / Sediment behaviour</th><th rowspan="2">Exokinematic</th><th colspan="3">Endokinematic</th><th rowspan="2">Biokinematic</th></tr>
<tr><th>Translation slumps</th><th colspan="2">Transposition
horizontal / vertical</th></tr>
<tr><td>Liquid</td><td colspan="2">even laminae
cross-stratification</td><td></td><td></td><td></td></tr>
<tr><td rowspan="2">Quasi-liquid</td><td colspan="2">remanié sand-waves</td><td>graded bedding
slurried bedding</td><td>clastic intrusions
auto-injections breccias</td><td>sand volcanoes
streamers</td><td rowspan="2"></td></tr>
<tr><td colspan="2">parting lineation
dendritic ridges</td></tr>
<tr><td rowspan="3">Hydro-plastic</td><td>frodescent marks, furrows, tool marks</td><td>"streaked out ripples", convolute bedding</td><td rowspan="3">slurry-slump bedding</td><td>corrugated bedding</td><td>cusps, load mark, small diapiric folds</td><td rowspan="2">surface traces of small animals</td></tr>
<tr><td colspan="2">deformed cross-stratification, erosion ripples</td><td>crumplet bedding</td><td>mud slumps</td></tr>
<tr><td>Quasi-solid</td><td colspan="2">" floating" slabs</td><td>slide-slump bedding</td><td>shredded bedding</td><td>guilielmites</td><td>bioturbates</td></tr>
<tr><td>Solid</td><td colspan="2">" pot holes"</td><td>slide-bedding</td><td>"jumbled block" structures</td><td></td><td>clear-cut traces</td></tr>
</table>

(a)

Causative stress	Class		Example
Gravitational unstable profile of bulk density	Continuous profile	single units	convolute lamination
	Discontinuous profile	single units	dish and pillar structure
		paired units (not pierced)	load casts
		paired units (pierced)	ball-and-pillow structures
		multilayer complexes units slumps	sand balls
Non-uniform confining loadings	single units		complex deformed cross-stratification
	paired units		faulting and folding due lateral spread of sand bodies
Downslope component of body force	slides		
	slumps		
Fluid flow	shear stress horizontal		simple deformed cross-stratification
	shear stress inclined		eroded and/or bent up laminae

(b)

Deformation mechanism / Driving force system		Exceed yield strength		Reduce yield strength	Liquidize			
		brittle	plastic		thixotropic	sensitive	liquefied	fluidized
Gravitational body force		soft-sediment faults	slumps, slides		slumps			
							complex recumb.fold	
Unequal confining load			loaded ripples		load ripples			
								clastic dykes
Gravitational unstable density gradient	continuous						convolute lamination?	
	single layer						dish structure?	
	two layer			clay, salt domes, cryoturbation	load casts, pseudonodules			
	multi-layer				ball-and-pillow			
							contort. heavy mineral bands	
Shear stress							simple recumb.fold	dish struct.? cusps
Other			rain prints, crystal growth, bioturbation					

(c)

Figure 1.13: (a) Classification of subaqueous sedimentary structures adapted from the original of Elliot (1965): considering elements of rheology and kinematic parameters. (b) Classification of soft-sediment structures from Allen (1982) based on the causative stress (driving forces); (c) "Working-classification" of soft-sediment deformation modified from the original of Owen (1985, 1987).

1.3 – The shelf-edge to base of slope: a brief review

1.3.1 - General aspects

The shelf–edge, slope and base-of-slope (continental rise) comprise the profile that links the shallow marine shelf with the basin floor. This profile is influenced by tectonic and sedimentary processes, that also control the margin profile (e.g. passive, convergent or strike slip margins; salt-influenced margin; carbonate platform) (Figure 1.14) (Emery, 1980; Pratson & Haxby, 1996). The shelf-edge area develops at the shelf-break, the point where average gradient changes from < 1° landward to > 1° seaward. The continental slope is the steepest physiographic part of the continental margin with a declivity that typically ranges from 2° to 5°, but varies from less that 1° to more than 25°. In modern shelf-margins, the shelf-break typically lies at water depths of 90 to 180 m, and the base of terrigenous clastic slopes can reach water depths between 1.5 and 3.5 km (Galloway, 1998; Pratson *et al*, 2007).

In this section some aspects of the evolution of the shelf-edge and the slope are summarized, focusing on the potential for occurrence of soft-sediment deformation structures in these environments.

1.3.2 – Slope

The pervasive gravitational potential gradient present on the slope implies that gravitational mass transport processes are important and result in seven facies that are the building blocks of slope depositional systems: (1) turbidite channel fills; (2) turbidite lobes; (3) sheet turbidites; (4) slide, slump and debris-flow sheets, lobes and tongues; (5) fine-grained turbidite fills and sheets; (6) contourite drifts and (7) hemipelagic drapes and fills (Galloway, 1998). Among them, turbidite channel fills, turbidite lobes, sheet turbidites, and slides, slumps and debris-flows deposits are prone to down slope detachment and *in situ* soft-sediment deformation structures.

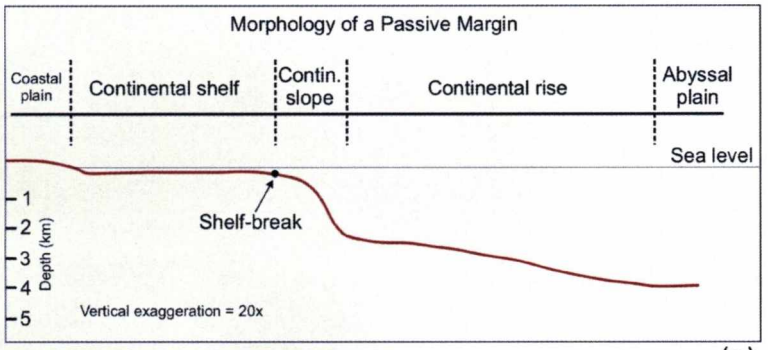

(a)

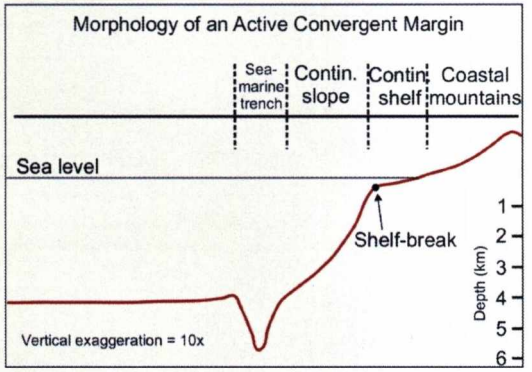

(b)

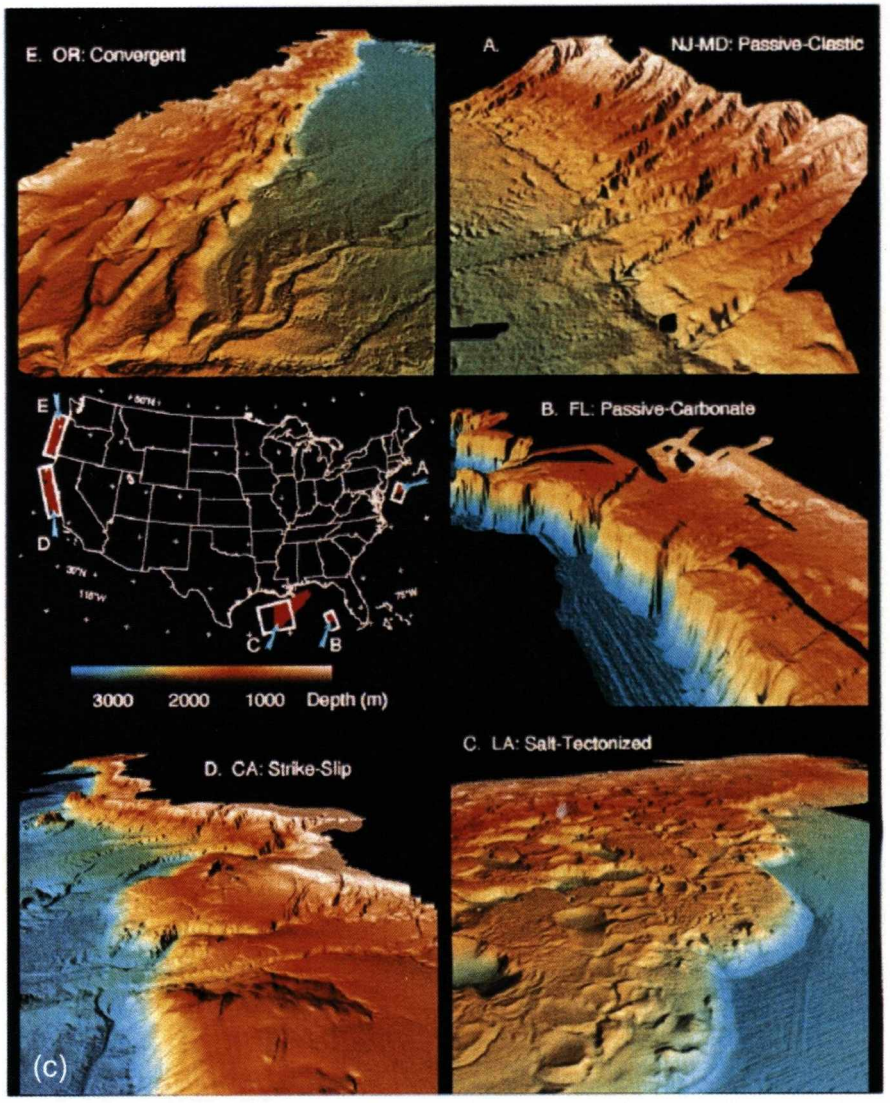

Figure 1.14: (a) and (b) Schematic view of the morphology of a passive and active margin respectively (from Brink *et al.*, 1992 *in* Nittrouer *et al.*, 2007). Note the clear differences in morphology and gradients. (c) Five types of continental margin/slope as a function of the tectonic environment and sediment deposition/deformation. Clockwise from top right: A - passive-clastic; B - passive-carbonate; C - salt-tectonized; D - strike-slip; E - convergent (from Pratson & Haxby, 1996).

The slope angle and shape are influenced by the interplay of many factors. At continental scales, plate tectonic processes create the general shape of the continental margin. Another fundamental factor that controls the shelf width and slope relief is accommodation space, which is controlled by thermal subsidence (passive margins), tectonic uplift (convergent margins), eustatic sea level and more locally by isostasy, compaction and faulting (Vail *et al.*, 1977; Jervey, 1988; Posamentier &Vail, 1988; Posamentier *et al.*, 1988; Pratson *et al.*, 2007).

At a broad scale, based on 150 seismic profiles across continental margins around the world, Adams & Schlager (2000) proposed that 80 % of slope profiles can be represented by three basic types of equation: the linear, the exponential and the Gaussian distribution (Figure 1.15). Geometry and inclination are dominated by depositional environment and sediment type. The Gaussian profile represents around 50% all studied slopes and is interpreted to be generated mainly by the redistribution and erosion of slopes with exponential profiles at the shelf-break, which reinforces the importance of remobilization of sediment and consequent soft-sediment deformation in the slope setting.

Considering the dynamics of the slope profile, Dailly (1983) proposed the concept of slope readjustment, in which slope angle evolves over time. It was used to explain the transition from carbonate (higher slope gradient) to siliciclastic (lower slope gradient) depositional regimes. More recently, Ross *et al.* (1994) used the slope readjustment concept to explain processes on the slope related to relative sea level rise and shelf-margin tectonics (Figure 1.16). Slope readjustment can explain the transition between the two basic types of basin margin: the progradational or "graded" and the erosional or "out-of-grade" (Hedberg, 1970). In this case, a significant oversteepening of the slope ("out-of-grade" margin) triggers long term mass wasting and depositional processes to establish an equilibrium to the slope ("graded" margin). Prather (2000, 2003) analysed the evolution of slopes above grade (out-of-grade slopes) and identified three types of accommodation space: (i) ponded basin; (ii) healed-slope and (iii) slope; found mainly in salt-based withdrawal and shale-based slopes, exemplified by the Gulf of Mexico (Figure 1.17). In contrast to the graded slopes, slopes above grade tend to accumulate large amounts of sediment in the upper- and mid-slope, which is accompanied by episodic mass wasting. *In situ* soft-sediment deformation structures may be more common in intra-slope basins (ponded basin accommodation space), mainly due to the loading caused

by the large volume of sediment trapped during basin fill process and the intercalation of distinct grain sizes and facies (distributary channel-lobe complexes and leveed-channel complex facies from Beaubouef & Friedmann, 2000).

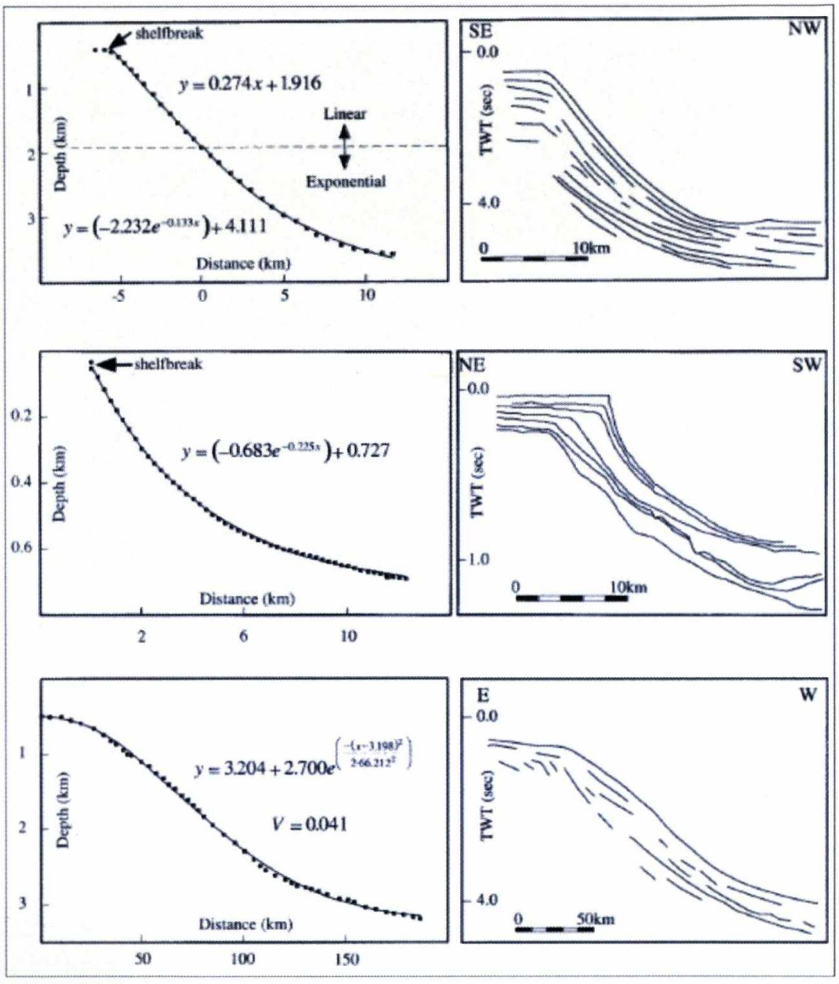

Figure 1.15: Examples from Adams & Schlager (2000) of three basic types of continental slope curvatures with their representative equation (left) and seismic profile sketch (right): (a) linear (and exponential) from Antarctic Peninsula Pacific margin; (b) exponential from Great Bahama Bank; (c) Gaussian (sigmoidal) from southwest Africa. See text for details.

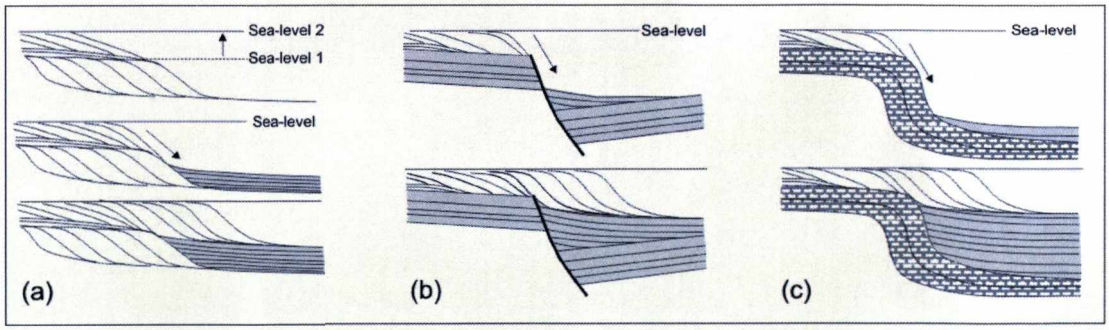

Figure 1.16: Three mechanisms that can lead to slope over-steepening and subsequent readjustment: (a) relative sea level rise; (b) tectonic mechanism (e.g. normal fault); (c) alternating carbonate-silicicalstic depositional regimes (from Ross et al., 1994).

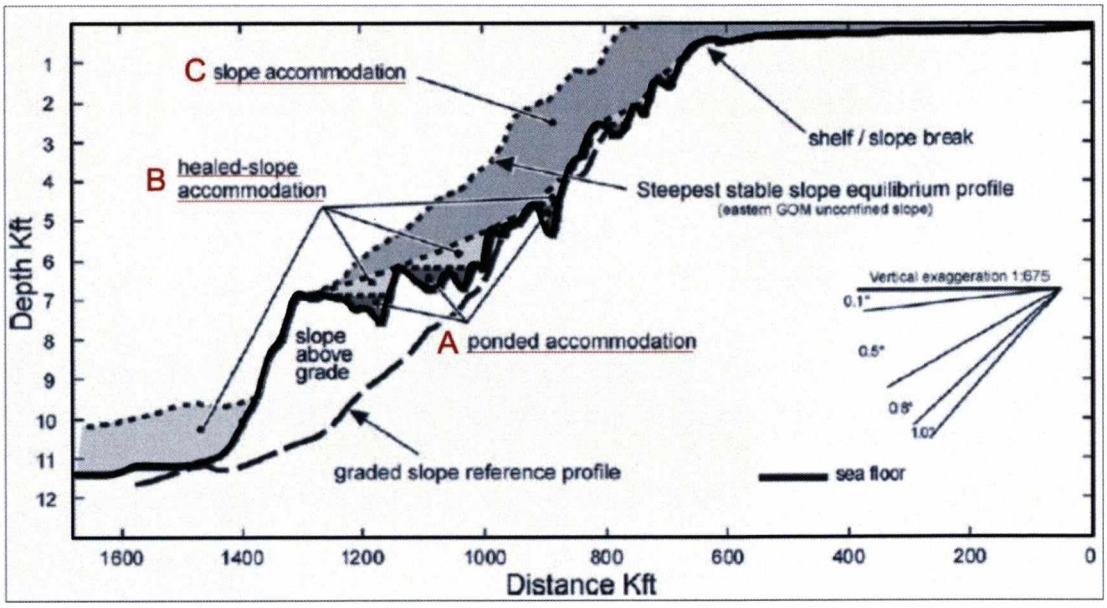

Figure 1.17: Types of accommodation space on the above-grade slopes: A - ponded; B - healed-slope and C - slope (from Prather, 2000). See text for details.

Slope systems are influenced by available grain size, flow density and thickness, sediment supply, type of sediment, the rate of sediment transport, climate, localized faulting and diapirism (Emery, 1980; Pratson & Haxby, 1996; Reading & Richards, 1994; Galloway, 1998; Kneller, 2003). Coleman & Prior (1988) reviewed a series of factors (Figure 1.18) that can result in strength reduction (e.g. excess of pore water pressure, gas generation, sedimentary loading) or stress increase (e.g. earthquake, oversteepening), which can create slope instabilities, resulting in mass movement and a new configuration of the slope. Most of these factors can be associated directly to trigger mechanisms described in Section 1.2.4. This fact emphasizes the importance of the submarine slope as a priority place for the occurrence of soft-sediment deformation structures.

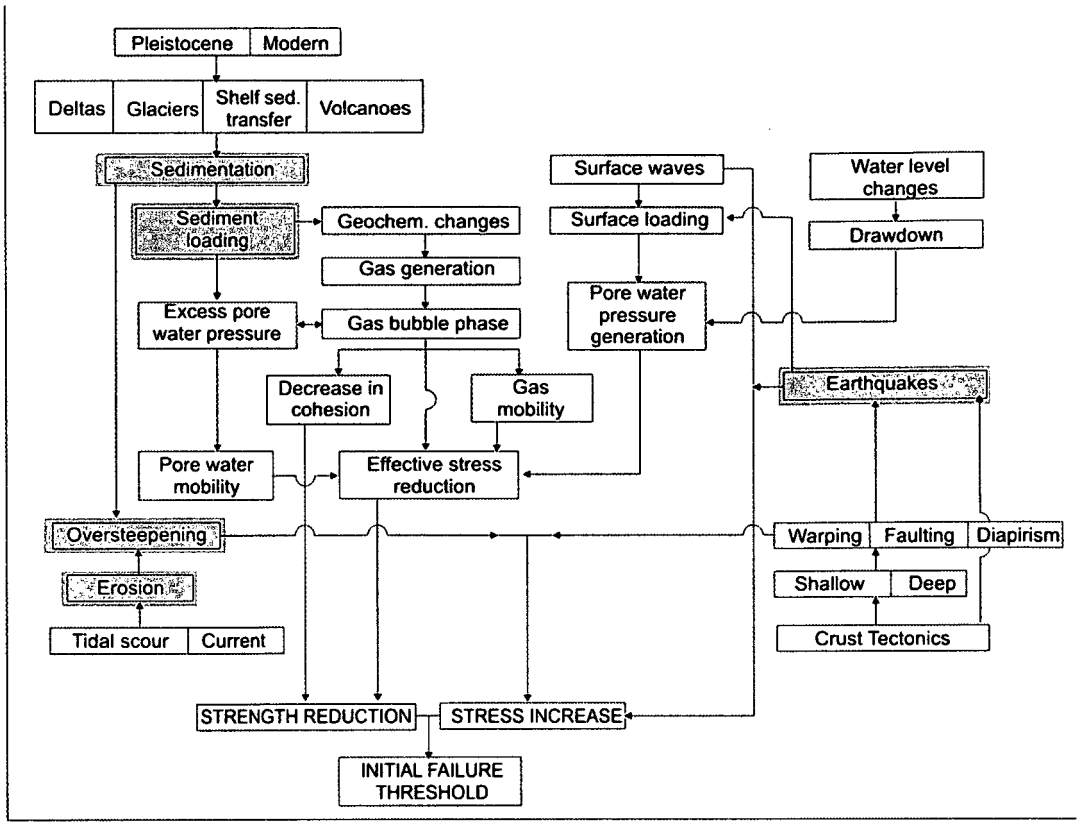

Figure 1.18: Combination of factors that can cause slope instabilities (from Coleman & Prior, 1988). Boxes shaded in grey are those agents directly addressed in this thesis.

Reading & Richards (1994) proposed 12 types of deep water depositional systems based on grain size and feeder system, the first influencing directly the slope gradient and consequently its stability. A grain size increase implies an increase in the stable slope gradient and the tendency for channels to migrate laterally. Galloway (1998) emphasized the importance of grain size in controlling slope morphology and in the generation of slump and debris flow deposits. Similarly to Hedberg (1970), he divided the slope system into constructional and destructional sections with emphasis on the distribution of facies. The constructional type is dominated by deposition of allochthonous sediment and includes many aprons, fans, basin-floor channels and contourite drifts with offlap and aggradational onlap or toplap architecture (Figure 1.19a). The destructional model is characterized by subregional slope retreat with the development of bounding surfaces (slides and mass wasting surfaces) with consequent redeposition of debris at the base of slope (Figure 1.19b). The loading of thick packages of sediment and the absence of mass transport complexes in the constructional case suggest that *in situ* soft-sediment deformation

structures are more likely to occur in this case while detached SSD structures is dominant in destructional slopes.

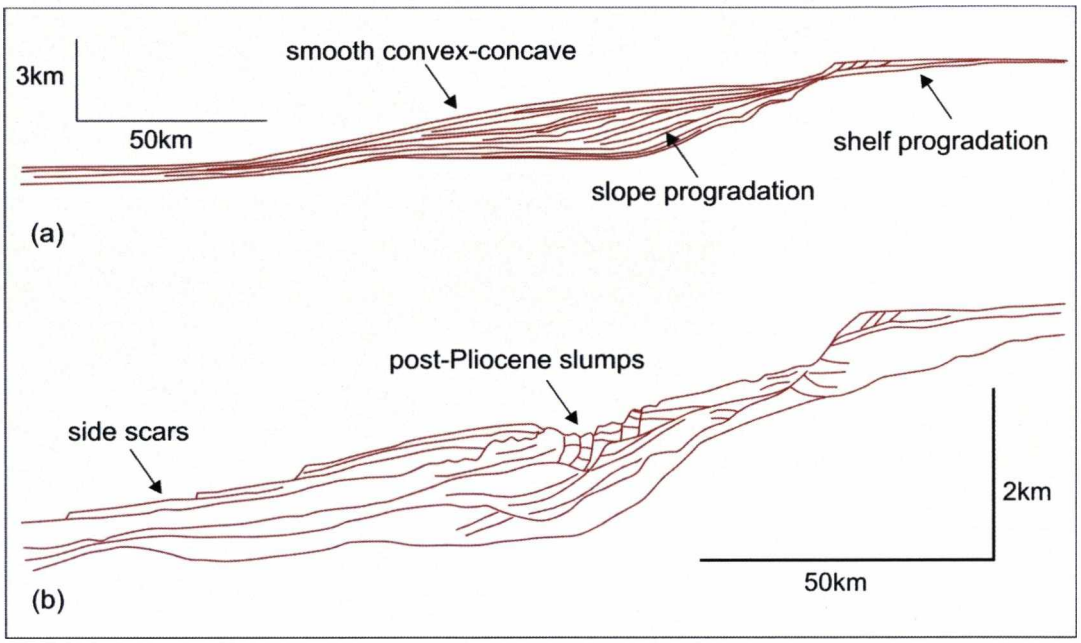

Figure 1.19: Schematic profiles showing examples from constructional (a) and destructional slopes (b) of the continental margin of Western Sahara (from Wynn *et al.*, 2000).

Sequence stratigraphy analysis (Posamentier &Vail, 1988; Posamentier *et al.*, 1988, Posamentier & Allen, 1999) has shown that sediment supply to the slope varies as a function of system tract. Higher rates of sediment supply favour greater development of soft-sediment deformation structures. *In situ* soft-sediment deformation is expected to occur in all systems tracts, while detached soft-sediment deformation will be more common during the falling-stage and the transgressive system tracts.

Discussion on soft-sediment deformation and slope evolution is normally restricted to the large packages of mass wasting products without detailed studies the deformational processes. In most detailed studies, the focus is typically on the understanding of the role of detached SSDS in the development of the equilibrium profile (Cronin *et al.*, 2000). The slope environment and associated processes are prone to the generation of *in situ* SSDS, but due to the scale of occurrence, the identification and study of this type of structure in the slope is still in its initial stages (Postma, 1983; Mount, 1993; Stromberg & Bluck, 1998; Moretti *et al.*, 2001, Hildebrandt & Egenhoff, 2007).

1.3.3 - Shelf-edge

From a physiographic point of view, the shelf-edge is a continuation of the shelf at its intersection with the slope. But while on the shelf, waves and currents predominate in moving sediment, gravity-driven mass movement becomes dominant at the shelf-break. The same factors that control the configuration of the slope (discussed above) will influence directly the shape and dynamics of the shelf-edge. This short review will focus on processes related to the development of shelf-edge deltas, which are particularly important for this thesis.

A different range of soft-sediment deformation structures have been recognized in the shelf-edge deltas compared to the slope. Coleman *et al.* (1983) listed some characteristics of modern deltas at the shelf-edge that can trigger sediment remobilisation and widespread soft-sediment deformation. These include: (1) extremely high depositional rates that do not allow pore fluids to escape, with consequent generation of high pore fluid pressures, decrease of sediment shear strength and subsequent subaqueous sediment instabilities; (2) biochemical degradation of organic material deposited by the deltas resulting in rapid production of methane gas that leads to further weakening of the sediments. The features produced by these processes include: (a) shallow-water rotational slumps and retrogressive landslides; (b) retrogressive landslide gullies and large depositional debris lobes; (c) sigmoidal progradational products of mass-movement processes; (d) shelf-progradation; (e) growth-faults; (f) retrogressive failures forming canyons and (g) massive shelf-edge instabilities that generate *in situ* fluid escape structures (Figure 1.20). These features have been studied in a series of deltas that include the Pliocene of Mississippi Canyon (Coleman *et al.*, 1983; Mayall *et al.*, 1992), the Carboniferous of the Clare Basin, Ireland (Martinsen, 1989; Pulham, 1989; Martinsen and Bakken, 1990); the Eocene Basin, Spitsbergen (Plink-Björklund *et al.*, 2001; Mellere *et al.*, 2002), the Permian Karoo Basin, South Africa (Wild, 2005; Charles, 2007) and the Neogene Niger Delta (Damuth, 1994; Meisling *et al.* 2000). Tables 1.1 and 1.2 illustrate some classic ancient and modern examples of shelf-edge deltas with soft-sediment deformation. Examples from ancient shelf-edge deltas are outcrop based (Table 1.1), while modern shelf-edge deltas are seismic data based (Table 1.2).

Subsurface studies concentrate on the largest features (slumps, slides and growth faults) (Edwards, 1981; Coleman *et al.*, 1983; Trincardi & Field, 1992; Damuth, 1994) and little work has been done on the sedimentary evolution and interpretation of soft-sediment deformation structures in this setting (Martinsen, 1989; Martinsen and Bakken, 1990; Mellere *et al.* 2002; Strachan, 2002; Wild, 2005). The studies of *in situ* soft-sediment deformation are restricted to thinner intervals associated with: (i) sand volcanoes, collapse depressions and sand dykes formed in gravity driven deposits, (ii) mud diapirs and load structures caused by loading by turbidites, (iii) water escape structures deforming well sorted sandstones that infill slump scars or heads of channels, and (iv) convolution and water escape structures in cross-bedded sections of tidal bar deposits.

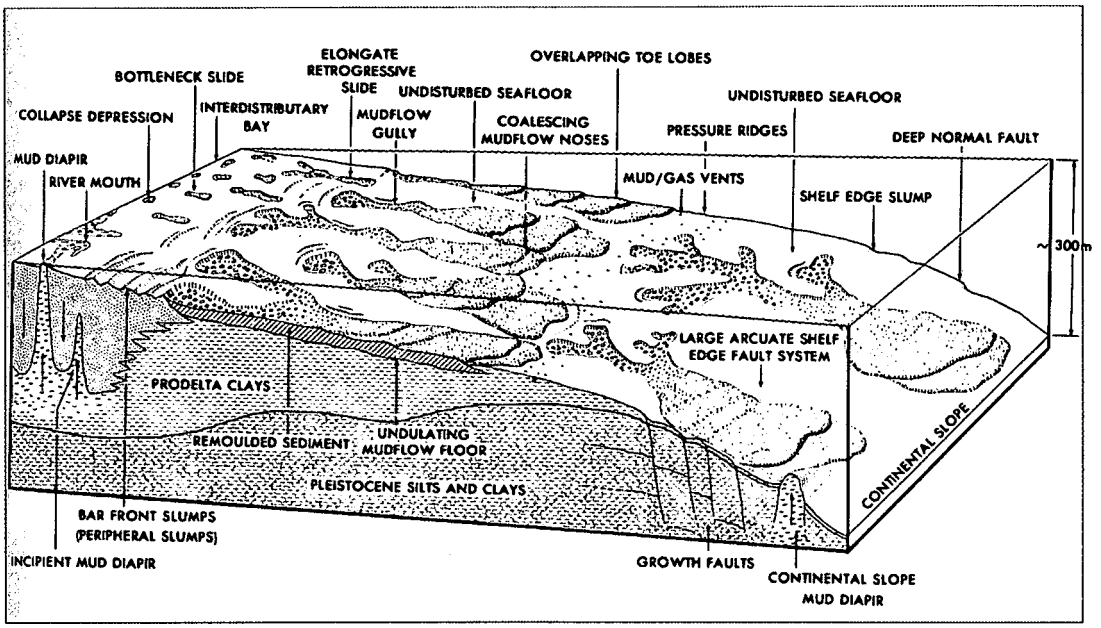

Figure 1.20: Sea bed features found between the river mouth and the shelf-edge of Mississippi River delta (from Coleman et al., 1983).

The development of shelf-edge deltas is normally associated with times of lowered sea level. Porębski & Steel (2003) related types of delta according to the position of sea level: (a) inner-shelf deltas, (b) mid-shelf deltas, (c) shelf-margin deltas and (d) bayhead deltas (Figure 1.21). The shelf-edge deltas, formed during the falling stage or lowstand system tracts, present characteristics including clinoforms that are well developed in height and length, upward thickening lobes, narrow feeder chutes, steep-fronted lobes, hyperpycnal flows and large scale slope failure and growth faulting. Table 1.3 compares the main characteristics of the mid-shelf deltas and shelf-margin deltas.

Occurrence	Age	Depositional environment	Total Thickness	Thickness of deformed section .	Position of the deformed section	Type of deformation	Deformation process	Reference
Clare Basin (west Ireland). Central Clare Group	Namurian (Upper-Carbonif.)	Fluvial-dominated deltas. Deformation confined to delta-front successions	Five cyclothems with avg thickness of 50-150m for the delta-front sequence.	Packets up to 60m. Around 50% of all delta-front sequence	Lower and intermediate section	Growth-faulting, slumping, clay diapirism, gravity sliding	Instabilities generated by undercompaction and overpressuring of rapdly deposited fine-grained sediments.	Pulham, 1989
Clare Basin (west Ireland). Gulf Island Formation	Namurian	Fine grained (mainly siltstone) turbidite in a delta-slope succession.	550m	410m (75%). Mudslumps and mudslides bodies from 15 to 50m thick.	Overall distribution. Mudslumps lower part; mudslides in the upper part. Water escape: late stage of slumps and slides or independent of the gravitational gliding	Slumping, sliding and water escape	Differential subsidence causing delta-slope oversteepening; high sediment accumulation rates leading to underconsolidation and loading due to turbidite deposition.	Martinsen, 1989; Collinson *et al.*, 1991.
Clare Basin (west Ireland). Ross Formation	Namurian	Deepwater turbiditic sandstone.	15m involving the "Ross slide" occurrence	Up to 6 m	Upper section of Ross Formation.	Slumping (dome and ridge structures) and later sand injection (dikes and sand volcanoes)	Liquidization of the sand bodies caused by the loadings, translation and cessation of the overlying slump	Strachan, 2002

Mississipi Canyon	Middle Pliocene	Shelf-edge delta	Two coarsening – upward delta sequences, around 120m each.	Intervals between 3 and 15 m thick. 30 to 50% of the two analyzed cycles	Lower section	Debris or mud flows and slumping of fine-grained sandstone and siltstone.	Instabilities due to progradation of a delta in a high angle slope.	Mayall *et al.*, 1992
Spitsbergen, Norway	Lower Cretaceous	Delta (from distributary channel to prodeltaic)	100 – 150m thick of deltaic deposits plus the upermost section of the underlying prodeltaic and delta slope deposits.	Two scars (at the same stratigraphic interval, 50-60 m deep.	On top of prodelta – delta slope interval and base of deltaic sequence	Brittle deformation with collapse of blocks (rotation and sliding). Infill of scars by slumping and debris-flow.	Slope failure caused by sediment loading and seismicity.	Nemec *et al.*, 1988
Spitsbergen, Norway	Eocene	Shelf-edge to slope deposits	Shelf-edge delta: packages of 0.5-1.5 m thick. Slope: Channel infill up to 5 m thick (beds from few centimetre to metre scale)	Shelf-edge delta: slumps up to 2 m thick. Slope: <1 m, up to 4.5 m thick. Shelf-edge estuary: Up to 1 m.	Shelf-edge deltas and estuaries: lower to medium section of the coarsening-thickening-upward packages	Shelf-edge: slumping Slope: water escape and slump scars or slumping of lobe margins Shelf-edge estuaries: tidal influenced channel margin collapse and water escape	Slumping triggered by steep slope. Water escape produced by loading.	Plink-Björklund *et al.*, 2001; Mellere *et al.*, 2002.
Karoo Basin	Permian	Slope to shelf	Coarsening-upward packages up to 50 m thick, thickness decreases to top.	Up to 10 m thick, decrease to top	Intermediate section	Slope: Water escape, density loading and "creep bodies" Slope/shelf-edge: MTCs and founder	Structures in the slope produced by rapid deposition in channels or creep MTCs and founder triggered by delta progradation and falling/lowstand stages of sea level.	Wild (2005); Charles (2007)

Table 1.1: Characteristics of ancient upper slope to shelf-edge deposits with emphasis to soft-sediment deformation process.

Occurrence	Depositional environment	Total Thickness	Thickness of deformed section .	Position of the deformed section	Type of deformation	Deformation process	Additional reference
Gulf of Mexico	Fluvial dominated delta	60-90 m, locally above 180 m	50 % of the mouth bar deposits in the Modern Mississipi delta.	Overall	Growth faults. Slumps and slides. Slide scars. Shale and salt diapirs at the lower slope.	Bar failure triggered by major floods, storms and hurricanes, oversteepening, mudlump activity, increase in pore pressure due to biogenic gas. Loading causing diapirism.	Lindsay *et al.*, 1984; Suter & Berryhill, 1985
Izmir Bay East Mditerranean Sea	Fluvial dominated	5-50 ms(4-40m for vel=1500m/s)	n.a.	n.a.	Imbricated slump blocks in lower prodelta slope	Seismic triggering of rapid deposited and unconsolidated sediments.	Aksu & Piper, 1983
Rhône Shelf, West Mediterranean Sea	Wave dominated	50m (each lowstand wedge)	Up to 50 m	Upper part of the wedge or the whole section	Retrogressive slumping and faulting at the *shelf-edge*	Slope failure and slump activated by the slope *oversteepening*	Tesson *et al.*, 1990
Niger Delta	Slope to shelf	n.a.	n.a.	Overall	Growth faults, mass transport. Fluid escape and diaprism.	Gravity driving due to rapid seaward sediment progradation associated to fluctuation of sea level. Differential loading causing fluidization.	Damuth, 1994; Davies, 2003

Table 1.2: Characteristics of modern shelf-margin deltas with emphasis to soft-sediment deformation process (modified from Porębski & Steel, 2003).

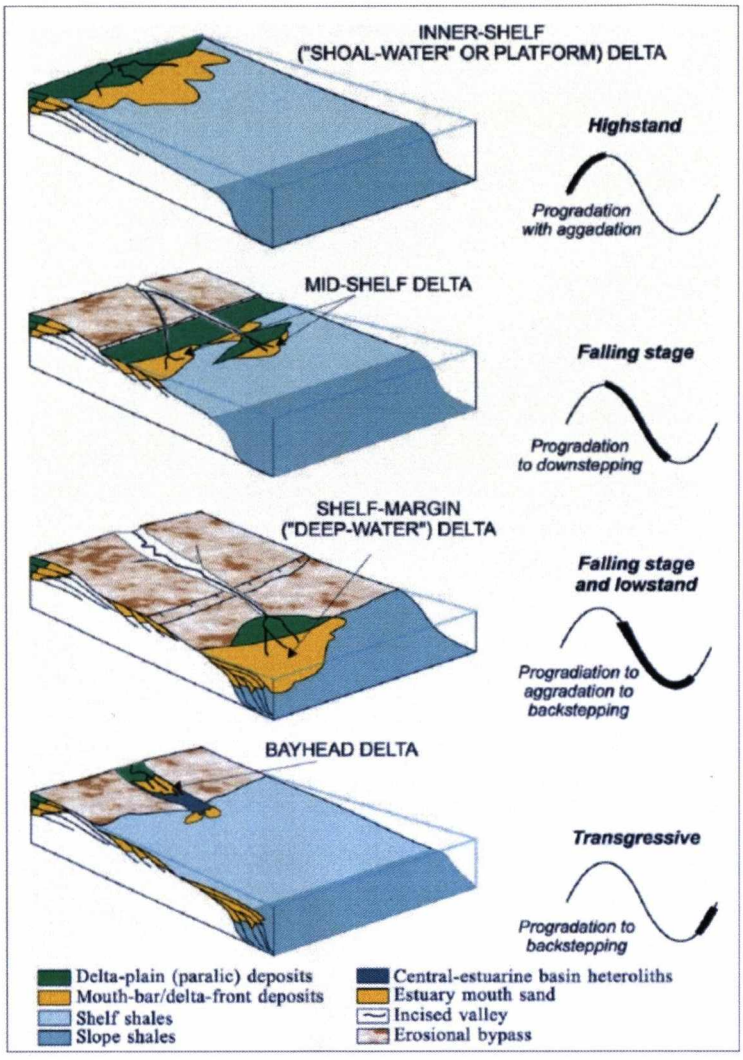

Figure 1.21: Classification of shelf-edges in terms of relative sea level change (from Porębski & Steel, 2003).

Steel *et al.* (2003) defined four types of shelf-edge delta based on relative sea level position at the shelf-break: (i) type A, where the delta contributed slightly to shelf-edge growth before being pushed back by base-level rise, reaching a modest thickness (<15m) and deposited during falling stage; (ii) type B, characterized by erosion caused by its distributary channel as a result of sea level falling below the shelf-edge and also characterized by the occurrence of significant amounts of soft-sediment deformation; (iii) type C, when the delta is re-established at the shelf-edge during sea level rise (late lowstand), just before transgression of the coastline back across the shelf; this type is considered the main component of shelf margin accretion during a single fall-to-rise cycle of relative sea level; and (iv) type D, that involves characteristics of type A to C and is developed continuously during falling stage and lowstand, but without shelf erosion (Figure 1.22).

	Mid-shelf deltas	Shelf-margin deltas
Shape	Erosional pods common	Lobate to strike elongated
Clinoform slope	<0.5°, but can be as much as 8°	Up to 8°, usually 3-6°
Clinoform height	Few tens of metres	Several hundred metres
Thickening trend	Seawards or no distinct trend	Seawards with maximum near shelf break
Dominant energy flux at delta front	Fluvial or wave	Fluvial or wave; tide influence may become important during late lowstand
Delta-top facies	Thin to absent delta plain; thick distributary channel sand below incised valley system; erosional bypass in places	No delta plain; thin fluvial distributaries where delta perches below shelf-edge. Erosional bypass common.
Delta-slope facies	Sandstones to heterolithic foresets; rare turbidite sands	Sandstone to heterolithic foresets; slumped mouth-bar sand embedded in prodelta shales; common hyperpycnal sand turbidites. Growth faults and diapirs.
Updip termination	Erosional pinchout within mid-shelf shales	Erosional pinchout within outer-shelf or upper slope shales
Downdip termination	Pinchout within outer-shelf shales	Pinchout within slope shales
Clinoform breakpoint trajectory	Horizontal to basinward falling	Basinward falling, aggraded to landward rising.
System tract	Falling stage	Falling stage to lowstand

Table 1.3: Main characteristics of shelf-margin deltas compared with mid-shelf deltas (from Porębski & Steel, 2003).

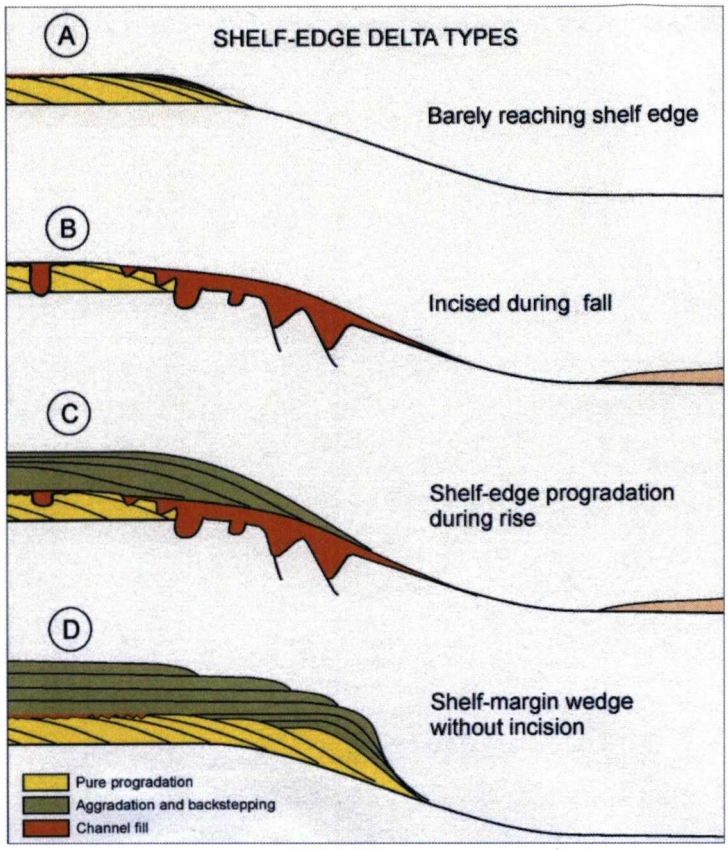

Figure 1.22: Shelf-edge types (from Steel et al., 2003). See text for details.

Other factors like fluvial supply, shelf width, shelf volume, shelf transport, tectonic activity (seismicity), basin energy and subsidence of the shelf-edge can have decisive roles in the progradation of deltas to the shelf-edge not necessarily during falling and lowstand time (Morton & Suter, 1996; Burgess & Hovius, 1998; Cronin *et al.,* 2000; Covault *et al.*, 2007).

Chapter 2 – The study areas

2.1 Gondwana and the origins of the Karoo and Neuquén Basins

The origins of the Karoo and Neuquén basins are related to late Palaeozoic convergence and accretion at the proto-Pacific margin and later break-up of Gondwana, respectively (Uliana *et al.*, 1989; de Wit & Ransome, 1992; Franzese & Spalletti, 2001, Franzese *et al.*, 2003, Milani & de Wit, 2008).

The Karoo Basin is a retro-arc foreland basin (Cole, 1992), one of a series of large basins (including the Paraná, Beacon and Bowen Basins) formed in association with the subduction and accretion of a palaeo-Pacific plate underneath western Gondwana (de Wit & Ransome, 1992; Veevers *et al.*, 1994; Lopéz-Gamundí & Rosselo, 1998) (Figures 2.1 and 2.2).

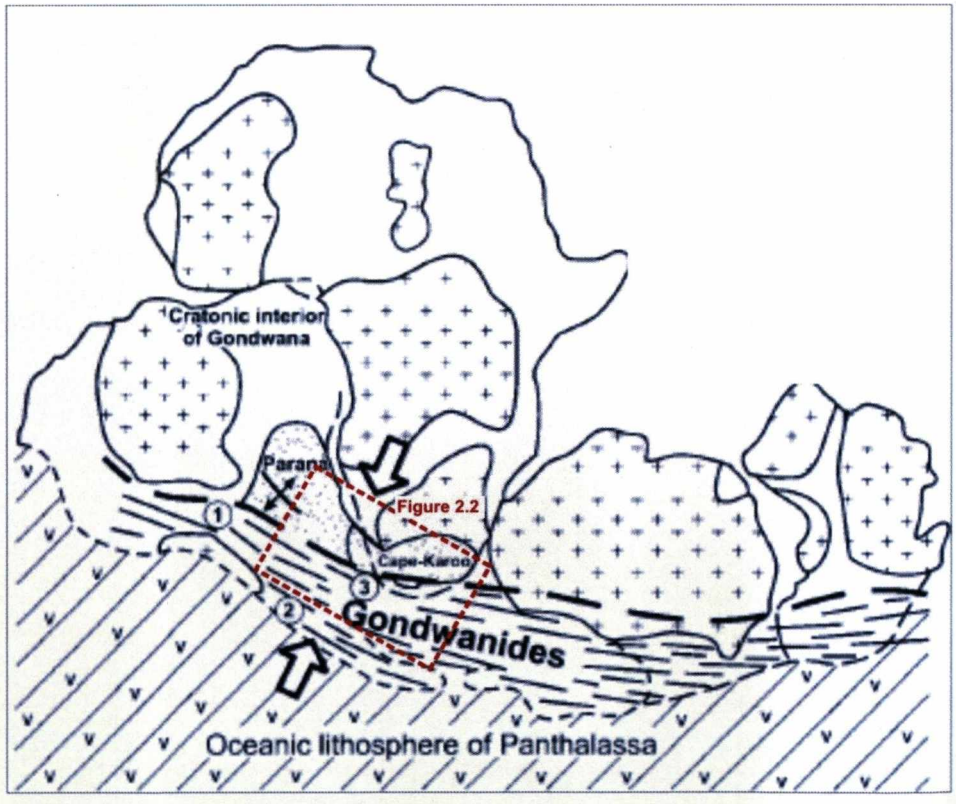

Figure 2.1: Regional tectonic setting of the souther margin of Gondwana during the Upper Palaeozoic (modified from Milani and de Wit, 2008). Note that the Cape Fold Belt is a small part of the large Gondwana orogeny (Gondwanides), which is well represented in South America. The Paraná, Karoo, Beacon and Bowen basins are related to the evolution of this orogeny.

The initiation of the Neuquén Basin as a Triassic intracontinental rift was linked to the thermo-mechanical collapse of the late Palaeozoic Gondwanides orogenic belt (Legarreta & Uliana, 1996) and the start of the Andean cycle (Franzese & Spalletti, 2001; Franzese *et al.*, 2003). The tectonic scenario was dominated by a strike-slip regime parallel to the continental margin with intraplate extension in the continent, resulting in NW-SE elongated depocentres that received the first deposits of the Neuquén basin and correlatives.

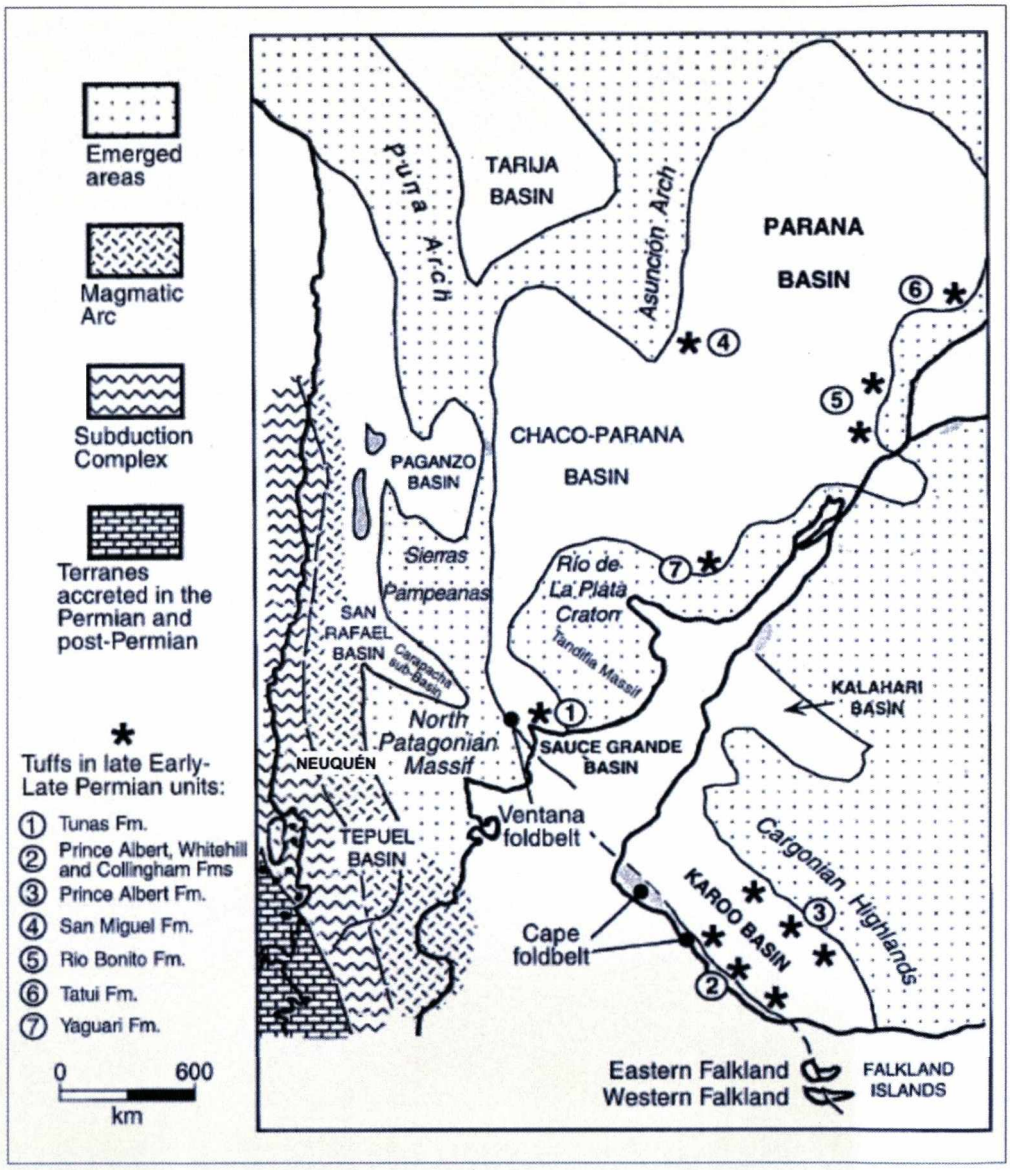

Figure 2.2: Palaeogeography and geotectonic setting of western Gondwana during the late Palaeozoic. Note that while the Karoo Basin is developing as a foreland basin behind the compressive system represented by the Cape and Ventana fold belts, the Neuquén region is still dominated by the magmatic arc associated with a subduction complex and is not yet a basin (from López-Gamundí & Rossello, 1998).

2.2 Karoo Basin

The Karoo Basin covers around 1,000,000 km^2, between 26° and 33°S and occupies a large part of present day South Africa. The fill can reach 10,000 m in thickness, and correlative successions are reported from Namibia and Zimbabwe (Figure 2.3). The Karoo Foreland Basin developed in response to lithospheric loading generated as a result of crustal shortening and thickening in the Cape Fold Belt (Catuneanu *et al.*, 1998) (Figure 2.4).

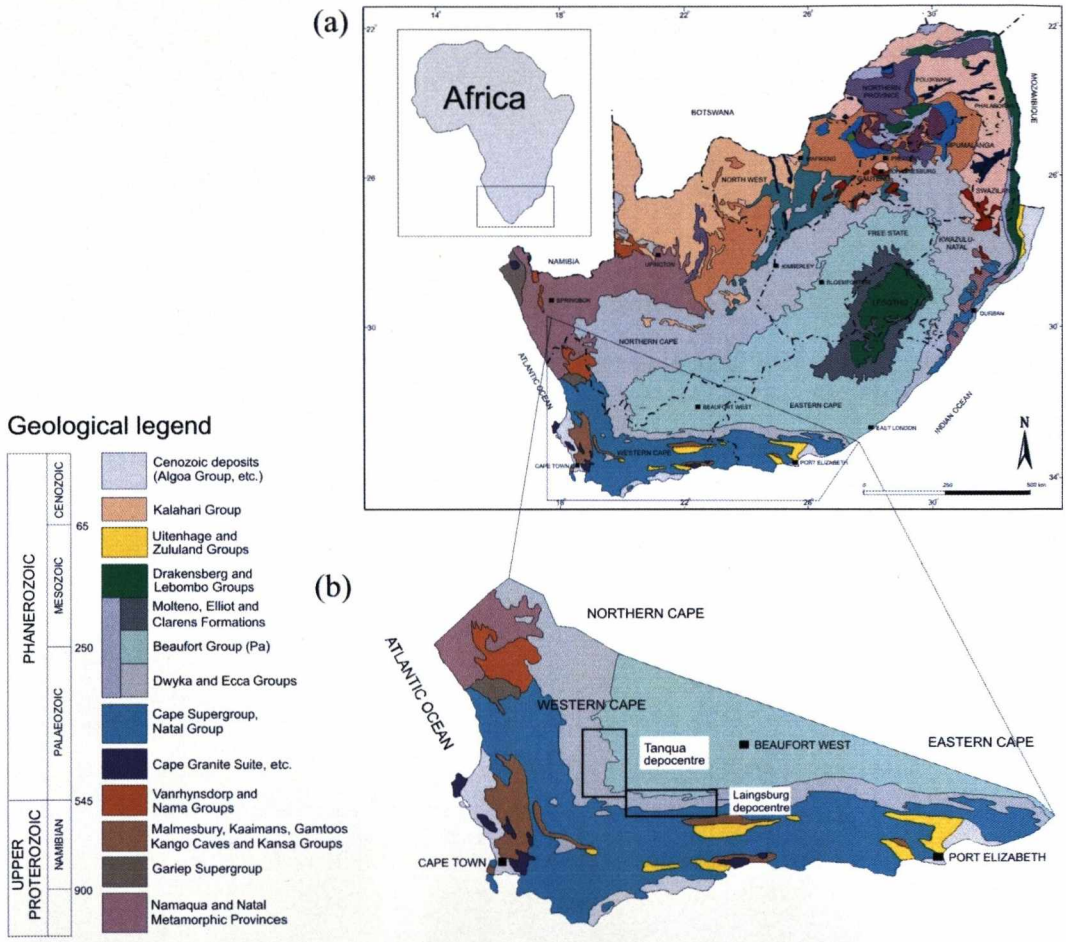

Figure 2.3: (a) Simplified geological map of South Africa, Lesotho and Swaziland; (b) Stratigraphic position and geology of south-western Karoo Basin and related geological section (compiled from Geological map of South Africa. Council for Geoscience, 2000). The Karoo Supergroup is represented by the following units: Dwyka Group (glacial); Ecca Group (marine); Beaufort Group (fluvial); Moteno, Eliot and Clarens Formations (fluvial-aeolian); and Drakensberg Group (basalts). The polygon indicates the position of the Tanqua and Laingsburg depocentres.

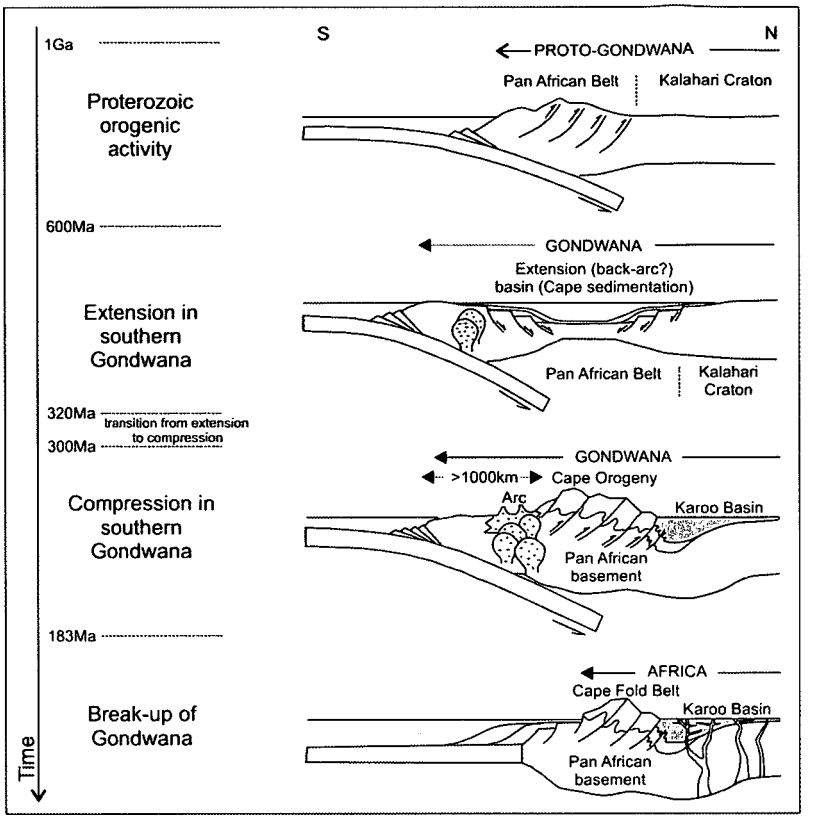

Figure 2.4: Crustal evolution of southern Africa. Karoo Basin is the shaded area (from Catuneanu *et al.*, 1998).

The Permo-Triassic Karoo Supergroup is represented by siliciclastic deposits of the basal Dwyka Group (glaciogenic), followed by the Ecca Group (marine) and culminating with the Beaufort Group (non-marine). The stratigraphic intervals studied in this research are part of the Ecca Group, exposed in the Tanqua and Laingsburg depocentres, SW Karoo Basin (Figure 2.5). The Karoo Supergroup has been traditionally viewed as influenced by the evolution of the Cape Fold Belt (CFB) syntaxis, the structural domain at the intersection the north and west branches of Cape Fold Belt (De Beer, 1995). The northeast oriented syntaxis was responsible for the bending of the CFB front, resulting in the north-northwest trending Cedarberg branch and the east-west trending Swartberg branch (Wickens, 1994). The Tanqua depocentre is positioned parallel to the Cedarberg branch while the Laingsburg depocentre is parallel to the Swartberg branch of the Cape Fold Belt.

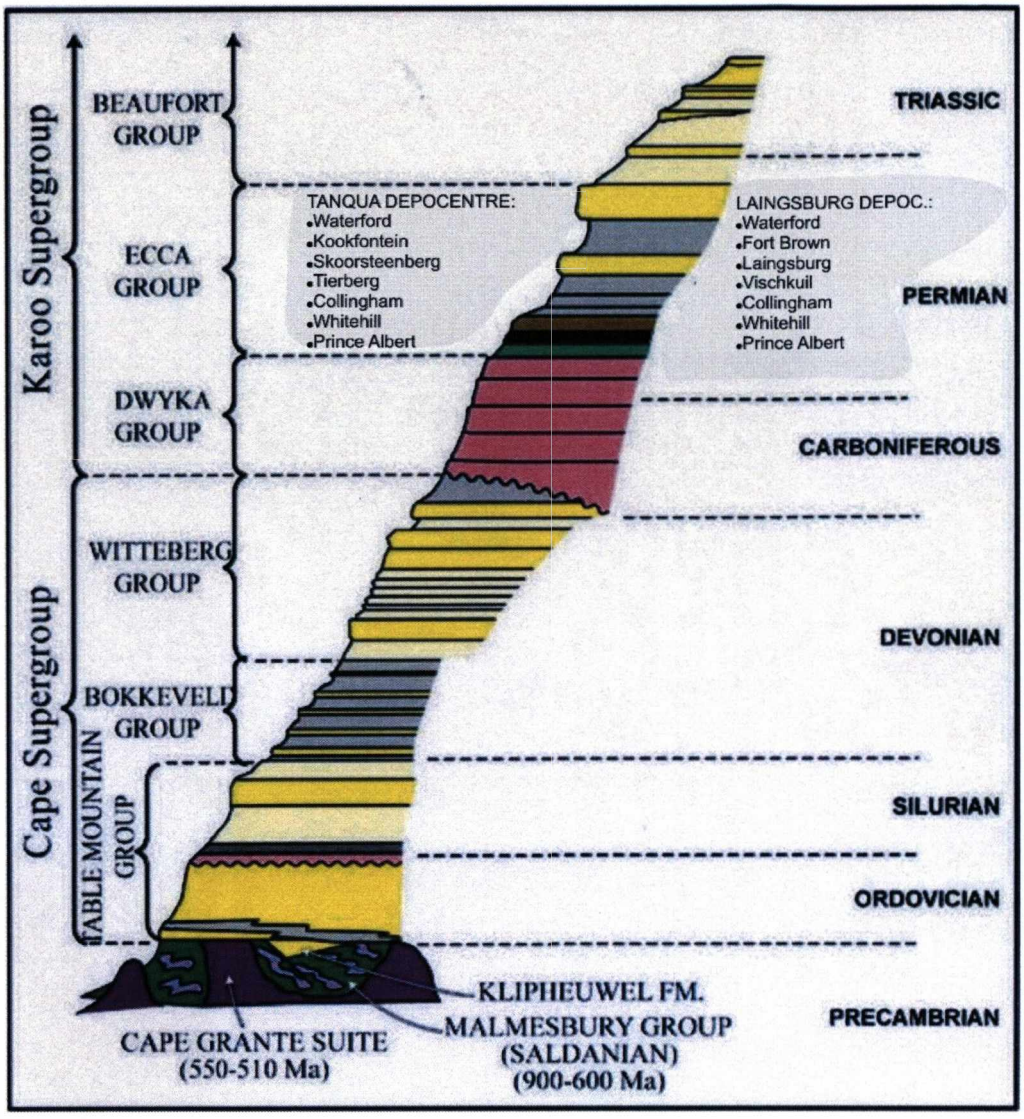

Figure 2.5: Lithostratigraphy of the Western Cape area (modified from Wickens, 1994). The Ecca Group is accompanied by the names of the formations in the Tanqua and Laingsbur`g depocentres.

Simultaneous shortening in the Cedarberg and Swaterberg branches of the CFB in the syntaxis area generated the NE trending antiforms of Hexriver, Bontberg and Baviananshoek and the adjacent synclines (De Beer, 1995). Influence of the CFB as a source area and/or as a control in the routeing for sediments of the Tanqua and Laingsburg depocentres is discussed in a series of works (De Beer, 1992; Wickens, 1994, Scott & Bouma, 2003, Flint *et al.*, 2004, King, 2005; Flint *et al.*, 2008). Van Lente (2004) demonstrated that the composition of the Ecca Group sedimentary rocks does not match with the adjacent CFB; the North Patagonian Massif being the most likely source terrain (cf. Figure 2.2). Structural analysis of King (2005) indicated the Hexriver Anticline as the main interference structure in the syntaxis area and the neighbouring De Doorns Sycline as a long lived structural low

on the sea floor that constituted the main entry point to the southwest Karoo Basin (Figure 2.6).

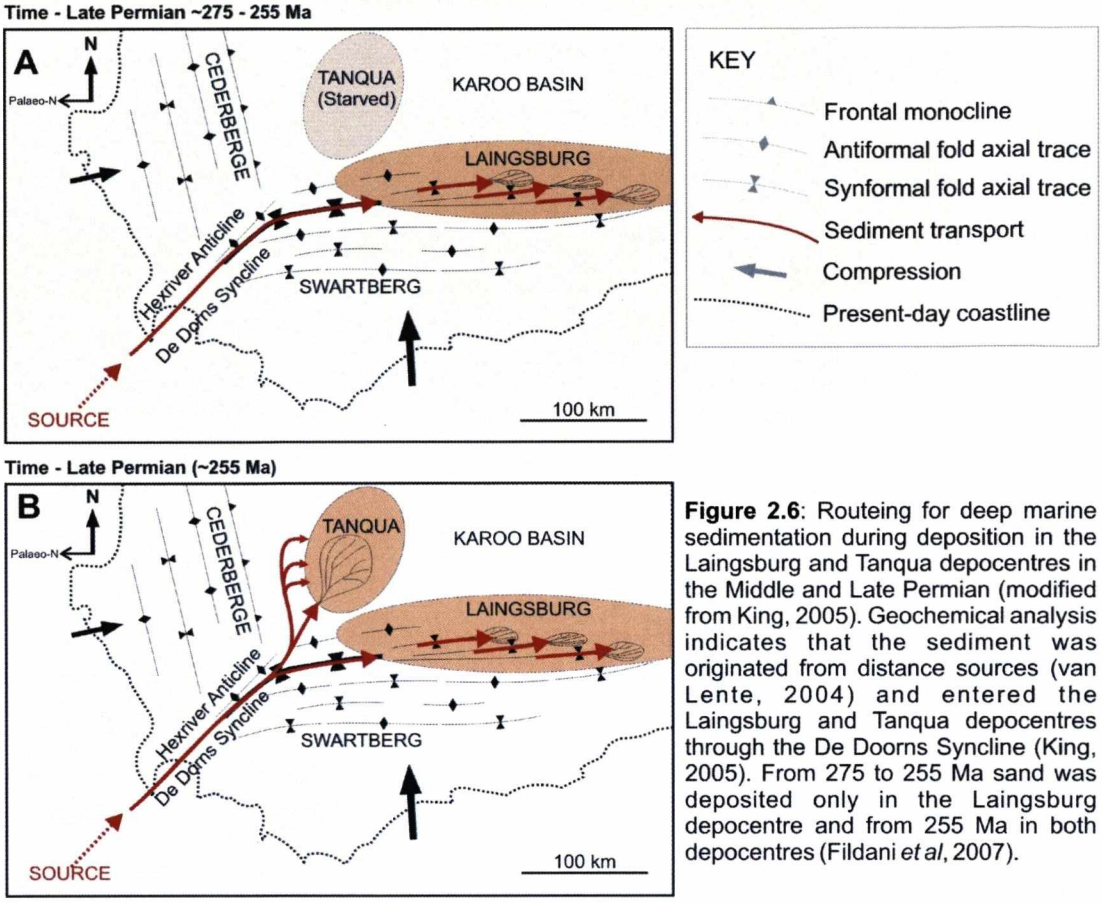

Figure 2.6: Routeing for deep marine sedimentation during deposition in the Laingsburg and Tanqua depocentres in the Middle and Late Permian (modified from King, 2005). Geochemical analysis indicates that the sediment was originated from distance sources (van Lente, 2004) and entered the Laingsburg and Tanqua depocentres through the De Doorns Syncline (King, 2005). From 275 to 255 Ma sand was deposited only in the Laingsburg depocentre and from 255 Ma in both depocentres (Fildani *et al*, 2007).

The exact timing for the formation of these structures has not been determined and the CFB may have formed after the deposition of the Ecca Group. It was proposed that major CFB compressional paroxysms occurred at 278, 258, 247 and 230 Ma (Hälbich *et al.*, 1983). Other results indicate 294, 276, 259, 239 and 223 Ma for the pulses of tectonism (Gresse *et al.*, 1992). Some concerns emerge from the generalization of the ages above because in the first case the samples were collected from a small area while in the second case dates were based only on six samples. Both studies dealt only with the growth of metamorphic minerals in cleavage planes. The only direct dating of the marine Karoo sediments is from interbedded volcanic ashes (Turner, 1999; Fildani *et al.*, 2007). Fildani *et al.* (2007), based on U-Pb single grain zircon ages from six ash beds in the lower fan deposits in both Tanqua and Laingsburg, suggested that the deep-water siliciclastic sedimentation began in the Laingsburg depocentre at 275 Ma resulting while the Tanqua depocentre was sand

starved (Tierberg Formation) during this time. At 255 Ma turbiditic sands deposition also initiated in the Tanqua depocentre and persisted in the two depocentres (Figure 2.7).

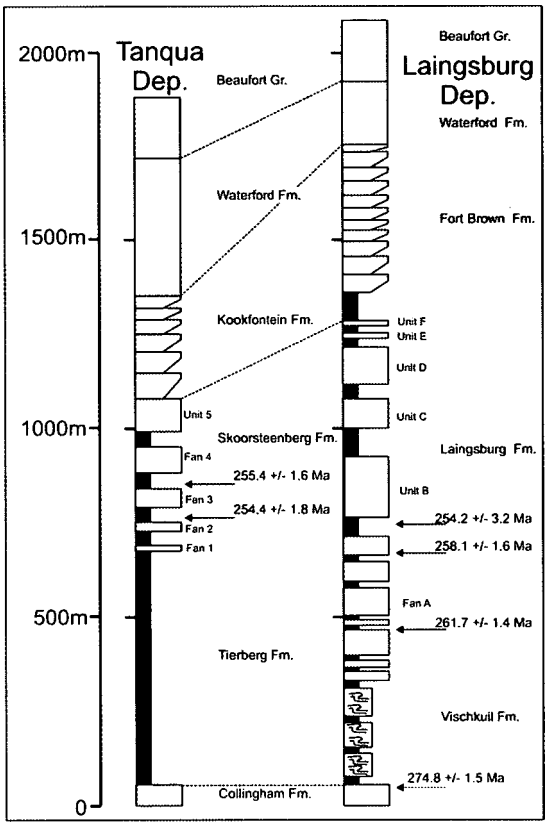

Figure 2.7: Indication of the correlation between the depocentres of Tanqua and Laingsburg based in Fildani *et al.* (2007). Sample position and ages are indicated in the figure.

2.2.1 Ecca Group stratigraphy in the Laingsburg and Tanqua depocentres

Deposition of the Lower Ecca Group followed the collapse of marine ice sheets and the subsequent sea level rise (Late Dwyka Group) (López-Gamundí, 1989; Anderson and Thomas, 1991; Visser, 1993, 1996) and comprises the Prince Albert Formation (carbonates and mudstones), Whitehill Formation (black, laminated, carbonaceous, pyrite-bearing marine shales), and Collingham Formation (turbidite siltstone and shale with yellowish layers of tuff) (Visser, 1992). These three formations in the southwest Karoo Basin indicate shallow open-marine environments (Prince Albert Fm), grading into reducing environment (Whitehill Fm) and followed by distal submarine fan facies associated with pelagic sedimentation and volcanic ashes (Collingham Fm) (Smith *et al.*, 1993). Their evolution was accompanied by

extensive volcanism in South Gondwana (López-Gamundí, 2006) that provided successive subaqueous ash beds through the Ecca Group (Fildani *et al.*, 2007). The Matjiesfontein Chert Bed occurring in the lower part of the Collingham Formation is a regionally extensive reworked subaqueous ash flow maker bed and is used to correlate the lower stratigraphy between the Tanqua and Laingsburg depocentres.

Tanqua depocentre

The Ecca Group in the Tanqua depocentre comprises a 1300 m thick (Wickens, 1994) conformable succession of marine siliciclastic sediments (Figure 2.8). Following deposition of the lower Ecca Group, deep-water deposits of the middle-upper Ecca Group includes basal grey mudstones and subordinate siltstones layers of the Tierberg Formation, followed by the four sand-rich submarine fans (Fans 1-4) overlain by a channelized lower slope succession (Unit 5) of the Skoorsteenberg Formation (Johnson *et al.*, 2001; Hodgson *et al.*, 2006). This is overlain by submarine slope and shelf-edge deltaic deposits of the Kookfontein Formation (Wild, 2005) and capped by shoreface deposits of the Waterford Formation marking the overall progradation of the basin margin to the north and northeast (Wickens, 1994) (cf. Figure 2.5). The studied outcrops are part of the Skoorsteenberg (cf. Chapter 3.1) and Kookfontein formations.

Kookfontein Formation

The Kookfontein Formation is characterised by coarsening- and thickening-upward silty-sandy successions that reflect progressive shallowing conditions associated with progradation (Wickens, 1994; Goldhammer *et al.*, 2000). Based on the identification and detailed description of 13 cycles over a thickness of 290 m, Wild (2005) interpreted the deposits of a lower slope to shelf succession, marked by the punctuated progradation of deltas over the shelf-edge, onto the upper slope. Repeated progradation of deltas over the shelf-edge led failure events (down slope slumping and sliding) on the mid to upper slope and foundering and creep around the shelf-edge. The analysed outcrops in this study cover cycles 2 to 4 in the Roosterberg area.

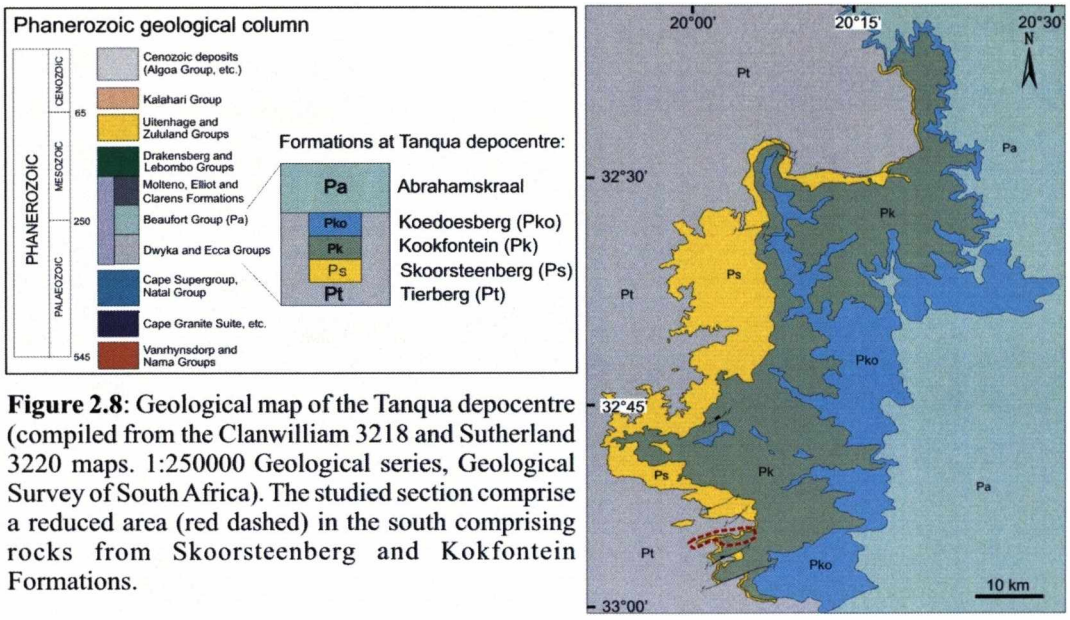

Figure 2.8: Geological map of the Tanqua depocentre (compiled from the Clanwilliam 3218 and Sutherland 3220 maps. 1:250000 Geological series, Geological Survey of South Africa). The studied section comprise a reduced area (red dashed) in the south comprising rocks from Skoorsteenberg and Kokfontein Formations.

Laingsburg depocentre

The Ecca Group in the Laingsburg area is up to 1900 m thick (Fildani *et al.*, 2007) (cf. Figure 2.7; Figure 2.9). The lower units (Prince Albert, Whitehill and Collingham Formations) are followed by up to 400 m of fine-grained turbidites with sporadic tuff layers plus a range of soft-sediment deformation features (Vischkuil Formation; Wickens, 1994; Sixsmith, 2000). It is overlain by the Laingsburg Formation: six sand-rich turbidite systems separated by hemipelagic and turbiditic mudstones, reflecting the gradual evolution from basin-floor through slope setting (Grecula, 2000; Sixsmith, 2000; Grecula *et al.* 2003). An upper slope to shelf-edge delta succession of the Fort Brown Formation and the transition to the Waterford Formation were the focus of this study.

Fort Brown Formation

Gradationally overlying the Laingsburg Formation, the Fort Brown Formation ranges in thickness from 80 to 205 m (Grecula, 2000; Sixsmith, 2000), consists of thin-bedded mudstones with interbedded sandstones in coarsening-upward packages towards the top of the formation. Charles (2007) considered the Fort Brown Formation as the product of shelf-margin deltas characterised by coarsening- and thickening-upward cycles of deltaic mouth bar sedimentation, with scour, deformation and influence of storm waves to the top. This author defined six

depositional cycles composed of five different facies associations developed in the upper slope setting. This thesis focuses on cycles 2 to 4 in the Heuningberg and Zootkloof areas.

Waterford Formation

The Waterford Formation is found in both Tanqua and Laingsburg depocentres and its transition to the overlying Beaufort Group is used as the upper marker for depocentre correlation (Wickens, 1994; Scott *et al.*, 2000). The 150 to 300 m thick succession of dominant fine- to medium-graded sandstones that abruptly or erosively overlie cyclic alternations of thin layers of mudstones and siltstones to very-fine grained sandstones. Soft-sediment deformation related to slumps and vertical loading are associated with thick sandstone layers. Minor previous work has produced a regional facies scheme (Rubidge *et al.*, 2000) and interpreted the deposits as deltaic (Jordaan, 1981).

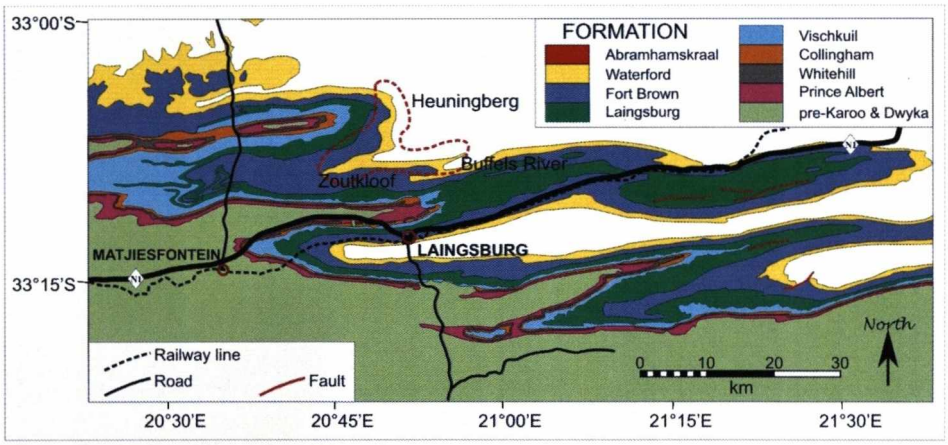

Figure 2.9: Geological map of the Laingsburg depocentre (compiled from the Ladismith 3320 map. 1:250000 Geological Series, Geological Survey of South Africa). The studied areas comprise three localities (Heuningberg, Zoutkloof and Buffles River) indicated by the red dashed line.

2.3 Neuquén Basin

The Neuquén Basin covers around 120,000 km^2 between 32° and 40° S, on the east side of the Andes of central-south Argentina and Chile. It is limited on its NE and S margins by the cratonic areas of the Sierra Pintada Massif and the North Patagonian massif, respectively, and the western boundary is the Andean Magmatic arc (Figure 2.10). The fill includes around 7000 m of sediments that range from Late Triassic to Early Cenozoic in age and comprises continental and marine siliciclastics, carbonates and evaporites (Figure 2.11). Geological understanding of the basin has benefited from the excellent quality of the outcrops plus the petroleum exploration data (reflection seismic lines and wells).

Figure 2.10: Neuquén Basin location and its geological boundaries (mod. from Howell et al., 2005). The study areas are north of Chos Malal and south of Zapala, at the Neuquén Province.

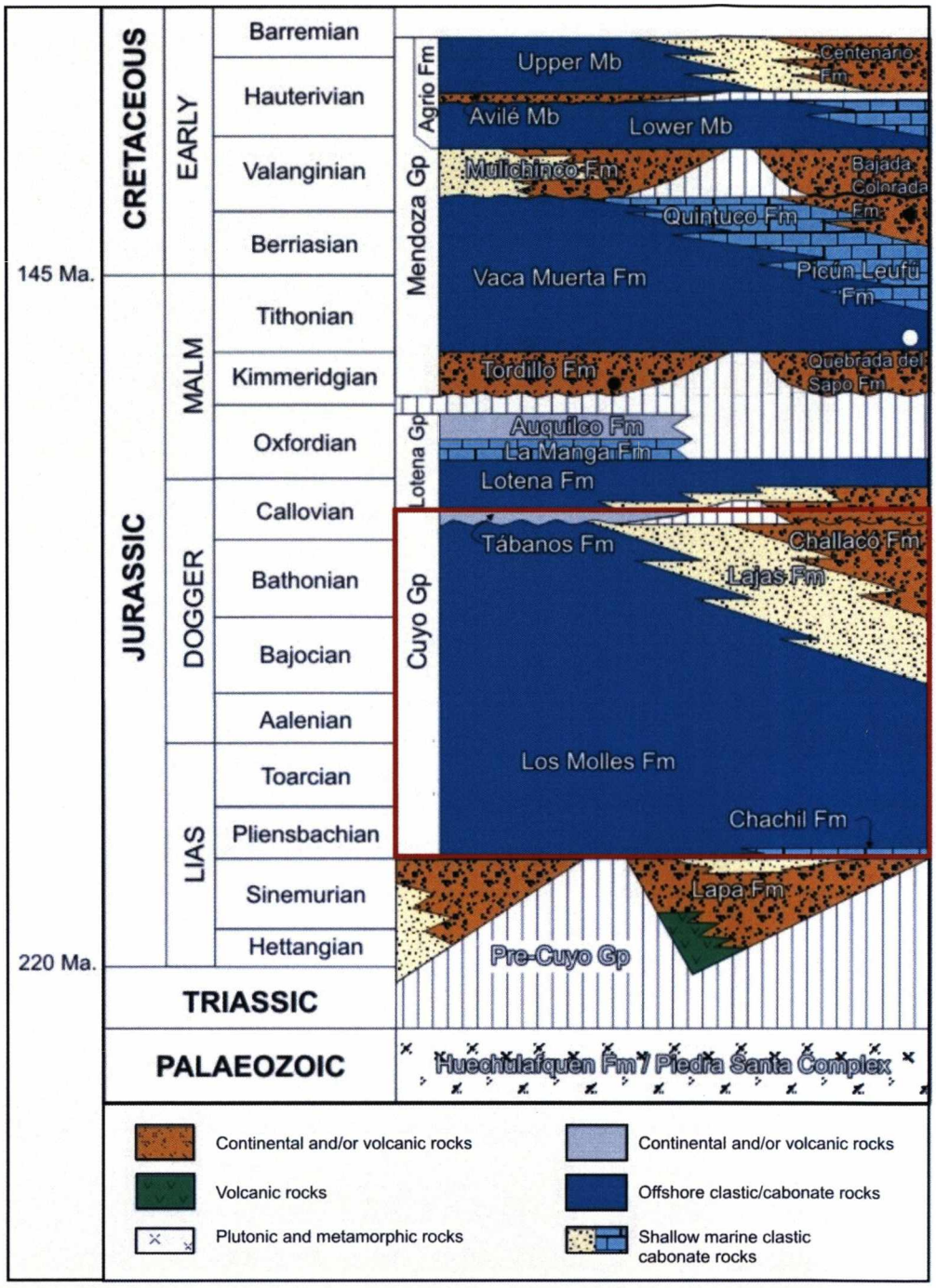

Figure 2.11: Chronostratigraphy of the Neuquén Basin until the Early Cretaceous (in Howell et al., 2005; after Legarreta & Gulisano (1989), Legarreta & Uliana (1991)). The studied interval comprises the Cuyo Group (Los Molles and Lajas Formations (red box).

Three main structural units were identified, from west to east: (a) the main Andean cordillera, located at the arc front and at the inner retro-arc area and dominated by the presence of Tertiary volcaniclastics successions; (b) the inner section of the Agrio Fold and Thrust Belt (FTB), composed of predominantly Jurassic-Lower Cretaceous marine units, deformed since the late Cretaceous time and comprising the studied outcrops in this study, and (3) the outer sector of the

Agrio FTB, formed by Cretaceous-Miocene rocks and deformed up to the late Miocene (Figure 2.12).

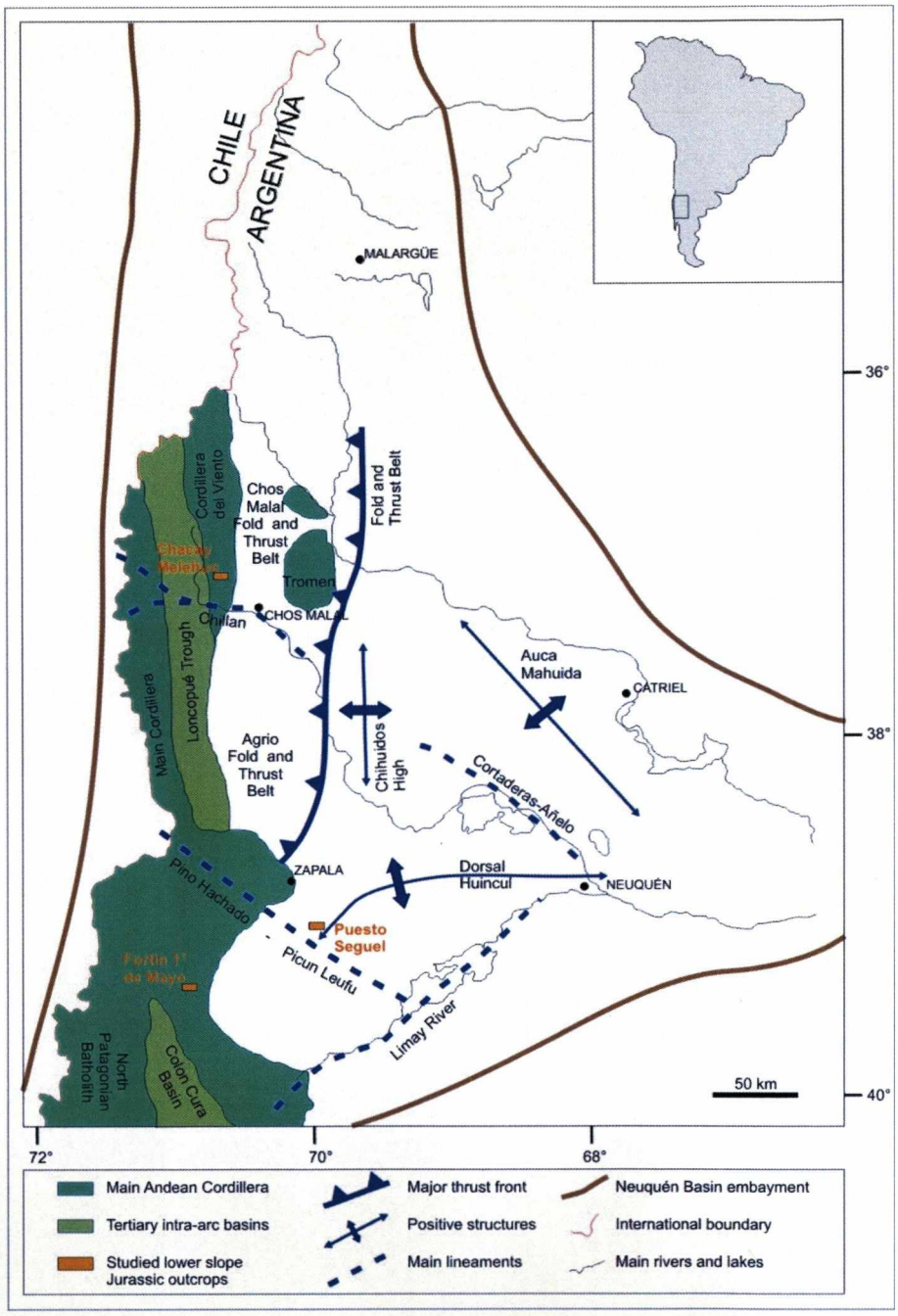

Figure 2.12: Main morphostructural units of the Andes in the central-south Neuquén Basin (from Zapata & Folguera, 2005) and the studied outcrops.

The tectonic and stratigraphic evolution of the Neuquén basin initiated during the Late Triassic and Early Jurassic as a product of extensional collapse of the Permian-Triassic orogenic belt. The Mesozoic Neuquén basin has a complex structural framework affected initially (Triassic and Early Jurassic, Figure 2.13a) by

the northeast oriented extension and later (late Jurassic-Cretaceous) by northwest oriented extension, fragmentation of western Gondwana and the Atlantic opening. The most conspicuous structure during this later phase is the Huincul dorsal, generated by the inversion of the earlier rifts depocentres, occurred during the Araucarian inversion in the Kimmeridgian (Figure 2.13b). The importance of this inversion is that it marked the reorganization of the Mesozoic stress field and coincided with the initiation of rifting along the eastern seaboard of Argentina and the conjugate margin of South Africa (Vergani *et al.*, 1995).

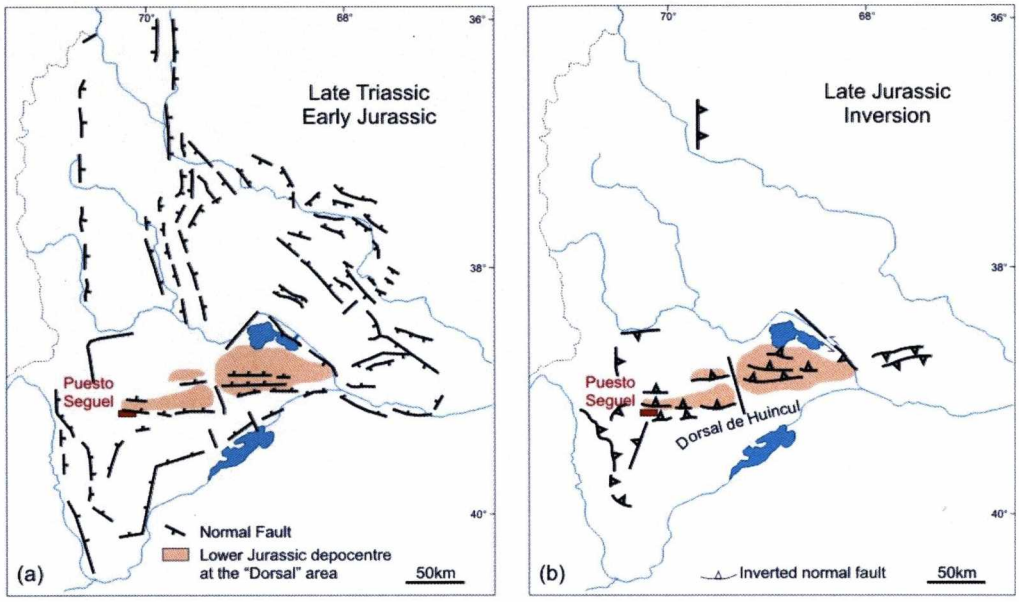

Figure 2.13: Representation of the main structural architecture during the Late Triassic/Early Jurassic (a) and Late Jurassic inversion (b). This later is particularly important in Puesto Seguel area (Chapter 4). The deposition of the Lajas Formation at Puesto Seguel area was controlled partially by the extensional pattern inherited from the Early Jurassic extension (a) and later inverted during the evolution of the Dorsal de Huincul, initiated in the Middle Jurassic with maximum effect in the Late Jurassic Araucanian inversion (b) (Figure after Vergani et al., 1995).

The evolution of the basin can be separated into three distinct phases (Vergani *et al.*, 1995; Howell *et al.*, 2005): (1) Late Triassic-Early Jurassic syn-rift phase; (2) Early Jurassic-Early Cretaceous post-rift phase; and (3) Late Cretaceous-Cenozoic foreland basin stage (Figure 2.14). The outcrops studied here are part of the Jurassic marine post-rift succession, which was influenced by the earlier rift geology. Characteristics of these three phases are described below:

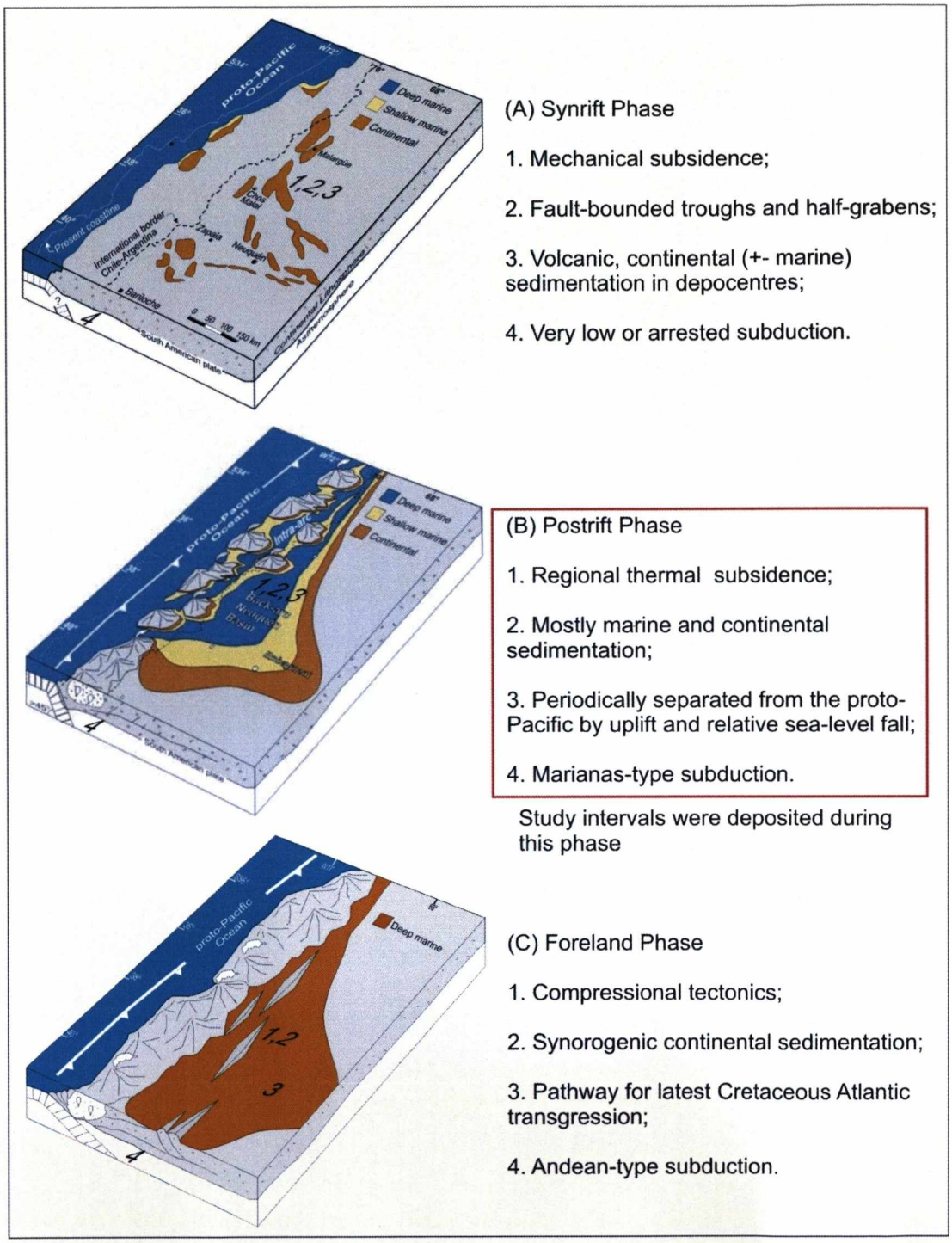

Figure 2.14: Schematic evolution of the Neuquén Basin from Late Triassic to Cenozoic with the three main evolutionary phases: (A) Late-Triassic - Early Jurassic rifting; (B) Jurassic- Early Cretaceous back arc basin and (C) Late Cretaceous foreland basin (from Howell et al., 2005). See text for details of each phase.

2.3.1 Late Triassic – Early Jurassic

During the Late Triassic-Early Jurassic syn-rift phase (Figure 2.14a), the tectonic system was dominated by a strike-slip regime subparallel to the western Gondwana margin (Franzese & Spalletti, 2001). This was reflected in the Neuquén area by a series of narrow, elongated half-grabens, controlled by three main trends of extensional faults (north-south, ENE-WSW and northwest-southeast), and are linked by transfer fault systems (Vergani *et al.*, 1995). These depocentres are marked by continental siliciclastic and volcaniclastic deposits of the Pre-Cuyo Group, and represent alluvial, fluvial, deltaic, lacustrine, and shallow-marine environments, with an abrupt transition from continental to marine sedimentation towards the uppermost part of the synrift succession (Franzese & Spalletti, 2001; Franzese *et al.*, 2003; Franzese *et al.*, 2006). The oldest interval consists of a heterogeneous assemblage of continental deposits associated with volcanic and pyroclastic members. An embryonic marine link between the Pacific Oceans and the Neuquén depocentre was established through southern Mendoza (Legarreta & Uliana, 1996)

2.3.2 Early Jurassic – Early Cretaceous

The Early Jurassic – Early Cretaceous post rift phase (Figure 2.14b) was related to a marine back-arc basin (Vergani *et al.*, 1995; Franzese et al., 2003). The period that involved thermal subsidence and back-arc extension resulted in a series of transgressive-regressive cycles controlled by subsidence rates, eustatic sea-level oscillations, and localized uplift that resulted in the deposition of the Cuyo, Lotena and Mendoza groups (Howell *et al.* 2005) (cf. Figure 2.11). The outcrops involved in this research are part of the Cuyo Group and more detailed description can be found in the introductions of Chapters 3 and 4.

Sedimentation in the Early Jurassic was initially influenced by minor activity and inherited topography from the syn-rift system (Vergani *et al.*, 1995; Burgess *et al.*, 2000; McIroy *et al.*, 2005). During this period depocentres coalesced and the area under marine influence enlarged during the Toarcian, associated with global eustatic sea level rise. From late Toarcian time onward, fault-controlled subsidence gradually decreased and the isolated rift depocentres of earlier Jurassic time were

gradually amalgamated into a single, broad basin in which the previous interbasin highs lost their identities (Legarreta & Uliana, 1996; Vergani *et al.*, 1995). This relative tectonic quiescence was affected during the Middle- Late-Jurassic by a new component of syn-sedimentary tectonic activity in the south and central part of the basin, related to the E-W oriented 'Dorsal Huíncul' strike-slip zone that inverted older extensional faults.

The Cuyo Group represents a depositional cycle that involved an initial period of Pliensbachian to Toarcian transgression, followed by rapid clastic progradation during the Aalenian to Bathonian and a relative sea level fall that culminated in basin desiccation during the middle Callovian (Legarreta & Uliana, 1996; Burgess *et al.*, 2000; Lanés, 2005). The study outcrops are from the Lower- and Middle-Jurassic Los Molles and Lajas formations, the main characteristics of which are described below.

Los Molles Formation

The post-rift stage in the Early-Jurassic was initiated by transgression and deposition of pelagic muds and turbidites of the Los Molles Formation, initially influenced by topographic elements related to faults active during the rifting event (Burgess et al., 2000). Towards the top, there is a reduction in the influence of rift palaeotopography on control of deposition and an increase in the relative amount of sandstone. Two sand-rich intervals from the Los Molles Formation; the Fortin Primero de Mayo slope channel complex and the progradational Chacay Melehue succession are discussed in Chapter 3.2. Sediments of this formation are diachronously overlain by sandy shallow marine strata of the Aalenian Lajas Formation.

Lajas Formation

According to McIlroy *et al.* (2005), the Middle Jurassic Lajas Formation comprises around 600 m of well exposed tide-dominated facies deposited within four unconformity-bounded sequences. Facies associations include tide-dominated deltas (present at Puesto Seguel study area and whose soft-sediment deformation structures are discussed in Chapter 4.2), sandy-heterolithic tidal channel fills and extensive progradational tidal-flat successions. Lajas Formation sedimentary facies suggest a high energy shelf and mesotidal ranges, in a palaeogeographic embayment that was

partially open to the north, with provenance of sediments from the east and southeast (Uliana & Legarreta, 1993; Vergani *et al.*, 1995).

2.3.3 Late Cretaceous - Cenozoic

The end of the Early Cretaceous (Figure 2.14c) marks the beginning of the compressional tectonic regime in the Neuquén and other correlative sub-Andean basins that lasted during the Late Cretaceous and the Cenozoic. The Neuquén region became a retro-arc foreland basin characterized by the inversion of previous extensional structures (Vergani *et al.*, 1995), the deposition of enormous amounts of continental sediments from the rising mountain chain to the west (Legarreta & Uliana, 1999), and the development of thin- and thick-skinned fold and thrust belts that result in the present-day configuration of the basin (Ramos & Folguera, 2005; Zapata & Folguera, 2005).

Chapter 3 – Soft-sediment deformation in the lower slope setting

Explanatory statement

The bulk of this chapter is in the form of a paper that is now in press: "Aseismic controls on *in situ* soft-sediment deformation processes and products in submarine slope deposits of the Karoo Basin, South Africa", by Oliveira, C.M., Hodgson, D.M. & Flint, S.S., *Sedimentology*. The references from the paper are presented together with the thesis references at the end of this volume. The role of each one of the authors was divided as follows: Oliveira – 80 % data collection, 70% of the interpretation and writing; Hodgson - 20% data collection, 15% of interpretation and editing of the text; and Flint - 15% of interpretation and editing of the text. The data on Karoo outcrop is supplemented in this chapter by additional examples from Neuquén Basin.

3.1 Karoo Basin – Waterfall area

Abstract

Intervals of soft-sediment deformation features including vertical fluid escape and load structures are common and well exposed in Permian lower slope deposits of the Tanqua Depocentre, Karoo Basin. The structures comprise mainly elongated flames, and load structures associated with ruptured sandstones and structureless siltstones, observed over a range of scales. The presence of an upper structureless siltstone layer linked to the flames, interpreted as a product of the debouching of fine grained material transported through the flame onto the palaeo-seabed, together with the drag and upward folding of lower sandstone layers are evidence that the flames were formed *in situ* close to the seabed by upward movement of sediment-rich fluids. Flames are oriented parallel to the deepwater palaeoslope in lateral splay deposits between two major slope channel complexes. Statistical correlation and regression analyses of 180 flame structures from seven stratigraphic intervals suggest a common mechanism for the deformation and indicate the importance of fluidization

as a deformation mechanism. Importantly, deformation occurred in an instantaneous and synchronous manner. Liquefaction and fluidization were triggered by depositional oversteepening in association with an inherited local NW topographic gradient. Seismic activity is not invoked as a trigger mechanism due to the restricted spatial occurrence of these features and the lack of indications of earthquakes during the time of deposition of the deepwater succession. The driving mechanisms involved a combination of vertical shear stress due to fluidization, development of an inverse density gradient and a downslope component of force associated with depositional slope of the lateral splay deposits. Ground penetrating radar profiles confirm the overall NE orientation of the flame structures and provide a basis for recognition of potential larger-scale examples of flames in seismic reflection datasets.

Keywords Karoo Basin, submarine slope, *in situ* deformation, soft-sediment deformation structures, flame structures, aseismic.

3.1.1. Introduction

Soft-sediment deformation structures is a collective term used to describe a variety of features that occur at a wide range of scales and form via mechanisms that promote the ductile deformation of sediments (Elliot, 1965; Lowe, 1975; Brenchley & Newall, 1977; Allen, 1982; Owen, 1987). An increase in pore pressure due to an interruption in the normal, gradual process of pore fluid expulsion through loading is the main factor that makes sediment behaviour change from that of a solid to a liquid (Allen, 1982; Maltman & Bolton, 2003). A deformation mechanism, normally liquefaction or fluidization, is necessary for temporary loss of sediment strength and is initiated by an external trigger (Owen, 1987). While the deformation mechanism is operating, the presence of externally applied stresses (driving forces) will define the style and amplitude of structures generated (Allen, 1982; Owen, 1987).

The products of soft-sediment deformation can be classified as (i) *in situ* (e.g. convolute lamination, load casts, flame structures and fluid escape structures), (ii) detached (e.g. slumps, slides, and debrites), and (iii) injected (e.g. clastic dykes and sills, and sand volcanoes) (Figure 3.1). *In situ* soft-sediment deformation occurs

without significant down slope movement (less than a few metres of dislocation) and generates smaller structures, typically below seismic resolution. A large range of structures can be generated by *in situ* deformation as a function of the direction of particle dislocation; if vertical, horizontal or a combination (Elliot, 1965; Brenchley & Newall, 1977; Owen, 2003). Absolute distance travelled by the sediment is difficult to ascertain and many of the features most likely lie between *in situ* and true mass movements (Maltman, 1994; Figure 3.1). Detached structures involve deformation and transportation of sediment down slope, initially by laminar flow processes for long distances (10s of m to km). Commonly, detached soft-sediment deformation products are represented by contorted bedding at different stages of disaggregation (Figure 3.1) with many well documented examples from outcrops and seismic datasets in submarine slope settings (e.g. Martinsen, 1989; McHugh *et al.*, 2002; Casas *et al.*, 2003; Posamentier, 2003). Finally, sand injectites involve pressure-driven remobilisation and forceful intrusion of sediment into surrounding strata, forming tabular and elongated bodies, some of them reaching tens of kilometres; normally injected along pre-existing or new fractures (Jolly & Lonergan, 2002).

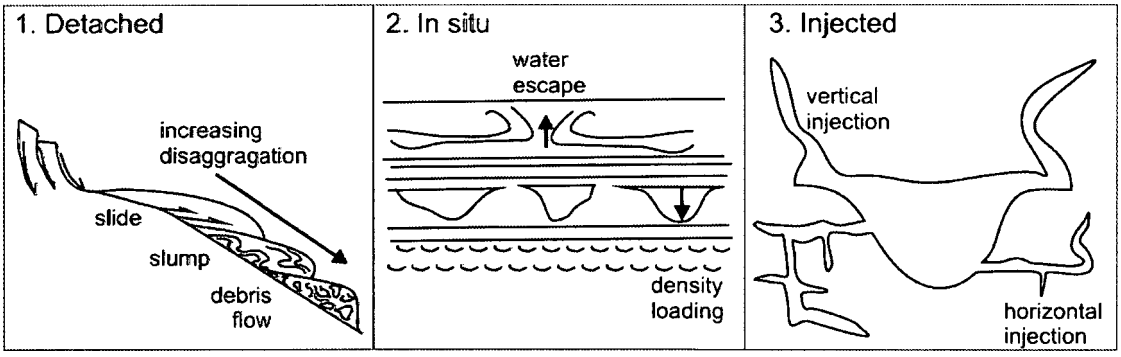

Figure 3.1: Three groups of post-depositional soft-sediment deformation processes and products are identified based on the distance and orientation of sediment transport: (1) detached – laminar to turbulent sediment transport via down slope mass flow for long distances (10s of m to km) under the presence of horizontal shear stress, (2) *in situ* – mainly vertical sediment transport with negligible down slope movement (a few metres) under the presence of vertical shear stress;and (3) injected – transport in subsurface in different orientations depending on local pressure gradient over distances from a few centimetres to kilometres. Note that there is a process continuum between these groupings, particularly groups 1 and 2. No scale implied.

Seismicity has been widely invoked as the initial cause of liquefaction (e.g. Ambraseys & Sarma, 1969; Seed, 1979; Obermeier, 1996) and dewatering (e.g. Neuwerth *et al.*, 2006; Montenat *et al.*, 2007) of fluid-saturated sediments. A large range of soft-sediment deformation structures recognized immediately after

earthquake events and in the geological record has been grouped as 'seismites' (Seilacher, 1969; Montenat *et al.*, 2007). However, deformation of loose sediment can be driven by many aseismic processes such as surface waves, rapid sedimentation, slope failure, artesian conditions, and escape of pore water and gas expansion (Owen, 1987, Maltman & Bolton, 2003).

The aim of this paper is to characterize the products of *in situ* soft-sediment deformation processes, represented mainly by intervals of flame structures in a submarine slope setting, where due to the narrow stratigraphic and geographic interval which they are located in requires that aseismic controls be invoked. The focus is on the geometry, internal features, and vertical and lateral associations of deformational facies, in order to investigate the mode of formation, the possible trigger mechanisms, the driving forces, and the scale of their occurrence. Flame structures are widely described in the literature, occurring in different depositional environments but with restricted dimensions; they are normally associated with load structures but can have different origins.

The study area is within the Tanqua depocentre, Karoo Basin, South Africa (Figure 3.2), and focuses on a 30 m thick succession of Permian submarine slope deposits exposed over a 4 km^2 area. Measurements of geometrical attributes and orientations from 180 structures in seven stratigraphic intervals were analysed statistically to investigate inter-dependencies between these parameters in order to develop a full interpretation.

3.1.2 Geological Setting

The Karoo Basin is one of a series of basins resulting from the subduction of the palaeo-Pacific plate under the western margin of Gondwana (de Wit & Ransome, 1992). The south-western part of the early Karoo Basin is subdivided into the Tanqua and Laingsburg depocentres, in which deepwater siliciclastic sediments of the Permian Ecca Group were deposited. Detailed stratigraphic correlation (Wild *et al.*, 2005; Hodgson *et al.*, 2006) and structural studies (King, 2005), combined with volcanic ash dating (Fildani *et al.*, 2007) indicate that deepwater deposition initiated first in the Laingsburg depocentre with later sand supply to the Tanqua depocentre

with broadly coeval deposition in the latest Permian (~255 Ma from Fildani *et al.*, 2007).

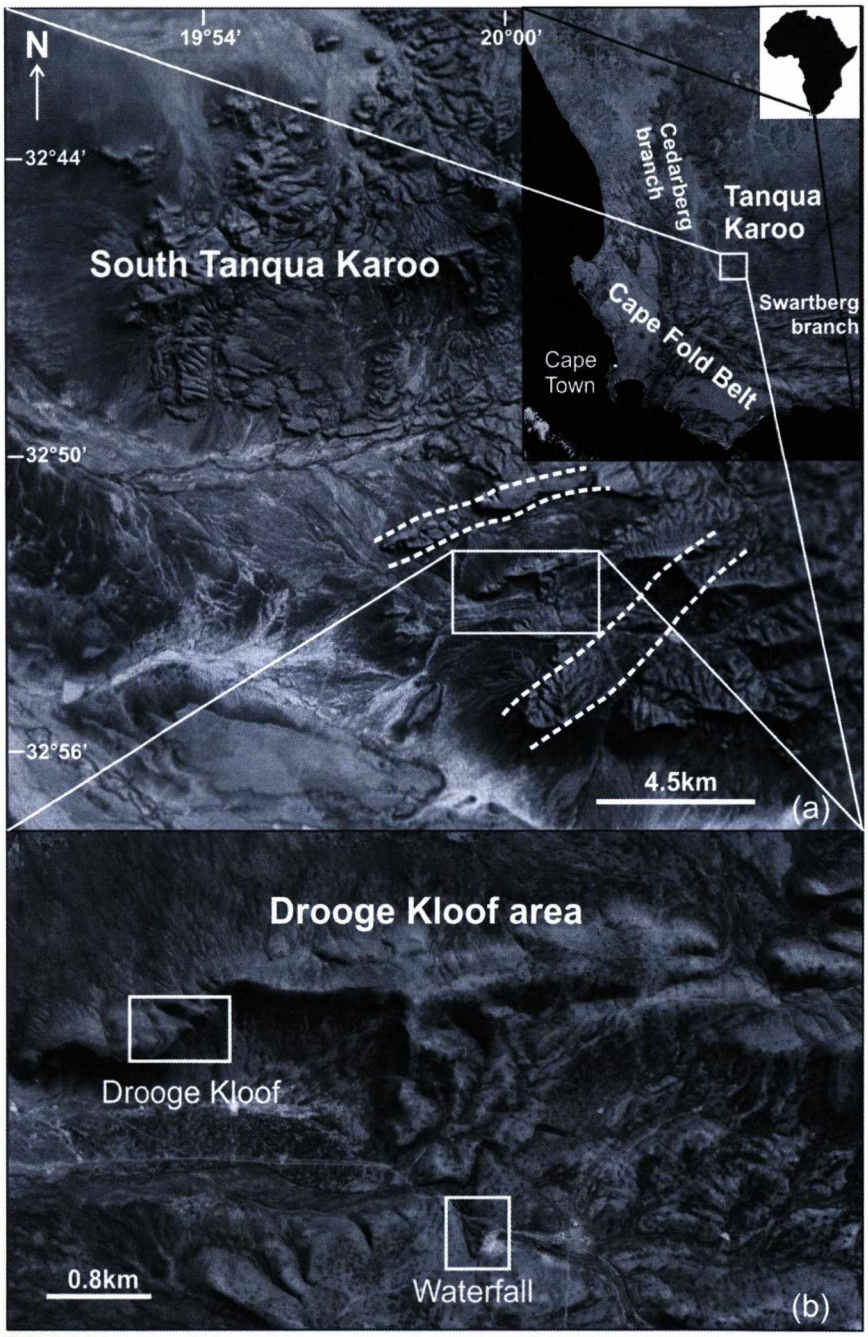

Figure 3.2: (a) Satellite image of the southern sector of the Tanqua depocentre, southwest Karoo Basin. The study area is highlighted. Dotted lines show the approximate position of the Klein Hangklip (north) and Groot Hangklip (south) slope channel complexes in Unit 5 (Wild *et al.*, 2005). (b) Detailed aerial photograph with the Drooge Kloof and Waterfall outcrops described in this study.

Stratigraphy of the Tanqua depocentre

The Permian Ecca Group in the Tanqua depocentre comprises a 1300 m thick conformable succession of marine siliciclastic sediments, overlying glacial deposits of the Dwyka Group (Westphalian to early Permian) and capped by fluvial deposits of the Beaufort Group (Permo-Triassic) (Figure 3.3). The basal Ecca Group is represented by marine mudstones of the Prince Albert and Whitehill Formations, overlain by distal turbidites and volcanic ashes of the Collingham Formation and basinal mudstone and siltstone of the Tierberg Formation (Wickens, 1994). The upper Ecca Group includes sand-rich submarine fan deposits of the Skoorsteenberg Formation overlain by submarine slope and shelf-edge deltaic deposits of the Kookfontein Formation, followed by shoreface deposits of the Waterford Formation marking the overall progradation of the basin margin to the north and northeast (Hodgson *et al.*, 2006).

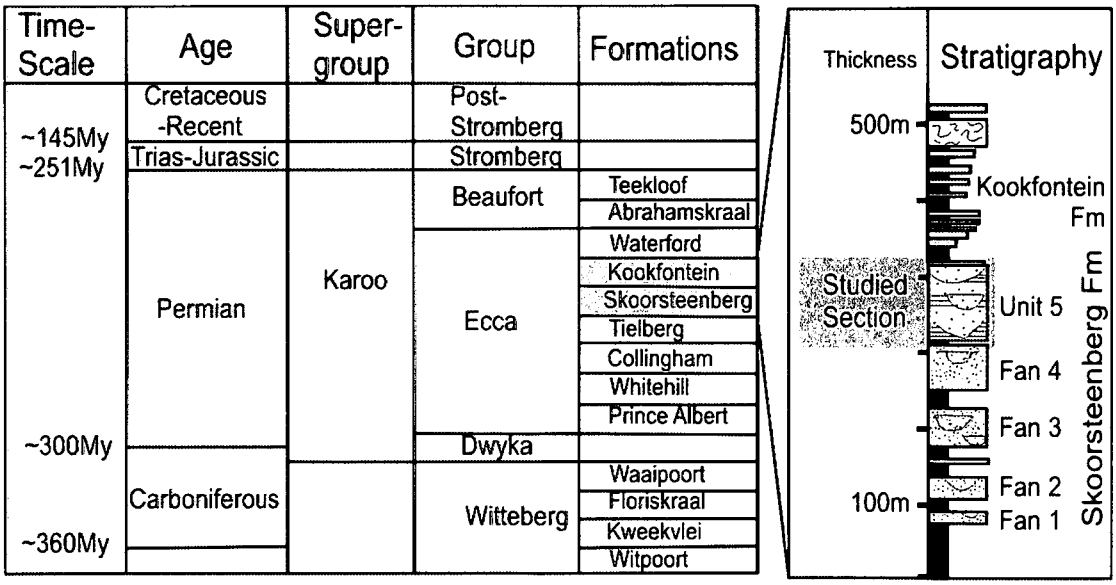

Figure 3.3: Simplified stratigraphy of the Tanqua depocentre showing the Skoorsteenberg and Kookfontein Formations. On the right, a general stratigraphic column with the studied Unit 5 highlighted (modified from Wild *et al.*, 2005).

The Skoorsteenberg Formation comprises around 400 m of deep-water sand-rich submarine fan complexes separated by fine-grained intervals (Wickens, 1994; Wickens & Bouma, 2000). Each submarine fan is interpreted as being deposited during a lowstand systems tract (LST), separated by mud-prone intervals that represent deposits of transgressive and highstand systems tracts (Goldhammer *et al.*, 2000; Johnson *et al.*, 2001). Hodgson *et al.* (2006) subdivided each fan into phases

of progradation (early LST), aggradation (middle LST) and retrogradation (late LST). The outcrops analysed in this study are part of Unit 5; multiple thick-bedded, sandstone-filled slope-channel complexes with abrupt lateral lithofacies changes into thin-bedded, ripple laminated sandstone sheet successions. In the southern Tanqua Hangklip area, Unit 5 comprises two vertically stacked, sub-parallel, NE-trending slope channel complexes 6 km apart, separated by early frontal splay and later lateral splay deposits in the Drooge Kloof/Waterfall area (Wild *et al.*, 2005).

Regional mapping using differential global positioning system technology (Hodgetts *et al.*, 2004) delineated distal and lateral thinning trends in the basin floor fans of the Skoorsteenberg Formation (Hodgson *et al.*, 2006). In the study area, the rate of thinning of Fans 2, 3 and 4 is much higher than elsewhere (Figure 3.4). Integration of this mapping with palaeocurrent analysis indicates that this trend is due to lateral onlap onto a mud-prone confining slope (Wild *et al.*, 2005, Hodgson *et al.*, 2006). Unit 5 is developed across this older bathymetry.

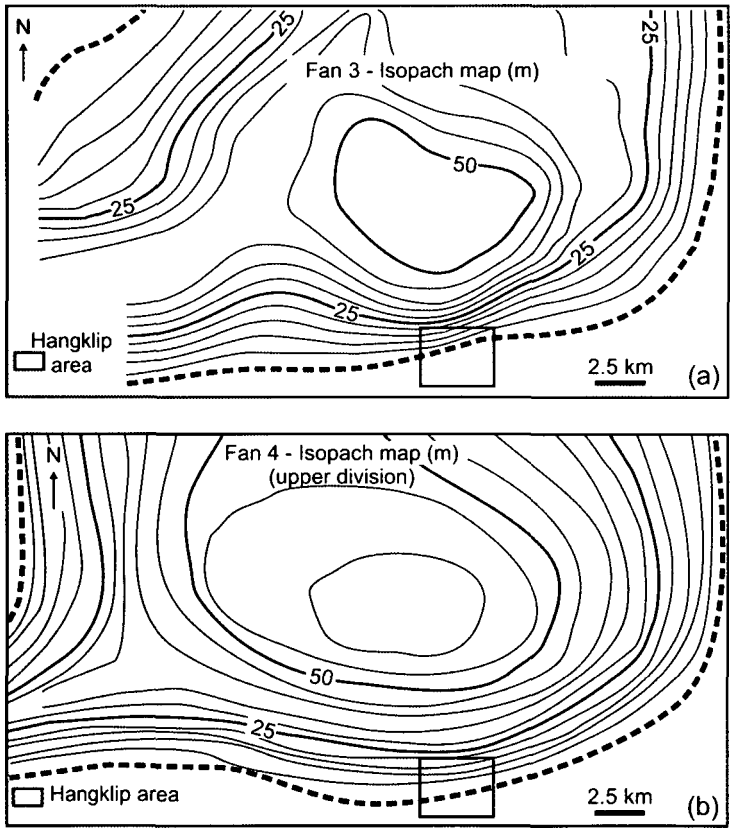

Figure 3.4: Isopach map of Fan 3 (a) and Fan 4 (b) at the south of Tanqua depocentre. The studied section is within the area marked by the rectangles. Note the high gradient and the pinch of the fans at the area of interest.

3.1.3 Methodology and dataset

In the study area, two outcrops, Waterfall and Drooge Kloof ridge, expose Unit 5 over a 4 km^2 area (cf. Figure 3.2). The Waterfall section is a shallow gully formed by the confluence of several ephemeral streams; the local topography provides good 3D control on the exposed deformation features. At Drooge Kloof ridge, the equivalent stratigraphic interval exposes the lateral transition from deformed to undeformed facies. Seven sedimentary logs were collected and beds were walked out between logs in order to capture lateral changes in facies and deformation features. The 30 m thick interval is characterized by three facies groups; (1) interbedded sandstone and siltstone, (2) bedded sandstone and (3) deformed sandstone and siltstone. A typical logged section shows the vertical arrangement of facies groups 1, 2 and 3 (Figure 3.5). Stratigraphic cross-sections show a tabular shape for the successive layers at this scale of observation and lateral transition between the different lithofacies groups (Figure 3.6). Detailed measurements of geometrical parameters were obtained from 180 deformation features from seven intervals and were analysed statistically in order to verify similarities among structures from distinct stratigraphic intervals.

Continuity and orientation of features in 3D was addressed via a 600 m^2 ground penetrating radar (GPR) survey, over frequencies of 100 MHz and 200 MHz, acquired on a flat surface of sandstone and targeting objectives 2-5 m below. In-lines were oriented N30E and were positioned to obtain the best possible coverage of the outcrop. The cross-lines were at 90° from the in-lines.

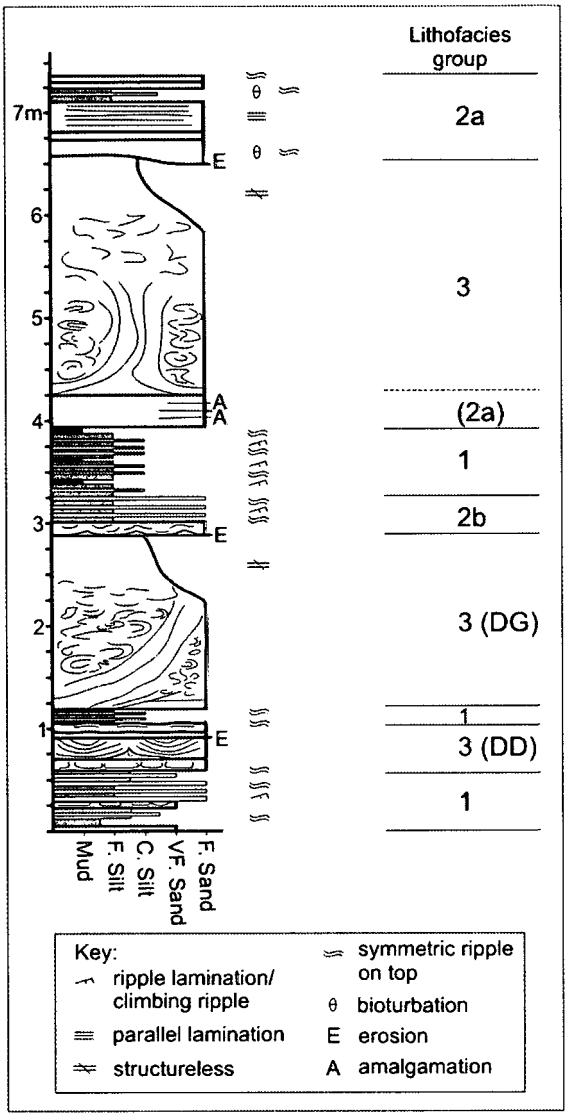

Figure 3.5: Log WF1, in the middle part of the Waterfall succession, illustrates the typical stacking pattern of the three groups of lithofacies. At the base of the log is a cycle of thickening- and coarsening-upward that culminates in the thick deformed interval. Deformed beds vary in thickness from 0.1m to 2.0 m. Two of the deformed layers (DG and DD) used for the statistical analysis are represented in this log.

Figure 3.6: (Next page) Stratigraphic correlation panel for the middle part of the Waterfall succession. Generally, layers are tabular with good lateral continuity. Numbers in circles indicate the dominant facies group for each interval. Lateral lithological transition is illustrated by using arrows between two lithofacies groups. Note that small scale deformed beds grade laterally into undeformed heteroliths. Erosional surfaces occur on top of the two thick (>1m) beds of deformed sandstone (lithofacies group 3), followed by deposition of bedded sandstone (lithofacies group 2). Inset map indicates the distribution of logs in the Waterfall gully. Beds DD, DF and DG were selected for statistical studies. Log coordinates on Appendix 1.

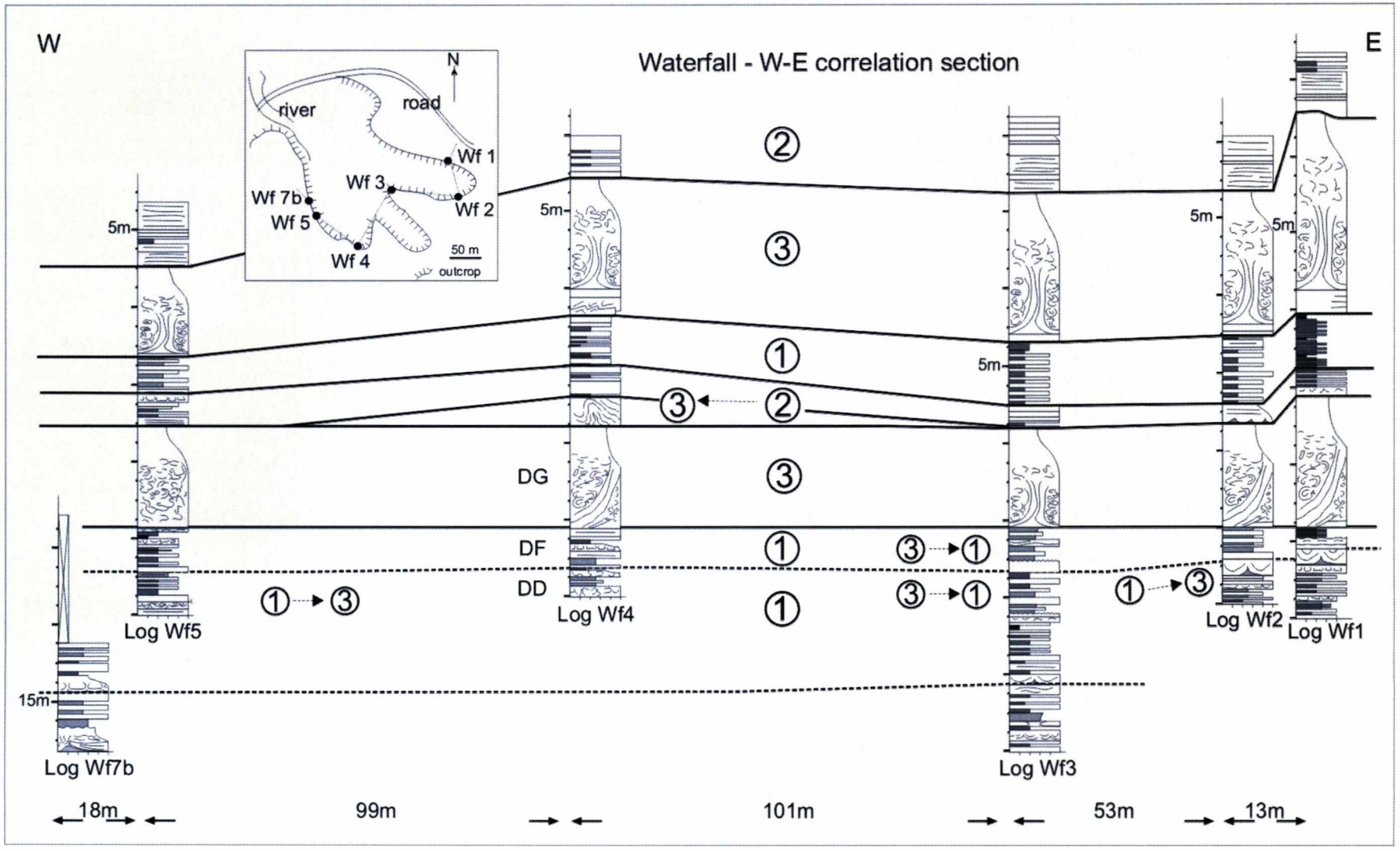
W
E
Waterfall - W-E correlation section
N
river
road
Wf 1
Wf 2
Wf 3
Wf 4
Wf 5
Wf 7b
50 m
outcrop
5m
15m
DG
DF
DD
Log Wf5
Log Wf4
Log Wf3
Log Wf2
Log Wf1
Log Wf7b
18m
99m
101m
53m
13m

Lithofacies description and interpretation

Lithofacies groups 1 and 2 comprise planar beds with variations in thickness and grain size; lithofacies 3 is characterized by the presence of extensive lateral sections rich in soft-sediment structures.

Lithofacies group 1

Group 1 comprises bedsets (0.3 to 0.8 m thick) composed of 1-10 cm thick beds of very fine- to fine-grained, normally graded and current ripple-laminated sandstone, interbedded with fine- to coarse-grained siltstone (Figure 3.7a, b). Rare mudstones with concretions and massive siltstones also occur. Bedsets thicken and coarsen upward at the base of the section. Symmetrical ripples on the top surfaces of sandstone beds are characteristic of this lithofacies group and crest lines sometimes show interference patterns between different trends. These ripples are formed only in the uppermost laminae and truncate underlying unidirectional current-ripple lamination within the bed. Load structures are observed in thicker, fine-grained sandstone layers. The vertical transition to other lithofacies groups is sharp and planar.

Lithofacies group 2

This group is characterized by fine-grained sandstone bedsets of average thickness 0.8 - 1.2 m, with individual graded beds varying from 0.03 to 1 m thick (Figure 3.7a, b). Minor thin beds of siltstone (< 5 cm) may be present. Sub-group 2a, includes sandstone beds up to 1 m thick which are massive to planar laminated (T_{ab}) and display symmetrical ripples on their top surfaces and some horizontal bioturbation traces. Sub-group 2b comprises thinner sandstone beds (up to 0.3 m) which are current ripple-laminated and also exhibits symmetrical ripples on their top surfaces. Beds can be amalgamated and the contacts are sharp and, sometimes, erosive (cf. Figures 3.5 and 3.6).

Lithofacies group 3

This group comprises bed-parallel intervals (0.3 to 1.2 m thick) of deformed strata that are >100 m in lateral extent and are bounded above and below by undeformed bedding (Figure 3.7a). Deformation comprises: (i) vertically-oriented and commonly hourglass-shaped, siltstone dominant, flame structures (Figure 3.7b);

(ii) folded fine-grained sandstone beds which are dissected by the flame structures (Figure 3.7b) and (iii) an overlying homogenous green structureless siltstone to very-fine grained sandstone with similar texture, composition, and blocky weathering style to the flame structures (Figure 3.7c).

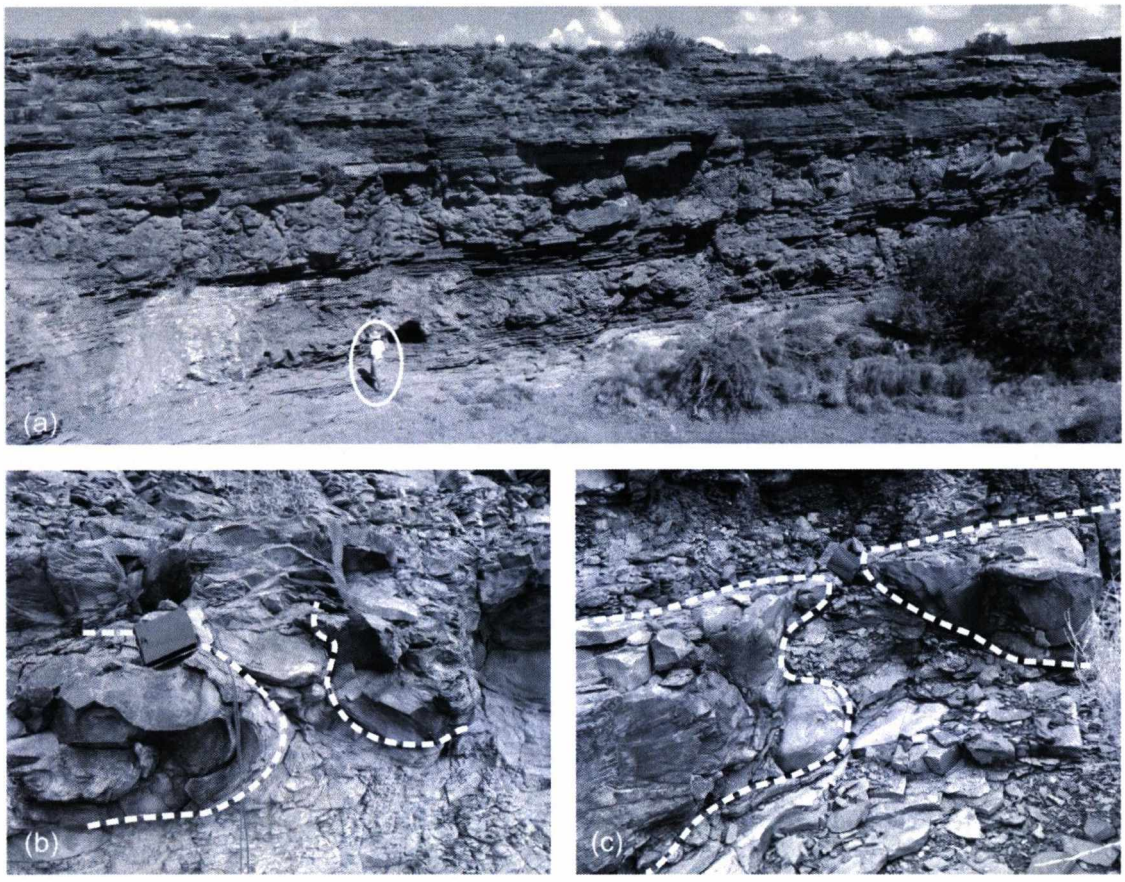

Figure 3.7: Characteristics of lithofacies group 3. (a) Partial view showing scale and tabular geometry of two thick (>1 m) deformed units and the intercalation between thin beds of sandstone and siltstone. Geologist circled for scale. (b) Detailed view of one small (compass for scale) vertical flame structure, showing the adjacent ruptured and contorted (folded) sandstone bed. (c) Flame structure and ruptured sandstone overlain by a 30 cm bed of structureless siltstone, with the same composition as the material in the core of the flame structure. Note the sharp contact between the siltstone bed and the underlying deformed sandstone/ flame structure.

Flame structures are downward connected to a thin basal layer and occur adjacent to concave-upward folded fine-grained sandstone beds. The flames are upright (no overturning or sense of shear) and elongate with a preferred horizontal orientation. Seven different morphologies of flame were identified in the Waterfall area (Figure 3.8). This classification was based on the 2D shape of the flames using the position and width of the flame narrowest point as the main parameter. Some truncation can be seen between superimposed flames. Alternating laterally with the flames are folded and ruptured fine-grained sandstone beds. They form symmetrical

and open, rounded- to angular-folds with upright axial planes. Typically, the sandstone beds maintain a constant thickness until points where they taper abruptly adjacent to the flame structures. Internal laminations are preserved within the sandstone beds with high wavelength folding of these laminae.

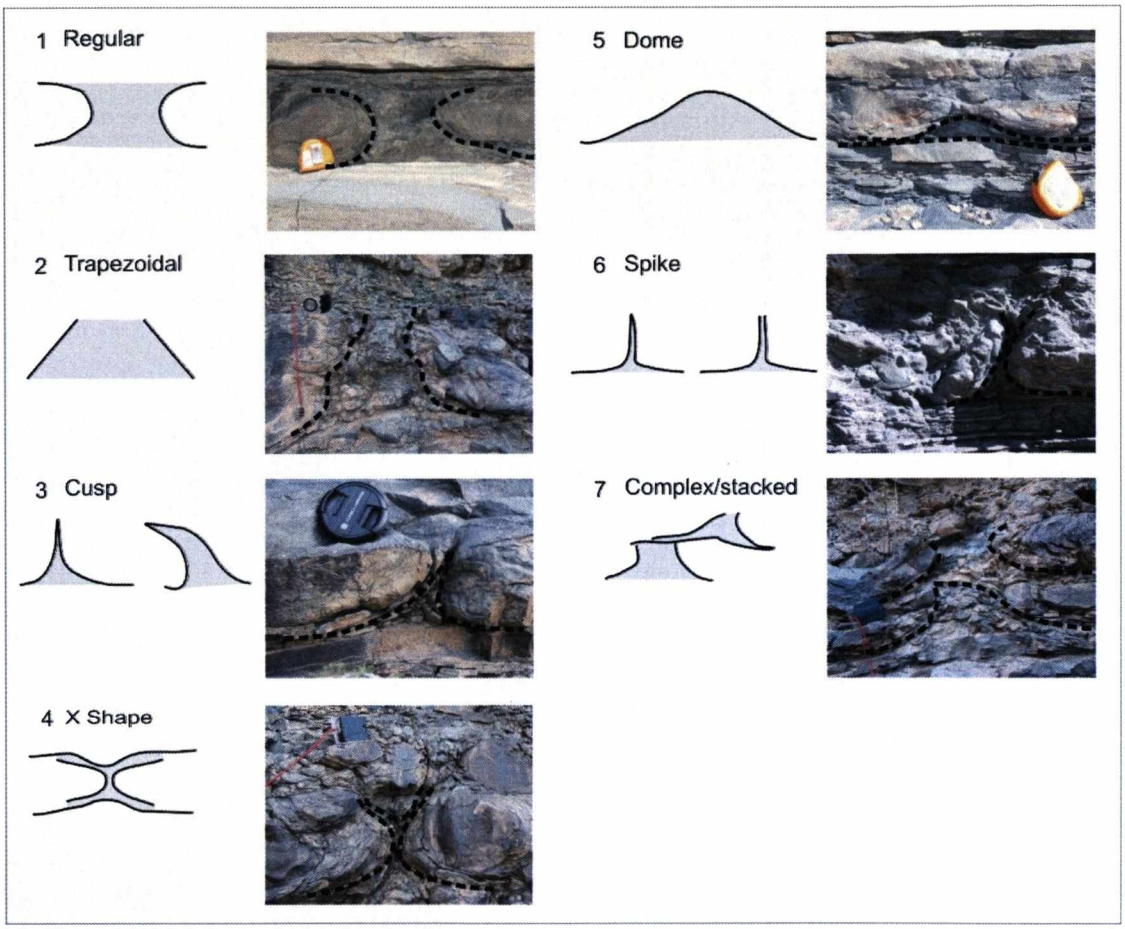

Figure 3.8: Simple classification of the types of flame structures identified in the study area. The classification considers only geometrical aspects of the structures, although the different morphologies are inferred to be linked to differences in bed thickness, rheology and pore pressure. The predominance of one style in a deformed interval will influence the statistical analyses of geometrical parameters. The most common shape is class 1 (regular), followed by classes 3 (cusp) and 6 (spike). Flame number 6 is 0.6 m high.

The homogeneous, green, finer grained layer above the ruptured and contorted sandstones bodies is connected directly to the flames, with a sharp contact on the underlying sandstone. Structureless siltstones (0.1-0.3 m thick) of the same distinctive facies also occur without underlying deformed sandstones and flames in this area. Subsidiary structures linked to the flames include sub-parallel grooves at

the contacts between ruptured sandstone and the flames, and elongated domes of the underlying bedding.

The top surface of the deformed interval is commonly gently undulating with concave lows between underlying flames filled by onlapping fine-grained sandstone beds (Figure 3.9a). Locally, the top surface preserves symmetrical ripple forms or metre-scale spoon-shaped depressions with sharp margins and ripples trending into the depression (Figure 3.9b, c). The lateral relationship between the deformed intervals and adjacent bedded-sandstone and/or thin-bedded sandstone-siltstone is transitional, occurring over a short distance (< 2m) without evidence of erosional truncation or faulting and is observed over different scales (Figure 3.10).

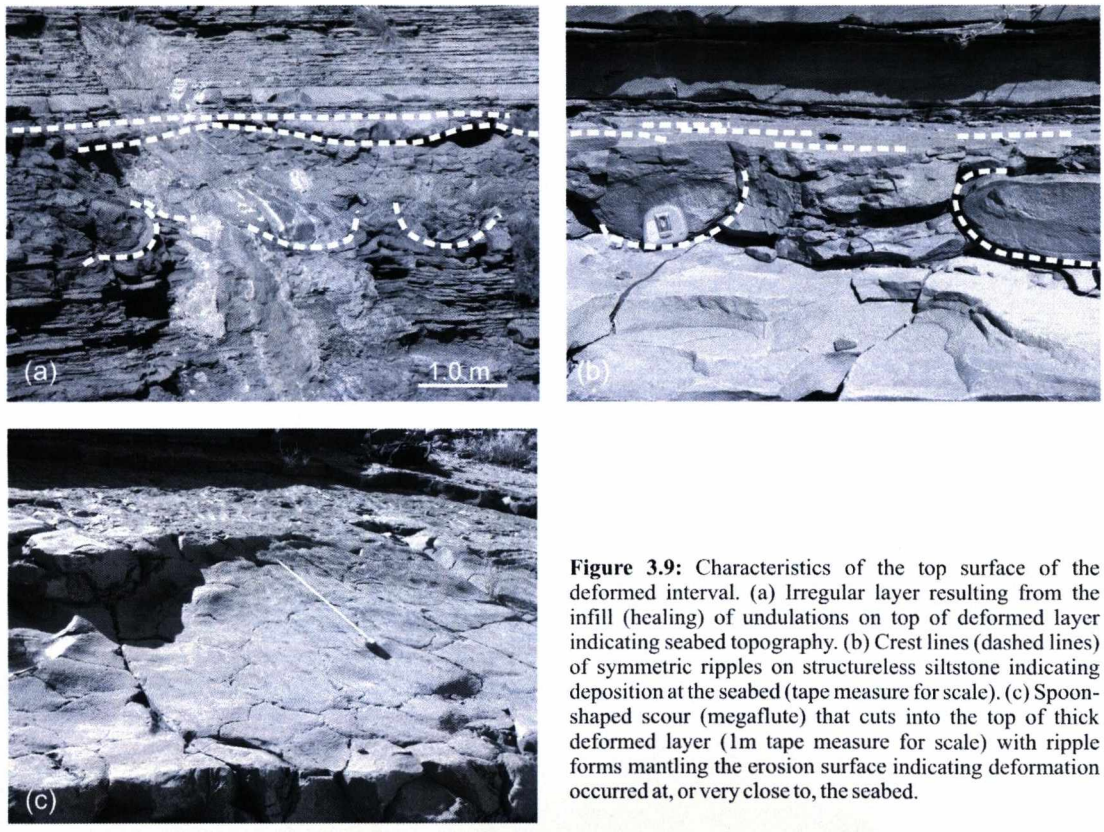

Figure 3.9: Characteristics of the top surface of the deformed interval. (a) Irregular layer resulting from the infill (healing) of undulations on top of deformed layer indicating seabed topography. (b) Crest lines (dashed lines) of symmetric ripples on structureless siltstone indicating deposition at the seabed (tape measure for scale). (c) Spoon-shaped scour (megaflute) that cuts into the top of thick deformed layer (1m tape measure for scale) with ripple forms mantling the erosion surface indicating deformation occurred at, or very close to, the seabed.

Interpretation

Lithofacies group 1 is interpreted as deposited by low concentration turbidity currents (cf. facies type C.2.3 of Pickering *et al.* (1986)), while lithofacies group 2 facies involves deposits of low concentration (2b) to erosive, high concentration (2a) turbidity currents. Together with lithofacies group 3 they form coarsening- and

thickening-upward 10-12 m thick packages, with deformed sandstones increasing to the top. These packages were interpreted by Wild *et al.* (2005) as lateral spill splay deposits. Metre scale (1-2 m) coarsening- and thickening-upward bedsets occur mainly in the lower-half of the 30 m thick studied interval. The upper-half is dominated by a thick interval of deformed sandstone, indicating an overall increase in the energy of the system. Also, the top of the deformed beds sometimes shows scouring that persists laterally for tens of metres and represents the base of the overlying cycle. The symmetrical ripples on the tops of turbidite beds were interpreted by Wild *et al.* (2005) as produced by the reworking of bed surfaces by orbital bottom currents and/or generated by large storm events.

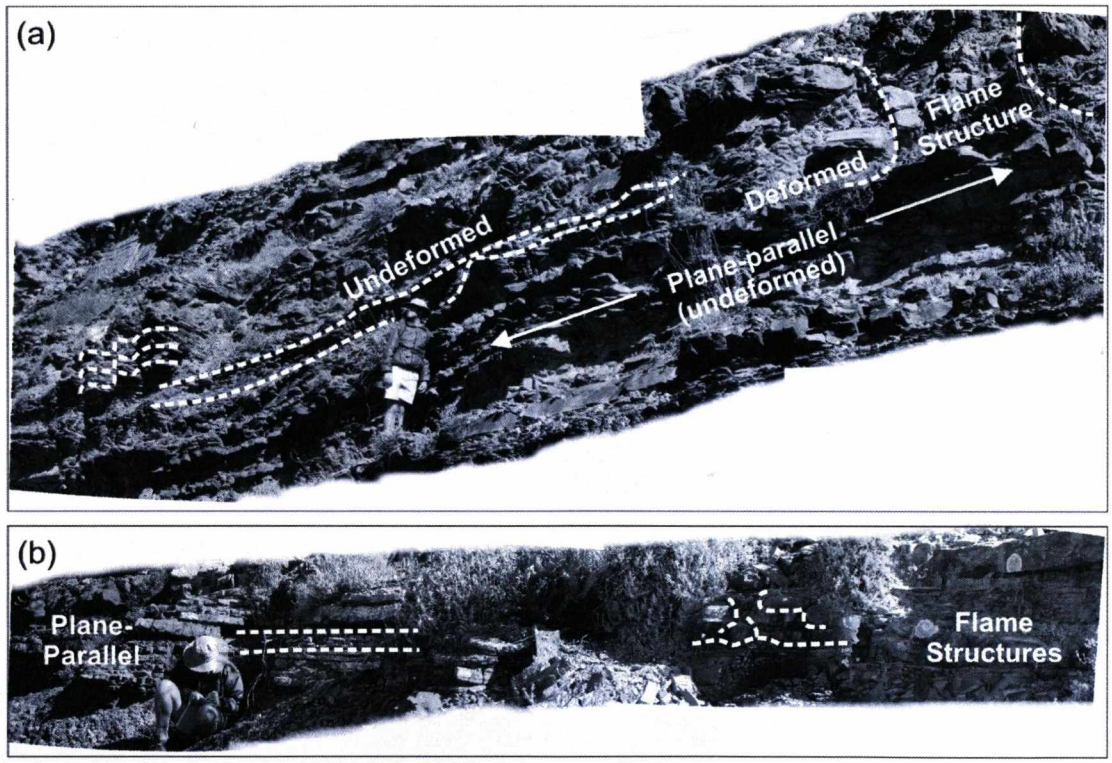

Figure 3.10: Large- (a) and small-scale (b) lateral changes in deformation in Drooge Kloof outcrop. No faulting or erosion is observed between deformed and undeformed material and this abrupt transition, therefore, indicates that the deformation occurred *in situ*.

The deformed beds were originally deposited from low to high concentration turbidity currents (lithofacies 2a and 2b). The capping structureless siltstone, the scarcity of preserved primary structures in the flame, the occurrence of (hydroplastic) lineations, and the ruptured sandstone beds and drag of underlying layers indicate that sediment-rich fluids escaped upward during development of the

flame structures. Therefore, these flames can be considered as a type of water escape structure (*sensu* Lowe, 1975). In addition, the ruptured sandstone may have loaded underlying units in response to extraction of fluids and sediment from units below, causing load structures (*sensu* Owen, 2003).

Based on the textural similarity and physical connection between the flame and the capping structureless siltstone bed combined with the infilling of topographic lows by overlying sandstone beds, it is interpreted that the deformation occurred at or near the seabed soon after deposition. In addition, the undulating top surfaces of deformed intervals indicate reworking by seabed currents (scours and ripples) (cf. Figure 3.9). The deposits were deformed *in situ* as indicated by the vertical orientation of the structures (absence of horizontal shear features such as asymmetric/vergent folding or overturned flames) and by the lateral transition into undeformed strata without indication of major disruptions like faults and erosion (cf. Figure 3.10).

Experimental production of deformation structures (Anketell *et al.*, 1969) showed that upward propagating vertical flames were able to retain their integrity until they reached the sediment–water interface, where they disintegrate, disperse and re-deposit sediment over the top of the deformed bed. The structureless bed found in the Waterfall area is interpreted to follow a similar process. Sometimes a planar surface is formed between the lower deformed/contorted interval and the upper structureless fine-grained interval. These surfaces are generated by the lateral spreading of highly fluidized sediment that came into contact with water and can be misinterpreted as the product of erosion caused by unrelated density currents (Anketell *et al.*, 1969). Where the distinctive green structureless siltstones are found sandwiched between undisturbed bedding they are interpreted to have flowed onto the seabed away from the source flame that is not exposed in the outcrop plane. Figure 3.11 summarizes the interpreted evolution of the flame structures. This is similar to the sequence of events proposed by Hildebrandt & Egenhoff (2007) for the formation of flame structures in massive sandstone sheets in a shallow marine environment. Details on the processes involved in the formation of the structures are presented below.

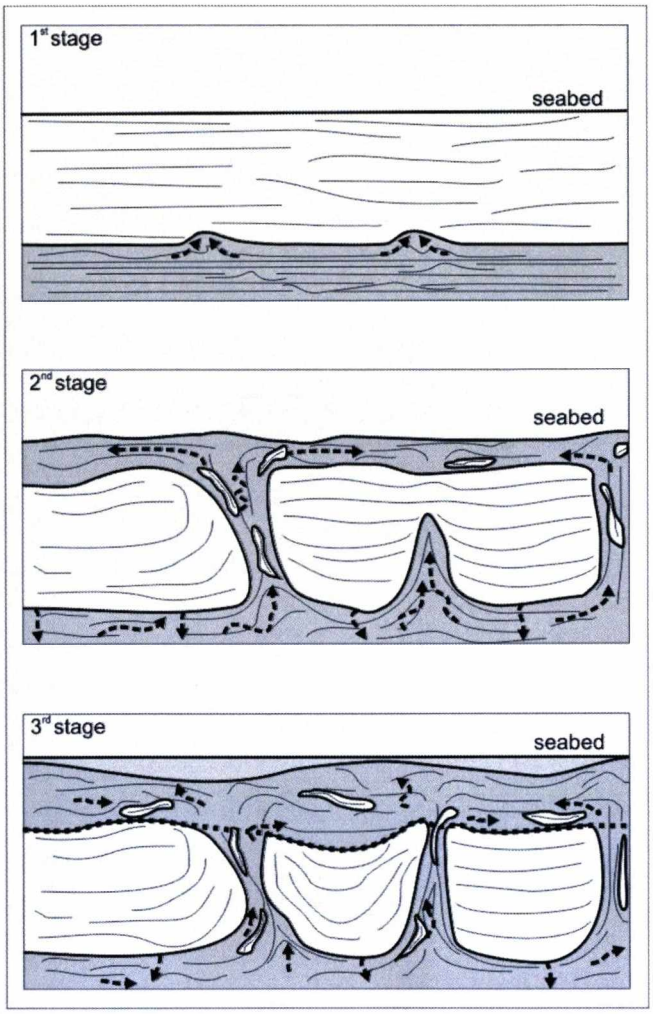

Figure 3.11: Cartoon to demonstrate the development of flame structures at Waterfall. In the first stage flames are nucleated in a lower siltstone bed with high pore pressures, approximately equidistant from each other and begin to migrate upward through the overlying fine sandstone bed. In the second stage this liquid-like material continues flowing upward resulting in the rupturing and folding of the non-consolidated sandstone. Occasionally, when it reaches the sea bottom the material begins to spread laterally and settles over the deformed sandstone. In the third stage, particle transportation gradually ceases. Topography is created on the seabed and later filled or exploited and scoured. Sometimes a surface resembling erosion is formed between the base of the debouched material and the contorted bed (dotted line in the 3rd stage). The origin of this surface is related to the deformation process without the action of any external agent (see text for detail). No scale implied.

Palaeocurrents and orientations of the flame structures

Sole marks (grooves) on the bases of undeformed sandstones indicate a SW-NE palaeocurrent azimuth, parallel to the interpreted NE-facing palaeoslope (Wild *et al.*, 2005; Hodgson *et al.*, 2006, Luthi *et al.*, 2006). Internal current ripple laminations within the laminated thin beds, however, indicate transport towards the NW (Figure 3.12a, b). The high angle between the grooves and the internal ripples varies from around 30° in beds at the base of the section, to around 90° in beds in the middle of the section. These data indicate an increasing divergence in palaeoflow

between the denser, basal part of each flow and its more dilute upper section, which appears to have been increasingly influenced by a local gradient at a high angle to the regional palaeoslope. The orientation of the internal ripples is consistent with the lateral splay depositional model proposed by Wild *et al.* (2005), in which flows spilled from a southern slope channel complex. An alternative interpretation for the divergence in flow direction of a single flow is the oblique reflection or deflection of the turbidity currents off intrabasinal topography (e.g. Kneller et al. 1991; Haughton 1994). However, regional mapping of Unit 5 shows no consistent pattern of thinning to indicate onlap (Wild 2005), plus the consistent relationship of bed base grooves and internal ripples over the Drooge Kloof area (Fig. 3.2), does not support the existence of local topography within Unit 5.

The orientation of the elongate flame structures shows a consistent WSW-ENE direction (Figure 3.12c), which is sub-parallel to the regional palaeoslope dip. The importance and interpretation of these orientations in the understanding of the deformational processes will be discussed below.

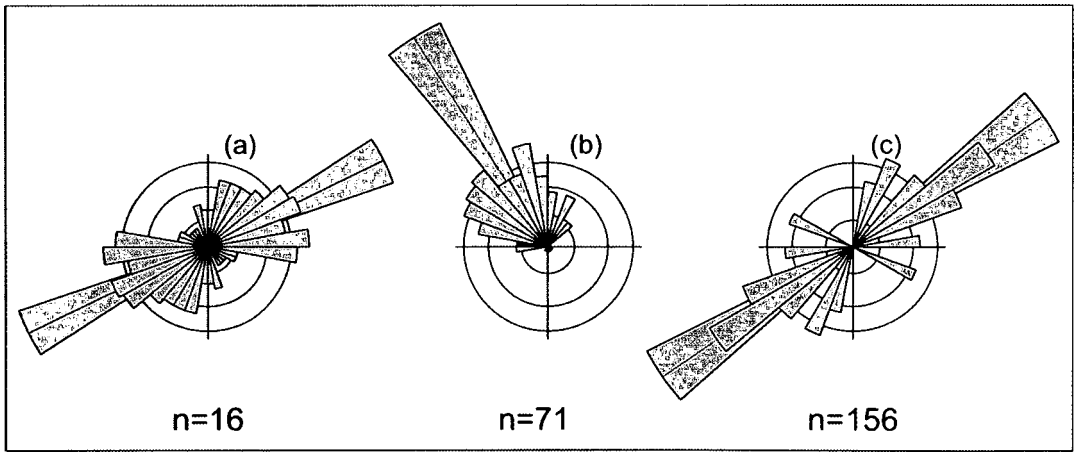

Figure 3.12: Orientation of sedimentary transportation at Waterfall: (a) grooves and (b) symmetrical ripples. Orientation of flame structures (c). This figure is complimented by Figures 3.17 and 3.18.

Ground Penetrating Radar acquisition

The Ground Penetrating Radar (GPR) survey was useful to verify the orientation of the flames in 3D and provides a high resolution link to the likely expression of geometrically similar but larger features that could occur in seismic reflection datasets from submarine slope environments. Here is presented a summary

of the results and interpretation. Detailed analyses are showing on Chapter 5. The target structures, extrapolated from the outcrop face, lay 2-5 m below the surface of exposed strata. After a simple processing workflow, the best result was obtained at 100 MHz frequency of acquisition (Table 3.1).

Acquisition Parameters		Processing workflow
Nominal antenna frequency	100MHz / 200MHz	Remove dead traces
Pulse Voltage	400V	Time cut
Recording length	512ns	Dewowing
Sample interval	0.8ns	AGC
Vertical stack	32	(Notchfilter)
Separation	1.0m (100MHz) 0.5m (200MHz)	Bandpass filter
		(Deconvolution)
Step size	0.1m	Migration

Table 3.1: Ground penetrating radar (GPR) survey acquisition and processing parameters.

In line Wf101, a clearly imaged vertical feature, characterized by low amplitude and discontinuous internal horizons, appears at the SW limit of the line and is interpreted as the expression of a flame structure (Figure 3.13). A flame structure of similar size and shape at the same stratigraphic interval can be observed at outcrop, 10 m from the GPR line (inset map in Figure 3.13). The laterally continuous high amplitude folded horizon positioned at 40 ns is interpreted as the expression of the ruptured sandstones. Just above and truncating the high amplitude folded horizon is a continuous low amplitude horizon that is interpreted as the capping homogeneous siltstone linked to the flames. The radar facies of the vertical structure (flame) and the truncating horizon are quite similar. At 20ns, a very high amplitude horizon just above the highest vertical feature and truncating the underlying horizons can be directly correlated to the main level of top scours and infill in the parent outcrop (cf. Figures 3.9 and 3.11). The horizons discontinuities, interpreted as produced by vertical structures, are oriented to ENE, essentially the same orientation obtained from outcrop measurements. A secondary trend points to the N.

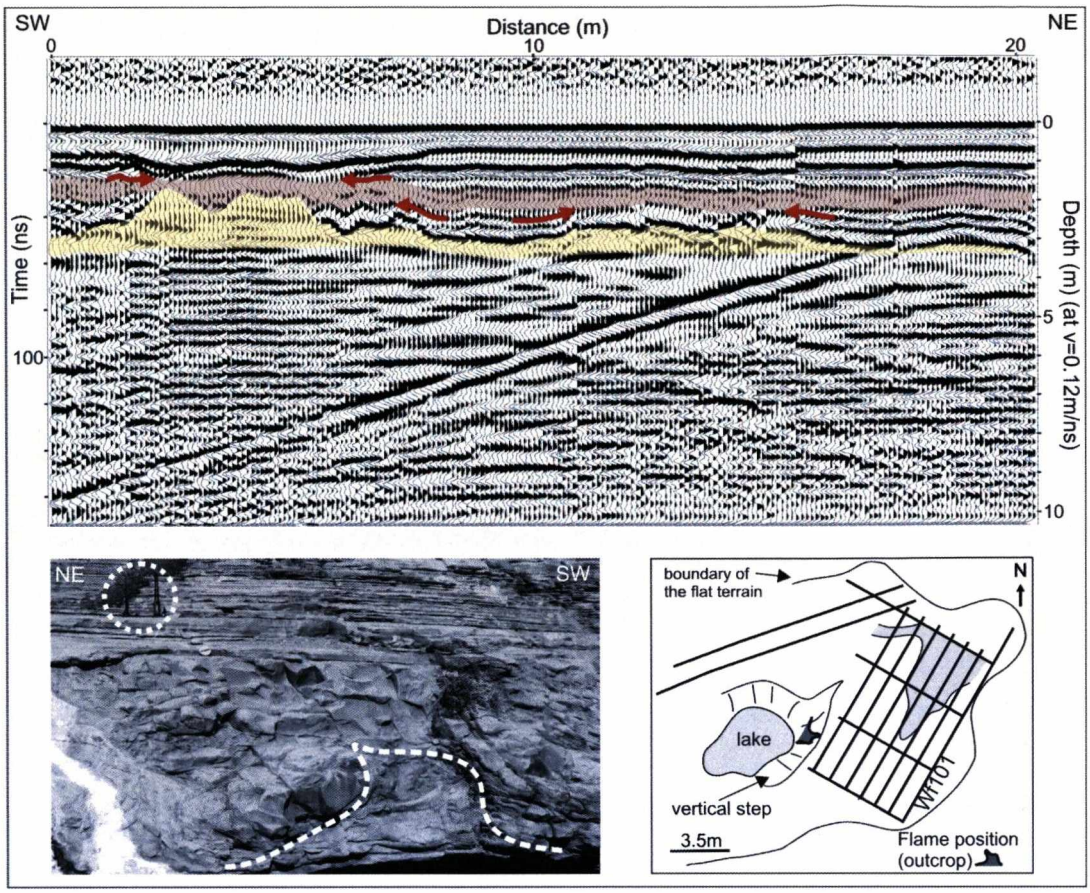

Figure 3.13: GPR section (Wf101) acquired across a surface just above one thick deformed layer and oblique to the general orientation of flames. The section captures some important features described in the outcrops: the light yellow group of horizons, with an undulating top is interpreted as the register of flame structures. The light orange horizon is interpreted as the structureless siltstone that is in connection with the flames at the SW part of the section. The folded strong reflectors between the coloured reflectors are interpreted as the ruptured sandstones. The orange horizons are truncating (see lower red arrows) the horizons interpreted as ruptured sandstones, as observed at the outcrops. The depression above the bigger flame is equivalent to the level of infill and scour at the outcrop. . The strong reflector dipping at a high angle to the NW is interpreted as a lateral reflection associated with a recent fracture and is not related to the original deposition or deformation. The photograph shows a lateral view of one flame occurring at the same level as the one interpreted in the GPR section. The GPR antenna (1 m high, in the white dotted circle) shows the approximate position of the section described above. The map shows the distribution of the acquired lines, and the relative position of line Wf101 and the flame described. It corresponds to part of the white coloured section on the Waterfall area on Figure 3.2. See Appendix 1 for GPR line coordinates.

3.1.4 Statistical analysis

Morphological measurements acquired from 180 flame structures included a) distance between adjacent flames; (b) basal flame width; (c) width at the narrowest point; (d) deformed layer thickness; (e) flame height; and (f) structureless siltstone thickness (Figure 3.14). This dataset was collected from seven different intervals (DA to DG) that varied in thickness but not in deformation style. The use of statistics

in the study of soft-sediment deformation structures is rarely cited (Potter & Pettijohn, 1963; Owen, 1995), despite being a common method in sedimentological investigations (e.g. Harper, 1998; Chen & Hiscott 1999a, b; Felletti, 2004; Sylvester, 2007). The presence of several intervals of different thicknesses with multiple examples of the same deformation feature facilitates the application of statistical analysis to improve the understanding of formation mechanisms. Methodology of data collection is discussed in Appendix 2 and raw data for statistical studies are listed considering each interval in Appendix 3, which contains the data for statistical studies in the other areas (Tanqua and Laingsburg depocentres at Karoo Basin and Neuquén Basin) discussed along this thesis.

After data preparation, simple linear regression analysis was undertaken to verify the relationship and correlation between the parameters at different scales. The numerical results presented in each graph are least square regression line, the correlation (r) and coefficient of determination (r^2) values. They were calculated through the use of the software Minitab (trademark of Minitab, Inc.). The least square regression line was chosen because it is one of the best ways to attenuate the errors related to the predicted straight line and the sum of the errors for each point. Values of r and r^2 give quantitative indication of the degree of strength among the studied population and the proportion of the response variable (y) that can be explained by the regression line model, respectively (Chatfield, 1989; Moore and McCabe, 2006). In general terms, bigger the values of r and r^2 stronger will be the relationship between the populations. Each parameter was analysed, both collectively and on a layer by layer basis. The influence of variability within a single deformed layer is discussed in Appendix 4. The following are the most significant cross-plotted parameters that are summarized for all surveyed beds.

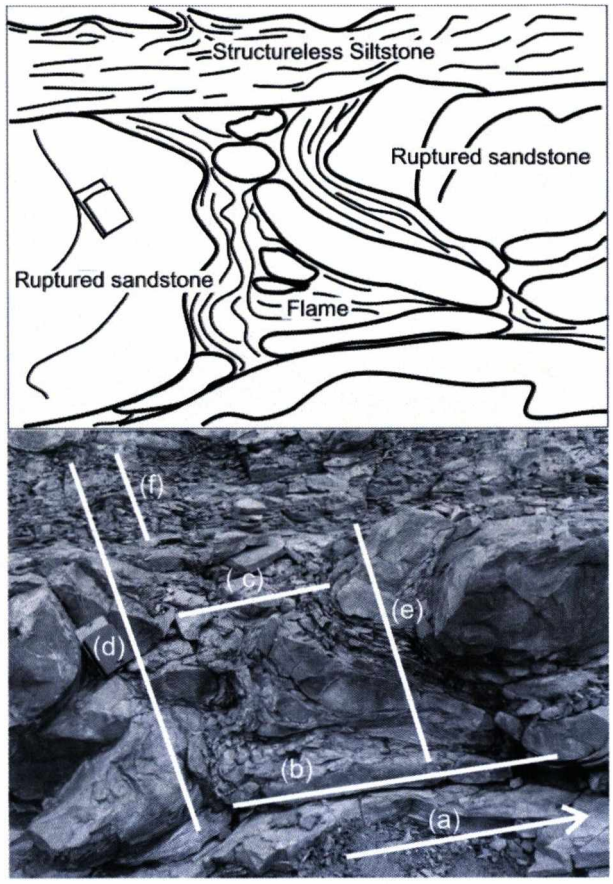

Figure 3.14: Sketch of a single flame structure showing the three main elements: flame, ruptured sandstone and structureless siltstone. Annotated photograph indicates the main geometrical parameters measured from 180 flames in 7 distinct intervals, for statistical evaluation: (a) distance between adjacent flames; (b) basal flame width; (c) width at the narrowest point; (d) deformed layer thickness; (e) flame height; and (f) structureless siltstone thickness.

Distance between adjacent flames (DN) *versus* basal width of flames (BW)

Statistical assessment

A positive linear association was obtained for the relationship between these two parameters. As the distance between adjacent structures increases, the basal dimension of the flames increase in a ratio DN/BW varying from 1:1 to 2:1 (Figure 3.15a). A similar positive linear correlation was obtained when considering each layer individually, although low values of correlation and high ratios occur for some intervals.

Interpretation

It is not clear what controlled the nucleation of the analysed flames. Factors such as material rheology, layer thickness, previous discontinuities, grain size and

pore-pressure may determine flame nucleation position and size (Nichols *et al.*, 1994). Rodríguez-Pascua *et al.* (2000) analysing pillow structures in lacustrine deposits, obtained similar ratios (2:1) when comparing synform range (distance between flames) and flame height. The ratio DN/BW around 2:1 partially reflects the differences of form and dimension between the anticlines (flames) and synclines (base of the ruptured sandstone) (cf. Figure 3.11). In this case, the distinct shape of the synforms (load casts) and antiforms (flames) can be explained in part by differential amplification due to the fluidization within the flame, which enhances the mobility of the sediment by adding to an upward-directed stress (Allen, 1982; Owen, 2003). The regular spacing between flames in each interval suggests, in case of the inexistence of structural controls (e.g. a regular fracture net), a synchronous and instantaneous origin for the structures. Also, it is an indication of the pervasiveness of the structure (Owen, 1985).

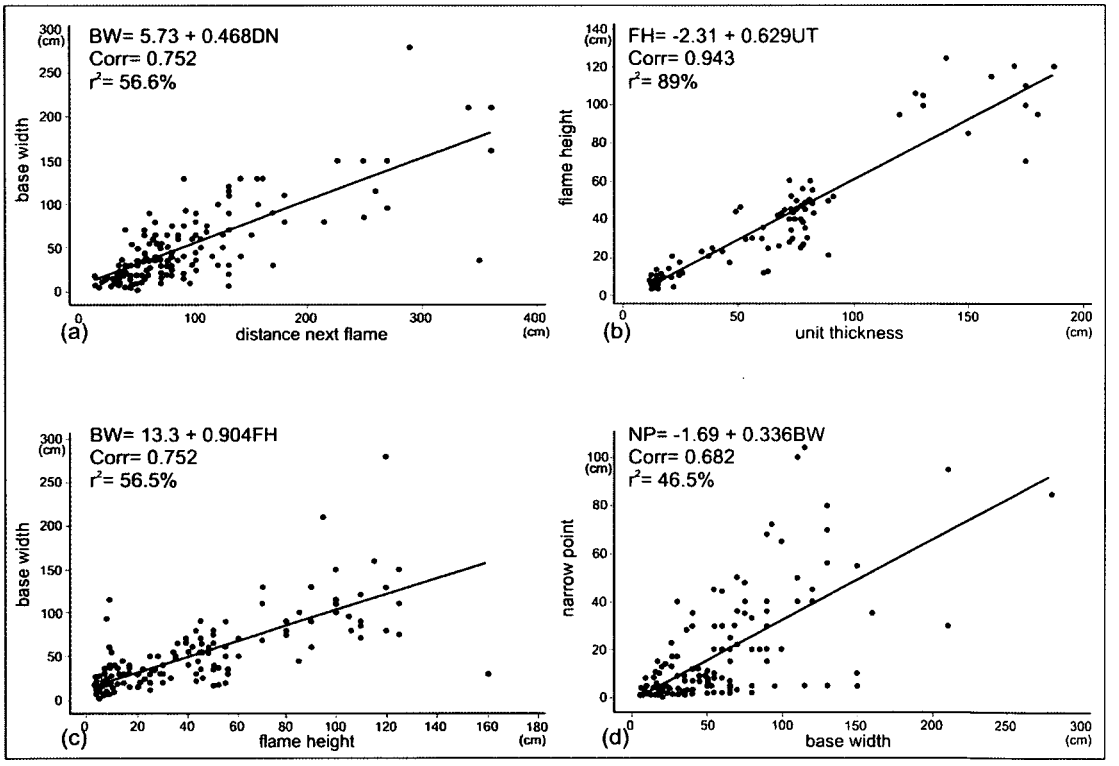

Figure 3.15: Least-square regression lines for the comparative study between distinct geometrical flame attributes: (a) Flame basal width (BW) as a function of the distance between adjacent flames (DN); (b) Height (FH) as a function of the deformed layer thickness (UT); (c) Flame basal width (BW) as a function of the flame height (FH); (d) Flame width at the narrowest position (NP) as a function of the basal width (BW). The dispersion on (d) is addressed in Figure 3.16. See text for detailed discussion.

Deformed layer thickness (UT) *versus* flame height (FH)

Statistical assessment

The deformed layer involves not only the vertical flame and the ruptured sandstone but also the structureless siltstone/very fine-grained sandstone deposited above the flame during deformation. A strong positive linear association is obtained for this relationship; as the deformed layer thickens, the associated flame gets higher, in a ratio UT/FH varying between 3:2 and 2:1 (Figure 3.15b). The correlation is poor when considering each layer in isolation, due to the effect of flame truncation in some cases.

Interpretation

The influence of layer thickness on the dimensions of the sedimentary deformation features in response to liquefaction and fluidization is reported in theoretical, laboratory and outcrop studies (e.g. Anketell & Dżułyński, 1968; Anketell *et al.*, 1970; Allen, 1985a, b; Nichols *et al.*, 1994; Owen, 1996b; Hindmarsh & Rijsdijk, 2000; Rijsdijk, 2001). Anketell & Dżułyński (1968) and Nichols *et al.*, (1994) modelled structures generated by unstable layer density contrasts and fluid escape mechanisms, respectively. They found a direct relationship between layer thickness and dimensions of the deformation feature, which is in accordance with our regression analysis. Other parameters analysed by these authors, such as change in density and strength, viscosity ratio, pressure variation and grain size and shape, were not evaluated in this work. It is interpreted that similar conditions for the deformation occurred in the successive layers.

In many cases the flame completely traverses the sandstone suggesting a UT/FH ratio equal to 1; however ratios >1 are obtained due to the presence of the structureless capping siltstone, which is part of the deformed bed but not part of the flame. Despite not reported with the same frequency of the events verified in laboratory experiments, this relationship between bed thickness and height of flame like structures has been noticed in nature. Allen (1985b) studied recent wrinkle marks (a centimetre scale intertidal sedimentary structure formed due to aseismic soft-sediment loading) and showed that the horizontal distance between the centres of pillow-shaped deformation features (DN) was 2-4 times the sand-layer thickness (UT). Here, values of approximately 1 were obtained for this same relationship. We

consider that differences in grain size, sediment composition, dimension of the structures and lithification can explain this difference.

Flame height (FH) *versus* flame basal width (BW)

Statistical assessment

A positive least-square regression line was obtained with a good correlation between the two parameters (Figure 3.15c). Outlier values associated with unusual flame shapes did not influence the results. An increase in the height of the flame is accompanied by an increase in the width of the flame, providing a FH/BW ratio of approximately 1:1. Individually, each layer shows lower values for correlation and ratios between 1:1 and 1:4.

Interpretation

Anketell *et al.* (1970) studied systems with reverse density gradients and predicted that systems developed in the absence of significant shear stress produce structures with the same proportions, at different scales. The dimensions of the structures were controlled by factors including viscosity ratio and thickness of layer (see above) involved in the deformation. This relationship is intrinsic to each structure. By analogy, the high degree of correlation can be interpreted as an indicator that similar sedimentological and stress conditions persisted during the deformation of distinct beds, generating structures with proportional horizontal and vertical dimensions.

Flame basal width (BW) *versus* flame narrowest point (NP)

Statistical assessment

This scatterplot is strongly influenced by the final shape of the flame, resulting in a positive least-square regression line with strong dispersion from the fitted line for the highest values (Figure 3.15d). The BW/NP ratio is 3:1. For each layer, despite a high degree of correlation and positive regression, the least-square regression lines show a distinct orientation (ratios varying from 20:1 to 1:1) that give

a fan-like pattern to the data. It is observed that the regression lines for each type of flame (cf. Figure 3.8) follow similar trends and can be clustered into two groups of narrow and large flames positioned below and above the total population regression line for BW vs. NP (Figure 3.16).

Interpretation

According to Allen (1982), the flames (which form anticlines) must grow at a rate inversely proportional to their width. Conceptually, fluidization will occur if the rate of growth equals or exceeds the settling rate of the grains. Based only on these aspects and considering the dome and spike shapes as end members of the flame shape classification (cf. Figure 3.8); it is suggested that the rate of flow during the formation of the spike-flames was greater than for the dome-flames. As distinct layers show the predominance of a certain shape, it is interpreted that slight differences in the grain concentration, density and size could impose distinct viscosity conditions during the deformation of each layer, which governed the final configuration of the flame.

The graph of the least square regression line for each bed plotted with least square regression lines for each flame type demonstrates the strong influence that flame morphology has on the dispersion of data in the relationship between BW and NP (Figure 3.16). The concentration of points in the upper part is a function of the number of samples; approximately 60% of all samples, that fit categories 1 (regular) and 7 (complex). The distribution of the regression lines for each bed emphasizes the relative importance of each flame style in the final configuration of the regression line. The best example is the bed C, where the flames of classes 3 and 6 control the positioning of the regression line. Also, bed A regression line is the one whose orientation is closer to the regression line for all samples. This behaviour can be explained by the fact that bed A contains the greatest variety of flame types.

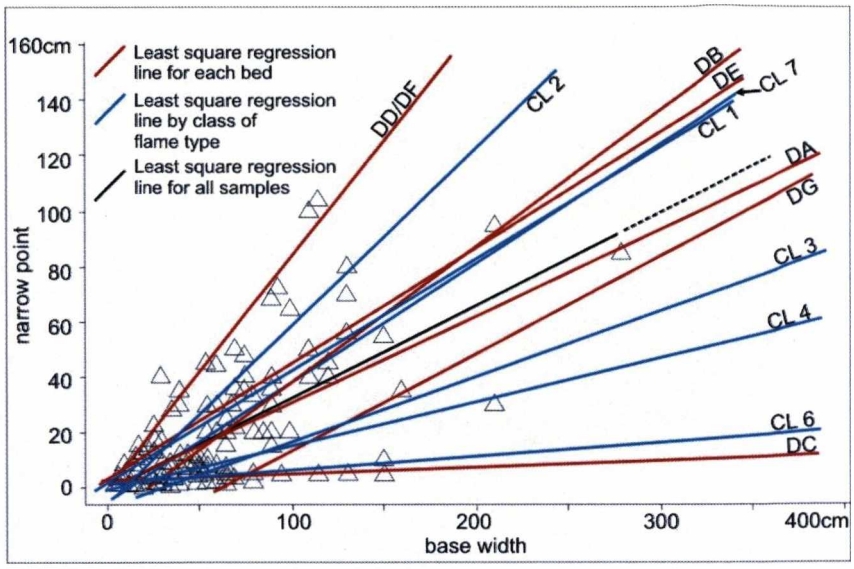

Figure 3.16: In order to emphasize the influence of teach type of flame (cf. Figure 3.8) in the relation between flame width at the narrowest point *versus* flame base width the extrapolation of the least-square regression lines are plotted for each bed (DA to DG) (red lines) and for each class of flame type (blue lines): regular (CL 1), trapezoidal (CL2), cusp (CL 3), x shape (CL 4), spike (CL 6) and complex (CL 7). Dome type (CL 5) has no statistical significance in the studied interval. The regression line for the whole population divides the graph into two distinct areas: the lower interval, dominated by the cusp (CL 3), x shape (CL4) and spike (CL 6) types; and the upper part dominated by flames with the regular (CL 1), trapezoidal (CL 2) and complex (CL 7) types. The lower group is characterized by narrow flames and the upper group by large flames. See text for discussion.

From the statistical relations we conclude that fluidization had an important role in bed deformation and this occurred under similar conditions of stress for a succession of beds. The data suggest that deformation occurred instantaneously and synchronously through each deformed layer rather than nucleating at a few discrete points and spreading laterally.

3.1.5. Discussion and interpretation

Owen (1987) proposed four key elements that control soft-sediment deformation: i) the initial characteristics of the sediment (e.g. grain size and packing); ii) the mechanism required to reduce the sediment strength; iii) the likely trigger mechanism, related to the action of an external agent, and iv) the driving force for the deformation. Deformation structures in Waterfall area were analysed based on these criteria.

Initial conditions

Soft-sediment deformation features can have more than one origin and a variety of structures can be produced by a single process (Lowe, 1975, Allen, 1982, Mills, 1983, Owen, 1987). However, these phenomena are more prevalent in subaqueous environments with alternating muds and sands (Lowe, 1975), loose packing (Obermeier, 1996) and high sedimentation rates (Allen, 1982). The narrow grain size range in the Karoo deposits and the interbedded turbidity siltstone and fine-grained sandstone satisfy these conditions. Importantly the same style of soft-sediment deformation is not exhibited elsewhere in the Unit 5 stratigraphy in the Tanqua area (which can be mapped for 40 km obliquely down dip) despite similar high rates of deposition and grain-size range (Wild, 2005; Wild *et al.*, 2005; Hodgson *et al*, 2006). This suggests that additional phenomena specific to the local study area were important in driving the deformation.

Deformation mechanism

The dominant morphology of the soft-sediment structures in the Drooge Kloof area reflects vertical grain dislocation by fluid escape (flames and ruptured sandstones) with secondary density loading caused by the ruptured sandstone (cf. Figure 3.11).

Lowe (1975) considered that sediment consolidation could result in water escape structures being generated by both liquefaction and fluidization. Vertical fluid escape occurs during the phase of re-sedimentation of a liquefied layer, generating a range of soft-sediment deformation structures (from pillars and dishes to load structures and dykes). During water escape, high flow rates favour fluidization, resulting in rapid bed expansion, increase in porosity and the sediment framework ceases to be grain-supported and becomes fluid-supported.

Load structures (*sensu* Owen, 2003) are formed by downward grain movement of an upper, denser layer into a lower bed, creating load casts and pseudonodules. Concomitant to the load cast/pseudonodule evolution, upward movement of the less dense layer results in flame structures. While liquefaction is considered to be the primary mechanism for the generation of load structures, the contribution of fluidization is not identified clearly in the geological record, despite the recognition that it is an important process (Allen, 1982, Owen, 2003, Maltman &

Bolton, 2003). In experimental modelling of seismites, Owen (1996b) and Moretti *et al.* (1999) emphasized the importance of liquefaction and fluidization as the main deformation mechanism for load structures and flame structures, respectively.

The relative importance of liquefaction *versus* fluidization in the studied section is assessed by morphological criteria: the lack of primary sedimentary structures in the flames and associated beds can be an indicator of turbulence caused by fluidization (Lowe, 1975). The vertical grooves in the contact area between the flame and the ruptured sandstone coupled with drag of the basal layer, both caused by the destabilization and upward movement of the particles, also indicate fluidization. The occurrence of the same style of deformation at distinct layers is an indicator that fluidization and liquefaction persisted through time as the main deformational mechanisms.

Trigger mechanism

The occurrence of a trigger is fundamental to the initiation of soft-sediment deformation (Maltman, 1994, Jones & Omoto, 2000, Maltman & Bolton, 2003). The increase in pore pressure is normally accompanied by a weakening of sediment strength caused by some type of loading or shearing, where pore fluid dissipation is prohibited or suppressed. Owen (1987) makes a distinction between three types of trigger: (i) those that influence directly the pore fluid pressure (ground water movement and escape of fluids from underlying layers), (ii) those related to impulsive stress (rapid sediment deposition, slope failure in response to undercutting and oversteepening, breaking waves and flood surges), and (iii) those associated with cyclic stress (earthquakes, surface waves, turbulent pressure associated with flow separation and glacial loading). Locat & Lee (2002), studying submarine landslides, outlined the same loading processes plus possible contributions by gas charging, gas hydrate disassociation, low tides, seepage and volcanic island processes.

In ancient systems, earthquake-induced deformation is commonly cited as the most likely trigger of soft-sediment deformation in diverse environments and tectonic settings (e.g. Moretti, 2000; Rosseti & Santos Jr, 2003; Neuwerth *et al.*, 2006; Moretti & Sabato, 2007; Sandeep & Jain, 2007; Spalutto *et al.*, 2007). Alternative trigger mechanisms invoked include rapid sediment deposition (Postma, 1983, Stromberg & Bluck, 1997; Moretti *et al.*, 2001), differential loading

(Needham, 1978; Dasgupta, 1998), storm waves (Alfaro *et al.*, 2002), groundwater movements (Owen, 1996a), steep depositional slope (Kleist, 1974; Postma, 1983) and oversteepening due to erosion (Alexander, 1987).

Although earthquake activity is traditionally favoured as an explanation for deformed sediments in ancient and modern environments (Obermeier, 1996; Sultan *et al.*, 2004; Montenat *et al.*, 2007), there is no evidence for seismicity at the time of deposition of the studied section, in this area of the Karoo Basin. The restricted extent of the deformation intervals (hundreds of metres) and the limited spatial and stratigraphic occurrence of this style of deformation are inconsistent with the larger area and stratigraphic interval likely to be affected by earthquake shock (cf. Obermeier, 1996). We note with caution the potential for circular reasoning in the interpretation of trigger mechanisms for *in situ* deformed intervals being earthquake induced (seismites), which could be used to infer a seismically-active setting, and vice versa.

The geological setting, the narrow stratigraphic interval affected, the deformation mechanism, and the discrete spatial distribution of deformation suggests rapid sediment deposition, differential loading, and locally steepened gradients as plausible deformation trigger mechanisms. When considering these mechanisms, there is no indication that the rate of deposition in the Waterfall area was greater than elsewhere in Unit 5 (Wild *et al.*, 2005; Hodgson *et al.*, 2006). Moreover, the possibility of differential loading caused by the adjacent Groot Hangklip and Klein Hangklip channel complex systems (cf. Figure 3.2) (Wild *et al.*, 2005) is not considered likely, because of the lateral distance to the axis of the channel complexes (>2 km) and absence of incision surfaces related to the channel complexes at the stratigraphic level of the studied interval.

The inherited topography, indicated by the lateral onlap and thinning of the underlying fans onto a local high in the study area (estimated at >1° by Hodgson *et al.*, 2006) resulted in a NW oriented local gradient (Figures 3.17a, b). Palaeocurrent indicators in the lateral splay deposits identify flow to the N-NW, at a high angle to the regional NE palaeoslope but approximately parallel to the local higher gradient inherited palaeoslope (Figure 3.17c). Therefore it is suggested that the association of an inherited topographic slope and the rapid deposition of lateral splay deposits caused a steeper local gradient. This gradient established an interstitial shear stress through slight movement and stretching (but not detachment) of parts of the

sediment pile, which increased pore pressures (Figure 3.17d). The presence of fine-grained sediment prevented the pore fluid from being drained which caused overpressure (Yassir, 1990) and subsequent fluidization of the bed and escape of fluids, when a threshold of stretching and pore pressures was exceeded.

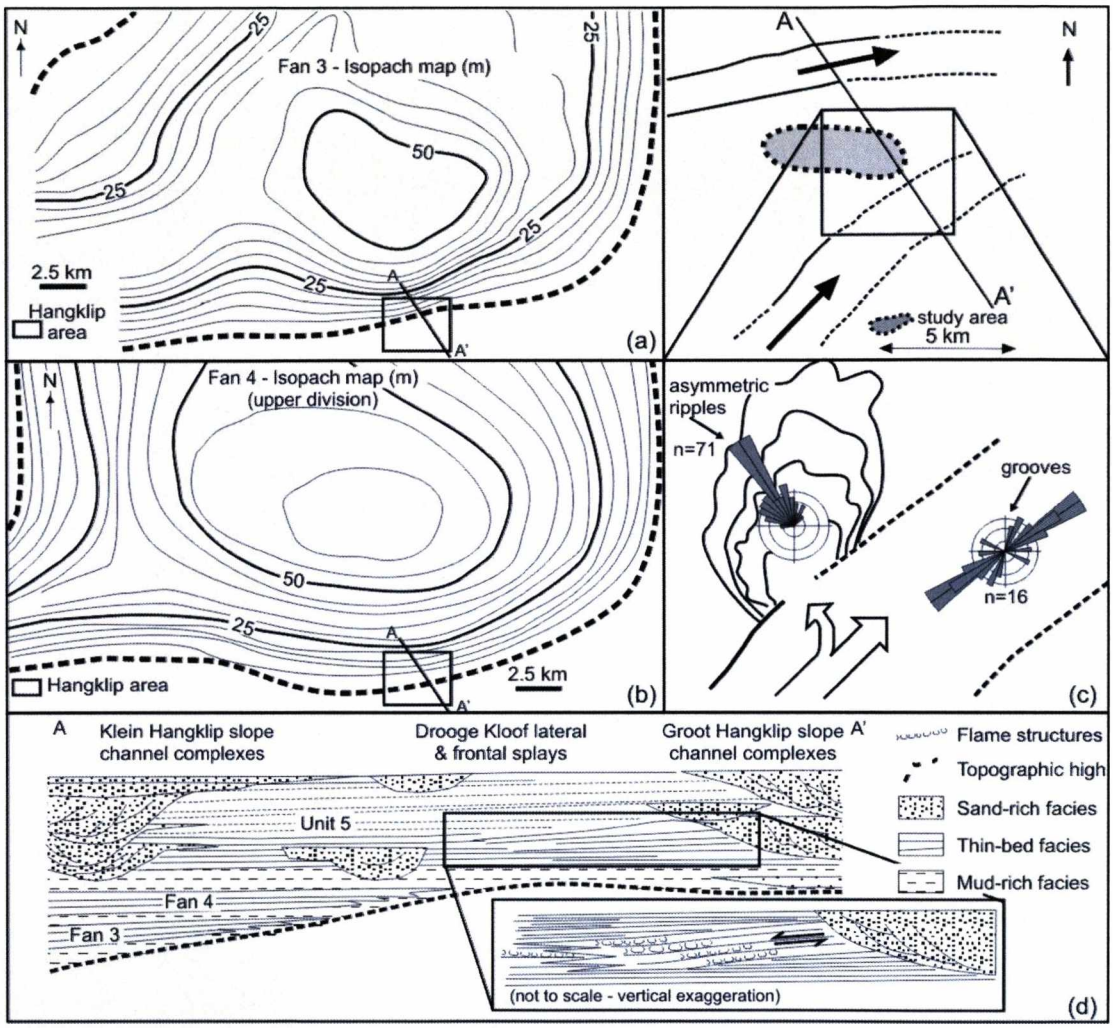

Figure 3.17: Environmental setting of deformation. (a) and (b) Isopach maps for the underlying Fans 3 and 4 respectively, showing abrupt thinning onto a palaeotopographic high in the study area indicating a slope of >1° (modified from Hodgson *et al.* 2006). (c) Palaeogeographic reconstruction, showing the study area between the two main channel complexes: Groot Hangklip (south) and Klein Hangklip (north), modified from Wild *et al.* (2005). Note, in the detail, the high angle between the grooves, which provides the general orientation for the regional palaeoslope, and the asymmetric ripples, that indicate deposition in a lateral splay. (d) Line A-A' cross-section parallel to the orientation of the asymmetric ripples and approximately orthogonal to the strike of the topographic high, showing the Drooge Kloof/Waterfall study section between the two channel complexes (from Wild *et al.*, 2005). This section shows the pinchout of the underlying fans 3 and 4 against a topographic high, and the flame rich NW oriented lateral splay deposits in Unit 5.

Driving force

In general, the deformation mechanism activated by a single trigger is not enough to cause substantial deformation in the sediment (Owen, 1987). A further condition must occur in tandem with the deformation mechanism in order to impose an additional deviatoric stress to cause effective deformation (strain). This 'driving force system' (*sensu* Owen, 1987) is strongly influenced by the depositional environment and can be organized into four classes (Allen, 1982; Owen, 1987): (i) a downward component associated with depositional slope, (ii) non-uniform distribution of the confining load, (iii) gravitationally unstable density gradient, and (iv) shear stress (tangential or vertical) acting within or at the surface.

The most common soft-sediment structures found in the Drooge Kloof area are water escape structures, indicating that grain movement was controlled by the vertical shear stress (driving force) due to the drag exerted by the vertically moving pore fluid during fluidization (Lowe, 1975; Owen, 1987). The occurrence of subsidiary load structures implies that an associated gravitational inverse density gradient was also present and resulted in the amplification of the original structures by the migration downwards of the ruptured sand beds (Allen, 1982; Owen, 1987; Hindmarsh & Rijsdijk, 2000). This was probably in response to the evacuation of underlying sediment during fluidization.

The elongation of the structures cannot be explained by these two driving forces and implies a local differential stress during remobilization (Collinson, 1994). Allen (1982) described a tendency of pseudonodules to be elongate parallel to the strike of the slope. However, elongate structures are also known to occur oblique or parallel to the palaeoslope direction (Allen, 1985b; Dasgupta, 1998; Moretti *et al.*, 2001). The WSW-ENE orientation of the elongated flames is sub-parallel to these channel complexes. The N-NW orientation of the current ripple lamination in undeformed beds indicates persistent flow at a high angle to the regional NE-directed palaeoslope during deposition of the host sediment. Despite not being interpreted as constructional levee deposits (Wild *et al.*, 2005), the general model is similar to one for the development of deformation in channel-levée complexes, where steep depositional gradients can result in sliding and/or slumping of levée-overbank deposits (e.g. Posamentier & Walker, 2006). In this study there is no evidence for down-slope detachment or dislocation of the lateral splay deposits to generate slumped intervals. However, 'attached' stretching of the sediment pile down local

slopes without detachment would be sufficient to create along strike weaknesses that control the spacing of elongate and vertically oriented, *in situ* structures From the discussion above, the deformation structures are thought to have been produced by the interaction of three driving forces: (1) a gravitationally inverse density gradient acting at the boundary of the deformed layers, (2) a vertical shear stress due to fluidization, and (3) a down-slope shear component related to the depositional slope of the lateral splay deposits (Figure 3.18).

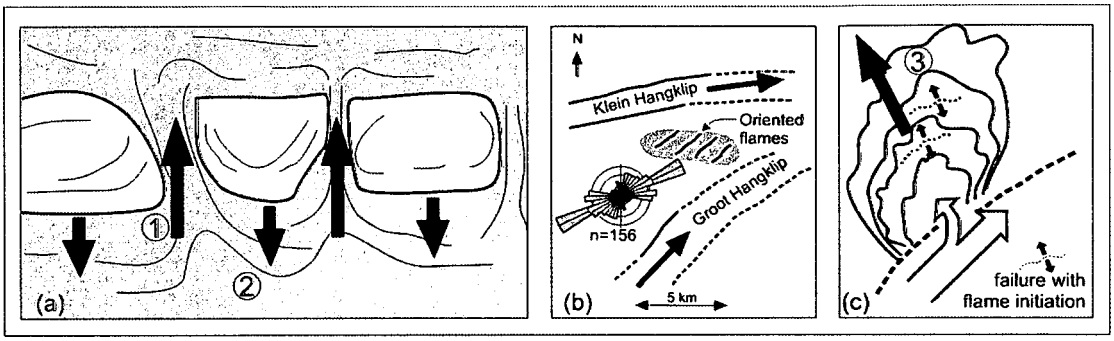

Figure 3.18: Driving forces present during the development of the studied structures. (a) Forces acting internally in each bed are represented by the upward vertical shear stress due to the fluidization (1) acting in the opposite direction to the secondary downward force associated with an inverse gradient caused by the denser deformed sandstone blocks (2). (b) Plan view with the flame orientation approximately down palaeoslope, indicated by the orientation of the channel complexes. This suggests a third driving force that controlled the elongation. (c) This force is interpreted as the down-slope component associated with lateral splay deposits in association with local steep topography (3) that created along-strike weakness planes in which the elongated flames developed. No scale implied in (a) and (c).

Length-scale of deformation

Two important aspects of this study, namely the orientation and the statistical response of the soft-sediment structures, require discussion on the occurrence of this style of deformation feature at larger scales. The orientation of structures indicates that a third dimension (horizontal length) of the flames can be longer than the components related to height and width (Figure 3.19). The statistical studies show that, over scales from centimetres to a few metres, structures follow a predictable linear pattern with a good level of correlation. Furthermore, the studied succession of alternating deformed-undeformed deposits reaches 30 m in the studied area. The GPR results indicate that at sub-seismic scales, the main structural and lithological variations related to the deformational features correspond to a radar-facies change.

Flame structures have been documented over a range of scales in this study (centimetre to metres scale), and the possibility of this style of deformation occurs at scales where identification is possible in seismic reflection sections is discussed here. The dimensions of flame structures and similar vertically oriented features as described from the outcrop studies are typically restricted to a few centimetres rarely reaching metre scale (e.g. Owen, 1995; Moretti, 2000; Rodríguez-Pascua *et al.*, 2000; Davies *et al.*, 2004; McLaughlin & Brett, 2004; Neuwerth *et al.*, 2006). Fluid escape structures reaching 4 m in height were found in an overlying stratigraphic succession (the Kookfontein Formation).

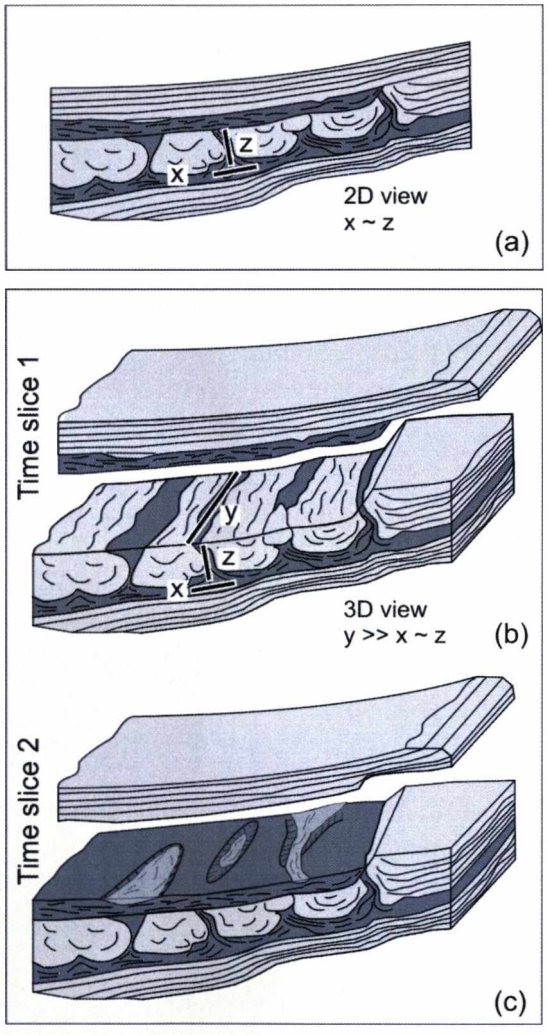

Figure 3.19: Cartoons to synthesize aspects of *in situ* deformed intervals. (a) Typical 2D (outcrop) with evenly spaced flames and an abrupt transition to undeformed strata. (b) Time slice 1 - 3D view of the same bed to show the elongation of the flame along y axis. (c) Time slice 2 - the surface expression of the debouched structureless siltstone on the seabed forms elongated topographic depressions that locally lead to scouring by turbidity current. No scale implied.

Laboratory studies have not attempted to predict the maximum height for flame structures before it fails because of the effects of gravity and lithostatic pressure.

However, large vertical *in situ* structures related to fluid escape such as gas chimneys and pock marks, are identifiable in seismic datasets (Hovland *et al.*, 1984; Heggland, 1998; Davies, 2003). Despite individual beds being under seismic resolution, it is expected that relatively thick packages (some tens of metres) of deformed beds, as in the Waterfall case, could develop a seismic response. It is expected that elongated flames would generate aligned tens of metre scale features (Figure 3.19) that could be detected in high resolution seismic data. Based on the response of the GPR in the present study, it is predicted that some large-scale *in situ* deformation packages could produce a 'chaotic' seismic facies similar to the seismic response of mass transport deposits (e.g. Embley, 1980; Damuth & Olson, 2001; Jenner *et al.*, 2007; Moscardelli & Wood, 2008). This seismic facies is interpreted to encompass a range of detached mass flow deposits on slopes including slides, slumps, and debrites, but rarely are *in situ* deformation processes invoked, which would have significant palaeo-environmental implications. Seismic modelling of soft-sediment deformation structures and their seismic response are discussed on Chapter 5.

3.1.6 Conclusions

From this study we conclude that processes resulting in intense deformation of metres thick sedimentary successions in submarine slope settings can occur *in situ* without significant dislocation of the sedimentary pile down slope. Elongate vertical fluid escape structures (flames) ruptured overlying sandstones and debouched homogenous silts onto the seabed via bed liquefaction and fluidization. Locally steepened gradients, in this case related to depositional topography, can overprint the effect of regional palaeoslope during build-up of pore pressures before the deformation process is initiated. The deformation was driven by a combination of stress orthogonal and parallel to bedding, expressed by fluid escape and density loading, and down slope stretching, respectively. Statistically significant geometrical/shape relationships for the products of soft-sediment deformation

processes are useful in helping to understand the trigger mechanisms and driving forces involved, and the prediction of distinct length scales of occurrence. Recognition and analysis of relatively large deformation structures at outcrop may assist in the interpretation of deformation features in seismic datasets. This approach stresses the importance of considering *in situ* deformation products as an alternative to detached down slope deformation deposits in subsurface datasets (core, well logs and seismic). Moreover, this study questions the validity of appealing to near-field or far-field earthquake activity as an explanation of large-scale *in situ* deformation; aseismic controls should be considered prior to invoking palaeoseismic controls on deformation processes.

3.2 – Neuquén Basin – Fortin 1° de Mayo and Chacay Melehue areas

3.2.1 Introduction

From Late Triassic to Early Jurassic time the Neuquén Basin of Western Argentina was characterized by extensional fault-controlled subsidence (Vergani *et al.*, 1995, Franzese *et al.*, 2006, cf. Chapter 2.3). Syn-rift continental siliciclastic/volcaniclastic deposits are overlain by deep marine mudstones and sandstone turbidite deposits of the Lower to Middle Jurassic Los Molles Formation (Legarreta & Uliana, 1996) (see Chapter 2), which is investigated here at the localities of Fortin 1° de Mayo and Chacay Melehue (cf. Figure 2.12). The objective was to analyse the soft-sediment deformation styles associated with a lower-slope channel complex at Fortin 1° de Mayo and with a progradational slope succession with intercalated mass transport deposits at Chacay Melehue. The two outcrops are located in the Main Andean Cordillera (Zapata & Folguera, 2005) and their present day exposure is related to the inversion of the Mesozoic rift system.

3.2.2 Fortin 1° de Mayo

General Aspects

The study area is a 300 m long road cut, up to 15 m high, on "Ruta 46", 75 km SW from the town of Zapala (Figure 3.20). It comprises a sand-prone turbidite channel complex from the Los Moles Formation (Figure 3.21), dated as Aalenian (Middle Jurassic) (Smith & Spalletti, 1995; Burgess & Flint, 1998) and characterized by a basal erosion surface that incises into marine mudstones; multiple internal erosion surfaces marked by truncation and the return to marine mudstones at the top of the succession. Bouma units, slump deposits and water escape structures are common features in those sandstones (Leanza *et al.*,2003). The tectonic structures at semi-regional scale are oriented NW-SE and were formed during the Cenozoic inversion of the former extensional Jurassic system. The most important structural elements around the study outcrop are the Catatún Anticline, and the Fortin 1° de Mayo and La Jardinera Synclines (Figure 3.21). The Fortin 1° de Mayo outcrop is

part of Catatún Anticline which form is picked out by the ridges formed by hard sandstone units.

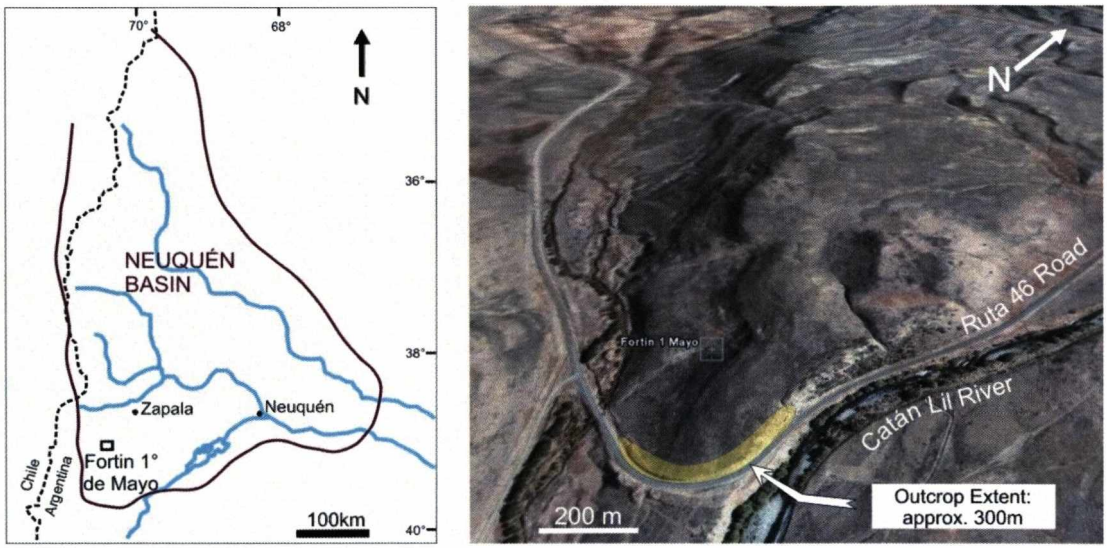

Figure 3.20: Location of the Fortin 1° de Mayo outcrop 75 km SW from the town of Zapala in the west border of the Neuquén Basin. The outcrop is approximately 300 m long in a road cut on the "Ruta 46" parallel to the Catán Lil River (Image from Google Earth ™).

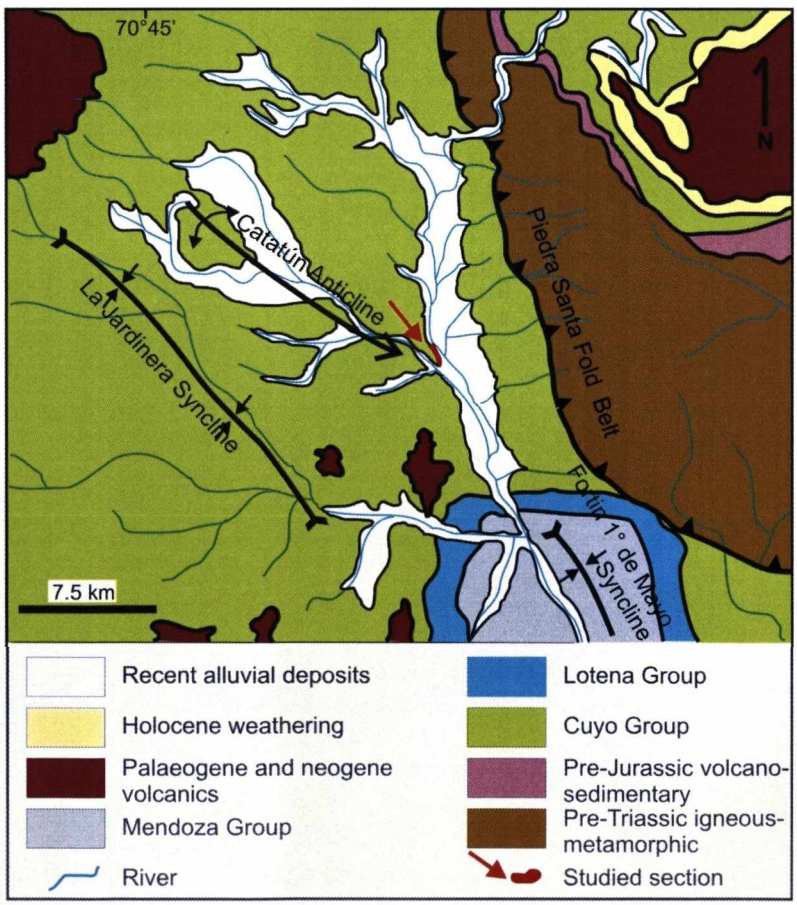

Figure 3.21: Geological map around Fortin 1° de Mayo. The studied outcrop is part of sandstone from the Los Molles Formation (modified from Leanza *et al.*, 2003).

The Aalenian in the southern Neuquén Basin represents a period of northward-progradation of the siliciclastic depositional system (Legarreta & Uliana, 1996). Rapid northward progradation of fluvial, deltaic and tidal systems provided a sediment source for deep-water deposition. The submarine channel units show evidence of sediment bypass that fed age–equivalent systems down-dip to the N-NE. By Aalenian time, fault topography was subdued and blanked by sediment but might still have been important in controlling routing of turbidity currents and large scale pattern of subsidence (Burgess & Flint, 1998) (Figure 3.22).

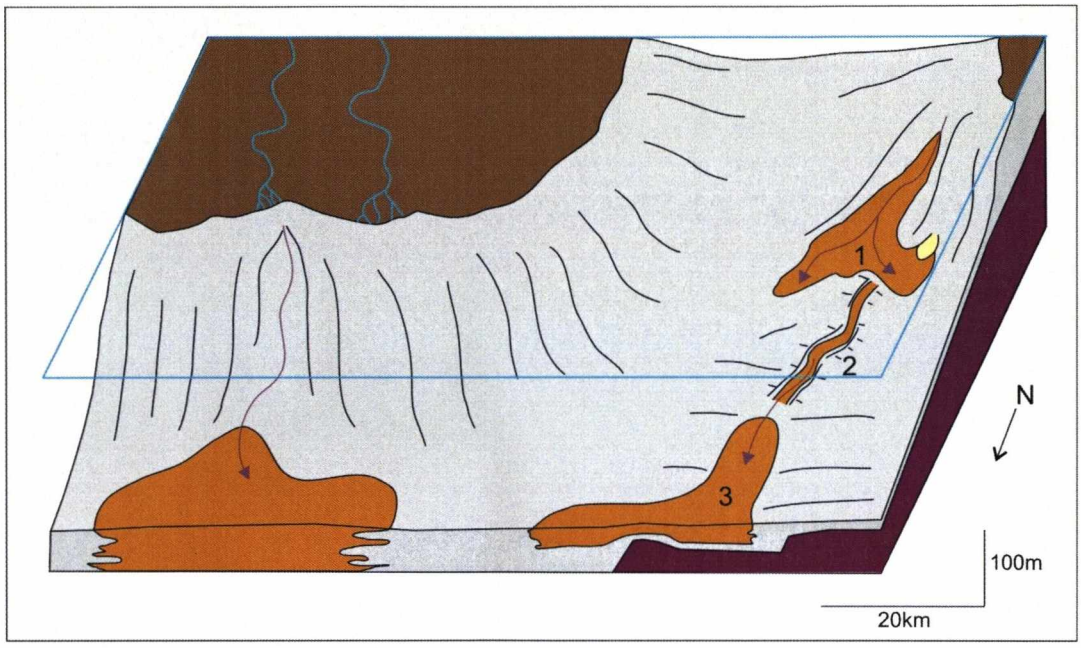

Figure 3.22: Schematic block diagram with the palaeogeography of Arroyo Jardinera (1), Fortin Primero de Mayo (2) and Morro del Aguilla (3) areas during the Aellian-Bajocian (180-169 Ma): they comprise a series of confined (Fortin Primero de Mayo) and unconfined (Arroyo Jardinera and Morro del Aguilla) turbidity deposits that are believed to be part of the same depositional system (after Burgess & Flint, 1998).

Description

Five logged sections (57 m total at cm scale resolution), were acquired along the outcrop. A composite log indicates a general fining-upward pattern, but with the intermediate section showing no preferential grading (Figure 3.23). The main lithofacies are: (i) coarse-grained sandstone with granules and pebbles, and intraclasts at the base of the system (Aa); (ii) medium-grained graded sandstone, divided in two subgroups: structureless sandstone (Ba) and sandstone with folds and flame structures (Bg); and (iii) mudstones, distributed in two subgroups: mudstone

(Ea) and deformed mudstone (Eb). Table 3.2 indicates the main characteristics of each lithofacies.

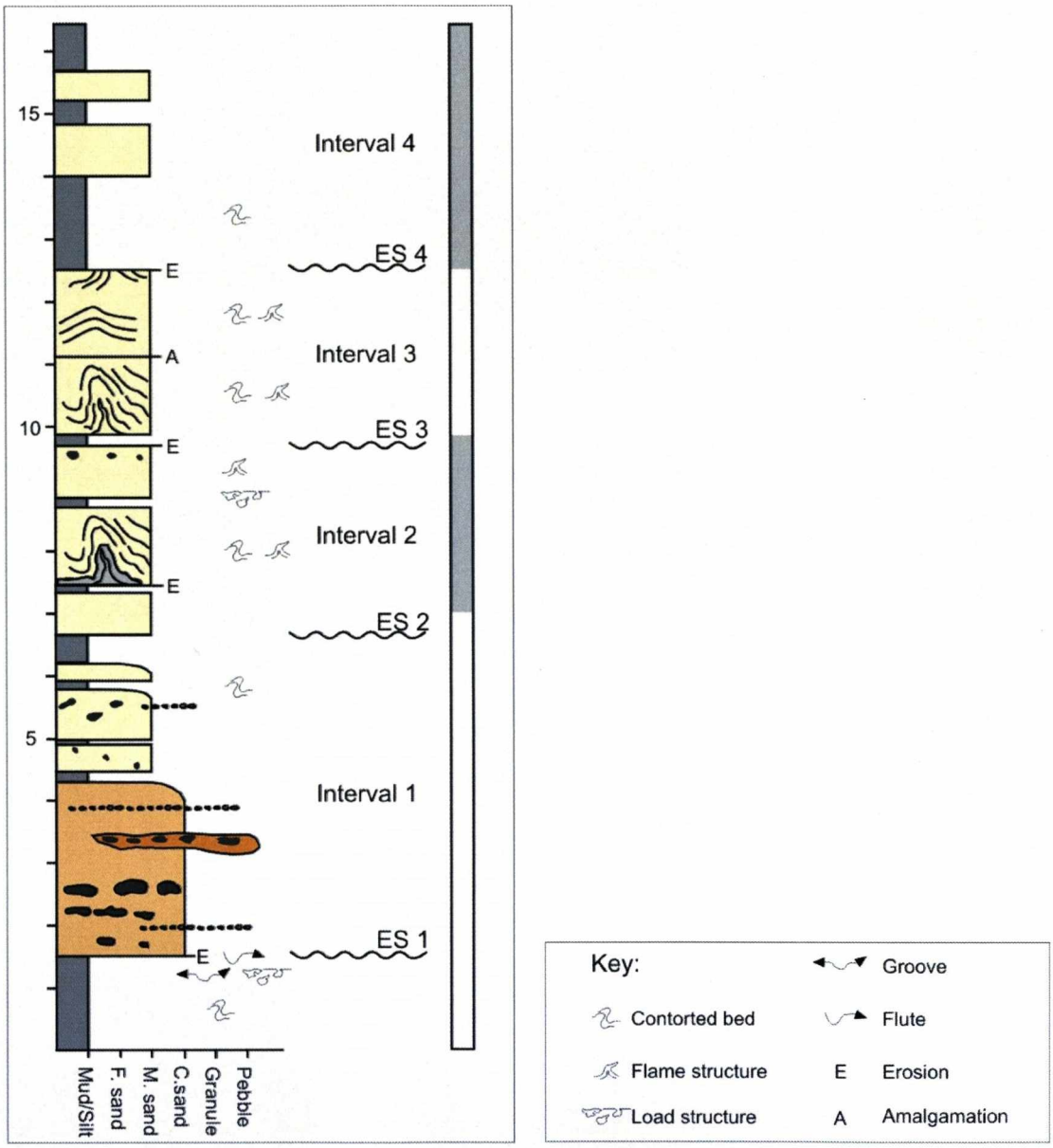

Figure 3.23: Composite log for the Fortin 1°de Mayo outcrop showing a general fining upward trend. Four main erosive surfaces (ES in the log) divide the logged section in four intervals used for reference in this study. See text for details about the lithofacies.

Correlation of the five logged sections combined with detailed mapping of lateral relationships identified four erosion surfaces that bound four distinct channel-fills (Figure 3.24). Mudstones from lithofacies Ea and Eb (Table 3.2) present at the base of this succession are truncated by Erosion Surface 1, which defines the base of the channel complex-fill. Above this surface a succession of coarse– to medium-grained sandstones (lithofacies Aa and Ba; Table 3.2), with basal erosive surfaces

and mudstone intraclasts, constitutes Interval 1 (characterized by lithofacies Aa, Ba, Ea and Eb) and is bound at the top by Erosion Surface 2 that is evident in the north of the outcrop where sandstones of lithofacies Aa are truncated and overlain by sandstones of lithofacies Bg of Interval 2. Soft-sediment deformation structures are restricted to the contact between the basal mudstone and the sandstone-fill of Interval 1. Structures include folding of bedding, overturning and rafting in the mudstone section (up to 1 m below the mudstone-sandstone contact) and load structures in the base of the sandstone. Decimetre scale flutes and grooves at the base of the sandstone indicate palaeoflow to the NE, at a high angle to the outcrop orientation (Figures 3.24 and 3.25).

Intervals 2 and 3 are characterized by the presence of tabular beds of lithofacies Ba and Bg and large scale folds and flame structures. Flame structures with a large range of scales (0.15 – 4 m high) comprise the most prominent class of soft sediment structure. The largest flames have their base at the same stratigraphic level as erosion surfaces 2 and 3, rarely rupturing the overlying bed. In contrast to the Waterfall section in Tanqua-Karoo, indication of material transported through the flame onto the seabed is not observed.

Lithofacies class	Lithofacies name	Lithology	Associated Lithofacies	Sedimentary /Soft-sediment deformation structures	Bounding surface	Single bed thickness	Geometry	Depositional/ Deformational Process
Aa	Coarse-grained sandstone/ conglomerate	Coarse-grained sandstone/ conglomerate Mudstone intraclasts	Eb	Massive with mudstone intraclasts up to 4 m long and parallel to basal erosive surface. Levels with granules and pebbles.	Loaded and erosive at the base. Internally sharp, erosive and amalgamated.	0.3 - 2.5 m. Thick beds can be product of lateral amalgamation.	Channelized	High concentration turbidity currents.
Ba	Structureless sandstone	Medium-grained sandstone. Minor fine grained sandstone.	Bg, Ea	Massive. Levels with mudstone clasts and rare pebbles.	Sharp. Amalgamated	0.05 -0.9 m.	Tabular. Also channelized	High concentration turbidity currents
Bg	Deformed sandstone	Medium-grained sandstone	Ba, Ea	Massive. Levels with mudstone clasts. Folds and flame structures.	Sharp	0.2 - 1.5 m	Tabular. Also channelized.	High concentration turbidity current or liquefaction
Ea	Mudstone	Claystone/ mudstone. Minor siltstone.	Ba, Bg, Eb	Fine laminated. Secondarily strucutureless.	Gradational laterally to lithofacies Eb and sharp or truncated on top.	<1cm (when laminated). Bed sets:0.05 to >5 m: below the base of the channel system	Tabular.	Low concentration turbidity currents and hemipelagic settling.
Eb	Deformed mudstone	Claystone/ mudstone. Minor siltstone and very-fine grained sandstone.	Aa, Ea	Occurrence of finely laminated siltstone and very-fine grained sandstone Overturned beds and rafts	Gradational laterally to lithofacies Ea and truncated at top.	<1cm (when laminated). Bed sets:0.5 - 1.5 m	Tabular.	Low concentration turbidity currents and hemipelagic settling.

Table 3.2: Lithofacies classification for the slope channel deposits of the Los Molles Formation, at Fortin Primero de Mayo, south Neuquén Basin.

Figure 3.24: Log correlation (a), sketch with main surfaces (b) and photo montage (c) of the Fortin 1° de Mayo outcrop with the indication of the erosive surfaces that define four slope channel fills. Observe the tabular beds and the homogeneous grain size (except for the northmost Interval 1) of the channel fills. Large flames occur in the lateral (margins?) of the outcrop and at the top of Interval 3. Noticeable erosion on top of Interval 3 is followed by dominant shales with channelized and tabular sandstone beds. See text for detail of each interval. Log coordinates on Appendix 1.

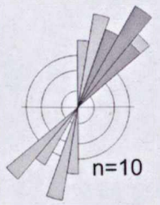

Palaeoflow
(at the erosive surface 1)
Flute
Groove

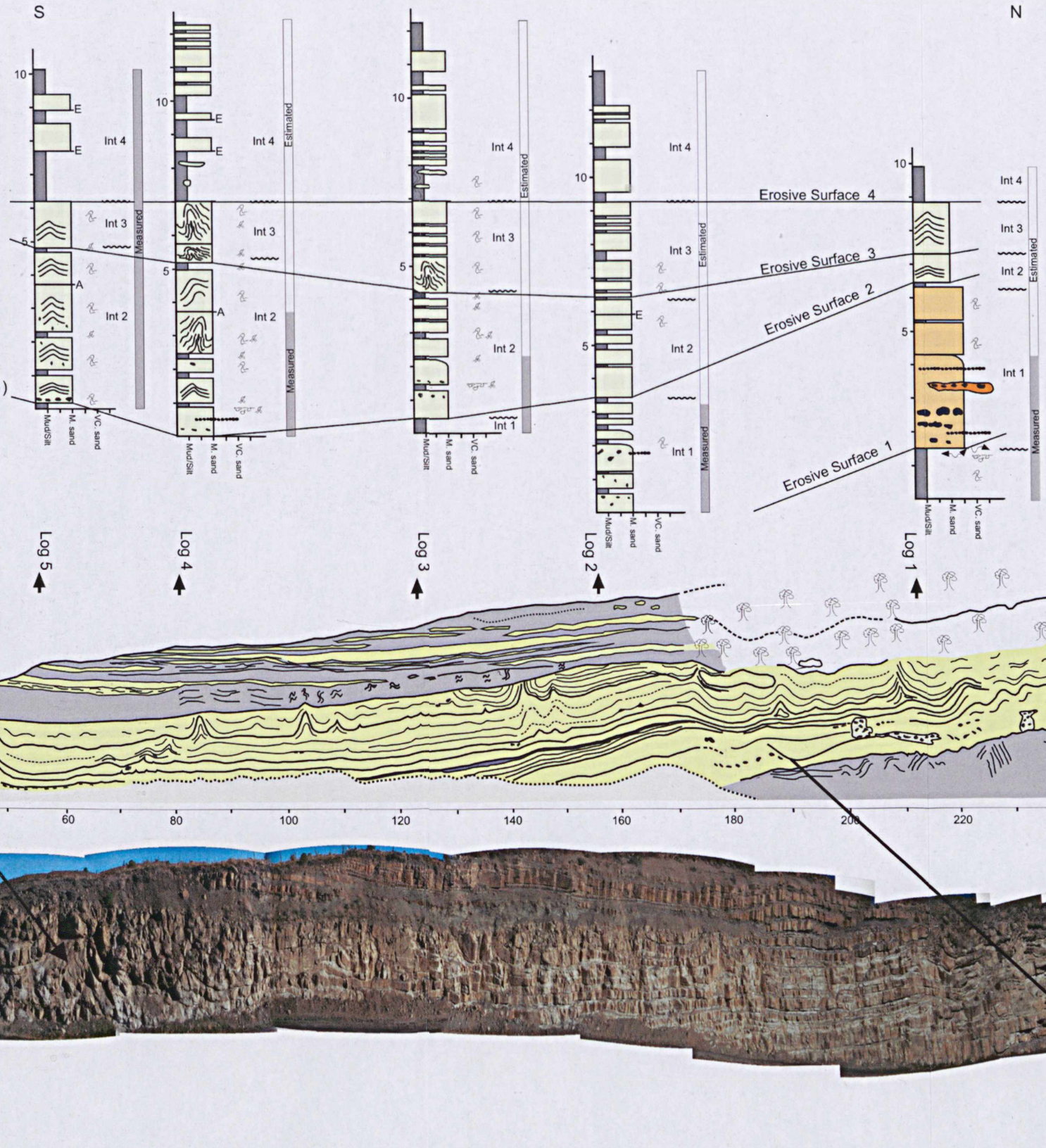

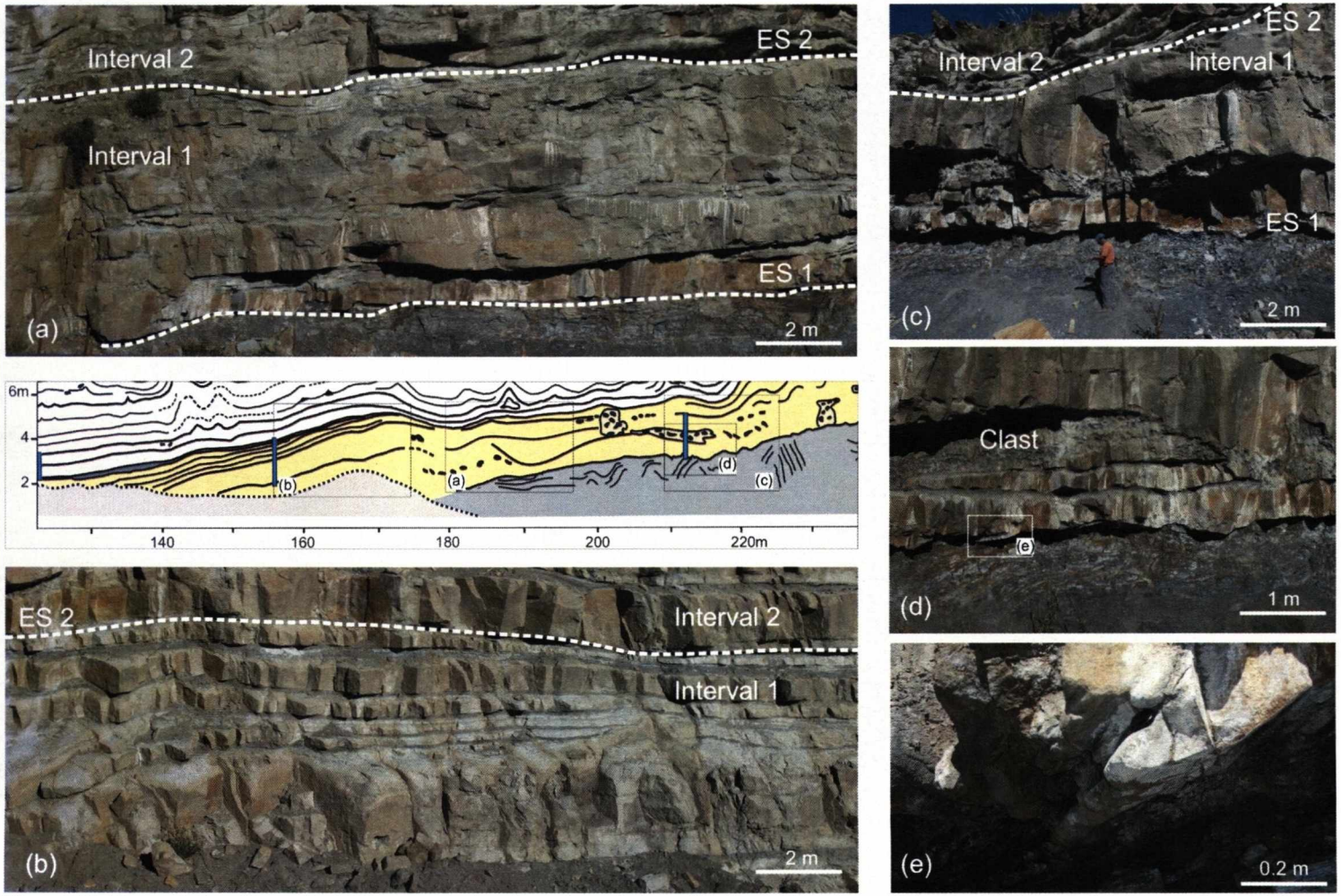

Figure 3.25: Characteristics of Interval 1: (a) Coarse-grained sandstone forms the base of the Fortin 1° de Mayo with low angle incisions and shale mega-clasts; (b) Tabular medium-grained sandstone with the upper contact with Interval 2 marked by subtle erosion; (c) View of the irregular channel base; (d) Detail of the deformed mudstone at the contact with the channel base and of the shale mega-clast parallel to the basal incision; (e) elongate wedge occurring at the channel base associated with flutes and grooves. The inset sketch shows the relative position of each photo.

Intervals 2 and 3 shows an increase in the dimension of the flames both upward and also toward the margins of the channel complex. It was not possible to identify any preferred orientation for the flame structures due to the 2D nature of the outcrop (Figure 3.26). The deformation of bedding by flame structures is not limited to the interval that the flames reside.

Common characteristics of intervals 2 and 3 are the homogeneous lithological composition and the dominant style of deformation (flame structures). Flames are developed at distinct stratigraphic levels: (i) nucleated just above Erosion Surface 2 and affecting intervals 2 and 3; (ii) nucleated within and affecting only Interval 2; (iii) nucleated above Erosion Surface 3 and affecting Interval 3; and (iv) nucleated in the intermediate section of Interval 2 and affecting the overlying beds and surfaces (cf. Figure 3.24).

Erosion Surface 4 marks the base of Interval 4, which includes lithofacies Ba, Ea and Eb. The base of this interval is marked by a major change in lithofacies with the deposition of up to 1.5 m of mudstone immediately above the deformed beds of Interval 3. Locally, flame structures in Interval 3 are truncated by Erosion Surface 4 (Figure 3.27). Lithofacies vary laterally between Ea and Eb with lithofacies Ba forming isolated decimetre channelized bodies and lenses of sandstone. The top of this interval consists of tabular sandstones beds intercalated with mudstone, without evidence for truncation. Soft-sediment deformation is restricted to overturned thin beds of lithofacies Eb, positioned just above Erosion Surface 4 (Figure 3.27).

The acquisition of geometrical parameters of flame structures for the statistical analysis was restricted to 8 structures in the central part of the outcrop, due to access restrictions. Raw data for statistical studies are listed in Appendix 3. The results are presented in Figure 3.28. Key observations are the homogeneous lithological composition and the dominant style of deformation (flame structures) that affect Interval 2 and 3.

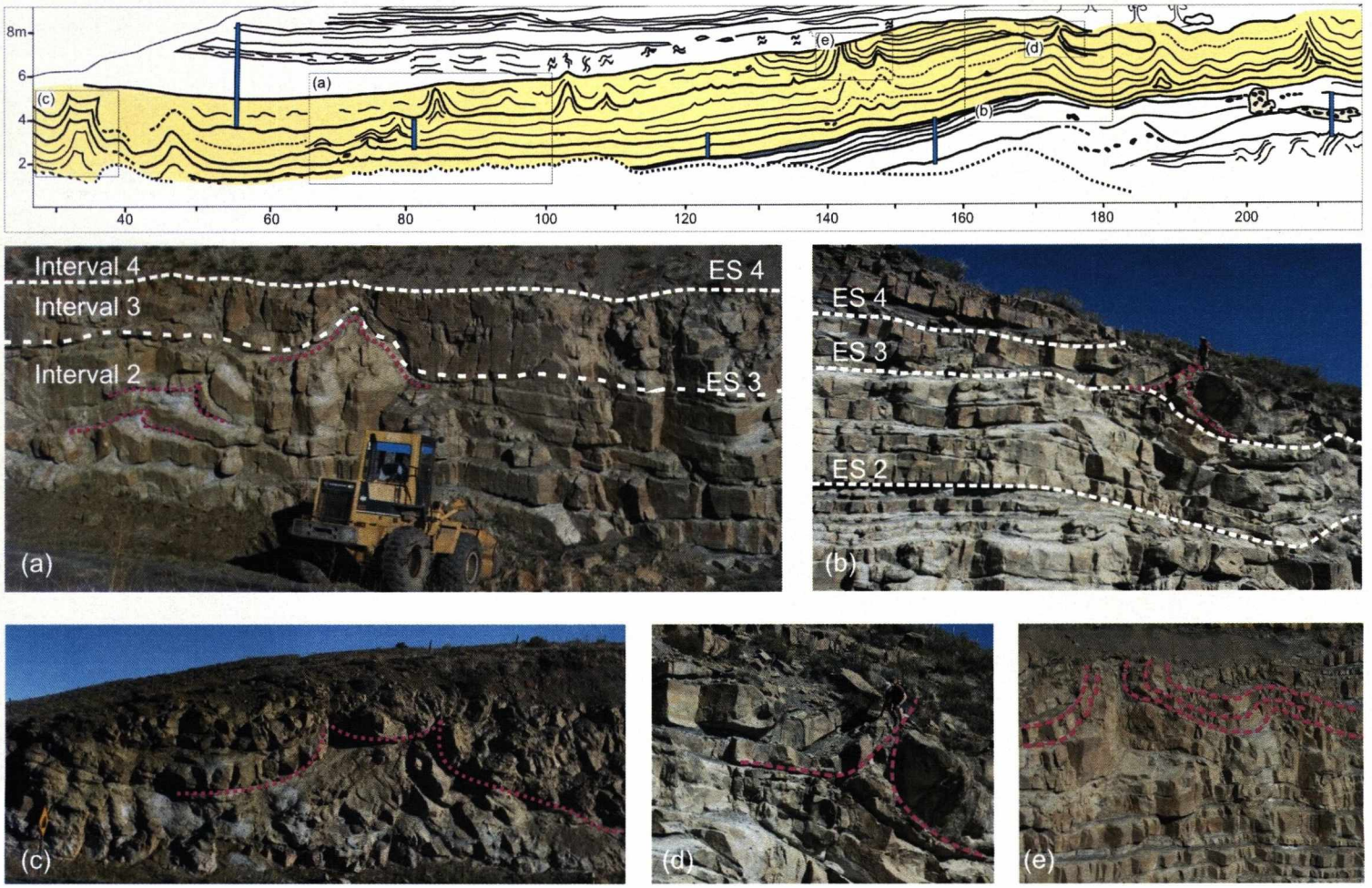

Figure 3.26: View of intervals 2 and 3. (a) Erosion surface 3, between these two intervals is not easy to observe due to amalgamation; note the size of the flames (dotted purple) increasing to the top; (b)To the north, erosion surface 3 controls the position of large flames; (c) Four metre high flame structure formed by simultaneous deformation of units 2 and 3; (d) Detail of the flame from (b), showing uncommon asymmetry between the two flanks; (e) Flame and associated flank folding on top of Unit 3. Observe the erosion on top of Unit 3. See sketch for scale.

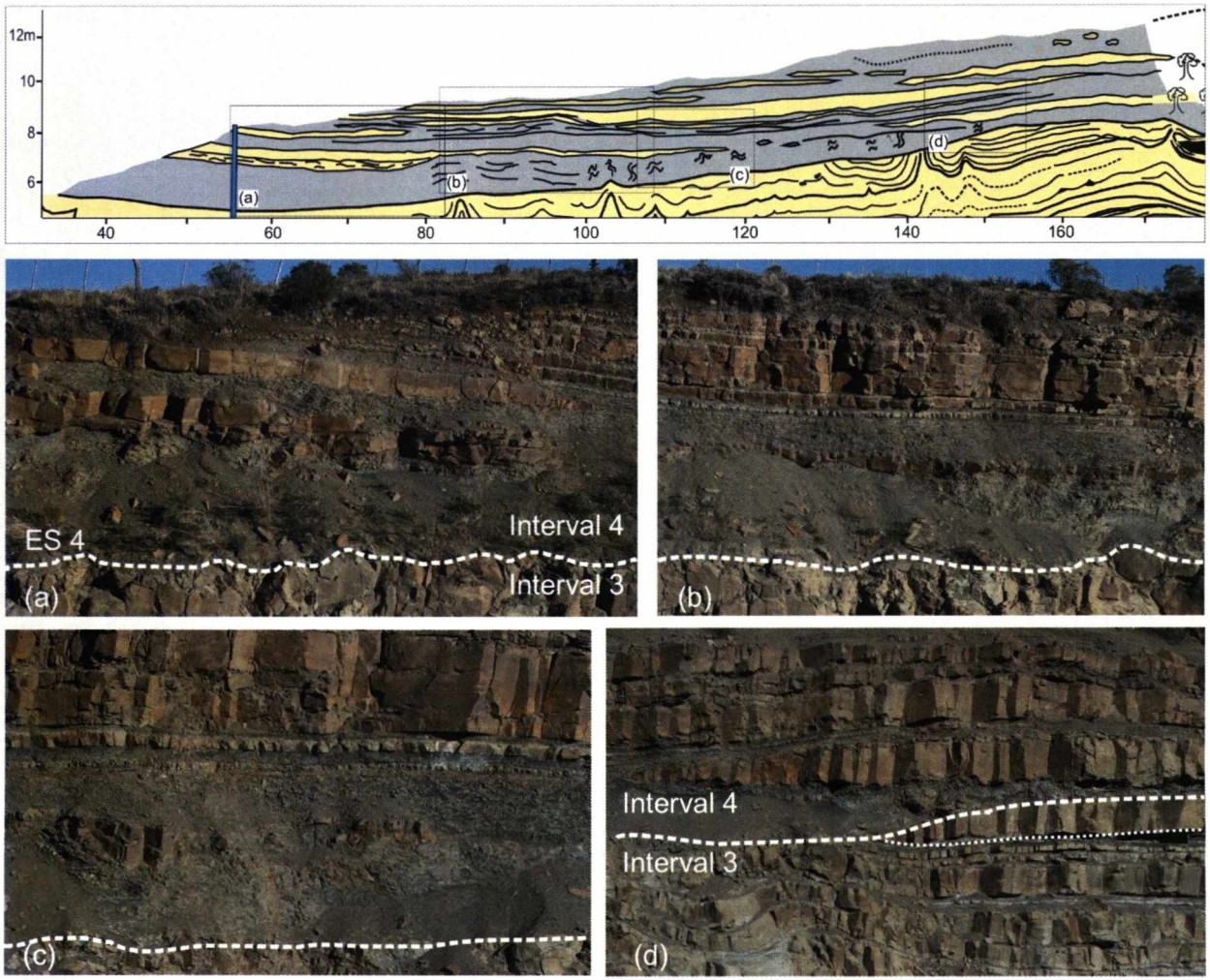

Figure 3.27: Interval 4. (a) and (b) Erosion surface 4 marks the base of Interval and is ovelain by mudstone intercalated with channelized sandstone and topped by tabular sandstone; (c) Detail of the highly deformed mudstone; (d) To the north, presence of sandstones lenses (base dotted) close to the contact between intervals 3 and 4. See sketch for scale.

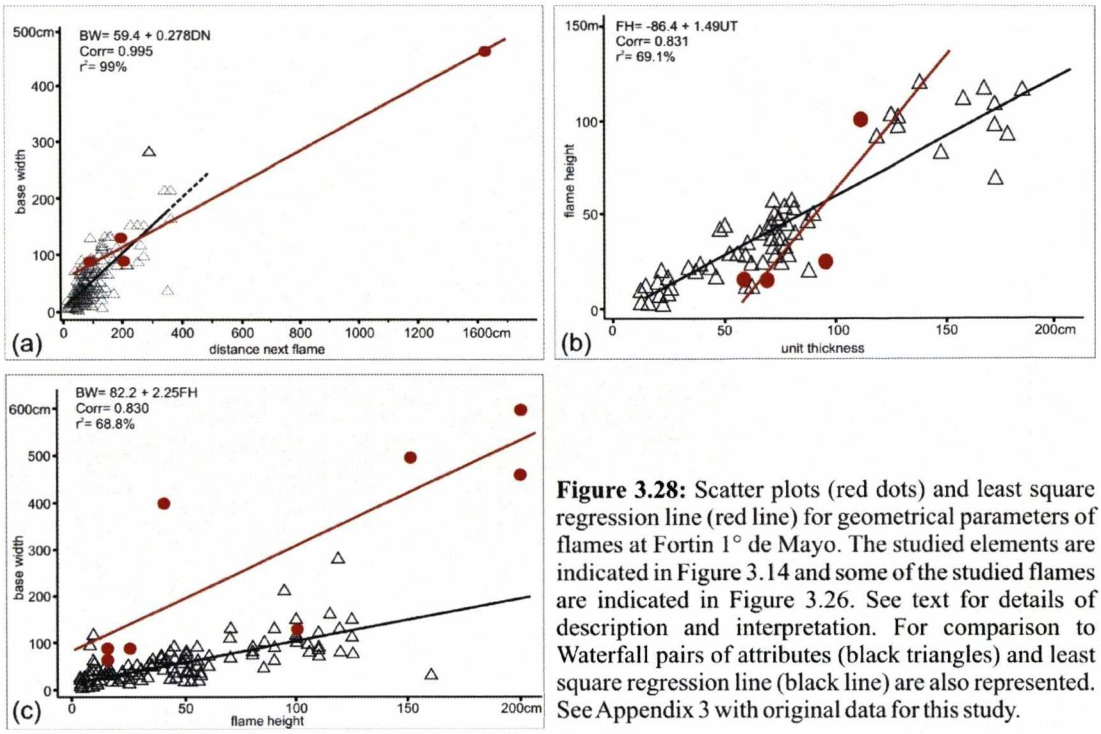

Figure 3.28: Scatter plots (red dots) and least square regression line (red line) for geometrical parameters of flames at Fortin 1° de Mayo. The studied elements are indicated in Figure 3.14 and some of the studied flames are indicated in Figure 3.26. See text for details of description and interpretation. For comparison to Waterfall pairs of attributes (black triangles) and least square regression line (black line) are also represented. See Appendix 3 with original data for this study.

Interpretation

Interpretation of the controls and trigger mechanism of the deformation of Fortin 1° de Mayo slope channel complex fill is limited because the margins of the complex are not exposed. The flame structures are preferentially distributed close to erosion surfaces and toward channel margins, indicating a stratigraphic control (cf. Figure 3.24). Several flame structures deform more than the interval that they sit in, affecting a variable thickness of section and indicating that the timing of deformation was not restricted to each cut and fill episode. For example, some flame structures nucleated low down and affected the whole sandbody (cf. south part of Figure 3.24). The distribution, height and style of flame structures at lower stratigraphic levels (intervals 1-3) in the channel complex and the lack of erosive truncation of the flame structures by the erosive surfaces within these intervals suggest that the deformation of the whole fill occurred simultaneously rather than sequentially. However, multiple phases of deformation can not be ruled out. The truncation of several flames by Erosion Surface 4 indicates that deformation took place close to the seabed. There is no clear evidence to indicate the trigger mechanism of the deformation, although possible controls include (1) rapid deposition and loading during channel-fill, (2) failure at the channel complex margins, (3) downslope movement of the whole

channel-fill increasing pore pressures and (4) seismicity. Each possible control is discussed below.

The Aalenian-Bajocian was a period of tectonic quiescence in the Neuquén Basin with thermal subsidence responsible for the enlargement of the basin (Legarreta & Uliana, 1996), and local fault activity (Vergani *et al.*, 1995). The first stages of inversion tectonics in the south of the Neuquén Basin are recorded in the Early Bajocian in the transition between the Los Molles and Lajas Formations (Freije *et al.* 2002). A fault is this area has not been identified in the present or previous studies and there is no regional indication for seismic activity during the evolution of the Fortin 1°de Mayo slope channel complex. Also, the sediment pile above the channel complex fill does not show evidence of abnormal loading that could have caused the instantaneous deformation of the studied section.

The deformation of the mudstone immediately below Erosion surface 1 supports an interpretation that invokes a component of down-slope sliding of the entire channel-fill. Here, shearing at the base would lead to the build-up pore pressures in mud-prone layers within the fill resulting in the deformation of several intervals. However, kinematic measurements of the shear fabric in the mudstones were not possible, and more deformation in Interval 1 would be predicted in this interpretation. The coarse grain size of Interval 1 may explain why no fluidization takes place in this interval. Alternatively, Interval 1 could have been consolidated before the event that caused the fluidization in intervals 2 and 3. Except for the asymmetry and truncation between the flanks of one large flame at the northern end of the outcrop (cf. Figure 3.26d), there is no evidence for along channel movements during the events that generated the flame structures. The symmetric pattern of the flame structures coupled with the absence of downslope vergence indicates that deformation of intervals 2 and 3 occurred *in situ*, with insignificant down slope movement.

The distribution of the largest flame structures and the occurrence of deformation at erosion surfaces suggest that the initiation of deformation is driven by failure at the channel margins. The flame structures, as in the Waterfall area, are interpreted as generated by instantaneous fluidization of sand. The presence of larger structures toward the channel margin and above the erosion surfaces indicates some control on the distribution of the structures. It is interpreted that the fine-grained material that mantles the main erosion surfaces concentrated higher amounts of fluid

prior to liquefaction that resulted in the distribution of the large flames. Also, large flames close to the channel margins are attributed to migration of fluids where the loading by the overlying sediment pile is small (Figure 3.29a).

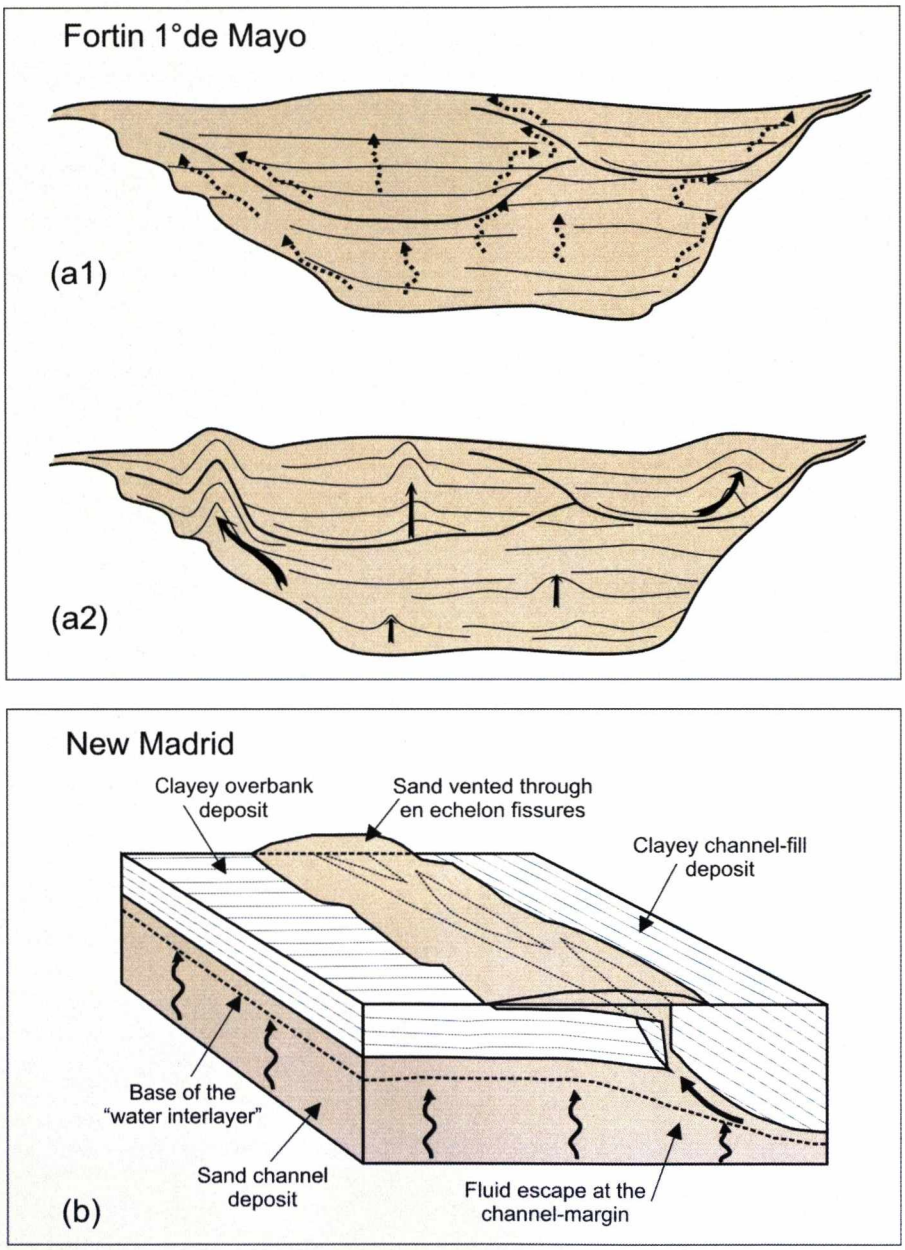

Figure 3.29: (a) Model for the development of flame structures in the channel deposits of Fortin 1° de Mayo. Liquefaction and fluidization of units 2 and 3 is followed by the upward escape of particles, controlled partially by the main erosion surfaces and by the channel margin (a1). The large flames are positioned at the less confined channel margin and in the upper levels (a2) and the black arrows indicate the relative flame size schematically. (b) Model for sand blows and dykes present at the margin of a channel in the New Madrid seismic zone. This is a possible analogue for the positioning of the Fortin 1° de Mayo flame structures (from Tuttle and Barstow, 1996). See text for details.

A possible explanation for the positioning of the flame structures can be found in a similar modern example in the New Madrid seismic zone, central United States, (Tuttle & Barstow, 1996) and by laboratory studies (Dobry & Liu, 1992; Fiegel & Kutter, 1994). Elongated sand blows and sandstone dykes, with dimensions similar to the flames of Fortin 1° de Mayo, occur along the margins of fine-grained channel-fill deposits after liquefaction triggered by seismic shock (Figure 3.29b). In this situation sand-prone channel-fill deposits are covered by clay-rich overbank and channel-fill deposits. The presence of sand dykes and other sedimentary structures at the interface between sand and mud support an interpretation that they were created by retardation of the upward flow of water due to the presence of the impermeable mud layer. This hypothesis found support in laboratory work (Dobry & Liu, 1992; Fiegel & Kutter, 1994), which indicated that the presence of a film of water or a "water interlayer" at the sand-mud interface was responsible for the soft-sediment deformation. It is believed that similar events occurred along erosion surfaces 2 and 3 in the study section, where a mudstone drape between intervals 2 and 3 could result in the concentration of fluid with consequent high pore pressures and the generation of larger flame structures.

The proximity of the largest flame structure to the margin of the channel complex at the south end of the outcrop is not constrained, due to the road cut. However, the topographic ridge representing the sand-rich channel complex dies out farther south, suggesting that the margin of the complex (if coarser-grained than the surrounding lithofacies) is close by. In this case a possible explanation for the process of formation could be similar to that invoked for the positioning of "sand blows" in the New Madrid seismic zone. In that case, positioning of sand bows were controlled by the concentration of stress in the boundary between channel and overbank areas associated with high hydraulic forces and loss of bearing strength in the upper part of the channel deposit.

The occurrence of one lens of sandstone at the base of Interval 4 (cf. Figure 3.27d) can be interpreted in more than one way: (1) as a sandstone dyke (Smith & Spalletti, 1995); (2) as the infill of topographic lows caused by deformation (Burgess & Flint, 1998); or (3) as a remnant geometry produced by the erosion of the sandstone above Interval 3. Typically, sand injection results in lateral or upward migration of sand (Lowe, 1975). However, it seems implausible that the sand was sourced from Interval 3 after a strong erosional event that truncated the flame

structures and would have removed any pore pressure build-up. Downward injection from Interval 4 can not be discounted, although no lineations were identified on the top surface of the sandstone lenses. The second and third options could explain the presence of the sandstone lens. In the second case, it would imply that the deformation of intervals 2 and 3 generated topography on the seabed in a similar process to that described in the Waterfall area.

Statistical analysis and comparison to Waterfall section

The results of the statistical analysis are influenced by the small amount of data of geometrical parameters, which means that interpretation must be taken with caution. For distance between adjacent flames *versus* basal width of the flames (Figure 3.28a) and for deformed layer thickness *versus* flame height (Figure 3.28b), the small number of points limit robust geological interpretation based only on the least square regression line. The largest flame measured for the first relationship (1440, 460) indicates the distance between flame structures is >50% greater than results from the Waterfall data. Except for a subtle rise between the two flames that may represent failed flame initiation, there is no evidence in the plane of the outcrop that justifies geometrically such a difference. Alternatively, the rise might be the "end" of a flame that grows into (or out) the plane of the outcrop. The other points obtained for the two relationships cited above fit well into the cluster of pairs for Waterfall, suggesting geometric similarities. For flame height *versus* flame basal width (Figure 3.28c) structures in Fortin 1° de Mayo with the same height of flames are wider than the ones found in Waterfall. One possible explanation could be related to differences in composition and grain size, finer grained in Waterfall. Grain size exerts an effective control on the liquefaction process and differences in grain size between successive beds control the development of voids that results in fluid escape structures (Nichols *et al.*, 1994; Obermeier, 1996). From the experiments conducted by Nichols *et al.*, 1994, it was observed that when the grain size of the basal layer (the one to be fluidized) was substantially less than that of the top layer; finer particles from the base layer infiltrated into the top layer by passing through its pore spaces resulting in flows without or with diminished burst out, resulting in small flames. Due to the small grain size such events are prone to occur in Waterfall area if compared to Fortin outcrops, certainly influencing in the flame dimensions.

3.2.3 Chacay Melehue

General Aspects

The Chacay Melehue outcrop comprises a 60 m thick section exposed for 8 km along the "Ruta 43" road between Chos Malal and Andacollo, in the south of the Cordillera del Viento (Figure 3.30).

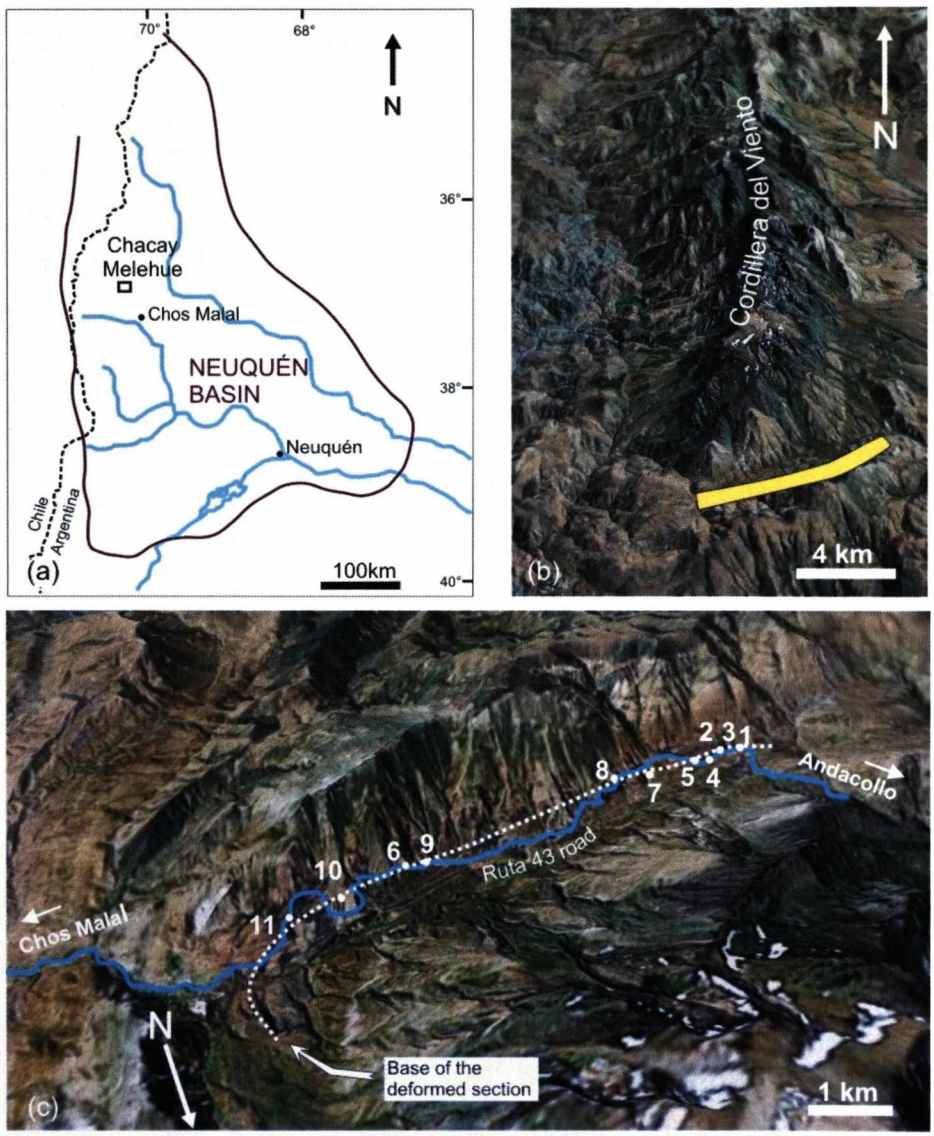

Figure 3.30: Location map for the Chacay Melehue outcrop, NW of the town of Chos Malal (a). The outcrop is positioned at the south of Cordillera del Viento (b), on the Ruta 46 road, between Chos Malal and Andacollo (c).The yellow strip on (b) shows the outcrop position and the numbers on (c) indicate the position of the sedimentological logs. Log coordinates in Appendix 1.

The highlands of the Cordillera del Viento were formed during Cenozoic inversion related to the evolution of the present day Andes. They are part of the Chos Malal fold belt and are composed of rocks from the Palaeozoic to Upper Jurassic (Figure 3.31). The study outcrop is a 55 m thick mud-prone turbidite succession with a thick debrite in the lower part of Bathonian to Lower Callovian Upper Los Molles Formation that can reach 800 m thick in the area (Figure 3.32). Within Los Molles Formation, the study section is preceded by a 90 m thick black shale that is rich in ammonites and volcaniclastic material and followed by 250 m of carbonaceous shale and topped by 400 m of black shales.

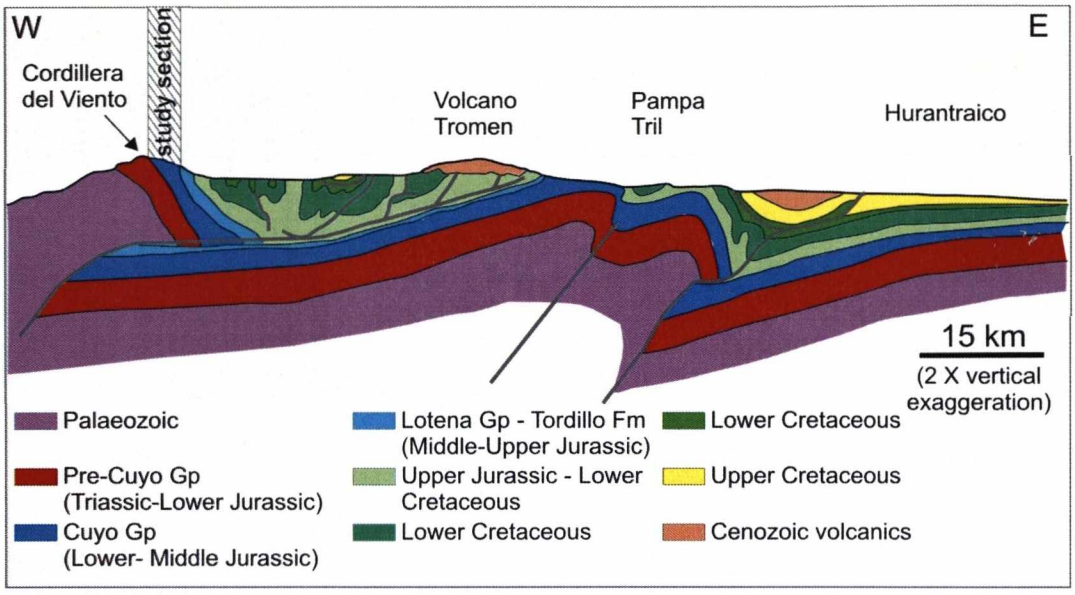

Figure 3.31: Structural section through the Cordillera del Viento at the Chos Malal Fold Belt, ilustrating the tectonic inversion that exposes of Mesozoic rocks from the Pre-Cuyo, Cuyo and Lotena Groups and the continental Tordillo Formation (from Kozlowski et al., 1996). The study interval is indicated in the geological section.

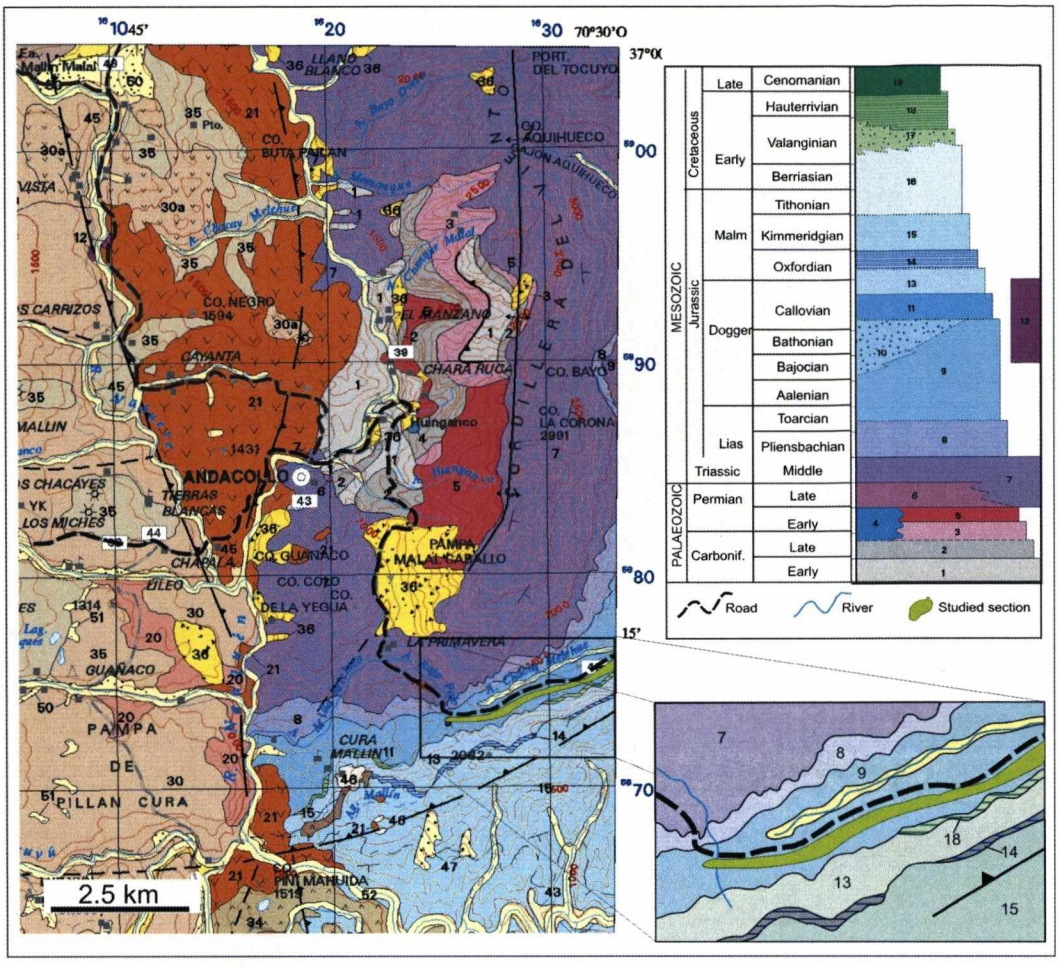

Figure 3.32: Northeast part of the Andacollo geological map (1:250,000) with the emphasis to the region around the Cordillera del Viento (after Rovere *et al.*, 2004). Two distinct regions are seen in the map: west of Andacollo is the domain of Cenozoic rocks and east of Andacollo is the domain of Mesozoic and Palaeozoic rocks. The studied section (detailed map) comprises Jurassic rocks which geological map is highlighted. Rocks in the detailed map are part of the following formations: 7- Choiyoi Group; 8 – La Primavera Formation; 9- Los Molles Formaton; 13 – Lotena Formation; 14 – La Manga and Auquilco Formations; 15 – Tordillo Formation and 18 – Agrio Formation.

According to Burgess & Flint (1998), during the Bathonian and Lower Callovian fault activity had probably ceased; however the distribution of sands suggests that there was not a simple transport path linking deep marine systems in the north with prograding deltaic and shelf systems in the south. This suggests the presence of significant basin floor topography. Two architectural styles developed in the area: thick amalgamated sandstones with some thin-bedded coarser-grained intervals to the south (Agua Fria) and coarse-grained channelized turbidites with associated large slumps deposits and debrites to the north (Chacay Melehue) (Figure 3.33). Palaeocurrents in the Chos Malal area indicate transport of sediments to the E and NE during this period (Burgess *et al.*, 2000).

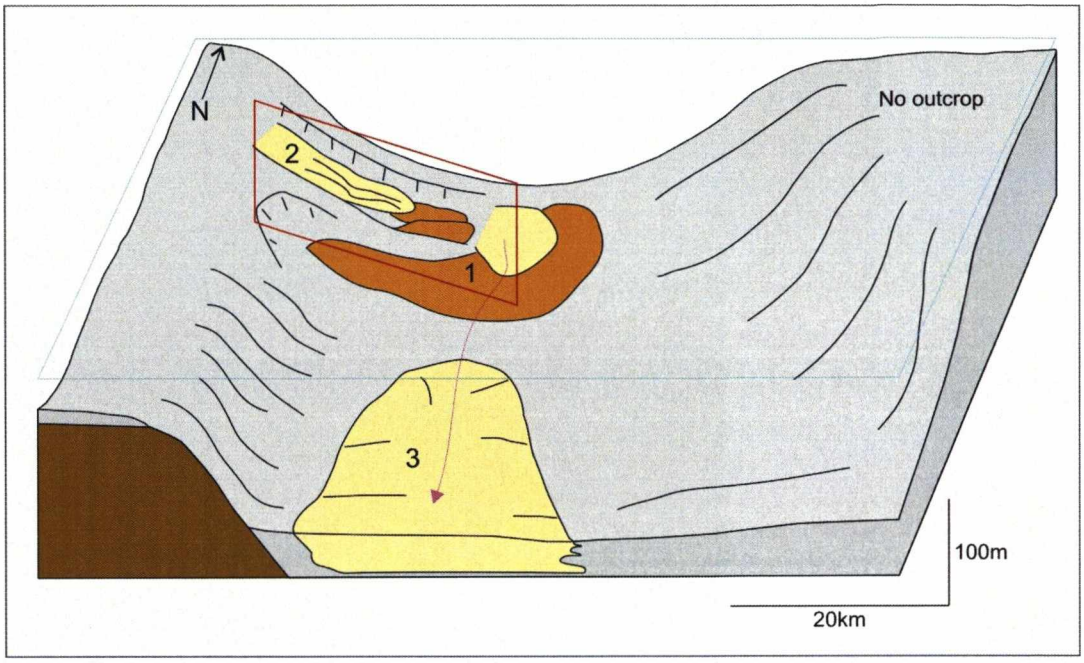

Figure 3.33: Schematic block diagram with the papaeogeography of the Chacay Melehue and Agua Fria areas during the Bathonian-Callovian (169-162 Ma): (1) slump at Chacay Melehue; (2) coarse grained turbidite at Chacay Melehue and (3) thin bedded turbidite at Agua Fria (after Burgess & Flint, 1998). The red polygon indicates the studied section.

Description

Eleven sedimentary logs were collected (a total of 530 m; cf. Figure 3.30) that led to the identification of the following lithofacies: (i) very coarse-grained sandstone/conglomerate (Aa); (ii) fine- to coarse-grained, thin- to thick-bedded graded sandstones divided into the following subgroups: structureless (Ba), planar-laminated (Bb); cross-stratified (Be) and deformed (Bg); (iii) planar-laminated thin (0.1-0.5 m) sandstone/siltstone interbeds (Ca); (iv) siltstone, divided in the subgroups structureless (Da) and planar-laminated siltstone/mudstone interbedded (Db); (v) mudstone, separated into mudstone (Ea) and deformed mudstone (Eb) and (vi) highly deformed beds of sandstone and siltstone, subdivided into: chaotic with matrix-supported rafts and deformed blocks (Fa); with vertical structures (Fb), and contorted (Fd). Table 3.3 indicates the main characteristics of each lithofacies.

Lithofacies class	Lithofacies name	Lithology	Associated Lithofacies	Sedimentary /Soft-sediment deformation structures	Bounding surface	Single bed thickness	Geometry	Depositional/ Deformational Process
Aa	Very coarse-grained sandstone/ conglomerate	Very-coarse-grained sandstone/ conglomerate. Clasts of mudstone and sandstone	Ba	Matrix-supported, clasts up to 3 m long parallel to the bedding. Levels with granules. Rare clast-supported intervals	Base erosive and sharp; top sharp to gradational.	1 - 7 m. Thick beds can be product of lateral amalgamation.	Channelized	High concentration turbidity current (?)
Ba	Structureless sandstone	Fine- to very coarse-grained sandstone. Rare granules.	Aa, Bb, Bg, Ca, Da, Db, Eb, Fd	Massive. Levels with mudstone clasts. Granules and pebbles close to base. Wavy on top. Load structures and flame structures.	Base sharp; top gradational and sharp. Amalgamated. Locally channelized.	0.2 - 6 m (amalgamated?).	Tabular. Also channelized	High concentration turbidity current
Bb	Planar-laminated sandstone	Fine- to coarse-grained sandstone	Aa, Ba, Ea, Fd	Parallel lamination. Symmetric ripples on top surface.	Base sharp; top gradational or sharp.	0.3 – 1 m	Tabular.	High concentration turbidity current with reworking
Be	Cross-stratified sandstone	Medium grained sandstone.	Ba, Fa	Low angle cross-stratification.	Base sharp; top sharp, locally gradational	1 – 5 m (amalgamated?)	Tabular (?)	Storm events (?)
Bg	Deformed sandstone	Fine to medium-grained sandstone	Ba, Ea	Large wavelength folds and flame structures.	Sharp. Base can be irregular.	0.2 - 2 m	Tabular. Also lens shape.	High concentration turbidity current or liquefaction

Ca	Planar-laminated sandstone/ siltstone interbedded	Fine-grained sandstone, siltstone and mudstone.	Ba,	Planar lamination. Mudclasts in the sandstone	Sharp	0.1 – 0.5 m	Tabular	Low to high concentration turbidity currents.
Da	Structureless siltstone	Siltstone	Ba, Ca	Massive. Secondary bed contortion and flames	Sharp	0.1 – 0.4 m	Tabular	Low concentration turbidity currents.
Db	Planar-laminated siltstone mudstone interbedded	Siltstone and mudstone.	Ba, Ca	Planar laminated	Sharp	0.1 – 1 m. Bed sets up to 14 m.	Tabular	Low concentration turbidity currents.
Ea	Mudstone	Claystone/ mudstone. Minor siltstone.	Ba, Bg, Eb, Fd	Finely laminated. Locally structureless.	Sharp	<1cm (when laminated). Bed sets up to 13 m.	Tabular.	Low concentration turbidity currents and hemipelagic settling.
Eb	Deformed mudstone	Claystone/ mudstone. Minor siltstone.	Aa, Ba, Ea	Deformed lamination	Sharp	<1cm (when laminated). Bed sets with 3 – 4 m	Tabular.	Low concentration turbidity currents and hemipelagic settling.

Fa	Highly-deformed sandstone/ siltstone with clasts.	Very-coarse-grained sandstone. Clasts of sandstone and mudstone.	Ea, Eb	Chaotic. Rich in contorted clasts of sandstone supported by fine grained matrix	Base erosive; top sharp.	5 – 12 m	Tabular and channelized	Debris flow.
Fb	Deformed sandstone/ siltstone with vertical structures	Siltstone to mudstone.	Ba	Flame structures	Base sharp; top irregular	0.5 – 0.8 m. Flame structure can reach 8 m high.	Tabular	Fluidization and/or liquefaction.
Fd	Contorted sandstone/ siltstone.	Mudstone and siltstone.	Ba, Db, Ea, Eb	Lamination is contorted.		Fine laminated (<2 cm beds). Bed sets from 4 to 14m.	Tabular	Slumps and slides

Table 3.3: Lithofacies classification for the deep water deposits of Los Molles Formation, at Chacay Melehue, south Neuquén Basin.

A composite log indicates the occurrence of four depositional units with a general coarsening- and thickening-upward trend, except for the lower unit (Figure 3.34). The 60 m thick interval is underlain and overlain by deep-water mudstone (Legarreta & Uliana, 1996). Unit 1 is a 10 to 20 m thick chaotic deposit, which is overlain by three coarsening- and thickening-upward sedimentary packages. Unit 2 is a 15 to 20 m thick package of marine mudstone punctuated by thin-bedded (0.05-0.1 m thick) medium-grained graded sandstones. Unit 3 is a 10 to 20m thick section of thin-bedded (0.05-0.1 m thick) fine-grained graded sandstone thickening upward to thick-bedded coarse-grained graded sandstone, locally folded with rotated bedding above listric normal faults. Commonly, Unit 3 is cut by an erosion surface that marks the base of Unit 4, which comprises 15-20 m of lenticular conglomerate and very-coarse-grained sandstone beds (Figure 3.34; 3.35).

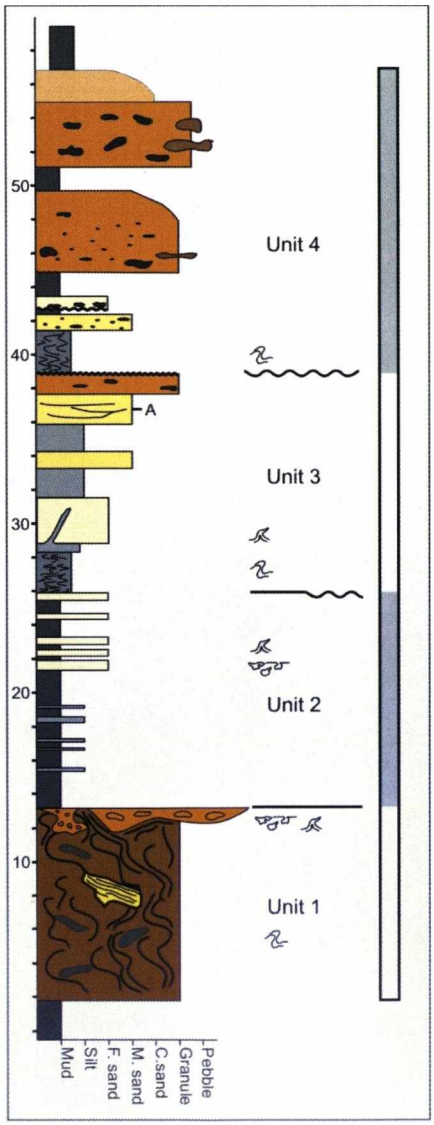

Figure 3.34: Composite log for the Chacay Melehue study area characterized by a coarsening- and thickening-upward succession overlying a basal chaotic interval. Four depositional cycles were identified (units 1 to 4) and main soft-sediment intervals are indicated (key for the symbols in Figure 3.23).

Unit 1 has a sharp basal contact with the underlying deep water mudstones and is sharply overlain by thin beds of Unit 2. It includes lithofacies Aa and Fa with secondary occurrences of facies B sandstones and deformed mudstone (Eb) (Table 3.3). Soft-sediment deformation in this unit is represented by two juxtaposed styles. The lower unit is represented by metre scale contorted rafts and blocks of different rocks without any preferential orientation that are supported by a coarse-grained siltstone. The upper style is large scale load structures of lenticular conglomerates and coarse-grained sandstones and associated flame structures (Figure 3.36). In the eastern section, there is a deep incision surface filled by thick (up to 3 m thick) conglomeratic beds, not found in the west.

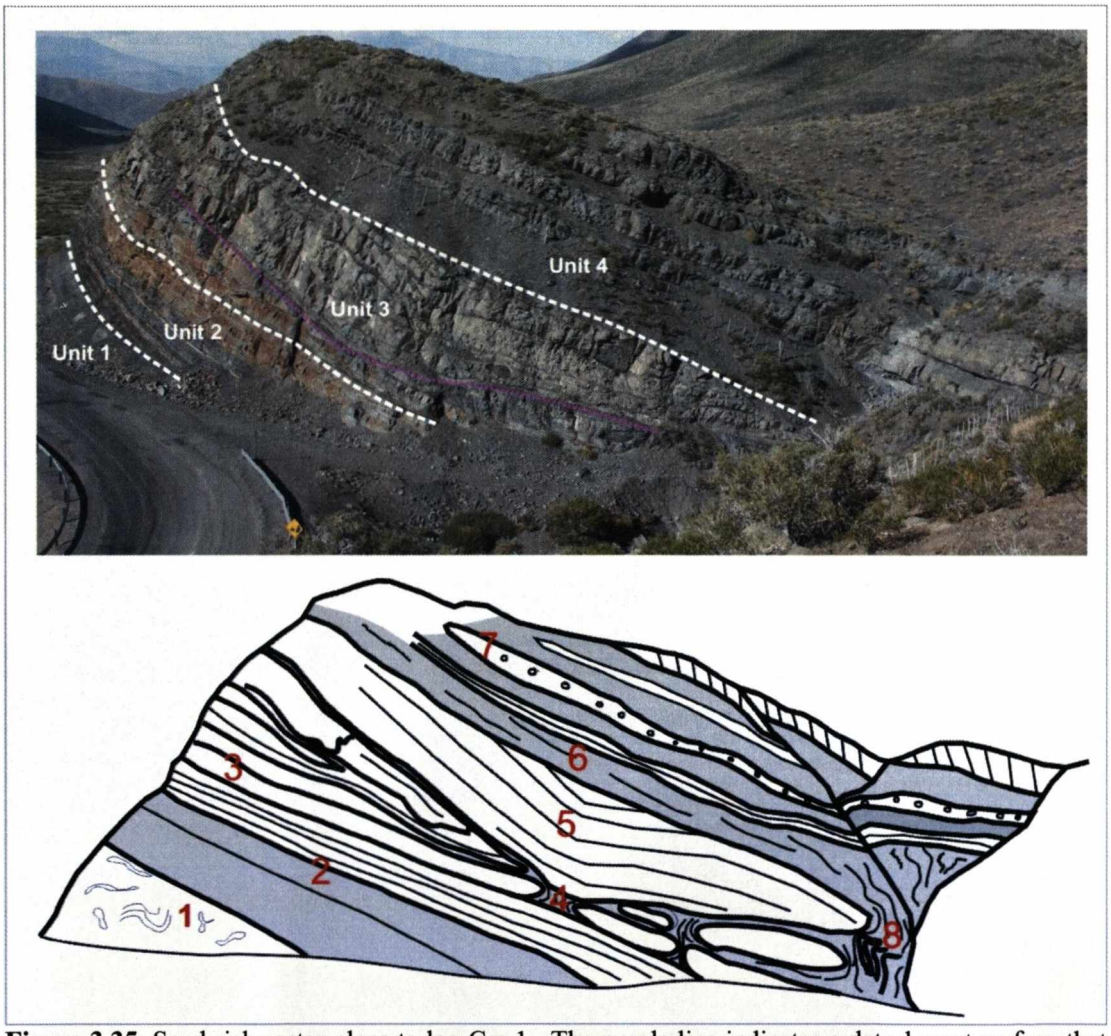

Figure 3.35: Sand rich sector close to log Cm 1. The purple line indicates a detachment surface that rotated the upper part of Unit 3. The sketch shows: (1) the chaotic Unit 1; (2) transition from the thin layers to thick sandstone beds on top of Unit 2; (3) disrupted sandstone beds at the base of Unit 3; (4) large flames at the base of Unit 3; (5) rotated beds above the detachment surface; (6) thin beds of Unit 4 deposited above the unconformity on top of Unit 3; (7) thick beds of coarse-grained sandstones to conglomerates on top of Unit 4; (8) local highly deformed section in lateral continuity to the detachment surface.

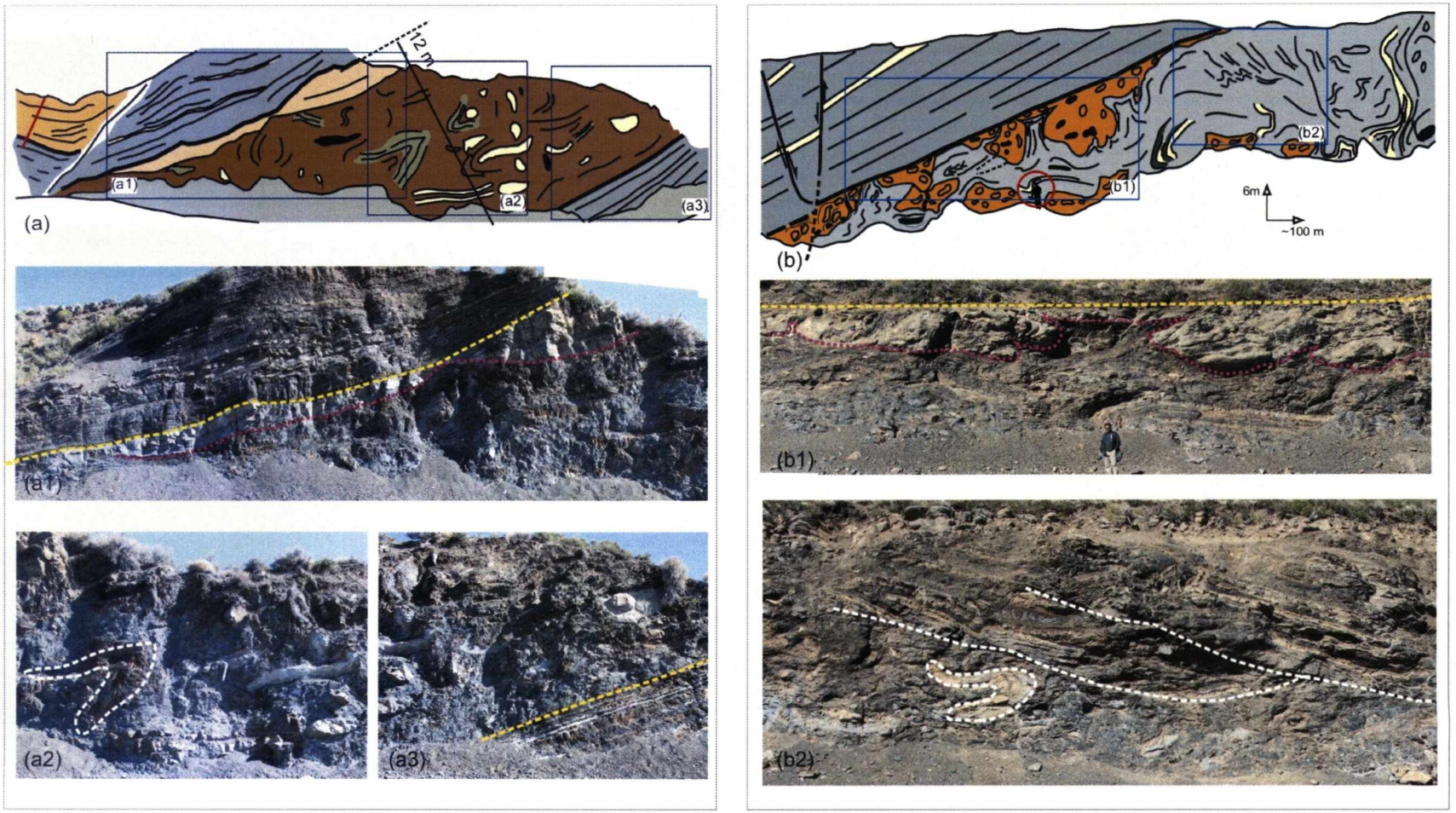

Figure 3.36: Unit 1 at the base of log Cm1 (a) and between logs Cm4 and Cm5 (b) (see Figure 3.40 for location). Note the sharp contact with the overlying shales (yellow dashed line) and the very-coarse sandstone that occur at the top, with irregular base (purple dotted line) without erosion (a1); Unit 1 is polymictic with large (> 1 m) folded rafts and blocks of shales (white dashed line), sandstones and volcanics (a2); Unit 1 is also in sharp contact with the underlying shales of Los Molles Formation. At the second locality, the coarse-grained top of Unit 1 shows metre-scale load and flame structures (b1) over the contorted and chaotic basal section, sometimes showing internal slide surfaces (b2).

Although slump folds must be considered with some caution as palaeoflow indicator, measurements of slump fold axis within Unit 1 indicate transportation along the direction E – W (cf. Figure 3.40) similar to the results obtained by Burgess *et al.* (2000) (see above).

Unit 2 has a sharp contact with underlying Unit 1 and comprises lithofacies Ba, Bb, Be, Db, Ea, Eb (Table 3.3). The occurrence of low angle cross stratification (Be) in the study section is exclusive to this unit. Soft-sediment deformation is restricted to the occurrence of thick deformed mudstone in logs Cm8a and Cm9. Minor small scale contorted beds, flame structures, and load structures are associated with siltstone and fine grained sandstone beds (Figure 3.37).

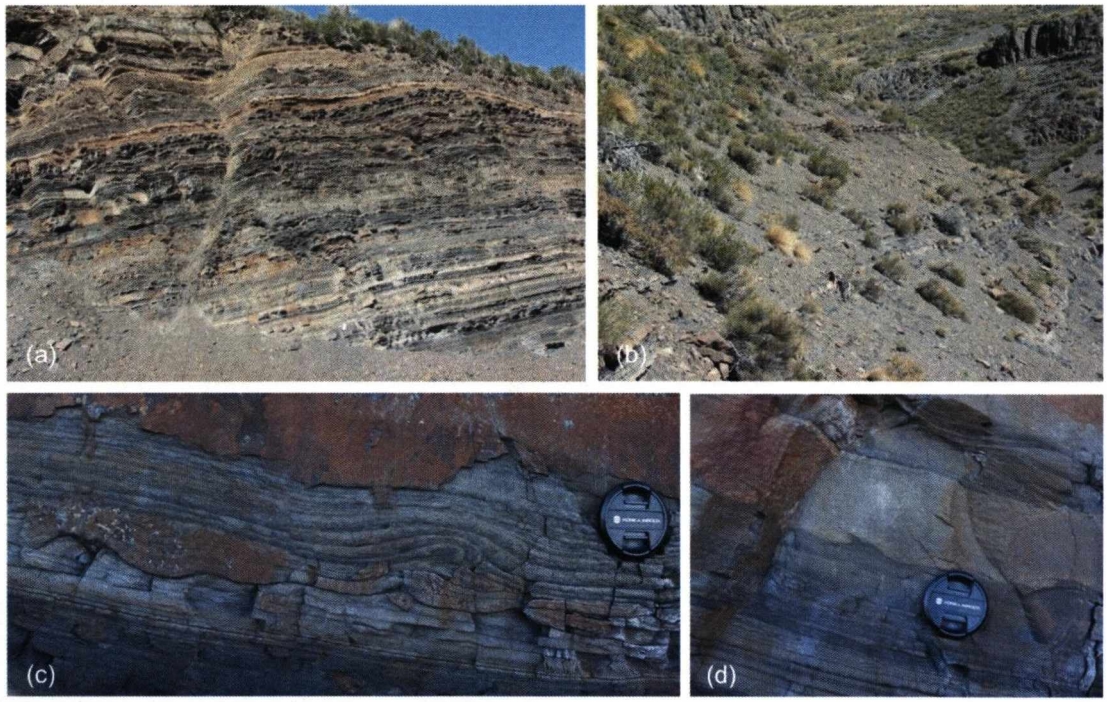

Figure 3.37: (a) Unit 2, west of log Cm5. The thick sandstone beds are in the transition to Unit 3 (the outcrop is 6 m high). The thickening- and coarsening-upward pattern not evident here is easily recognized toward the west (cf. Figure 3.35); (b) Transition Unit 2 - Unit 3 at log Cm6, reflecting the dominance of mudstone in the distal position. The thick bed on top is the top of Unit 4; (c) and (d) Centimetre-scale soft-sediment folds, load structures and flame structures at the sandy top of Unit 2, at the position of log Cm2. See Figure 3.40 for location.

Unit 3 shows a sharp contact with the underlying Unit 2, with local erosion and soft-sediment deformation. To the east the contact with Unit 2 is transitional. The main lithofacies are Ba, Bb, Bg, Ca, Da, Db, Ea, Eb (Table 3.3). Unit 3 is a coarsening- and thickening-upward section, generally coarser than Unit 2. Soft-

sediment deformation structures are represented by flames and sand injectites nucleated in the mudstones at the base of the unit (Figure 3.38). Geometric differentiation between these structures is made considering their relationship with the adjacent rocks: flames are characterized by the rupture of an unconsolidated overlying sediment with possible debouching (or creation of structures like mud volcanoes) at the surface of the deposit at the time of deformation (e.g. Figure 3.38a); meanwhile, sand injection is characterized by the cutting of well defined successive beds, presence of lateral sand injections in different stratigraphic levels and the deformation of the host rock (e.g. Figure 3.38d, e). For genetic considerations consult Chapter 3.1.1. The flames/sand injections can reach 8 m in height, cutting beds of coarse grained sandstone and they correlate laterally to contorted mudstone (Figure 3.38e). At the west side a large unconformity separates underlying fine-grained parallel sandstone-laminated beds from a 10-15 m thick package of medium- to coarse-grained thick (metre scale) sandstone beds. The sandstone beds are tilted at a steeper dip than the underlying beds (cf. Figure 3.35). Laterally, the unconformity is associated with a highly deformed interval that grades upward into a steep fault with a 3m vertical displacement and a listric fault zone marked by the lateral interruption of the thick sandstone beds of Unit 4.The upper limit of Unit 3 is marked by an erosion surface that forms an angular unconformity in the west. Measurements of the axis of soft-sediment folds at the base of Unit 3 indicate movement to ENE (cf. Figure 3.40).

Unit 4 is composed of lithofacies Aa, Ba, Bb, Bg, Ea and Eb (Table 3.3). It is characterized by thick, coarse-grained sandstone beds and well- to poorly-sorted pebble to boulder conglomerate beds with rounded clasts of sandstone and, flat and elongated clasts of mudstone. Soft-sediment deformation structures are restricted to localized contorted sandstones and mudstones in the base of the unit (Figure 3.39).

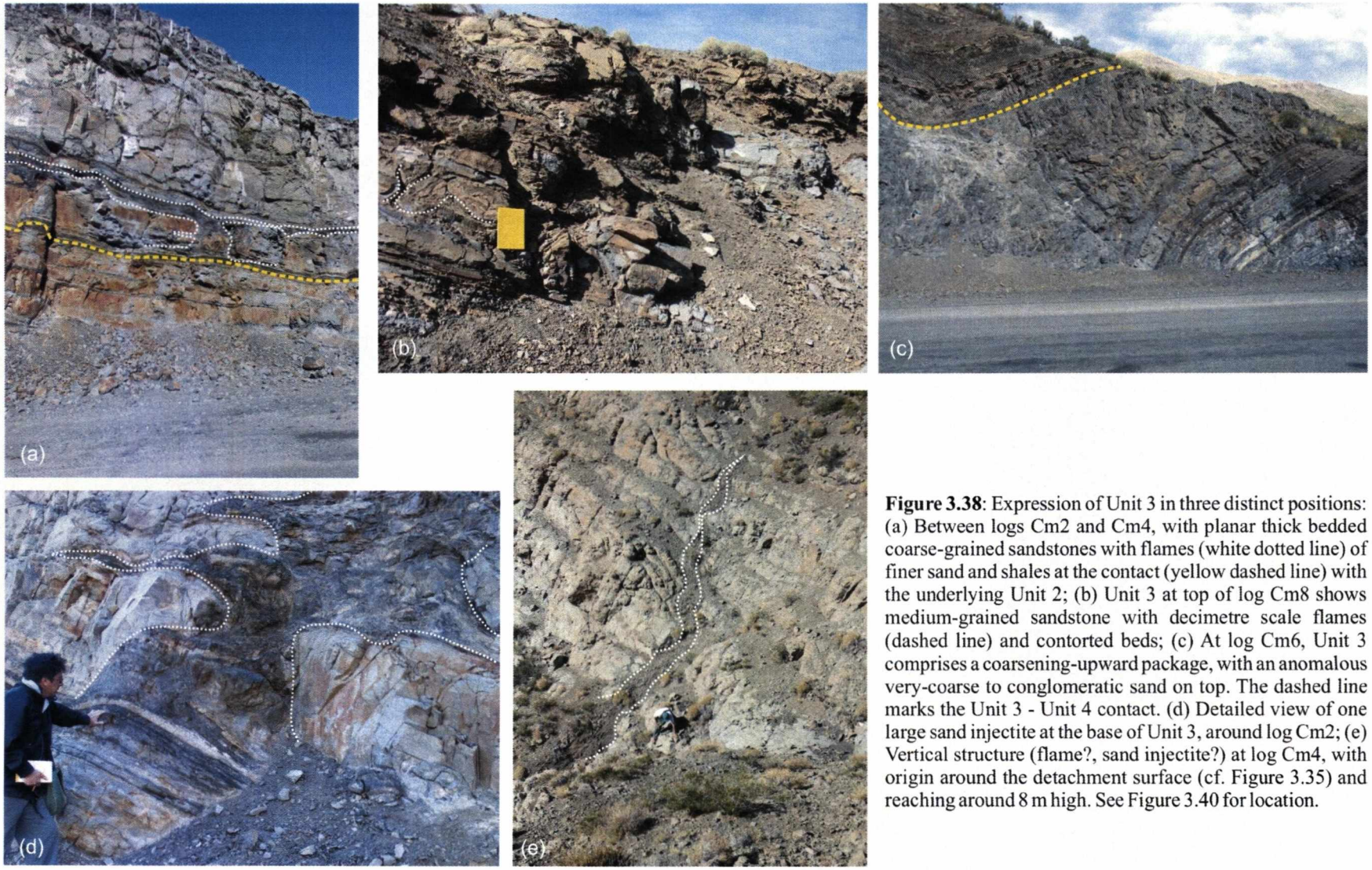

Figure 3.38: Expression of Unit 3 in three distinct positions: (a) Between logs Cm2 and Cm4, with planar thick bedded coarse-grained sandstones with flames (white dotted line) of finer sand and shales at the contact (yellow dashed line) with the underlying Unit 2; (b) Unit 3 at top of log Cm8 shows medium-grained sandstone with decimetre scale flames (dashed line) and contorted beds; (c) At log Cm6, Unit 3 comprises a coarsening-upward package, with an anomalous very-coarse to conglomeratic sand on top. The dashed line marks the Unit 3 - Unit 4 contact. (d) Detailed view of one large sand injectite at the base of Unit 3, around log Cm2; (e) Vertical structure (flame?, sand injectite?) at log Cm4, with origin around the detachment surface (cf. Figure 3.35) and reaching around 8 m high. See Figure 3.40 for location.

Figure 3.39: (a) Thick beds of very coarse-grained sandstone and conglomerate on top of Unit 4 at log Cm2; (b) Above detailed view of the well-sorted pebble conglomerate at the base of the bed in (a) and below poorly-sorted cobble/boulder conglomerate around log Cm3; (c) Medium-grained sandstone bed (1 m thick) at the top of log Cm11 at the same stratigraphic position and down dip related to (a). See Figure 3.40 for location.

Correlation between the sedimentary logged sections was based on the mapped distribution of the units described above and aided by good lateral exposure. A correlation panel was established approximately parallel to regional palaeoslope (Figure 3.40). There is a general reduction in sandstone content to the east, although all logs indicate an overall coarsening- and thickening-upward trend. Faults are common and can be separated into two groups, with normal faults in the west and reverse faults in the east. Fault planes are oriented approximately NW-SE. Hinge line orientation for folds at the base of Unit 1 and near the contact of Unit 2 with Unit 3 varies between N-S and NW-SE.

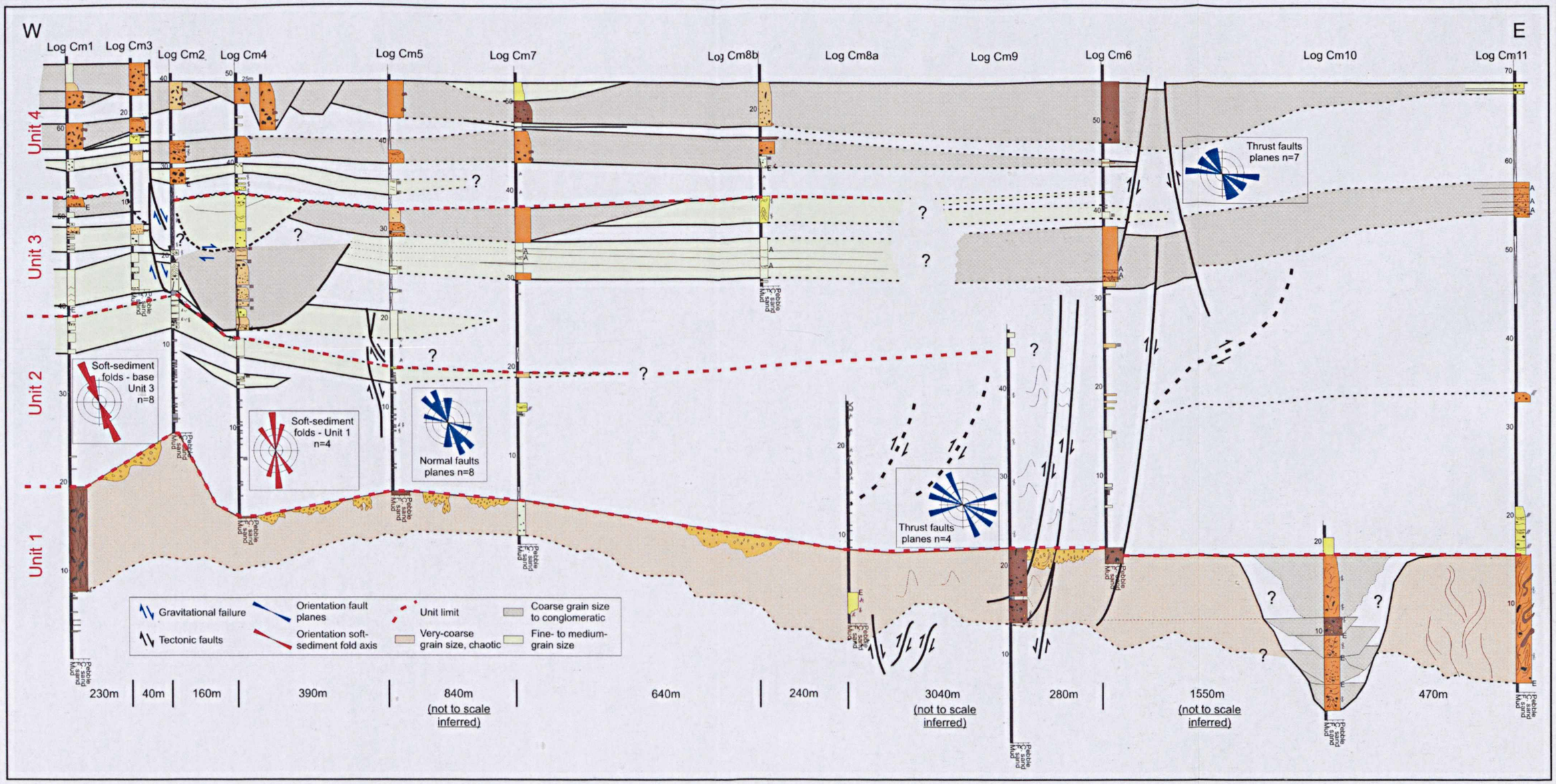

Figure 3.40: Chacay Melehue geological section indicating the correlation between the logs acquired. It is oriented parallel to regional slope, with the distal section at the east side. The section is divided into four major units separated by unconformites. Orientation of tectonic fault planes and of soft- sediment folds axis is shown. See text for detailed description of each unit and interpretation of the geological evolution.

Interpretation

This section was interpreted as an unstable submarine slope environment by Burgess et al. (2000) based on the lithofacies associations, high degree of variability and instability indicators. The chaotic deposits that comprise Unit 1 are interpreted as debrites, based on the unsorted contorted rafts of intra-formational sediment supported by fine-grained matrix, the localized folding, and the textural immaturity. The debrite is abruptly overlain by sandstones and conglomerates. Unit 1 shows two phases of soft-sediment deformation: the first was formed by the down slope evolution of the debris flow. The second phase resulted from deposition of younger coarse-grained sandstones and conglomerates that produced load structures and secondary flame structures. The chaotic facies and the hinge line orientation of the folds in the debrites (cf. Figure 3.40) suggests that sediment was transported to the east, subparallel to the Chacay Melehue palaeoslope (in agreement with Burgess *et al.*, 2000). The irregular distribution of the conglomerate bodies on top of the debrite, without evidence for erosion, suggests either passive infill of existing topographic lows and/or active loading by emplacement of the conglomerates. Either process could have resulted in the large scale (up to 4 m high) foundering structures.

The uppermost package (formed by units 2 to 4) is interpreted to comprise turbidites because of the stratigraphic position in the deep water slope deposits of Los Molles Formation, the normal grading of individual sandstone beds, and the divisions of parallel lamination above structureless graded division. Overall, these beds fine and thin to the east over 7 km down depositional dip, a distance consistent with such a rate of change on a submarine slope (Sprague et al., 2003). This is corroborated by palaeocurrent measurements (cf. Burgess *et al.*, 2000) and the concentration of erosion surfaces that limit each unit on the west side (cf. Figure 3.40). To the east erosion surfaces are not present and the contacts between the units become sharp and concordant.

Soft-sediment deformation in units 2 to 4 is concentrated at the base of each unit and affects mainly the muddy interval with local generation of contorted beds. It is interpreted as slumping probably caused by loading due to emplacement of the coarser material over the mud-prone section. Deformation is enhanced because the finer material was deposited directly over erosive surfaces creating local sites of instability. Particularly interesting is the base of Unit 3, where large (up to 8 m high) mud injection, small intraformational folds and listric-shaped normal faults affect the

sandy section and occur at the same stratigraphic level as the deformed mudstone down dip. The normal faults are interpreted to be generated by gravitational slope failure and control the rotation of an entire section of the overlying Unit 3 (cf. Figure 3.35 and 3.40, Unit 3 between logs Cm3 and Cm4). The unconformity described in the Unit 3 is interpreted as the detachment of those faults, supported by the localized stratigraphic position of the faults without equivalents along the studied section, their listric shape, the rotation of the overlying bedding with thickening toward the footwall, and the detachment at the same stratigraphic interval as the slumping. Flame structures are represented as isolated occurrences, and are the product of deformation of the mud interval that deformed the immediately overlying bed. One flame cuts a succession of sandstone beds without causing deformation of the overlying beds (cf. Figure 3.38e). A possible explanation is that it was injected in a process similar to sand injectites, probably fluidization and hydraulic fracturing (Jolly & Lonergan, 2002).

It is thought that deformation of the complete package was driven by down slope movement of sand-prone packages deposited on a muddy slope. The trigger mechanism(s) that initiated the deformation in the diverse units is not easy to elucidate. It could be related to seismicity, as fault activity during the evolution of the post-rift Cuyo Group has been documented (Vergani *et al*, 1995), or could simply be initiated by the loading and oversteepening caused by rapid progradation and consequent failure of the slope.

Tectonic events are recorded by normal faults oriented NW-SE that follow the general structural framework imprinted by the rift system that preceded and in part controlled the deposition of the Los Molles Formation. Post-depositional thrust faults show a general WNW-ESE trend and are associated with inversion of the older normal faults and are not related to slope collapse structures.

In contrast to the Waterfall and Fortin Primero de Mayo examples, detached soft-sediment deformation processes are dominant at Chacay Melehue. They are represented by a complicated interaction between sediment gravity currents, mass flows and gravitational failure processes on a submarine slope, generating predominantly downslope-translated soft-sediment deformation structures (thick debrites and slumps with common slump-folds and gravitational faults).

Chapter 4 – Soft-sediment deformation in shelf-edge/upper slope settings

4.1 – Karoo Basin – Heuningberg and Roosterberg areas

4.1.1 – Introduction

In this chapter, the shelf-edge to upper slope succession of the Kookfontein and Fort Brown formations in the Roosterberg and Heuningberg areas in the Tanqua and Laingsburg depocentres (Figure 4.1, cf. regional geological maps on Figures 2.8 and 2.9) is analysed with the aim of establishing the relationship between the style of deformation and profile position.

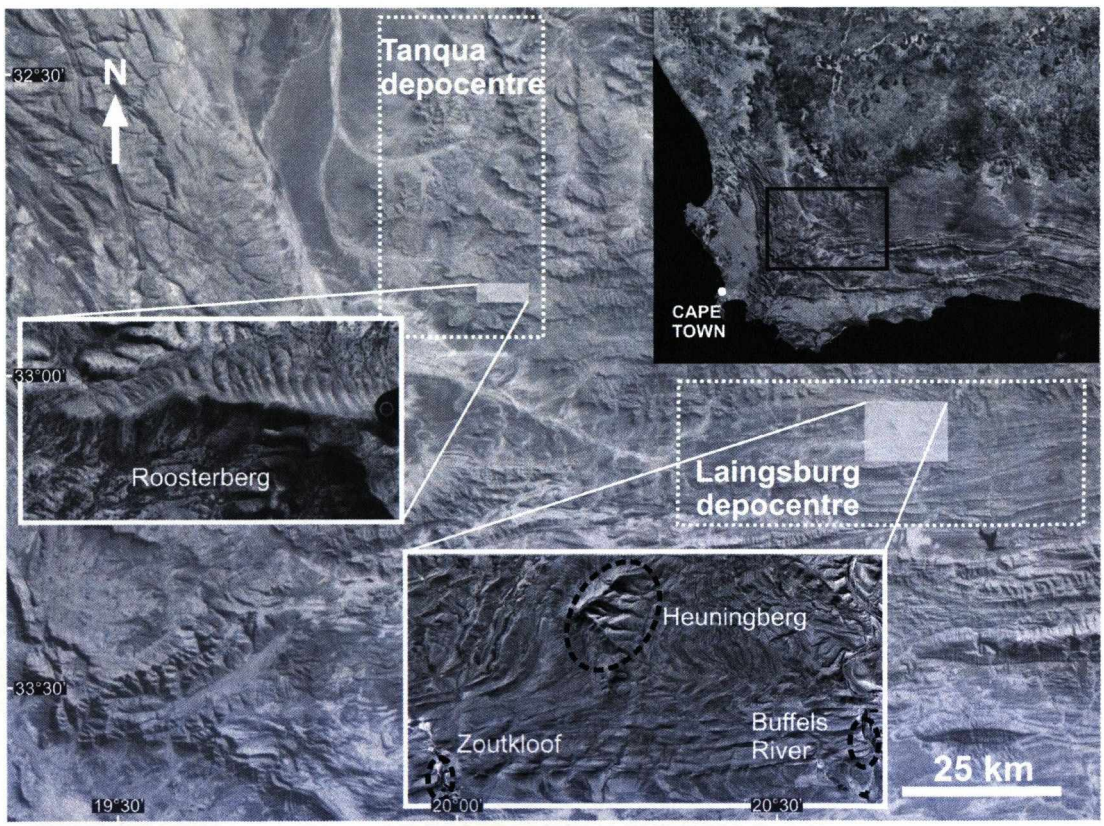

Figure 4.1: Aerial photo and satellite view of the shelf-edge/upper slope deposits of the Roosterberg area (Tanqua depocentre) and Heuningberg, Zoutkloof and Buffels River areas (Laingsburg depocentre).

Data acquisition was based on outcrop logging, lateral and vertical mapping and correlation of deposits within each study areas. In the Tanqua depocentre, the studied section is part of the proximal part of an overall north oriented progradational upper slope and shelf-edge that evolve to ramp type outbuilding (Wild, 2005) (Figure 4.2). Eight logs (total of 360 m), aligned along the E-W oriented Roosterberg range, were acquired in the Roosterberg area of the Tanqua depocentre covering depositional cycles 2 to 4 as defined by Wild (2005) (Figure 4.3).

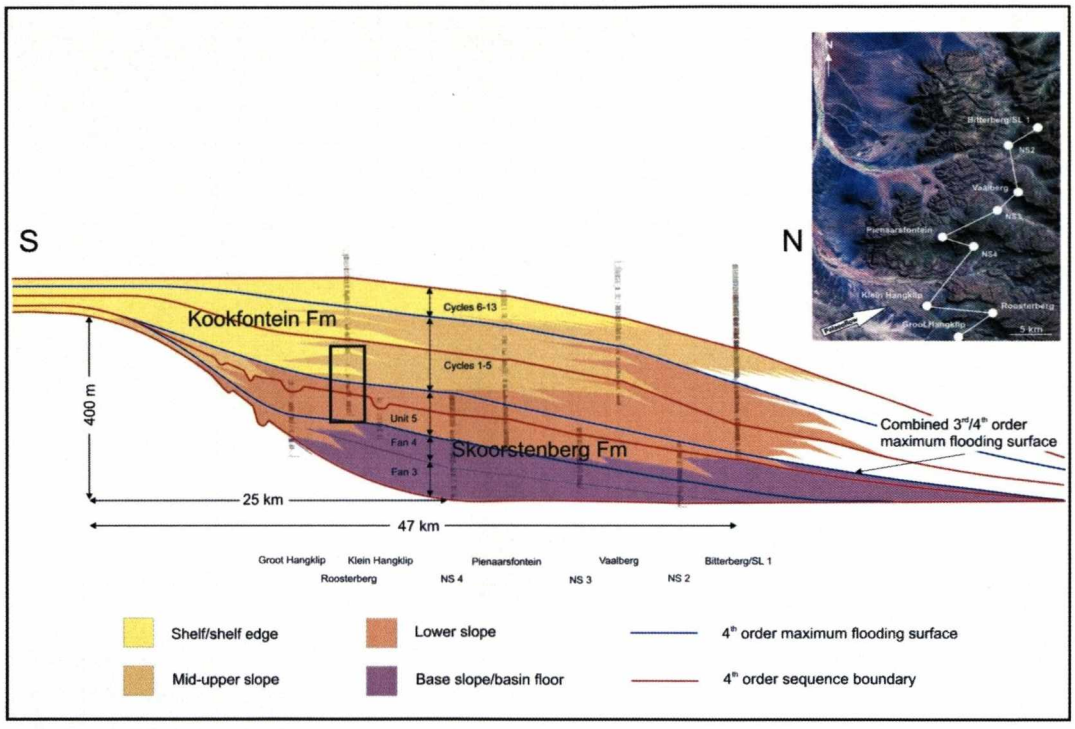

Figure 4.2: Sequence stratigraphic framework and depositional environments of the Upper Skoorsteenberg Formation (basin-floor fans 3 & 4 and Unit 5, lower slope to base of slope wedge) and the Kookfontein Formation (Cycles 1-13, prograding slope and shelf edge) (from Wild, 2005) at the Tanqua Depocentre (after Wild, 2005). The studied section is represented by the black square and comprises shelf to shelf-edge deposits of the Kookfontein Formation (Cycles 2 to 4).

In the Heuningberg area, Charles (2007) characterised ENE oriented, coarsening and thickening-upward cycles of mouth bar sediments deposited onto the upper slope; with scour, deformation and the influence of storms increasing upwards, interpreted preliminarily as parasequences, owing to the presence of well-defined flooding surfaces and absence of sequence boundaries, expressed on the upper slope as correlative conformities (Figure 4.4). Thirteen logs (total of 411 m) were acquired in the Laingsburg depocentre, in the Heuningberg, Zoutkloof Farm and Buffels River areas. The focus of the investigation was the deformed sandy section of depositional

cycles 2 to 4 as defined by Charles (2007) in the Heuningberg area (Figure 4.5) with complementary information from the stratigraphically younger outcrops from Zoutkloof Farm and Buffels River (cf. Figure 4.1). Mapping of lateral changes in the facies and deformational style was possible due to the good exposure of the deformed intervals (cf. Figure 4.3). No attempt was made to correlate cycles between the two areas (which are 100 km apart) due to exposure and logistical considerations. Therefore any cycle in the Tanqua section has no implied spatial or temporal equivalence to a cycle in the Laingsburg section.

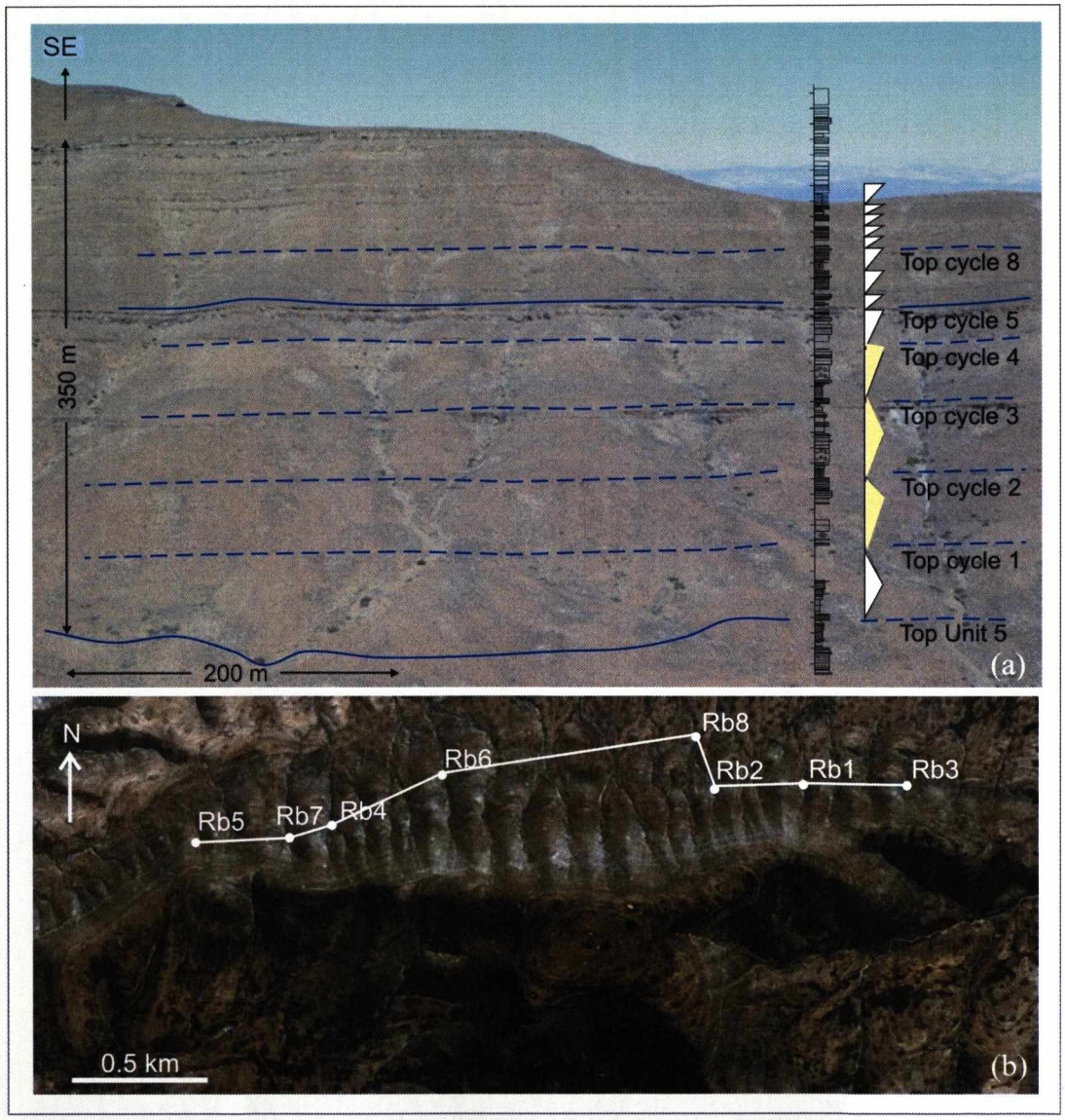

Figure 4.3: (a) Photograph of the west part of Roosterberg (around log Rb5) showing log section and distribution of depositional cycles in the Kookfontein Formation (Wild, 2005). The three cycles (2, 3 and 4) investigated in this study are highlighted; (b) Aerial view of Roosterberg pointing the position of the base of the acquired log. The white line shows the orientation of the correlation section on Figure 4.6.

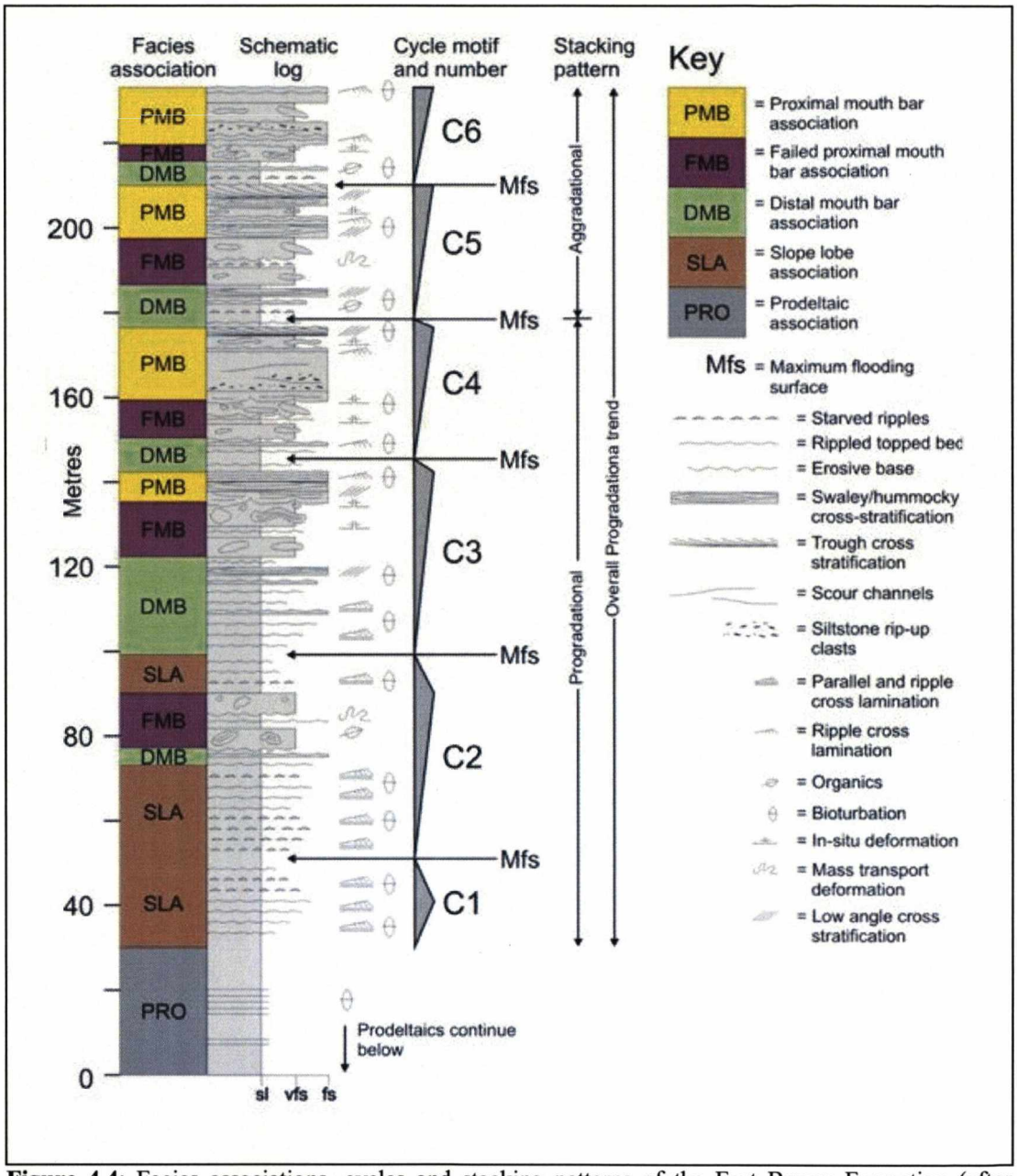

Figure 4.4: Facies associations, cycles and stacking patterns of the Fort Brown Formation (after Charles, 2007).

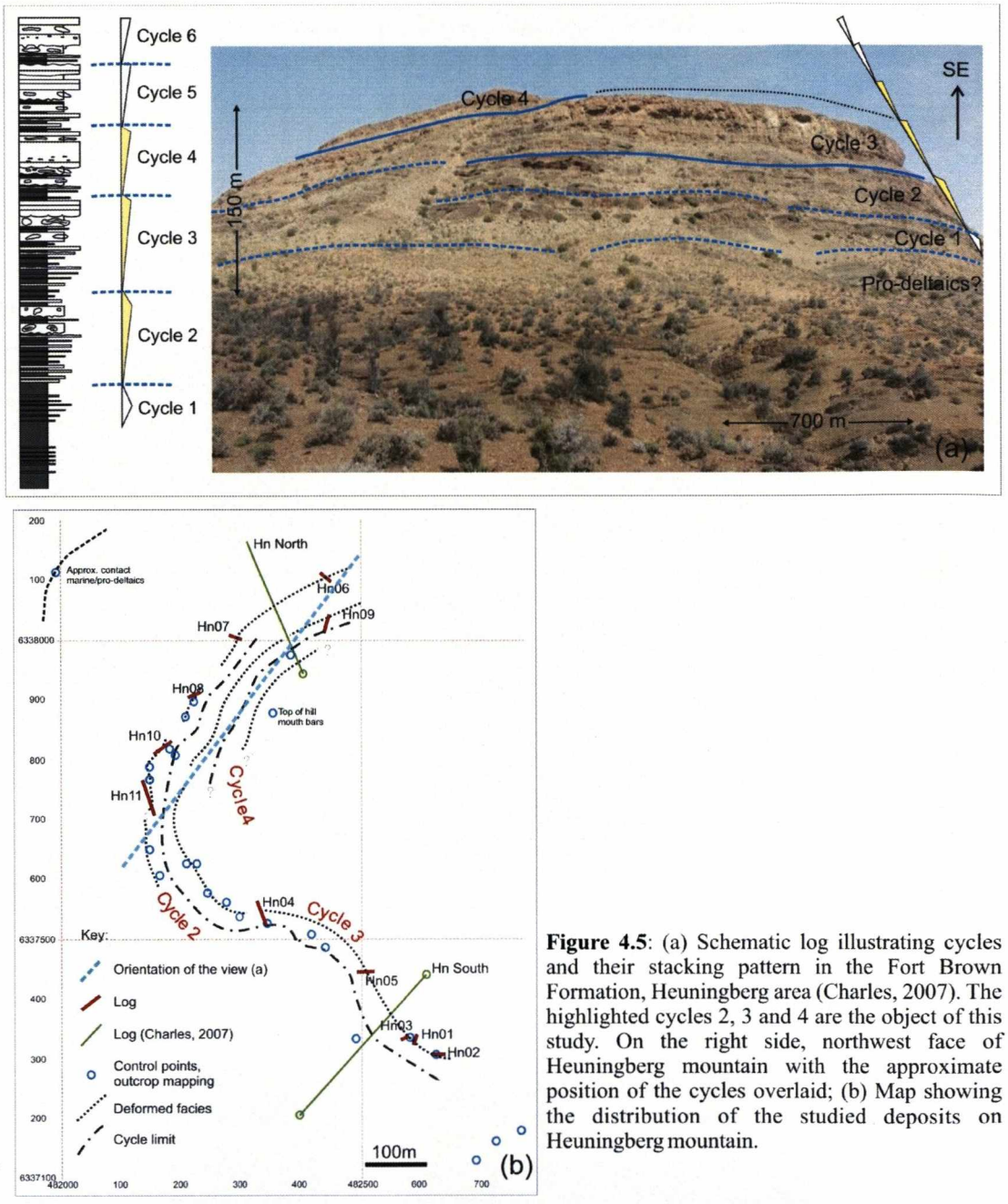

Figure 4.5: (a) Schematic log illustrating cycles and their stacking pattern in the Fort Brown Formation, Heuningberg area (Charles, 2007). The highlighted cycles 2, 3 and 4 are the object of this study. On the right side, northwest face of Heuningberg mountain with the approximate position of the cycles overlaid; (b) Map showing the distribution of the studied deposits on Heuningberg mountain.

4.1.2 – Facies and Facies associations.

Here, the facies and facies associations identified in both study areas will be described to synthesise one generic framework for the analysis of intervals of soft-sediment deformation. The main lithofacies are described in Table 4.1. The lithofacies classes are based on the scheme of Pickering *et al.* (1986), with classes A-E defined on grain-size differences and class F on the basis of internal organization

and soft-sediment deformation style. Accompanying the class designation (A-F), indices a-f indicate internal depositional or deformational sedimentary structures. Four facies associations were defined based on the internal facies distribution (Table 4.2).

Log correlation panels are shown in figures 4.6 and 4.7, for the Roosterberg and Heuningberg areas respectively and a summary with the main characteristics for each cycle is given in Table 4.3. Both study intervals lie stratigraphically above basin-floor fan and erosive submarine slope channel/levee systems (Grecula et al. 2003; Sixsmith et al., 2004; Hodgson *et al.*, 2006, Flint *et al.*, 2008), and below shelf and fluvial strata (Wickens 1994; Wild 2005). The Roosterberg cycles in Tanqua are prefixed with 'R', and the Heuningberg cycles in Laingsburg with 'H'.

Lithofacies class	Lithofacies name	Sub-classes	Lithology	Associated Lithofacies	Sedimentary structures	Bounding surface	Single bed thickness	Geometry	Depositional/ Deformational Process
Aa	Coarse-grained sandstone/ conglomerate		Coarse-grained sandstone/ conglomerate	Fa, Fc	Chaotic, clast supported, dewatering fabrics. Highly deformed sadstone blocks. Outcrop type: *Buffles River*	Sharp	0.7m	Tabular	Rapid deceleration of high concentration turbidity current or debris flow.
Ba	Structureless sandstone	l – loaded base o – bioturbed w – symmetric ripple on top g – rip-up clasts	Very fine- to fine-grained sandstone	Bb, Bc, Bd, Be, Ca, Db, Fa, Fb, Fe	Massive, block weathering. Rare wavy on top.	Sharp. Also loaded and erosive base. Amalgam.	0.2-1.5m. Up to: 5m.	Tabular. Rarely channel.	Rapid deceleration of high concentration turbidity current or liquefaction
Bb	Planar-laminated sandstone			Ba, Bc, Bd, Be, Ca, Db, Dc, Ea, Fb	Parallel lamination. Commonly grading to massive or low-angle cross stratification. Symmetric waves on top. Rare rip-up clasts.	Sharp. Also gradational on top.(Tbc) and base.	0.02-0.1m. Bed sets: 0.15-2.0m (anomal. 3.5m and 6.0m)	Tabular. Rarely channel.	High concentration turbidity currents
Bc	Ripple-laminated sandstone			Ba, Bb, Bd, Ca, Cb, Db, Dc	Ripple lamination. Symmetric wave ripples on top.	Sharp and gradational. (Tbcd-Tbc). Rare loaded base	0.03-0.12m. Bed sets: 0.2-4.0m	Tabular	High concentration turbidity currents

Bd	HCS sandstone	l – loaded base o – bioturbed w – symmetric ripple on top g – rip-up clasts	Fine-grained sandstone	Ba, Bb, Bc Fb, Fd	Hummock-cross stratification	Sharp. Base can be erosive.	0.3-0.7m (0.1-1.0m)	Tabular and channel.	Storm events.
Be	Cross-stratified sandstone		Very fine- (rare) to fine-grained sandstone	Ba, Bb, Bd, Ca, Fb	Low-angle cross stratification, grading to ripple and planar laminated. Rip-up clasts when erosive base.	Sharp and erosive.	1.0-1.3m (0.2-1.7m)	Associated with channels; also tabular.	Storm events
Bf	Undulate-laminated sandstone		Very fine- to fine-grained sandstone	Ba, Bc, Fb	Wavy laminated. Rare event.	Sharp	0.2-0.8m	Tabular	Low to high concentration turbidity currents.
Ca	Planar-laminated sandstone/siltstone interbedded	l – loaded base o – bioturbed w – symmetric wave on top	Fine-grained siltstone to fine-grained sandstone	Ba, Bb, Bc, Bd, Be, Cb, Db, Dc, Ea	Parallel lamination. Symmetric waves on top. Some soft-sediment deformation. Bioturbed. Characteristic of coarsening-upward sequences.	Sharp and gradational.	0.02-0.1m. Bed sets: avg 1.0m, up to 13m in Roosterberg.	Tabular	Low to high concentration turbidity currents.
Cb	Ripple-laminated sandstone/siltstone interbedded			Ba, Bb, Ca, Db, Dc	Ripple lamination. Symmetric waves on top.	Sharp and gradational (Tbc, Tc).	0.02-0.1m. Bed sets: 0.25-1.0m.	Tabular	Low to high concentration turbidity currents
Da	Structureless siltstone	l – loaded base o – bioturbed w – symmetric wave on top	Fine- to coarse-grained siltstone	Ba, Bb, Dc, Fa, Fb, Fd	Massive, blocky weathering. Occurrence of foundering	Sharp	0.2-1.0m (thickest: liquefaction?)	Tabular	Low-concentration turbidity currents

Db	Planar-laminated siltstone	l – loaded base o – bioturbed w – symmetric wave on top	Fine- to coarse-grained siltstone	Ba, Bb, Bc, Ca, Cb, Dc, Ea	Parallel lamination. Characteristic of coarsening-upward and agradational sequences.	Sharp and gradational.	≤0.01m. Bed sets: 0.2-2.5m, up to 8.5m.	Tabular	Low-concentration turbidity currents
Dc	Ripple-laminated siltstone	l – loaded base o – bioturbed w – symmetric wave on top	Fine- to coarse-grained siltstone	Ba, Bb, Ca, Db, Ea	Ripple lamination. Characteristic of coarsening-upward sequences. Symmetric waves on top.	Sharp and gradational	0.01-0.04m. Bed sets: 1.0-6.5m, up to 13.0m.	Tabular	Low-concentration turbidity currents
Ea	Claystone		Claystone/ mudstone	Ba, Be, Da, Db, Dc	Structureless. Occurrence of fine laminated silty clays	Gradational at base and sharp or truncated on top.	<1cm (when laminated). Bed sets:10-200cm.	Tabular and lens shape.	Hemipelagic settling.
Fa	Highly deformed sandstone siltstone with rafts	i – silty matrix n – sandy matrix	Fine-grained siltstone to fine-grained sandstone. Rafts rarely medium grained sandstone to conglomerate	Aa, Ba, Da, Fb, Fc, Fd.	Chaotic, rich in deformed rafts of coarser material (normally fine grained sandstone or coarser) than the matrix (coarse grained siltstone to fine grained sandstone)	Sharp, also erosive in the base. Amalgam.	2.0-7.0m (1.0-10.0m)	Tabular	Rapid deceleration of high concentration turbidite current or debris flow.

Fb	Deformed sandstone/siltstone with vertical structures	*i* – silty matrix n – sandy matrix s – "squeeze" component	Fine-grained siltstone to fine-grained sandstone	Ba, Bb, Da, Fa, Fc, Fd, Fe	*SSD structures:* flames (dominant), also load casts, pseudonodules. Rare pillar and dish.	Sharp, also truncated on top. Amalgam. Loaded base.	0.2-1.5m (up to 3.0m)	Tabular to convex to top.	*In situ* deformation associated with liquefaction plus down slope mass movement (slumping, debris flow).
Fc	Structureless sandstone/ siltstone with foundering			Fb, Fe	Structureless presenting less deformed lens/rafts of sandstones. Commonly lenticular sandstone bodies on top. Small pseudonodules and ball and pillow	Sharp.	0.4-1.8m (Anomalous >3m)	Tabular to convex to base.	Passive foundering of denser sand bodies in a silty/sandy liquefied bed.
Fd	Contorted sandstone siltstone	r – disrupted and lenticular layering v – convolute lamination		Da, Fa	Chaotic, presenting matrix and rafts contorted. Sometimes difficult to distinguish from facies Fa.	Sharp, also erosive in the base.	0.6-2.0m (0.3-2.7m)	Tabular and lens shape	Slumping of slope edge deposits.
Fe	Sandstone/siltstone with detached load structures (pseudonodules, ball and pillow)			Fb, Fc	Load structures (pseudonodules and ball and pillow) of sandstone in a structureless siltstone/sandstone matrix.	Sharp	0.1-1.0m	Irregular	*In situ* deformation associated with liquefaction.

Table 4.1: Lithofacies classification for the shelf-edge/upper slope deposits of Kookfontein and Fort Brown Formations in the Tanqua and Laingsburg depocentres, respectively.

Facies association number	Facies association name	Main Lithofacies	Secondary Lithofacies	Characteristics
1	Interbedded sandstone and/or siltstone	Ba, Bb Ca Db, Dc Ea	Bc, Be Cb Da, Dd Fb, Fd	• Coarsening-upwards beds • Some aggradation • Rare fining-upwards beds • Common wave ripples on top.
2	Thick sandstone	Ba,Bb,Bc,Bd,Be	Bf Ca, Cb Da, Db Fa, Fb, Fd	• Channel geometry (some) • Coarse beds • Rare fine laminated beds • Low angle cross-stratification (LCS) mainly in Zoutkloof and Buffels River localities • Some symmetric wave ripples on top • Loaded base (common) • Bioturbation • Base showing amalgamation and erosion • Lateral gradation from B to F lithofacies • B and C divisions of the Bouma sequence are common.

3	Deformed – *in situ*.	Fb, Fc, Fe Da	Aa Ba, Bb,Bc, Bd, Be, Bf Ca Db Fa, Fd	• Vertical structures (flames) dominate • Loaded base • Structureless sandstone (Ba) and siltstone (Da) facies can be related to layer liquefaction
4	Deformed - detached	Fa, Fd	Aa Ba, Bfb, Bf Ca, Cb Da Fb, Fc, Fe	• Fd facies: slumps dominate • Fa facies: debrites dominate • Deformed sandstone rafts of a range of sizes (cm to m) • Structureless sandstone (Ba) and siltstone (Da) facies can be related to layer liquefaction • Channelized shape is common. • Some symmetric wave ripples on top.

Table 4.2: Lithofacies association for shelf-edge/upper-slope deposits of the Kookfontein Formation (Tanqua depocentre) and Fort Brown Formation (Laingsburg depocentre).

East

West

Cycle R4

Cycle R3

Cycle R2

Rb3 log

Rb1 log

Rb2 log

292m

569m

Rb7 log

Bed G

Rb5 log

Rb4 log

473m

545m

Bed F

Bed E

Bed D

Bed C

Bed B

Bed A

Rb6 log

Rb8 log

1092m

Key:

- Ripple lamination (also climbing ripple)
- Parallel lamination
- Cross-bedding (low angle)
- Hummock cross-stratification
- Structureless
- Tbc Bouma cycle
- Wavy on top
- Concretion
- Plant material
- Bioturbation
- Soft-sediment deform. (not-specified)
- Flame structure
- Slump-related structure
- Raft
- Pseudonodule, ball-and-pillow struc.
- Pillar-and-dish struc.
- Load cast
- E Erosion
- A Amalgamation
- Rip-up clast

- Mudstone/claystone
- Thin-layers siltstone dominated
- Translated dominated deformation (debrites, slump dep.)
- Thin-layers sandst. dominated
- Sandstone
- *In situ* dominated deformation (flame, load structures, etc.)

Bed A Selected for statistical analysis

1 Facies association (refers to Table 2)

Figure 4.6: Correlation section Roosterberg area, Tanqua depocentre. This log section is located on Figure 4.3 and log coordinates are on Appendix 1.

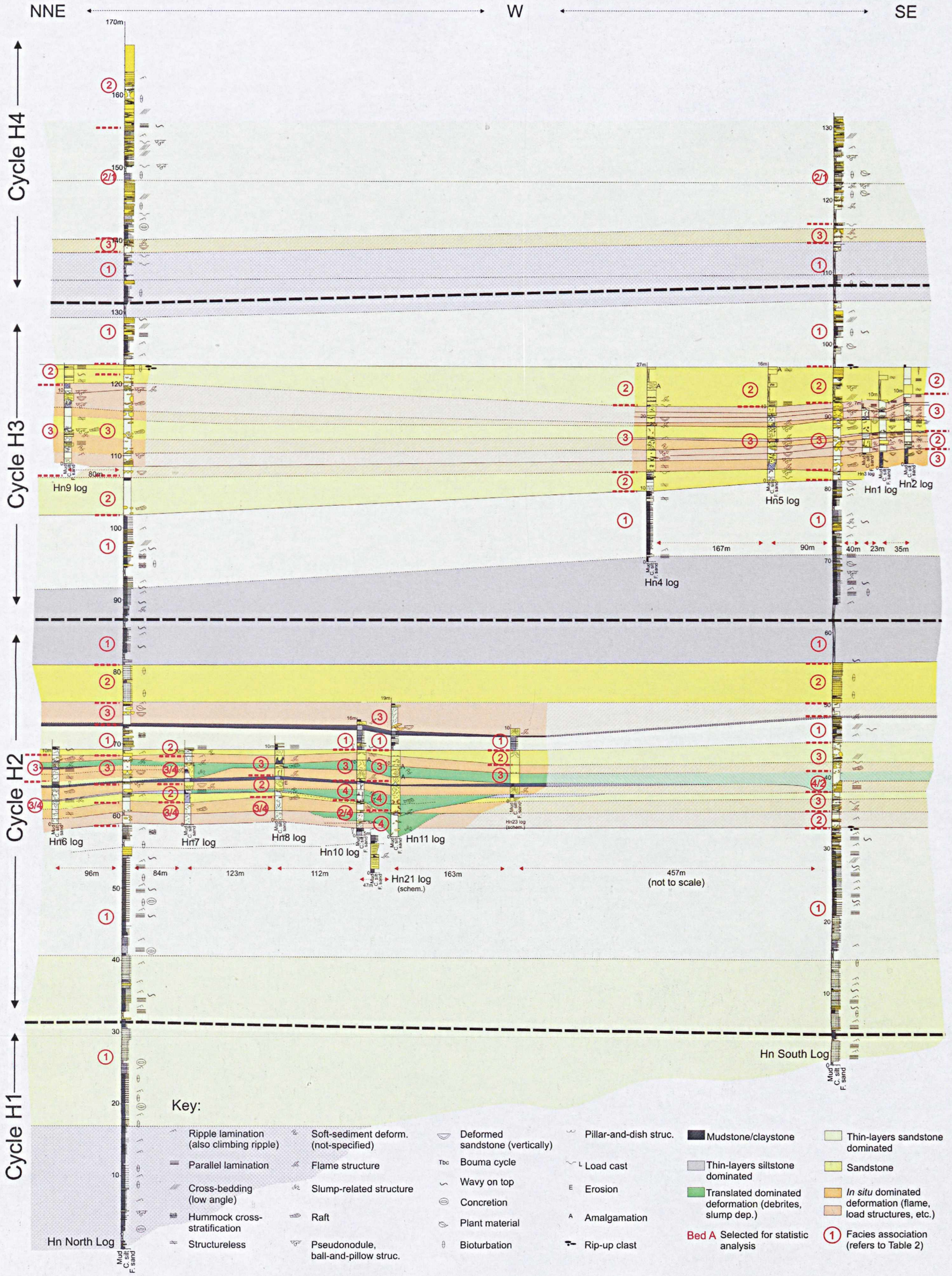

Figure 4.7: Correlation section Heuningberg area, Laingsburg depocentre. Logs Hn North and Hn South are from Charles (2007). This log section is located on Figure 4.5 and the coordinates are on Appendix 1.

CHARACTERISTIC		ROOSTERBERG (TANQUA DEP.)			HEUNINGBERG (LAINGSBURG DEP.) (Charles, 2007)		
GENERAL	Number of cycles (regional) identified in work to date	13 (Wild, 2005)			6 (Charles, 2007)		
	Subcrop	Thin slope succession (<100m)			Thick slope succession (500m)		
	Stacking pattern	Progradationa/Aggradational			Progradational/Aggradational		
		CYCLE R2	CYCLE R3	CYCLE R4	CYCLE H2	CYCLE H3	CYCLE H4
Total thickness		48m	48m	> 40m	55m	46m	~ 40m
Deformed section thickness		12-14m	12-18m	10-15m	17m	15-17m	4m (discont.)
Deformed/Total section thickness (%)		25-29%	25-38%	25-37%	31%	33-37%	10%
Cycle symmetry							
Facies association sequence		1-4-3-2-1	1-4-3-2-1-(2)	1-(4)-3-2-1	1-4/3-1-3-2-1	1-2-3-2-1	1-(3)-2
Dominant deformation category		Detached	Detached	*In situ*	Detac./*In situ*	*In situ*	*In situ*
Unidirectional palaeocurrents (ripple foresets)		N	N-NW	N-NW	E-NE (Charles, 2007)		
Bidirectional palaeocurrents (symmetrical ripple crests)		E-W	NE-SW	E-W	NE-SW		

Table 4.3: Summary of main characteristics for depositional cycles in the Roosterberg (Tanqua depocentre) and Heuningberg (Laingsburg depocentre) study areas.

4.1.3 Stratigraphy of study intervals

Recent studies by Wild (2005) and Charles (2007) proposed a model for the architectural organization and geological evolution of the interpreted upper slope to shelf-edge successions exposed in the Tanqua and Laingsburg depocentres. In both study areas, the stratigraphy was divided into mappable coarsening- and thickening-then fining- and thinning-upward cycles bounded by regional mudstones. Thirteen cycles of coarsening- and thickening-upward packages of siltstone to fine-grained sandstone in the Kookfontein Formation in the Tanqua depocentre were split by Wild (2005) in two groups: cycles 1-5 exhibit a broadly progradational stacking pattern with decreasing thickness upwards, while cycles 6-13 form an aggradational stacking pattern of progressively thinner packages. This change was interpreted by Wild (2005) as the transition from upper slope (cycles 1-5) to shelf environments (cycles 6-13) (Figure 4.8a). The cycles studied at Roosterberg (cycles 2-4) were deposited in an upper-slope to shelf-edge setting and comprise a aggradational section within the general progradational basal sequence. Six coarsening- and thickening–upward cycles in the Fort Brown Formation, Laingsburg depocentre, exhibit a progradational-to-aggradational stacking pattern (Figure 4.8b) and are interpreted as product of upper slope to shelf-edge deltas (Charles, 2007). Cycles 2-4 studied at Heuningberg area characterized a progradational stacking pattern.

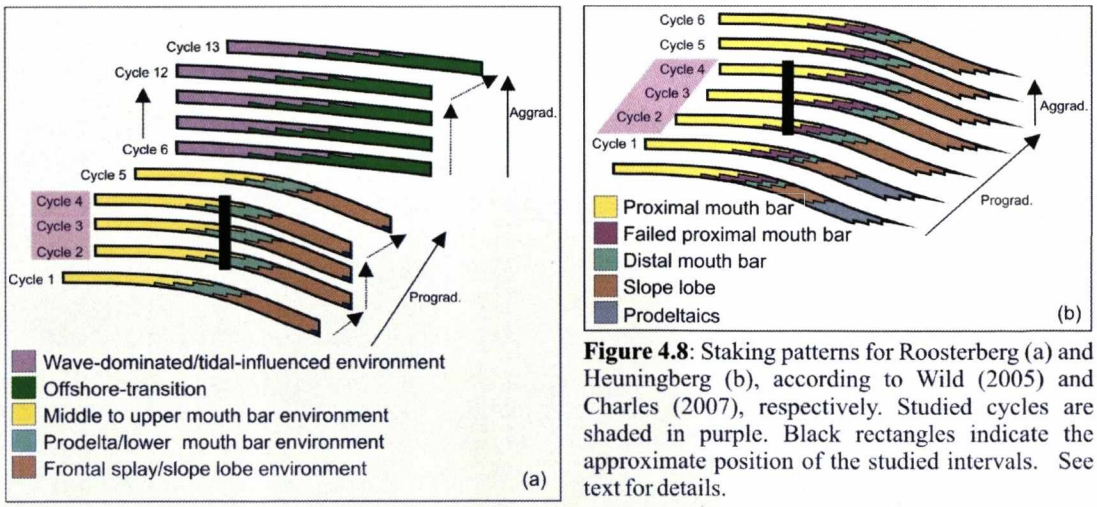

Figure 4.8: Staking patterns for Roosterberg (a) and Heuningberg (b), according to Wild (2005) and Charles (2007), respectively. Studied cycles are shaded in purple. Black rectangles indicate the approximate position of the studied intervals. See text for details.

A similar large-scale stratigraphic succession of facies is identified in all studied cycles (Figures 4.6 and 4.7) in both areas. The bases and tops of cycles are

defined by extensive, typically metre-thickness, mudstone intervals. The main body of each cycle is characterized by a lower interval dominated by thin intercalated siltstone and fine-grained sandstone beds, followed by an intermediate section dominated by soft-sediment deformed facies, overlain by thick-bedded fine-grained sandstone. The top section of the cycles can vary from fine grained thinning-upward packages to sharp tops. The resemblance is also expressed in the cycle thickness (40 to 55 m) and the average percentage (around 30%) of deformed strata (Table 4.3). Table 4.4 summarizes main aspects of the facies distribution and the interpreted depositional/deformational setting for each cycle in both depocentres that will be discussed in more detail in the sections below.

Description

In Roosterberg outcrop, three coarsening- and thickening to fining- and thining-upward cycles show a common upward succession of facies association 1-4-3-2-1 (Tables 4.2 and 4.3 and Figure 4.6). The 48 m thick Cycles R2 and R3 are similar and form an asymmetric profile, composed of a basal section of coarsening-upward interbedded siltstone-sandstone (class 1, Table 4.2), with subordinate soft-sediment deformation (mainly Cycle R2). This is followed by a deformed interval showing the predominance of deformed transported facies (class 4, Table 4.2) over *in situ* deformed facies (class 3, Table 4.2); capped by thick planar-laminated to cross-stratified sandstone (class 2, Table 4.2) with secondary soft-sediment deformation structures and channel incisions. At the top of Cycle R2, a 4 m thick package of coarsening- and thickening-upward siltstone and laminated sandstone is overlain by 3 m of fining-upward mud-prone heteroliths culminating with the deposition of a 2 metre thick mudstone that demarcates the top of the cycle. More complex relations are found on top of Cycle R3, with the 15 m thick package of planar-laminated normal graded coarse siltstone to mudstone on the east side (log Rb4) contrasting with the deposition of mud-prone heteroliths that grade upward to a planar- and ripple-laminated siltstone on the west side (log Rb8). The top of Cycle R3 is characterized by deposition of 1.5 m of mudstone used as a regional marker. Cycle R4 is thinner (38 m) and less deformed than the older cycles. It is distinguished by the predominance of *in situ* deformation over detached deformation and is organized in a vertical facies association succession 1-(4)-3-2-1 (Table 4.4).

Facies distribution and interpretation		ROOSTERBERG (TANQUA DEP.)			HEUNINGBERG (LAINGSBURG DEP.)		
		CYCLE R2	CYCLE R3	CYCLE R4	CYCLE H2	CYCLE H3	CYCLE H4
Lower section	*Facies*	Cb, Dc Fa, Fb, Fc, Fe (sec.)	Cb, Dc Da, Fe (sec.)	Bb, Bc, Ca, Dc	Ca, Cb, Db, Dc Bd, Be (sec.)	Cb, Db, Dc Bd, Be (sec.)	Cb, Dc
	Interpretation	Low density turbidity currents, mid slope environment + failure to the top, upper slope	Low density turbidity currents, mid slope environment + loading to the top	Low to high density turbidity currents, mid slope environment	Lower to mid mouth bar, shelf-edge/upper slope environment	Lower to mid mouth bar, shelf-edge environment	Lower to middle mouth bar, shelf environment
Intermediate section (deformed)	*Facies*	Fa, Fb, Fd	Fa, Fb, Fd	Bc, Bd, Fb, Fe	Fa, Fb, Fc, Fd	Bd, Be Fa, Fb, Fc, Fe	Ba, Bb Fb, Fc, Fe
	Interpretation	Progradation and failure of the delta front, shelf-edge/ upper slope environment	Progradation and failure of the delta front, shelf-edge/ upper slope environment	Progradation and failure of the delta front, shelf-edge environment	Progradation and failure of mid- upper mouth bar, shelf-edge environment	Progradation and failure of mid- upper mouth bar, shelf-edge/shelf environment	Middle mouth bar, shelf environment, locally *in situ* instabilities
Upper section	*Facies*	Bb, Bd Fb (sec.)	Ba, Bb, Bd, Be Fe (sec.) Ca, Dc (top)	Bb, Bc, Bd	Ba, Bc, Fc(sec.)	Be, Ca, Dc	Ba, Bb, Be Fb, Fe (sec.)
	Interpretation	Mouth bars, shelf edge environment	Mouth bar, fluvial dominated storm wave influence, late flooding and retrogradation, shelf environment	Mouth bar, shelf environment	Upper mouth bar, shelf environment, followed by flooding	Delta front progradation lateral migration, shelf environment.	Upper mouth bar, shelf environment, locally *in situ* instabilities
Facies association		1-4-3-2-1	1-4-3-2-1-(2)	1-(4)-3-2-1	1-4/3-1-3-2-1	1-2-3-2-1	1-(3)-2

Table 4.4: Facies distribution and interpretation for the studied cycles at Roosterberg (Tanqua depocentre) and Heuningberg (Laingsburg depocentre).

The succession in the Heuningberg area contains fewer detached facies in comparison to the Roosterberg outcrops (green beds in Figures 4.6 and 4.7). The vertical succession of facies associations is not as well organized and predictable as in Roosterberg although a general distribution of facies can be described by 1-(2)-3-(4)-2-1 (Tables 4.2 and 4.3), from base to top. Also, cycle thickness and the degree of deformed facies decrease upwards.

Cycle H2 is characterized by aggradational to thickening- and coarsening-upward packages of siltstone to fine-grained sandstone that, together with lower Cycle H3, differ from the lower cycle sections in the Roosterberg area by the presence of hummocky- and low angle- cross-stratification below the intermediate section of deformed packages. The middle/upper Cycle H2 shows a complex interaction of detached and *in situ* deformed strata, followed by deposition of thick beds of undeformed fine-grained sandstone and an overlying 4 m thick fining- and thinning-upward package at the top of this cycle. Cycle H3 is similar to Cycle H2 but is distinguished by the preponderance of *in situ* deformation in the middle section and by the occurrence of 8-10 m thick interval of a coarsening- and thickening-upward siltstone to fine-grained sandstone just above the intermediate deformed interval and separated from this by an erosive surface. The coarsening- and thickening-upward package of coarse-grained siltstone to fine-grained sandstone that caps the H4 Cycle is characterized by a coarsening- and thickening-upward package and by the dominance of low angle-cross -stratification and minor occurrences of deformed facies.

Interpretation

The common tripartite succession for each cycle is here interpreted as the result of the migration of a delta onto and sometimes over the shelf-edge (Wild, 2005) culminating with: (i) the initial deposition of turbidites on the slope, normally represented by facies association 1; (ii) followed by a deformed sedimentary package originating from the failure of the delta front when it reached the shelf-edge/upper slope, represented by facies associations 3 and 4 and (iii) culminating with a mouth bar/shoreface deposited above the failed material, facies association 2. Variations can be seen from cycle to cycle and laterally within a cycle; and this is interpreted as a function of the relative position of the delta in relation to the shelf-edge.

Cycles R2 and R3 in Roosterberg follow the succession described above with a well developed down-slope detached facies association suggesting that the delta front reached beyond the shelf-edge. The same model can be used for Cycle R4, although the predominance of *in situ* deformation deposits over detached deformation deposits suggests that Cycle R4 was deposited in a more stable setting than the underlying cycles, which Wild (2005) interpreted to be related to a decrease in slope angle due to sediment accretion.

At the top of Cycle R2, the 4 m thick finer-grained package of coarsening- and thickening-upward mudstone to coarse siltstone is interpreted as formed in a backstepping trend. At the top of Cycle R3 lateral changes are interpreted as a product of the combination of relative sea-level rise with lateral delta lateral switching to the east during transgression. An overall relative sea level rise culminates in the deposition of the 1.5 m thick mudstone that marks regionally the end of this cycle.

Similarly to Roosterberg, the stratigraphic succession for Cycles H2 and H3 in Heuningberg is interpreted as the product of delta progradation over the shelf-edge with the initial deposition of (pro-delta) turbidity currents on the slope, followed by deformation processes at the delta front (in situ and detached) and capped by mouth bar deposits (Charles, 2007). In contrast to Roosterberg, there is an abrupt reduction in the proportion of detached facies between Cycles H2 and H4, which is interpreted as a change from slope to shelf deposition with consequent reduction in detached facies.

The coarsening- and thickening-upward siltstone to fine-grained sandstone deposited just above the mouth bar deposits that succeed the deformed interval on top of Cycle H3, is interpreted as a product of the lateral migration of the delta before flooding and closure of the cycle.

In both depocentres, the upward reduction in the proportion of detached facies points to more stable depositional conditions being established over time. An alternative interpretation is that detached processes moved down-slope and are not preserved in the shallower cycles rather than an overall decrease in the gradient. This alternative is supported by the overall progradation in both depocentres. In Roosterberg the dominant depositional environment varied from shelf-edge/upper- and middle-slope (Cycles R2 and R3) to shelf-edge (Cycle R4), while in

Heuningberg it began in a shelf-edge/upper-slope (Cycle H2), through the shelf-edge (Cycle H3) and culminated with the deposition on the stable shelf (Cycle H4).

Facies present in the Tanqua-Laingsburg shelf-edge deposits are similar to those identified in Pliocene deposits of the Mississippi Canyon (Mayall *et al.*, 1992) and in the Eocene of Spitsbergen (Plink-Björklund *et al.*, 2001), with the presence of fine to very fine laminated to structureless sandstone/siltstone beds, interbedded ripple-laminated sands and soft-sediment deformed beds. The internal organization of the studied deltas in the Mississippi Canyon is similar to that in the Karoo with deformed intervals in the intermediate section of each clinoform and interpreted as part of the upper delta slope. It is interesting to note that in the Spitsbergen case the soft-sediment deformation is concentrated in the lower- and middle-slope, this can be explained by the presence of distributary channels and chutes that transported sediment through the shelf-edge to be deposited on the slope and subsequently deformed by slumping. In the Karoo case, chutes, channels and canyons crossing the shelf-edge are rarely identified, which implies that deposition was concentrated in the shelf-edge and upper slope, followed by subsequent deformation. Also, the Spitsbergen slope was much steeper (3-4°; Steel *et al.*, 2000; Steel & Torben, 2002) compared with the estimated gradient of 0.5° (Wild, 2005) for Tanqua. This characteristic could result in the transportation of the sediment far from the upper slope with deposition and deformation occurring predominantly in the middle and lower slope.

4.1.4 – Sediment mobilisation

The wide variety of soft-sediment deformation structures found in the shelf-edge deposits of the Tanqua and Laingsburg depocentres is analysed in detail considering the area of occurrence and the stratigraphic position.

Tanqua Depocentre (Roosterberg area)

i) *Cycle R2*

Soft-sediment deformation

Soft-sediment deformation features are widespread in Cycle R2. The basal heterolithic interval R2A (Figure 4.9) includes flame structures in thin fine-grained sandstone layers and pseudonodules in siltstone/fine-grained sandstone, with poor lateral continuity (Figure 4.9a, b, c). Near to the top is a localized chaotic interval showing lateral wedging. The highly deformed interval R2B can be divided into three domains (R2B1, R2B2 and R2B3) delimited by sharp boundaries. Basal R2B1 is characterized by deformed layers of fine-grained sandstone, with preserved internal laminations, separated by vertically oriented flame structures, within a siltstone matrix. Laterally, the degree of sandstone deformation changes, although identification of discrete flame structures is still possible in areas of increased deformation. The overlying 6-8 m thick R2B2 is characterized by a lack of internal organization and the presence of metre-scale contorted blocks of fine- to medium-grained sandstone supported by a structureless siltstone to fine-grained sandstone matrix (Figure 4.9d, e). Interval R2B3 is marked by the occurrence of large vertical flames of siltstone up to 1.5 m high, separated by ruptured fine-grained sandstone (Figure 4.9f, g). Sometimes it is possible to observe the material from the flame above and locally truncating the sandstone (Figure 4.9g). Interval R2C includes thick beds of fine-grained sandstone characterized by large flames reaching 4 m in height (Figure 4.10a) and by a succession of flames in erosionally confined beds (Figure 4.10b).

The flame orientation in Cycle R2 has a general E-W trend, with a change in orientation from ESE-WNW in the basal section to ENE-WSW in the upper section. Palaeocurrents obtained from current ripple foresets indicate flow to the north while symmetrical ripple crestlines indicate flow to E-W (Figure 4.11).

Interpretation

The dominance of vertically oriented structures in the intercalated thin beds of siltstone and sandstone of R2A can be explained by loading caused by the influx of sand over mud rich layers resulting in an increase in pore pressure and subsequent liquidization of these beds. As a consequence, two processes occurred: i) density inversion that produced pseudonodules of fine-grained sandstone in a structureless siltstone/mudstone matrix and ii) vertical shear due to fluidization of the mud layer that produced flame structures and broke through the overlying unconsolidated sandstone (Figure 4.9a, b). The appearance of the first chaotic deposits interpreted as

products of laminar debris flow processes (log Rb8 between 17-20 m, Figure 4.6) at the top of R2A indicates slope instability.

R2B records general substrate perturbation in the study area. The lowest part (R2B1, figure 4.9) is deformed by folding and disruption of the bedset but preserves some layering and vertical dewatering, is interpreted as a product of slumping. No measurements of asymmetry or slump noses orientation were taken. Unit R2B2 is distinguished due to the total lack of stratification and the increase in contorted sandstone blocks of different sizes (Figure 4.9d, e), interpreted as products of debris-flow processes. Here, the distinguishing between slumps and debrites was made considering the degree of internal organization of the intervals: ductile deformation with folds and some preservation of the original strata was classified as slump and brittle deformation with chaotic internal organization was classified as debrite. The degree of deformation decreases to the top of this succession with the appearance of pseudonodules and ball-and-pillow structures in the sandier part (at 32 m, log Rb8) and undeformed layers of sandstone (at 20 m, log Rb6) interpreted here as products of passive foundering into the top of the debrite.

The 2 m thick highly continuous interval R2B3 (Figure 4.9f, g) is characterized by a change in grain size (fine-grained sandstone) and deformational style (large amplitude flames) in relation to R2B2. This package is interpreted to be generated by fluidization of the upper part of the mud-prone deposits due to loading by the overlying thick sand deposits. In this case the rapid deposition of the overlying sandstone probably increased the pore pressure and caused instantaneous vertical fluid escape that generated flames up to 1.5 m high. Bed architecture suggests spreading of the fluidized material over the ruptured sandstone (Figure 4.9g), indicating that deformation occurred at or just below the seabed, similarly with the structures described at Waterfall (cf. Figures 3.7 and 3.11).

The upper R2C interval, dominated by fine-grained sandstone mouth bar facies, is characterized by large scale dewatering features in a sand-rich environment (Figure 4.10a) associated with erosive surfaces (Figure 4.10b). This can interpreted as: (a) the product of fluidization generated by the high amount of water in the system, caused by the progressive transgression in the upper part of the cycle; (b) loading/unloading caused by thick packages of sand (succession of beds represented by the yellow interval on top of Cycle R2, Figure 4.6) during the mouth bar

migration on top of the cycle and, (c) to a lesser extent by the instability caused by the erosion and associated deposits, (cf. Figure 4.10b; Dasgupta, 1998).

When flame structure orientations and the palaeocurrent direction given by the current-ripple foresets are separated by deformed intervals (Figure 4.11), the lower R2A interval (heterolithic) and the upper R2C interval (mouth bar) indicate a 90° angle between palaeoflow and the flame orientation. The intervening R2B slumps and debris-flows show no preferred flame orientation. The along strike orientation of the flames in intervals R2A and R2C suggests two possible controls on flame positioning: *i*) upward "injection" of flames from an underlying liquidized bed caused by loading in the frontal part of the deposition, or *ii*) fluid escape oriented in accordance with extensional stress in the proximal part of the deposit. The "injection" of flames would imply some down slope inclination for the flame axial plane (e.g. Butler & Tavarnelli, 2006) that is not observed in the studied area. Thus, it is suggested that the fluidization of an underlying bed was induced probably by loading/unloading during deposition of the subsequent bed when resultant flames would be oriented parallel to the strike extensional weakness lines in the overlying layer. Symmetrical ripple crestline orientations indicate re-working by waves and/or geostrophic currents at a high angle to the preferential slope direction.

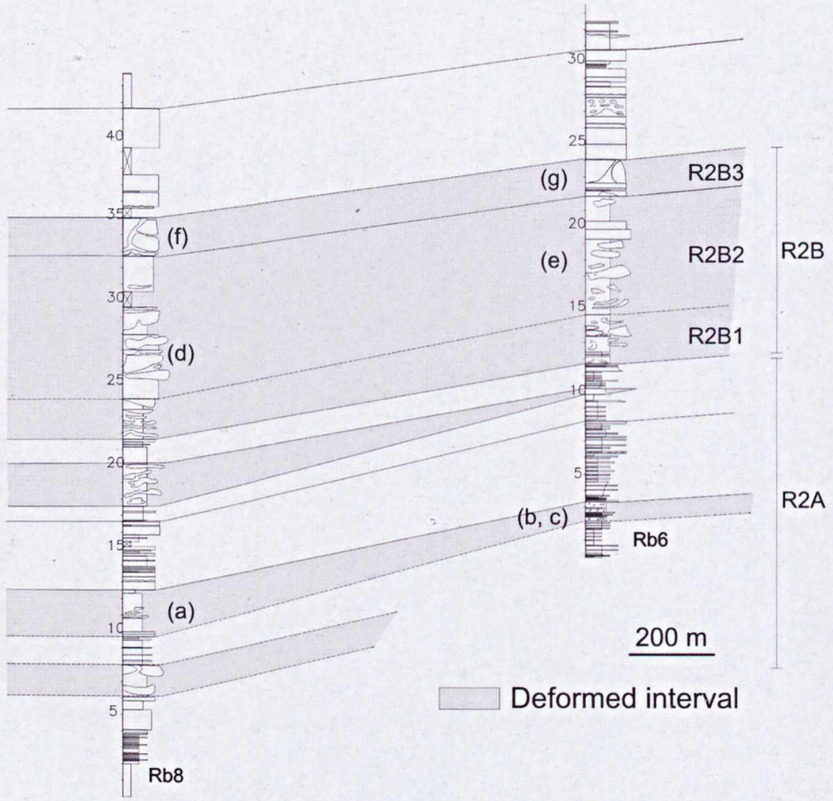

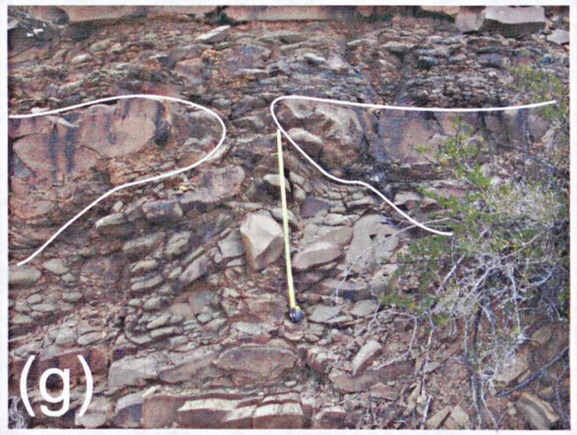

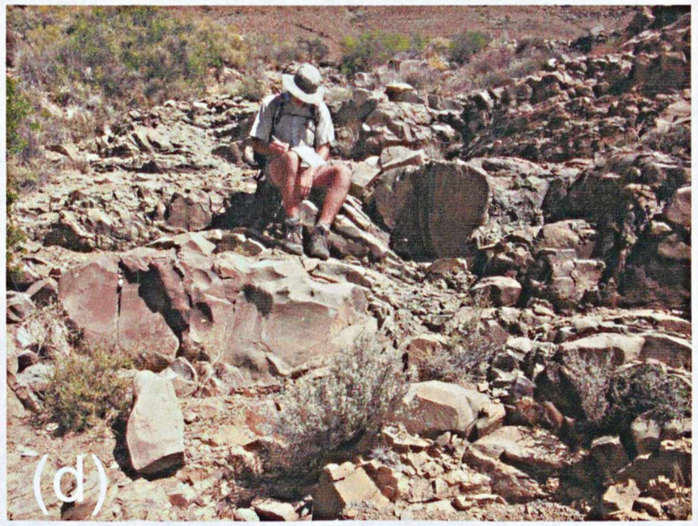

Figure 4.9: View of the deformation in Cycle R2 lower (R2A) and middle (R2B) intervals. In R2A, deformation is vertical dewatering of specific sandstone layers in a dominantly thin bedded section (a) (stick 1.8m long for scale), the lateral transition from deformed (b) to undeformed (c) occurs over a few metres. The R2B interval is characterized by thick debrites and slumps (d and e) - R2B2 - with top dominated by vertical dewatering features (f and g, tape measure 1m long for scale) - R2B3 -. The interval R2B1 is in an intermediate stage between R2B2 and R2B3.

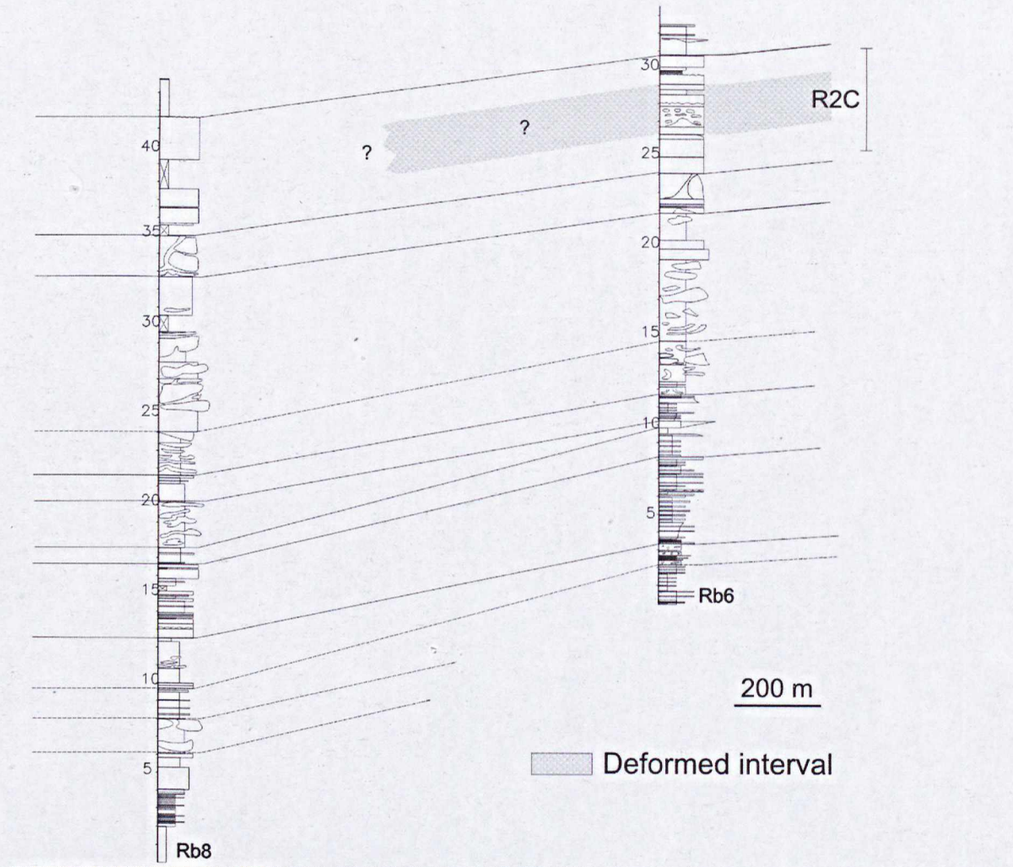

Figure 4.10: View of the deformation in Cycle R2 upper sandstone rich interval R2C. It shows localized metre-scale deformation, with predominance of vertical dewatering structures (a). In some places (b) it is possible to identify rare successive events of deformation associated with erosional surfaces (dashed lines). Geologist 1.8 m for scale.

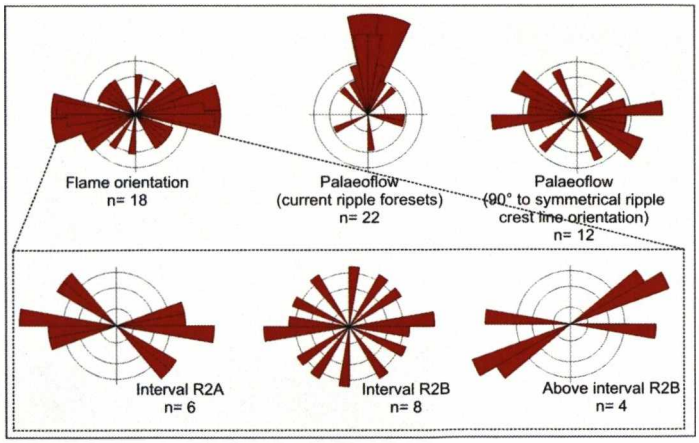

Figure 4.11: Cycle R2 flame orientation and palaeoflow obtained from current-ripple foresets (unidirectional) and from symmetrical crest lines (bidirectional). Below is the flame orientation considering the distinct deformation intervals in Cycle R2.

ii) Cycle R3

Soft-sediment deformation

Soft-sediment deformation features occur in the lower two-thirds of Cycle R3. The basal heterolithic deposits contain only a few pseudonodules and flames, which are overlain by two highly deformed intervals R3A and R3B (Figures 4.12 and 4.13). R3A is highly deformed and characterized by chaotic scattered, deformed sandstone blocks in a fine-grained sandstone matrix (Figure 4.12a, b) or by medium-grained folded sandstone in a siltstone to fine-grained sandstone matrix (Figure 4.13a). There is a tendency for the deformation to decrease upwards (Figure 4.12c). R3B is less deformed and varies laterally from totally deformed (log Rb4) to undeformed (log Rb7) over only 200 metres, without truncation (Figures 4.13). On the east side, vertical flame structures at different scales are the dominant deformational product and they are overlain by a structureless finer grained layer that sometimes truncates the flame structures (Figure 4.12d).

The interval between 65 and 75 m in log Rb8 involves the top of R3A, R3B and the base of the uppermost sandstone (highlighted log section in Figure 4.12) and constitutes a good example of features formed by vertical *in situ* soft-sediment deformation processes These include ruptured sandstone beds (Figure 4.12c), flame structures (Figure 4.12d-e) and pillar and dish structures (Figure 4.12f). On the west side, around log Rb4, a highly deformed interval dominated by folded and contorted sandstone bounded by sharp contacts is the main deformational feature (Figure 4.13a, b). Laterally-equivalent undeformed deposits include current-ripple and

parallel-laminated to hummocky cross-bedded fine grained sandstone (log Rb7, figure 4.6). The laminated fine-grained sandstone package that overlies R3B has little soft-sediment deformation; just pillar and dish structures on the east side and smaller perturbations related to channel evolution to the west (Figures 4.6, 4.12 and 4.13).

Flame structures found in the basal heterolithic section show predominantly E-W orientations, while measurements of the few flames around the deformed intervals R3A and R3B show no preferential orientation. Symmetrical ripple crestlines suggest 2 possible direction of flow: N-S and SW-NE. Current ripple foresets agree with the palaeoflow to the NNW measured by Wild (2005) (Figure 4.4).

Interpretation

The rare occurrence of pseudonodules and flames in the heterolithic basal section of Cycle R3 is attributed to sporadic events of liquidization that affected those beds. The highly deformed interval R3A is interpreted as a product of mass movement, similar to the interval R2B2 in Cycle R2. Two basic differences from the former can be identified in interval R3A: *i*) the absence of the "slump" transitional layer (R2B1) separating it from the underlying heteroliths and *ii*) the lateral transition from a debrite (Figure 4.12a, b) on the east side to a slump deposit (Figure 4.13a, b), denoted by the increase in folding of the silty matrix and of the sandstone blocks on the west side. The differentiation between slump deposits and debrites in this outcrop is not easy due to the lack of lateral exposure and different weathering conditions in the different positions. As in the equivalent sedimentary package (R2B2) in Cycle R2, there is a tendency for the occurrence of foundering at the top of the deformation succession, which is interpreted to indicate that the setting became more stable with a decrease in down slope movement.

Interval R3B is characterized by strong lateral variation in the deformational facies. On the east side (log Rb8), the preservation of some bedding, the presence of flames and the structureless cap over the ruptured sandstone layers (Figure 4.12d, e) indicate that the down slope stress was less intense than on the west side (between logs Rb4 to Rb5) (Figures 4.6, 4.13a, b). The intensely deformed slumped section (log Rb4) changes laterally (over 200 m) to undeformed parallel beds with low angle hummocky cross-stratification (log Rb7). The lateral transition between the two

outcrops is not exposed. However, considering the internal characteristics (folding and contorted beds) and the distribution of the sedimentary facies at the upper part of Cycle R3, it is possible to interpret the deformed interval as the product of a slump in a mouth bar deposit.

In the upper section of R3, the deformation (pillar-and-dish structures and deformed sandstone associated with channels) reflects the decreasing proportion of silt and mud in the succession and the increase in the action of storms (hummocks), wave reworking (symmetrical ripples) and channel incision.

The interpretation above corroborates the regional interpretation of Wild (2005) that considered the intermediate deformed section (R3A and part of R3B) as product of progradation and subsequent failure of the delta front; and the overlying undeformed sandstone deposited in a mixed fluvial- / storm wave-influenced upper mouth bar environment.

Between 67 and 75 m in log Rb8 (highlighted in Figure 4.12), the sequence of events associated with vertical particle dislocation illustrates stratigraphic changes in the deformation style (ruptured elongated sandstone, flames, pillar and dish structures) and in the deformational process (from density driven in the lower part to vertical shear associated with upward particle movement during fluidization in the upper part) related to an increase in the proportion of sand in the pre-deformation deposits.

Despite the broadly orthogonal orientation of the outcrop to the general NNW palaeoflow indicators (Wild, 2005), the comparison between the east and west exposures of Cycle R3, over a distance of 1.5 km, suggest the west part was close to the delta front (slumps, channel incisions, truncations, hummocky cross-stratification) while the east side was farther down slope (debrites and/or fluid escape structures).

As in Cycle R2, the flame orientation in the basal heterolithic section is E-W, which is at a high angle to the main NNW palaeoflow indicators, suggesting the orientation of the slope controlled the flame orientation. Deformed intervals R3A and R3B do not show preferential flame orientation, as expected for their chaotic deformational facies. Symmetric ripple crestlines indicate action of waves and storm-waves varying from high angle (SW-NE) to low angle (N-S) in relation to the interpreted palaeoslope orientation.

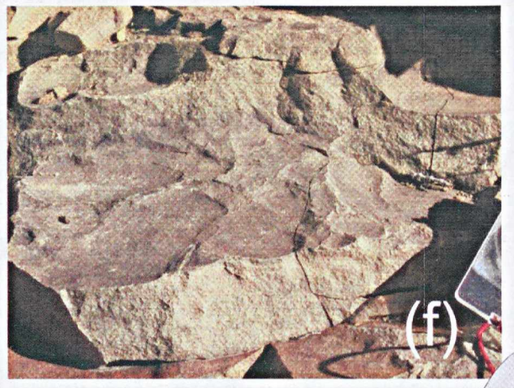

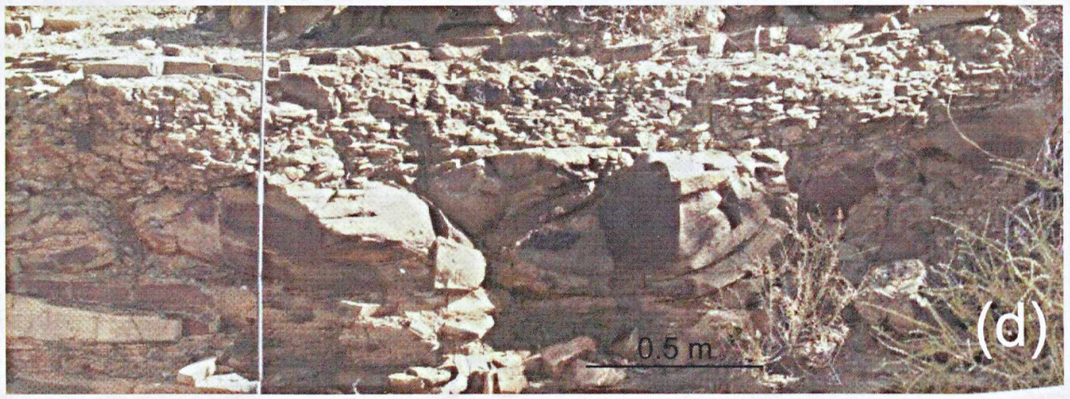

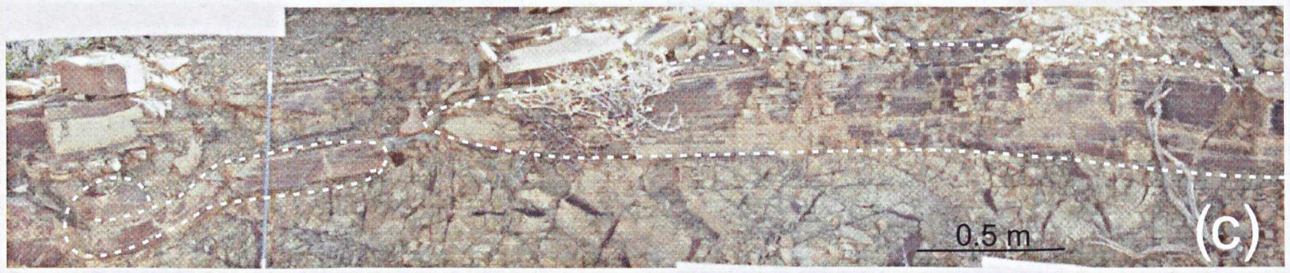

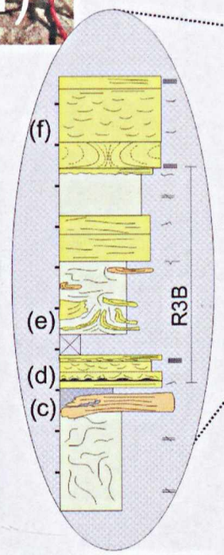

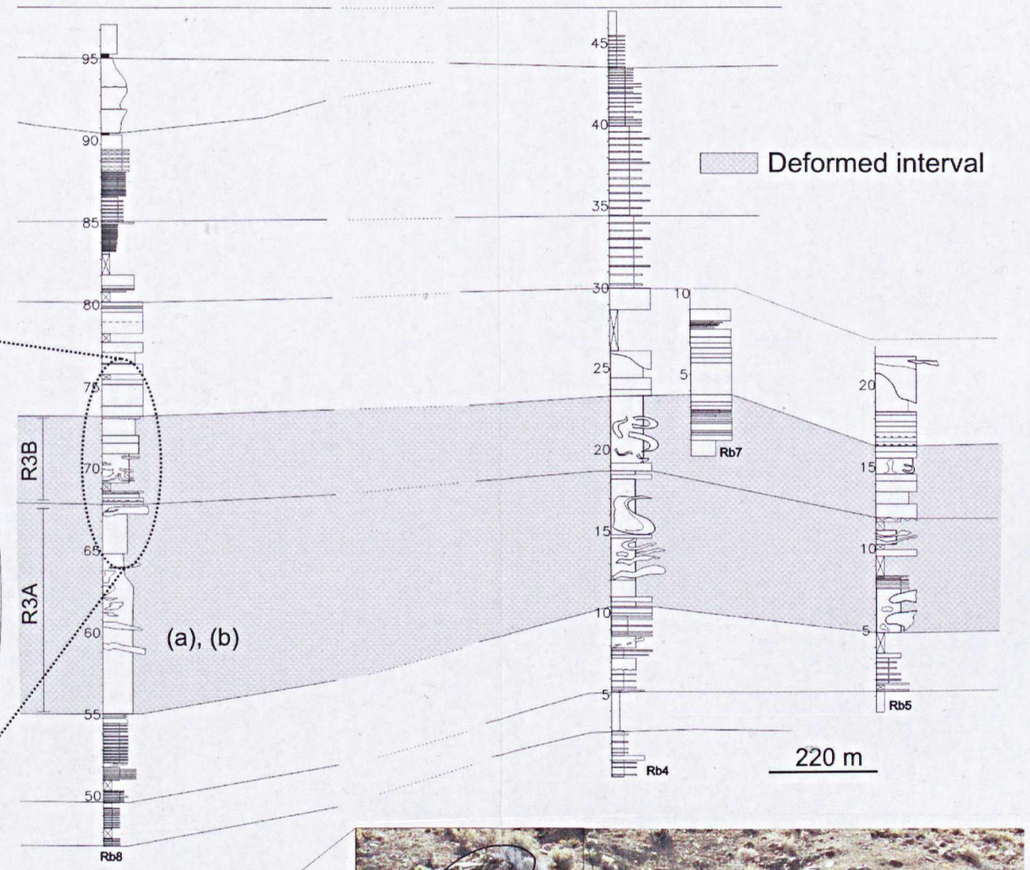

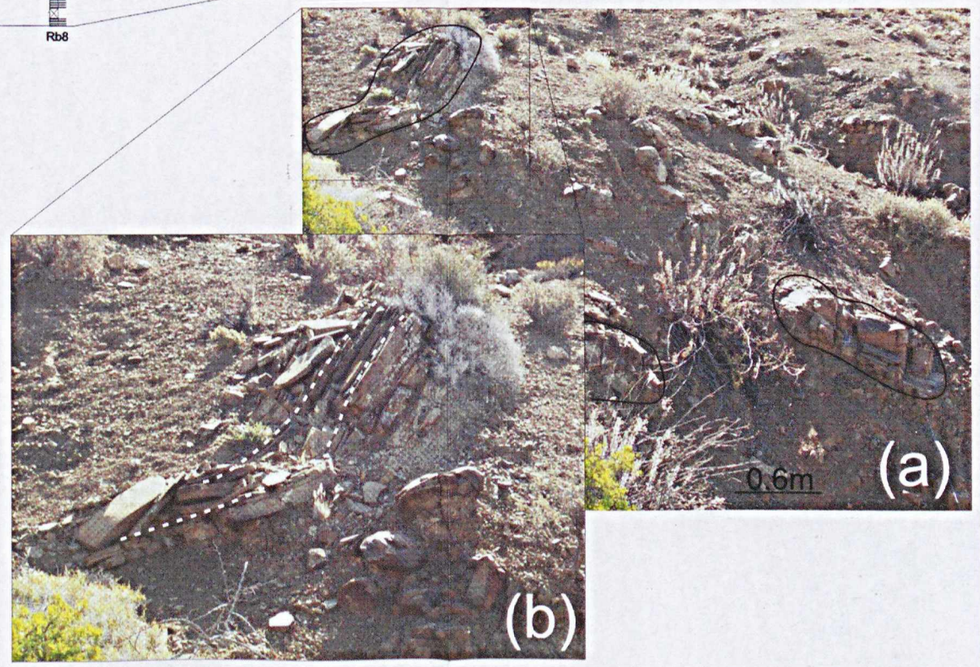

Figure 4.12: View of Cycle R3 East side (log Rb8) deformation for the intervals R3A and R3B. Interval R3A is highly deformed (a) presenting rafts of sandstone with folded or bent layering (b, for bending detail). On top of this interval the sandstone rafts are more preserved and normally horizontal (c), suggesting passive sinking of the sandstone layer. Reaching the interval R3B, the deformation degree is small with preservation of most of the original internal layering. In this case, the soft-sediment deformation structures are indicative of vertical deformational events: it is dominated by vertical flames and by an overlying/truncating structureless layer that occurs at different scales (d and e). The high degree of deformation stops in the sandstone dominated sequence above the interval R3B, although pillar and dish structures are common in a layer (f) close to its base.

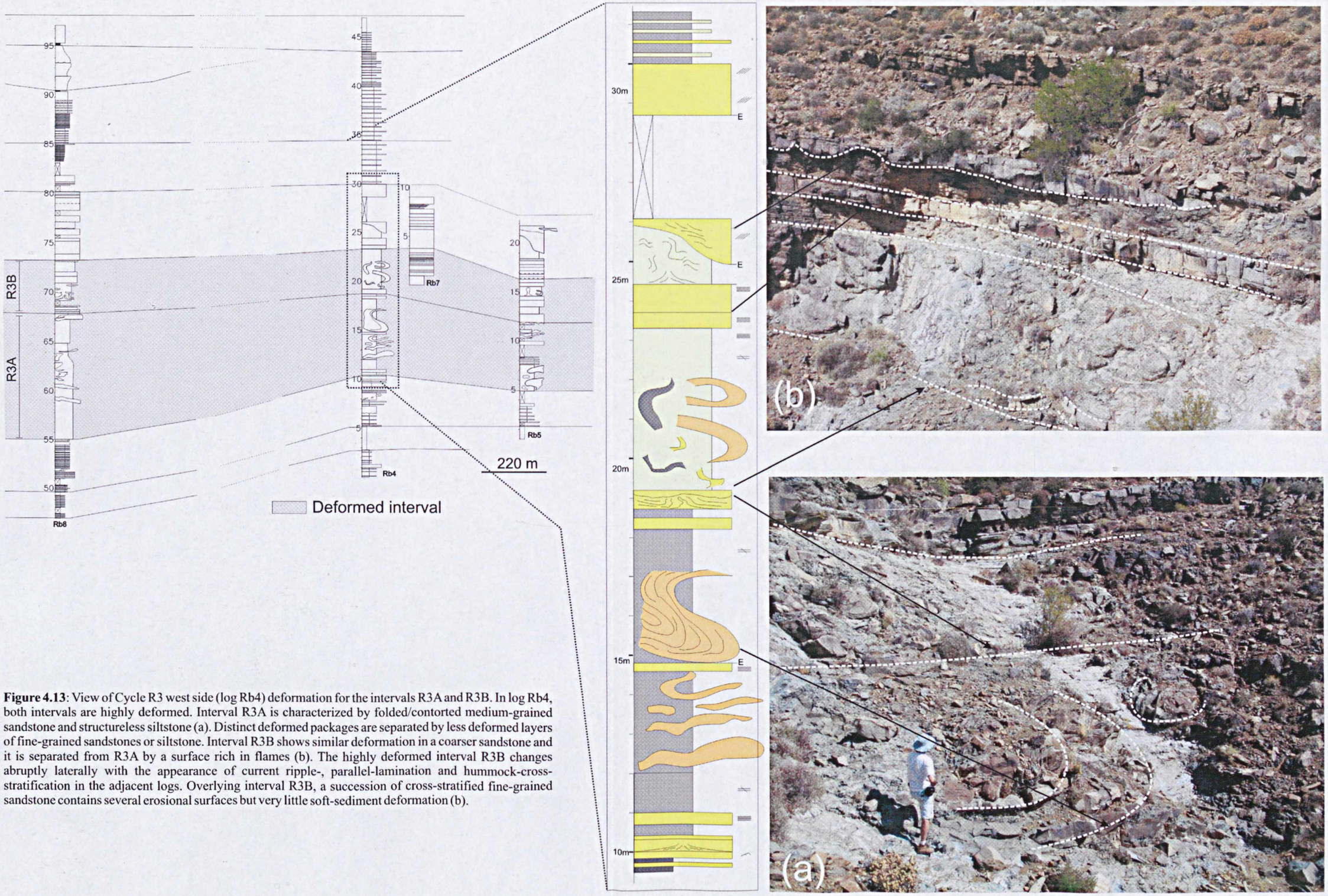

Figure 4.13: View of Cycle R3 west side (log Rb4) deformation for the intervals R3A and R3B. In log Rb4, both intervals are highly deformed. Interval R3A is characterized by folded/contorted medium-grained sandstone and structureless siltstone (a). Distinct deformed packages are separated by less deformed layers of fine-grained sandstones or siltstone. Interval R3B shows similar deformation in a coarser sandstone and it is separated from R3A by a surface rich in flames (b). The highly deformed interval R3B changes abruptly laterally with the appearance of current ripple-, parallel-lamination and hummock-cross-stratification in the adjacent logs. Overlying interval R3B, a succession of cross-stratified fine-grained sandstone contains several erosional surfaces but very little soft-sediment deformation (b).

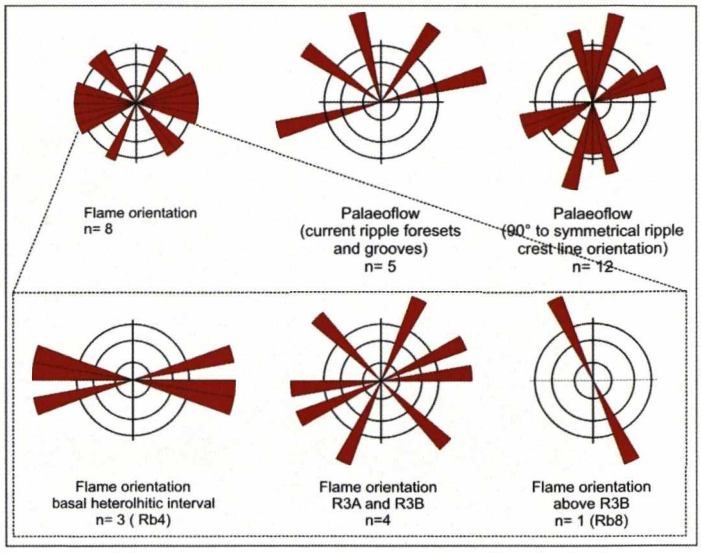

Figure 4.14: Cycle R3 flame orientation and palaeoflow obtained from current-ripple foresets (unidirectional) and grooves (bidirectional); and from symmetrical crest lines (bidirectional). Below is the flame orientation considering the different stratigraphic intervals in Cycle R3.

iii) Cycle R4

Soft-sediment deformation

Soft-sediment deformation structures are seen in the upper half of Cycle R4 (Figure 4.6). The lower half, composed of thin layers of heterolithic material, does not show deformation at the scale of observation. The upper half can be divided into four distinct sediment packages. Three of them, R4A, R4B and R4C (Figures 4.15 and 4.16), indicate post-depositional sediment mobilization. R4A is dominated by a siltstone matrix, normally structureless, punctuated by thin beds containing flames and pseudonodules. Locally, it is possible to observe an interval composed of a succession of flames deforming the overlying sandstone that shows variation in thickness with thinning towards the flames (Figure 4.15b). The transition between intervals R4A and R4B is marked by erosive contact and locally load casts and pseudonodules. R4B marks a depositional change in Cycle 4, with the dominance of fine-grained sandstone to the top of the cycle. The separation between cycles R4B and R4C is marked in the east by a thin layer of medium-grained sandstone with rip-up clasts (Figure 4.6). Thick sandstone beds in R4B and R4C are marked by flames (Figure 4.14c) and high amplitude folding (Figure 4.16b). Like the interval R4A, R4B and the base of R4C contain many small-scale flame structures, load casts, pseudonodules and ball-and-pillow structures (Figure 4.15d and 4.16c). Interval R4C is marked by the major increase in hummocky and low-angle cross stratification that are present all around. The lateral transition from deformed to undeformed strata

occurs abruptly without truncation within tens of metres (Figure 4.16c). Well preserved low angle cross-stratified layers with pseudonodules and flame structures formed laterally to massive sandstone with contorted blocks and a loaded/irregular base, without evidence for erosion or truncation. R4C is followed by deposition of a thick and amalgamated package of fine-grained sandstone with ripple cross-lamination and localized hummocky cross stratification and an abrupt reduction in the extent of soft-sediment deformation structures. Flame structures in the three deformed sections are strongly oriented E-W (Figure 4.17). Current ripple foresets indicate palaeoflow to the NNW (Wild, 2005).

Interpretation

In contrast to cycles R2 and R3, where slump deposits and debrites are common, the structures found in Cycle R4 are predominantly products of vertical movement of particles due to escape of fluids (flames) and unstable density contrast (pseudonodules and load casts), and also restricted slumping (intraformational folding). This observation is in accordance with Wild (2005) who interpreted the increase in foundering structures (and the decrease in detached deformation) in the upper cycles as related to stabilization of the shelf, occurring in upper mouth bar and delta top distributary channel deposits in a more proximal environment than the underlying Cycle R3.

The structureless character and the presence of flames and pseudonodules in the successive fine-grained beds of R4A sandwiched between ticker sandstone packages (Figures 4.6, 4.15) and followed by deposition of the thick sandstone packages (R4A and R4B), suggest that liquidization occurred caused by the stepping of the upper sandstone beds over this interval. Speculatively, if section R4A was restricted in extent the inability of fluid to escape could cause the entire liquefaction of this layer, creating conditions for the development of the observed pseudonodules, flames and small slumps. One line of evidence for the coupling between sand deposition and deformation of the underlying siltstone is provided by the structure illustrated in Figure 4.15b, which indicates that syndepositional deformation of the sandstone bed was induced by vertical flow of the underlying siltstone.

The sand rich intervals R4B and R4C are interpreted as mouth bars in which deformation (Figures 4.15c, d and 4.16b, c) was driven by: i) folding of metre scale sandstone package result of the initial slumps close to the shelf-edge (Figure 4.16b);

ii) migration of successive bars (as evidenced by the thin layer of medium grained sandstone with rip-up clasts in the boundary R4B-R4C, just above high amplitude flames) and iii) secondarily by storm events affecting the shelf-edge. The possibility of storms causing deformation can be reasoned by the reduction in occurrence of deformation structures (above R4C) coincident with a reduction in the amount of hummocky cross-stratification (Figure 4.6).

Abrupt lateral changes, without truncation, in the continuity of some layers (Figure 4.16c) indicate the complexity of the deformational processes shown by the correlation between logs, revealing different degrees of down slope movement of the sedimentary package.

The E-W flame orientation in the deformed intervals is given mainly by the flames in R4B and R4C. The structureless siltstone rich interval R4A shows more variation in flame orientation due to the presence of slumped intervals. As in the other intervals the flame orientation is at almost 90° to the NNW palaeoflow indicators, implying an association between these orientations and the slope.

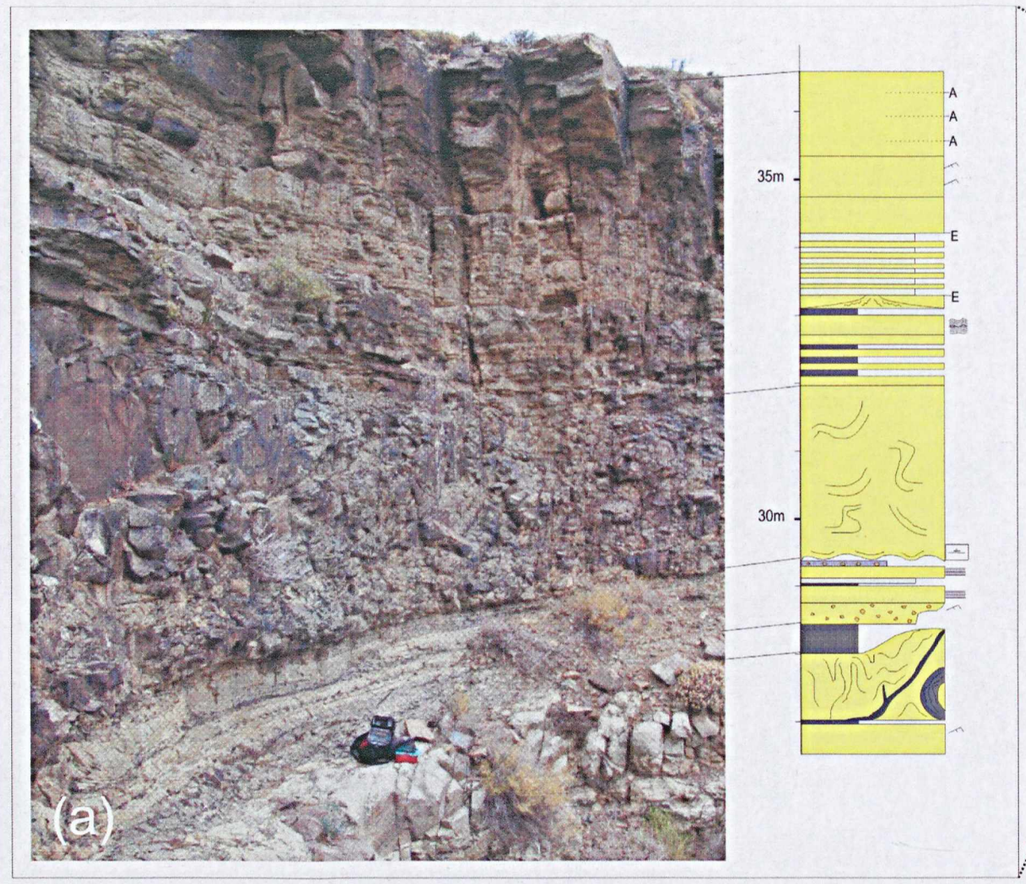

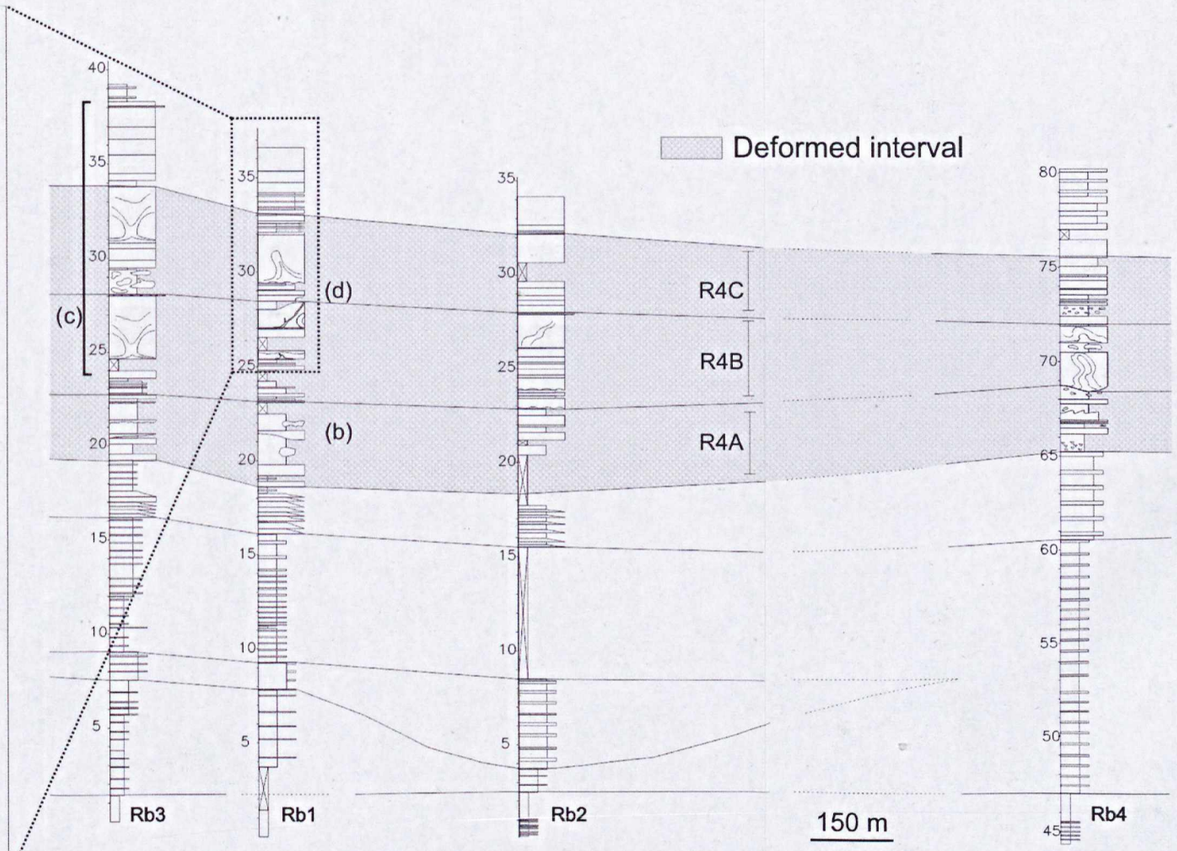

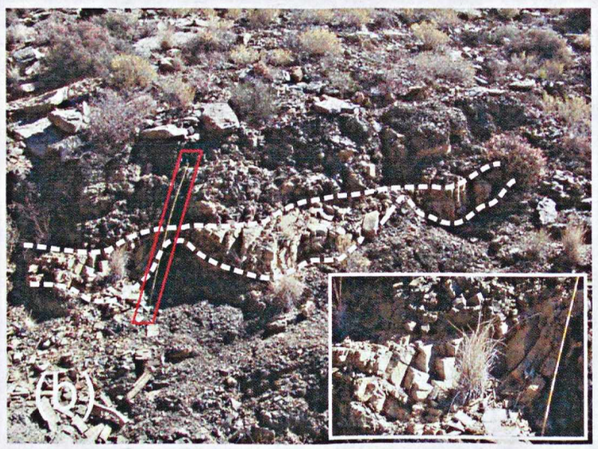

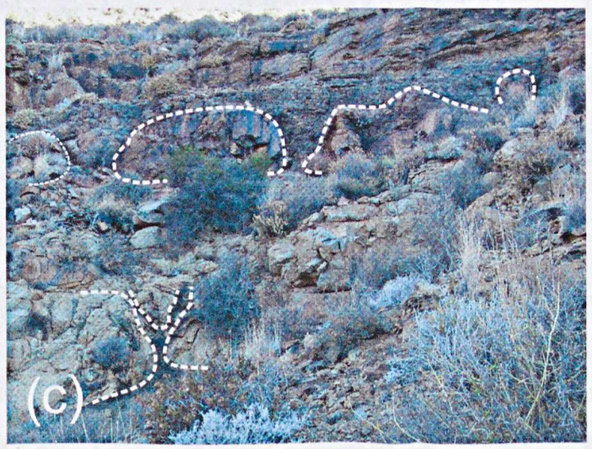

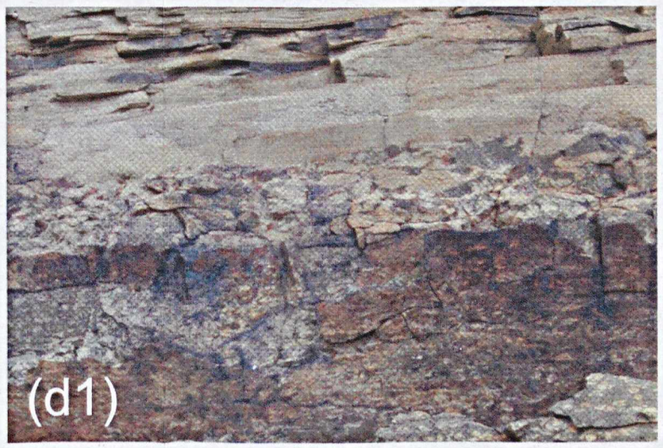

Figure 4.15: View of Cycle R4 east side (logs Rb1 to Rb3) deformation for the intervals R4A, R4B and R4C. Layering is well preserved in all intervals (a) and deformation is dominated by load structures/flames (foundering) (b) (highlighted pole 1.8 m high for scale), flames (c) (log Rb3 for scale) and load casts and pseudonodules (d). Details of the load casts can be seen in the upper part of photo d (d1). Detailed view of (b) (white square) indicates thickening of bedding for thick part of the deformed sandstone. Two levels of flames can be seen in (c); the upper shows strong deformation with apparent flow of fine material from the flames that spread over the ruptured sandstone.

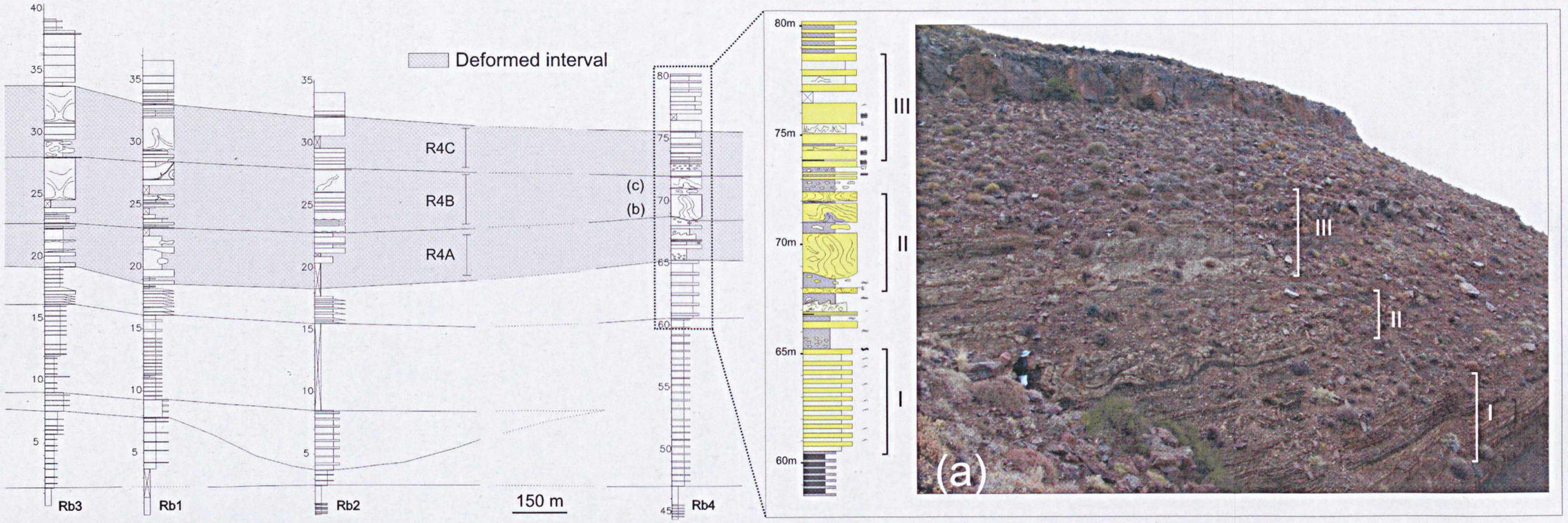

Figure 4.16: View of Cycle R4 west side (log Rb4) deformation for the intervals R4A, R4B and R4C. Less deformed than Cycles R2 and R3, the original bedding is normally preserved in Cycle R4 (a) and the deformation is characterized by folding (b) pseudonodules and flames (c1) and base loading (load casts) (c2). The lateral transition between deformed and undeformed occurs abruptly within a few metres (10 m) as indicated by photos c1 and c2, where well preserved low angle cross-stratificated layers with pseudonodules (base of c1) and flame structures (top of c1) levels developed lateral to a massive sandstone with contorted blocks and loaded/irregular base (c2).

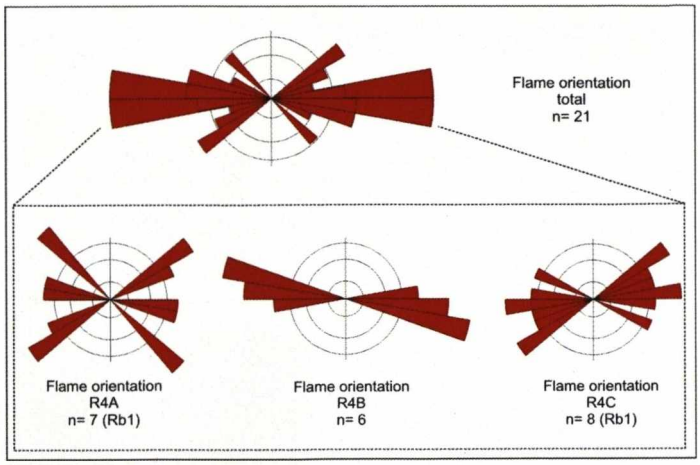

Figure 4.17: Cycle R4 flame orientation. Below is the flame orientation considering the different stratigraphic intervals in Cycle R4.

Laingsburg Depocentre (Heuningberg area)

i) Cycle H2

Soft-sediment deformation

This cycle presents a complex interaction between *in situ* and detached deformation facies (facies association 3 and 4, Table 4.2) with abrupt lateral and vertical changes (cf. Figure 4.7). Detailed logging and mapping with focus on the deformational facies were undertaken on the NW face of Heuningberg Mountain. The deformed section was divided into four intervals (H2A to H2D) bounded by centimetre thick beds of mudstone to fine-grained siltstone (Figure 4.18). Interval H2A is dominated by coarse-grained siltstone to very fine-grained sandstone with blocky weathering, which complicates the identification of soft-sediment deformation features. Only rafts of deformed sandstone can be discerned in this interval. Around the base of log Hn10, the layering is preserved and cut by a 1.5 m deep erosion surface with clasts at the base and filled by structureless fine-grained sandstone and sandstone blocks (Figure 4.19). Interval H2B includes a range of deformational styles with strong lateral variation: large flames (1 m high) deform and rupture the overlying thick massive sandstone layers in log Hn7; to the south, channel incision through underlying sandstones (rare brittle deformation is observed) is marked on log Hn8 and with a chaotic interval in log Hn10 (Figure 4.20). Interval H2C is composed of fine-grained sandstone, which is structureless or shows blocky

weathering. Where soft-sediment deformation structures are recognizable, the dominant features are flame structures and associated deformed sandstone with bedding bent upwards. Also, truncations are present toward the base of this interval. Around log Hn7, a 1.5 m deep erosion surface is overlain by massive sandstone. Flame orientations were obtained for one layer and the result shows a preferential E-W orientation (Figure 4.21). Interval H2D, close to the top of the study interval, presents flame structures and foundering structures deforming a 3-4 m thick section of sandstone beds. At the NW, around log Hn11 and at the base of H2D, a prominent 1 m thick massive fine-grained sandstone is ruptured by flame shaped siltstone oriented SW-NE that extends for more than 100 m (Figure 4.22). The basal deformed sandstone bed presents a homogeneous thickness and growth strata is not observed. Palaeoflow is to the E-NE (Charles, 2007).

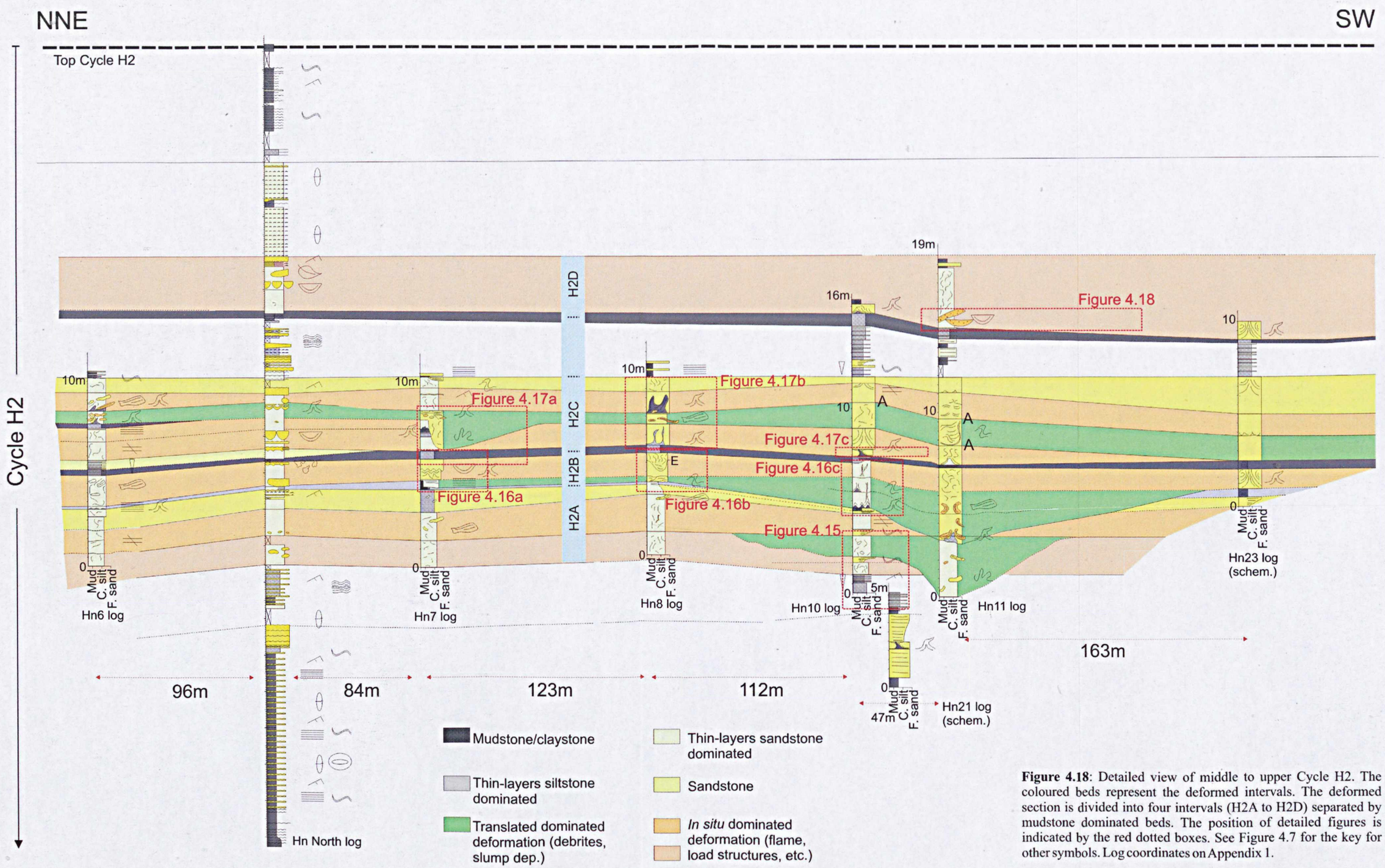

Figure 4.18: Detailed view of middle to upper Cycle H2. The coloured beds represent the deformed intervals. The deformed section is divided into four intervals (H2A to H2D) separated by mudstone dominated beds. The position of detailed figures is indicated by the red dotted boxes. See Figure 4.7 for the key for other symbols. Log coordinates on Appendix 1.

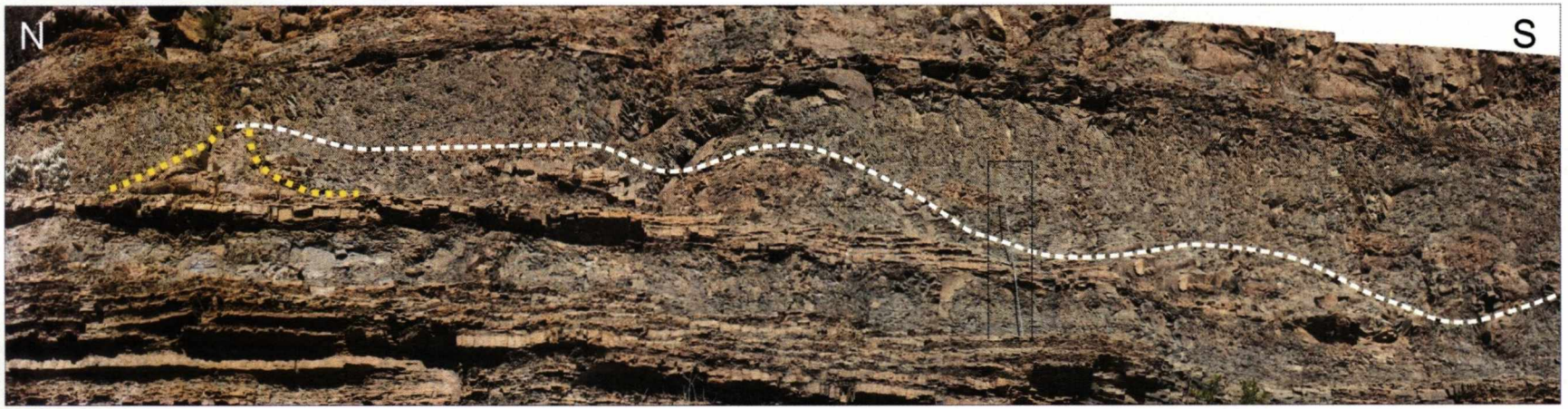

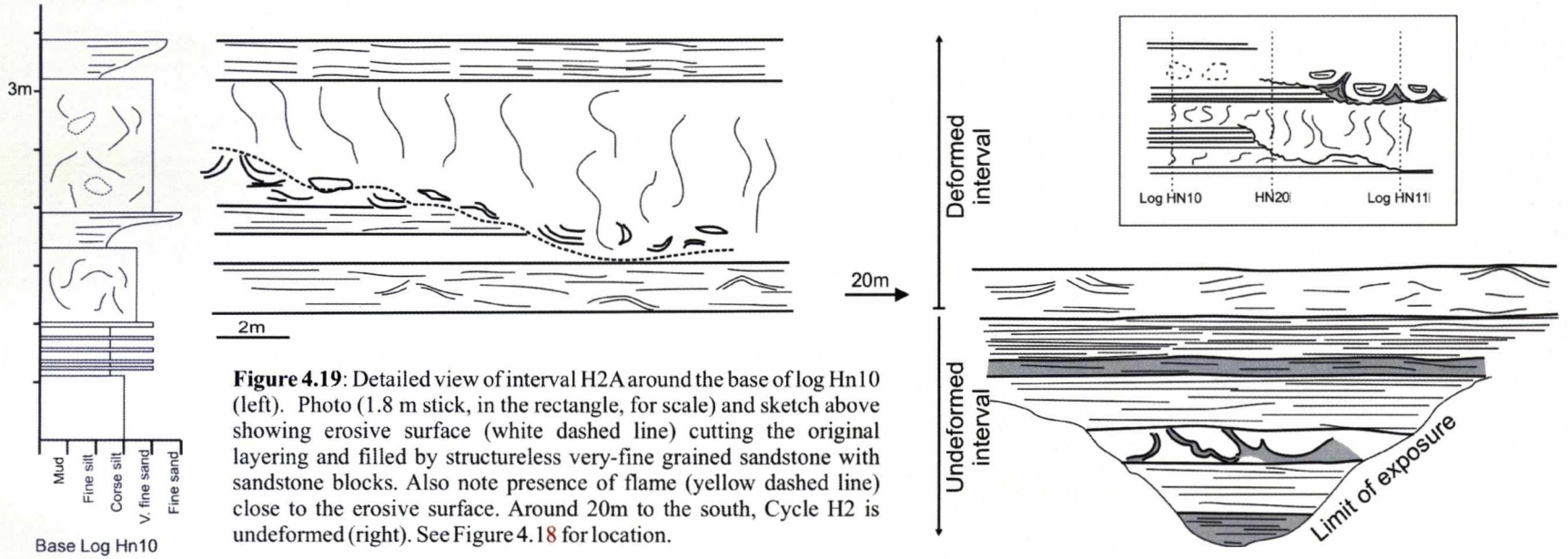

Figure 4.19: Detailed view of interval H2A around the base of log Hn10 (left). Photo (1.8 m stick, in the rectangle, for scale) and sketch above showing erosive surface (white dashed line) cutting the original layering and filled by structureless very-fine grained sandstone with sandstone blocks. Also note presence of flame (yellow dashed line) close to the erosive surface. Around 20m to the south, Cycle H2 is undeformed (right). See Figure 4.18 for location.

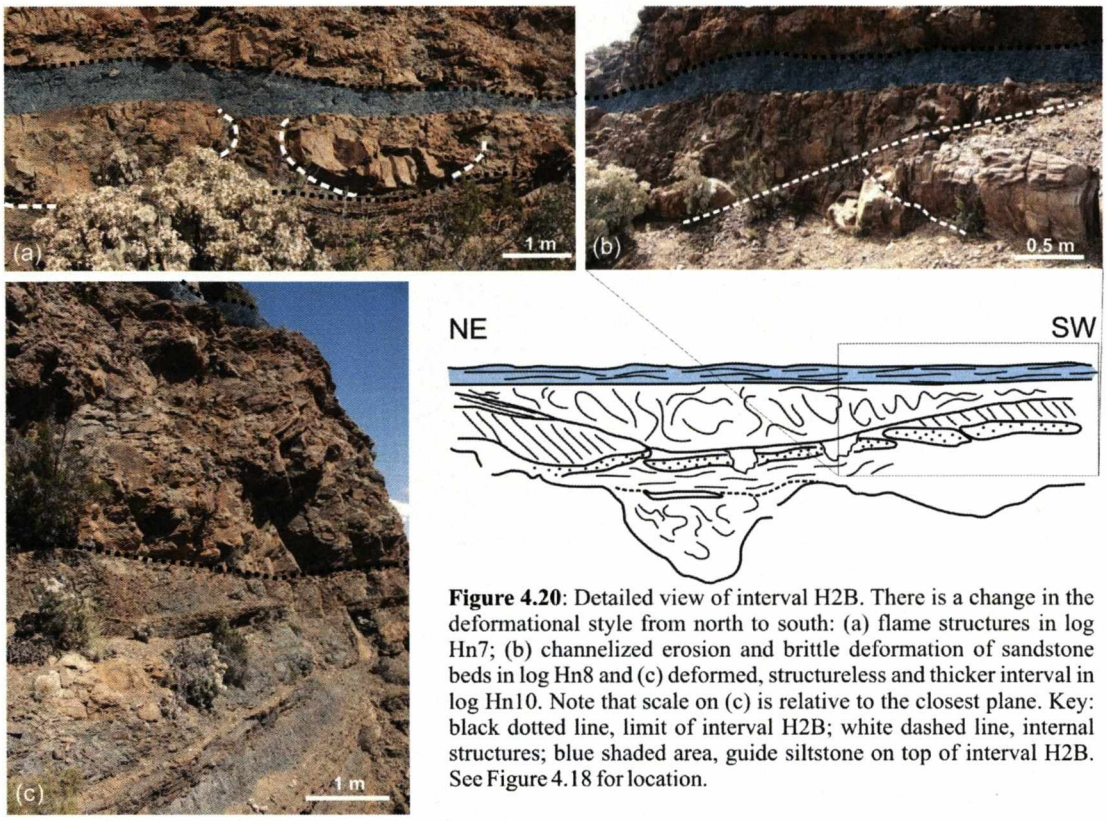

Figure 4.20: Detailed view of interval H2B. There is a change in the deformational style from north to south: (a) flame structures in log Hn7; (b) channelized erosion and brittle deformation of sandstone beds in log Hn8 and (c) deformed, structureless and thicker interval in log Hn10. Note that scale on (c) is relative to the closest plane. Key: black dotted line, limit of interval H2B; white dashed line, internal structures; blue shaded area, guide siltstone on top of interval H2B. See Figure 4.18 for location.

Interpretation

In contrast to Roosterberg, where large packages of translation-dominated facies of deformed sandstone are dominant (cf. green coloured beds on Figure 4.6), and are interpreted as having reached the mid-slope; deformation found in the intervals H2A to H2C of Cycle H2 occurred at the shelf-edge (Wild, 2005; Charles, 2007; cf. Table 4.4). It is interpreted that loading caused by progradation of mouth bar deposits at the shelf-edge created conditions for partial or total liquidization of beds that, associated with the lower depositional gradient of mouth bar deposits, resulted in the domain of *in situ* soft-sediment deformation structures and in minor local slump deposits and debrites. Erosion surfaces are interpreted, based on sedimentary facies of their infill, as the product of mass flow (cf. Figures 4.19 and 4.21a). Deformation of the unconsolidated beds adjacent to the erosive surfaces is common and could originate from the unloading/loading related to the erosion and infill (Dasgupta, 1998). The deformation at the base of H2D is interpreted as associated with the fluidization of the underlying finer-grained bed (cf. Figure 4.22), caused by the weight of a thick mouth bar deposit above. The fact that this bed is undeformed and massive to the SW indicates that deformation was post-depositional. However, the contorted blocks in the deformed zone indicate that deformation

occurred when the bed was not completely lithified. Interval H2D is disconnected from the underlying deformed intervals by a muddy interval interpreted as a flooding surface and is considered as a product of further progradation of the delta front.

The strong oriented flame structures (Figures 4.21 and 4.22), approximately parallel to the direction of the slope, reinforces that they were controlled by channel incisions along the slope (cf. Figure 4.21). However, the oriented deformation at the base of interval H2D can not be easily explained because there is no evidence of large incisions/scours or changes of thickness along the deformed bed at the scale of observation. Speculatively, large incisions or differential loading could occur laterally to the studied outcrops and drive the oriented structures parallel to their elongated axis.

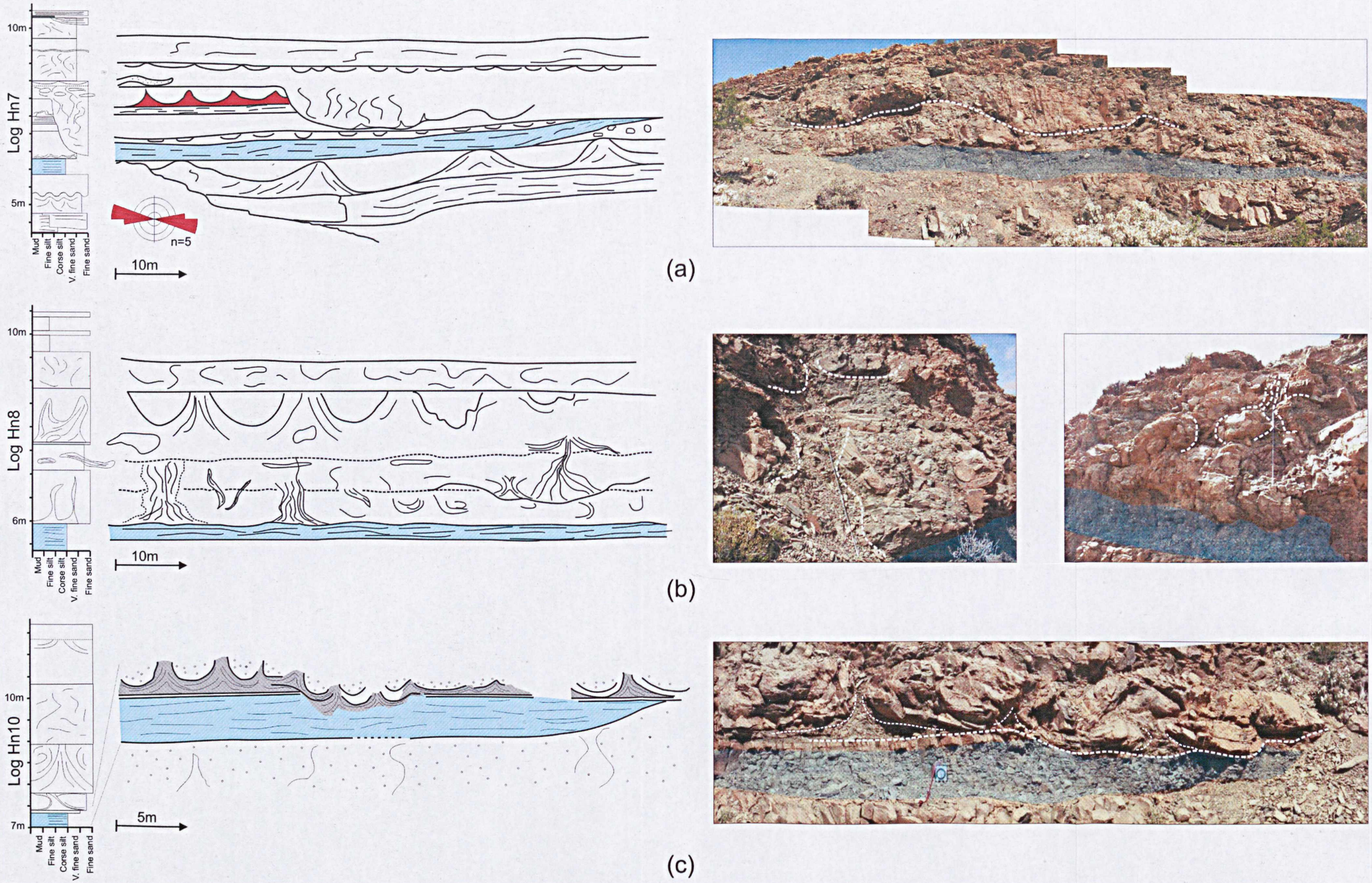

Figure 4.21: Detailed view of soft-sediment deformation in the interval H2C: (a) log Hn7; interval H2C is positioned above the reference siltstone (light blue) and is characterized by thin layers with vertical flames and truncated by a 1.5 m deep incision filled by structureless sandstone. Flame orientation obtained for the highlighted bed (red) is E-W. Notice below the reference layer large flames from the underlying interval H2B; (b) log Hn8; interval dominated by flame structures and localized truncations; (c) log Hn10; incision eroding part of the reference siltstone and presenting flames just above the erosive surface. See figure 4.18 for location.

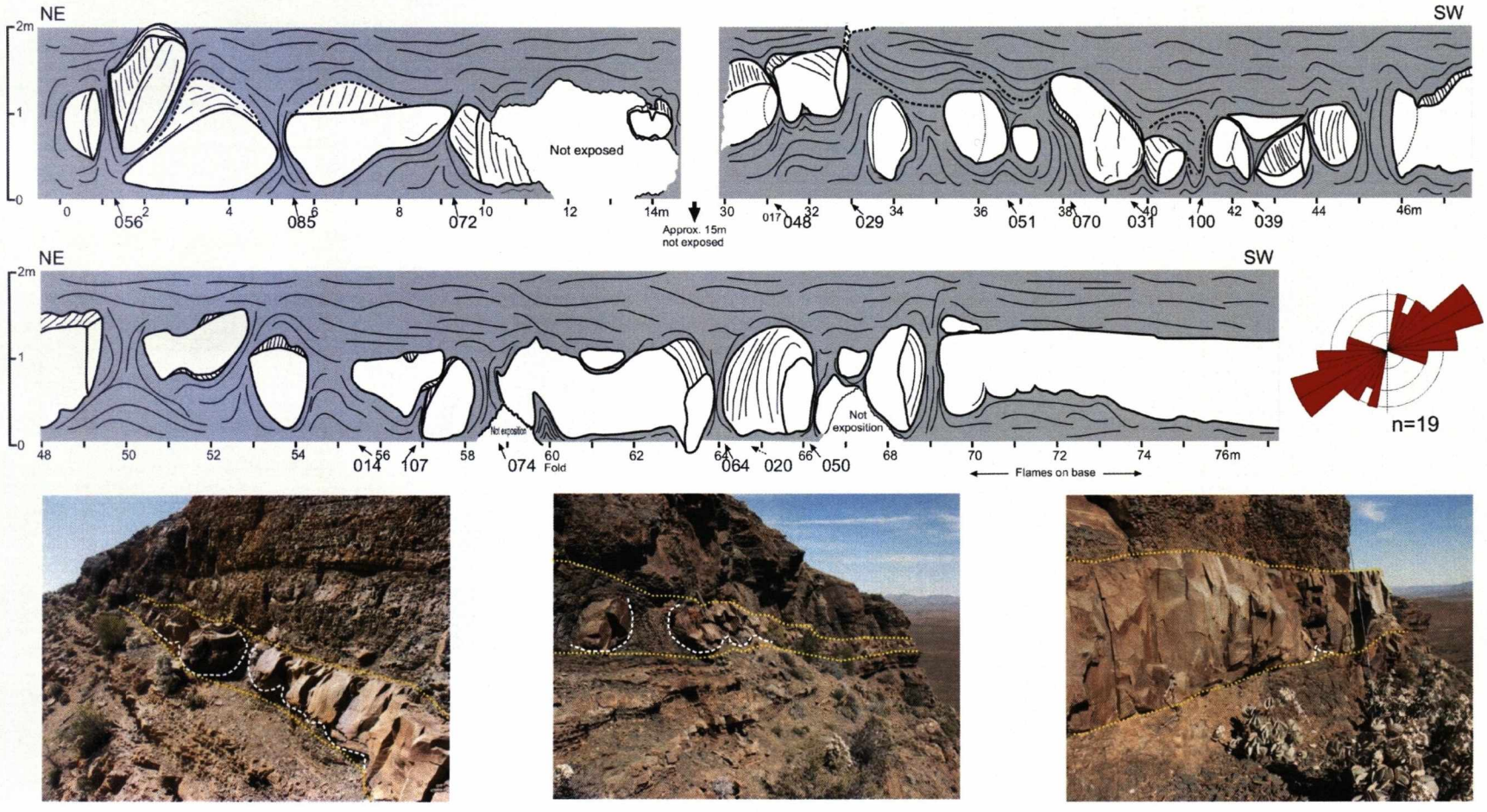

Figure 4.22: Sketch of lateral variation of the soft-sediment deformation in one single sandstone layer in interval H2D.The fine grained sandstone (white) was ruptured by a laminated siltstone (grey) producing flames and sandstone blocks with rounded margins. The flame orientation is strongly SW-NE. The photos provide some examples of the deformed and preserved sandstone (bounded by yellow dotted line) and some flame structures are highlighted (white dashed line). See figure 4.18 for location.

ii) Cycle H3

Soft-sediment deformation

Cycle H3 is dominated by facies association 3 (deformed *in situ*, Table 4.2) with the occurrence of flames, load casts, detached pseudonodules, foundering structures and sandstone blocks without evidence of horizontal transportation. The presence of facies association 4 (deformed detached, Table 2) is marked by the occurrence of structureless sandstone, rafts and minor truncations. Detailed mapping of the SW face of Heuningberg focused on the lateral and vertical distribution of flame structures and the acquisition of data for statistical analysis (Figure 4.23). Lateral transition of deformational facies is evident in the horizon at the base of logs Hn1 and Hn2. The SE limit is characterized by blocks of laminated sandstone "floating" in a structureless siltstone matrix with the intensity of block deformation increasing downwards (Figure 4.24). Around 130 m to the NW (log Hn5) in the same layer the sandstone is ruptured by flame structures resulting in elongated sandstone bodies parallel to the WSW-ENE oriented flame structures. Continuing towards the NW, at 170 m from log Hn5, log Hn4 shows that the amount of siltstone decreases abruptly, the sandstone is preserved and the flame structures are restricted to its base (Figure 4.25).

Overlying beds show similar behaviour with *in situ* soft-sediment structures that vary laterally and stratigraphically from layer to layer (Figure 4.26). In beds CD1, CD2 and CD3 at the SE end of the panel (cf. Figure 4.23), superimposed flame structures are interrupted by truncations. There is no preferential orientation to the flames in these beds (Figure 4.27), which contrasts with the lower part of this cycle and of Cycle H2, where flames are strongly oriented.

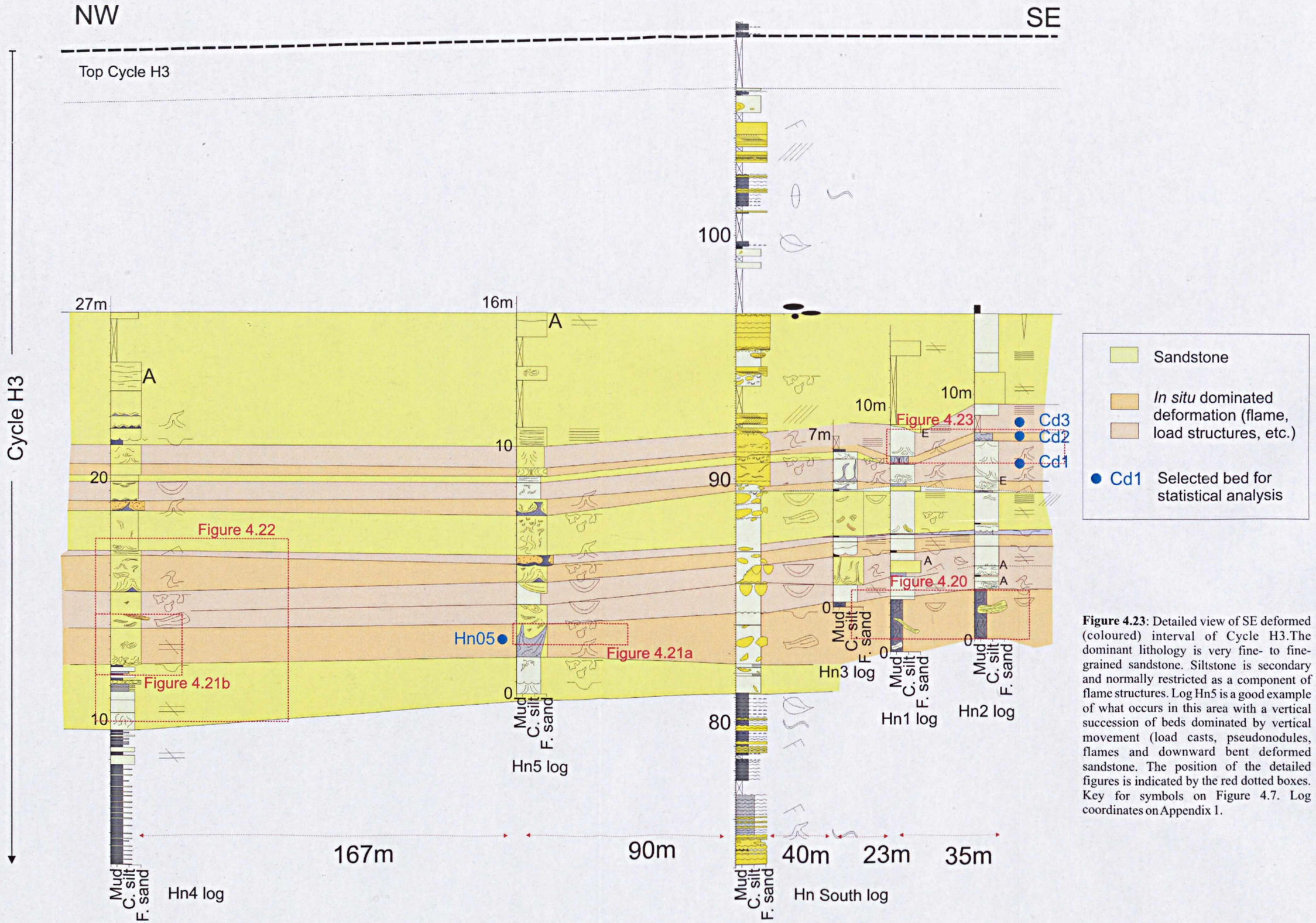

Figure 4.23: Detailed view of SE deformed (coloured) interval of Cycle H3.The dominant lithology is very fine- to fine-grained sandstone. Siltstone is secondary and normally restricted as a component of flame structures. Log Hn5 is a good example of what occurs in this area with a vertical succession of beds dominated by vertical movement (load casts, pseudonodules, flames and downward bent deformed sandstone. The position of the detailed figures is indicated by the red dotted boxes. Key for symbols on Figure 4.7. Log coordinates on Appendix 1.

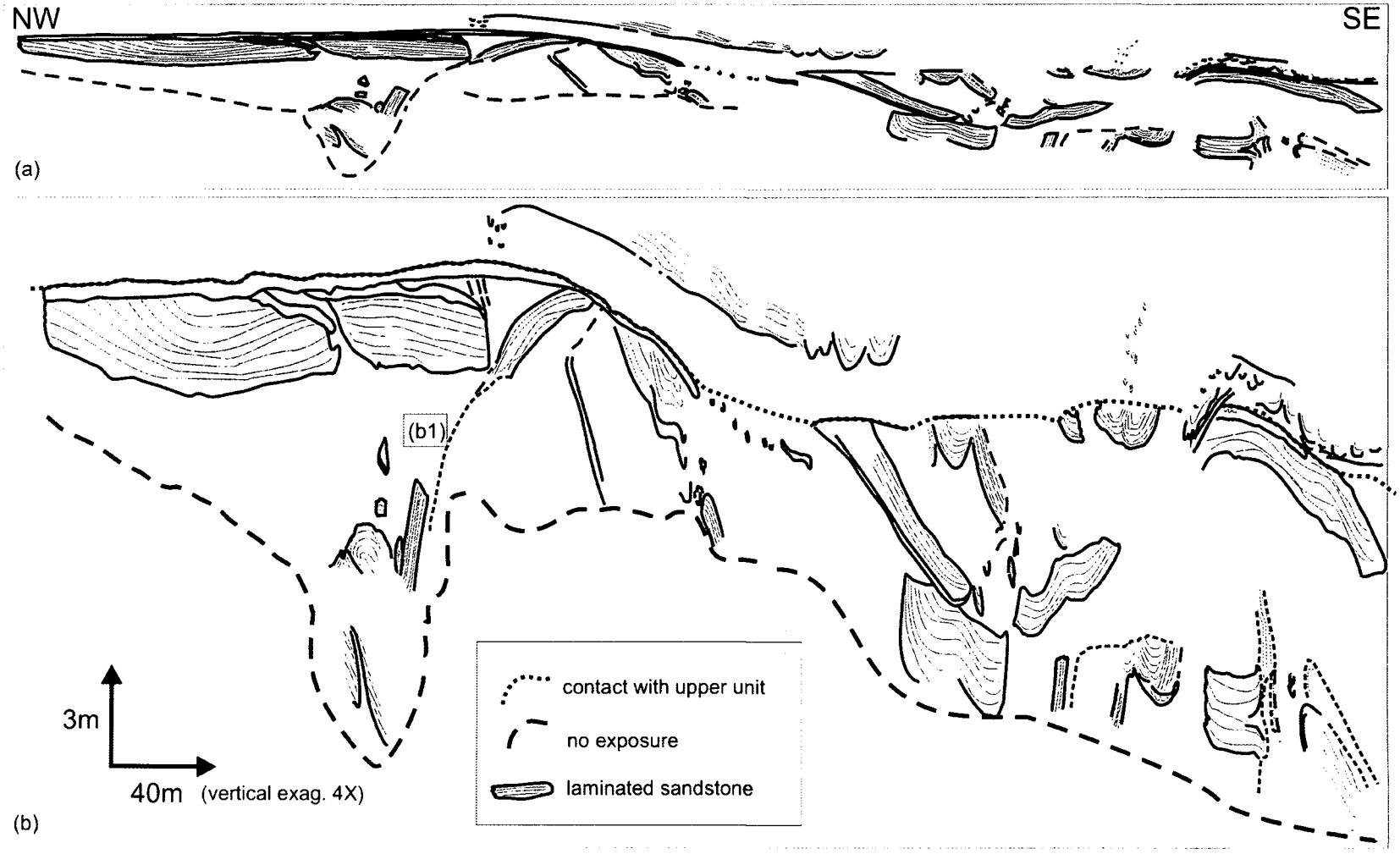

Figure 4.24: (a) Sketch of the base of logs Hn1, Hn2 and Hn3 with metre blocks of fine sandstone in a coarse siltstone matrix. (b) Same drawing with a 4 times vertical exaggeration to highlighted internal structures. The degree of deformation increases downwards. In some positions one track for block dislocation is suggested in the outcrop (b1). See Figure 4.23 for location.

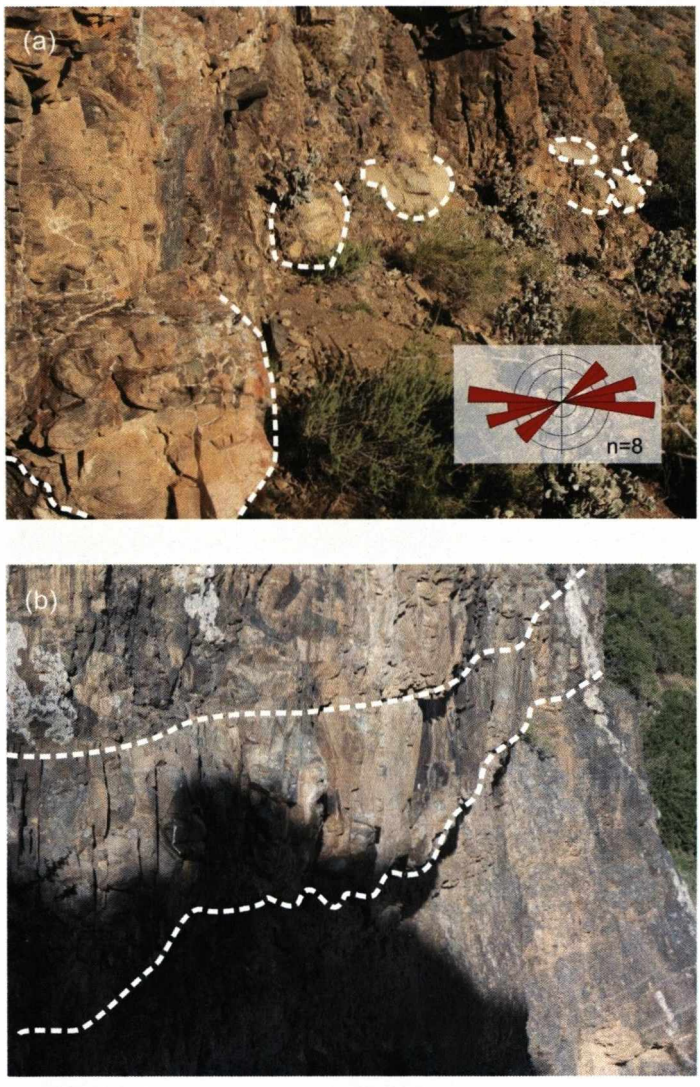

Figure 4.25: Lateral changes in a basal bed of Cycle H3: (a) log Hn5 with "rods" of sandstone, around 60 cm diameter on top of an approximately 1 m thick structureless siltstone with flames. The flames are oriented WSW-ENE. Photo was taken along the flame orientation; (b) log Hn4, thick massive sandstone with flames and load casts at its base. See Figure 4.23 for location and scale. The two outcrops are equivalent to bed "B" on Figure 4.26.

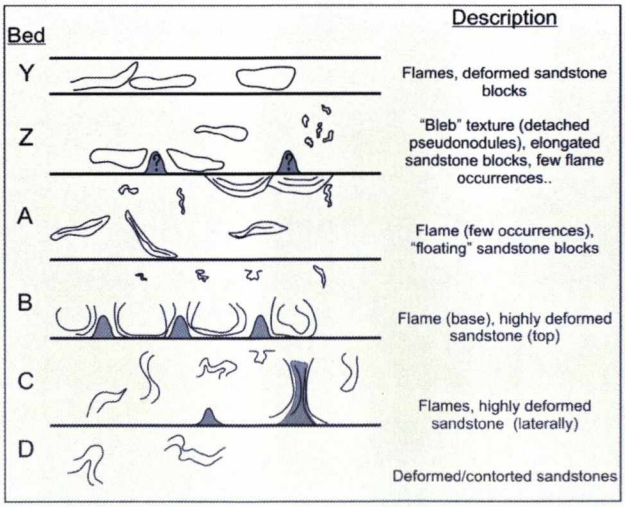

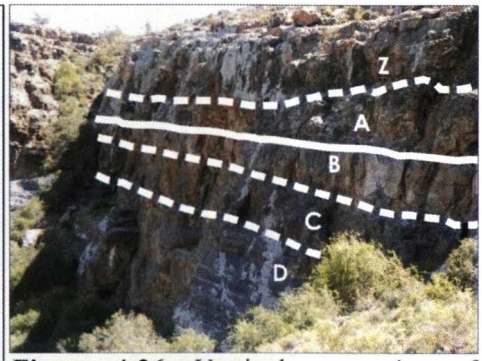

Figure 4.26: Vertical succession of deformed beds close to log Hn4. Observe the slight changes in the in situ deformation style from bed to bed. See Figure 4.23 for location.

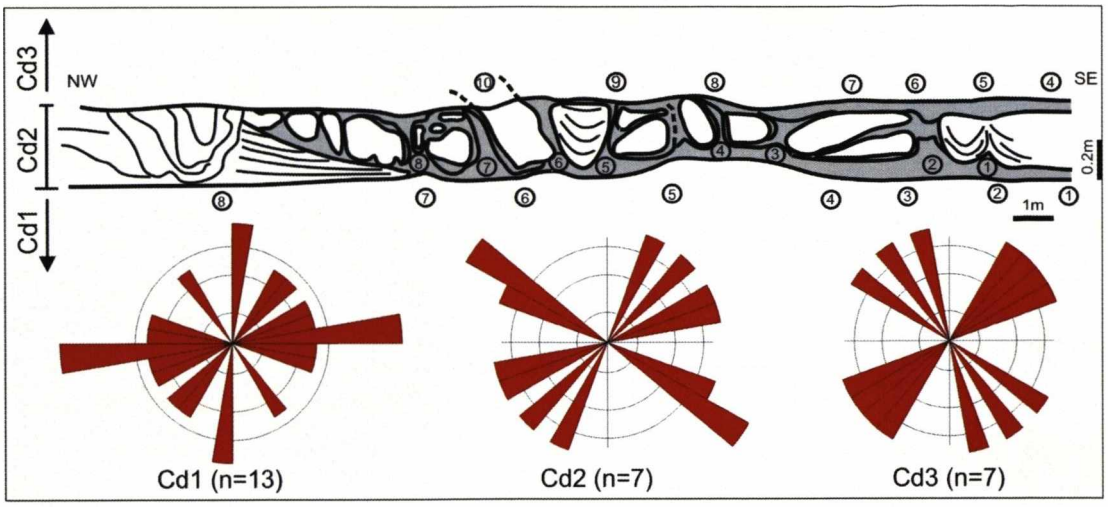

Figure 4.27: Sketch of the bed Cd2. In grey are represented the siltstones and associated flame structures and in white the deformed sandstones, some of them rotated. Numbers represent the position of the flames in the beds Cd1, Cd2 and Cd3. Rose diagrams for the flame orientation show the lack of preferential orientation in the analysed beds. See Figure 4.23 for location. Original data are in Appendix 3.

To the NW of log Hn4 this cycle is exposed in a cliff and comprises a thick section of highly deformed fine-grained sandstone that forms the prominent top of the SW face of Heuningberg Mountain (Figure 4.28). Due to the vertical nature of this face, it was not possible to complete the log. However, clear bedding, mainly in the lower section, large vertical flames (up to 5 m high) and possible erosive surfaces are noted. The NW face (log Hn9) resembles the SW face with parallel bedding accompanied by *in situ* vertical deformation with lateral variation in style and degree of deformation. The good exposure allowed the rare tracking of a deformation zone crossing stratigraphy from one level to another (Figure 4.29a) and the identification of a particular deformational style (Figure 4.29b) characterized by ruptured sandstones and flame structures overlaid by sandstone beds with growth sections.

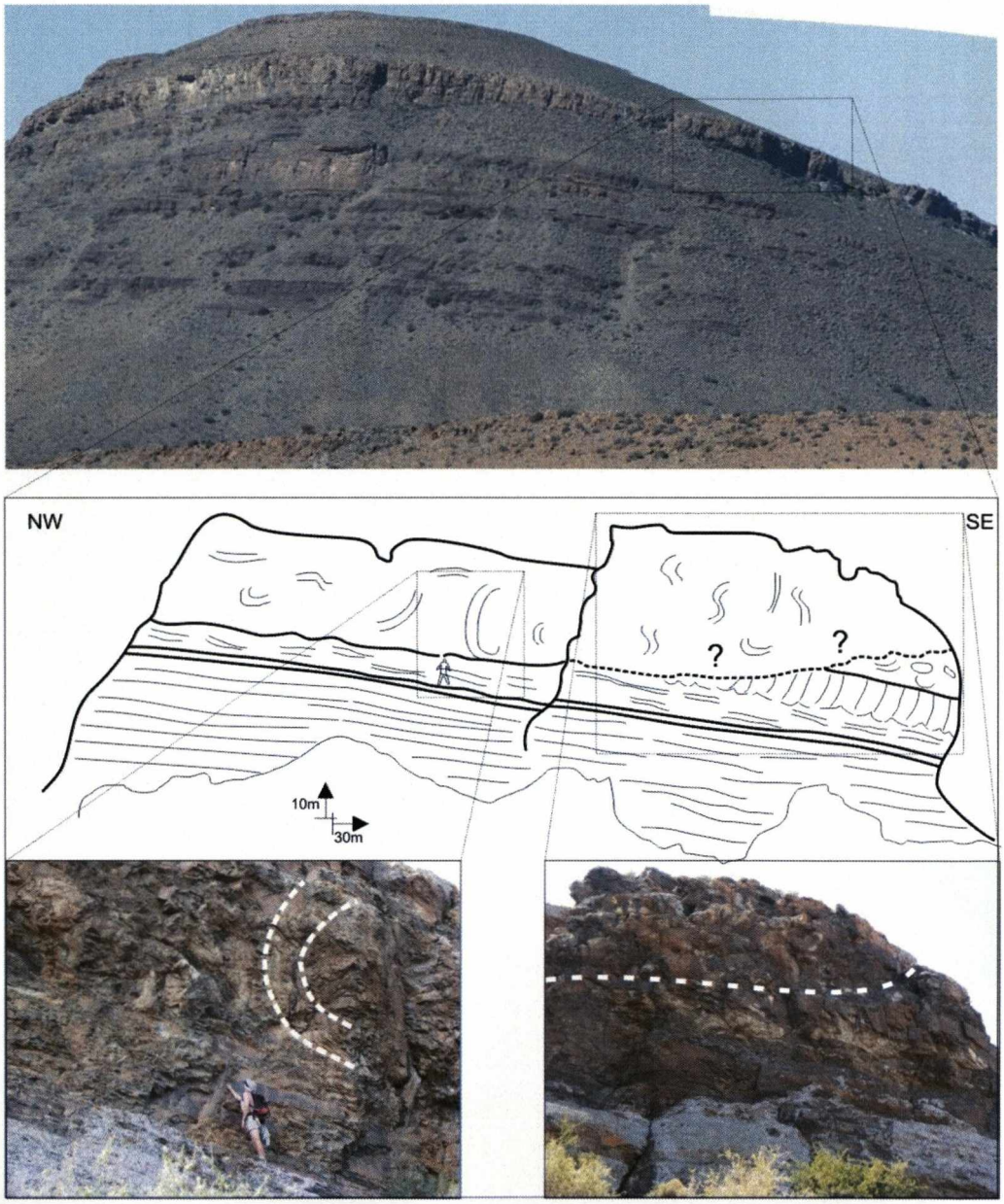

Figure 4.28: Frontal view of Heuningberg Mountain showing the cliff that comprises the deformed portion of Cycle H3. Below, detailed view from the SE part: presence of parallel bedding at the base of the interval and contorted blocks and flames to top (left photo). Also presence of an incision surface suggesting deep erosion (right photo).

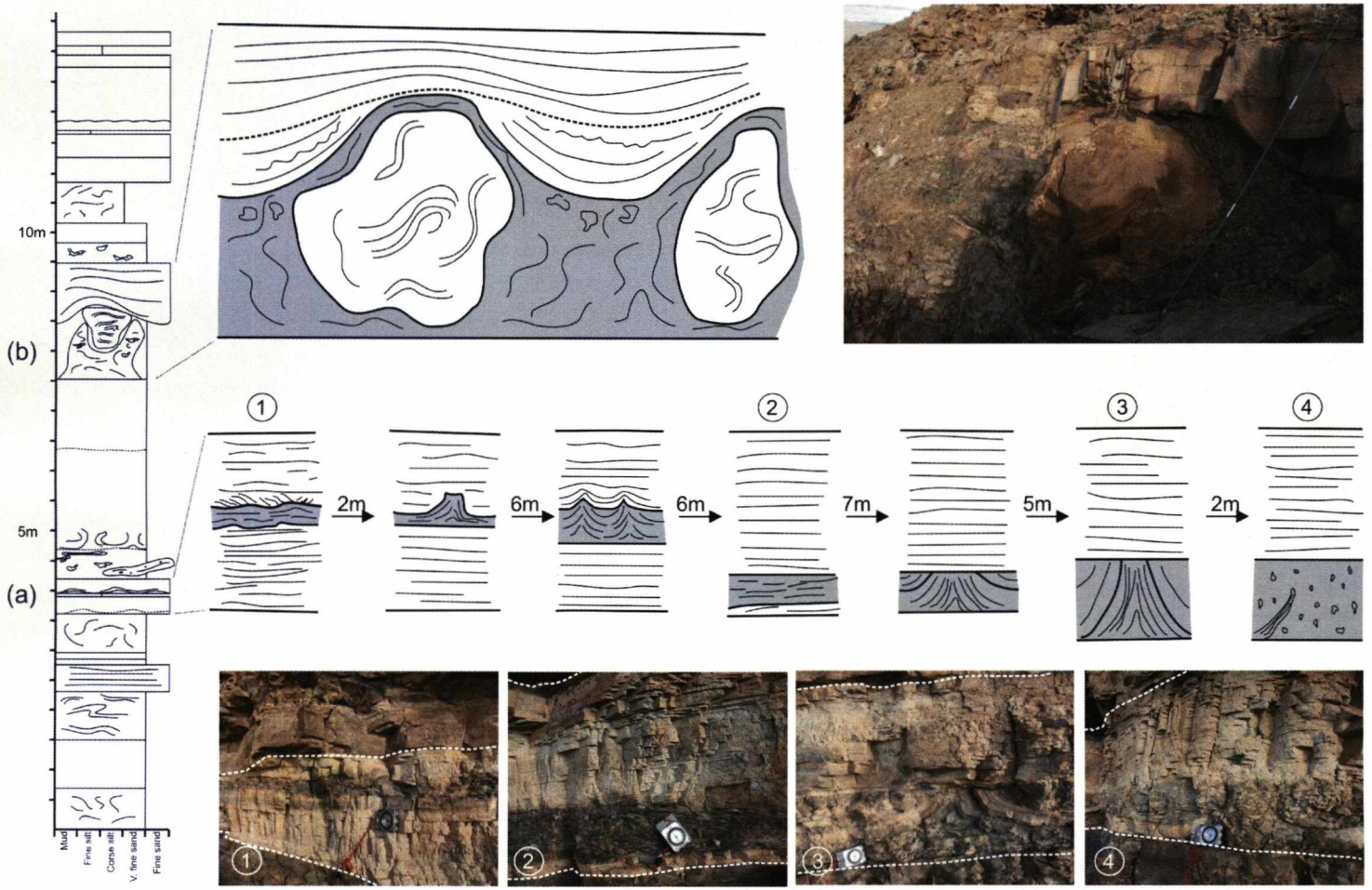

Figure 4.29: Soft-sediment deformation styles present in Cycle H3 on the NW face of Heuningberg. (a) At 4m on log Hn9 is a 0.8 m sandstone bed with intercalated flame-rich deformed siltstone that "jumps" from one level to another along the 30 m lateral extent of the exposition. Dashed lines in the photos indicate bed top and base. (b) Between 7.5 m and 9.5 occurs soft-sediment deformation of one bed in two distinct times: first generation of flame structure with the rupture, plastic deformation and rotation of the sandy rich part; followed by sandstone presenting growth section.

Interpretation

Except for the central part (cf. Figure 4.28), the predominance of *in situ* deformation in successive beds indicates that similar depositional/deformation found in Cycle H2 persisted through Cycle H3. A continuous supply of sand to the shelf-edge created the conditions for common liquefaction (load casts, pseudonodules, foundering blocks) and fluidization (flame structures). The lower 1-2 m thick bed shows a lateral variation in the style of deformation and a increase in the magnitude of deformation to the SE, from flames (log Hn4) to a disrupted layer (logs Hn1 and Hn2) that "floated" and sank in the mobile substrate, increasing the degree of deformation while moving downward (Figure 4.24). This occurrence is particularly important to prove that the deformation process here was *in situ* foundering. In this case: (i) there is no evidence of oriented flow in the siltstone matrix; (ii) the sandstone raft close to the top is parallel to the bedding and shows internal lamination preserved and undeformed; (iii) the detached blocks began to sink with one rotation of the elongated axis between 10° and 35° in relation to the original bedding and (iv) the sunken blocks become contorted when they reach the deepest part. The orientation of the outcrop is broadly orthogonal to the E-NE palaeocurrents (Charles, 2007). It implies that these variations are occurring along strike. Possible causal events could be the collapse of the channel margin or change in sediment supply across the delta front, thus changing the imposed loading. This interpretation is supported by the large amount of scours described by Charles (2005).

Around log Hn9 (Figure 4.29a) a well exposed 1 m thick parallel laminated bed shows two levels with *in situ* deformation structures that can help us to understand the abrupt lateral transition between the deformed and undeformed material observed in a large number of beds. In this example, when the deformation ceases in one layer it appears in another bed. If it is considered that the entire package deformed simultaneously, the accommodation space required for deformation in one layer could be compensated by the deformation in another, in a way that the whole system would be in equilibrium in a 3D compensation model (Figure 4.30). As shown in the former sections of this thesis, fluidization with vertical escape of fluids is many times accompanied by the generation of load structures resulting in the internal organization of the deformed section (see Chapter 3.1), however sometimes is not possible to observe the "compensating load structures" and the section seems to be unbalanced. The model envisaged from the

outcrop around log Hn9, suggests that when soft-sediment deformation occurs simultaneously in a succession of beds, deformation can be nucleated and distributed through the entire volume under deformation in the sense to be in equilibrium when the deformation process ceases. It is believed that laboratory tests could evaluate this hypothesis, however experiments conducted to evaluate *in situ* soft-sediment deformation do not report the 3D reorganization of the deformation in simultaneously deformed beds (Kuenen, 1958; Nichols *et al*, 1994; Owen, 1996; Moretti *et al*, 1999).

The structures described at the top of log Hn9 (Figure 4.29b) show the controlling of subsequent sandstone deposition by the former soft-sediment deformation structures (flames and ruptured sandstones) indicating the occurrence of differential compactation indicated by the growth strata in the overlying bed.

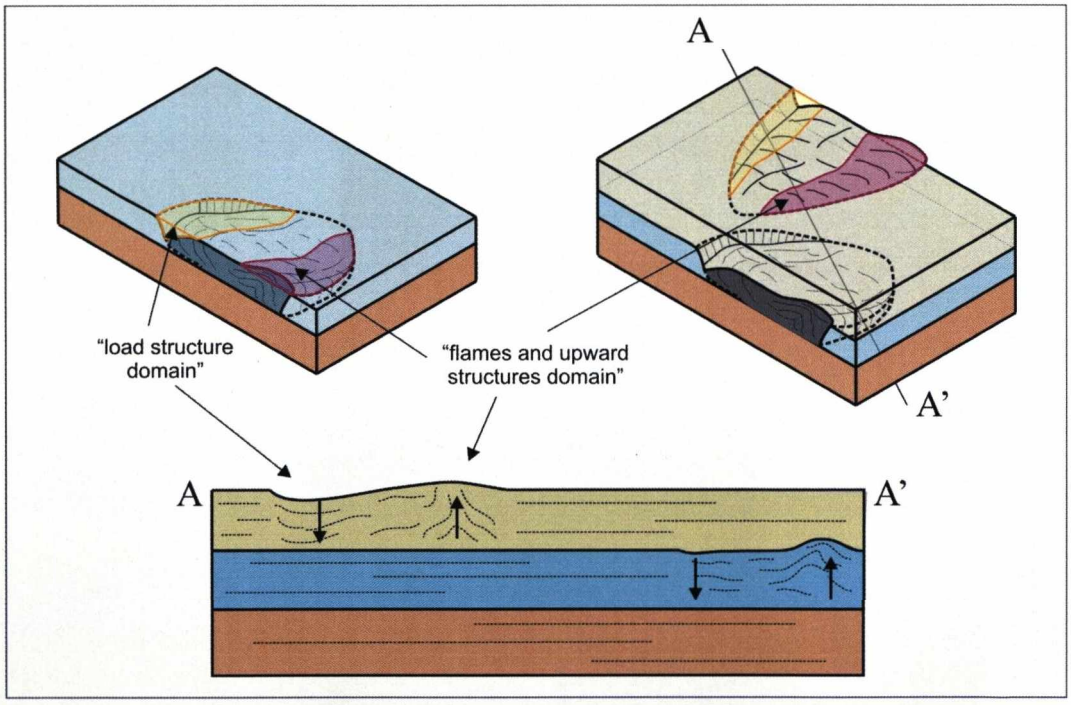

Figure 4.30: Diagram illustrating possible mechanism of deformation for single and multiple beds. In case of a single bed (upper left), upward and downward compensation occur inside the same deformed bed. In case of multiple beds (upper right), vertical movements can occur in different beds resulting in a final volumetric compensation. Section A-A' illustrates possible outcrop view of deformation involving multiple beds.

iii) Cycle H4

Soft-sediment deformation

This cycle (Figure 4.7) is characterized by the occurrence of *in situ* soft-sediment deformation structures, represented by centimetre-scale load casts and pseudonodules distributed vertically and horizontally through the sedimentary package. No detached soft-sediment structures are observed. Two 2 m thick beds contain flame structures and vertically deformed sandstones. The lowest one (around 15 m from the base of the cycle) shows a lower level dominated by dispersed sandstone rafts in a siltstone matrix while the upper section is dominated by flame structures. The degree of deformation varies laterally in both cases. Flames are strongly oriented WNW – ESE (Figure 4.31).

Interpretation

The presence of load casts and pseudonodules in Cycle H4 is interpreted as the product of localized soft-sediment deformation resulting from loading caused by the rapid deposition of fine-grained sandstone over thin beds of siltstone to very-fine-grained sandstone in a shelf environment. Deformation is normally restricted to the contact between two beds, not requiring full bed liquefaction. The thick interval illustrated in Figure 4.31 presents slight differences in the deformational process. At level 1, preservation of the internal bedding and the lateral boundary indicates brittle deformation of the bedding parallel elongated sandstone blocks. Allied to the absence of flame structures this suggests that deformation here occurred by the failure and collapse of a sandstone layer into the lower liquefied siltstone, through the process of foundering, similar to the one described in detail in Cycle H3 (cf. Figure 4.24). Levels 2 and 3 are the product of vertical downward dislocation of the sandstones (load casts and pseudonodules) and the vertical upward movement of the finer-grained lithology (flames), caused by liquefaction and fluidization of these layers. Level 2 shows components of horizontal movement, indicated by the elongation of the deformed sandstones and by the presence of some truncation (see Figure 4.31, level 2 at NE part).

The lack of detached soft-sediment deformation fits with the general stacking pattern for the Heuningberg area (cf. Figure 4.8b). In that case Cycle H4 initiates a period of aggradation with the deposition of successive proximal mouth bar facies in the study area, which is expected to occur in a flatter shelf environment and

consequently less favourable for the occurrence of detached soft-sediment deformation..

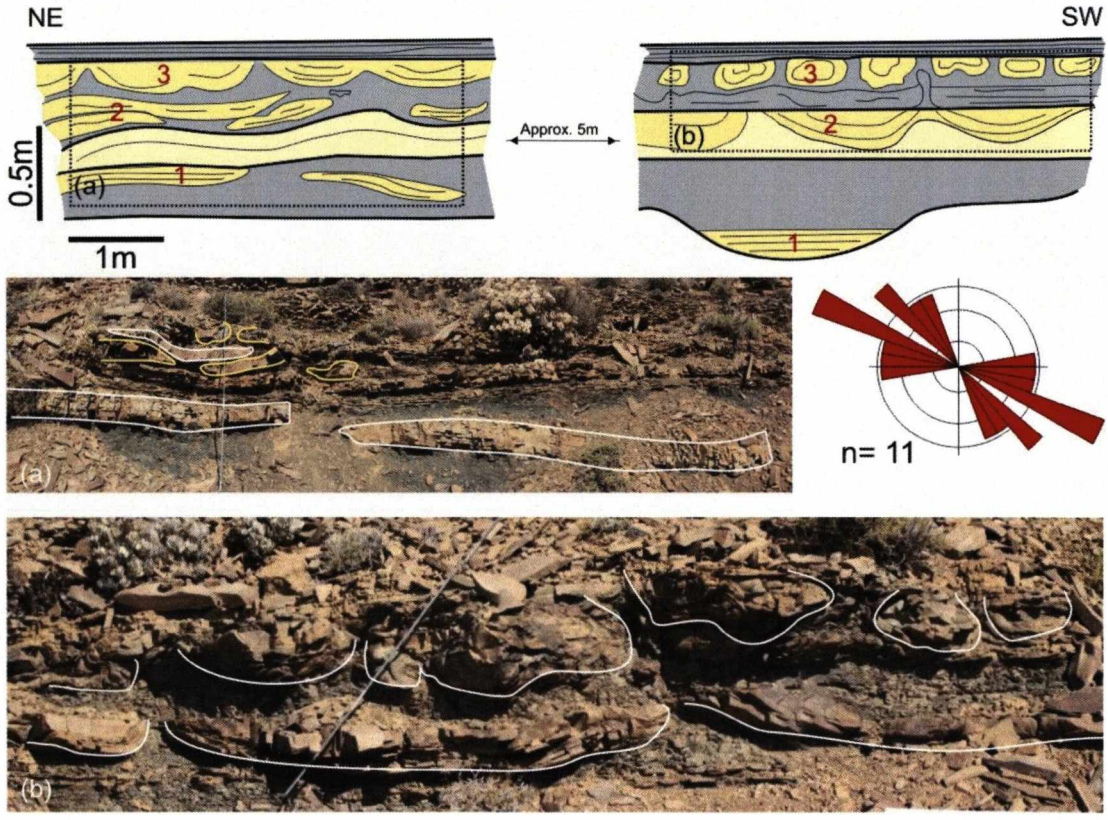

Figure 4.31: Composite deformed bed at base of Cycle H4. Sketch show 3 styles of deformation with lateral changes in the intensity of deformation: level 1 is dominated by "floating" elongated sandstones, sub-parallel to bedding, in a siltstone matrix; level 2 shows a mixing of flame structures, deformed sandstone blocks and truncation and level 3 is dominated by flame structures. Photos (a) and (b) are detail from the sketches above; some structures are highlighted by white or yellow continuous lines. Measurements of the orientation from level 3 indicate a strong WNW-ESE orientation.

consequently less favourable for the occurrence of detached soft-sediment deformation.

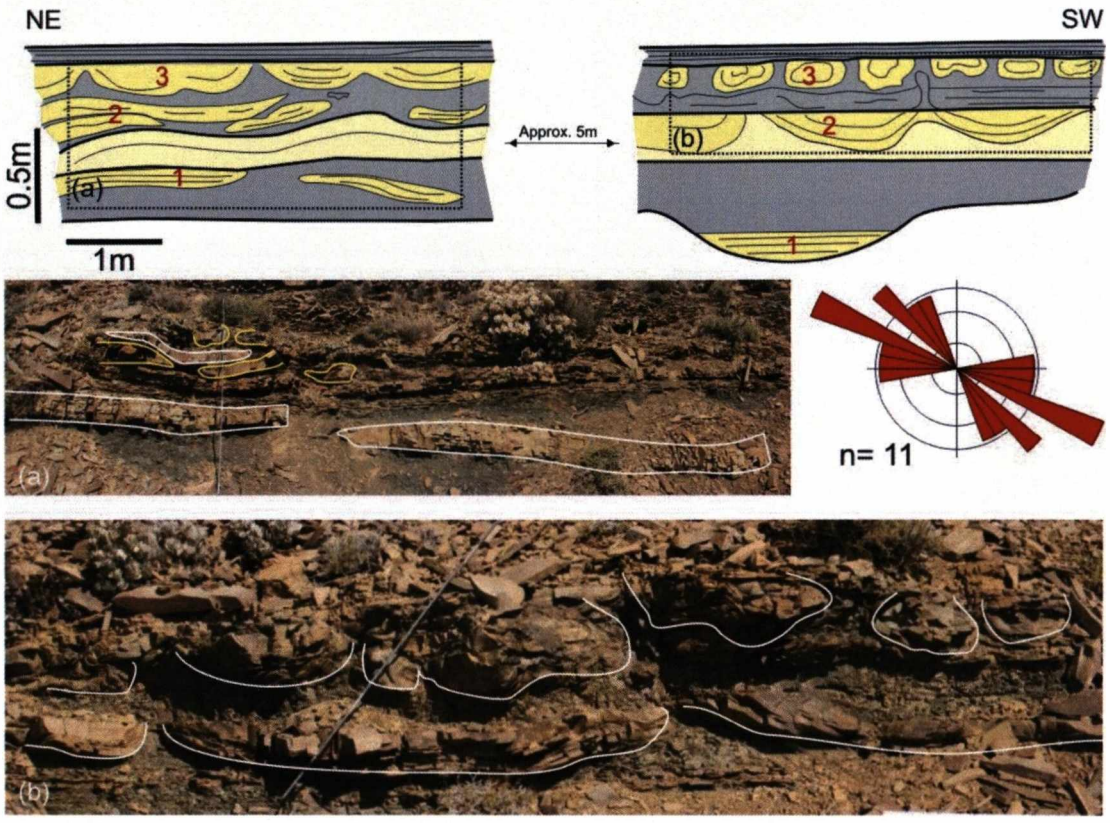

Figure 4.31: Composite deformed bed at base of Cycle H4. Sketch show 3 styles of deformation with lateral changes in the intensity of deformation: level 1 is dominated by "floating" elongated sandstones, sub-parallel to bedding, in a siltstone matrix; level 2 shows a mixing of flame structures, deformed sandstone blocks and truncation and level 3 is dominated by flame structures. Photos (a) and (b) are detail from the sketches above; some structures are highlighted by white or yellow continuous lines. Measurements of the orientation from level 3 indicate a strong WNW-ESE orientation.

4.1.5 Zoutkloof and Buffels River areas

These two areas are located 5.5 km to SW and 7.0 km to SE of Heuningberg Mountain (cf. Figure 4.1), respectively, and expose a stratigraphic interval younger than the ones studied in Heuningberg. One log was acquired in each area reaching a total of 260 m. The objective here was to analyse the deformation style and identify any distinct pattern in the upper stratigraphic levels. Initial correlation by Charles (2007) positioned the outcrop at Zoutkloof Farm just above Cycle H4 in Heuningberg, separated by a possible maximum flooding surface and exposing Cycles 5 and 6 plus the upper undivided section. The aerial photo-interpretation of the topographic expression of anticlines and synclines also indicates that Zoutkloof is stratigraphicaly above Cycle H4, but is of inadequate detail to confirm if it is exactly above H4. The mapped features also indicate that the outcrop in the Buffels River, 10 km east from Zoutkloof, exposes the stratigraphic interval approximately equivalent to the top of Zoutkloof (Figure 4.32).

Soft-sediment deformation

Zoutkloof is characterized by high frequency (<10 m thick) cycles of coarsening- and thickening-upward siltstone to fine-grained sandstone of facies association 1 and 2 (Table 4.2). These packages form thicker cycles, varying from 35 to 50 m thick, on the same scale as the ones described in Heuningberg. Here, cycles H5 and H6 are broadly equivalent to cycles 5 and 6 of Charles (2007) and are followed by Cycle H7 (Figure 4.32).

The facies associations are not vertically organized as they are in Roosterberg and Heuningberg, where it is possible to identify an intermediate deformed section for each cycle. At Zoutkloof Cycle H5 is characterized by facies association 3 (deformed *in situ*), while cycles H6 and H7 present facies association 4 (deformed detached). In particular, the stratigraphy described in Zoutkloof is important for the characterization of an uncommon deformation style (Figure 4.33) and by the good lateral exposure of the deformation along the outcrop (Figure 4.34). Palaeocurrents are oriented to the NE (Charles, 2007) and flame structures show no preferential orientation.

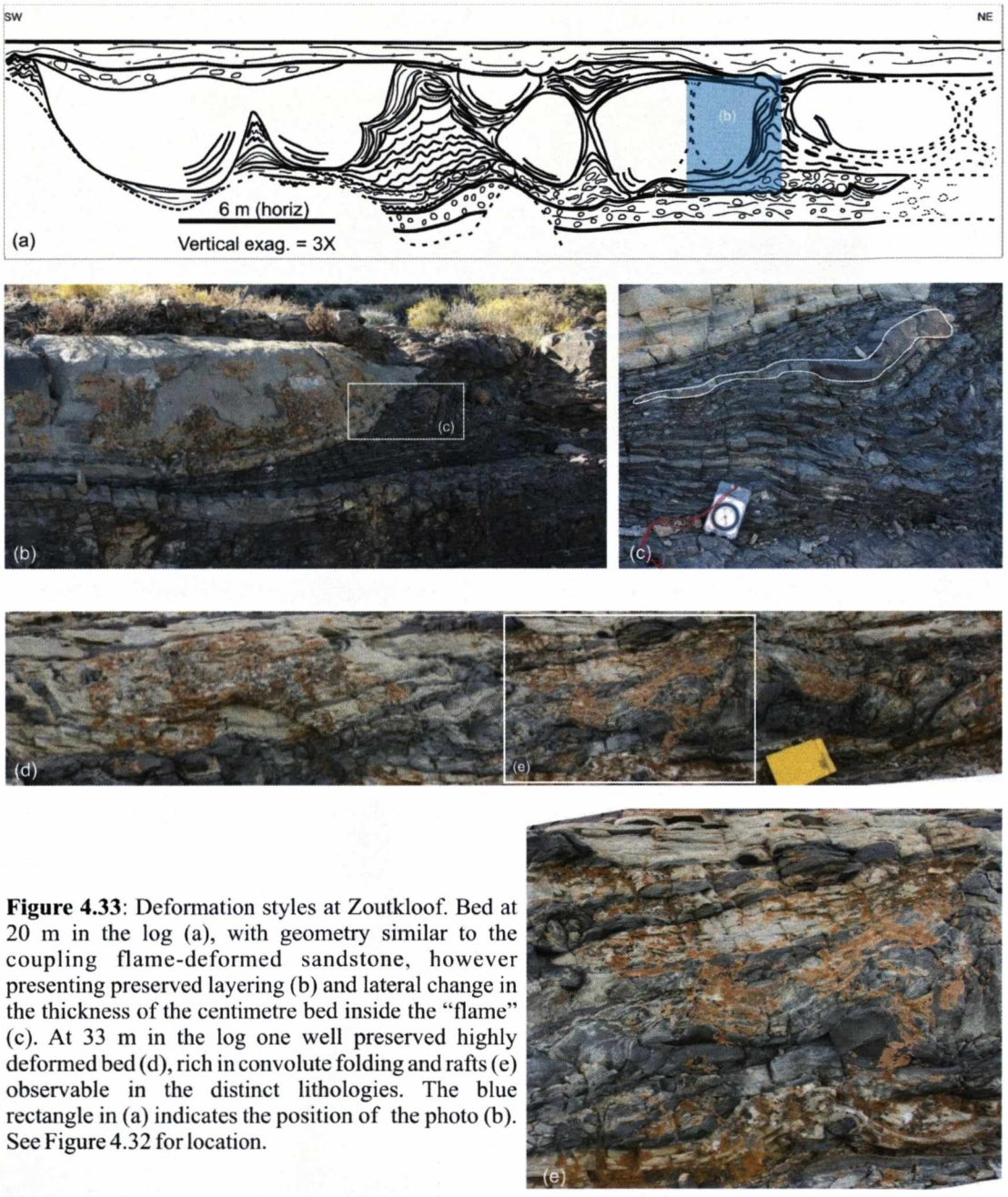

Figure 4.33: Deformation styles at Zoutkloof. Bed at 20 m in the log (a), with geometry similar to the coupling flame-deformed sandstone, however presenting preserved layering (b) and lateral change in the thickness of the centimetre bed inside the "flame" (c). At 33 m in the log one well preserved highly deformed bed (d), rich in convolute folding and rafts (e) observable in the distinct lithologies. The blue rectangle in (a) indicates the position of the photo (b). See Figure 4.32 for location.

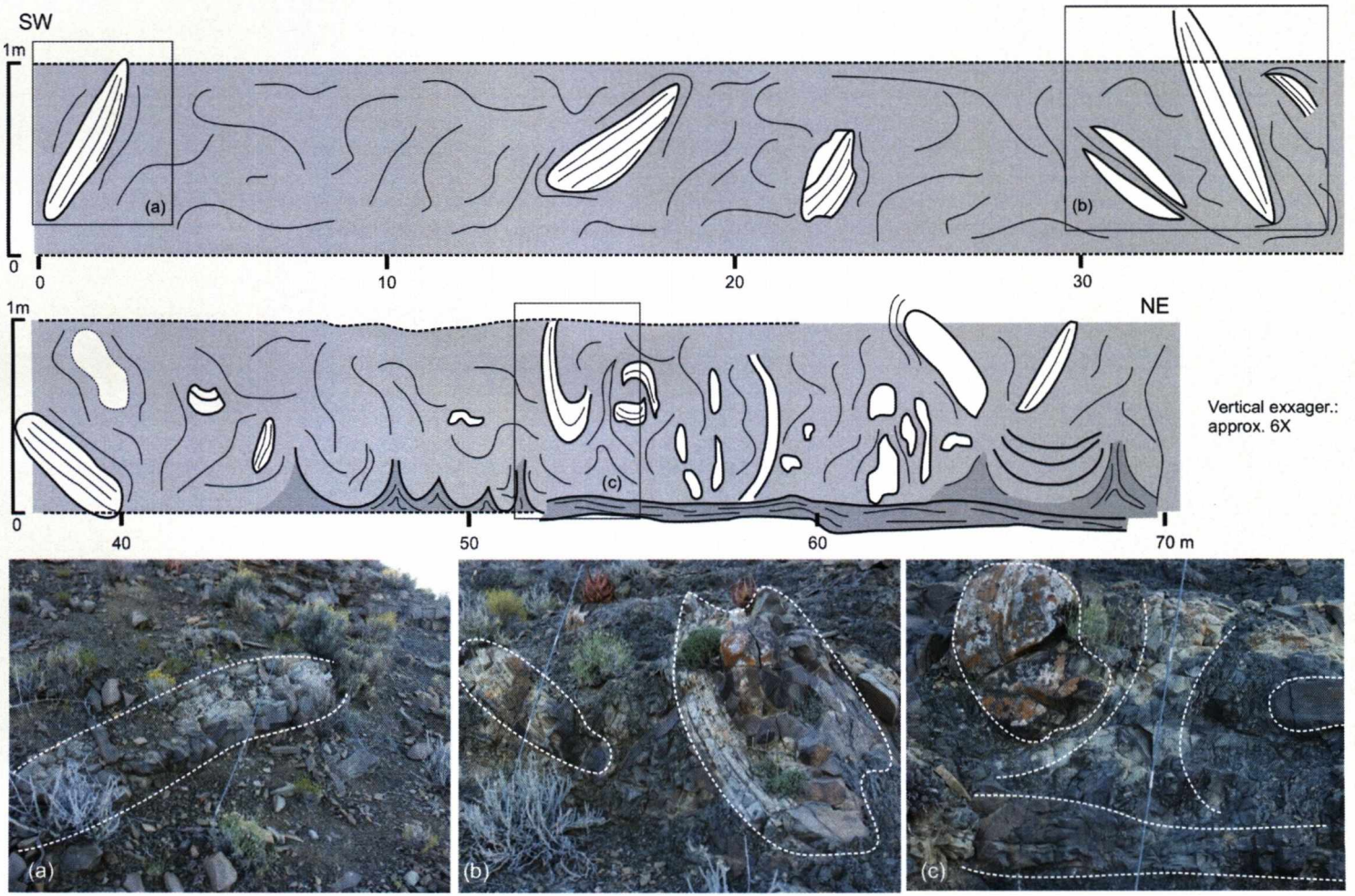

Figure 4.34: Lateral change in the degree of deformation in a bed (58 m in Zoutkloof log) positioned inside a thick (52 - 63 m in the log), highly deformed interval. In the SW part, rafts of fine grained sandstone up to 3 m long (a) are found dispersed in highly deformed siltstone to very-fine grained sandstone matrix. Walking along this interval to the NE, the number of dispersed rafts increases and become closer (b), culminating with the association of rafts, flames structures and preserved bedding at the NE boundary (c).

The presence of coarsening- and thickening-upward cycles in the Buffels River area is not clear. The most distinctive characteristic is the presence of thick intervals (up to 10 m thick) of highly deformed very-fine grained sandstone with rafts (facies association 4, Table 4.2) in a siltstone matrix overlain by 5 m thick planar laminated- and low-angle cross-stratified fine-grained sandstones. These occurrences are similar to the intermediate and upper sections of cycles studied at Roosterberg and Heuningberg, but it is not possible to be exactly sure of their relative stratigraphic position. *In situ* soft-sediment deformation is restricted to some intervals and is represented by load casts and pseudonodules and small flames. The most conspicuous soft-sediment deformation features are the elongated and sub-parallel (up to 5 m long) sandstone rafts present in the deformed intervals. Good exposures allow a 3D view of the WSW-ENE oriented flame structures (Figure 4.35). NW-SE orientation of the symmetrical ripple crest lines indicates palaeocurrents along the azimuth SW-NE.

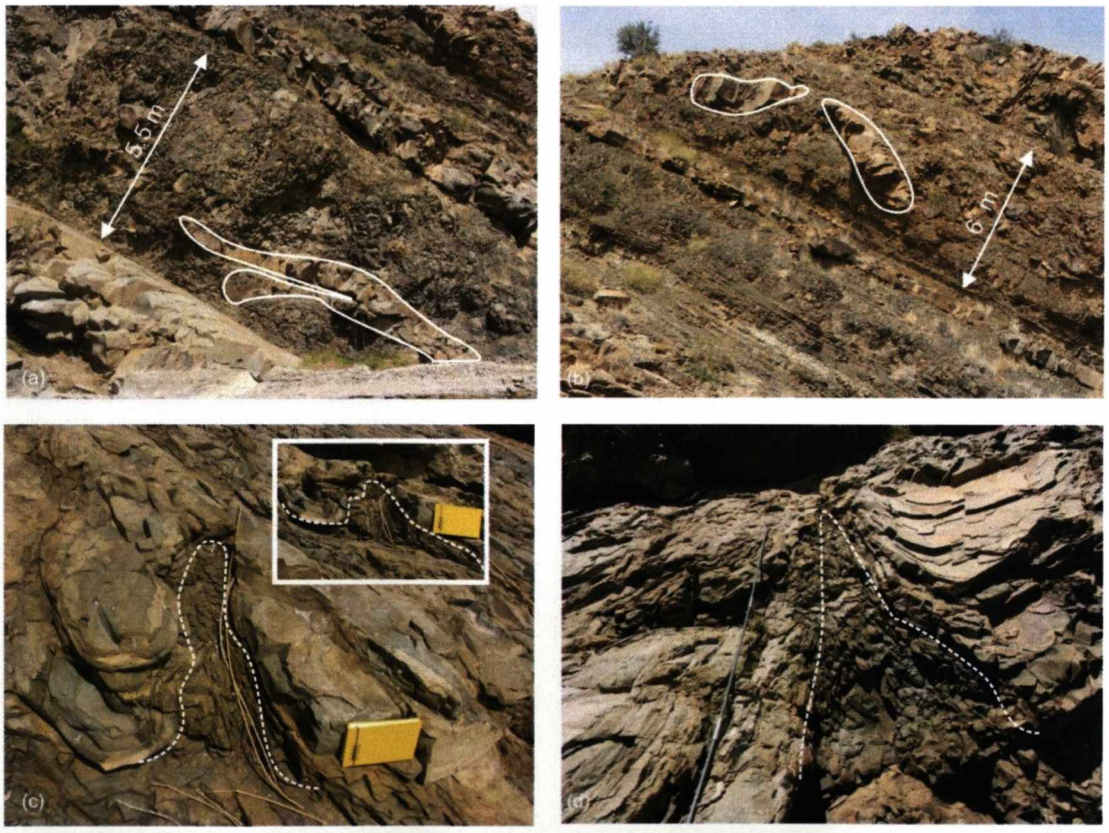

Figure 4.35: Soft-sediment deformation at Buffels River. (a) and (b) Thick packages of debrites, positioned at 75-81 m and 88-94 m in the log and characterized by large elongated rafts, up to 6 m long, sub-parallel to bedding; (c) and (d), the first positioned at 14 m in the log and the second in an isolated outcrop, are plan view of elongated flame structures in different scales. The inset rectangle in (c) is the frontal view of the same flame structure. The stick in (d) is 1.8 m long.

Interpretation

Cycle H5 in Zoutkloof is dominated by *in situ* deformation features; the presence of a 10 m thick succession of beds with many pseudonodules and intense deformation at 25 and 33 m in the Zoutkloof log (Figure 4.33) are indicators of vertical loading and liquidization of the interval without significant lateral dislocation. The atypical bed at 25 m (Figure 4.33a) is interpreted to have formed by loading caused by emplacement of the thick bed of sandstone over a stratified and unconsolidated finely laminated bed. In this case, the sandstone bed squeezed the underlying thin layers that escaped laterally and become thicker toward the flame, resulting in a type of soft-sediment deformation structures nominated here as squeezed structure. In contrast to the flame structures described above, the preservation of the internal layering indicates that fluidization was secondary in this episode with deformation interpreted as occurring under plastic behaviour. However, the deformation in the bed at 33 m (Figure 4.33d) is considered as a product of total liquefaction and mixing of distinct lithologies, generating the contorted pattern observed. It is nominated as convolute bed and is interpreted as formed by liquefaction intrusion (Lowe, 1975), i.e., the intrusion of liquefied sediment masses generally accompanied by complete obliteration of primary structures in the intruded sediment and intense deformation of surrounding strata. It must not be confused with convolute lamination which is considered as a type of soft-sediment fold (sense Lowe, 1975), formed by hydroplastic or laminar liquefied flowage that deform primary laminations without obliterating them.

The Zoutkloof succession is interpreted as representing a position up dip in relation to Heuningberg, in a stable shelf to shelf-edge environment, characterised by cycles of coarsening- and thickening-upward, similar to the underlying Cycle H4 at Heuningberg. The *in situ* deformation of Cycle H5 (with no evidence of detachment) supports this interpretation. From cycles H6 and H7 in the Zoutkloof log, deformational facies 4 (Table 4.2) is interpreted as the product of debris flows and slumps dispersed through the vertical succession and marks the re-introduction of instabilities in the system, which could be caused by lateral shifts of the delta front. At Buffels River the successions of thick debrites and cross-laminated sandstone, is thought to equate to a stratigraphic position equivalent to the mid and upper Zoutkloof succession and persists to the upper stratigraphic intervals. The orientation of the symmetrical ripple crests suggests palaeoflow E-W, which would indicate that

Buffels River is positioned down dip in relation to Heuningberg and Zoutkloof. However this must be considered carefully as the orientation of ripple crests normally indicates reworking not necessarily at the same orientation of the original deposition trend as seen in the Heuningberg area.

4.1.6 – Statistical studies

Roosterberg Area

Observations

Measurements of geometrical parameters (Figure 3.14) were taken from 19 flames in 7 distinct predominantly vertically oriented deformed layers (beds A to G, Figure 4.6), from Cycle R2 and at the base of Cycle R3. They were selected considering different scales of flame occurrences (few centimetres to 4 m in height) and they were compared to the extensive dataset from the lower slope *in situ* deformation from the Waterfall area (see Chapter 3). The results of the statistical analysis, summarized in Figure 4.36, show a high degree of correlation (from 0.712 to 0.992) between the cross-plotted parameters. Distance to next flame (DN) *versus* base width (BW) (Figure 4.36a) shows the least square regression line almost parallel with the one obtained for the Waterfall lower slope deformation and the dimension of the studied parameters is broadly equivalent in the two areas. The ratio DN/BW varies between 0.5:1 and 1.5:1. Unit thickness (UT) *versus* flame height (FH) (Figure 4.36b) is characterized by a high degree of correlation, similar to that obtained from the Waterfall outcrops and the ratio UT/FH is approximately 1.2:1. Flame height *versus* base width (Figure 4.36c) ratio is between 0.8:1 and 1.3:1. In this case, large structures (beds F and G) show a tendency for flames with narrow bases compared to Waterfall and thinner beds from Roosterberg. The large spread of the cross-plotted pairs found in the case of base width *versus* narrow point (NP) (Figure 4.36d), ratio BW/NP around 3.5:1, is related to the different styles of flames found (Figure 3.16) and is similar to the result provided by the Waterfall data.

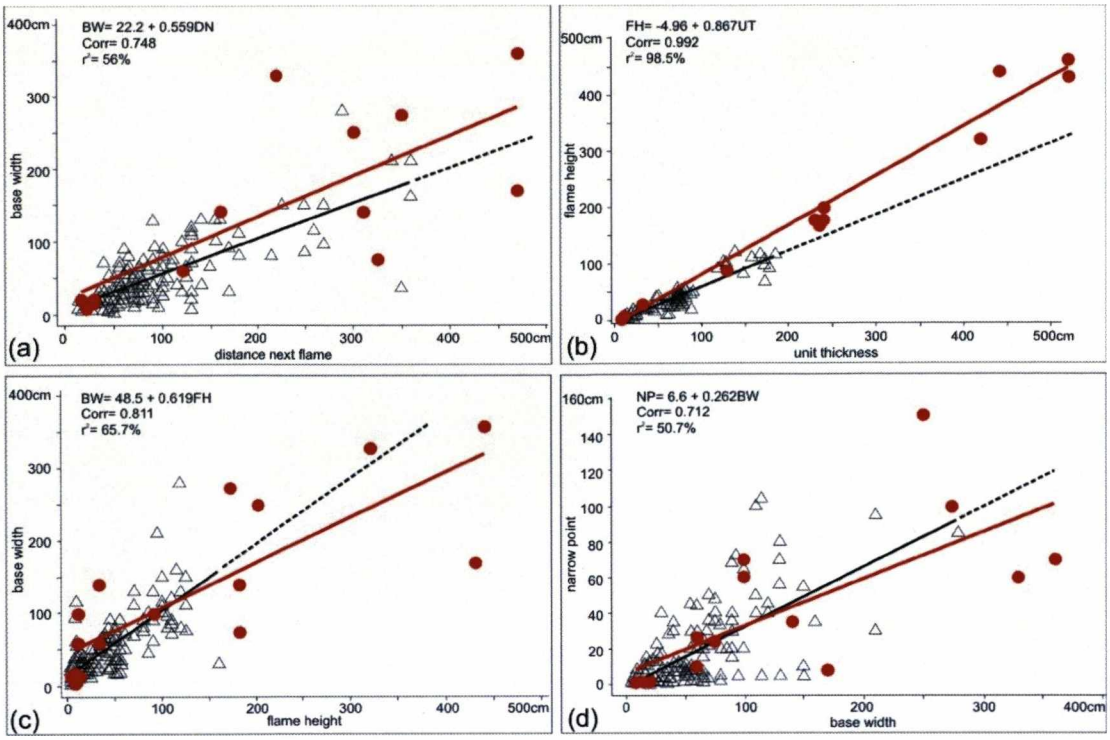

Figure 4.36: Cross plots (red dots) and least square regression line (red line) for geometrical parameters of flames at Roosterberg. The studied elements are indicated in Figure 3.14 and the position in the Roosterberg outcrop is in Figure 4.6. See text for details of description and interpretation. For comparison Waterfall pairs of attributes (black triangles) and least square regression line (black line) are also represented.

Interpretation

Due to the large amount of data and results obtained from the Waterfall area (Section 3.1.4), all statistical analyses of geometric parameters of flames in other localities will be compared to this large dataset in order to verify if similar conditions persisted in different times and depositional environments. Roosterberg data present a good fit with Waterfall data. The differences (crossplot flame height *versus* base width, for example) can be attributed to changes in the large scale flame style (Figure 4.10). Compared to Waterfall, samples from Roosterberg are positioned in a stratigraphic interval (Cycle R2 and base of Cycle R3) that was subject to considerable lateral stress, which resulted in the occurrence of detached soft-sediment structures, due to the instability of the shelf-edge upper slope. However, the effect of such stress is not registered in these particular beds, in the field or suggested by the statistical analysis. Also, the responses from Roosterberg indicate that flame structures occurring at a larger scale preserve basically the same geometrical characteristics as small scale examples (from Waterfall). The large

structures (beds E, F and G, Figure 4.6) were associated with mouth bar deposits, where a large amount of sediment is loading the underlying strata.

Heuningberg, Zoutkloof and Buffels River Area

Observations

The analysis included measurements from 55 flames from the different outcrops (Figure 4.37), displayed together with pairs from each outcrop highlighted. Complementary regression analysis for each interval from the Heuningberg area is presented in Appendix 4. Due to the small number of points, data from Zoutkloof and Buffels River are not individualized in different intervals. Distance to next *versus* base width (Figure 4.37a) shows a result similar to the Waterfall section; a DN/BW ratio of 1.5:1 to 2:1 and unusual values for Zoutkloof. Unit thickness *versus* flame height (Figure 4.37b) is characterized for a great range of samples where the flame and layer thickness have close values (ratio approx. 1:1). For the least square regression line, UT/FH varies from 1.1:1 to 1.4:1. Flame height *versus* base width (Figure 4.37c) shows spreading of the points and departure from the least square regression line related to Waterfall data. The FH/BW ratio varies from 0.3:1 to 0.9:1 and is lower than values found for Waterfall (around 1:1). Base width *versus* narrow point (Figure 4.37d) shows a peculiar concentration of the points in the equivalent lower half part of the distribution for Waterfall, with a BW/NP ratio from 5:1 to 6.5:1.

Interpretation

Pairs with large values of distance to next *versus* base width are related to one bed (cf. Figure 4.33a) in which the flames are interpreted to be produced by a different process (see section 4.1.5) if compared to the origin of the flames in general (see section 3.1.5), which could explain the anomalous response. The graph for unit thickness and flame height indicates that, at least in 40% of the samples, flames ruptured the layer completely, i. e., the ratio UT/FH is 1:1. This phenomenon was also observed at Waterfall, but in that case the spreading of material transported through the flame onto the seabed (and also considered part of the deformed bed) is implied in values below the 1:1 straight line in the graph (Figure 4.38) and it is an

effective difference between the two areas. One possible cause for this difference can be attributed to the higher slope gradient in the case of Laingsburg data avoiding the settling of the extruded material that flowed down-slope. An additional factor could be the occurrence of erosion related to the truncations produced by channels and debris flows, as described in Cycles H2 and H3. When observing the results from flame height *versus* base width values, beds CD2 and CD3 are the most likely to have caused the spreading of points away from the least square regression line. This can be explained because the succession that contains bed CD also contains a complex series of truncations (Figure 4.23) that may have partially eroded the flames, resulting in an alteration in the relation FH/BW. Base width *versus* narrow point is a relationship that depends on the type of flame, as indicated with Waterfall data (see section 3.1.4). Types 3 and 4 are the dominant style in Heuningberg and the cross-plotted pairs are distributed in the region dominated by flame types 3 and 4 in the graph for Waterfall data which implies a good match between the two areas.

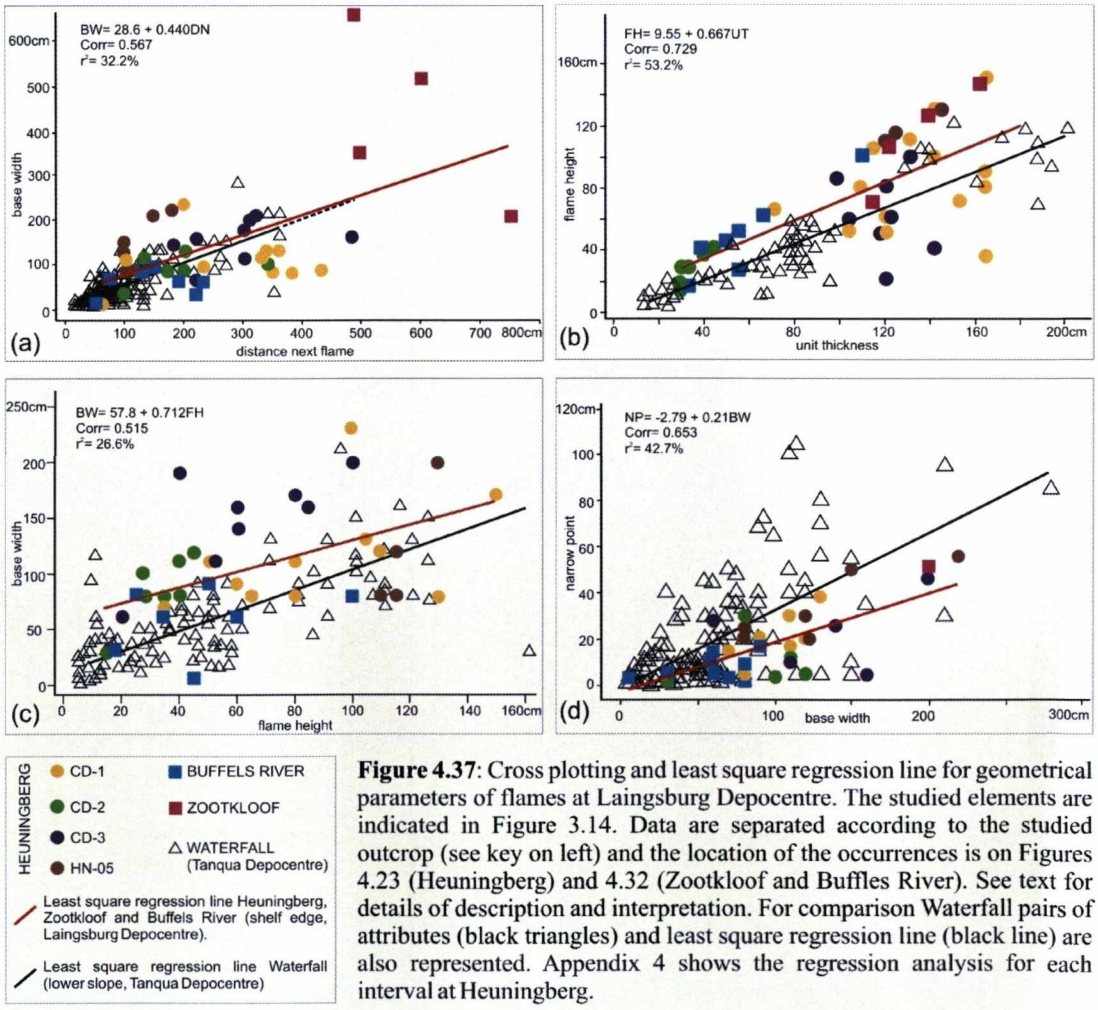

Figure 4.37: Cross plotting and least square regression line for geometrical parameters of flames at Laingsburg Depocentre. The studied elements are indicated in Figure 3.14. Data are separated according to the studied outcrop (see key on left) and the location of the occurrences is on Figures 4.23 (Heuningberg) and 4.32 (Zootkloof and Buffles River). See text for details of description and interpretation. For comparison Waterfall pairs of attributes (black triangles) and least square regression line (black line) are also represented. Appendix 4 shows the regression analysis for each interval at Heuningberg.

Considering the similarity between the result of the statistical analysis for the shelf–edge deposits in Roosterberg and Heuningberg areas with the lower-slope deposits of Waterfall (Chapter 3), it is considered that similar rheological conditions could have existed during the *in situ* deformation in these different areas and palaegeographic settings. It appears that different depositional environments can generate deformational structures with similar characteristics if the grain-size range is similar. Therefore, flame structures are not diagnostic of a particular environment. In fact they are the response to particular stress conditions (deformation mechanism and driving force) that act during sediment deformation, independent of the depositional environment.

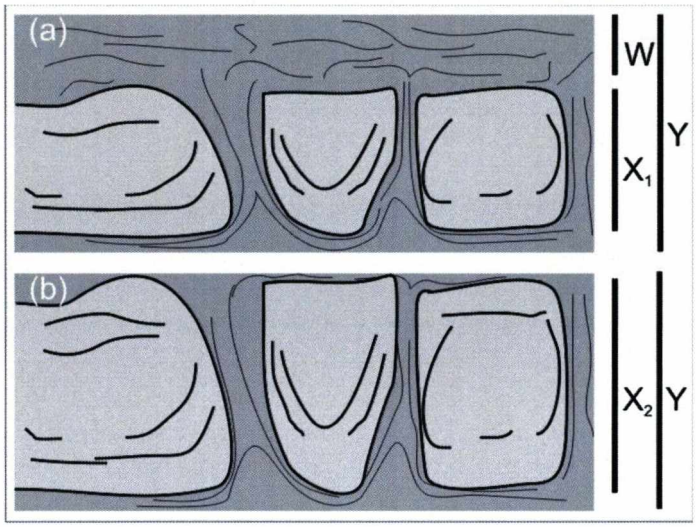

Figure 4.38: Diagram illustrating situation of flames (X) that resulted in the total break up of the overlying sandstone (pale grey). (a) finer grained material moving upward and spreading (W) over the broken sandstone; in this case X1<Y, where X1 is the height of flame and Y the thickness of the deformed bed, a common occurrence at Waterfall; (b) again the sandstone is ruptured by the fine grained material, but in this case there is no deposition of the structureless bed (or it was eroded) over the broken sandstone; in this case X2≈Y, generating a ratio approximately 1:1 that is common in Heuningberg.

4.1.7 – Complementary aspects

One major characteristic of shelf-edge deltas is the range of scales and great abundance of slope controlled and gravity-driven soft-sediment deformation intervals (see Chapter 1.3). In ancient and modern shelf-edge deltas; growth faults, slumps and slides occur in a range of settings varying from the collapse of the upper slope and channel margins to retrogressive failure of the shelf margin and triggered

by distinct events, while *in situ* soft-sediment deformation is less common (Martinsen, 1989; Melere *et al.*, 2002) (cf. Chapter 1.3; Tables 1.1 and 1.2). In many cases (almost 100% of seismic based examples) the small scale *in situ* structures are overprinted by the large scale detached features (slump and slide deposits, and debrites) and are considered as secondary features (for references see Table 1.1 and 1.2).

Compared to published examples (cf. Chapter 1.3), Heuningberg and Roosterberg are unique in exhibiting a large range of *in situ* and detached soft-sediment deformation structures. Detailed outcrop based work in other shelf-edge settings (Martisen, 1989; Collinson *et al.*, 1991; Plink-Björklund *et al.*, 2001; Mellere *et al.*, 2002; Strachan, 2002) identified structures related to specific events such as slump evolution and growth faults. The main difference in the Karoo examples is the overall distribution of well developed *in situ* soft-sediment deformation structures in distinct stratigraphic intervals and generated under different conditions of deformational processes. One possible explanation for this particularity could be the low angle of the Karoo slope, estimated as ~0.5° (Wild, 2005), that would contribute to the generation and preservation of *in situ* soft-sediment structures.

Growth faults are synsedimentary deformation structures commonly present at the shelf-edge (Tables 1.1 and 1.2; Edwards, 1976; Edwards, 1981; Bhattacharya & Davies, 2001; van Heijst *et al.*, 2002) occurring associated with slides and slumps, and consequently function of the slope gradient. A series of factors control the evolution of growth faults. The most cited are: (i) high sedimentation rate and loading, normally due to progradation of the sediment pile; (ii) excess of pore pressure, due to loading or presence of gas; (iii) high slope angle, that increases slope instabilities; and (iv) density contrast. At Roosterberg, the loading caused by the prograding delta, accompanied by a density contrast, created initial conditions that resulted in slumping and *in situ* deformation, but no growth faulting. In ancient lithified strata it is not possible to evaluate the role of pore pressure. Thus, the most likely factor in the absence of growth faults on the Karoo shelf-edge was probably the low angle of the slope.

4.2 – Neuquén Basin – Puesto Seguel area

4.2.1 Introduction

The Middle Jurassic Lajas Formation comprises 600 m of tide-dominated facies, which includes tide-dominated deltas, sandy heterolithic tidal channel fills and extensive progradational tidal-flat successions cut by heterolithic tidal channel fills (McIlroy *et al.*, 2005). The studied section is part of the tide-dominated deltas facies association and was chosen due to the excellent exposure of an interval of flame structures macroscopically similar to the ones found in the Waterfall area in the Tanqua Karoo (cf. Section 3.1). The objective here was to analyse the geological constraints, the deformational style, and the statistical distribution for the flame structures, and to compare/explore similarities and differences in the observations and results with the Waterfall data. The outcrop is located near the W-E trend of the Dorsal de Huíncul (see Chapter 2.3), a structure that originated as an extensional transfer zone that was later inverted and deformed by strike-slip movements (Vergani *et al.*, 1995). The effects of the Dorsal can be seen from the Middle Jurassic (Bajocian) to the Late Jurassic (Kimmeridgian), with a peak in activity between the Bathonian and Callovian (Vergani *et al.*, 1995; Freije *et al.*, 2002). The deposition of the Lajas Formation in this area was partially controlled by a N-S fault-controlled embayment generated during the rift-phase (Late Trissic-Early Jurassic) (McIlroy *et al.*, 2005) that preceded the main phase of inversion of the Dorsal de Huíncul (cf. Figure 2.13). Palaeocurrents for this interval around the Arroyo Picún Leufú indicate transport to the NW (Freije *et al.*, 2002).

4.2.2 Puesto Seguel

General Aspects and Description

The area around Puesto Seguel consists of the upper Los Molles Formation and the lower Lajas Formation (Aalenian-Bajocian) on the north flank of the Picún Leufú Anticline (Figure 4.39). Gulisano & Hinterwimmer (1986) identified two sedimentary successions: (a) the lower part characterized by deltaic deposits with fluvial and tide influence and (b) the upper part characterized by marginal marine, probably deltaic with strong influence of tides and secondarily fluvial. The studied

interval is part of the lower succession. The Picún Leufú Anticline is an asymmetric structure presenting a gentle north flank, oriented approximately east-west generated by transpression and associated with the evolution of the Dorsal de Huíncul.

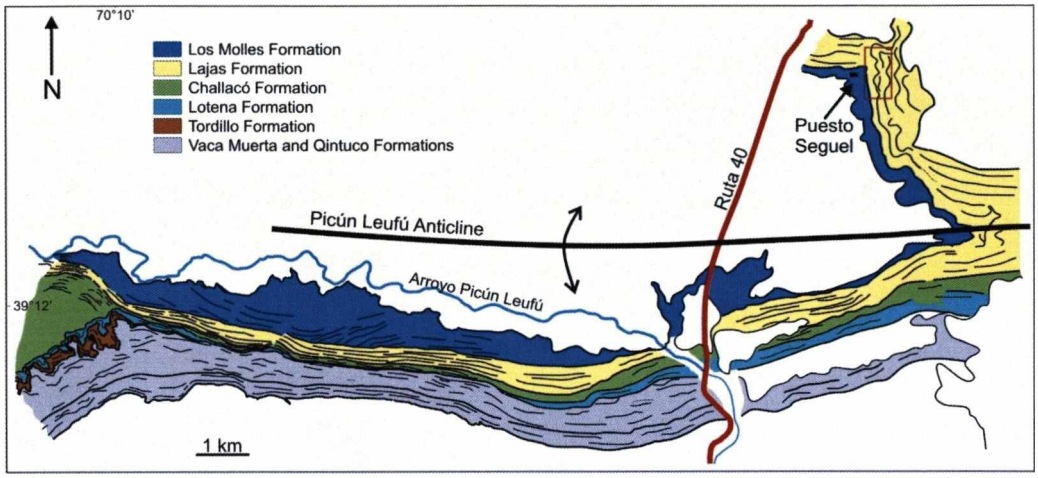

Figure 4.39: Geological map of Picún Leufú Anticline at Puesto Seguel area (interpreted from satellite image and modified from Galisano & Hinterwimmer, 1986 and Freije *et al.*, 2002). The studied outcrop (highlighted in the red polygon) is part of Lajas Formation.

The studied outcrop is 30 km south of Zapala and 6 km NNE of the bridge over the Picún Leufú River on the Ruta 40 highway (Figure 4.40). It comprises a succession of coarsening- and thickening-upward cycles, dominated by the following lithofacies: (i) tabular beds of planar-laminated fine-grained sandstone (Bb), intercalated with (ii) centimetre-scale thin beds of mudstone and very-fine grained sandstone with organic material (Cc), which grades laterally to (iii) deformed sandstone/siltstone interbeds rich in flame structures (Fb) and are topped by (iv) thick (up to 3 m) beds of cross-stratified fine- to medium-grained sandstone (Be) (Figure 4.41). Table 4.5 indicates the main characteristics of each lithofacies and Figure 4.42 illustrates some depositional structures.

Two intervals of flame structures were the main target for investigation in this outcrop. Interval 1 provides an excellent example of a lateral transition from facies Cc and Bb (undeformed bedsets) to facies Fb (deformed). Eight detailed logs (cm-scale), comprising a total of 13 m, were acquired and correlated along the 2 m thick bedset around the lateral transition between deformed and undeformed beds (Figure 4.43). In the south part, beds of facies Cc are overlain by beds of facies Bb. Beds of the underlying group (facies Cc) are parallel with very thin mudstone drapes. Small scale soft-sediment deformation is represented by load-casts of the sand-rich

beds over the mud-rich beds in the intermediate section, overturned flame structures that verge to the north, and micro-scale growth-faults dipping north in the basal section. The overlying group (facies Bb) is characterized by thicker beds (up to 0.4 m thick) of fine-grained sandstone with load casts, flame structures and some convolution and rotation of sandstone blocks (Figure 4.44).

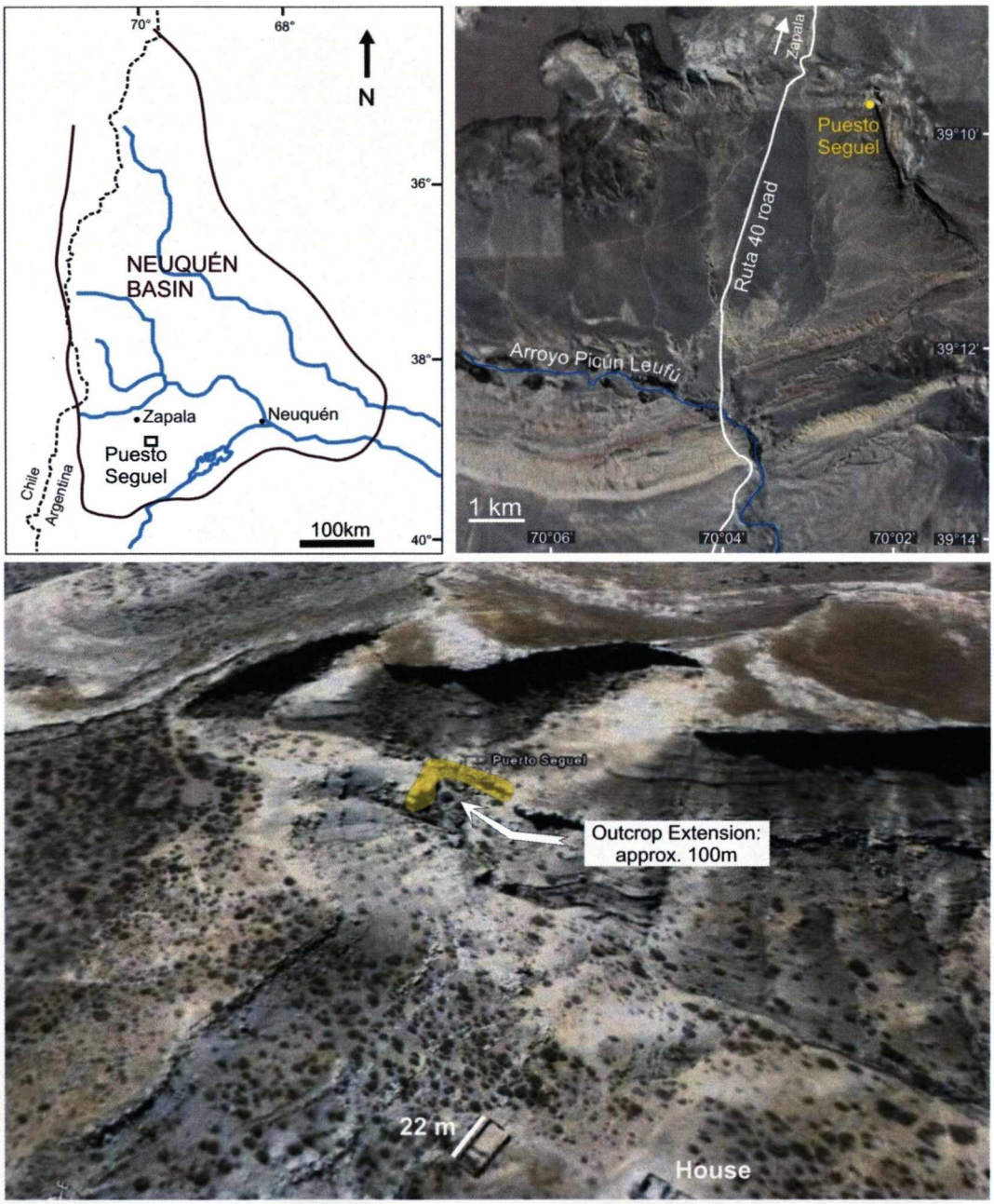

Figure 4.40: Location map for the Puesto Seguel outcrop, SSE of the town of Zapala (a), at 6 km NNE of the bridge of the Ruta 46 road over the Arroyo Picún Leufú river (b).The yellow strip on (c) shows the studied outcrop position, part of the Lajas Formation.

The north section of Interval 1 (facies Fb) is highly deformed with vertically oriented flame structures that can reach up to 1 m in height. They are similar in morphology to the ones found in the Waterfall area (cf. section 3.1). They differ as the disruption and convolution affect a succession of centimetre scale sandstones and mudstones; while at Waterfall the deformation normally involves no more than two or three sandstone beds (Figure 4.45).

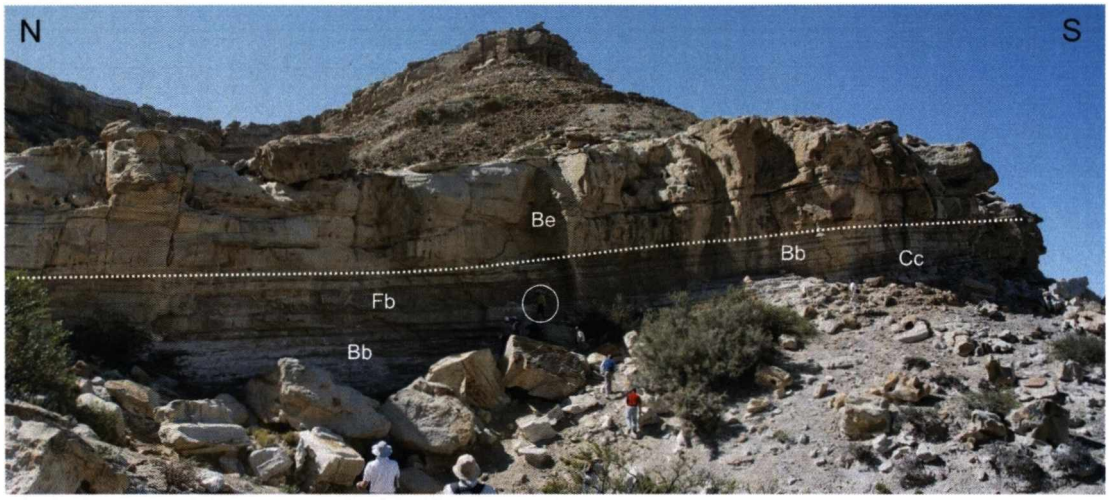

Figure 4.41: General view of the studied outcrop (interval 1) of the Lajas Formation at Puesto Seguel. The lower half is composed of facies Bb, Cc and Fb; the upper part (above dotted line) is composed of facies Be (see Table 4.5 and text for detail). The geologist highlighted in the circle is at the level of the soft-sediment deformed bed set that passes laterally into undeformed beds (right of the photograph).

The lateral transition between deformed and undeformed strata is sharp and marked by a small listric normal fault, which disrupted parallel beds that become contorted in the hanging wall block (Figure 4.46). Using sedimentological criteria it is possible to follow less disturbed beds in both sides of the fault (e.g. beds 2 and X) (cf. Figure 4.46). The upper part is marked by the deposition of a wedge of sandstone with same facies Cc and controlled by the underlying fault. The flames are oriented approximately to the east, although the outcrop is rather 2D, which does not permit a good visualization of flame axis.

Interval 2 includes a Cc lithofacies bedset overlain and partially eroded by a thick channelized package of lithofacies Be. Soft-sediment deformation occurs in two beds in the lower section (Cc facies) and comprises the disruption of the sandstone beds and vertical flame structures up to 0.3 m thick and oriented to the north (Figure 4.47). Measurements of geometric parameters were collected for the statistical analysis and are represented in the graphs in Figure 4.48.

Lithofacies class	Lithofacies name	Lithology	Associated Lithofacies	Sedimentary /Soft-sediment deformation structures	Bounding surface	Single bed thickness	Geometry	Depositional/ Deformational Process
Bb	Planar-laminated sandstone	Fine- to medium-grained sandstone	Cc	Parallel lamination. Symmetrical wave-ripples on top. Rare occurrence of low angle cross-lamination	Sharp. Base can be irregular due to loading.	0.1-1 m	Tabular.	Subtidal mouth bar
Be	Cross-stratified sandstone	Medium-grained sandstone.		Low angle cross-stratification to through cross-stratification. Large tree trunks to the top	Base sharp; top sharp, secondarily gradational	≈1 m. Bed sets up to 5m. (amalgamated)	Lenticular	Distributary channels (?)
Cc	Ripple laminated sandstone/ very-thin sandstone-mudstone interbeds	Fine-grained sandstone, siltstone and mudstone.	Bb, Fb	Ripple –lamination. Planar lamination in the very-thin beds. Flaser and lenticular bedding. Mud drapes Load and flame structures. Secondary growing faults. Organic material. Symmetric waves on top.	Sharp	0.02 – 0.2 m for the ripple laminated sandstone. <0.01m (bed sets up to 0.2m) for the very-thin sandstone/mudstone	Tabular	Subtidal (McIlroy *et al*, 2005).
Fb	Deformed sandstone/ siltstone with vertical structures	Siltstone to mudstone.	Cc	Flame structures. Contorted bedding	Sharp	0.2 – 1.5 m.	Tabular	Fluidization and/or liquefaction.

Table 4.5: Lithofacies classification for the tide-dominated delta facies from Lajas Formation, at Puesto Seguel, south Neuquén Basin.

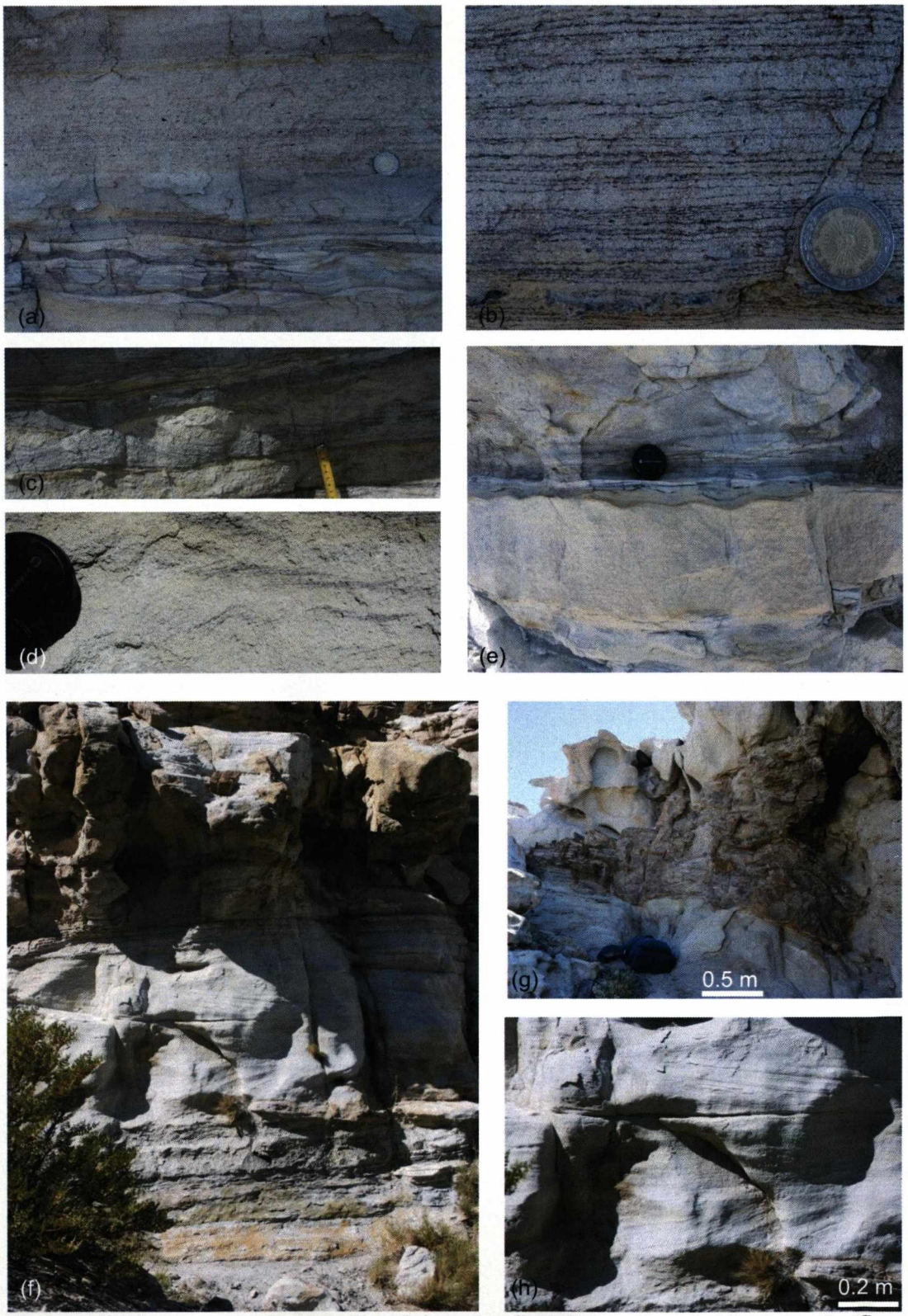

Figure 4.42: Sedimentary structures (not deformational) at Puesto Seguel. (a) Facies Cc, flaser bedding at the base; (b) Facies Cc, very thin bedding separated by mud laminae; (c) Facies Cc, lenticular bedding; (d) Facies Cc, climbing ripples in a sand rich bed (lens cap, 5 cm diameter, for scale); (e) Facies Bb, wavy on top of a planar laminated sandstone; (f) Facies Be, thick bed of cross-stratified sandstone, with the top rich in organic material (vertical scale: approx. 3m high); (g) Facies Be, presence of large fossilized tree trunks in the upper part; (h) Facies Be, details of the well sorted grain size and cross stratification in the lower interval.

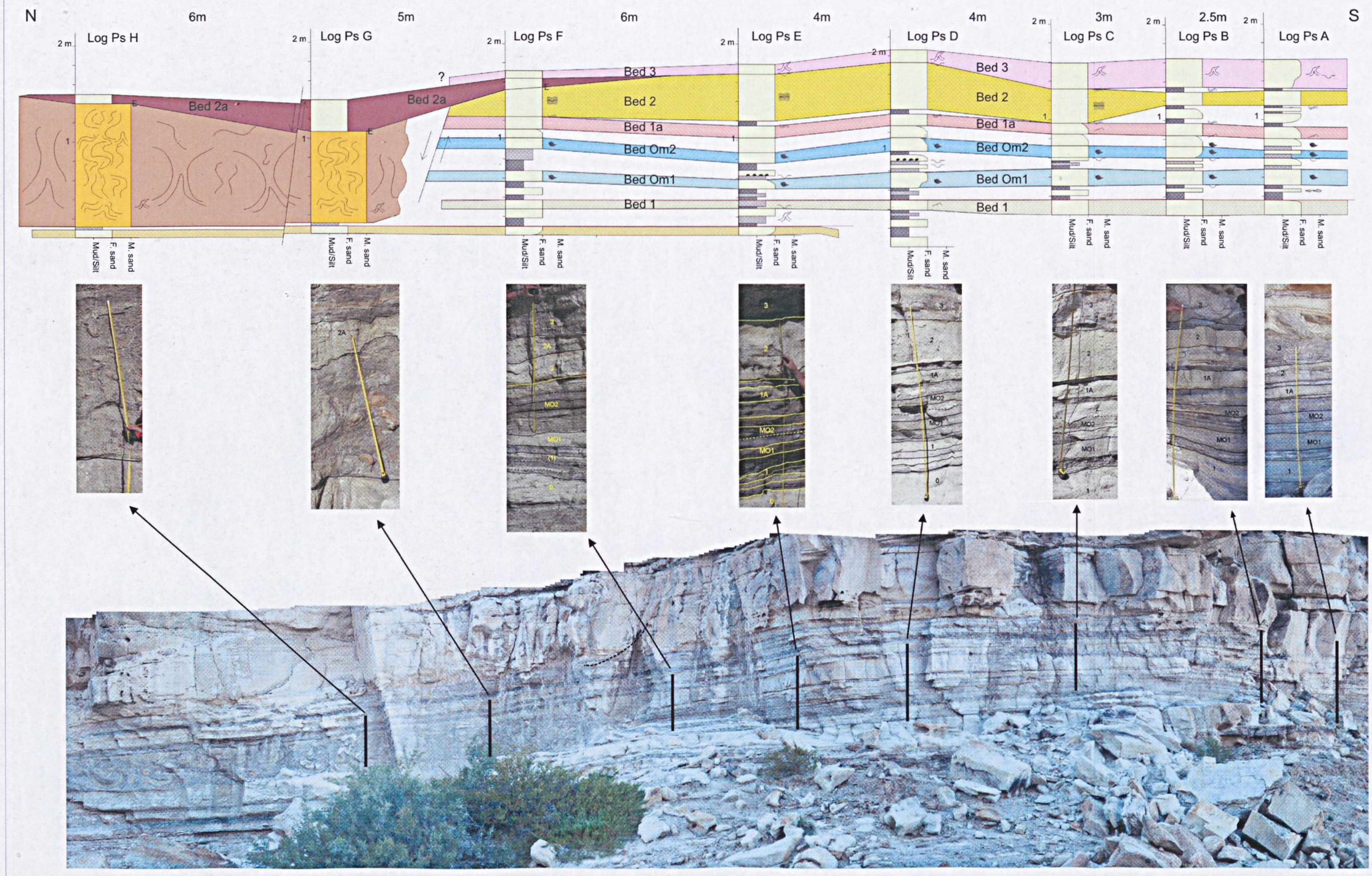

Figure 4.43: Interval 1 from Puesto Seguel outcrop with the distribution of logs along the outcrop and the correlation among them. The south part can be divided in two sections; the lower one is compound basically of facies Cc that persists up to the bed 1a and is overlain by thicker beds (beds 2 and 3) of facies Bb. To the north, it grades abruptly to one thick bed of facies Fb. The boundary between these two laterally distinct groups of facies is marked by a normal fault. See key for the symbols lateral to Puesto Seguel logs in Figure 4.6. Log coordinates on Appendix 1.

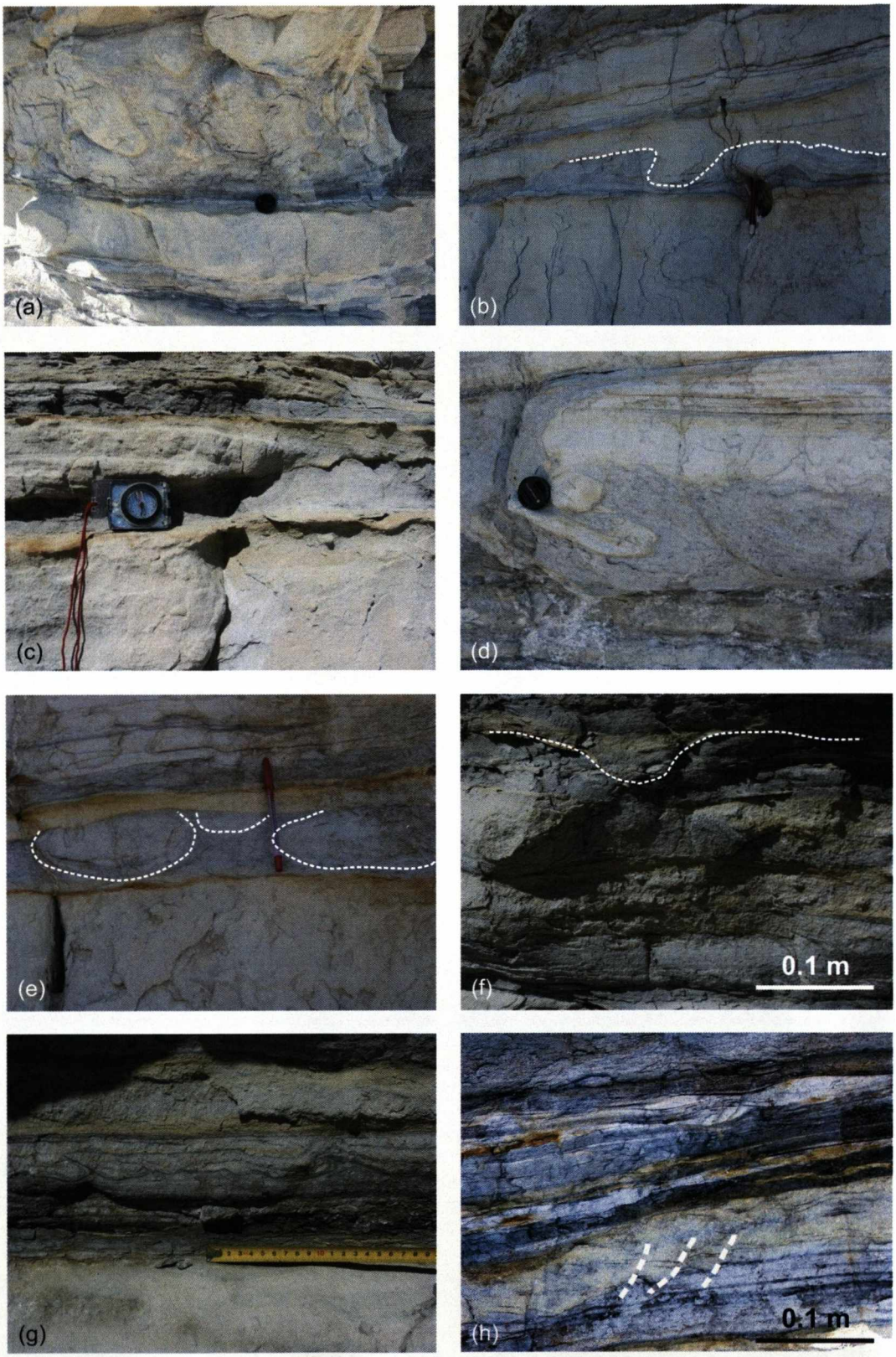

Figure 4.44: Soft-sediment deformation structures (SSDS) in facies Bb, upper Interval 1 south: (a) chaotic, rotated sandstone blocks and flames; (b) dm-scale load structure; (c) loading and erosion (?); (d) ruptured and sunk sandstone; (e) classic dm-scale flame structure. SSDS at facies Cc, lower Interval 1 south: (f) load structure (7 cm deep); (g) cm-scale flame-structures with vergence to north; (h) cm-scale normal fault (4-5 cm is the dashed plane) dipping north and associated load structure.

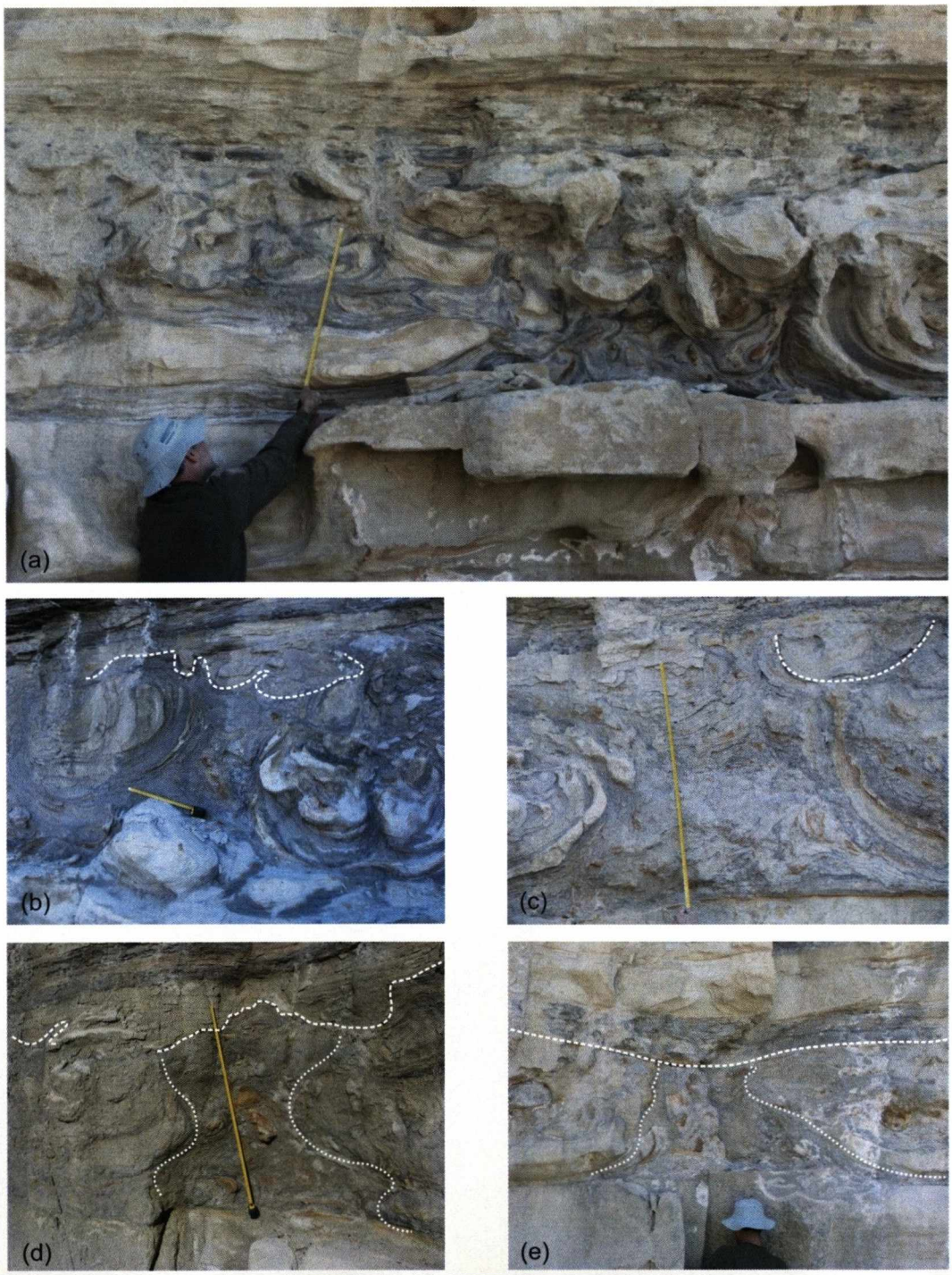

Figure 4.45: Soft-sediment deformation structures (SSDS) in facies Fb, Interval 1 north: (a) convolution and folding associated with flame structure (right); (b) and (c) regular type flame structure with load-casts and pseudonodules on top (dashed line); (d) fill of topographic low on top of the section (above dashed line); (e) bending of the overlying bed over the top of one flame (differential compaction ?). Tape measure is 1 m long.

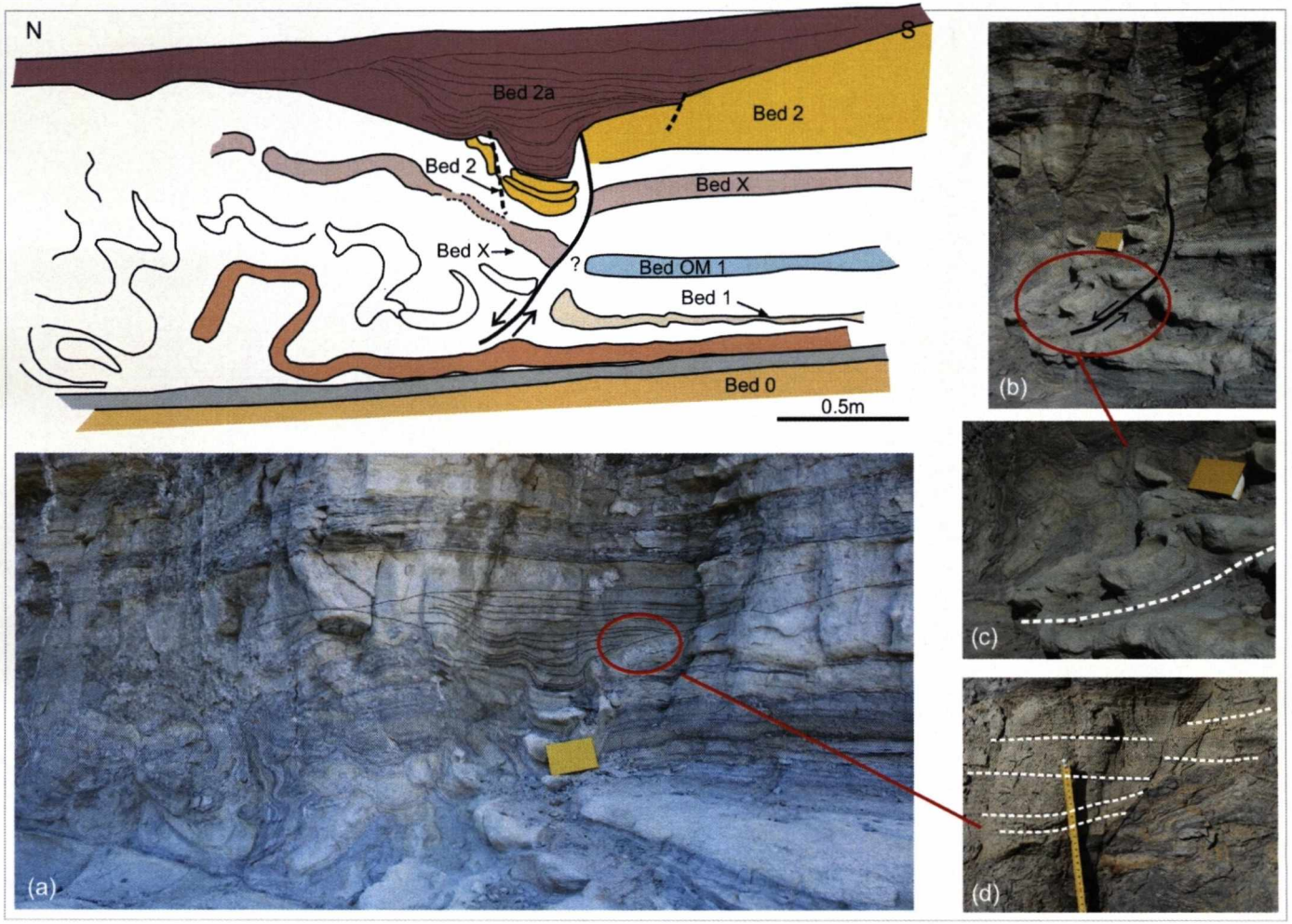

Figure 4.46: View if the transition between highly deformed bedset and plan-parallel beds at Interval 1. The sketch indicates the abrupt transition bounded by a normal fault. Observe that some beds are tracked in the deformed part and began folded by soft-sediment deformation. In the fault zone is deposited an unconformable bed (bed 2a) partially deposited while the fault was active. (a) Transition zone with emphasis to beds 2a and 2; (b) Fault plan; (c) Detail of the fault detachment with the development of one flame structure above it; (d) Detail of bed 2a fill evidencing internal unconformity.

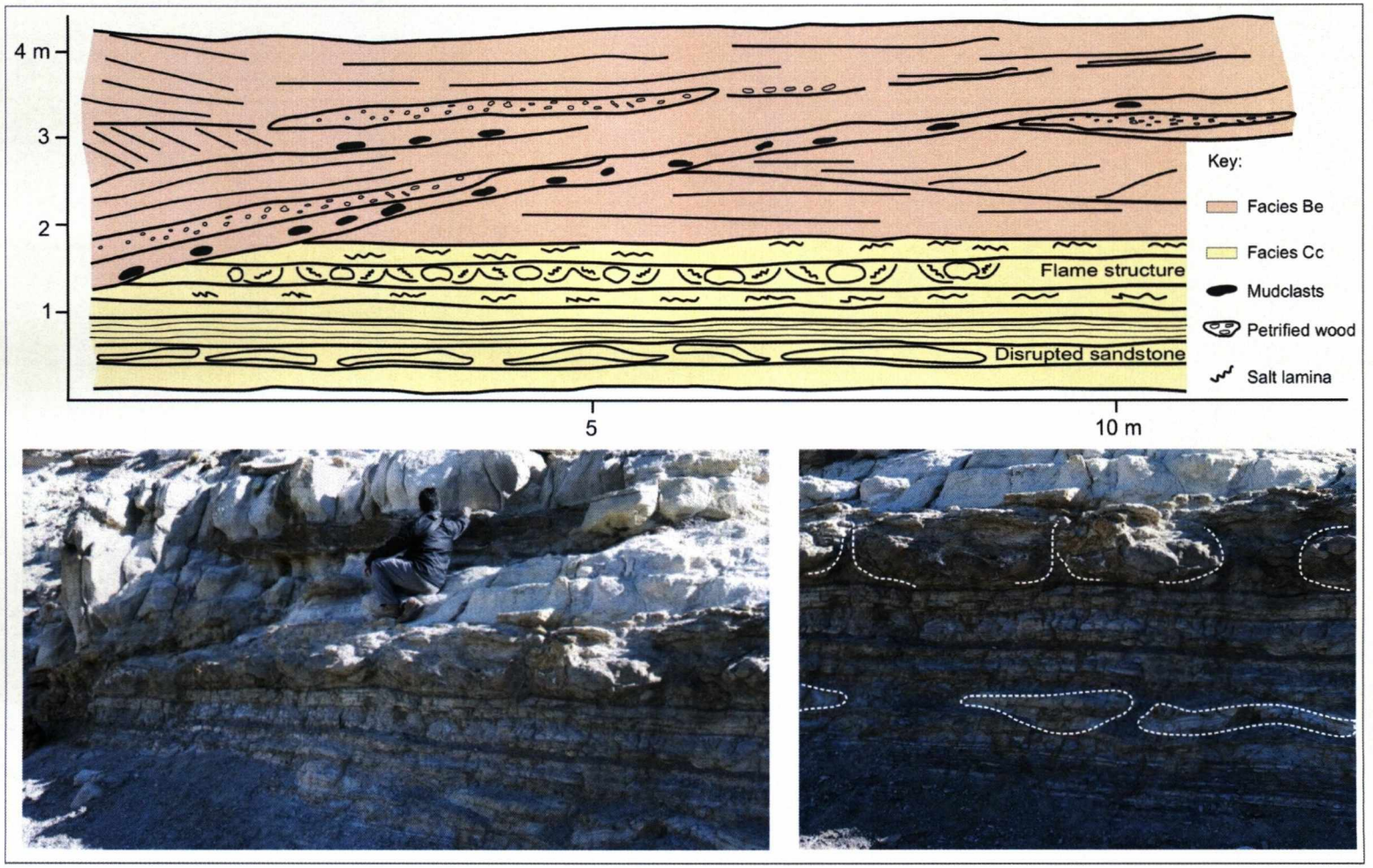

Figure 4.47: View of Interval 2. In this case the thick package of sandstone of facies Be was deposited immediately above and shows an erosive contact with the deformed bed in the lower facies Cc package. Soft sediment deformation is represented by flame structures and disrupted sandstones. (presence of salt laminae is considered as product of modern diagenesis). Left photograph show the contact between the lower and the upper sections and the right photograph (2 m high section) show detail of the two deformed beds. Log coordinates on Appendix 1.

Interpretation

The grain-size and the style of soft-sediment deformation structures found at Puesto Seguel are similar to the ones found at the Waterfall section and in some intervals of Heuningberg and Roosterberg outcrops. Thus, as in the other studied outcrops, liquefaction and fluidization are interpreted as the deformational mechanisms that generated such structures (cf. Chapter 3.1.5).

A possible trigger for the soft-sediment structures at Puesto Seguel could be the differential loading caused by the mouth bar/distributary channels at the top of each cycle. For Interval 2 it is supported by the abrupt change from facies Cc to Be, with the occurrence of the flame rich interval just below the erosive base of the thick sands (Figure 4.47). The presence of large tree trunks in the upper section of the Interval 2, suggests high energy and rapid sediment deposition that could cause deformation of the underlying package. However, the expected decrease in deformation with the increase in distance was not possible to test due to restrict length of exposure. For Interval 1, at least 1 m of tabular beds, dominantly of sandstone, occur between the deformed section and the thick sandstones at the top of the cycle indicating a uniform loading over Interval 1 and consequently differential loading is not expected as a trigger mechanism for deformation.

The Puesto Seguel locality lies approximately 20 km to the east of the main Lajas Formation outcrops in the Charahuilla area, where a 300 m thick succession is exposed, from basal tidal deltas through cycles of tidal channel and tidal flat deposits, capped by fluvial deposits (McIlroy *et al.*, 2005). Regional structural interpretations show that those outcrops lie within a fault-bounded southern embayment to the main Neuquen basin, while the Puesto Seguel area is outside of this feature (McIlroy *et al.*, 2005). The bounding faults were active in the Triassic but subtle, fault-related topography was still sufficient in Lajas times to provide additional amplification of tidal range to macrotidal conditions. Within the embayment succession soft-sediment deformation is not present in the main Lajas section, except for in the basal tidal deltas (McIlroy *et al.*, 1995). The reason for deformation in these deposits has been related to their stratigraphic position as the first clastic deposits to prograde over a muddy platform, resulting in foundering and collapse (McIlroy *et al.*, 1999). In the Seguel area the studied deformed deposits do not lie at the base of the Lajas Formation. It is considered likely that there was a subtle westerly tilt to the shelf in the Seguel area, related to the underlying substrate

(McIlroy et al., 2005). This subtle slope is thought to have initiated slow down-slope movement (creep) that acted as the trigger for the small-scale growth faulting and related soft-sediment deformation features in this local area. The effect of earthquakes is not likely due to geographic and stratigraphic restriction in the area of the deformation.

Soft-sediment deformation structures can be produced by the tidal flux and the tidal bore and are represented by small scale wrinkle marks, folds, flowslides, flow rolls and flame structures (Wells *et al*, 1980; Greb & Archer, 2007). Alternatively the overturned flame structures as well as the centimetre scale growth faults at the base of the "undeformed" section of the Interval 1 (cf. Figure 4.44g, h) could have originated by similar process that imprinted the north vergence for the structures.

The probably trigger mechanisms for the soft-sediment deformation structures at Puesto Seguel given the possible controls described above are the differential loading and a local oversteepening related to the main Lajas deposits to the west, with the contribution of the tidal flux and tidal bore in the generation of small-scale structures.

Three driving forces are considered as main forces acting during the evolution of the structures: (i) vertical stress caused by fluidization was dominant during the evolution of the large flame structures; (ii) horizontal stress acted during the formation of the small flames and, probably, the centimetre-scale faults; and (iii) density inversion in the evolution of the load structures. The possibility that gravitational body forces acting downward on a gentle slope is not rejected, due the occurrence of chaotic "slumped facies" (cf. Figure 4.44a) and the configuration of the normal fault, but in this case it would be secondary as there is not indication of preferential orientation, other than the vertical flames, in the highly deformed interval.

In contrast to the outcrops discussed in previous sections, the transition between deformed and undeformed strata is well exposed at Puesto Seguel. The normal fault that bonds the deformed facies can be interpreted as a non-tectonic fault because (i) the fault is restricted to a 1 m interval and listric in shape, which differs to the post-deformational faults that cut the outcrop from top to base (cf. Figure 4.46); (ii) the hanging wall fill is dominated by soft-sediment deformation; and (iii) the indication, from the bed thickening trends that the clastic-wedge above the fault

was deposited, at least partially, when the fault was active. It is interpreted that the normal fault synchronously developed in the boundary of the deformed section in order to compensate, in a single deformed interval the upward and downward particle movement caused by the soft-sediment deformation process.

A high degree of correlation and good fit of the least square regression lines to the cluster of points were obtained for the cross-plotted attributes of Puesto Seguel flame structures (Figure 4.48).

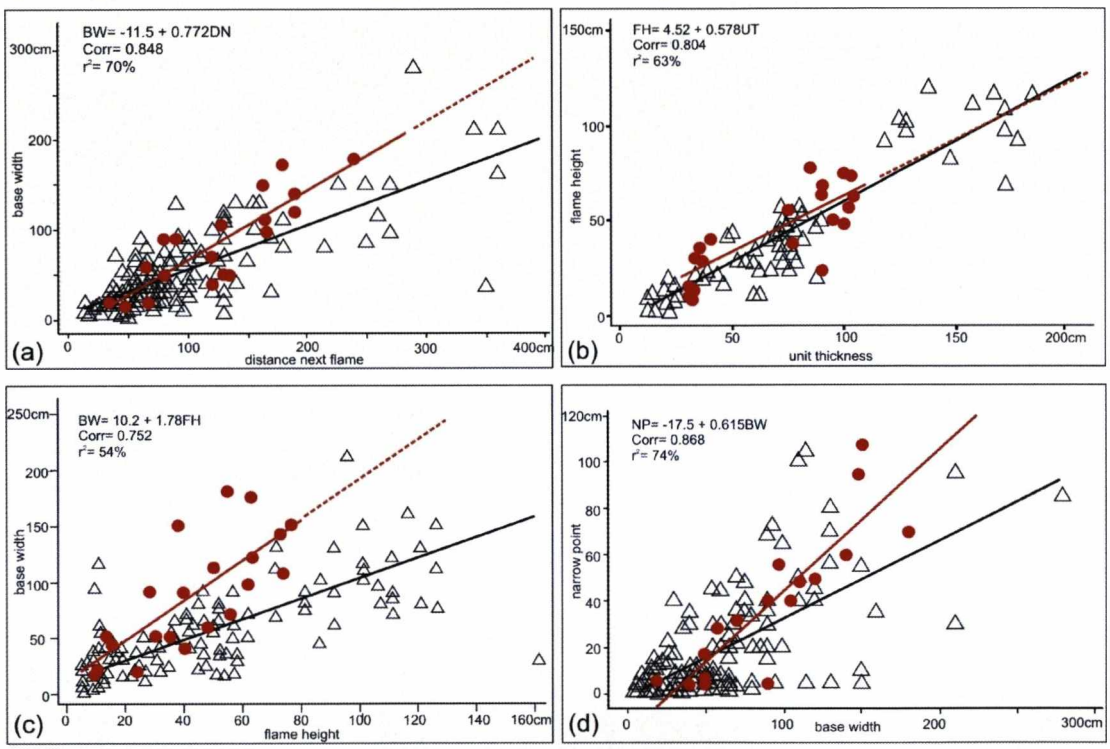

Figure 4.48: Cross plots (red dots) and least square regression line (red line) for geometrical parameters of flames at Puesto Seguel. The studied elements are indicated in Figure 3.14. See text for details of description and interpretation. For comparison Waterfall pairs of attributes (black triangles) and least square regression line (black line) are also represented.

In general, the results were similar to the ones identified in the Waterfall area in the case of the relationship between the distance between flames *versus* basal width of the flames (Figure 4.48a). For the deformed layer thickness *versus* flame height (Figure 4.48b), despite the close grouping of the points and the regression line with the results from Waterfall, care is needed because the paired distribution constitutes two distinct clusters of data. This aspect will be discussed later (Chapter 6.3) in comparison with other datasets. For flame height *versus* base width (Figure 4.48c) greater values for the base width are obtained for the same flame height. The composition of the deformed beds can be the explanation for such variation (cf.

Section 3.2.2 – Interpretation). Data for base width *versus* narrow point are distributed along the trend (Figure 4.48d) that reflects the behaviour of flames with regular shape (cf. Figure 3.8 and 3.16), which agrees with the most common flame shape found at Puesto Seguel. Except for some discrepancy in the relationships between flame height and base width, values from Puesto Seguel are close to Waterfall results and suggest that processes involved in both cases were comparable and independent of the depositional setting: shallow water deltaic *versus* submarine slope turbidites.

Chapter 5 – Multi-scale analysis of deformation

5.1 Introduction

As documented by many previous studies (Elliot, 1965; Lowe, 1975; Brenchley & Newall, 1977; Allen, 1982; Owen, 1987) soft-sediment deformation structures occur over a wide range of scales, varying from a few centimetres/millimetres (e.g. wrinkle marks, desiccation cracks, dishes) to hundreds/thousands of cubic meters (mass transport complexes). Among the structures discussed in this study the most important are slump deposits and debrites (detached structures), and flame structures and load structures (*in situ* structures). The first group occurs at distinct scales (centimetre to hundreds of kilometres), while flame structures/load structures are traditionally described at scales varying from centimetres to a few metres, with rare examples reaching some hundreds of metres (e. g. loading of basalts in water saturated sands; Needham, 1978).

As discussed in chapters 3 and 4, *in situ* soft-sediment structures, notably flame structures, show a marked internal organization and preferential orientation in a large number of the studied outcrops. Also, the statistical studies show linear trends for internal parameters of flame structures, suggesting that flames maintain the same proportions over a range of scales. The objective here is to investigate the scale dependence of these features, using different methods of data acquisition (ground penetrating radar (GPR) and X-ray tomography) and data treatment (serial sectioning of hand specimens, GPR profiles, tomographic imaging and seismic modelling). Centimetre-scale analysis is provided by serial sectioning and tomography, metre-scale by GPR, and tens to hundreds of metres-scale by seismic modelling.

5.2 Hand specimen studies

Centimetre-scale samples from deformed intervals were collected in the Tanqua depocentre with the objective of analysing the shapes of soft-sediment deformation structures in three dimensions. Two methods were tested: X-ray tomography and

serial sectioning. The results in both cases were limited although some information about shape and orientation were extracted. Analyses were made from core from the SL1 research borehole, two hand specimens (R2 and R3) of load structures from Roosterberg (Figure 5.1), and one sample of folded material (Wf1) from a flame rich interval in the Waterfall area (cf. Figures 3.6 and 3.7). The borehole SL1 was drilled at the locality of Bitterberg, around 25km NE of Roosterberg, that penetrates the Unit 5 of Skoorstenberg and the thirteen cycles of Kookfontein Formation in the Tanqua depocentre (Wild, 2005). Sample SL1 is part of the basal cycle of the Kookfontein Formation.

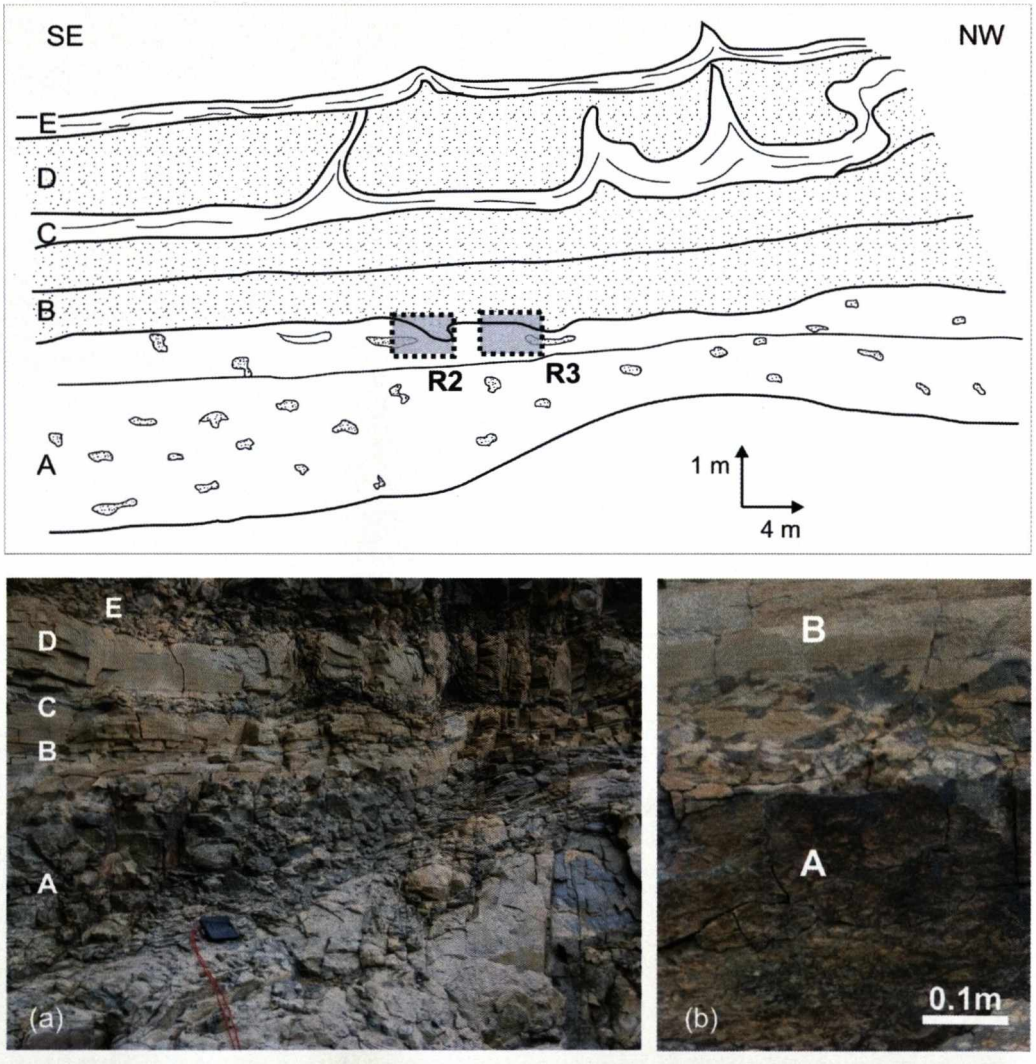

Figure 5.1: Sketch and photographs of an interval dominated by *in situ* soft-sediment deformation: load structures (beds A and B) and flame structures (beds C and E). Samples for hand specimen studies were collected from the transition between intervals A and B. Photos: (a) general view of the outcrop; (b) detailed view of the load casts and pseudonodules from B to A. This interval is part of Cycle R4 and its location is shown in Figure 4.15a.

5.2.1 Computed tomography (CT)

X-ray computed tomography (CT) is a non-destructive technique that permits visualization of the internal structure of objects, determined by variations in density and atomic composition. Its use in geosciences has increased since the 1980's (Mees *et al.*, 2003). It is based on the attenuation of X- or gamma-rays, generating digital images which map the numerical values of the linear attenuation coefficient, with resolution from 0.01 to 1.0 mm, depending on the energy of the radiation and the composition of the sample (Duliu, 1999). To obtain a section through the object the source and receptor (gantry) rotates around the sample. The emission and reception of collimated X- or gamma-rays in different directions produces voxels (a number of volumetric units with prismatic shape whose dimension is approximately equal to the beam diameter; Figure 5.2). A single value of linear attenuation coefficient (μ) is produced for each voxel. As the attenuation coefficient μ is a function of density and effective atomic number of the sample, information about density and chemical composition of the sample can be obtained. The final CT image is obtained by the attribution of an image pixel for each voxel, where colours or shades of grey are proportional to the correspondent numerical value of attenuation coefficient. By assembling together successive sections it is possible to obtain a 3D representation of the investigated structures.

In the case of samples from this study, one fourth generation tomography Picker was used, with 1200 receivers adjusted to register adjacent sections spaced 1mm apart. The generation of a tomography is a function of the device configuration. The fourth generation tomography consists of a fixed complete ring of detectors and a single X-ray source that rotates around the object being scanned. Maximum applied voltage was 130 kV and 100 mA current, time of sampling was regulated to the maximum (4s) in order to obtain best quality CT images. No special sample preparation was required for the acquisition.

Due to the regular shape, one 60cm long and 3 inch diameter core section (C2) from the SL1 research borehole (base of the core at 129 m depth), with convoluted and folded lamination was selected for the initial test. Afterwards, the study focused on samples R3 and Wf1.

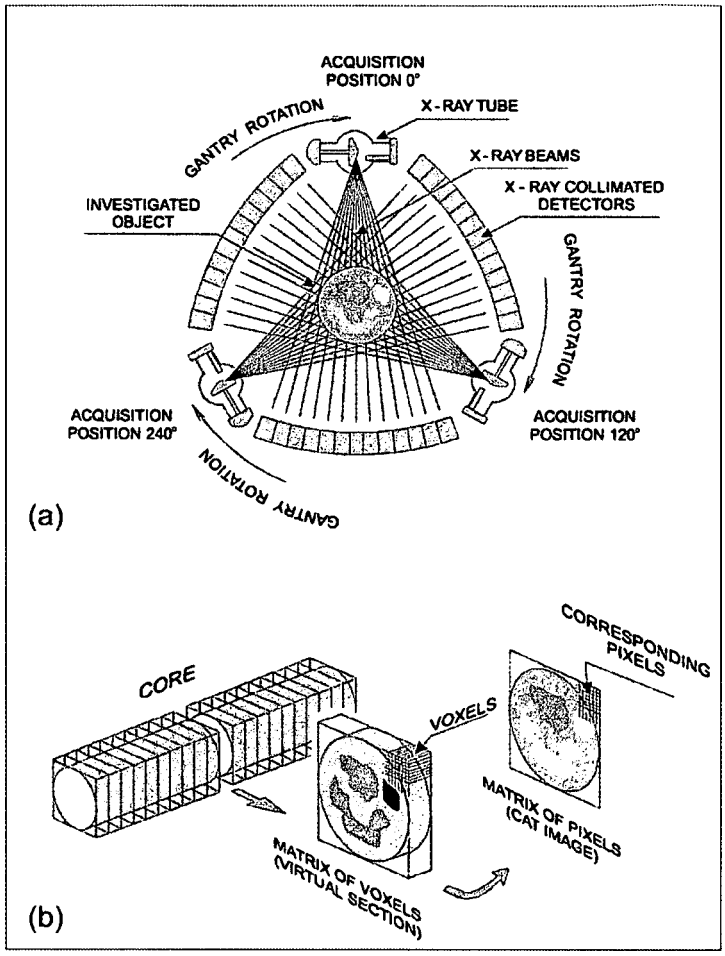

Figure 5.2: (a) Schematic view of the projection acquisition of a third generation of CT – Computed Tomography. X-ray source and detectors are combined and rotate around the object to be investigated. (b) The product of the rotation of the combination X-ray emission-detection around the sample is a virtual section through the sample whose thickness is equal to the diameter of the radiation beam. The section can be decomposed in units of volume (voxels) each one of them contains an average value of linear attenuation coefficient (μ), that can be mapped if one pixel is attributed to each value and represents the CT image (from Duliu, 1999).

The quality of the CT images was affected mainly by *beam hardening*, an artefact at the edge of the object created by an increase in the mean X-ray energy while it passes through the scanned object, and secondarily by *ring artefacts*, characterized by concentric rings that are a function of the internal characteristic of the equipment (Ketcham & Carlson, 2001) (Figure 5.3). Two visualisation techniques were tested: (1) volume rendering, based on attribution of one RGB colour and associated opacity for each voxel of CT values, and (2) isocontouring, i.e. the map of the isosurfaces that mark the boundaries of objects. The result for core sample C2 was largely influenced by the effect of beam hardening, thus the rendering was effective only in the central part of the core (Figure 5.4). The rendering allowed identification of main sedimentological discontinuities as well as

the mapping of centimetre scale pseudonodules. However the analysis of orientation was not possible due to the small area of imaging.

Because of the irregular shape of sample R3, artefacts associated with beam hardening were difficult to differentiate from actual material variations. The sharp contact between the upper denser layer and the lower siltstone (cf. Figure 5.1) is clear in the CT image. The identification of pseudonodules was possible by using rendering and opacity (Figure 5.5). The same procedure was used in the analysis of the folded sample Wf1 which showed indications of the internal folding (Figure 5.6). Unfortunately the analysis of trends or internal organization of the samples (two key objectives of the study) was not possible. One limiting factor was the mineralogical similarities (Van Lente, 2005) (and consequent poor CT contrast) between the different lithofacies. In conclusion, despite the high potential of this methodology for 3D analysis of SSDS, its effectiveness needs to be tested in a larger range of samples.

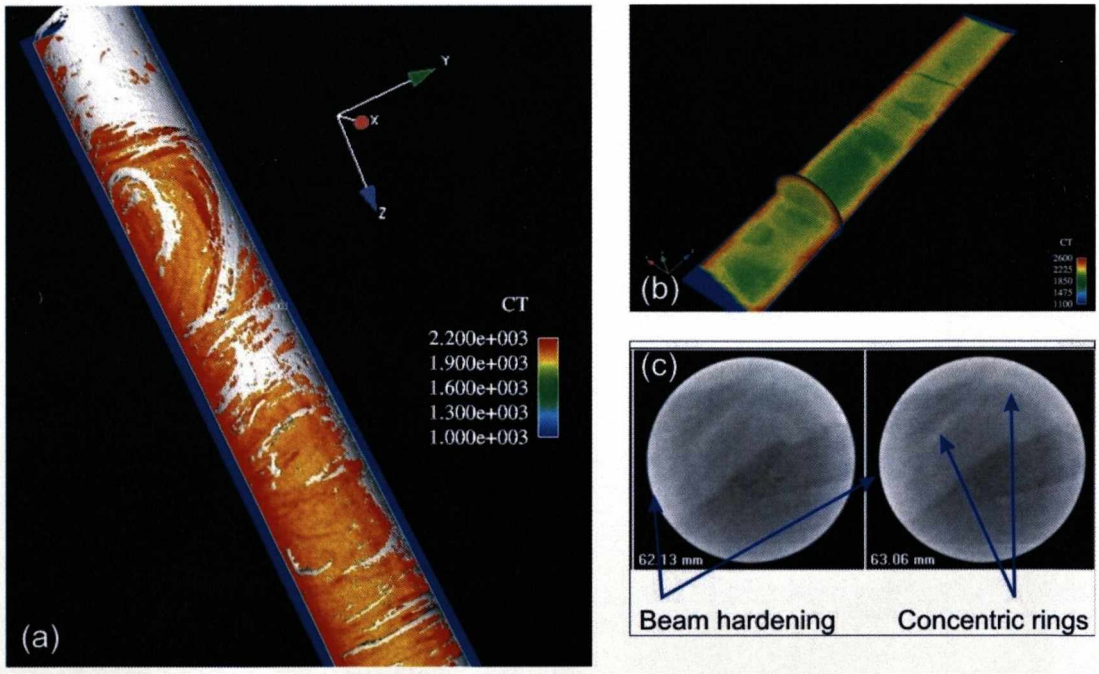

Figure 5.3: CT image from core C2: (a) General view of the core, the white part is related to high CT values due to beam hardening; (b) CT image of one slice of core C2, orthogonal to the acquisition planes, the beam hardening is indicated by the orange colour in the extremity of the core; (c) Two successive CT images from core C2 with beam hardening (white boundary) and concentric rings.

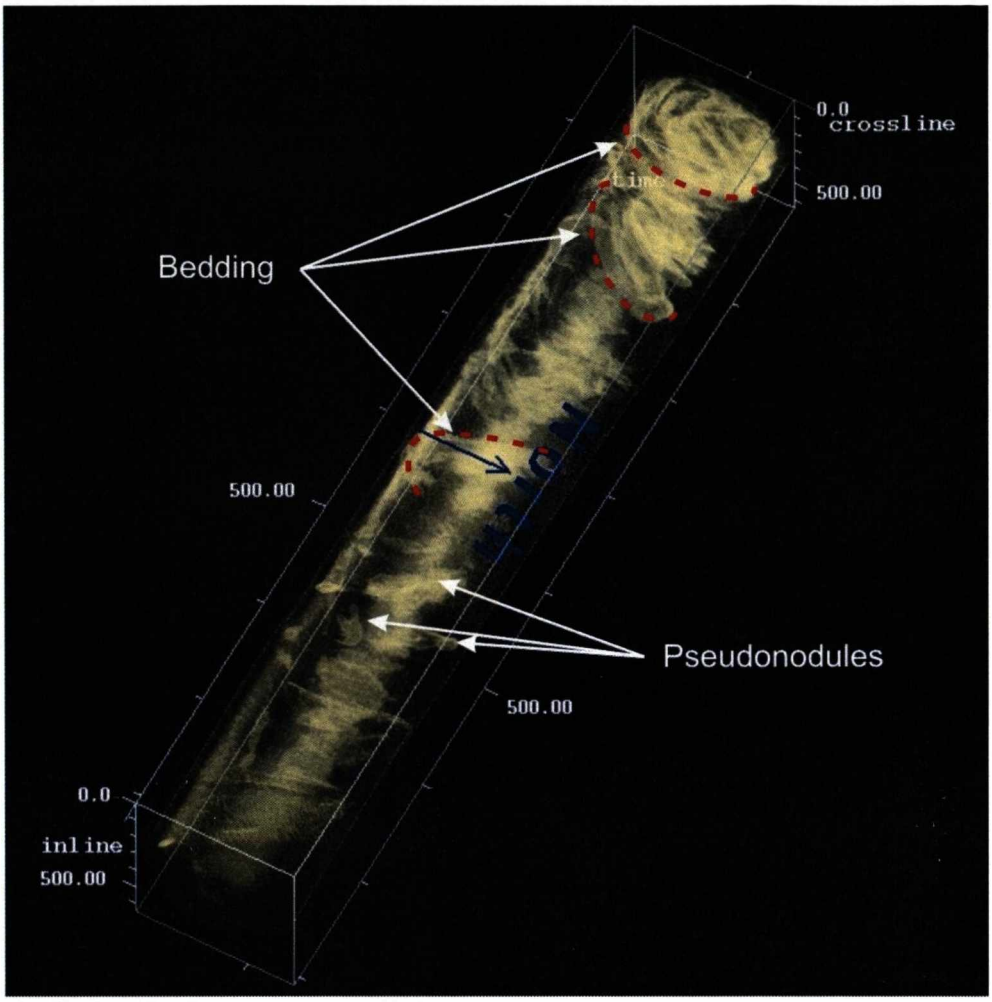

Figure 5.4: Rendering of core C2 with opacity adjusted to permit the visualization of CT values around 1900. In the lower part it is possible to distinguish distinct bodies interpreted as pseudonodules and in the upper part surfaces revealing the stratigraphic contacts sometimes associated with folding.

5.2.2 Serial sections

Serial sectioning is a novel approach to the study of small scale soft-sediment deformation. The technique has been used in studies of pore morphology (Cooper, 1994). The methodology is simple and consists of: (1) collection of oriented decimetre-scale rock samples; (2) cutting the sample in parallel slices at 0.5 – 1.0 cm spacing, normally oriented orthogonal to the feature to be investigated; (3) image scanning of each surface (300 dpi or higher); (4) loading of each image file of the successive slices in parallel, preferentially with separation equal to the distance between each plane in the original rock, in software that permits the tracking of a 2D object with superposition of values for z axis (vertical axis); in this study GOCAD

was used; (5) interpretation of the different features in the successive slices; (6) correlation between the interpreted features; (7) interpolation of the correlative shape in each slice to build up a 3-D volume (Figure 5.7).

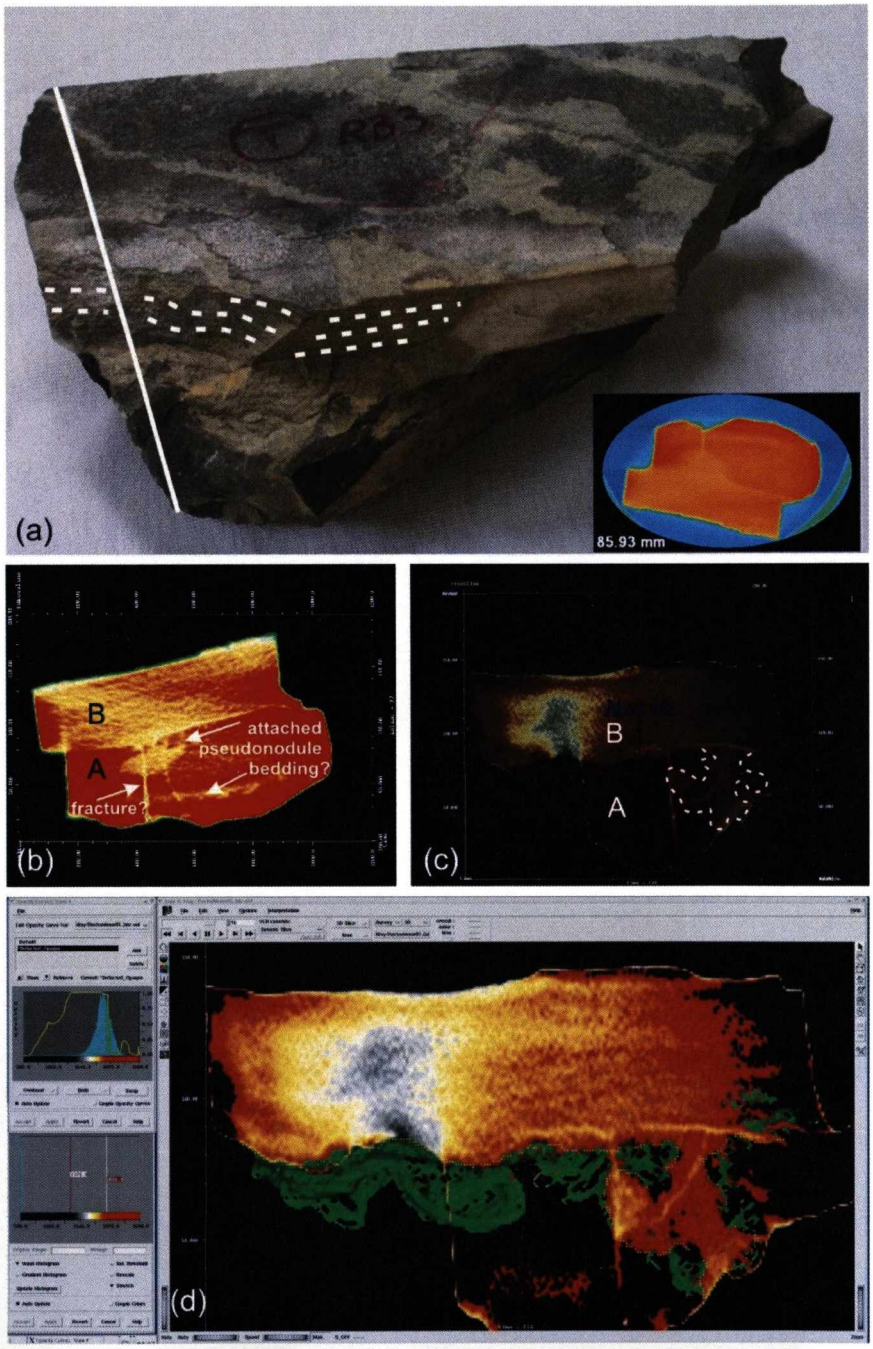

Figure 5.5: Tomography of sample Rb3: (a) Dashed lines show the fine-laminated sandstone overlying a massive siltstone to very fine-grained sandstone. The straight white line over the sample indicates the position of the tomographic section shown on the lower right side of the photograph (the acquisition was made with the sample upside down); (b) Visualization of one slice of R3 showing a pseudonodule attached to bed B (higher CT values in yellow); (c) Opacity used to emphasize the pseudonodules (dashed line) in bed A; observe that lower values of CT (green and yellow area) make identification of other features difficult; (d) One technique used to solve the problem in (c) was to isolate areas of anomalous values (small yellow dot indicates the limit of the detection) in order to observe subtle load casts (green body).

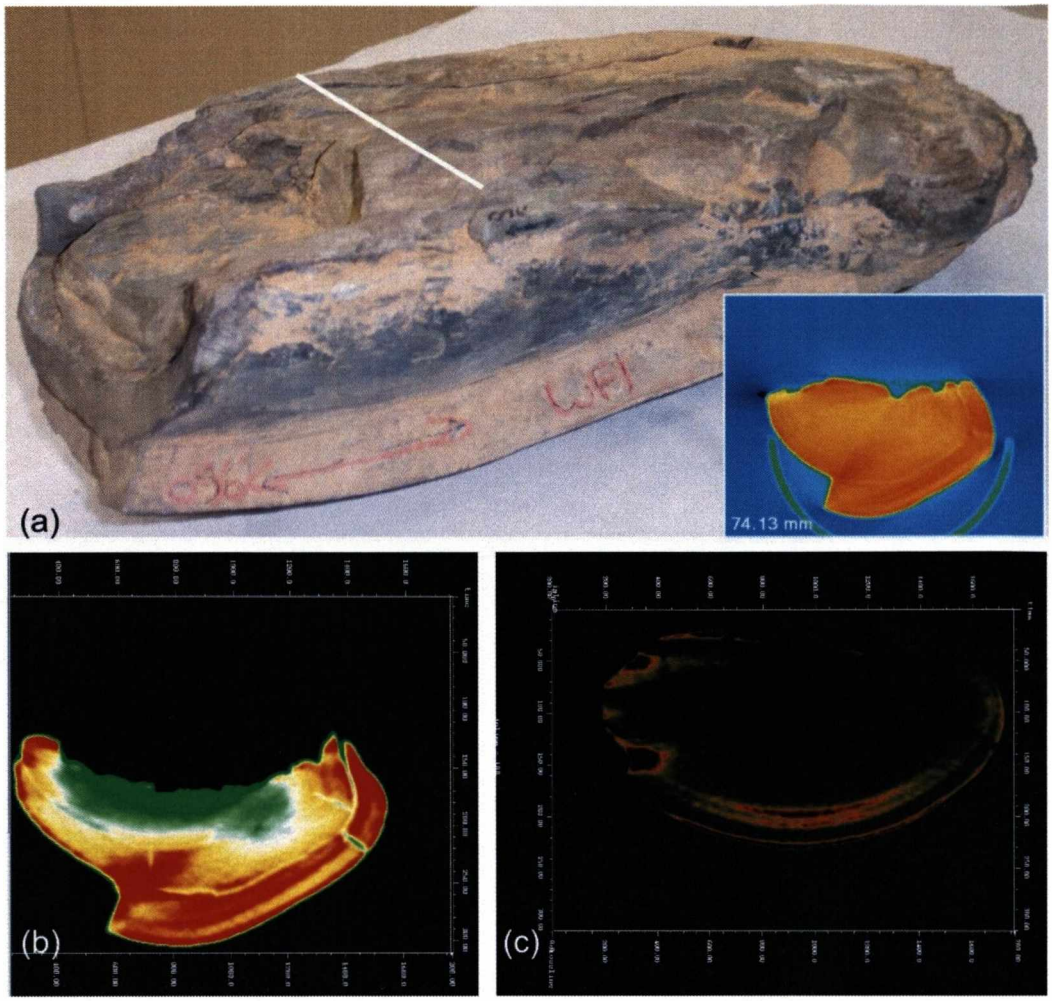

Figure 5.6: Tomography of sample Wf1: (a) The straight white line over the sample indicates the position of the tomographic section (lower right side of the photo). The semicircle below the sample is a plastic device used to stabilize the sample during acquisition; (b) Visualization of one slice of Wf1 indicating the internal bedding; different values for CT (see the different colour zones) makes mapping of the same geological characteristics (bedding for example) impossible by using just one criteria for visualization; (c) Opacity volume adjusted to visualize the red areas from (b), with high values of CT; note that important geological information is lost in the other values of CT (black in the image).

Some restrictions are inherent to the serial slicing method: (1) resolution orthogonal to the slices is normally between 0.5 and 1 cm, and is a function of the space between successive slices, that is conditioned by the degree of preservation of the sample, its susceptibility to cutting and saw characteristics; (2) display of the structures after interpretation is only possible in an axis perpendicular to the plane of each rock slice; (3) the technique is only applicable to well cemented rock samples, or samples set in resin.

For this study, sample R2 was used as it captures the base of a fine-grained sandstone bed and the load structures from this sandstone in the underlying siltstone (cf. Figure 5.1). At the end of interpretation 13 bodies, varying from 1-10 cm long

had been defined as distinct expressions of load structures (Figure 5.8). Some of these structures represent the coalescence of two or more bodies. When displayed individually it was possible to image the spatial evolution of each body along planes parallel to the original acquisition planes. One of the best examples is represented by the base of the sandstone and adjacent structures, where it was possible to register the different stages of the evolution of the load features (Figure 5.9). Small structures, positioned a few centimetres below and detached from the sandstone base, are here interpreted as pseudonodules (from detached pseudonodules to ball-and-pillow structures) (Figure 5.10). Three of these bodies (red, pink and white in Figure 5.10) present similar conical shapes with the tips pointing broadly to the south. This orientation can be interpreted as an indicator that some bed parallel shear could have taken place during the development of the load structure, leading to elongation.

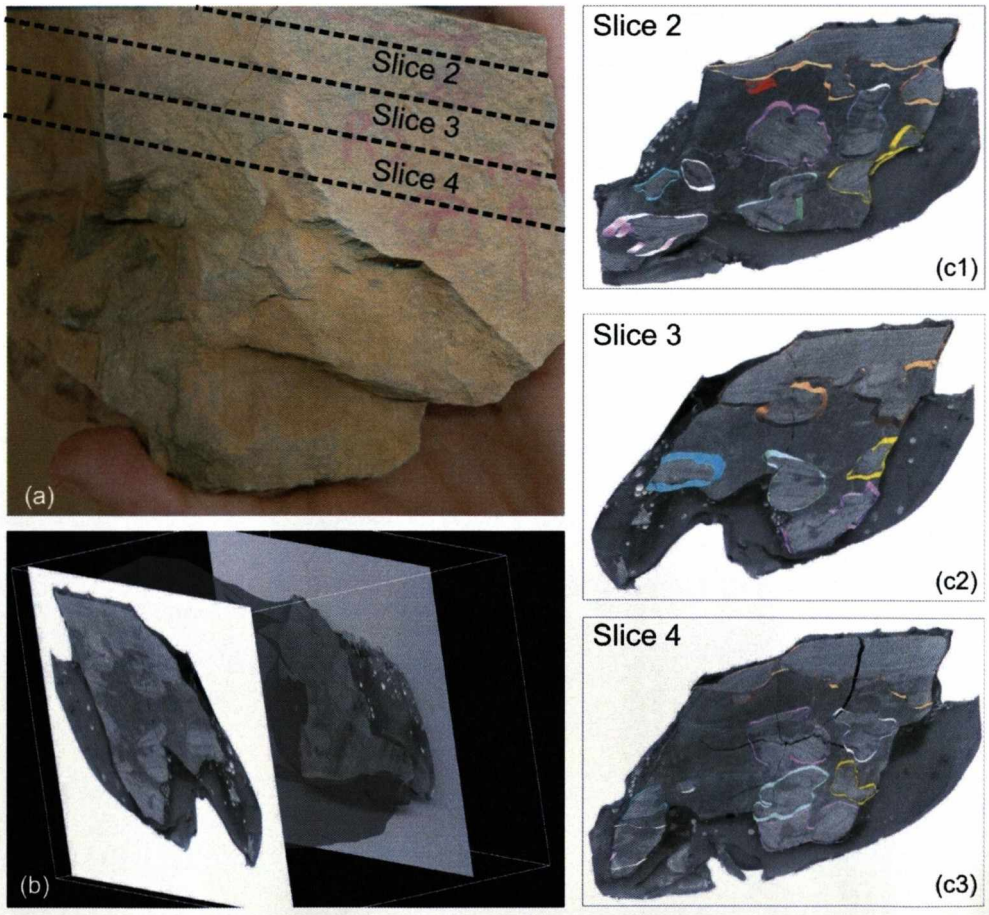

Figure 5 .7: Three steps in serial sections analysis: (a) View of sample R2 used for the serial sectioning and study of centimetre size soft-sediment deformation; (b) Scan images from the rock slices loaded and prepared for interpretation; (c) Three rock slices from sample R2, showing load casts, attached and detached pseudonodules. Each structure is interpreted for different slices. For each load structure one different colour is attributed.

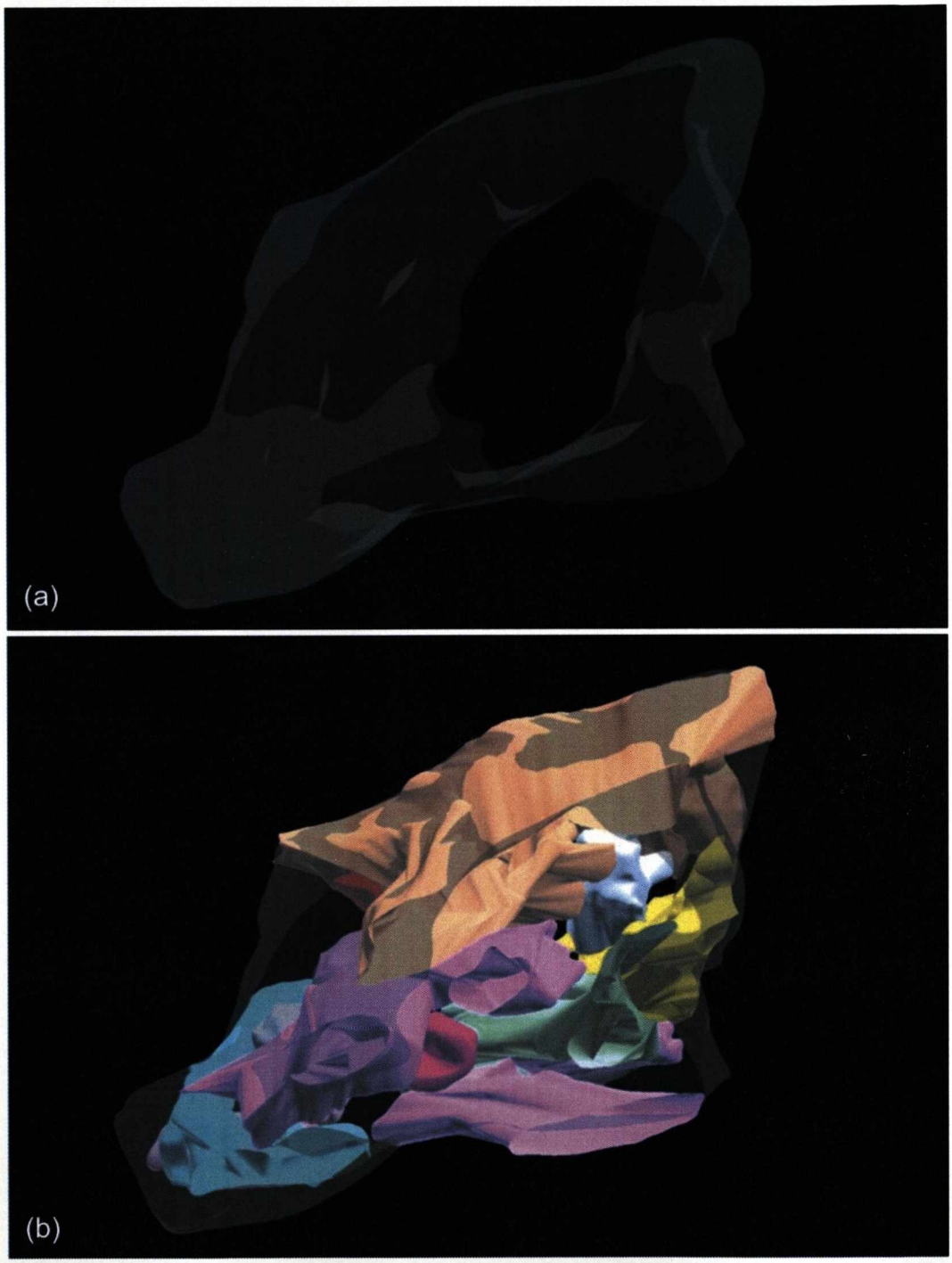

Figure 5.8: (a) Reconstitution of the external shape of sample R2 based on the outline of its slices; (b) Population of the external shape with the bodies interpreted in each slice and subsequent correlation and interpolation.

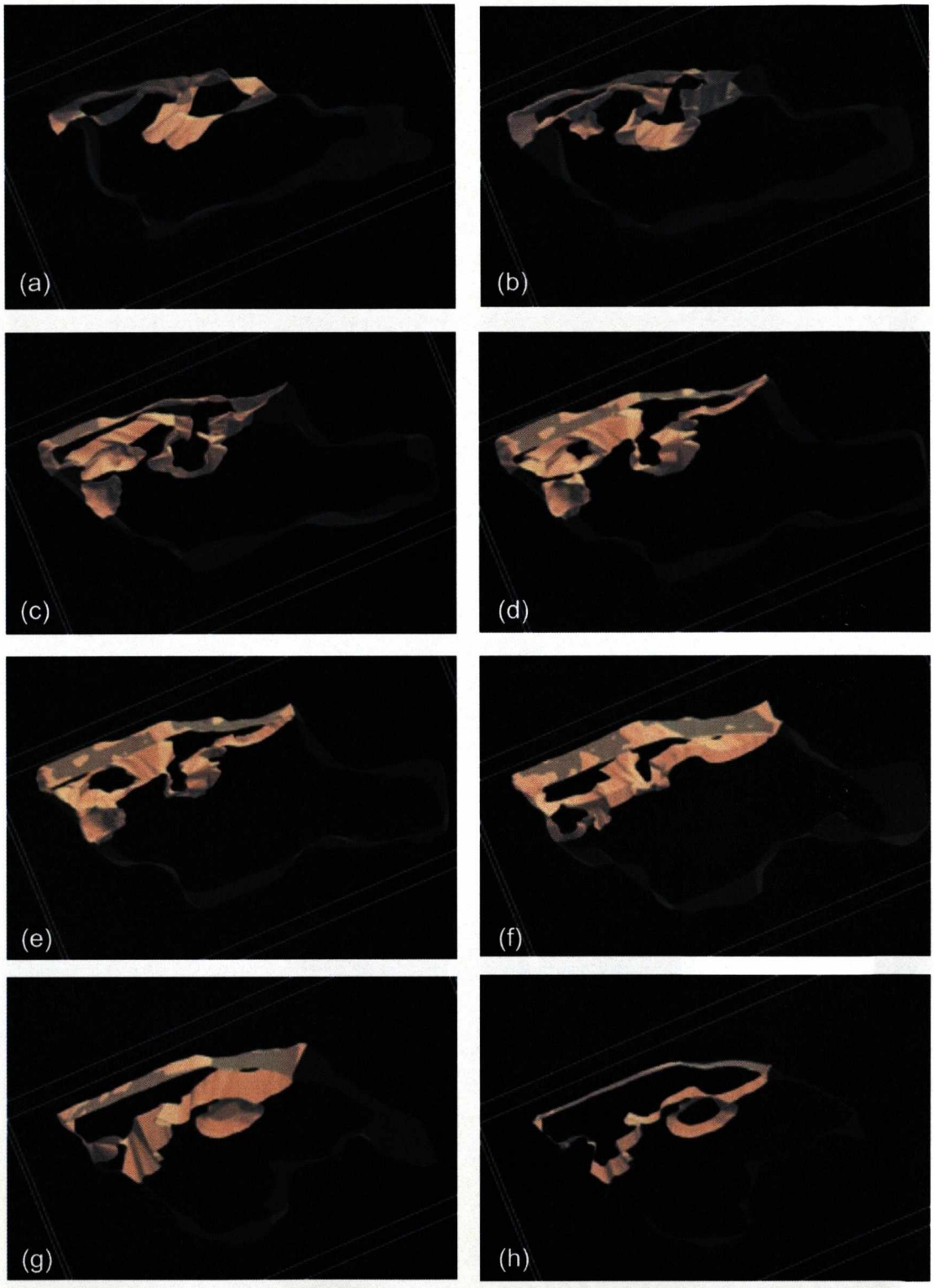

Figure 5.9: Spatial evolution of load structures at the base of the upper sandstone bed represented by successive and continuous interpreted slices from N to S: (a) left - simple load cast, right - pendulous load cast; (b) to (e) left - detached pseudonodule, right - attached pseudonodule; (f) left - simple load cast + detached pseudonodule, right - pendulous load cast; (g) and (h) left - pendulous load cast, right - detached pseudonodule.

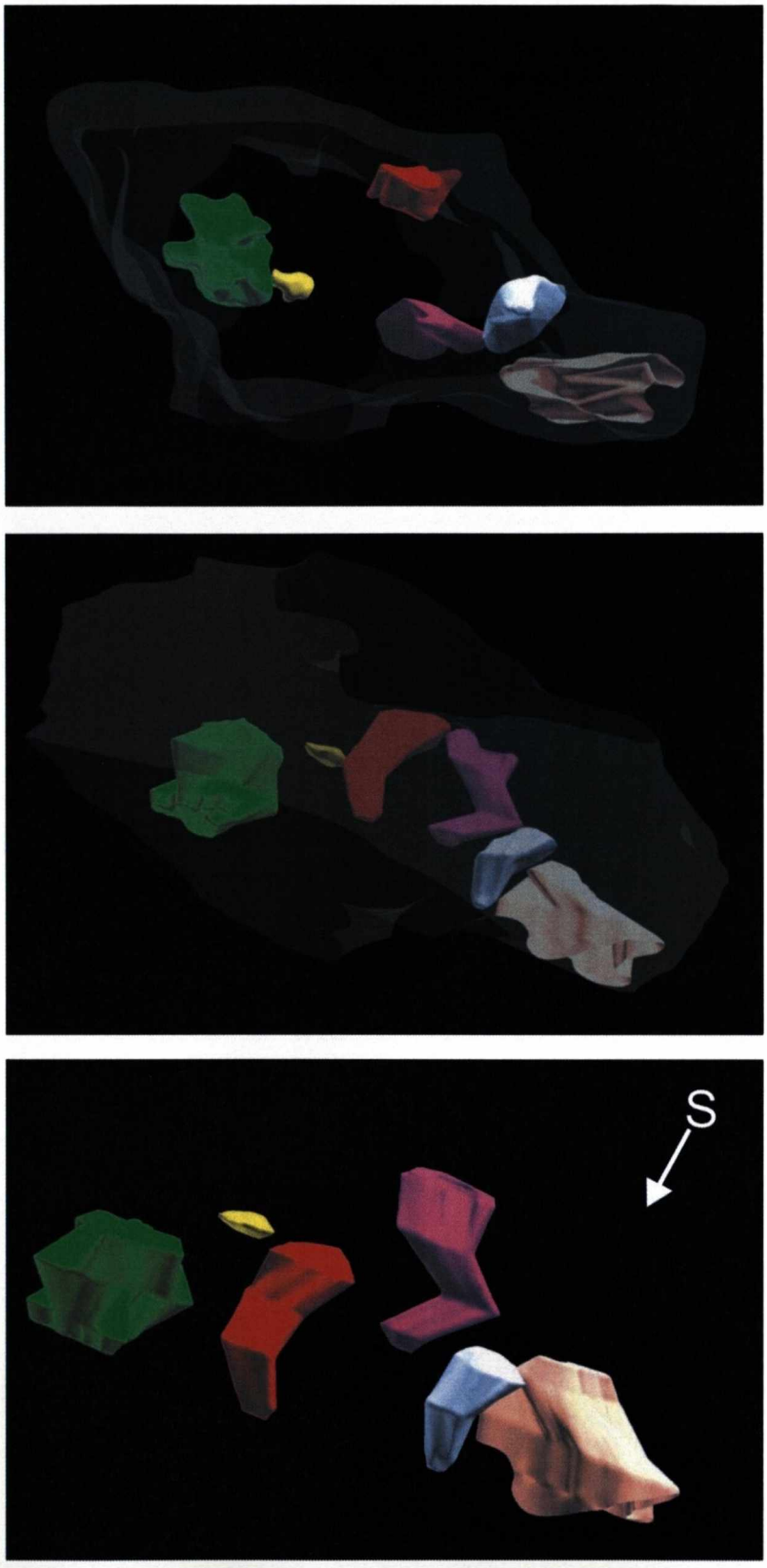

Figure 5.10: Small detached-pseudonodules and ball-and-pillow structures up to 4 cm long: (a) frontal view; (b) 3D view from the top, and (c) map view, three of the bodies (red, pink and white) are oriented with the tip pointing to south.

Allen (1982) discussed two possible origins for pseudonodules and ball-and-pillow structures: (i) downslope movement of interbedded sand and mud, and (ii) gravitational instability of layered sediments due to a density contrast. Allen considered (i) to be unlikely due to the development of identical structures in experiments involving only vertical movement of particles, the possibility of oblique descent of the sand bodies and the absence of other indicators of internal shear planes parallel to bedding. In the study area, although there is no field evidence for lateral movement during the formation of detached pseudonodules and ball-and – pillow structures, the result of this smaller scale of analysis suggests that some lateral movement can occur, but on the scale of a few centimetre. This result reinforces origin (i) as a possible driving for the formation of pseudonodules, with implications for the interpretation of the environment where the deformation occurred.

Although a good result was obtained during the study of pseudonodules, further studies with samples from different areas are required in order to evaluate the efficiency of this methodology in the study of soft-sediment deformation.

5.3 Ground Penetrating Radar (GPR)

The objective of this section is to add further 3-D control to the shapes of the flame structures in the Waterfall study area (Chapter 3). Aspects of acquisition and interpretation are discussed including the applicability for imaging of vertical structures.

5.3.1 Introduction and methodology

Ground penetrating radar (GPR) is a non-invasive geophysical technique that detects discontinuities in the shallow subsurface (<50m) and is similar in principle to reflection seismic (Davis and Annan, 1989; Neal, 2004). The radar produces a short pulse of high frequency (10-1000 MHz) electromagnetic energy that is transmitted into the ground, then reflected back from shallow discontinuities (bed boundaries, lithology changes and internal structures) and collected/recorded by an

antenna/receiver at the surface (Figure 5.11). The propagation and the detection of the signal is a function of the electrical properties of the geological material and is primarily controlled by water content in soils, rock type, and fractures (Davis and Annan, 1989). The material properties that control the behaviour of the electromagnetic energy are: (1) dielectric permittivity (ε), i.e., the amount of electric field energy stored during each cycle of the alternating electric field at a specific frequency; (2) electrical conductivity (σ), i.e., a measure of the ability of the material to transport charge on application of a static field and (3) magnetic permeability (μ), i.e., the magnetic equivalent of dielectric permittivity, is a measure of magnetic field energy stored and lost through induced magnetisation. Velocity (v) and attenuation (α), i.e. the exponential decline of amplitude with the distance travelled, are two characteristics that describe the propagation of high frequency radio waves in the ground. These characteristics are highly influenced by ε and σ, respectively, and can be represented by the following simplified equations:

(i) Velocity v

$$v = \frac{c_0}{\sqrt{\varepsilon_r}},$$

Where, c_0 is the electromagnetic wave velocity in a vacuum (3×10^8 m s^{-1}) and ε_r is the relative dielectric permittivity;

(ii) Attenuation constant α

$$\alpha = \frac{\sigma}{2}\sqrt{\mu/\varepsilon},$$

Where, σ is the electrical conductivity, μ is the magnetic permeability and ε is the dielectric permittivity.

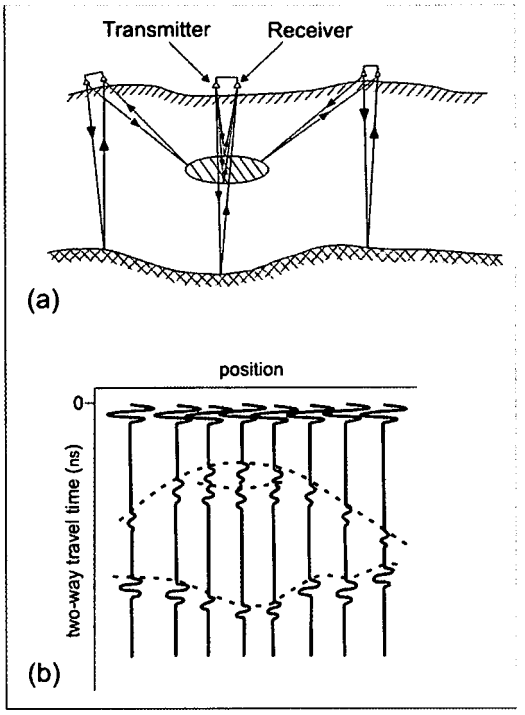

Figure 5.11: (a) Conceptual view of a radar survey as used for a reflection profile along three positions for transmitter/receiver during acquisition. (b) Resulting radar section from the model in (a) (from Davies & Annan, 1989).

Table 5.1 shows velocity and attenuation at the frequency of 100 MHz for distinct geological materials. Freshwater has a high ε and consequent low velocity if compared with air and typical rock-forming minerals. In general for rocks, sediments and soil, lower ε implies higher v, and lower σ equates to lower α (Neal, 2004). When a propagating electromagnetic wave encounters a subsurface discontinuity in terms of ε, σ or μ, part of the energy is reflected back. The strength of this energy captured by the GPR equipment will be a function of the reflection coefficient that expresses the contrast between the properties at the interface of adjacent bodies. The greater the contrast, the larger the reflection coefficient and the signal amplitude that is captured by the antenna will be.

Material	*K*	σ (mS/m)	*V* (m/ns)	α (dB/m)
air	1	0	0.3	0
distilled water	80	0.01	0.033	2×10^{-3}
fresh water	80	0.5	0.033	0.1
sea water	80	3×10^{4}	0.01	10^{3}
dry sand	3-5	0.01	0.15	0.01
saturated sand	20-30	0.1-1.0	0.06	0.03-0.3
limestone	4-8	0.5-2	0.12	0.4-1
shales	5-15	1-100	0.09	1-100
silts	5-30	1-100	0.07	1-100
clays	5-40	2-1000	0.06	1-300
granite	4-6	0.01-1	0.13	0.01-1
dry salt	5-6	0.01-1	0.13	0.01-1
ice	3-4	0.01	0.16	0.01

Table 5.1: Dielectric constant (K), electrical conductivity (σ), velocity (V) and attenuation (α) for common geological material at 100 MHz (from Davis & Annan, 1989).

The use of the GPR method for the study of sedimentary rocks is largely focused on architectural and stratigraphic characterization (Neal, 2004, and references therein). Fractures, faults and folds generate reflections not related to the primary sedimentary bedding that can generate major electromagnetic discontinuities responsible for the deterioration of the GPR image quality; this can lead to misinterpretation when such events are not properly identified. Faults and fractures are the most common vertical structures identified in GPR profiles (Green *et al*, 2003; Rossetti, 2003, Theune *et al.*, 2006), in scales varying from a few metres (Reiss *et al.*, 2003) to hundreds of metres (Bakker & Van der Meer, 2003).

5.3.2. Planning and acquisition

The depth of penetration and resolution of the radar are influenced by the equipment characteristics, frequency of the signal and rock properties (Table 5.2). In a similar way to reflection seismic, higher frequencies imply higher resolution and less

penetration (depth). Thus the type of equipment and frequency of the signal must be considered in relation to the position, lateral continuity and thickness of the objective.

Central frequency (Mhz)	Maximum depth (m)
1000	1
400	2
200	4
100	25
50	30
25	40
10	50

(a)

Central frequency (Mhz)	Resolution (m) (theoretical)
200	0.125-0.25
100	0.25-0.5
50	0.5-1
25	1-2

(b)

Table 5.2: (a) Maximum radar depth penetration as a function of the central frequency, based on results from hardware companies. (b) Theoretical resolution as a function of the central frequency, considering velocities of 0.1 m/ns. (from Porsani, 1999).

The first step was to establish the geological objective and the general configuration of the survey. A 600 m^2 survey was acquired on a flat surface of sandstone, targeting flame structures 2-5 m below, with the objective of imaging the flame shapes and verifying their orientations. In-lines were oriented N30E, spaced 1 m from each other, and positioned to obtain the best possible coverage of the outcrop, while the cross-lines were positioned 5 m from each other and at 90° from the in-lines. This configuration was oblique to the general orientation of flames (WSW-ENE) from the adjacent outcrops and arranged in order to contemplate the range of scale of the studied structures and, at the same time, to attend questions of logistic and time. The occurrence of one flame in a vertical face contiguous with the survey helped in the determination of the acquisition parameters (Figures 5.12 and 3.14).

Two acquisition techniques were used in Waterfall: (i) the common offset or reflection sound and (ii) the common mid point (CMP) (Figure 5.13). The first was used to map the subsurface discontinuities in the whole survey. The second was used to measure the velocity of the sedimentary package.

The acquisition parameters (see Table 3.1) were chosen to ensure penetration of 4 m, coupled with the best possible vertical resolution. Among the acquisition parameters, the nominal antenna frequency, the vertical stack and step size were analysed. The vertical resolution is given by $\lambda/2$ to $\lambda/4$ where λ is the wavelength. If $\lambda = v/f$, and $v=0.12$ m/ns, obtained from the CMP survey, than the vertical resolution for a frequency of 100 MHz will vary between 0.6 m and 0.3 m, while for 200 MHz it will

vary between 0.3 m and 0.15 m. Both are in the range of the bed thicknesses at Waterfall. The step size was chosen to be tight (0.1 m) in order to improve the lateral resolution. The two antennae (transmitter and receiver) were oriented orthogonal to the line direction with separation varying between 0.5 m (200 MHz) and 1.0m (100 MHz) in order to avoid signal saturation in the top portion of the trace, following test and quality analysis in the field. The separation of 1 m for 100 MHz satisfied the empirical relationship that the separation must be 20% of the target depth (Jol & Bristow, 2003) while the separation of 0.5 m for the 200 MHz survey was at the limit for the base of one deformed interval.

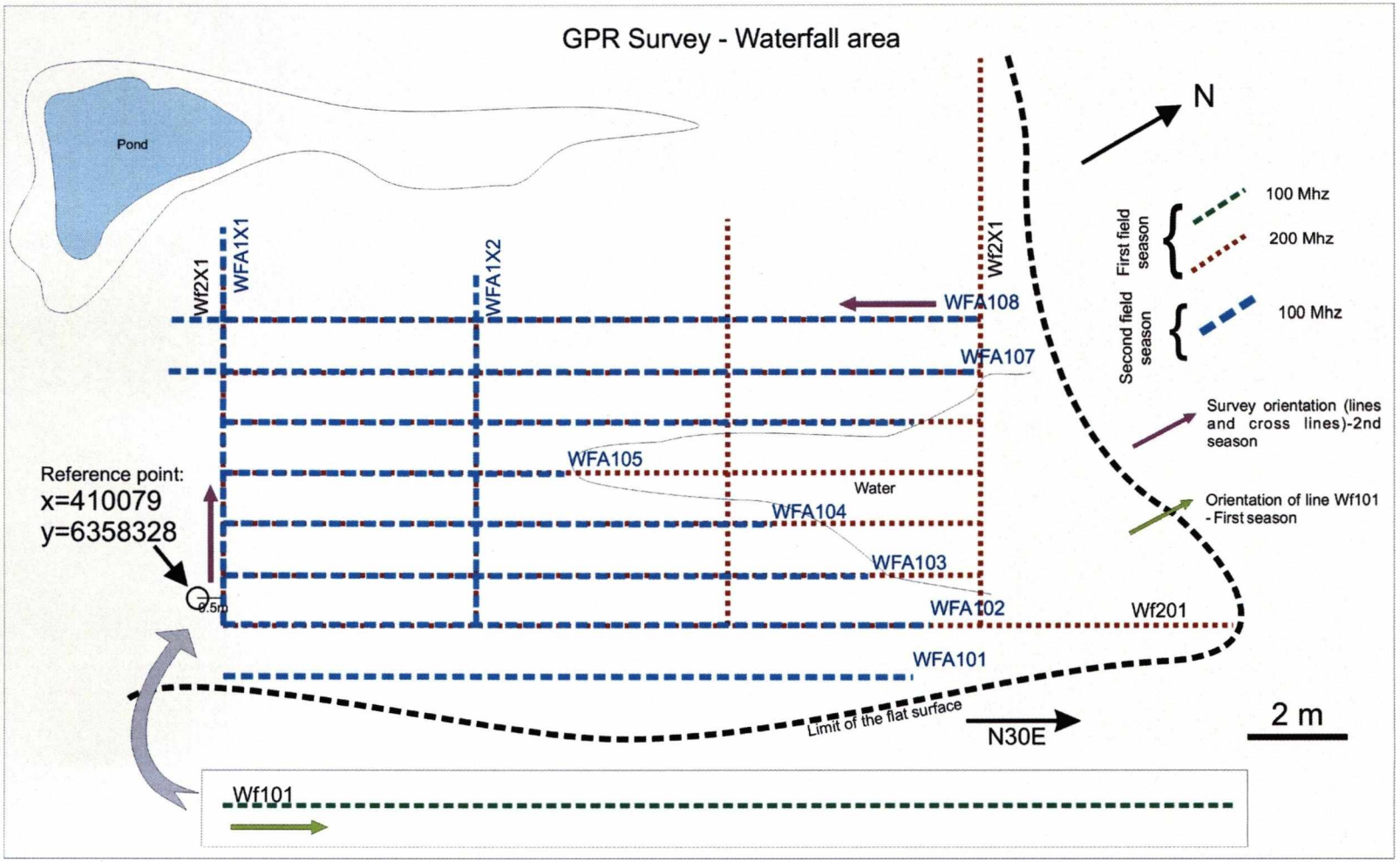

Figure 5.12: Map view of the Waterfall GPR survey. Inlines were 1 m spaced, oriented N30E and referred to the coordinate of one point at the south of the survey. Crosslines are at 90° to the inlines and 5 m separated. The acquisition was done in two field seasons: the first at 200 MHz (after some test lines at 100 MHz and 200 MHz) and the second exclusively at 100 Mhz lines. Note the presence of a flooded area that was not sampled in the second season. See lines coordinates on Appendix 1.

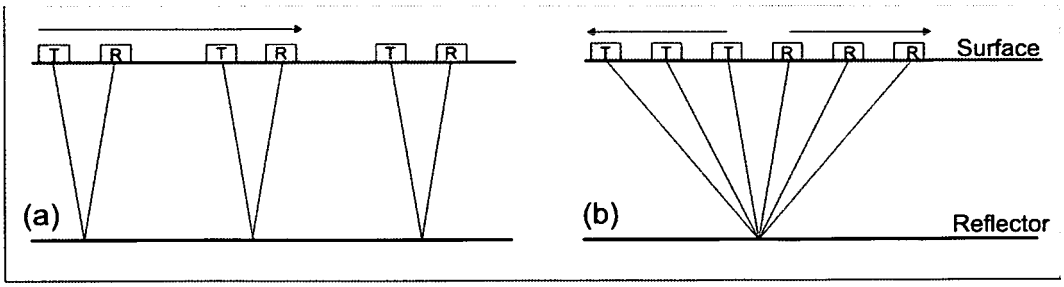

Figure 5.13: Acquisition techniques used in Waterfall: (a) common offset; (b) common mid-point (CMP). T is the position of the transmitter and R is the receiver, arrows indicate direction of dislocation of T and R. See text for detail.

5.3.3 GPR processing

Although simpler compared to the processing involved of seismic reflection data, the processing of GPR data follows the same steps used for seismic data. Basically, the objective is to recover the signal for deeper reflectors where amplitude is diminished by attenuation and to increase the signal:noise ratio. The basic workflow for the processing is presented in Table 3.1 and was obtained after a series of tests that involved the inclusion of other steps like deconvolution and FK filtering in some special cases.

The same workflow, with some changes in the parameters, was used to process the two different sets of lines (100 MHz and 200 MHz). In general, the quality of the lines was poor but better in the set acquired with 100 MHz frequency (Figure 5.14). Among the factors that affected the quality of the GPR in Waterfall, the most important were: (i) rock homogeneity (siltstones and fine sandstones), (ii) the verticality of the flame structures and (iii) the problems with coupling the equipment with the rock surface. The 200 MHz lines were not able to image the depth of the flame structures probably because of the ringing in the upper reflectors and wrong definition of the acquisition parameters (for example small separation). The steps and parameters used for processing are briefly described below:

- Data preparation: due to the flat surface it was not necessary to undertake a static correction for topographic effects; the dead traces were removed and the first arrival was moved to time zero (time-zero drift correction);

- Signal-saturation correction (dewowing): a dewowing filter (5 ns window) was used to remove the "wow" induced by signal saturation due to the airwave, ground-wave and near-surface wave;
- Application of gain: this was used to amplify the weak signal at the level of the objective, due to progressive attenuation with increase in travel time. The AGC was applied with window length=25ns and scaling factor=1). This amplified the weak, deeper signal, but required equalisation of amplitude of all signals and noise;
- Application of filters: normally one bandpass filter (f = {30,70,270,310}) was used, based on analysis of the frequency spectrum, to eliminate very low and very high amplitudes, normally associated with noise. In lines WFA104 and WFA105, a localized (spike shape) high amplitude value was identified, with the peak frequency around 144MHz. This was interpreted as a product of the acquisition equipment, which caused a deterioration of the signal/noise ratio. It was removed using a notch filter (f= {136,142,147,151});
- Migration: Kirchhoff's migration (velocity = 0.12 ns) was applied in order to remove the effects of diffractions and distortions.

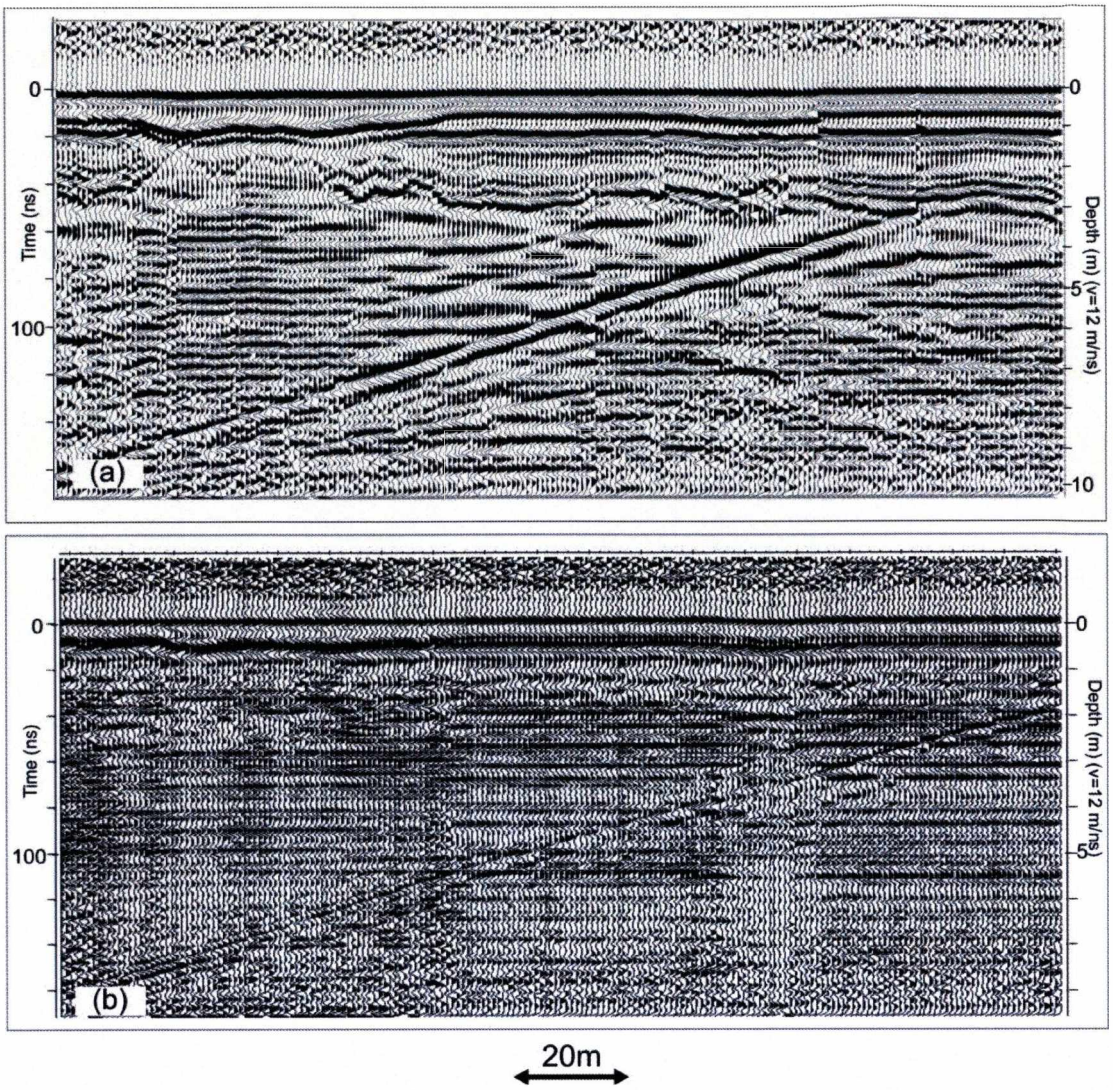

Figure 5.14: Comparison of line Wf101 acquired with the frequencies of 100 MHz (a) and 200 MHz (b). See text for details about quality evaluation and sequence of processing. Deconvolution and filtering, out of the normal processing workflow, was applied in the 200 MHz case in order to try to increase the signal/noise ratio, without good results.

5.3.4. Interpretation

The interpretation of the GPR lines focused on two aspects: (i) to identify radar facies and to correlate them with Waterfall lithofacies, and (ii) to confirm the orientation of the flame structures. The identification and interpretation of radar facies was discussed in Chapter 3.1 (cf. Figure 3.13). The structures are identified in the GPR profiles by their vertical shape, by the lateral changing in the signal amplitude and truncations, and by the bent reflectors. This section focuses on the interpretation of the main trend for the structures and some discussion about identification of vertical structures using GPR data.

Line Wf101 permitted the identification and interpretation of five horizons (Figure 5.15) affected to different degrees by the soft-sediment deformation structures: (1) base of "red" reflector, related to the topographic low above the flames; (2) and (3) top and base of the "blue" interval, at the top section of the interval between the main level of flames and the base of the "red" reflector, probably associated with a ruptured bed; (4) "violet" reflector, associated with the base of the structureless siltstone; and (5) "orange" section, representing the main interval of flames. The interpretation was based on stacked (i.e. not-migrated) and migrated GPR sections. The presence of diffractions and distortions in non-migrated sections was related to the soft-sediment structures and used to help in the interpretation (Figure 5.16).

Figure 5.17 summarizes the distribution and 2D dimensions (along inlines and crosslines) of the radar features interpreted as products of soft-sediment deformation. This interpretation was based on the stratigraphic level of the occurrence compared to the position in the face of the adjacent outcrop and dimensions of the local exposed structures. This single map permits the observation of the effect of the flame structure on the five distinct horizons: where just one colour is present it means that the structure is affecting just one level; superposition of colours means that the structure is disrupting distinct beds. After the interpretation and plot of the distinct structures, a WSW-ENE trend and a secondary N-S trend of the "ellipse bodies" were mapped. The main trend coincides with the orientation of the flame structures in the nearby outcrops. It is important to emphasize that better constraint for the flame orientation would be obtained if the controlling lines (x-lines) were closer.

The study shows that elongate flame structures (i) can be identified both vertically and horizontally by the GPR method, (ii) can extend horizontally further (at least a few metres) than is observed in outcrop and (iii) can be organized forming parallel trends of structures. This result corroborates the interpretation about the control of driving forces, other than vertical ones, in the formation *in situ* soft-sediment deformation structures.

The use of GPR in the study of small scale soft-sediment deformation is rarely cited in the literature (Liberty *et al.*, 2003). Therefore, the Waterfall dataset represents a relatively rare and novel applicability of GPR.

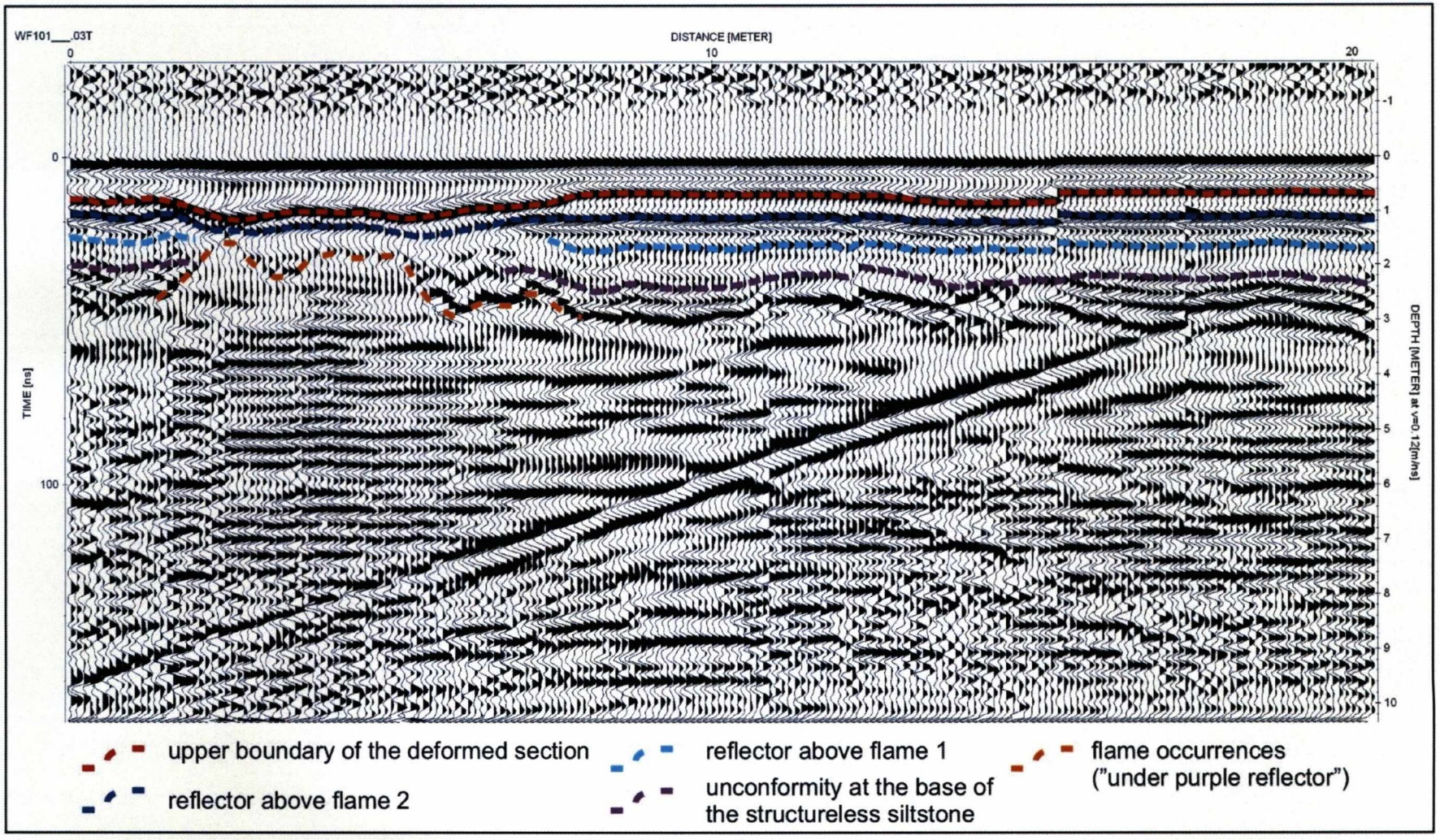

Figure 5.15: Stacked section Wf101 showing the 4 reflectors selected for the study of the degree of deformation related to each vertical structure. The method involves the identification and mapping of the points where these horizons were affected by the growing of the flame structures nucleated below the purple reflector.

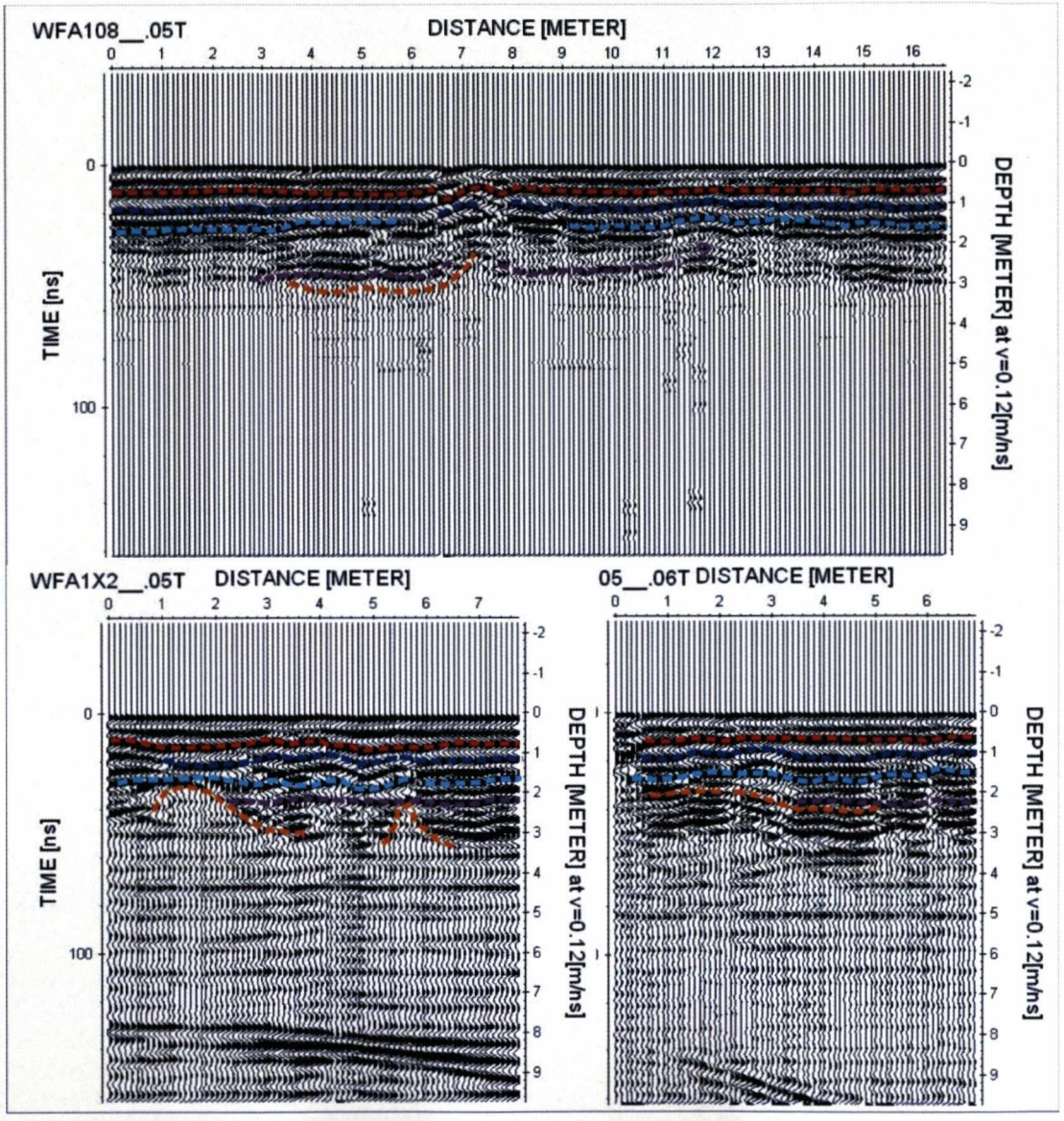

Figure 5.16: Interpreted stacked sections Wfa108 (a), Wfa1x2 (b) and Wfa105. Key for the colours is in Figure 5.15 and location is in Figure 5.12.

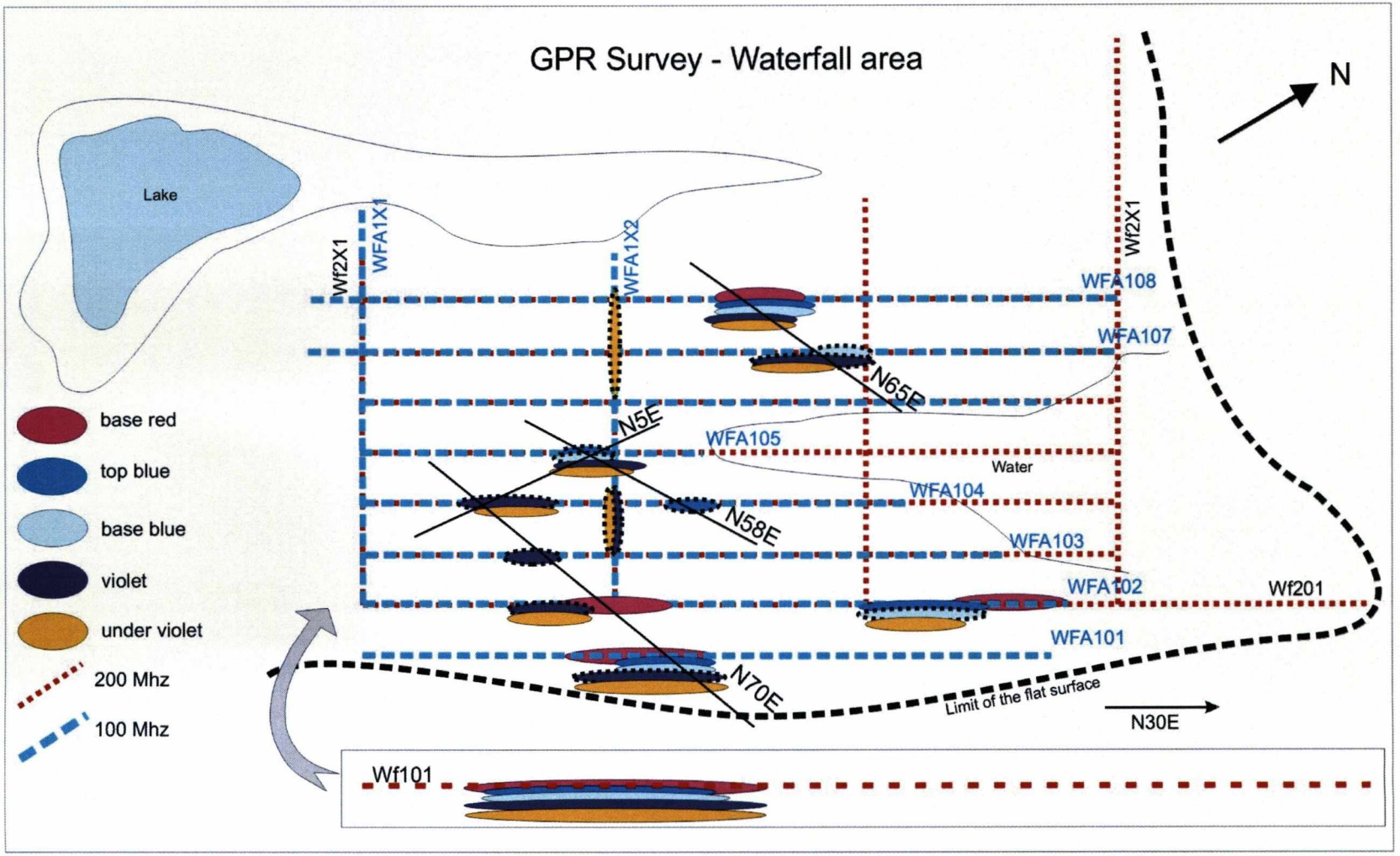

Figure 5.17: GPR survey map for 200 MHz and 100 MHZ and the distribution of seismic features, interpreted from the 100 MHz data, as the response of soft sediment deformation considering the distinct horizons (See Figures 5.15 and 5.16 for reference). Line Wf101 was shot in the same position as line WFA102. The orientation of some trends for the interpreted structures is displayed on the map.

5.4 Seismic modelling

5.4.1 Introduction

In situ deformation structures intercalated with gravity driven deposits discussed in chapters 3 and 4 raises the possibility that at least some chaotic deposits interpreted in seismic sections might represent *in situ* soft-sediment deformation rather than MTCs. In order to evaluate the seismic response for this type of process-product, seismic modelling was undertaken on the Waterfall section.

One key question to be considered is the vertical and lateral resolution of the seismic data. The vertical resolution is the minimum layer thickness that can be detected by a given seismic signal and is function of the wavelength (λ) of the signal. The dominant wavelength is given by:

$$\lambda = \frac{v}{f},$$

where v is the velocity and f the dominant frequency. Normally the vertical resolution is limited to $\lambda/4$. The range of seismic velocities in the subsurface is normally between 2000 and 5000 m/s (increasing downwards), while the dominant frequency varies between 20 and 50 Hz (decreasing downwards) (Yilmaz, 2001). For these values, the typical seismic wavelengths vary from 40 to 250 m, which implies a vertical resolution between 10 and 60 m, decreasing with depth (Figure 5.18). These numbers can be optimized once amplitude effects help to map below the vertical resolution limit and special high resolution seismic acquisition is pushing the dominant frequency to higher values.

Lateral resolution marks the minimum horizontal distance between two reflection points where they are recognized as separate points. It is defined by the Fresnel zone, that is the region of constructive reflection interference surrounding the geometrically predicted reflection point (Okoye & Uren, 2000), which is a function of the wavelength (and consequently frequency), velocity and depth of the reflecting interface. The Fresnel zone, in terms of frequency, is given by:

$$r = \frac{v}{2}\sqrt{\frac{t_0}{f}},$$

where r is the radius of the wavefront, t_0 is the time (two-way travel time) that it takes for the energy arrive to a receiver at the surface.

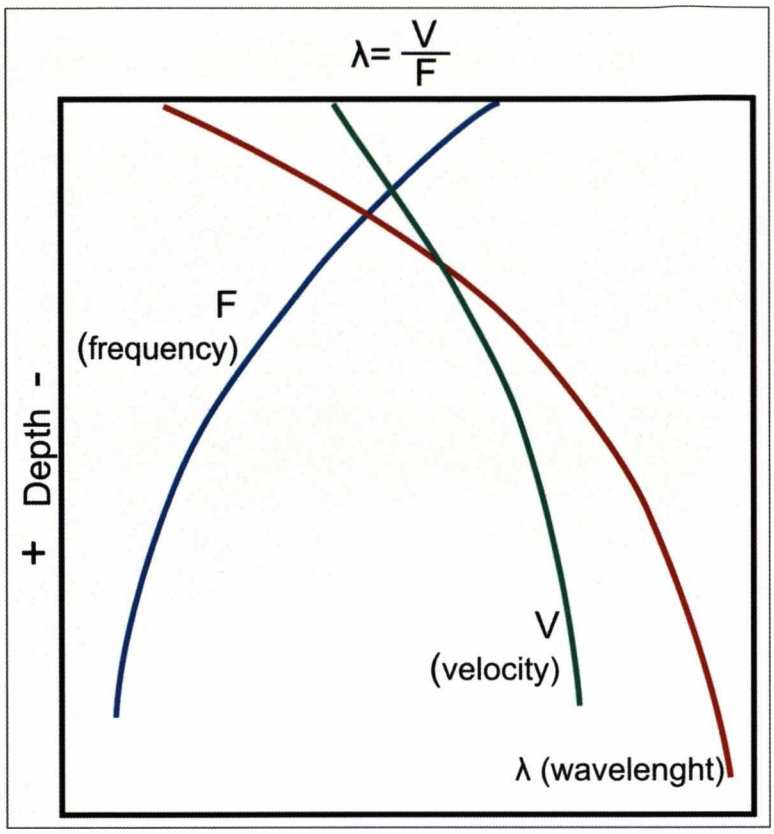

Figure 5.18: Increase of the wavelength λ and consequent decreasing in the vertical resolution with depth (from Brown, 1993).

The 1990s marked a major advance in the acquisition and processing of high resolution data (e.g. high quality 3D multichannel seismic and multibeam echo-sounder data) with focus mainly on seabed and shallow subsurface strata. It was accompanied by a consequent improvement in the quality (and resolution) of imaging of deeper reflectors. Table 5.3 indicates the resolution obtained in different published studies.

The focus in this section is to test the synthetic seismic response of a velocity based geological model with *in situ* soft-sediment deformation considering changes in the thickness of the model and in the peak frequency for the incident seismic wave, consequently with direct influence on seismic resolution.

Locality	Geophysical Method		Frequency	Resolution (V –vertical; H – horizontal)	Maximum depth	Reference
Scotian Slope, Canada	Digital high resolution seismic reflection	Air gun	180 Hz (centre) (0 to 400Hz)	1.0 m (V)	0.5 s (TWT) [1]	Mosher *et al.*, 2004
		Sparker	1500 Hz (centre) (500 – 2500 Hz)	0.2 m (V)	0.05 s (TWT)	
	Multibeam sonar		30 kHz	53 m (H) (for 1500m wd [2])	surface	
			95 kHz	5 m (H) (for 100 m wd)	surface	
Sigsbee Scarpment, Gulf of Mexico (lower edge of the continental slope)	Side scan sonar		120 kHz	5 m (H) (?)	surface	Eddy Lee & George, 2004
	Subbottom profile		2-8 kHz	1 m (V) (?)	225m (0.3 s TWT) 50 m effective	
Cape Basin (offshore – South Africa)	High-resolution multichannel seismic reflection	Air gun	250Hz	3 m (V), at the seafloor.	1 s (TWT)	Weigelt & Uenzelmann-Neben, 2004
Tambaredjo oil field, Suriname, (Palaeocene)	High-resolution three dimension seismic	6.25 m bin size in both directions	n.a.	2.5-4 m (V)	Interval positioned at 350m deep (Palaeocene)	Rabelo *et al.*, 2007.
St Lawrence Estuary,Canada (Quaternary)	High-resolution single-channel sparker		200Hz	1.25 m (V), at the sea floor	300 m (0.5 s TWT)	Pinet *et al.*, 2008
Adriatic Shelf, Italy (Quaternary)	Very high-resolution 3D seismic		n.a.	Decimetre scale (V)	100 m	Marsset *et al.*, 2004

Table 5.3: Vertical and lateral high-resolution obtained by different geophysical methods. They are extensively used for studies of the seafloor and the first 1.0 s (TWT) (between 750 m and 1000m) of subsurface stratigraphy. [1] TWT = two way time; [2] wd = water depth.

5.4.2 Methodology

The seismic modelling was based on zero-offset wavefield, i.e. wave propagation with source and receiver at the same point. The shot records were simulated using the concept of exploding reflectors, where the wavefield was generated by multiple sources positioned along the reflecting interfaces, which were exploded without delays, in order to simulate a horizontal plane wave. The reverse time migration (Baysal *et al.*, 1983) was used; a migration algorithm based on the extrapolation back in time while using the stacked section to be the boundary condition (Yilmaz, 2001). Migration was implemented through a finite-difference solution of the two-dimensional acoustic wave equation (McMechan, 1983). Figure 5.19 indicates the steps of the seismic modelling, from the initial velocity model to the reverse time migrated section. The main inputs are the velocity model; the size of the cell (h), that will condition the dimension of the model, and cutoff frequency (f) for one wavelet generated by the Gaussian second derivative. The definition of the dimension of the cell (h) is fundamental for the difference finite solution in order to avoid numerical dispersion, and is related to the minimum velocity of the model (v_{min}) and the cutoff frequency (f) by the relation

$$h = \frac{v_{min}}{w.f_{max}},$$

where w is the maximum number of samples (5 in practical terms) by wavelength considering the maximum frequency and f_{max} is the maximum cutoff frequency. Thus, the ideal solution for the modelling will follow the relation above, forcing one of the variables out of this ideal relationship will imply the introduction of distortions in the modelled migrated section.

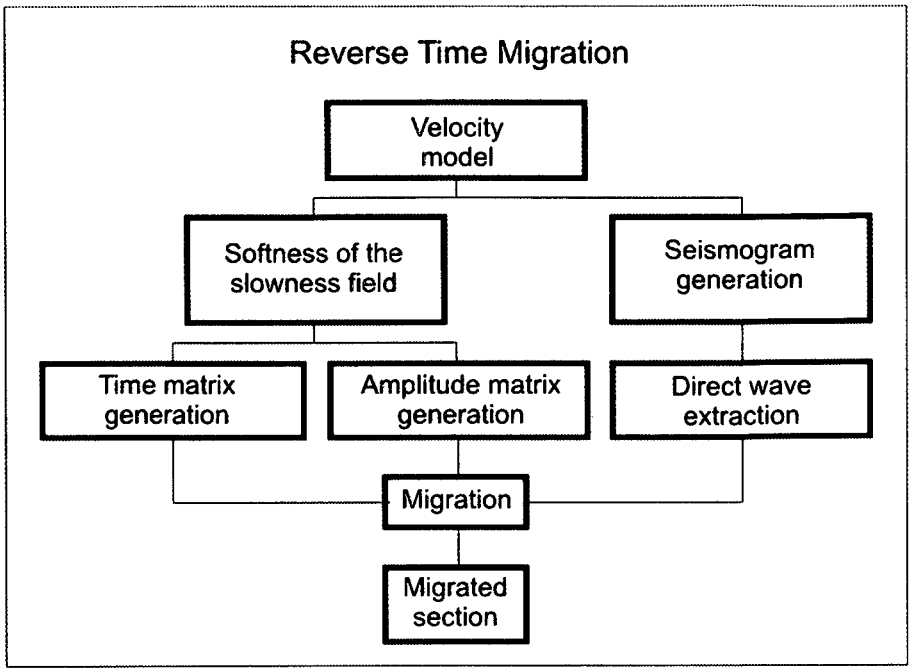

Figure 5.19: Flowchart of the reverse time migration processing.

5.4.3 Parameters and construction of the model

Construction of the geological model was based on the interpretation and correlation of the Waterfall sedimentary succession according to the following steps:

1. Drawing of the lateral extension of the deformed beds, considering different geometries for the flames. Flames 1, 4, 6 and 7 were created maintaining the proportions around base width, flame height and distance between adjacent flames based on the measured relationships obtained from Waterfall studied structures. Flames 2 and 5, more conceptual, have a regular shape with the spread of the material from the flame above them. Flame 3 has an irregular shape measured directly from the outcrop in Heuningberg (Figure 5.20).
2. Drawing of the undeformed beds and of the lateral extensions of the flames without deformation, characterising the transition from deformed-undeformed.
3. Expansion of the original dimensions of the model (38 m x 100 m) by a factor of 2 (76 m x 200 m). The objective was to create a model that was more "visible" for the lower frequencies but maintaining the proportionality and plausible dimensions (Figure 5.21). In this case,

the smallest Flame 1 is 1.5 m high while the thickest Flame 2 is 3 m high, with vertical dimensions compatible with equivalent structures described in Roosterberg (Chapter 4) and Chacay Melehue (Chapter 3).

4. Division of the model into a grid of 380 x 1000 cells to be populated with seismic velocities of the distinct intervals. Based on the Waterfall stratigraphy and correlation, three zones were defined by the dominant lithology (Figure 5.22), and divided into: (i) sandstone (white in the model), (ii) mudstone/siltstone undeformed (pink in the model), and (iii) mudstone/siltstone deformed (red in the model).

5.4.4 Analysis of the results and interpretation

In order to populate the model with realistic data, different velocities, varying between 2500 m/s and 3100 m/s, for Neogene and Upper Cretaceous sandstones and mudstones/siltstones of the South Atlantic continental margin were used. The estimated central frequency for these intervals was 500 Hz and the selected value of h (size of the cell in the model) equal to 1 m (five times the scale of the model). The choice of h=1 m was justified in order to accommodate the range of calculated vertical resolutions, between 10 and 15 m. The result of the test with different velocities for the model is shown in Figure 5.23. Exceptionally, the model 3 sandstone velocities are higher than the mudstone velocity of the proposal models. Velocity models 1 and 3 are characterized by the highest contrast of velocity and generate noisy synthetic seismic sections, with the nucleation of vertical conical features that decrease the signal/noise ratio. In both models, the deepest deformed horizons (Flames 1, 2 and 3) are poorly defined or not defined.

Models 2 and 4 reproduce with good definition flames 2 to 7. Model 4 shows inverted polarity in relation to the other models. Also, in comparison to model 2, model 4 is higher in conical noise and creates "false flames" such as the ones observed just above the dipping reflector above Flame 5. Considering that velocity model 2 resulted in the best quality, it was selected for the test of resolution, varying the thickness of the model and the frequency of the wave.

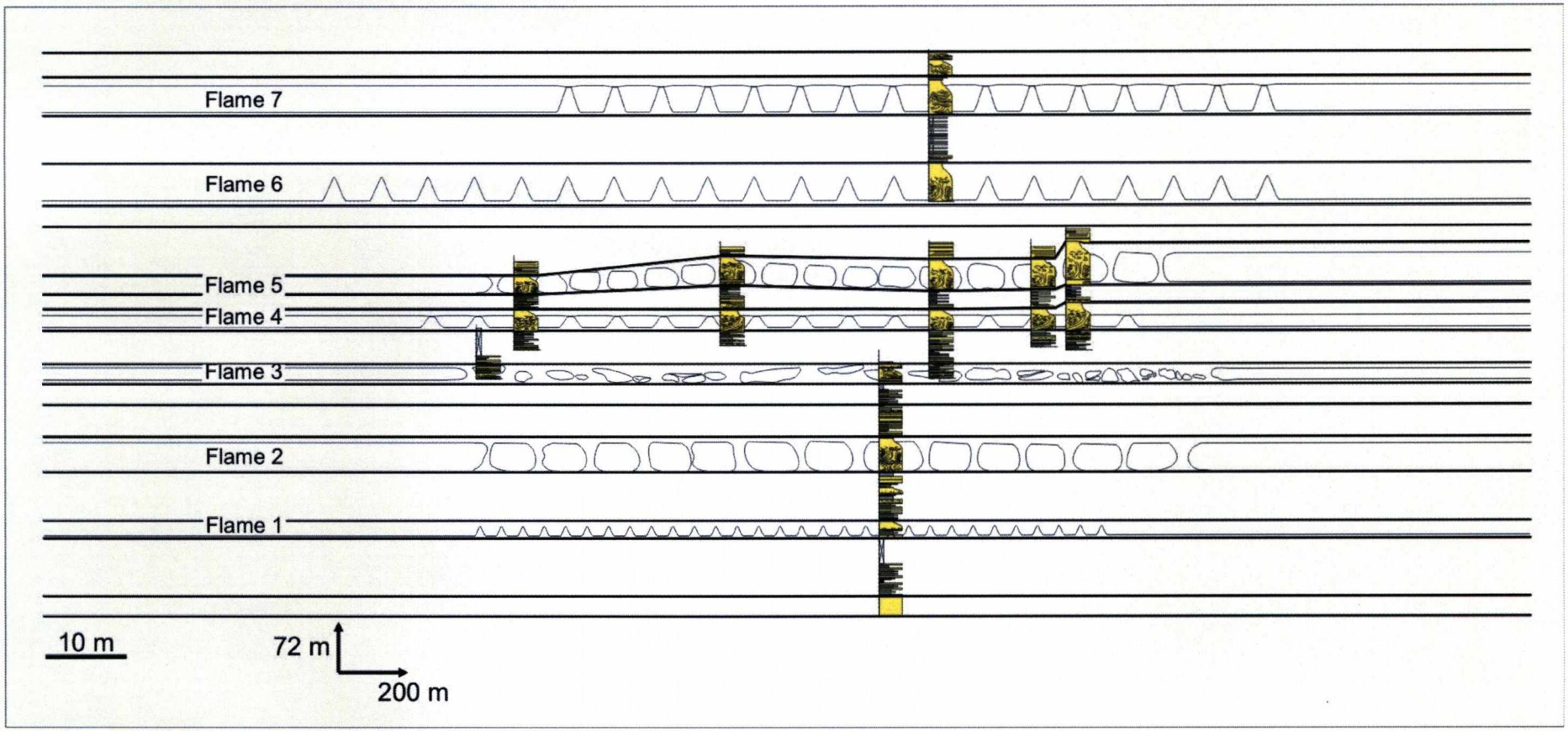

Figure 5.20: Geological model constructed based on the Waterfall correlation (logs attached to the model). Seven deformed intervals were defined at the scale of the model and they were built considering real examples and dimensions from the outcrops (see text for more information).

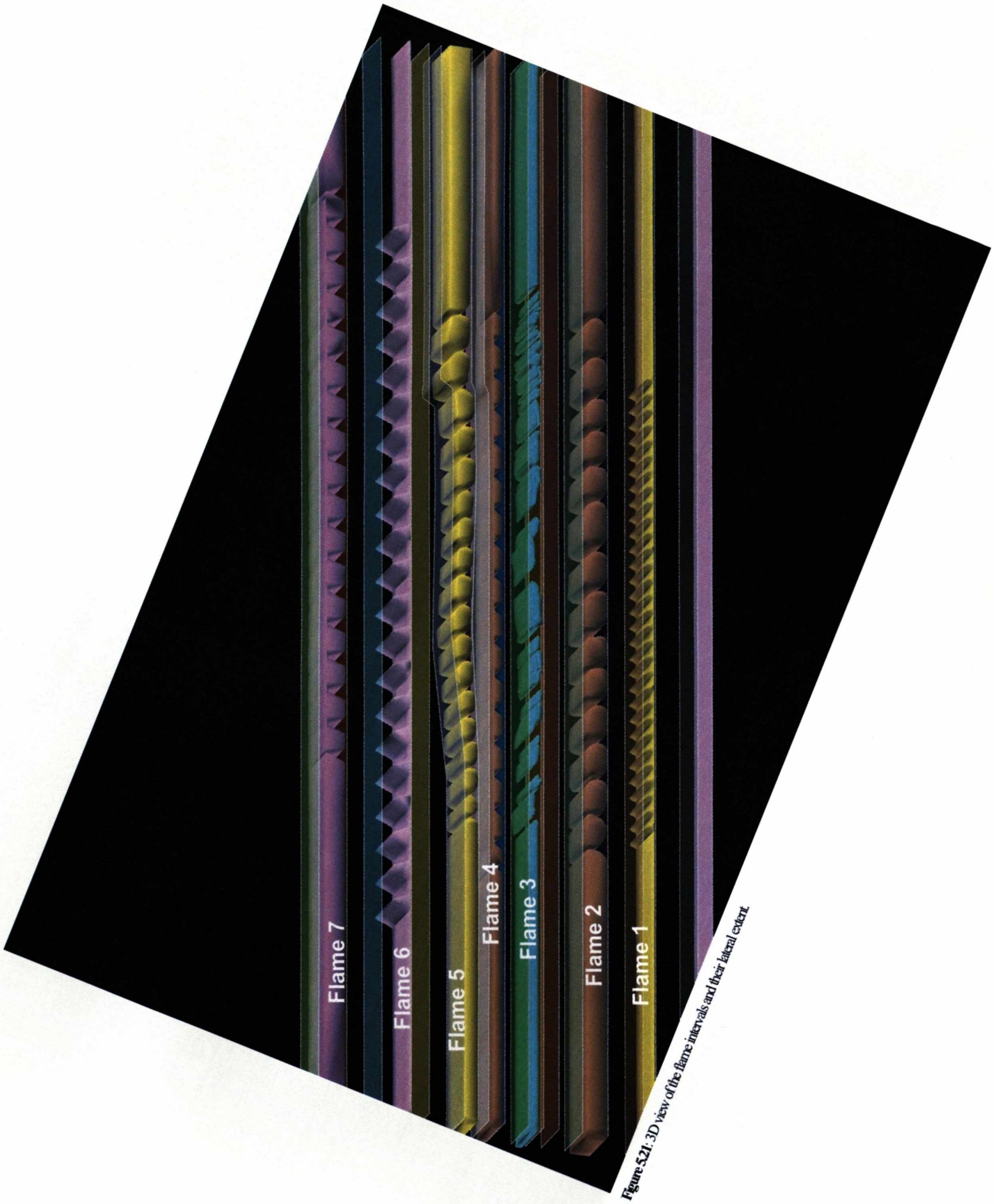

Figure 5.21: 3D view of the flame intervals and their lateral extent

Figure 5.22: Velocity model based on the geological model. The intervals were separated into three zones, one for the sandstones and two for the mudstones/siltstones (one associated with the flames and one not deformed). The separation of the mudstone/siltstone intervals into two zones permitted more possibilities for population with distinct velocities.

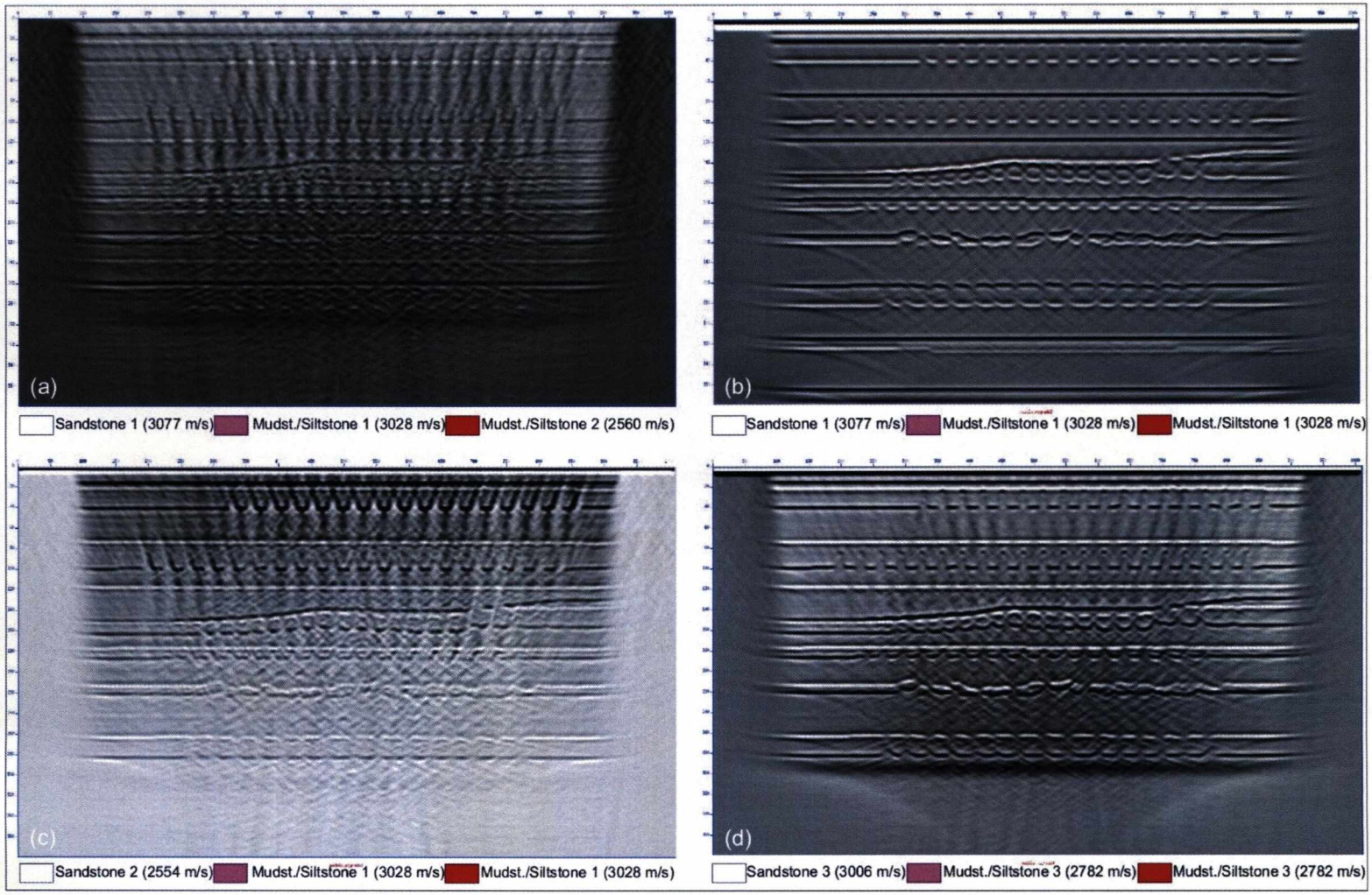

Figure 5.23: Seismic modelling considering distinct velocity for the 3 velocity zones: (a) Model 1: three velocities of Neogene rocks; (b) Model 2: two velocities for Neogene rocks (vel sandst > vel siltstone); (c) Model 3: two velocities for Neogene rocks (vel sandst < vel siltstone); (d) Model 4: two velocities for Cretaceous rocks. The colour code and the distribution of rock seismic velocities is in Figure 5.22. Parameters for modelling: h=1 m; f=500 Hz

Table 5.4 indicates the selected frequencies and cell dimensions for testing, and the associated theoretical vertical resolution. Three different ranges of frequencies were selected with distinct objectives: (i) 100 Hz associated with highest values of central frequency for high resolution seismic acquisition focusing on targets overlain by 1-2 km of strata; (ii) 500 Hz associated with highest values of frequency for targets with 500 to 1000 m of sedimentary cover; and (iii) 3000 Hz for a frequency range found in special surveys like sub-sea bottom profiles for targets less than 100 m below the sea floor.

Frequency (Hz)	H (cell dimension) (m)	Velocity (m/s)	Vertical resolution (m) (v=3000 m/s)
50	2.0	Sandstone: 3077m/s Mudstones /Siltstones: 3028 m/s	15
100	2.0		7.5
100	5.0		7.5
500	0.4		1.5
500	1.0		1.5
500	1.2		1.5
500	2.0		1.5
3000	0.1		0.25
3000	0.2		0.25

Table 5.4: Pairs of frequency and cell dimension (h) used for the seismic modelling based on velocity model 2. The last column shows the calculated vertical resolution considering the velocity of 3000 m/s.

The same velocities from model 2 were maintained for the test with the new frequencies. It is important to stress that such high frequencies would not be expected in lithified, deeply buried strata, but this does not invalidate the comparative analysis for different frequencies and thicknesses. For shallower rocks, considering the same frequencies above, the values of vertical resolution would be approximately 2/3 (v~2000 m/s) of the one presented in Table 5.4.

A 500 Hz pulse was applied for different scales of the geological model (Figure 5.24). For h=0.4 m, i.e. twice the size of the original model, there is no definition of the structures in the deformed intervals. For that frequency, the ideal size for the recognition of the flames would be with h=1.0 m, that means a dimension five times the size of the original model. Considering a pulse with frequency of 100 Hz, the limit of definition for the beds with some indication of deformation would for a model with h=2 m, ten times the size of the original geological model (Figure 5.25a). For the sampling of the actual outcrop size much higher frequencies would be necessary (Figure 5.25b).

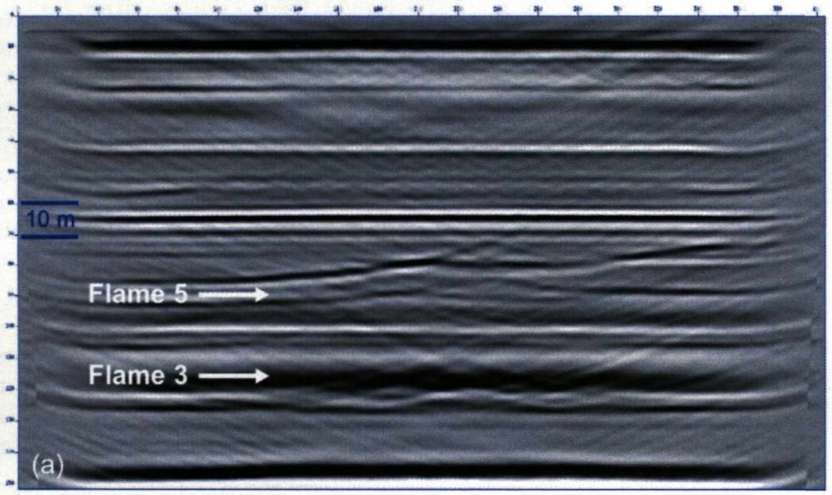

h=0.4 m

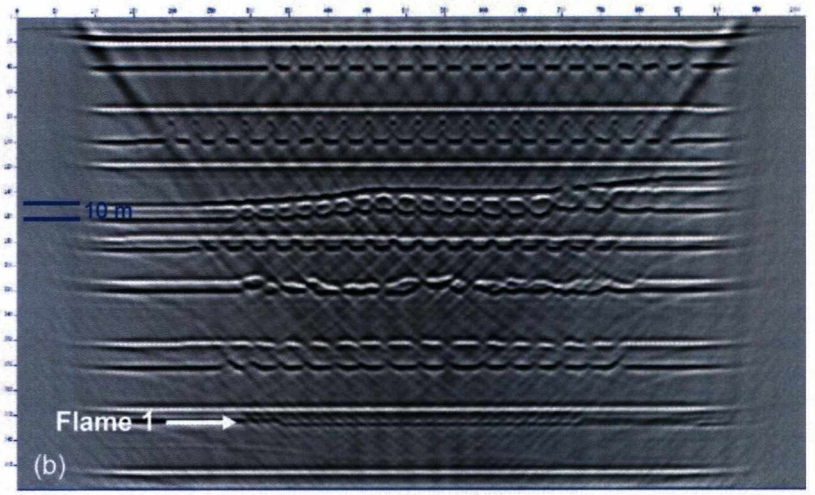

h=1.0 m

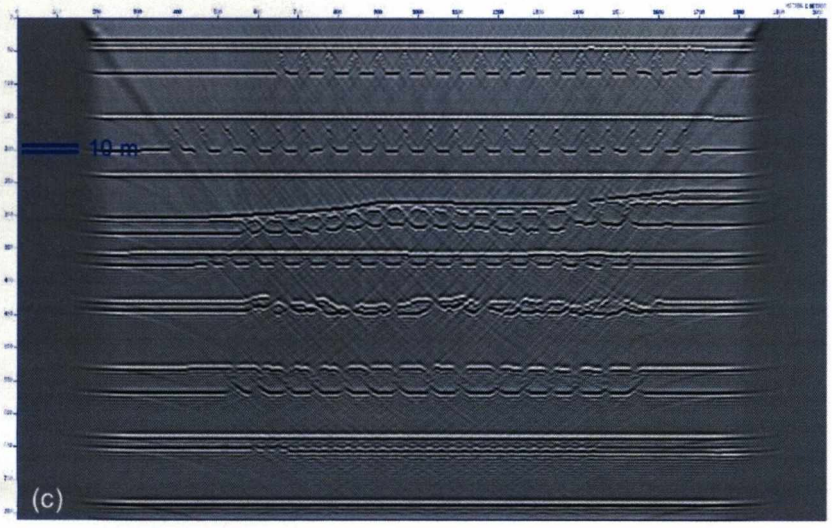

h=2.0 m

Figure 5.24: Seismic modelling for different dimensions of velocity model 2 considering the incidence of one wavelet with frequency of 500 Hz: (a) h=0.4 m (total depth = 152 m), twice the dimension of the original model, it is not possible to identify the flames in the deformed intervals; (b) h=1.0 m (total depth 380 m), five times the size of the original model, the "ideal" dimension for the frequency of 500 Hz, top and base of the deformed intervals with flames are identified; (c) h=2.0m (total depth 760 m), 10 times the dimension of the original model, as the structures are bigger than the ones in the "ideal" situation (h=1.0 m), all events will be visible. More noise is introduced to the section.

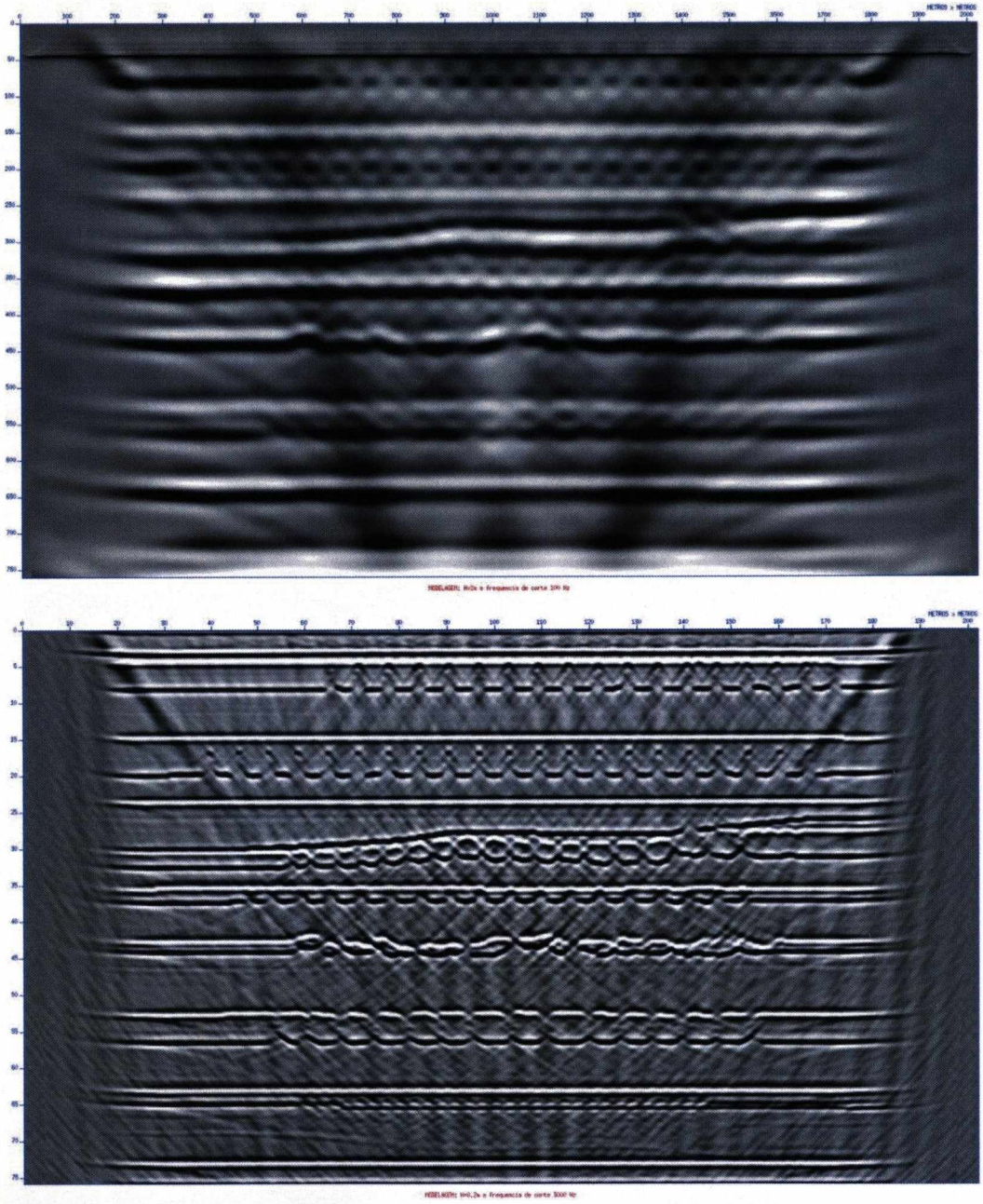

Figure 5.25: (a) Seismic model for f=100 Hz and h=2.0 m, in this case the geological model must be at least 10 times the outcrop size for the deformed interval to be sub-sampled during the seismic modelling; (b) Seismic model for f=3000 Hz and h = 0.2 m, only very high frequencies not used in standard surveys are able to sample the model at the original outcrop scale. Seismic velocities are the same as for velocity model 2 (Figure 5.22).

Interpretation

As the only change in the initial models was related to changes in the velocity (Figure 5.23), it is interpreted that this seismic model was sensitive to large changes in the internal velocities, implying the addition of high frequency noise in models 1, 3 and 4. The results indicate that for the dimensions of the original geological model

only deformation close to the seabed (a few hundred metres) could be imaged and only with the use of non-conventional geophysical surveys (e. g. sub-bottom profile or single-channel sparker). For more deeply buried sandstone packages (> 1000 m), even with very high dominant frequencies (between 100 Hz and 500 Hz), the dimensions of the geological model would need to be 5 to 10 times the size of the original model. From the data above it is estimated that for shallow sedimentary packages (<1000 m burial depth), the flames would need be around 3 to 7 times the size of the measured examples to be imaged, given that vertical resolution will be around 2/3 of the resolution for deeper rocks (cf. Table 5.4).

It is important to consider that the presence of oil or gas in the situation above could increase the impedance contrast, consequently affecting the amplitude of the signal and altering the appearance of the seismic section. Variation in density and velocity of rocks involved in the deformation packages would largely influence the final result (cf. Figure 5.23). Parallel to the geological characteristics of the rocks, for available 3D seismic data, modern (pre-stack) migration and deconvolution processes help to increase the resolution and the signal-to-noise ratio (Yilmaz, 2001). In the field of seismic attributes, the development of techniques among them related to the spectral decomposition (e.g. Q estimation and Q compensation, and spectral decomposition-based inversion for seismic reflectivity) (Chopra *et al.*, 2006; Wang, 2006; Chopra & Marfurt, 2008) has improved the recuperation of reflectivity below the seismic resolution.

For the geological model the range of the tested flames were between 1 and 3 m high. Along the mapped areas in Neuquen and Karoo basins it was possible to map features up to 5 m high. This range of scale has been sampled by modern high resolution geophysical surveys (Trincard *et al.*, 2004; and references from Table 5.3). Otherwise the seismic modelling indicates that for deeper strata the size of the structures would need to be much bigger in order to be sampled by a compatible frequency. From this it is concluded that: (1) flame structures should be considered when interpreting high resolution data from shallow sedimentary packages; (2) the seismic modelling above provides indications of a likely seismic response for analogous structures.

The multi-scale approach considered in this chapter complements effectively the observations from the outcrops. Hand specimens are demonstrated to be effective in providing information about the shape and orientation of centimetre-scale load structures, while GPR furnished the same type of information for metre scale flame structures. Finally, the seismic modelling gave a strong indication as to the expected geometry of flame structure intervals when sampled by high-resolution geophysical methods using realistic ranges of frequencies and velocities. Obviously, systematic testing of hand specimen techniques are necessary to evaluate different types and dimension of structures. Also, there is a large range of methodologies for seismic modelling that could be tested in the investigation of this type of deformation.

Chapter 6 – Discussion

6.1 – Classification of soft-sediment deformation structures

In chapters 3 and 4 a range of soft-sediment deformation structures were described, with emphasis on the spatial and temporal setting, likely trigger mechanisms and driving forces. The objective of this chapter is to explore generic aspects of the processes and products in different depositional environments, culminating in a revised classification scheme. Table 6.1 summarizes the soft-sediment structures found in the study areas.

Among the structures in Table 6.1, four of them are not classed as separate structures in the available systems of classification for soft-sediment deformation features. They are: (1) structureless (cf. Figures 3.7 and 3.14); (2) ruptured and folded sandstone (cf. Figures 3.7 and 4.22), (3) convolute bed (cf. Figure 4.33b) and (4) squeezed structure (cf. Figure 4.33a). The first three of these are related to deformed beds rather than a specific type of structure, but they are associated with soft-sediment deformation processes and products and therefore considered as one type of structure. The structureless and the ruptured and folded sandstones are closely associated and are easily explained when associated with bed liquidization (liquefaction and fluidization) that produce flame structures as observed in the Waterfall area (Chapter 3.1). The convolute bed is interpreted as produced by the liquefied intrusion of a laminated bed confined by two undeformed beds, controlled by simple shear parallel to bedding (see Chapter 4.1.5). It can be considered as an intermediate case of the strucutureless soft-sediment deformation bed. The squeezed structure is a parent feature of the flame structures, created by loading of the denser upper layer in a laminated bed deforming under plastic behaviour, and secondary fluidization, which expanded laterally and upwards.

Type of deformation	Category	Frequency	Locality	Dimension	Environment	Deformation mechanism	Driving force
Flame structure	Fluid escape *In situ*	Abundant	WF, FM, CM, RO,HN, ZF, BR, PS	0.05-4 m (V and H)	Deltas/shoreface; shelf-edge; lower slope channel and MTC, intra-channel	Fluidization,	Vertical shear (particles moving upwards); inverted density gradient; subtle downslope force
Dish structure	Fluid escape *In situ*	Rare	RO, HN	0.05 m (V) 0.1 m (H)	Shelf-edge delta	Liquidization	Vertical and horizontal shear (due to moving particles)
Structureless bed	Fluid escape/ lateral spreading *In situ*/detached	Common	WF, RO	0.5 m (thickness)	Shelf-edge delta and lower slope intra-channel	Fluidization	Vertical and horizontal shear
Ruptured and folded sandstone	Fluid escape/ loading (?) *In situ*	Common	WF, CM, HN	0.2–1.5 m (V)	Deltas/shoreface; shelf-edge; lower slope channel and MTC, intra-channel	Fluidization, brittle	Vertical shear; downslope stretching
Load cast	Load structure *In situ*	Abundant	(WF), FM, CM, RO, HN, ZF, BR	0.02-0.5 m	Shelf-edge delta; lower slope channel, intra-channel and mass transport complex	Liquefaction	Inverted density gradient
Pseudonodule (Attached and Detached)	Load structure *In situ*	Common	WF, RO, HN, ZF	0.02-0.1 m	Shelf-edge delta; lower slope intra-channel.	Liquefaction	Inverted density gradient
Ball-and-pillow	Load structure *In situ*	Rare	RO, ZF	0.02-0.1 m	Shelf-edge delta	Liquefaction	Inverted density gradient
Squeezed structure	Load structure/ fluid escape *In situ*	Rare	ZF	Up to 1.5 m high	Shelf-edge delta	Liquidization/slide	Inverted density gradient; lateral shear; non-uniform confining load.

Foundering structure	Load structure *In situ*/detached	Uncommon	CM**, RO, HN	Up to 5 m long	Shelf-edge delta, lower slope lobe (?)	Liquefaction	Inverted density gradient
Convolute lamination	Density instabilities * *In situ*	Rare	RO	0.3-0.5 m (thickness)	Shelf-edge delta	Liquefied flow	Vertical shear; inverted density gradient; secondary lateral movement (downslope force?)
Fold	Loading/mass movement Detached/*In situ*	Common	FM, CM, RO	0.02-2 m	Shelf-edge delta; lower slope.	Slide/slump	Downslope component of gravitational force, laminar shear
Slide/Fault	Mass movement Detached	Rare	CM	10 m (thickness)	Lower slope	Slide/ britte (elastic flow)	
Slump	Mass flow Detached	Common	(FM), CM, RO, HN	Up to 10 m (thickness)	Shelf-edge delta, lower slope.	Slide (elastic flow)	
Contorted blocks/rafts	Mass flow Detached	Common	CM, RO, HN, ZF, BR	Up to 12 m (thickness)	Shelf-edge delta, lower slope.	Debris flow (plastic flow)	
Convolute bed	Fluid escape/ mass flow *In situ*/detached	Uncommon	HN, ZF	1 m (thickness)	Shelf-edge delta	Liquefied intrusion/ liquefied flow (?)	Horizontal shear
Mud injection	Injectite *In situ*	Rare	CM	Up to 8 m high	Lower slope.	Fluidization	Hydraulic fracturing

Table 6.1: Characteristics, depositional environment and deformation processes related to the soft-sediment deformation structures found in the study areas. Key for occurrence: WF – Waterfall; FM – Fortin Primero de Mayo; CM – Chacay Melehue; RO – Roosterberg; HN – Heuningberg; ZF – Zoutkloof; BR – Buffels River; PS – Puesto Seguel. * Allen (1982) considered the most plausible, despite other explanations consider also by horizontal stress. ** Conglomerates and coarse-grained sandstones on top of debrites.

Table 6.2 summarizes the various associations among the described structures that are interpreted as a function of the dominant deformation mechanism and driving force. The associations DA1, DA2 and DA3 (Table 6.2) are described in outcrops (Howard & Lohrengel II, 1969; Needham, 1978; Cheel & Rust, 1986; Mount, 1993; Owen, 1996a; Dasgupta, 1998; Moretti, 2000; Moretti *et al.*, 2001; Alfaro *et al.*, 2002; McLaughlin & Brett, 2004; Hildebrandt & Egenhoff, 2007) and in experiments (Kuenen, 1958; Anketell & Dżułyński, 1968; Anketell *et al.*, 1970; Nichols *et al.*, 1994; Owen, 1996b; Moretti *et al.*, 1999). Typically, they originate from the liquidization of fine-grained sediment that is deformed to the final configuration by the action of forces including inverse density gradient (vertical), non-uniform confining load (vertical) or shear stress (horizontal or vertical) caused by fluidization.

Name	**Soft-sediment deformation structure association**	**Locality**	**Example(s)**
DA 1	Flame structure + ruptured sandstone + structureless (+ dish)	WF, RO	Figures 3.7, 3.8, 3.14, 4.12
DA 2	Load cast + pseudonodule + ball-and-pillow	RO, ZF	Figure 4.15
DA 3	Elements of DA 1 and DA 2 + foundering structure	RO, HN, FM	Figures 4.26, 4.31, 4.45c, 5.1
DA 4	Debris flow + load structure or foundering structure on top	RO, HN, CM	Figures 3.36, 4.12c
DA 4a	Similar to DA 4 but at larger scale (outcrop). Occurrence of *in situ* deformation just above slump/debrite intervals	RO, HN	Figures 4.6. 4.7
DA 5	Slump scar + flame structure	RO	Figures 4.19, 4.21
DA 6	Flame structure + mud injection	CM	Figure 3.38d, e
DA 7	Flame structure + sandstone fold	FM	Figure 3.26e
DA 8	Fold + load cast + flame	CM	Figure 3.37c, d

Table 6.2: Distinct associations between soft-sediment deformation structures related to the dominant deformation mechanism and driving force. See text for details. Key for locality: see Table 6.1.

Classes DA 4 and DA 4a are related to the occurrence of *in situ* soft-sediment deformation in the latter stages of formation of mass transport deposits. Few examples of these interactions are found in the literature, among them: (i) extensional zones in slumps, with the development of late normal faults (Martinsen and Bakken, 1990); (ii) low gradient shallow-water collapse depressions generated by the decrease in the volume of the sediment-gas-water system (Coleman and Prior, 1988); (iii) sand volcanoes, collapse depressions and clastic dykes on top of slumps or on top of immediately overlying beds, produced by the upward movement or

sinking of sediment in response to escaping pore waters (Martinsen, 1989). In the Karoo Basin and Neuquén Basin examples two models are proposed: (1) for class DA4 it is interpreted that deformation was associated with the localized non-uniform loading and/or inverse density gradient caused by the deposition of thick sandstone packages over muddy slumps/debrites, partly controlled by topographic irregularities on top of the slump deposit/debrite. From the case studies, an example of this relationship is the large scale load structures on top of debrites at the base of Chacay Melehue section (see Chapter 3.2.3, cf. Figure 3.36b); (2) for the thickest beds of class DA4a there is no clear indication of any relationship between the underlying slump/debrites and the overlying beds that are dominated by water escape features. The repetition of this pattern mainly in cycles R2, R3 and R4 at Roosterberg (cf. Figure 4.6, *in situ* deformation dominated beds overlying detached deformation dominated beds) suggests that loading caused by rapid deposition of sand over the mud-prone mass movement deposits was enough to increase the pore pressure, causing liquidization of the underlying deposits with consequent fluid escape and generation of load structures in the overlying sandstone beds.

Class DA 5 is interpreted to originate from the effect of differential loading caused by partial removal of the overburden via localized slumping, in a similar manner to that proposed by Dasgupta (1998) (cf. Figure 4.21a). The association found in DA6 can be explained by considering that flame structures are a particular type of sediment injection structure (Lowe, 1975), generated by fluidization but with a distinct mechanism of intrusion (cf. Lowe, 1975; Jolly & Lonergan, 2002). In general, the same associations of distinct soft-sediment deformation structures (Table 6.2) can be observed laterally along the outcrops (cf. Figures 4.24-4.25, 4.31, 4.34).

A classification scheme

Based on the information above a new scheme for the classification of soft-sediment structures is proposed. Among the current classification systems, the most comprehensive are those of Elliot (1965), Allen (1982) and Owen (1987) (cf. Figure 1.13). These are genetic schemes, i.e., the classifications themselves reveal something about the evolutionary history of the structures. In the scheme proposed here the philosophy of those classifications is incorporated, based around the distance of fluid plus sediment movement and the stress condition, set within the background deformation mechanism (Figure 6.1). In this sense it is similar to the

larger scheme proposed by Elliot (1965). Throughout this study, the emphasis has been on the interplay between *in situ* and detached (transported downslope) structures, which form one of the main horizontal axes of the proposed scheme. Stress condition constitutes the vertical axis in the proposed classification. The deformation mechanism is fundamental in the changing of the stress conditions in order to cause deformation and, therefore, is the background to the proposed classification.

As in any classification, the proposed scheme does not cover all possibilities. The main restriction is related to the representation of the dominant stress, because different types of stress can be acting at the same time or in the same space within a determined area. Thus on a 2D graph as shown in Figure 6.1, representation of the dominant stress is difficult for structures with components of compressive normal and lateral shear (e. g. foundering structures). The advance over similar classification systems is that the scheme provides a comprehensive link between different structures (products) and indicates the general tendency for the increase in slope instability. Another characteristic is that it reflects dominant structures found in shelf edge to slope setting in the studied outcrops and, therefore, can be used as reference to compare other analogues. It is very important to highlight that the situation represented by the graph is not static and a recurrence of one type of structure can occur at any time and at different scales through a deformational process continuum. For example, *in situ* deformation can occur in the late stages of mass transport complex emplacement because at a certain time the mass transport complex became stable enough to initiate a new cycle of *in situ* deformation at a different level in the hierarchy of deformation, making it difficult to depict on the graph.

Different types of *in situ* soft-sediment deformation structures can occur associated with a single event or can evolve from a previous type. Figure 6.2 indicates the links between distinct structures described from the Karoo and Neuquén basins, governed mainly by sediment liquefaction and/or fluidization. This evolutionary scheme (Figure 6.2) helps in the understanding of the interrelations between the *in situ* structures classification (Figure 6.1). It is important to emphasize differences between foundering structures (Figure 6.2a) and load structures (Figure 6.2b). Foundering structures are generally more flat-based, with internal structures preserved and showing abrupt contact (brittle rupture?) with the source bed, suggesting that deformation occurred when the overlying bed was semi-consolidated.

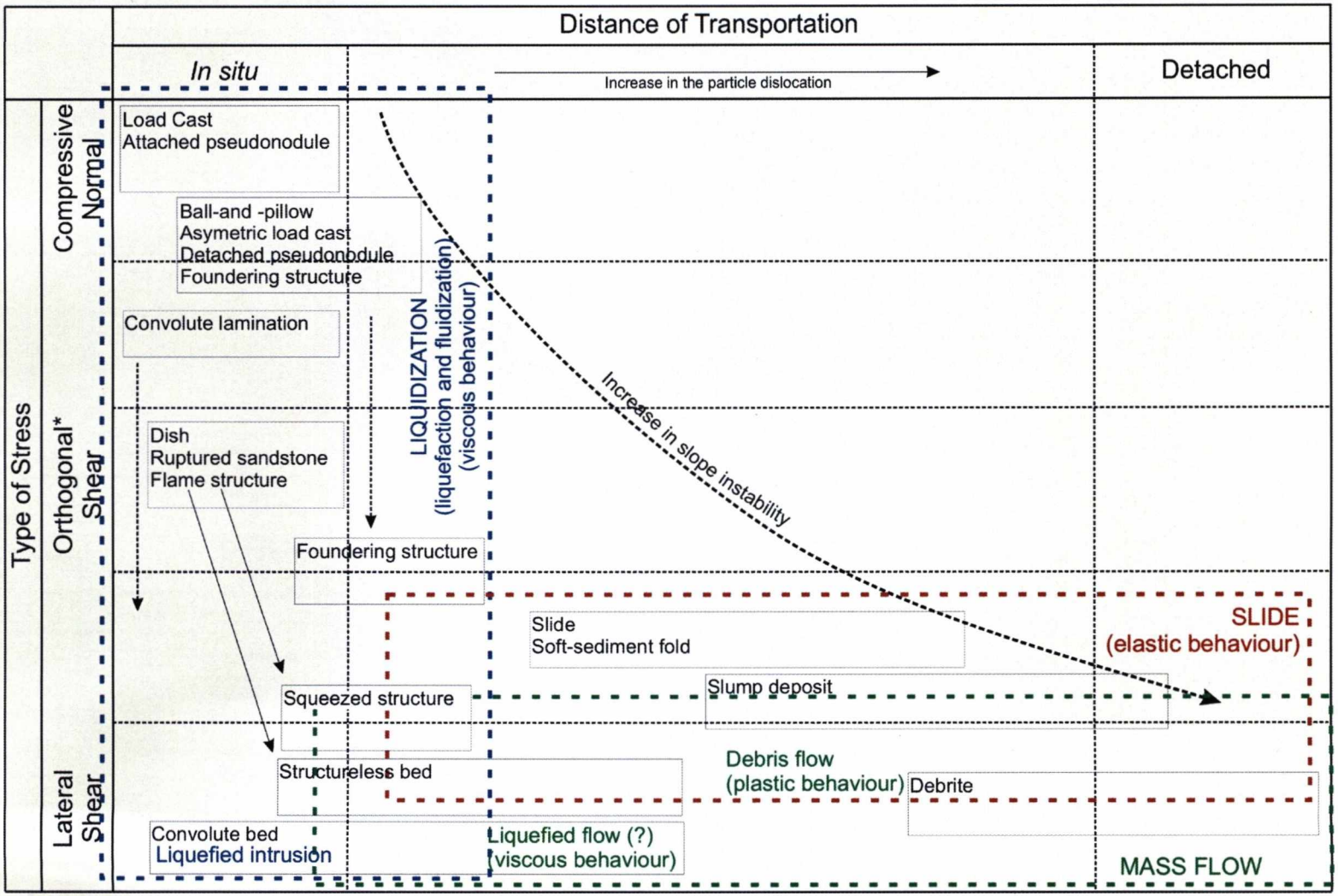

Figure 6.1: Classification scheme for soft-sediment structures found in the Karoo and Neuquén basins, based on the distance of transportation and type of stress, with the indication of the dominant deformation mechanism (dashed rectangles). It does not include the injection and normal faults, the first because complexity of stress involved that will depend on particular conditions and the second due to the occurrence of brittle behaviour and tensile lateral stress. Arrows indicate linkages between structures and dominant stress (continuous arrows) or structures affected by two or more type of stress, in different areas of the graph (dashed arrow). Large detached arrow indicates the general trend for the slope instability. See text for details about deformation mechanisms. (*relatively to bedding).

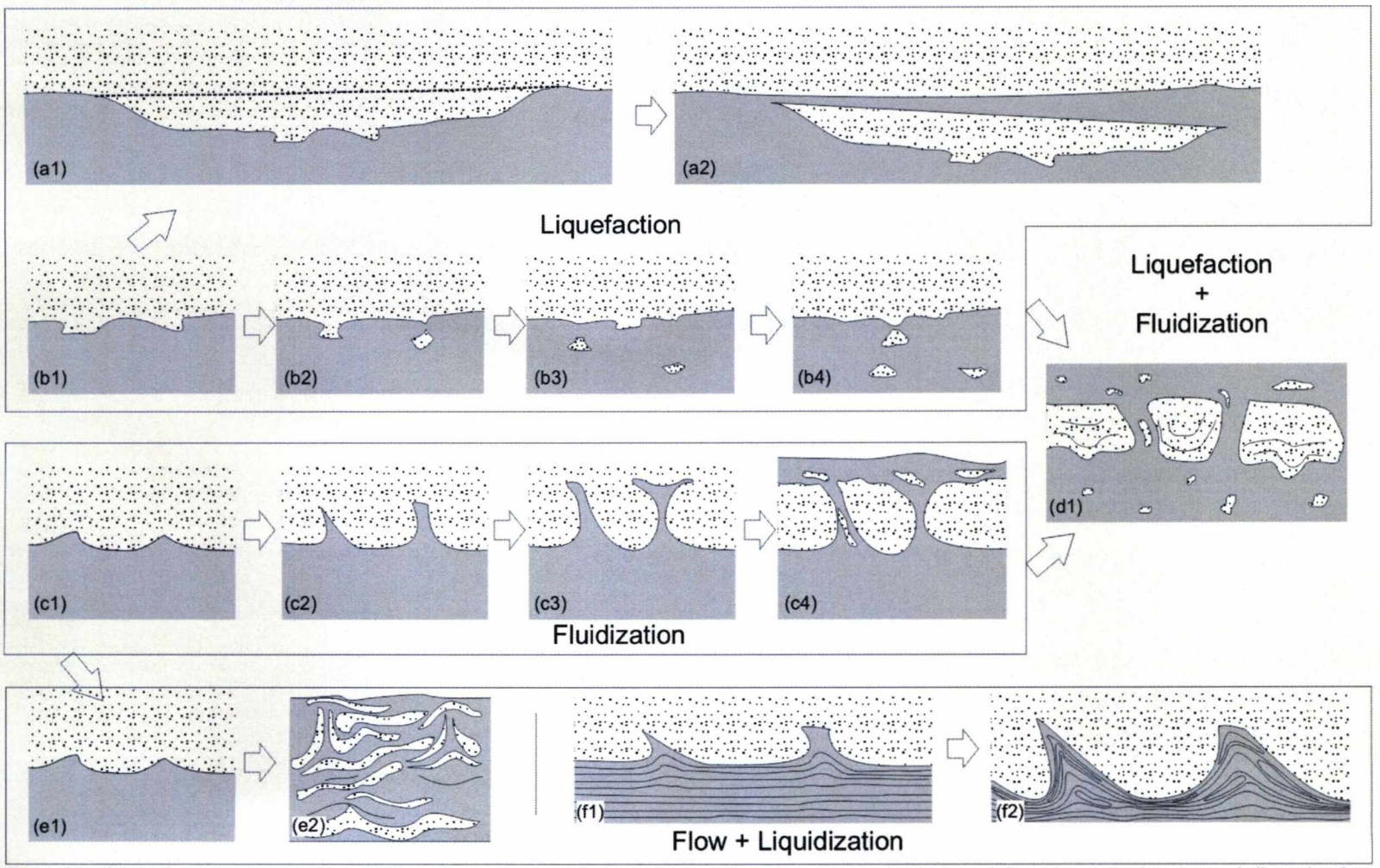

Figure 6.2: Sketch of main *in situ* soft-sediment deformation structure types in the study areas grouped according to the dominant deformation mechanism. Arrows indicate situations resulting in the generation of a sequence of distinct structures with the same origin. The structures represented are: (a) foundering structure; (b) load structures: (b1) simple load cast, (b2) attached and detached pseudonodules, (b3 and b4) detached pseudonodule and ball-and-pillow structure; (c) flame structure, culminating in ruptured sandstone and structureless bed (c4); (d1) load structures and flame structures may occur associated; (e) convolute bed and (f) squeezed structure.

6.2 – Comparison of processes, triggers and products from shelf-edge, upper and lower slope settings

Chapter 3 introduced the methodology used for analysis of the deformation processes that affected deposits in a variety of depositional settings in the study areas. This followed schemes proposed by Allen (1982) and Owen (1987) in which the deformation processes were separated into three main aspects: the trigger, the deformation mechanism and the driving force. This division helped to avoid misunderstanding between the causes of deformation, the deformational process and the products of deformation. The objective in this section is to compare the deformational processes in the distinct depositional settings, and to establish similarities and differences between them.

Table 6.3 summarize depositional environments, and deformation processes and their products in the Karoo and Neuquén basin outcrops. The identified trigger mechanisms present distinct characteristics according to the relative position on the depositional profile (Table 6.4). The trigger for deformation can be the combination of more than one factor, implying that a sequence of events can culminate in deformation. As an example, failure can be initiated by a combination of oversteepening, earthquake activity, rapid sediment accumulation, release of gas and gas hydrate, low tides, storm waves and/or groundwater seepage (Prior & Coleman, 1978; Wells *et al.*, 1980; Lee *et al.*, 2007, Nittrouer *et al.*, 2007). As discussed in Chapter 1 the identification of trigger mechanisms in ancient rocks is difficult and can cause some circularity in the argument once trigger mechanism may be, in part, specified because of the interpreted setting. Therefore the interpretation presented here is also influenced by this effect. Criteria used to minimize the uncertainty were: the lateral/areal extension of the deformation, the local stratigraphic context, the lithological contrasts and the changes in the geometry of the neighbouring rocks. Overall, the trigger for deformation in the Karoo and Neuquén examples was interpreted to be loading associated with rapid sediment deposition that led to an increase of pore fluid pressure and subsequent bed liquidization. In the shelf-edge to upper slope examples (Chapter 4), failure was caused by sediment loading due to progradation of the delta, combined with an underlying unstable mud-prone slope. In the middle-lower slope settings (Chapter 3), failure occurred due to sediment loading combined with an underlying inherited topographic slope. Finally, earthquake

triggering of the deformation is only considered a possibility for the lower-slope deposits of the Chacay Melehue area due to possible reactivation of the boundary fault. None of the other examples presented in this thesis have any direct link to seismic activity as a trigger for deformation.

It has long been recognized that loading causes the build up of high pore water pressure with consequent liquefaction of the sediment (Seed, 1979; Obermeier, 1996) (cf. Chapter 1.2). Liquefaction and fluidization are considered the main deformation mechanisms that result in soft-sediment deformation structures (Lowe, 1975, 1976; Allen, 1982; Maltman & Bolton, 2003); also interpreted as the deformation processes that produced the structures studied in this research (Table 6.5). Deformation associated exclusively with liquefaction and fluidization is interpreted as occurring mainly in a vertical orientation, orthogonal to bedding. When the major displacement direction is parallel to bedding, mass movement occurs, and commonly the products are divided into slides and mass flow deposits (*sensu* Varnes, 1958) (cf. Figure 1.11). Translational slides and rotational slides (slumps) are characterized by elastic behaviour and (simple and/or pure) shear failure (Nardin *et al.*, 1979). This process generated the slump deposits, soft-sediment folds and rare rotational block in the Karoo and Neuquén datasets. Related to mass flow processes, debris flows (Lowe, 1979; Nardin *et al.*, 1979), are interpreted as the process that produced the debrites and associated deformation in the study outcrops. This process is characterized by plastic behaviour with shear distributed throughout the sediment. Liquefied intrusion (Lowe, 1975) is interpreted as the most likely process that generated deformation in the Zoutkloof area (cf. Figure 4.33d, e). The intruded sediment is highly viscous and generally concordant and involves the distribution but not total elutriation of finer grain sizes. Alternatively, incipient liquefied flow (Lowe, 1976, 1979; Nardin *et al.*, 1979) may occur and, in this case, the material behaves like a viscous fluid with sediment supported by dilatancy, the upward displacement of fluid. Rare brittle deformation occurs affecting mainly metre scale sandstone beds that fail under the presence of adjacent liquidized and deformed beds.

Locality	Depositional Environment	Soft-sediment deformation structures	Trigger	Deformation mechanism	Driving force
Waterfall, Tanqua	Lower-slope, intra-channel	Flame structure *, load structure **	Local steepening gradient/ rapid sediment deposition	Liquefaction and fluidization	(1) Gravitationally inverse density gradient; (2) vertical shear stress; (3) down- slope component of body force.
Fortin Primero de Mayo, Neuquén	Lower-slope, slope channel	Flame structure, fold	Failure of the channel complex margins or upstream failure	Fluidization	(1) Non-uniform distribution of the confining load; (2) down-slope component of body force.
Chacay Melehue, Neuquén	Lower-slope	Contorted blocks and rafts, load structure, flame structure, mud injection, normal fault,	Rapid sediment deposition; slope failure; oversteepening; earthquake (?)	Liquefaction and fluidization; slide, mass flow; brittle deformation	(1) Down- slope component of body force; (2) gravitationally inverse density gradient; (3) normal shear stress; (4) hydraulic fracturing; (5) non-uniform distribution of the confining load
Roosterberg (Cycle R2), Tanqua	Middle- and upper-slope; shelf-edge	Flame structure, load structure, contorted blocks and rafts, foundering structure,	Rapid sediment deposition; slope failure; loading/unloading caused by delta progradation	Liquefaction and fluidization; mass flow	1) Gravitationally inverse density gradient; (2) vertical shear stress, (3) down- slope component of body force
Roosterberg (Cycle R3), Tanqua	Middle- and upper-slope; shelf-edge	Contorted blocks and rafts; flame structure; foundering structure	Slope failure; loading/ unloading caused by delta progradation	Liquefaction and fluidization; mass flow	(1) Down- slope component of body force (2) gravitationally inverse density gradient; (3) vertical shear stress
Roosterberg (Cycle R4), Tanqua	Shelf-edge	Flame structure, load structure, intraformational fold (high amplitude)	Rapid sediment deposition; loading/unloading caused by delta progradation	Liquefaction and fluidization, slide	1) Gravitationally inverse density gradient; (2) vertical shear stress; (3) down- slope component of body force (restricited).

Heuningberg (Cycle H2), Laingsburg	Upper-slope; shelf-edge	Flame strucuture; load structure (rare); rafts and chaotic intervals.	Slope failure; loading/ unloading caused by debris flow incisions or by delta progradation; rapid sediment deposition	Liquefaction and fluidization; mass flow; brittle deformation (rare)	(1) Non-uniform distribution of the confining load; (2) down-slope component of body force; (3) vertical shear stress
Heuningberg (Cycle H3), Laingsburg	Shelf-edge	Flame structure; load structure; foundering structure; contorted sandstone.	Rapid sediment deposition; slope or channel margin failure.	Liquefaction and fluidization; mass flow (?)	(1) Vertical shear stress; (2) gravitationally inverse density gradient; (3) down- slope component of body force (restricited).
Heuningberg (Cycle H4), Laingsburg	Shelf	Load structure; flame structure; sandstone rafts (rare); foundering	Rapid sediment deposition	Liquefaction and fluidization	1) Vertical shear stress; (2) gravitationally inverse density gradient; (3) down- slope component of body force (restricited).
Zoutkloof, Laingsburg	Shelf to shelf-edge	Flame structure; load structure; squeezed bed; contorted blocks and rafts	Rapid sediment deposition; slope failure	Liquefaction and fluidization; mass flow; liquefied intrusion	1) Vertical and lateral shear stress; (2) non-uniform distribution of the confining load; (3) down- slope component of body force
Buffels River, Laingsburg	Shelf-edge; upper slope (?)	Contorted blocks and rafts; flame structure and load structure (restricted)	Slope failure	Liquefaction and fluidization; mass flow	(1) Down- slope component of body force; (2) Vertical shear stress; (3) gravitationally inverse density gradient
Puesto Seguel, Neuquén	Delta	Flame structure, fault	Loading/ unloading caused by delta progradation	Liquefaction and fluidization	(1) Vertical shear stress; (2) non-uniform distribution of the confining load; 3) down- slope component of body force.

Table 6.3: Summary of the deformational processes associated with each study interval. *The term 'flame structure' includes the associated ruptured and folded sandstone, and the structureless bed. **The term 'load structure' includes load casts, pseudonodules, ball-and-pillow and pillar-and-dish structures.

Trigger Mechanisms - Karoo and Neuquén Outcrops			
Type of trigger	Depositional environment		
	Lower-slope	Upper-slope/ shelf-edge	Shelf / Delta
Oversteepening	(Y)		Y
Rapid sediment deposition	Y	Y	Y
Failure (slope)	(Y)	Y	(Y)
Loading/unloading due to delta/mouth bar progradation		Y	
Failure of channel margin (?)	Y	Y	
Earthquake (?)	Y		

Table 6.4: Summary of the trigger mechanisms interpreted in the Karoo and Neuquén basins considering the depositional environment.

Deformation mechanism	Depositional environment		
	Lower-slope	Upper-slope/ shelf-edge	Shelf / Delta
Liquefaction	Y	Y	Y
Fluidization	Y	Y	Y
Liquefied intrusion (?)		Y	
Slide	Y		
Mass Flow (debris flow, liquefied flow)	Y	Y	
Brittle deformation	Y	Y	

Table 6.5: Summary of the deformation mechanisms interpreted for soft-sediment deformation in relation to depositional profile position, Karoo and Neuquén basins.

The driving forces, although identified as crucial for the generation of soft-sediment deformation (Lowe, 1975), have only recently been systematically separated as the third component necessary for the development of soft-sediment deformation structures (Allen, 1982; Owen, 1987, 1996b). The interpreted driving forces are represented in Table 6.6 and can be separated into two groups: (1) forces related to the generation of *in situ* deformation structures: gravitationally inverse density gradient, vertical/normal shear stress and non-uniform distribution of the confining load; (2) down-slope component of body force associated with detached deformation structures, that are equivalent to gravity driven processes and the related mass movement described by Varnes (1958) and Mulder & Cochonat (1996).

Secondarily, hydraulic fracturing drove the deformation in a rare occurrence of mud injection in Chacay Melehue.

Driving forces	Depositional environment		
	Lower-slope	Middle-slope/ shelf-edge	Shelf / Delta
Gravitationally inverse density gradient	Y	Y	Y
Vertical/normal shear stress	Y	Y	Y
Non-uniform distribution of the confining load	Y	Y	
Down-slope component of body force	Y	Y	Y
Hydraulic fracturing	Y		

Table 6.6: Summary of driving forces interpreted for soft-sediment deformation features in relation to depositional profile position, Karoo and Neuquén basins.

The position of sea level exerts a fundamental control on sedimentation patterns and soft-sediment deformation processes, and therefore the stratigraphic distribution of deformation features in the shelf and slope areas (Posamentier *et al.*, 1988; Posamentier & Vail, 1988; Posamentier *et* al., 1992; Trincard & Field, 1992; Kolla *et al.*, 2000; McHugh *et al.*, 2002). In particular, the progradation of deltas to the shelf-edge is interpreted as occurring in the late stage of the base-level fall and in stages of early base level rise, while gravity flows record a maximum during late stage of forced regression and a minimum during the highstand normal regression (Porębski & Steel, 2003).

The sand-prone shelf-edge components of clinoforms (cycles) studied in Tanqua and Laingsburg depocentres have the highest concentration of soft-sediment deformation features and are interpreted as deposited during the falling stage and lowstand system tracts in a progradational/aggradational character similar to type D shelf-edges from Steel *et al.* (2003) (cf. Figure 1.22). In this case, it is suggested that deposition and soft-sediment deformation occurred in the upper-slope/shelf-edge during time of high sediment supply, but with minor amounts of sediment bypass to the lower-slope and basin floor. This is indicated by the absence of widespread incisions and down-dip sand-prone fans. Wild (2005), studying the shelf-edge deposits of the Tanqua depocentre, related the transition from the point-sourced sand-rich basin-floor fan deposits of the Skoorsteenberg Formation to the shelf-edge deposits of the Kookfontein Formation to be associated with a shallowing and

lengthening of the slope. This resulted in a decrease in sediment transport efficiency to the basin-floor and a transition from incision and bypass processes to sediment accretion, which is an additional factor controlling deposition and deformation in the upper-slope/shelf-edge setting.

6.3 – Comparative analysis of the statistical response

In chapters 3 and 4, the statistical behaviour of the dimensions for different geometric components of flame structures was discussed by the use of cross plots, correlation and regression analysis. A statistical approach aids interpretation of the timing of deformation, the predicted length scales of the deformation products, and the identification of relationships between different geometric parameters. In this section, the best fit regression lines (sometimes extrapolated for better comparison with other regression lines) for each pair of characteristics in each interval of deformation are analysed with the objective of identifying differences and similarities in the shapes of products and deformational processes (Figure 6.3). The least-square regression line and the regression line equation, and values of correlation and coefficient of determination (r^2) for the total of the samples are represented in each plot. Normally this combined regression line is strongly influenced by the greater amount of data from the Waterfall interval. The graphs just represent the extrapolation of the regression lines; the distribution of the points in each class is represented in figures 3.15 (Waterfall), 3.28 (Fortin), 4.36 (Roosterberg), 4.37 (Heuningberg and others in the Laingsburg depocentre) and 4.48 (Puesto Seguel). Appendix 4 shows graphs with individual beds. In all these cases graphs are respecting the limits of data occurrence and, therefore, can be used to elucidate questions about data extrapolation.

Distance between adjacent flames (DN) *versus* basal width of flames (BW)

Figure 6.3a presents the least-square regression lines for all study intervals. The results for the Karoo outcrops (Waterfall, Roosterberg and Heuningberg) are similar despite different depositional environments that the host sediments were deposited in (from lower slope to shelf-edge delta). The orientation of the regression line of Fortin 1° de Mayo is influenced by the small number of sample flames and by

an 'anomalous' value (cf. Chapter 3.2.2 and Figure 3.28), although the distribution of the other pairs are similar to the Karoo trend. The least-square regression for Puesto Seguel presents a divergent trend in relation to the Karoo group but the correlation is based on a large amount of data and without the influence of anomalous values. The cause of this difference can be related to factors associated with the nucleation of flames such as material rheology, layer thickness, previous discontinuities, grain size and pore pressure differences (cf. Chapter 3.1). Among the studied outcrops, Puesto Seguel is the only one that presents a clear normal fault in the transition from deformed to undeformed sediments. This can be an indicator of differences associated with sediment rheology that influenced the nucleation of flames.

Deformed layer thickness (UT) *versus* flame height (FH)

Several authors have indicated a direct relationship between the bed thickness and the dimensions of the deformation structures (see Chapter 3.1; Anketell & Dżułyński, 1968; Anketell *et al.*, 1970; Allen, 1985a, b; Nichols *et al.*, 1994; Owen, 1996b; Hindmarsh & Rijsdijk, 2000; Rijsdijk, 2001) but little work has been attempted to quantify this relationship (Allen, 1985b). The results obtained through the statistical analysis (Figure 6.3b) indicate a high degree of similarity between the behaviour of the flames from Waterfall, Heuningberg and Puesto Seguel despite different depositional conditions and deformation controls. Again, the data from Fortin 1° de Mayo show an atypical behaviour that can be explained by the small number of samples obtained in this interval (cf. Figure 3.28). The trend of Roosterberg is slightly different from the average trend and a possible explanation for this can be related to the much larger thickness of the deformed beds, that can reach up to 5 m (cf. Figure 4.36) when compared to the other outcrops where maximum thickness reaches no more than 2 m (cf. Figures 3.15, 4.37 and 4.48).It is important to have in mind that the linearity of the relationships will not necessarily be the same at larger scales. Due to the low amount of very large scale structures it was not possible to verify the consistency of the result for such scale. See discussion ahead about the range of scale for *in situ* soft-sediment deformation structures.

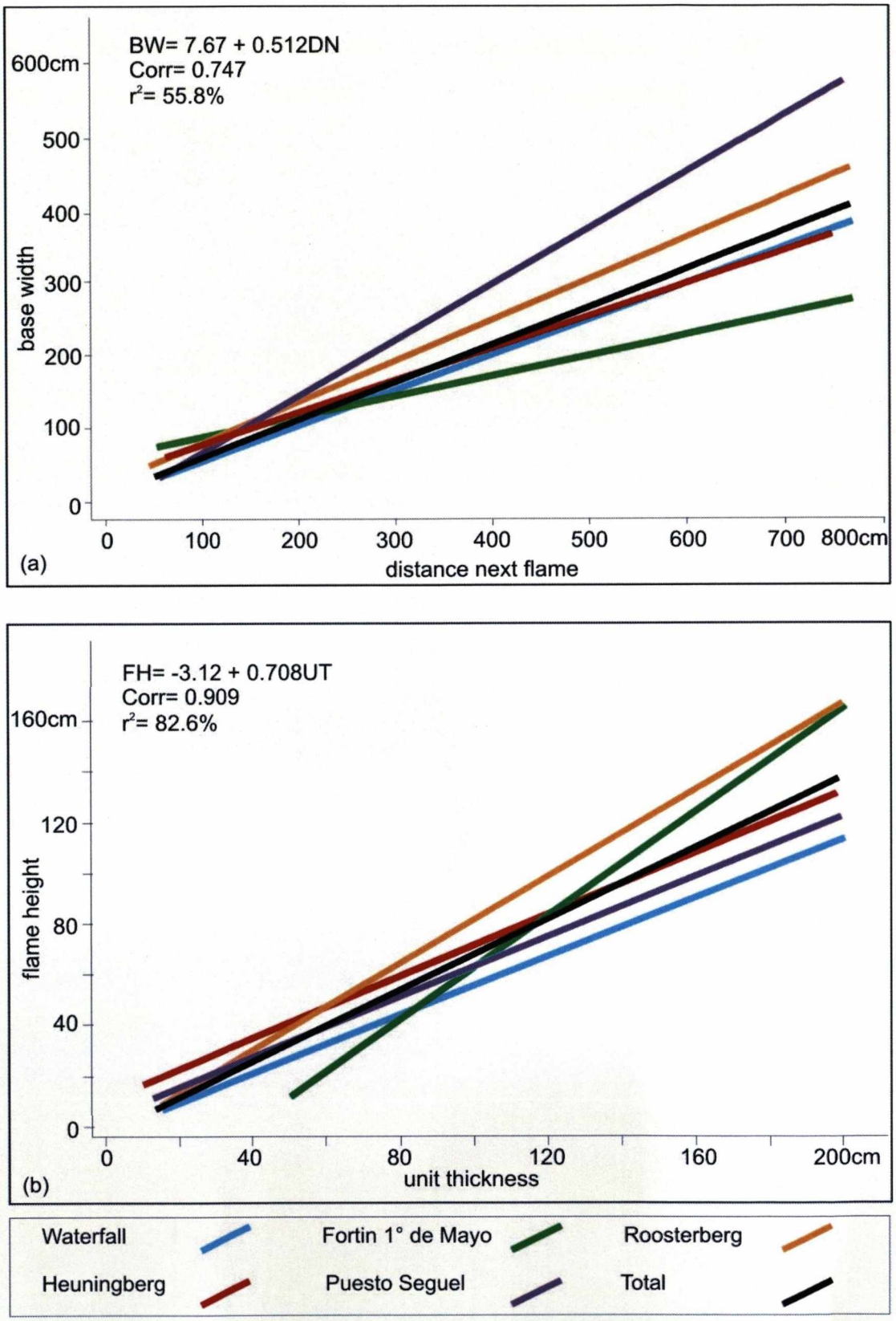

Figure 6.3: Plot of the best fit regression line for the each sampled interval and the response for all intervals together (black line) for the following relations: (a) distance between adjacent flames (DN) versus basal width of flames (BW); (b) deformed layer thickness (UT) versus flame height (FH).

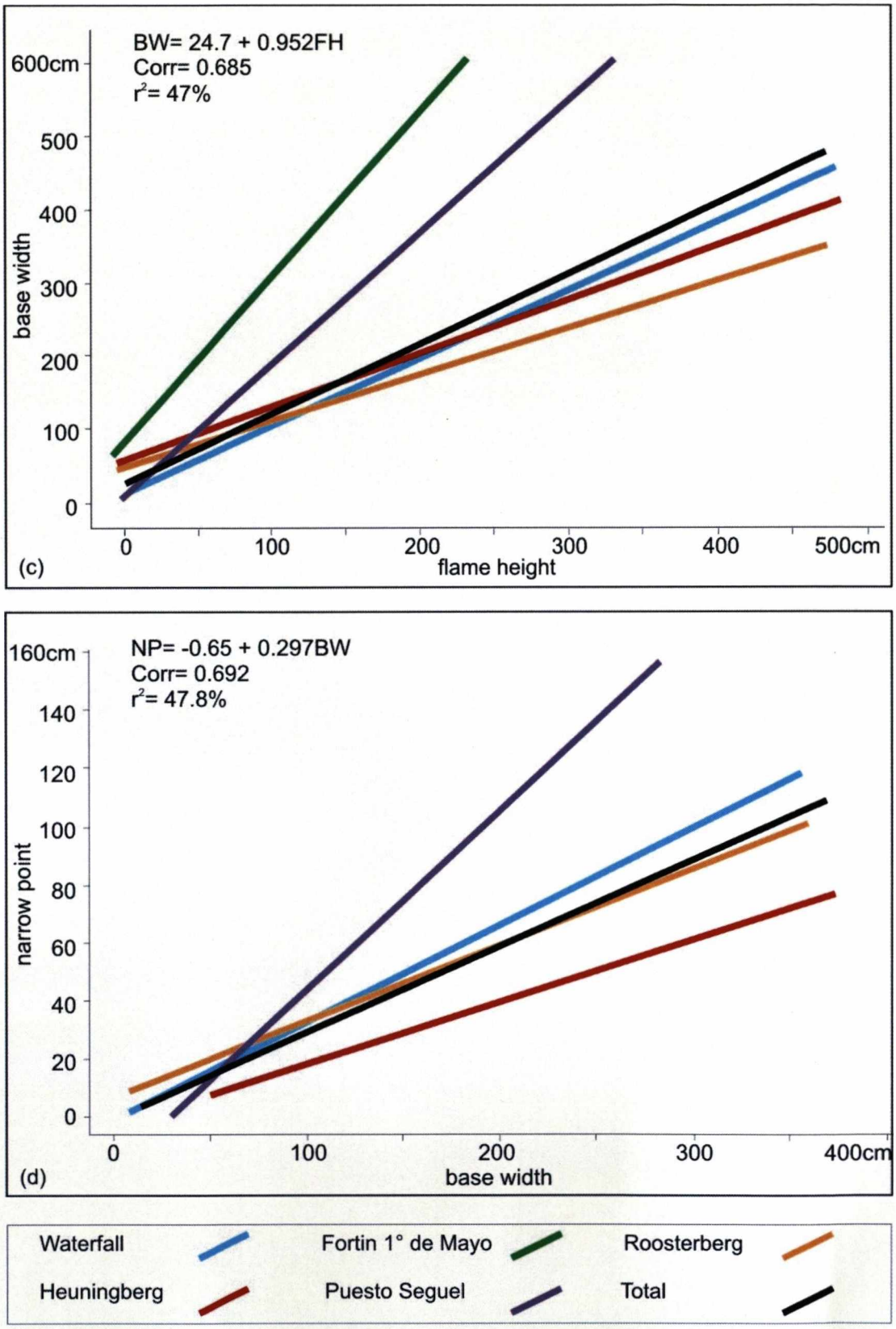

Figure 6.3 (cont): (c) flame height (FH) versus flame basal width (BW); (d) flame basal width (BW) versus flame narrowest point (NP). Each colour represents one of the study intervals (see key above). The regression line equation, the correlation and the square of correlation (r2) in the left upper side of each graph are related to the total number of samples.

The UT/FH ratio for the total of the samples is approximately 3:2 and can be considered as a good approximation for the quantification of this relationship. However, two facts need to be considered during the analysis of these parameters. First, the thickness of the deformed bed that will be a function of whether material transported upward through the flame is deposited on the seabed, as discussed in Chapter 3.1.4 and 4.1.6 (cf. Figure 4.38), and consequently could influence the statistical relationship. Second, it was noticed that when considering sub-groups from each population (e.g. Figures 4.37, 4.48, and Appendix 4) there is a tendency for a trend different from the one observed for the whole population. It is interpreted that this is a function of the regular/constant thickness of the intervals which normally results in a steep regression line. To avoid this problem it is necessary to sample different intervals with distinct thicknesses in the same area.

Flame height (FH) *versus* flame basal width (BW)

The Karoo and Neuquén datasets show two distinct trends for this relationship (Figure 6.3c). According to the graph, for the same width of flame there is a tendency for shorter flames in the Neuquén case, interpreted to be caused by differences in the composition and grain size, as discussed in Chapter 3.2.2. In general, the occurrences from Neuquén involve a coarser grain size and less intercalated fines than the examples found in the Karoo Basin, which could imply restrictions to the upward migration of the particles, producing "shorter" flames ($< \frac{FH}{BW}$) compared to the ones from the Karoo.

Flame basal width (BW) *versus* flame narrowest point (NP)

In this case the different trends of the least-square regression lines are intrinsically related to the flame type (cf. Figure 3.8, 3.16) and were discussed in details in the respective sections in Chapters 3 and 4. Figure 6.3d shows the distinct trends as a function of the dominant style of flame. As the Waterfall and Roosterberg data present flames of different types, the regression line is positioned without any preferential trend (cf. Figures 3.15 and 4.36). In contrast, the regression lines for Heuningberg and Puesto Seguel deviate from the general trend (black line) because they are richer in types 3 and 4, and type 1 flame structures, respectively.

Range of scale of the *in situ* soft-sediment deformation structures

In general, the consistency of the results presented in Figure 6.3 suggests that flames that originated in different environments and with different scales can have similar final configuration of measurable parameters. Anketell *et al.* (1970) made a similar observation from tens of laboratory experiments with reversed density gradient. The structures developed in each experiment were essentially similar even though the compositions of the model materials used were different, suggesting that such materials can behave in a similar manner under deformation. More tests must be done with other populations, but the behaviour found in the present analysis suggests that, under certain basic conditions (cf. Section 3.1.5), the deformation style and dimensions in different depositional settings might be predictable at distinct scales.

Figure 6.4 illustrates a hypothetical situation where the dimensions of two geometrical attributes of one regular structure present a linear relationship, analogous to the results obtained from the studied flame structures. The scales of sampling of each of the discussed methods were plotted considering the observations and discussions in Chapter 5. Taking as an example the dimensions of the flame structures, these range from 0.03 to 5 m. For structures outside of this range it would be necessary to use other methods (Figure 6.4). Chapter 5 discussed the application of serial slices and tomographic studies for scales sub-outcrop, and in addition these techniques can provide information on the 3D shape of the deformed units.

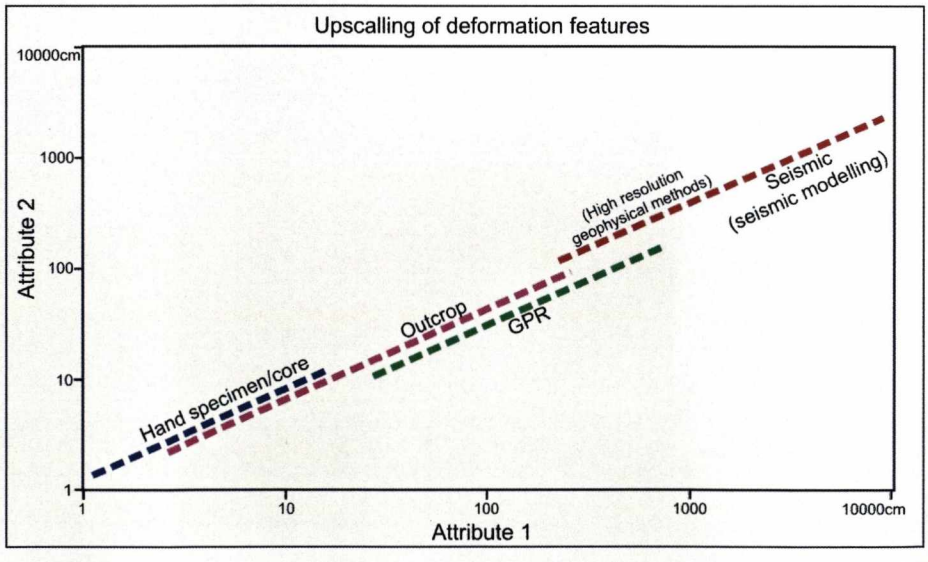

Figure 6.4: Hypothetical view of a linear relation between two attributes and the range of scale covered by each one of the methods used or discussed in this thesis. See text for discussion.

For larger scales, despite the seismic modelling suggesting that large flame structures at outcrop scale can be registered by high resolution geophysical methods, care must be taken in order to avoid the incorrect interpretation of very large structures using seismic data without the background of field observations.

Chapter 7: Conclusion and Recommendations

7.1 General conclusions

The objectives and key questions stated at the beginning of this thesis (Section 1.1.2) are used here to frame presentation of the pertinent scientific conclusions resulting from this research.

7.1.1 Pre-requisite conditions and processes

1. *What are the most common types of SSDS found between the shelf-edge and the lower slope?*

Eight classes of soft-sediment deformation structures (SSDS) associations were recognised in this study, some of which are widely reported in the literature, while others, such as the association of *in situ* SSDS with the latter stages of mass movement, are not. In this case deformation is associated with deposition of thick sandstone packages over unconsolidated muddy slump/debrite facies, causing foundering of the sand into the mass movement deposit or causing deformation of the sandstone by fluid escape from the underlying bed. Seven types of flame structures were defined based on statistically significant differences in geometry. The main control on shape is considered to be the degree of fluidization and flame maturity.

2. *What criteria can be used to differentiate detached vs. in situ structures?*

In situ soft-sediment deformation structures can be easily mistaken for translational structures in subsurface data (core, well and seismic) if not carefully analysed and can result in a misinterpretation of the depositional/deformational environment. In this study it was observed that processes resulting in intense deformation of several metre-thick successions in submarine slope settings can occur *in situ* without significant downslope dislocation of the sedimentary pile. Criteria to identify *in situ* structures include vertical positioning of folds and deformation features (no lateral shear), preferential orientation of the structures and the lateral passage of deformed beds into undeformed strata without truncation. *In situ* SSDS may breech the sea floor, producing local seabed topography due to debouching of fine grained material through flames onto the sea bed. The seabed topography could then influence overriding sediment-laden gravity currents.

3. *What are the pre-requisite conditions and trigger mechanisms that govern the initiation of deformation that forms distinct soft- sediment deformation structures?*

Loading due to rapid sediment deposition, with a component of local steeper gradients in the slope, is the interpreted overall trigger for deformation, based on detailed stratigraphic analysis and the distribution of the SSDS. In the datasets used there was no evidence of seismicity.

The narrow grain size range, mainly in the Karoo deposits, and the interbedded siltstone and fine-grained sandstone turbidites are considered fundamental to establish suitable pre-requisite conditions for soft-sediment deformation to occur. Comparison of the results from the Karoo and Neuquén datasets indicates that flame height may be controlled by grain size; the coarser grained Neuquén systems have shorter flames than the fine-grained sandstone Karoo deposits. More work is required to substantiate this finding.

4. *What processes and stress conditions acted during the deformation?*

Liquefaction and fluidization were largely the main deformation mechanisms that governed the *in situ*-soft sediment deformation structures. These two processes also occur associated with slides and mass flows that produced the detached soft-sediment deformation structures.

Normal compressive and normal shear stresses were associated with the origin of *in situ*-soft sediment deformation structures, while lateral stresses were associated with the origin of detached soft-sediment structures. Naturally mixed structures could be generated where the different stresses are combined. Soft-sediment deformation structures evolve through several stages as a process continuum depending on the boundary condition, and examples of each stage can be misinterpreted as different structures. This thesis has reconstructed the evolutionary stages of development of these features.

The proposed classification system is data driven, based on detailed measurements and statistical assessment of the products of deformation processes within well documented depositional and stratigraphic contexts. This system provides a reliable link between different structures. Four types of deformation product, not explicitly present in published classifications include (1) structureless; (2) ruptured and folded sandstones; (3) convolute bed and (4) squeezed structures.

5. *What type of force could amplify or conduct the deformation?*

The interpreted low angle slope in the Karoo Basin seems to be the major factor that dictated the style of the soft-sediment deformation structures in the Karoo system. *In situ* SSDS are produced by a gravitational inverse density gradient concomitant with vertical shear stress promoted by fluidization. This work has highlighted the importance of the downslope component of body force as a third component in oriented structures.

7.1.2 Stratigraphic and geographic distributions

1. *What is the preferential stratigraphic and profile position for the occurrence of SSDS?*

Similar structures are produced in different depositional environments. This indicates that independently of the trigger mechanism, similar rheological conditions can occur during the soft-sediment deformation process. In this study *in situ* and detached deformation structures are identified in deposits from shelf-edge to base of slope settings and consequently cannot be used independently to define the depositional environment.

Soft-sediment deformation is stratigraphicaly controlled in shelf-edge deltas of the Tanqua depocentre. The same succession of facies is found in all cycles and comprises: (1) basal section of coarsening-upward interbedded siltstone-sandstone, with subordinate soft-sediment deformation; (2) intermediate deformed interval showing the predominance of deformed transported facies over *in situ* deformed facies; and (3) upper section of undeformed thick, planar-laminated to cross-stratified sandstone. This succession is considered as the result of the migration of a delta onto and sometimes over the shelf-edge resulting in: (i) initial deposition of turbidites on the upper slope; (ii) followed by a deformed sedimentary package originating from the failure of the delta front when it reached the shelf-edge/upper slope and (iii) mouth bar/shoreface deposited above the failed material.

The internal organization of the Karoo deltas is similar to that in the Pliocene of Mississipi Canyon with deformed intervals in upper slope deposits; this situation differs from the Eocene of Spitsbergen where soft-sediment deformation is concentrated in the lower- and middle-slope. The explanation for this difference can

be related to the high slope gradient in Spitsbergen (3°-4°) if compared with the Karoo (~ 0.5°). In Spitsbergen the presence of distributary channels and chutes transported sediment through the shelf-edge region to be deposited on the slope. In the lower gradient Karoo systems, chutes, channels and canyons crossing the shelf-edge are rarely identified, which implies that deposition/deformation was concentrated in the shelf-edge and upper slope. This relatively low slope gradient may also explain the absence of growth faults in the Karoo system.

Although the scale of individual SSDS in shelf-edge delta deposits are larger in the Tanqua area the actual degree of disorganization with abrupt lateral transition of the deformed facies is greater in the Laingsburg depocentre. Ongoing stratigraphic work (Flint, 2008, *pers. comm.*) suggests that the Tanqua margin was of lower gradient than at Laingsburg and the finding from this thesis provide independent support to this hypothesis. Generically, this indicates that scale of individual SSD intervals does not necessarily equate with a higher degree of deformation.

2. *Are* in situ *and detached structures associated? If so, what is the spatio-temporal nature of this relationship?*

In low gradient settings, the products of detached deformation (slumps, slides, MTDs) can be accreted onto the upper slope, and *in situ* deformed strata stay 'attached'. In high gradient settings *in situ* deformation may develop in detached flows, sometimes leading to transformation into turbidity currents. This could lead to a stratigraphic paradox where more detached and *in situ* deformation structures are found in lower gradient settings because they are not preserved on higher gradient margins. Also, the scale and number of deformation structures need not correlate to the seismicity and/or gradient of a basin margin.

3. *Do SSDS follow a preferential orientation?*

Orientation of flame structures is poorly reported in the literature but the studied examples have preferential orientations which provide information on the dynamics of the depositional/deformational environment as well as local stress conditions during formation.

7.1.3 Scale of occurrence

1. *Are the large scale in situ soft-sediment deformation features observable on seismic sections? Can these structures be misidentified as detached (mass transport deposits) in seismic sections?*

Morphology of flame structures is independent of outcrop scale, as shown by statistical relationships. This characteristic allows prediction of the dimension/geometry of flame structures at outcrop scale. Extrapolation to scales below or above the range of outcrop limits must be done with care. The methodological basis for the evaluation of these out of outcrop scale situations are initiated here but still need to be effectively evaluated. From this study it is considered likely that some of the chaotic features observed in seismic sections can have a component of *in situ* soft-sediment deformation. Although seismic modelling indicated possible response of *in situ* soft-sediment deformation structures to the method, more work needs to be done in order to evaluate this possibility.

2. *What methods could be used to the study of features below and above the average outcrop scale?*

For samples below outcrop scale, serial sections show that macro-scale *in situ* deformation can actually include micro-scale translational movement. This is particularly new in relation to load structures; the lateral migration of pseudonodules is described in the literature as associated with the process of foundering but this study has found that detached pseudonodules are elongated parallel to direction of movement.

3. *Are the* in situ *structures predictable at different scales?*

At least at outcrop scale, the statistical studies indicated a consistent relationship between geometrical parameters, resulting in proportional dimensions at different scales particularly in the case of flame structures. Structures produced in bothj shelf-edge and lower slope deposits are similar, which indicate that same rheological conditions occur in a variety of settings.

7.2 Recommendations

A. The methodology proposed with the use of statistical analyses in the study of morphology and processes related to flames must be tested on different datasets in order to confirm if the final configuration of the flames can be predicted independently of the depositional setting.

B. More work is required to test the apparent sensitivity of SSDS morphology to grain size and lithology. The volume and pressure of pore water prior to deformation is a key control on the style and scale of deformation, and this will be a function of grain-size, packing, and pore shape. Possible laboratory testing could be considered to investigate these parameters further.

C. Physical modelling of the specific geological situations is recommended. For example, to test interpretations such as: (i) Waterfall flame structures controlled by palaeotopography; (ii) Fortin Primero de Mayo flame structures associated with local unconformities; (iii) Generation of sea bed topography by debouching of sediment due to fluid escape; (iv) 3D analysis of the effect of compensation by the distribution of flame structures at different stratigraphic levels.

D. For the Karoo study area, this was the first work on the soft-sediment deformation structures and their sedimentological setting. There is scope to extend the studies more widely across the Laingsburg depocentre, in tandem with further stratigraphic studies.

E. Based on the encouraging results of seismic modelling, a new research direction would be the acquisition and analysis of ultra-high frequency shallow seismic reflection surveys for the first hundred metres of the sea-bottom in targeted slope environments to investigate the occurrence and morphology of *in situ* SSDS as identified in this work. A linked objective would be to find and study present day examples of debouching of soft-sediment material through flames onto the sea bed, and the extent to which such processes are related to gas escape pockmarks and other such features.

References

Abbot, D.H.; Embley, R.W. & Hobart, M.A. (1985) Correlation of shear strength, hydraulic conductivity, and thermal gradients with sediment disturbance: South Pass region, Mississippi Delta. *Geo-Marine Letters*, **5**, 113-119.

Adams, E.W. & Schlager, W. (2000). Basic types of submarine slope curvature. *Journal of Sedimentary Research*, **20**, 814-828.

Aksu, A.E. & Piper, D.J.W. (1983) Progradation of Late Quaternary Gediz delta, Turkey. *Marine Geology*, **54**, 1-25.

Alexander, J. (1987) Syn-sedimentary and burial related deformation in the Middle Jurassic non-marine formations of theYorkshire Basin. *In:* Jones, M.E. & Preston, R.M.F. (eds) *Deformation of sediments and sedimentary rocks.* Geological Society, London, Special Publications, **29**, 315-324.

Alfaro, P., Delgado, J., Estévez, A., Molina, J.M., Moretti, M. & Soria, J.M. (2002) Liquefaction and fluidization structures in Messinian storm deposits (Bajo Segura Basin, Betic Cordillera, southern Spain). *International Journal of Earth Sciences*, **91**, 505-513.

Allen, J.R.L. (1977) The possible mechanics of convolute lamination in graded sand beds. *Journal of the Geological Society*, **134**, 19-31.

Allen, J.R.L. (1982) *Sedimentary Structures: Their Character and Physical Basis.* Developments in Sedimentology, 30. Elsevier, Amsterdam, vol 2, 663p.

Allen, J.R.L. (1985a) *Principles of Physical Sedimentology.* Chapman & Hall, London, 272p.

Allen, J.R.L. (1985b) Wrinkle marks: an intertidal sedimentary structure due to aseismic soft-sediment loading. *Sedimentary Geology*, **41**, 75-95.

Allen, J.R.L. (1994) Fundamental properties of fluids and their relation to sediment transport processes. *In:* Pye, K (ed.) *Sediment Transport and Depositional Processes.* Blackweel Scientific Publication, 25-60.

Ambraseys, N & Sarma, S. (1969) Liquefaction of soils induced by earthquakes. *Bulletin of the Seismological Society of America*, **59**, 651-664.

Anderson, J.B. & Thomas, M.A. (1991) Marine ice-sheet decoupling as a mechanism for rapid, episodic sea-level change: the record of such events and their influence on sedimentation. *Sedimentary Geology*, **70**, 87-104.

Anketell, J.M. & Dżułyński, S. (1968) Transverse deformational patterns in unstable sediments. *Annales de la Societe Geologique de Pologne*, **38**, 411-416.

Anketell, J.M., Cegła, J. & Dżułyński, S. (1969) Unconformable surfaces formed in the absence of current erosion. *Geologica Romana*, **8**, 41-46.

Anketell, J.M., Cegła, J. &, Dżułyński, S. (1970) On the deformational structures in systems with reverse density gradients. *Annales de la Societe Geologique de Pologne*, **40**, 3-30.

Bakker, M.A.J. & Van der Meer, J.J.M. (2003) Structure of a Pleistocene push moraine revealed by GPR: the eastern Veluwe Ridge, The Netherland. *In*: Bristow, C.S. & Jol, H.M. (eds) *Ground Penetrating Radar in Sediments*. Geological Society, London, Special Publication, **211**, 143-151.

Baysal, E., Kosloff, D.D. & Sherwood, J.W.C. (1983) Reverse time migration. *Geophysics*, **48**, 1514-1524.

Beaubouef, R.T. & Friedmann, S.J. (2000) High resolution seismic/sequence stratigraphic framework for the evaluation of Pleistocene intra slope basins, Western Gulf of Mexico: depositionsl models and reservoir analogs. *In:* Weimer, P., Slatt, R.M., Coleman, J., Rosen, N.C., Nelson, H., Bouma, A.H., Styzen, M.J. & Lawrence, D.T. (eds) *Deep-water Reservoirs of the World.* GCSSEPM Foundation 20th Annual Bob F. Perkins Research Conference, 40-60.

Bhattacharya, J.P. & Davies, R.K. (2001) Growth faults at the prodelta to delta-front transition, Cretaceous Ferron sandstone, Utah. *Marine and Petroleum Geology*, **18**, 525-534.

Bitzer, K., Salas, J. & Ayora, C. (2000) Fluid pressure, flow velocities and transport processes in a consolidating sedimentary column with transient hydraulic properties. *Journal of Geochemical Exploration*, **69-70**, 127-131.

Bouma, A.H. (1979) Continental slopes. *In*: Doyle, L.J. & Pilkey, O.H. (eds) *Geology of Continental Slopes*. Society of Economic Paleontologists and Mineralogists, Special Publication, **27**, 1-15.

Brenchley, P.J. & Newall, G. (1977) The significance of contorted bedding in the Upper Ordovician sediments of the Oslo region, Norway. *Journal of Sedimentary Petrology*, **47**, 819-833.

Brink, K.H., Bane, J.M., Church, T.M., *et al.* (1992) *Coastal Ocean Processes: a Science Prospectus*. Technical Report WHOI-92-18, Woods Hole Oceanographic Institute, 88p.

Brown, A.R. (1993) *Interpretation of Three-Dimensional Seismic Data*. American Association of Petroleum Geologists Memoirs, **42**, 2-3.

Burgess, P.M. & Flint, S.S. (1998) *Sequence Stratigraphy of Jurassic Turbidite Systems in the Neuquen Basin, Argentina: A combined outcrop and subsurface study*. Final Report, StratGroup, University of Liverpool.

Burgess, P.M. & Hovius, N. (1998) Rates of delta progradation during high stands: consequences for timing and deposition in deep-marine systems. *Journal of the Geological Society*, **155**, 217-222.

Burgess, P.M., Flint, S.S. & Johnson, S. (2000) Sequence stratigraphic interpretation of turbidite strata: An example from Jurassic strata of the Neuquén basin, Argentina. *Geological Society of America Bulletin*, **112**, 1650-1666.

Butler, R.W.H. & Tavarnelli, E. (2006) The structure and kinematics of substrate entrainment into high-concentration sandy turbidites: a field example from Gorgoglione "flysch" of southern Italy. *Sedimentology*, **53**, 655-670.

Canals, M., Lastras, G., Urgeles, R., Casamor, J.L., Mienert, J., Cattaneo, A., De Batist, M., Haflidason, H., Imbo, Y., Laberg, J.S., Locat, J., Long, D., Longva, O., Masson, D.G., Sultan, N., Trincardi, F. & Bryn, P. (2004) Slope failure dynamics and impacts from seafloor and shallow sub-seafloor geophysical data: case studies from COSTA Project. *Marine Geology*, **213**, 9-72.

Casas, D., Ercilla, G., Baraza, J., Alonso, B. & Maldonado, A. (2003) Recent mass-movement processes on the Ebro continental slope (NW Mediterranean). *Marine and Petroleum Geology*, **20**, 445-457.

Catuneanu, O., Hancox, P.J. & Rubidge, B.S. (1998) Reciprocal flexural behaviour and contrasting stratigraphies: a new basin development model for the Karoo retroarc foreland system, South Africa. *Basin Research*, **10**, 417-439.

Charles, A.J. (2007) *Stratigraphic development and sedimentary processes in shelf-margin delta deposits: An example from the Fort Brown Formation, Karoo Basin, South Africa*. Unpubl. M.Sc. report, University of Liverpool, 21p.

Chatfield, C. (1989) *Statistics for Technology*, 3rd edition, Chapman and Hall, 381p.

Cheel, R.J. & Rust, B.R. (1986) A sequence of soft-sediment deformation (dewatering) structures in Late Quaternary subaqueous outwash near Otawa, Canada. *Sedimentary Geology*, **47**, 77-93.

Chen, G. & Hiscott, R.N. (1999a) Statistical analysis of facies clustering in submarine-fan turbidite succession. *Journal of Sedimentary Research*, **69**, 505-517.

Chen, G. & Hiscott, R.N. (1999b) Statistical analysis of turbidite cycles in submarine fan successions: tests for shot-term persistence. *Journal of Sedimentary Research*, **69**, 486-504.

Chopra, S. & Marfurt, K.J. (2008) Emerging and future trends in seismic attributes. *The Leading Edge*, **27**, 298-318.

Chopra, S., Castagna, J. & Portniaguine, O. (2006) Seismic resolution and thin-bed reflectivity inversion. *Recorder*, **31**, 19-25.

Cole, D.I. (1992) Evolution and development of the Karoo Basin. *In:* De Wit, M.J. & Ransome, I.G.D. (eds) *Inversion Tectonics of Cape Fold Belt, Karoo and Cretaceous Basins of Southern Africa*, Procèedings of the conference on inversion tectonics of the Cape Fold Belt, Cape Town, South Africa. A.A.Balkema, Rotterdam, 87-99.

Coleman, J.M. & Prior, D.B. (1988) Mass wasting on continental margins. *Annual Review Earth Planetary Science*, **16**, 101-119.

Coleman, J.M., Prior, D.B. & Lindsay, J.F. (1983) Deltaic influences on shelf edge instabilities processes. *In:* Stanley, D.J. & Moore, G.T. (eds) The Shelfbreak, Critical Interface on Continental Margins. Society of Economic Paleontologists and Mineralogistis, Special Publication, **33**, 121-137.

Collinson, J. (1994) Sedimentary deformational structures. *In:* Maltman, A.J. (ed) *The Geological Deformation of Sediments*. Chapman and Hall, London, 95-125.

Collinson, J. D., Martinsen, O., Bakken, B. & Kloster, A. (1991) Early fill of the Western Irish Namurian Basin: a complex relationship between turbidites and deltas. *Basin Research*, **3**, 223-242.

Cooper, M.R. (1994) *Diagenetic Evolution and Implications for the Reservoir Properties of Selected Shallow Marine and Aeolian Sandstones*. Unpubl. Ph.D. thesis, University of Liverpool, 184p.

Covault, J.A., Normark, W.R., Romans, B.W. & Graham, S.A. (2007) HIghstand fans in the California borderland: The overlooked deep-water deposition system. *Geology*, **35**, 783-786.

Cronin, B.T., Hartley, A.J., Celik, H., Hurst, A., Türkmen, I. & Kerey, E. (2000) Equilibrium profile development in graded deep-water slopes: Eocene, Eastern Turkey. *Journal of the Geological Society*, **157**, 943-955.

Dailly, G.C. (1983) Slope readjustment during sedimentation of continental margins. *In:* Watkins, J.S. & Drake, C.L. (eds) *Studies in continental marine geology*. American Association of Petroleum Geologists, Memoirs, **34**, 593-608.

Damuth, J.E. (1994) Neogene gravity tectonics and depositional processes on the deep Niger Delta continental margin. *Marine and Petroleum Geology*, **11**, 320-346.

Damuth, J.E. & Olson, H.C. (2001) Neogene-Quaternary contourite and related deposition on the West Shetland Slope and Faeroe-Shetland Channel revealed by high-resolution seismic studies. *Marine Geophysical Researches*, **22**, 369-399.

Dasgupta, P. (1998) Recumbent flame structures in the Lower Gondwana rocks of the Jharia Basin, India – a plausible origin. *Sedimentary Geology*, **119**, 253-261.

Davis, J.L. & Annan, A.P. (1989) Ground-penetrating radar for high-resolution mapping of soil and rock stratigraphy. *Geophysical Prospecting*, **37**, 531-551.

Davies, N.S., Turner, P. & Sansom, I.J. (2004) Soft-sediment deformation structures in the Late Silurian Stubdal Formation: the result of seismic triggering. *Norwegian Journal of Geology*, **85**, 233-243.

Davies, R.J. (2003) Kilometer-scale fluidization structures formed during early burial of a deep-water slope channel on the Niger Delta. *Geology*, **31**, 949-952.

De Beer, C.H. (1992) Structural evolution of the Cape Fold Belt syntaxis and its influence on syntectonic sedimentation in the SW Karoo Basin. *In:* De Wit, M.J. & Ransome, I.G.D. (eds) *Inversion Tectonics of Cape Fold Belt, Karoo and Cretaceous Basins of Southern Africa*, Proceedings of the conference on inversion tectonics of the Cape Fold Belt, Cape Town, South Africa. A.A.Balkema, Rotterdam, 197-206.

De Beer, C.H. (1995) Fold interference from simultaneous shortening in different directions: the Cape Fold Belt syntaxis. *Journal of African Earth Sciences*, **21**, 157-169.

De Wit, M.J. & Ransome, I.G.D. (1992) Regional inversion tectonics along the southern margin of Gondwana. *In:* De Wit, M.J. & Ransome, I.G.D. (eds) *Inversion Tectonics of Cape Fold Belt, Karoo and Cretaceous Basins of Southern Africa*, Proceedings of the conference on inversion tectonics of the Cape Fold Belt, Cape Town, South Africa. A.A.Balkema, Rotterdam, 15-21.

Dobry, R. & Liu, L. (1992) Centrifugue modeling of soil liquefaction. *Tenth World Conference on Earthquake Engineering*. Post-conference Proceedings, **11**, 6801-6809.

Duliu, O.G. (1999) Computer axial tomography in geosciences: an overview. *Earth-Science Reviews*, **48**, 265-281.

Dżułyński, S. & Walton, E.K. (1965) *Sedimentary Features of Flysch and Greywackes.* Developments in Sedimentology 7, Elsevier, Amsterdam, 274p.

Eddy Lee, Y.-D. & George, R.A. (2004) High resolution geological AUV survey results across a portion of the eastern Sigsbee Escarpment. *American Association of Petroleum Geologists Bulletin*, **88**, 747-764.

Edwards, M.B. (1976) Growth faults in Upper Triassic deltaic sediments, Svalbard. *American Association of Petroleum Geologists Bulletin*, **60**, 341-355.

Edwards, M.B. (1881) Upper Wilcox Rosita delta system of south Texas: growth-faulted shelf edge deltas. *American Association of Petroleum Geologists Bulletin*, **65**, 54-73.

Elliot, R.E. (1965) A classification of subaqueous sedimentary structures based on rheological and kinematical parameters. *Sedimentology*, **5**, 193-209.

Embley, R.W. (1980) The role of mass transport in the distribution and character of deep-ocean sediments with special reference to the North Atlantic. *Marine Geology*, **38**, 23-50.

Emery, K.O. (1980) Continental Margins – classification and petroleum prospects. *American Association of Petroleum Geologists*, **64**, 297-315.

Felletti, F. (2004) Statistical modelling and validation of correlation in turbidites: an example from the Tertiary Piedmont basin (Castagnola Fm., Northern Italy). *Marine and Petroleum Geology*, **21**, 23-39.

Fildani, A., Drinkwater, N.J., Weislogel, A., McHargue, T., Hodgson, D.M. & Flint, S.S. (2007) Age control on the Tanqua and Laingsburg deep-water systems: New insights on the evolution and sedimentary fill of the Karoo basin, South Africa. *Journal of Sedimentary Research*, **77**, 901-908.

Fiegel, G.L. & Kutter, B.L. (1994) Liquefaction mechanism for layered soils. *Journal of Geotechnical Engineering*, **120**, 737-775.

Flint, S.S., Hodgson, D.M., Sixsmith, P., Grecula, M. & Wickens, H. DeV. (2008) Deepwater basin floor/slope deposits of the Laingsburg Depocenter, Karoo Basin, South Africa. In: Nilsen, T., Shew, R, Stefans, G. and Studlick, J. (eds) *Atlas of Deepwater Outcrops*. American Association of Petroleum Geologists, **ST56**, 326-329.

Flint, S.S., Hodgson, D.M., King, R.C., Potts, G.J., van Lente, B. & Wild, R.J. (2004). *The Karoo Basin Slope Project: Phase 1*. Industry consortium report (unpublished), University of Liverpool, (CD-Rom).

Franzese, J.R. & Spalletti, L.A. (2001) Late Triassic-early Jurassic continental extension in southwestern Gondwana: tectonic segmentation and pre-break-up rifting. *Journal of South American Earth Sciences*, **14**, 257-270.

Franzese, J.R., Spalletti, L., Gómez Pérez, I. & Macdonald, D. (2003) Tectonic and paleoenvironmental evolution of Mesozoic sedimentary basins along the Andean foothills of Argentina (32° - 54°). *Journal of South American Earth Sciences*, **16**, 81-90.

Franzese, J.R., Veiga, G.D., Schwarz, E. & Gómez-Pérez, I. (2006) Tectonostratigraphic evolution of a Mesozoic graben border system: the Chachil depocentres, southern Neuquén Basin, Argentina. *Journal of the Geological Society*, **163**, 707-721.

Freije, H., Azúa, G., González, R., Ponce, J.J. & Zavala, C. (2002) Actividad tectónica sinsedimentaria en el Jurásico del sur de la Cuenca Neuquina. *V Congreso de Exploración y Desarrollo de Hidrocarburos*. Mar del Plata. Acta CD, 17p.

Galloway, W.E. (1998). Siliciclastic slope and base-of-slope depositional systems: component facies, stratigraphic architecture, and classification. *American Association of Petroleum Geologists Bulletin*, **82**, 627–643.

Gill, W.D. & Kuenen, P.H. (1957) Sand volcanoes on slumps in the Carboniferous of County Clare, Ireland. *Quarterly Journal of the Geological Society*, **113**, 441-460.

Goldhammer, R.K., Wickens, H. DeV., Bouma, A.H. & Wach, G. (2000) Sequence stratigraphic architecture of the Late Permian Tanqua submarine fan complex, Karoo Basin, South Africa. *In:* Bouma, H.D. & Stone, C.G. (eds) *Fine-Grained Turbidite Systems*. American Association of Petroleum Geologists, Memoir **72** and Society for Sedimentary Geology, Special Publication **68**, 165-172.

Greb, S.F. & Archer, A.W. (2007) Soft-sediment deformation produced by tides in a meizoseismic area, Trunagain Arm, Alaska. *Geology*, **35**, 435-438.

Grecula, M. (2000) *Stratigraphy and architecture of tectonically controlled turbidite systems: Laingsburg Formation, Karoo Basin, South Africa.* Unpubl. Ph.D. thesis, University of Liverpool, 291p.

Grecula, M., Flint, S., Potts, G., Wickens, H. DeV. & Johnson, S. (2003) Partial ponding of turbidite syatems in a basin with subtle growth-fold topography: Laingsburg-Karoo, South Africa. *Journal of Sedimentary Research*, **73**, 603-620.

Green, A., Gross, R., Holliger, K., Horstmeyer, H. & Baldwin, J. (2003) Results of 3-D georadar surveying and trenching the san Andreas fault near its northern landward limit. *Tectonophysics*, **368**, 7-23.

Gresse, P.G., Theron, J.N., Fitch, F.J. & Miller, J.A. (1992) Tectonic inversion and radiometric resetting of the basement in the Cape Fold Belt. *In:* De Wit, M.J. & Ransome, I.G.D. (eds) *Inversion Tectonics of Cape Fold Belt, Karoo and Cretaceous Basins of Southern Africa*, Proceedings of the conference on inversion tectonics of the Cape Fold Belt, Cape Town, South Africa. A.A.Balkema, Rotterdam, 217-228.

Gulisano, C. & Hinterwimer, G. (1986) Facies deltaicas del jurásico médio em El oeste del Neuquén. *Boletín de Informaciones Petroleras*, YPF, **8**, 2-32.

Hälbich, I.W., Fitch, F.J. & Miller, J.A. (1983) Dating the Cape orogeny. *In:* Söhnge, A.P.G. & Hälbich, I.W. (eds) *Geodynamics of the Cape Fold Belt.* Special Publication Geological Society South Africa, **12**, 149-165.

Harper, C.W. (1998) Thickening and/or thining upward patterns in sequences of strata: tests of significance. *Sedimentology*, **45**, 657-696.

Haughton, P.D.W. (1994) Deposits of deflected and ponded turbidity currents, Sorbas Basin, Southeast Spain. *Journal of Sedimentary Research*, **A64**, 233-246.

Hedberg, H.D. (1970) Continental margins from viewpoint of the petroleum geologist. *American Association of Petroleum Geologists Bulletin*, **54**, 3-43.

Heggland, R. (1998) Gas seepage as an indicator of deeper prospective reservoirs. A study based on exploration 3D seismic data. *Marine and Petroleum Geology*, **15**, 1-9.

Hildebrandt, C. & Egenhoff, S. (2007) Shallow-marine massive sandstone sheets as indicators of palaeoseismic liquefaction – An example from Ordovician shelf of Central Bolivia. *Sedimentary Geology*, **202**, 581-595.

Hindmarsh, R.C. & Rijsdijk, K.F. (2000) Use of a viscous model of till rheology to describe gravitational loading instabilities in glacial sediments. *In:* Maltman, A.J., Hubbard, B. & Hambley, M.J. (eds) *Deformation of Glacial Materials*. Geological Society, London, Special Publications, **176**, 191-201.

Hobbs, B.E., Means, W.D. & Williams, P.F. (1976) *An Outline of Structural Geology*. John Wiley & Sons, Inc. 571p.

Hodgetts, D., Drinkwater, N.J., Hodgson, D.M., Kavanagh, J., Flint, S.S., Keogh, K.J. & Howell, J.A. (2004) Three dimensional geological models from outcrop data using digital data collection techniques: an example from the Tanqua Karoo depocentre, South Africa. *In:* Curtis, A. & Wood, R. (eds) *Geological Prior Information Science and Engineering*. Geological Society, London, Special Publications, **239**, 57-75.

Hodgson, D.M., Flint, S.S., Hodgetts, D., Drinkwater, N.J., Johannessen, E.J. & Luthi, S.M. (2006) Stratigraphic evolution of fine-grained submarine fan systems, Tanqua depocenter, Karoo Basin South Africa. *Journal of Sedimentary Research*, **76**, 20-40.

Hovland, M., Judd, A.G. & King, L.H. (1984) Characteristics features of pockmarks on the North Sea Floor and Scotian Shelf. *Sedimentology*, **31**, 471-480.

Howard, J.D. & Lohrengel II, C.F. (1969) Large non-tectonic deformational structures from Upper Cretaceous rocks of Utah. *Journal of Sedimentary Petrology*, **39**, 1032-1039.

Howell, J.A., Schwarz, E., Spallletti, L.A. & Veiga, G.D. (2005) The Neuquén Basin: an overview. *In:* Veiga, G.D., Spallletti, L.A., Howell, J.A. & Schwarz, E. (eds) *The Neuquén Basin, Argentina: A Case Study in Sequence Stratigraphy and Basin Dynamics*. Geological Society, London, Special Publications, **252**, 1-14.

Jenner, K.A., Piper, D.J.W., Campbell, D.C. & Mosher, D.C. (2007) Lithofacies and origin of late Quaternary mass transport deposits in submarine canyons, central Scotian Slope, Canada. *Sedimentology*, **54**, 19-38.

Jervey, M.T. (1988) Quantitative geological modeling of siliciclastic rock sequences and their seismic expression. *In:* Wilgus, C.K., Hastings, B.S., Kendall, C.G.St.C.; Posamentier, H.W., Ross, C.A. & Van Wagoner, J.C. *Sea-level changes: an integrated approach*. Society of Economic Paleontologists and Mineralogists, Special Publication, **42**, 47-69.

Johnson, S.D., Flint, S.S., Hinds, D. & Wickens, H. DeV. (2001) Anatomy of basin floor to slope turbidite systems, Tanqua Karoo, South Africa: sedimentology, sequence stratigraphy and implications for the subsurface prediction. *Sedimentology*, **48**, 987-1023.

Jol, H.M. & Bristow, C.S. (2003) GPR in sediments: advice on data collection, basic processing and interpretation, a good practice guide. *In:* Bristow, C.S. & Jol, H.M. (eds) *Ground Penetrating Radar in Sediments*. Geological Society, London, Special Publication, **211**, 9-27.

Jolly, R.J.H. & Lonergan, L. (2002) Mechanisms and controls on the formation of sand intrusions. *Journal of Geological Society*, **159**, 605-617.

Jones, A.P. & Omoto, K. (2000) Towards establishing criteria for identifying trigger mechanisms for soft-sediment deformation: a case study of Late Pleistocene lacustrine sands and clays, Onikobe and Nakayamadaira basins, northeastern Japan. *Sedimentology*, **47**, 1211-1226.

Jones, M. (1994) Mechanical principles of sediment deformation. *In:* Maltman, A. (ed.) *The Geological Deformation of Sediments*, Chapman & Hall, 37-71.

Jordaan, M.J. (1981) The Ecca-Beaufort transition in the western parts of the Karoo basin. *Trans. Geol. Society of South Africa*, **84**, 19-25.

Ketcham, R.A. & Carlson, W.D. (2001) Acquisition, optimization and interpretation of X-ray computed tomographic imagery: applications to the geosciences. *Computers & Geosciences*, **27**, 381-400.

King, R.C. (2005) *The structural evolution of the Cape Fold Belt and SW Karoo Basin: implications on sediment storage and routeing to the SW Karoo Basin.* Unpubl. Ph.D. thesis, University of Liverpool, 327p.

Kleist, J.R. (1974) Deformation by soft-sediment extension in the coastal belt, Franciscan Complex. *Geology*, **2**, 501-504.

Kneller, B. (2003) The influence of flow parameters on turbidite slope channel architecture. *Marine and Petroleum Geology*, **20**, 901-910.

Kneller, B., Edwards, D., McCaffrey, W. & Moore, R. (1991) Oblique reflection of turbidity currents. *Geology*, **14**, 250-252.

Kolla, V., Biondi, P., Long, B. & Fillon, R. (2000) Sequence stratigraphy and architecture of the Late Pleistocene Lagniappe delta complex, northeast Gulf of Mexico. *In:* Hunt, D. & Gawthorpe, R.L. (eds) *Sedimentary Responses to Forced Regression.* Geological Society of London, Special Publications, **172**, 291-327.

Koslowski, E.E., Cruz, C.E. & Sylwan, C.A. (1996) Geologia structural de la zona de Chos Malal, Cuenca Neuquina, Argentina. *XIII Congreso Geologico Argentino y III Congreso de Exploración de Hidrocarburos*, **1**, 15-26.

Kuenen, P.H. (1958) Experiments in Geology. *Transactions of the Geological Society of Glasgow*, **23**, 1-28.

Kuenen, P.H. & Migliorini, C.I. (1950). Turbidity currents as a cause of graded bedding. *The Journal of Geology*, **58**, 91-127.

Kuribayashi, E. & Tatsuoka, F. (1975) Brief review of liquefaction during earthquakes in Japan. *Soil and foundation*, **15**, 81-92.

Lanés, S. (2005) Late Triassic to Early Jurassic sedimentation in northern Neuquén Basin, Argentina: Tectosedimentary evolution of the first transgression. *Geologica Acta*, **3**, 81-106.

Lash, G.G. (1985) Accretion-related deformation of an ancient (early Paleozoic) trench-fill deposit, central Appalachian orogen. *Geological Society of America Bulletin*, **96**, 1167-1178.

Leanza, H.A., Repol, D., Escosteguy, L. & Salvarredy Aranguren, M. (2003) *Estratigrafia Del Mesozóico em La Comarca de Fortín 1° de Mayo, cuenca Neuquina sudoccidental, Argentina.* Servicio Geológico Minero Argentino, Instituto de Geologia y Recursos Minerales, Buenos Aires, Serie Contribuiciones Técnicas – Geologia, **1**, 21p.

Lee, H.J., Locat, J., Desgagnés, P., Parsons, J.D., McAdoo, B.G., Orange, D.L., Puig, P., Wong, F.L., Dartnell, P. & Boulanger, E. (2007) Submarine mass movements on continental margins. *In:* Nittrouer, C.A., Austin Jr, J.A., Field, M.E., Kravitz, J.H., Syvitski, J.P.M. & Wiberg, P.L. (eds) *Continental Margin Sedimentation: From Sediment Transport to Sequence Stratigraphy.* International Association of Sedimentologists, Special Publication, **37**, 213-274.

Legarreta, L. & Gulisano, C.A. (1989) Análisis estratigráfico secuencial de la Cuenca Neuquina (Triásico suprior-Terciario inferior, Argentina) *In:* Chebli, G. & Spalletti, L. (eds) *Cuencas Sedimentarias Argentinas*. Serie Correlácion Geológica, Universidad Nacional de Tucumán, **6**, 221-243.

Legarreta, L. & Uliana, M.A. (1991) Jurassic-Cretaceous marine oscillations and geometry of back arc basin fill. Macdonald, D.I.M. (ed.) *Sedimentation, Tectonics and Eustasy – Sea-level Changes at Active Margins.* International Association of Sedimentologists, Special Publications, **12**, 429-450.

Legarreta, L. & Uliana, M.A. (1996) The Jurassic succession in the west-central Argentina: stratal patterns, sequences and paleogeographic evolution. *Palaeogeography, Palaeoclimatology, Palaeoecology*, **120**, 303-330.

Legarreta, L. & Uliana, M.A. (1999) El Jurássico y Cretácico de la Cordillera Principal y la Cuenca Neuquina. 1. Facies Sedimentarias. *In:* Caminos, R. (ed.) *Geología Argentina.* Instituto de Geología e Recursos Minerales, Anales, **29**, 399-416.

Liberty, L.M., Hemphill-Haley, M.A. & Madin, I.P. (2003) The Portland Hills Fault: uncovering a hidden fault in Portland, Oregon using high-resolution geophysical methods. *Tectonophysics*, **368**, 89-103.

Lindsay, J.F., Prior, D.B. & Coleman, J.M. (1984) Distributary-mouth bar development and role of submarine landslides in delta growth, South Pass, Mississipi Delta. *American Association of Petroleum Geologists Bulletin*, **68**, 1732-1743.

Locat, J. & Lee, H.J. (2002) Submarine landslides: advances and challenges. *Canadian Geotechnical Journal*, **39**, 193-212.

López-Gamundí, O.R. (1989) Postglacial transgressions in Late Paleozoic basins of western Argentina: a record of glacioeustatic sea level rise. *Palaeogeography, Palaeoclimatology, Palaeoecology*, **71**, 257-270.

López-Gamundí, O.R. (2006) Permian plate margin volcanism and tuffs in adjacent basins of west Gondwana: Age constraints and common characteristics. *Journal of South America Earth Sciences*, **22**, 227-238.

López-Gamundí, O.R. & Rossello, E.A. (1998) Basin fill evolution and palaeotectonic patterns along the Samfrau geosyncline: the Sauce Grande basin-Ventana foldbelt (Argentina) and Karoo basin-Cape foldbelt (South Africa). *Geologische Rundschau*, **86**, 819-834.

Lowe, D.R. (1975) Water escape structures in coarse-grained sediments. *Sedimentology*, **22**, 157-204.

Lowe, D.R. (1976) Subaqueous liquefied and fluidized sediment flows and their deposits. *Sedimentology*, **23**, 285-308.

Lowe, D.R. (1979) Sediment gravity flows: their classification and some problems of application to natural flows and deposits. *In:* Doyle, L.J. & Pilkey, O.H. *Geology of the Continental Slopes.* Society of Economic Paleontologists and Mineralogists. Special Publication, **27**, 75-82.

Lowe, D.R. & LoPiccolo, R.D. (1974) The characteristics and origins of dish and pillar structures. *Journal of Sedimentary Petrology*, **44**, 484-501.

Luthi, S.M., Hodgson, D.M., Gell, C.R., Flint, S.S., Goedbloed, J.W., Drinkwater, N.J. & Johannessen, E.P. (2006) Contribution of research borehole data to modelling fine-grained turbidite reservoir analogues, Permian Tanqua-Karoo basin-floor fans (South Africa). *Petroleum Geoscience*, **12**, 175-190.

Maltman, A.J. (1984) On the term 'soft-sediment deformation'. *Journal of Structural Geology*, **6**, 589-592.

Maltman, A.J. (1994) Introduction and overview. *In:* Maltman, A.J. (ed) *The Geological Deformation of Sediments.* Chapman and Hall, London, 1-35.

Maltman, A.J. & Bolton, A. (2003) How sediment become mobilized. *In*: Van Rensbergen, P., Hillis, R.R., Maltman, A.J. & Morley, C.K. (eds) *Subsurface Sediment Mobilization.* Geological Society, London, Special Publications, **216**, 9-20.

Martinsen, O.J. (1989) Styles of soft-deformation on a Namurian (Cartboniferous) delta slope, Western Irish Namurian Basin, Ireland. *In:* Whateley, M.K.G. & Pickering, K.T. (eds) *Deltas: sites and traps for fossil fuels.* Geological Society, London, Special Publications, **41**, 167-177.

Martinsen, O.J. & Bakken, B. (1990) Extension and compression zones in slumps and slides in the Namurian of Count Clare, Ireland. *Journal of the Geological Society*, **147**, 153-164.

Marsset, T., Marsset, B., Thomas, Y., Cattaneo, A., Thereau, E. Trincardi, F. & Cochonat, P. (2004) Analysis of Holocene sedimentary features on the Adriatic shelf from 3D very high resolution seismic data (Triad survey). *Marine Geology*, **213**, 73-89.

Mayall, M.J., Yeilding, J.D., Oldroyd, J.D., Pulham, A.J. & Sakurai, S. (1992) Facies in a shelf-edge delta – an example from the subsurface of the Gulf of Mexico, Middle Pliocene, Mississippi Canyon, Block 109. *American Association of Petroleum Geologists Bulletin*, **76**, 435-448.

McHugh, C.M.G., Damuth, J.E. & Mountain, G.S. (2002) Cenozoic mass-transport facies and their correlation with relative sea-level change. *Marine Geology*, **184**, 295-334.

McIlroy, D., Flint, S.S. & Howell, J.A. (1999) Applications of High Resolution Sequence Stratigraphy to Reservoir Prediction and Flow Unit Definition in Aggradational Tidal Successions. Proc. 19th GCSEPM Research Conference, Houston, 121-132.

McIlroy, D., Flint, S.S., Howell, J.A. & Timms, N. (2005) Sedimentology of the tide-dominated Jurassic Lajas Formation, Neuquén Basin, Argentina. *In:* Veiga, G.D., Spalletti, L.A., Howell, J.A. & Schwarz, E. (eds) *The Neuquén Basin, Argentina: A Case Study in Sequence Stratigraphy and Basin Dynamics*. Geological Society, London, Special Publications, **252**, 83-107.

McLaughlin, P.I. & Brett, C.E. (2004) Eustatic and tectonic control on the distribution of marine seismites: examples from the Upper Ordovician of Kentucky, USA. *Sedimentary Geology*, **168**, 165-192.

McMechan, G.A. (1983) Migration by extrapolation of time-dependent boundary values. *Geophysical Prospecting*, **31**, 413-420.

Mees, F., Swennen, R., Van Geet, M. & Jacobs, P. (2003) Applications of X-ray computed tomography in geosciences. *In:* Mees, F., Swennen, R., Van Geet, M. & Jacobs, P. (eds) *Applications of X-ray Computed Tomography in Geosciences.*, Geological Society, London, Special Publication, **215**, 1-6.

Meisling, K.E., Kanschat, K.A., Armentrout, J.M., Dyer, R., Tsakma, J.J. & Bassey, F.A. (2000) Slope deformation control on trap and reservoir

development in turbidite systems, southeastern Niger Delta, offshore Nigeria. *American Association of Petroleum Geologists, 2000 Annual Meeting Expanded Abstract*, p. 97.

Mellere, D., Plink-Björklund, P. & Steel, R.J. (2002) Anatomy of shelf deltas at the edge of a prograding Eocene shelf margin, Spitsbergen. *Sedimentology*, **49**, 1181-1206.

Milani, E.J. & De Wit, M.J. (2008) Correlations between the classic Paraná and Cape-Karoo sequences of South America and southern Africa and their basin infills flanking the Gondwanides: du Toit revisited. *In:* Pankhurst, R.J., Trouw, R.A., Brito Neves, B.B. & de Wit, M.J. (eds) *West Gondwana: Pre-Cenozoic Correlations Across the South Atlantic Region.* Geologic Society of London, Special Publications, **294**, 319-342.

Mills, P.C. (1983) Genesis and diagnostic value of soft-sediment deformation structures – a review. *Sedimentary Geology*, **35**, 83-104.

Montenat, C., Barrier, P., d'Estevou, P.O. & Hibsch, C. (2007) Seismites: An attempt to critical analysis and classification. *Sedimentary Geology*, **196**, 6-30.

Moore, D.S. & McCabe, G.P. (2006) *Introduction to the Practice of Statistics – Fifth Edition*, W.H. Freeman and Company, New York, 800p.

Moretti, M. (2000) Soft-sediment deformation structures interpreted as seismite in middle-late Pleistocene aeolian deposits (Apulian foreland, southern Italy). *Sedimentary Geology*, **135**, 167-179.

Moretti, M. & Sabato, L. (2007) Recognition of trigger mechanisms for soft-sediment deformation in the Pleistocene lacustrine deposits of the Sant'Arcangelo Basin (Southern Italy): Seismic shock vs. overloading. *Sedimentary Geoloogy*, **196**, 31-45.

Moretti, M., Alfaro, P., Caselles, O. & Canas, J.A. (1999) Modelling seismites with a digital shaking table. *Tectonophysics*, **304**, 369-383.

Moretti, M., Soria, J.M., Alfaro, P. & Walsh, N. (2001) Asymmetrical soft-sediment deformation structures triggered by rapid sedimentation in turbiditic deposits (Late Miocene, Guadix Basin, southern Spain). *Facies*, **44**, 283-294.

Morton, R.A. & Suter, J.R. (1996) Sequence stratigraphy and composition of Late Quaternary shelf-margin deltas, Northern Gulf of Mexico. *American Association of Petroleum Geologists Bulletin*, **80**, 505-530.

Moscardelli, L. & Wood, L. (2008) New classification system for mass transport complexes in offshore Trinidad. *Basin Research*, **20**, 73-98.

Moscardelli, L., Wood, L. & Mann, P. (2006) Mass-transport complexes and associated processes in the offshore area of Trinidad and Venezuela. *American Association of Petroleum Geologists Bulletin*, **90**, 1059-1088.

Mosher, D.C., Piper, D.J.W., Campbell, D.C. & Jenner, K.A. (2004) Near-surface geology and sediment-failure geohazards of central Scotian Slope. *American Association of Petroleum Geologists Bulletin*, **88**, 703-723.

Mount, J.F. (1993) Formation of fluidization pipes during liquefaction: examples from the Uratanna Formation (Lower Cambrian), South Australia. *Sedimentology*, **40**, 1027-1037.

Mulder, T. & Cochonat, P. (1996) Classification of offshore mass movements. *Journal of Sedimentary Research*, **66**, 43-57.

Nagtegaal, P.J.C. (1965) An approximation to the genetic classification of non-organic sedimentary structures. *Geologie en Mijnbouw*, **44**, 347-352.

Nardin, T.R., Hein, F.J., Gorsline, D.S. & Edwards, B.D. (1979) A review of mass movement processes, sediment and acoustic characteristics, and contrasts in slope and base-of-slope systems versus canyon-fan-basin floor systems. *In:* Doyle, L.J. & Pilkey, O.H. *Geology of the Continental Slopes.* Society of Economic Paleontologists and Mineralogists. Special Publication, **27**, 61-73.

Neal, A. (2004) Ground-penetrating radar and its use in sedimentology: principles, problems and progress. *Earth-Sciences Reviews*, **66**, 261-330.

Needham, R.S. (1978) Giant-scale hydroplastic deformation structures formed by the loading of basalt onto water-saturated sand, Middle Proterozoic, Northern Territory, Australia. *Sedimentology*, **25**, 285-295.

Nemec, W., Steel, R.J., Gjelberg, J., Collinson, J.D., Prestholm, E. & Øxnevad, I. E. (1988) Anatomy of collapse and re-established deata front in the lower Cretaceous of eastern Spitsbergen: gravitational sliding and sedimentation processes. *American Association of Petroleum Geologists Bulletin*, **72**, 454-476.

Neuwerth, R., Suter, F., Guzman, C.A. & Gorin, G.E. (2006) Soft-sediment deformation in a tectonically active area: The plio-Pleistocene Zarzal

Formation in the Cauca Valley (Western Colombia). *Sedimentary Geology*, **186**, 67-88.

Nichols, R.J., Sparks, R.S.J. & Wilson, C.J.N. (1994) Experimental studies of the fluidization of layered sediments and the formation of fluid escape structures. *Sedimentology*, **41**, 233-253.

Nittrouer, C.A., Austin Jr, J.A., Field, M.E., Kravitz, J.H., Syvitski, J.P.M. & Wiberg, P.L. (2007) Writing a Rosetta stone: insights into continental-margin sedimentary processes and strata. *In:* Nittrouer, C.A., Austin Jr, J.A., Field, M.E., Kravitz, J.H., Syvitski, J.P.M. & Wiberg, P.L. (eds) *Continental Margin Sedimentation. From Sediment Transport to Sequence Stratigraphy.* International Association of Sedimentologists, Special Publication, **37**, 1-48.

Obermeier, S.F. (1996) Use of liquefaction-induced features for paleoseismic analysis – An overview of how seismic liquefaction features can be distinguished from other features and how their regional distribution and properties of source sediment can be used to infer the location and strength of Holocene paleo-earthquakes. *Engineering Geology*, **44**, 1-76.

Okoye, P.N. & Uren, N.F. (2000) Fresnel zone and spatial resolution for *P*- and *SH*-waves in transversely isotropic media. *Geophysics*, **65**, 1168-1178.

Owen, G. (1985) *Mechanisms and controls of deformation in unconsolidated sands: an experimental approach.* Unpubl. Ph.D. thesis, University of Reading, 674p.

Owen, G. (1987) Deformation processes in unconsolidated sands. *In:* Jones, M.E. & Preston, R.M.F. (eds) *Deformation of sediments and sedimentary rocks.* Geological Society, London, Special Publications, **29**, 11-24.

Owen, G. (1995) Soft-sediment deformation in Upper Proterozoic Torridonian sandstones (Applecross Formation) at Torridon, northwest Scotland. *Journal of Sedimentary Research*, **A65**, 495-504.

Owen, G. (1996a) Anatomy of water-escape cusp in Upper Proterozoic Torridon Group sandstones, Scotland. *Sedimentary Geology*, **103**, 117-128.

Owen, G. (1996b) Experimental soft-sediment deformation structures formed by liquefaction of unconsolidated sands and some ancient examples. *Sedimentology*, **43**, 279-293.

Owen, G. (2003) Load structures: gravity-driven sediment mobilization in the shallow subsurface. *In*: Van Rensbergen, P., Hillis, R.R., Maltman, A.J. &

Morley, C.K. (eds) *Subsurface Sediment Mobilization*. Geological Society, London, Special Publication, **216**, 21-34.

Pickering, K., Stow, D., Watson, M. & Hiscott, R. (1986) Deep-water facies, processes and models: A review and classification scheme for modern and ancient sediments. *Earth-Sciences Reviews*, **23**, 75-174.

Pinet, N., Duchesne, M., Lavoie, D., Bolduc, A. & Long, B. (2008) Surface and subsurface signatures of gas seepage in the St. Lawrence Estuary (Canada): Significance to hydrocarbon exploration. *Marine and Petroleum Geology*, **25**, 271-288.

Piper, D.J.W., Cochonat, P. & Morrison, M.L. (1999) The sequence of events around the epicentre of the 1929 Grand Banks earthquake: initiation of debris flows and turbidity current inferred from sidescan sonar. *Sedimentology*, **46**, 79-97.

Plink-Björklund, P., Mellere, D. & Steel, R.J. (2001) Turbidite variability and archictecture of sand-prone, deep-water slopes: Eocene clinoforms in the Central Basin, Spitsbergen. *Journal of Sedimentary Research*, **71**, 895-912.

Porębski, S.J. & Steel, R.J. (2003) Shelf-margin deltas: theirs stratigraphic significance and relation to deepwater sands. *Earth-Science Reviews*, **62**, 283-326.

Porsani, J. L. (1999) *Ground Penetrating Radar (GPR): Proposta metodológica de emprego em estudos geológicos-geotécnicos nas regiões de Rio Claro e Descalvado, SP*. Umpubl. PhD thesis, IGCE, UNESP, Brazil, 145p.

Posamentier, H.W. (2003) Depositional elements associated with a basin floor channel-levee system: case study from the Gulf of Mexico. *Marine and Petroleum Geology*, **20**, 677-690.

Posamentier, H.W. & Allen, G.P. (1999) *Siliciclastic Sequence Stratigraphy – Concepts and Applications*. SEPM Concepts in Sedimentology and Paleontology, **7**, 204p.

Posamentier, H.W. & Vail, P.R. (1988) Eustatic controls on clastic deposition II – Sequence and system tract models. *In:* Wilgus, C.K., Hastings, B.S., Kendall, C.G.St.C.; Posamentier, H.W., Ross, C.A. & Van Wagoner, J.C. *Sea-level changes: an integrated approach*. Society of Economic Paleontologists and Mineralogists, Special Publication, **42**, 125-154.

Posamentier, H.W. & Walker, R.G. (2006) Deep-water turbidites and submarine fans. *In:* Posamentier, H.W. & Walker, R. (eds) *Facies Models Revisited.* Society for Sedimentary Geology, Oklahoma, 399-520.

Posamentier, H.W., Jervey, M.T. & Vail, P.R. (1988) Eustatic controls on clastic deposition I – Conceptual framework. *In:* Wilgus, C.K., Hastings, B.S., Kendall, C.G.St.C.; Posamentier, H.W., Ross, C.A. & Van Wagoner, J.C. *Sea-level changes: an integrated approach.* Society of Economic Paleontologists and Mineralogists, Special Publication, **42**, 109-124.

Posamentier, H.W., Allen, G.P., James, D.P. & Tesson, M. (1992) Forced regressions in a sequence stratigraphic framework: concepts, examples, and exploration significance. *American Association of Petroleum Geologists Bulletin*, **76**, 1687-1709.

Postma, G. (1983) Water escape structures in the context of a depositional model of a mass flow dominated conglomeratic fan-delta (Abrioja Formation, Pliocene, Almeria Basin, Spain). *Sedimentology*, **30**, 91-103.

Potter, P.E. & Pettijohn, F.J. (1963) *Paleocurrents and Basin Analysis.* Springer-Verlag, Berlin, 296p.

Prather, B.E. (2000). Calibration and visualization of depositional process models for above-grade slopes: a case study from Gulf of Mexico. *Marine and Petroleum Geology*, **17**, 619-638.

Prather, B.E. (2003). Controls on reservoir distribution, architecture and stratigraphic trapping in slope settings. *Marine and Petroleum Geology,* **20**, 529-545.

Pratson, L.F. & Haxby, W.F. (1996) What is the slope of the U.S. continental slope? *Geology*, **24**, 3-6.

Pratson, L.A., Nittrouer, C.A., Wiberg, P.L., Steckler, M.S., Swenson, J.B., Cacchione, D.A., Karson, J.A., Murray, A.B., Wolinsky, M.A., Gerber, T.P., Mullenbach, B.L., Spinelli, G.A., Fulthorpe, C.S., O'Grady, D.B., Parker, G., Driscoll, N.W., Burger, R.L., Paola, C., Orange, D. L., Field, M.E., Friedrichs, C.T. & Fedele, J.J. (2007). Seascape evolution on clastic continental shelves and slopes. *In:* Nittrouer, C.A., Austin Jr, J.A., Field, M.E., Kravitz, J.H., Syvitsky, J.P.M. & Wiberg, P.L. (eds) *Continental Margin Sedimentation: From Sediment Transport to Sequence Stratigraphy.*

International Association of Sedimentologists, Special Publication, **37**, 339-380.

Prior, D.B. & Coleman, J.M. (1978) Disintegrating retrogressive landslides on very-low-angle subaqueous slopes, Mississippi Delta. *Marine Geotechnology*, **3**, 37-60.

Pulham, A.J. (1989) Controls on internal structure and archictecture of sandstone bodies within Upper Carboniferous fluvial-dominated deltas, County Clare, western Ireland. *In:* Whateley, M.K.G. & Pickering, K.T. (eds) *Deltas: Sites and Traps for Fossil Fuels.* Geological Society, London, Special Publications, **41**, 179-203.

Rabelo, I.R., Luthi, S.M. & Van Vliet, L.J. (2007) Parameterization of meander-belt elements in high-resolution three-dimension seismic data using the GeoTime cube and modern analogues. *In:* Davies, R.J., Posamentier, H.W., Wood, L.J. & Cartwright, J.A. (eds) *Seismic Geomorphology: Applications to hydrocarbon Exploration and Production.* Geological Society, Special Publication, **277**, 121-137.

Ramos, V. & Folguera, A. (2005) Tectonic Evolution of the Andes of Neuquén: constraints derived from the magmatic arc and foreland deformation. *In:* Veiga, G.D., Spalletti, L.A., Howell, J.A. & Schwarz, E. (eds) *The Neuquén Basin, Argentina: A Case Study in Sequence Stratigraphy and Basin Dynamics*. Geological Society, London, Special Publications, **252**, 15-35.

Reading, H.G., & Richards, M. (1994) Turbidite systems in deep-water basin margins classified by grain size and feeder system. *American Association of Petroleum Geologists Bulletin*, **78**, 792-822.

Reiss, S., Reicherter, K.R. & Reuther, C-D. (2003) Visualization and characterization of active normal faults and associated sediments by high-resolution GPR. *In*: Bristow, C.S. & Jol, H.M. (eds) *Ground Penetrating Radar in Sediments*. Geological Society, London, Special Publication, **211**, 247-255.

Rettger, R.E. (1935) Experiments on soft-rock deformation. *American Association of Petroleum Geologists Bulletin*, **19**, 271-292.

Rijsdijk, K.F. (2001) Density-driven deformation structures in glacigenic consolidated diamictits: examples from Traeth y Mwnt, Cardiganshire, Wales, U.K. *Journal of Sedimentary Research*, **71**, 122-135.

Rodrígues-Pascua, M.A., Calvo, J.P., De Vicente, G. & Gómez-Gras, D. (2000) Soft-sediment deformation structures interpreted as seismites in lacustrine sediments of the Prebetic Zone, SE Spain, and their potential use as indicators of earthquake magnitudes during the Late Miocene. *Sedimentary Geology*, **135**, 117-135.

Ross, W.C., Halliwell, B.A., May, J.A., Watts, D.E. & Syvitsky, J.P.M. (1994). Slope readjustment: A new model for the development of submarine fans and aprons. *Geology*, **22**, 511-514.

Rosseti, D.F. (2003) Delineating shallow Neogene deformation structures in northeastern Pará State using Ground Penetrating Radar. *Anais da Academia Brasileira de Ciencias*, **75**, 235-248.

Rosseti, D.F. & Santos Jr, A.E. (2003) Events of sediment deformation and mass failure in Upper Cretaceous estuarine deposits (Cametá Basin, northern Brazil) as evidence of seismic activity. *Sedimentary Geology*, **161**, 107-130.

Rovere, E.I., Caselli, A., Tourn, S., Leanza, H.A., Hugo, C.A., Folguera, A., Escosteguy, L., Geuna, S., González, R., Colombino, J.E. & Danieli, J.C. (2004) *Hoja Geológica 3772-IV, Andacollo, Provincia de Neuquén.* Servicio Geológico Minero Argentino, Instituto de Geologia y Recursos Minerales, Boletín number **298**, 104p. Buenos Aires.

Rubidge, B.S., Hancox, P.J. & Catuneanu, O. (2000) Sequence analysis of the Ecca-Beaufort contact in the southern Karoo of South Africa. *South African Journal of Geology*, **103**, 81-96.

Saller, A.H., Noah, J.T., Ruzuar, A.P. & Schneider, R. (2004) Linked lowstand delta to basin floor fan deposition, offshore Indonesia: An analog for deep-water reservoir systems. *American Association of Petroleum Geologists Bulletin*, **88**, 21-46.

Sandeep, S. & Jain, A.K. (2007) Liquefaction and fluidization of lacustrine deposits from Lahaul-Spiti and Ladakh Himalaya: Geological evidences of paleoseismicity along active fault zone. Sedimentary Geology, **196**, 47-57.

Scott, E.D. & Bouma, A.H. (2003) Source-to-sink: the importance of the updip coastal area in defining deep-water sand characteristics. *In:* Roberts, H.H., Rose, N.C., Fillon, R.H. & Anderson, J.B. (eds) *Shelf Margin Deltas and Linked Down Slope Petroleum Systems: Global Significance and the Future*

Exploration Potential. GCSSEPM 23rd Annual Foundation Bob F. Perkins Research Conference, Houston Texas, 577-596.

Scott, E.D., Bouma, A.H. & Wickens, H. DeV. (2000) Influence of tectonics on submarine fan deposition, Tanqua and Laingsburg subbasins, South Africa. *In:* Bouma, H.D. & Stone, C.G. (eds) *Fine-Grained Turbidite Systems.* American Association of Petroleum Geologists, Memoir **72** and Society for Sedimentary Geology, Special Publication **68**, 47-56.

Seed, H.B. (1979) Soil liquefaction and cyclic mobility evaluation for level ground during earthquakes. *Journal of the Geotechnical Engineering Division.* American Society of Civil Engineers, **105**, GT2, 201-255.

Seed, H.B. & Idriss, I.M. (1982) *Ground motions and soil liquefaction during earthquakes.* Earthquake Engineering Research Institute, Berkeley, California, 134p.

Seilacher, A. (1969) Fault-graded beds interpreted as seismites. Sedimentology, **13**, 155-159.

Sixsmith, P.J. (2000) *Stratigraphy development of a Permian turbidite system on a deforming basin floor: Laingsburg Formation, Karoo Basin, South Africa.* Unpubl. Ph.D. thesis, University of Liverpool, 229p.

Smith, R.D.A. & Spalletti, L.A. (1995) Erosional, depositional and post-depositional features of a turbidite channel-fill, Jurassic, Neuquen Basin, Argentina. *In:* Poickering, K.T., Hiscott, R.N., Kenyon, N.H., Ricci Lucchi, F. and Smith, R.D.A. (eds) *Atlas of Deep Water Environments: Architectural style in turbidite systems.* Chapman & Hall, London,162-166.

Smith, R.H.M., Eriksson, P.G. & Botha, W.J. (1993) A review of the stratigraphy and sedimentary environments of the Karoo-aged basins of South Africa. *Journal of African Earth Sciences*, **16**, 143-169.

Spalutto, L., Moretti, M., Festa, V. & Tropeano, M. (2007) Seismically-induced slumps in Lower-Maastrichtian peritidal carbonates of the Apulian Platform (southern Italy). *Sedimentary Geology*, **196**, 81-98.

Sprague, A.R., Sullivan, M.D., Campion, K.M., Jenson, G.N., Goulding, F.J., Garfield, T.R., Sickafoose, D.K., Rossen, C. & Jennette, D.C. (2003). The physical stratigraphy of clastic strata: A hierarchical approach to the analysis of genetically related stratigraphic elements for improved reservoir

prediction. *National AAPG/SEPM meeting abstracts, Houston, Texas, March 10-13.*

Steel, R.J. & Torben, O. (2002) Clinoforms, clinoform trajectories and deepwater sands. *In:* Armentrout, J.M.. (ed.) *Sequence Stratigraphy Models for Exploration and Production.* GCSSEPM Foundation 22nd Annual Bob F. Perkins Research Conference, 367-380.

Steel, R.J., Porębski, S.J., Plink-Bjorklund, P., Mellere, D. & Maija, S. (2003) Shelf-edge delta types and their sequence-stratigraphic relationships. *In:* Roberts, H.H., Rose, N.C., Fillon, R.H. & Anderson, J.B. (eds) *Shelf Margin Deltas and Linked Down Slope Petroleum Systems: Global Significance and the Future Exploration Potential.* GCSSEPM 23rd Annual Foundation Bob F. Perkins Research Conference, Houston Texas, 205-230.

Steel, R.J., Crabaugh, J., Schellpeper, M., Mellere, D., Plink-Bjorklund, P., Deibert, J. & Loeseth, T. (2000) Deltas vs. rivers on the shelf edge: their relative contributions to the growth of shelf-margins and basin floor fans (Barremian and Eocene, Spitsbergen). *In:* Weimer, P., Slatt, R.M., Coleman, J., Rosen, N.C., Nelson, H., Bouma, A.H., Styzen, M.J. & Lawrence, D.T. (eds) *Deep-water Reservoirs of the World.* GCSSEPM Foundation 20th Annual Bob F. Perkins Research Conference, 981-1009.

Stow, D.A.V. (1994) Deep sea processes of sediment transport and deposition. *In*: Pye, K. (ed) *Sediment Transport and Depositional Processes.* Blackwell Scientific Publication. 397p.

Stow, D.A.V., Reading, H.G. & Collinson, J.D. (1996). Deep seas. *In* Reading, H.G. (ed) *Sedimentary Environments: Processes, Facies and Stratigraphy* 3rd Edition. Blackwell Science Ltd., 395-453.

Strachan, L.J. (2002) Slump-initiated and controlled syndepositional sandstone remobilization: an example from the Namurian of County Clare, Ireland. *Sedimentology*, **49**, 25-41.

Stromberg, S.G. & Bluck, B. (1998) Turbidite facies, fluid-escape structures and mechanisms of emplacement of the Oligo-Miocene Aljibe Flysch, Gibraltar Arc, Betics, southern Spain. *Sedimentary Geology*, **115**, 267-288.

Sultan, N., Cochonat, P., Canals, M., Cattaneo, A., Dennielou, B., Haflidason, H., Laberg, J.S., Long, D., Mienert, J., Trincardi, F., Urgeles, R., Vorren, T.O. & Wilson, C. (2004) Triggering mechanisms of slope

instability processes and sediment failures on continental margins: a geotechnical approach. *Marine Geology*, **213**, 291-321.

Suter, J.R. & Berryhill Jr, H.L. (1985) Late Quaternary shelf-margin deltas, northwest Gulf of Mexico. *American Association of Petroleum Geologists Bulletin*, **69**, 77-91.

Sylvester, Z. (2007) Turbidite bed thickness distributions: methods and pitfalls of analysis and modelling. *Sedimentology*, **54**, 847-870.

Tesson, M., Gensous, B., Allen, G.P. & Ravenne, Ch (1990) Late Quaternary deltaic lowstand wedges on the Rhône continental shelf, France. *Marine Geology*, **91**, 325-332.

Theune, U., Rokosh, D., Sacchi, M.D. & Schmitt D.R. (2006) Mapping fractures with GPR: A case study from Turtle Mountain. *Geophysics*, **71**, B139-B150.

Trincardi, F. & Field, M.E. (1992) Collapse and flow of lowstand shelf-margin deposits: An example from eastern Tyrrhenian Sea, Italy. *Marine Geology*, **105**, 77-94.

Trincardi, F., Cattaneo, A., Correggiari, A. & Ridente, D. (2004) Evidence of soft sediment deformation, fluid escape, sediment failure and regional weak layers within the late Quaternary mud deposits of the Adriatic Sea. *Marine Geology*, **213**, 91-119.

Turner, B.R. (1999) Tectonostratigraphical development of the Upper Karoo foreland basin: orogenic unloading versus thermally-induced Gondwana rifting. *Journal of African Earth Sciences*, **28**, 215-238.

Tuttle, M. & Barstow, N. (1996) Liquefaction-related ground failure: a case study in the New Madrid seismic zone, central United States. *Bullentin of Seismological Society of America*, **86**, 636-645.

Twiss, R.J. & Moores, E.M. (2007) Structural Geology. 2nd edition. W.H. Freeman and Company, New York. 736p.

Uliana, M.A. & Legarreta, L. (1993) Hydrocarbon habitat in a Triassic-to-Cretaceous sub-andean setting: Neuquén Basin, Argentina. *Journal of Petroleum Geology*, **16**, 397-420.

Uliana, M.A., Biddle, K.T. & Cerdán, J. (1989) Mesozoic extension and the formation of Argentine sedimentary basins. *In:* Tankard, A.J. & Balkwill, H.R. (eds) *Extension tectonic and stratigraphy of the North Atlantic margins.* American Association of Petroleum Geologists, Memoirs, **46**, 599-614.

Vail, P.R., Mitchum Jr, R.M. & Thompson III, S. (1977) Seismic stratigraphy and global changes of sea level, Part 4: Global cycles and relative changes in the sea level. *In:* Payton, C.E. (ed.) *Seismic Stratigraphy – applications to hydrocarbon exploration.* American Association of Petroleum Geologists Memoirs, **26**, 83-97.

Van Heijst, M.W.I.M., Postma, G., van Kesteren, W.P. & de Jongh, R.G. (2002) Control of syndepositional faulting on systems tract evolution across growth-faulted shelf-margin: An analog experimental model of the Miocene Imo River field, Nigeria. *American Association of Petroleum Geologists Bulletin*, **86**, 1335-1366.

Van Lente, B. (2004) *Chemostratigraphic trends and provenance of the Permian Tanqua and Laingsburg Depocentres, Southwestern Karoo Basin, South Africa.* Unpubl. PhD thesis, University of Stellenbosch, 339p.

Van Loon, A.J. & Brodzikowski, K. (1987) Problems and progress in the research of soft-sediment deformations. *Sedimentary Geology*, **50**, 167-193.

Varnes, D.J. (1958) Landslide types and processes. *In:* Eckel, E.D. (ed) *Landslides and Engineering Practice.* Highway Research Board, Washington, DC, Special Report, **29**, 20-47.

Veevers, J.J., Cole, D.I. & Cowan, E.J. (1994) Southern Africa: Karoo Basin and Cape Fold Belt. *In:* Veevers, J.J. & Powell, C.McA. (eds) *Permian-Triassic pangean basins and foldbelts along the panthalassan margin of Gondwanaland.* Geological Society of America, Memoirs, **184**, 223-279.

Vergani, G.D., Tankard, A.J., Belotti, H.J. & Welsink, H.J. (1995) Tectonic evolution and paleogeography of the Neuquén Basin, Argentina. *In:* Tankard, A.J., Suárez S., S. & Welsink, H.J. (eds) *Petroleum basins of South America.* American Association of Petroleum Geologists, Memoirs, **62**, 383-402.

Visser, J.N.J. (1992) Deposition of the Early to Late Permian Whitehill Formation during a sea-level highstand in a juvenile foreland basin. *South Africa Journal of Geology*, **95**, 181-193.

Visser, J.N.J. (1993) Sea-level changes in a back-arc foreland transition: the late Carboniferous-Permian Karoo Basin of South Africa. *Sedimentary Geology*, **83**, 115-131.

Visser, J.N.J. (1996) Controls on Early Permian shelf deglaciation in the Karoo Basin of South Africa. *Palaeogeography, Palaeoclimatology, Palaeoecology*, **125**, 129-139.

Walker, R.G. (1978). Deep-water sandstone facies and ancient submarine fans: models for exploration for stratigraphic traps. *American Association of Petroleum Geologists Bulletin*, **62**, 932-966.

Wang, Y. (2006) Inverse Q-filter for seismic resolution enhancement. *Geophysics*, **71**, v51-v60.

Weigelt, E. & Uenzelmann-Neben, G. (2004) *American Association of Petroleum Geologists*, **88**, 765-780.

Wells, J.T., Prior, D.B. & Coleman, J.M. (1980) Flowslides in muds on extremely low angle tidal flats, northeastern South America. *Geology*, **8**, 272-275.

Wickens, H. DeV. (1994) *Basin floor fan building turbidites of the southwestern Karoo Basin, Permian Ecca Group, South Africa.* Unpubl. Ph.D. thesis, University of Port Elizabeth, 233p.

Wickens, H. DeV. & Bouma, A.H. (2000) The Tanqua Fan Complex, Karoo Basin, South Africa – outcrop analog for fine-grained deepwater deposits. *In*: Bouma, H.D. & Stone, C.G. (eds) *Fine-Grained Turbidite Systems*. American Association of Petroleum Geologists, Memoir 72 and Society for Sedimentary Geology, Special Publication, **68**, 153-164.

Wild, R.J. (2005) *Sedimentological and sequence stratigraphic evolution of a Permian lower slope to shelf succession, Tanqua depocentre, SW Karoo Basin, South Africa*. Unpubl. Ph.D. thesis, University of Liverpool, 368p.

Wild, R.J., Hodgson, D.M. & Flint, S.S. (2005) Architecture and stratigraphic evolution of multiple, vertically-stacked slope channel complexes, Tanqua depocentre, Karoo Basin, South Africa. *In:* Hodgson, D.M. & Flint, S.S. (eds) *Submarine Slope Systems: Processes and Products*. Geological Society, London, Special Publication, **244**, 89-111.

Woodcock, N.H. (1978) Soft-sediment deformation: a review. *In:* Fitches, W.R. & Maltman, A.J. *Conference Report: Deformation of soft sediments. Journal of the Geological Society*, **135**, 245-251.

Wynn, R.B., Masson, D.G., Stow, D.A.V. & Weaver, P.P.E. (2000) The Northwest African slope apron: a modern analogue for deep-water systems

with complex seafloor topography. *Marine and Petroleum Geology*, **17**, 253-265.

Yassir, N.A. (1990) The undrained shear behaviour of fine grained sediments. *In*: Knipe, R.J. & Rutter, E.H. (eds) *Deformation Mechanisms, Rheology and Tectonics*. Geological Society, London, Special Publication, **54**, 399-404.

Yilmaz, Ö. (2001) *Seismic Data Analysis – Processing, Inversion, and Interpretation of Seismic Data.* Society of Exploration Geophysicists, Tulsa, OK; 2 vol., 2027p.

Youd, T.L. (1977) Discussion of 'Brief review of liquefaction during earthquakes in Japan' by E. Kuribayashi and F. Tatsuoka. *Soils and foundation*, **17**, 82-85.

Zapata, T. & Folguera, A. (2001) Tectonic evolution of the Andean Fold and Thrust Belt of the southern Neuquén Basin, Argentina. *In:* Veiga, G.D., Spalletti, L.A., Howell, J.A. & Schwarz, E. (eds) *The Neuquén Basin, Argentina: A Case Study in Sequence Stratigraphy and Basin Dynamics.* Geological Society, London, Special Publications, **252**, 37-56.

Appendix 1

Location of logs, GPR lines and outcrops within Karoo and Neuquén studied successions.
UTM, WGS84 - Central meridians: Neuquén , 69 W and Karoo 21 E

A 1.1 Upper and lower contacts of the logs.

Basin and Locality	Log Position	Log name	Base of Log		Top of Log	
			X	Y	X	Y
Karoo - Tanqua	Waterfall	WF1	410052	6358330	410050	6358343
Karoo - Tanqua	Waterfall	WF2	410054	6358317	410061	6358310
Karoo - Tanqua	Waterfall	WF3	410001	6358322	410017	6358312
Karoo - Tanqua	Waterfall	WF4	409979	6358223	409976	6358193
Karoo - Tanqua	Waterfall	WF5	409938	6358313	409933	6358304
Karoo - Tanqua	Waterfall	WF6	409994	6358648	410003	6358635
Karoo - Tanqua	Waterfall	WF7	409893	6358466	409898	6358424
Karoo - Tanqua	Waterfall	WF7b	409933	6358330	#	#
Karoo - Tanqua	Roosterberg	Rb1	415511	6360245	415488	6360166
Karoo - Tanqua	Roosterberg	Rb2	415009	6360265	415004	6360195
Karoo - Tanqua	Roosterberg	Rb3	415803	6360205	415781	6360162
Karoo - Tanqua	Roosterberg	Rb4	413444	6360195	413443	6360064
Karoo - Tanqua	Roosterberg	Rb5	412899	6360136	412900	6360108
Karoo - Tanqua	Roosterberg	Rb6	413917	6360340	413919	6360265
Karoo - Tanqua	Roosterberg	Rb7	413269	6360148	413269	6360148
Karoo - Tanqua	Roosterberg	Rb8	414942	6360535	414882	6360246
Karoo - Laingsburg	Heuningberg	HN01	482586	6337328	482590	6337343

Karoo - Laingsburg	Heuningberg	HN02	482617	6337311	482636	6337310
Karoo - Laingsburg	Heuningberg	HN03	482565	6337337	482575	6337341
Karoo - Laingsburg	Heuningberg	HN04	482342	6337527	482326	6337568
Karoo - Laingsburg	Heuningberg	HN05	482494	6337449	482519	6337450
Karoo - Laingsburg	Heuningberg	HN06	482439	6338113	482447	6338107
Karoo - Laingsburg	Heuningberg	HN07	482285	6338013	482297	6338010
Karoo - Laingsburg	Heuningberg	HN08	482216	6337910	482229	6337914
Karoo - Laingsburg	Heuningberg	HN09	482448	6338045	482426	6338026
Karoo - Laingsburg	Heuningberg	HN10	482156	6337817	482180	6337834
Karoo - Laingsburg	Heuningberg	HN11	482133	6337773	482154	6337712
Karoo - Laingsburg	Heuningberg	HN North	482195	6338441	482404	6337948
Karoo - Laingsburg	Heuningberg	HN South	482396	6337210	482606	6337450
Karoo - Laingsburg	Heuningberg	HN21	482144	6337768	#	#
Karoo - Laingsburg	Heuningberg	HN23	482161	6337610	#	#
Karoo - Laingsburg	Buffels River	BR	489238	6334370	489088	6334567
Karoo - Laingsburg	Zoutkloof Farm	ZF	478890	6333418	478781	6333552
Neuquén	Puesto Seguel	PS1	410805	5664877	#	#
Neuquén	Puesto Seguel	PSA	410779	5664827	#	#
Neuquén	Puesto Seguel	PSH	410806	5664840	#	#
Neuquén	Puesto Seguel	PS4 (interval 2)	410795	5664939	#	#
Neuquén	Fortin 1° de Mayo	FM01	355808	5638035	#	#
Neuquén	Fortin 1° de Mayo	FM02	355832	5637971	#	#
Neuquén	Fortin 1° de Mayo	FM03	355832	5637925	#	#
Neuquén	Fortin 1° de Mayo	FM04	355835	5637891	#	#
Neuquén	Fortin 1° de Mayo	FM05	355811	5637878	#	#
Neuquén	Chacay Melehue	CML1	360256	5872685	360305	5872572

Neuquén	Chacay Melehue	CML2	360504	5872736	360504	5872625
Neuquén	Chacay Melehue	CML3	360477	5872633	360467	5872606
Neuquén	Chacay Melehue	CML4	360664	5872769	360641	5872682
Neuquén	Chacay Melehue	CML5	361029	5872908	361124	5872780
Neuquén	Chacay Melehue	CML6	365497	5874485	365544	5874446
Neuquén	Chacay Melehue	CML7	361843	5873109	361909	5873033
Neuquén	Chacay Melehue	CML8a	362389	5873448	362331	5873385
Neuquén	Chacay Melehue	CML8b	362270	5873236	362227	5873165
Neuquén	Chacay Melehue	CML9	365215	5874499	365275	5874457
Neuquén	Chacay Melehue	CML10	366844	5875259	366854	5875243
Neuquén	Chacay Melehue	CML11	367283	5875420	367314	5875297

Note: When the top pf log is not showed is due its small dimension.

A 1.2 GPR lines at Waterfall

Coordinates GPR lines 2nd acquisition

	Start		End	
Line	X	Y	X	Y
WFA101	410087,4	6358339,2	410080,5	6358327,4
WFA102	410086,7	6358340,1	410079,7	6358328.0
WFA103	410085,3	6358339,6	410078,8	6358328,5
WFA104	410083,4	6358338,4	410077,9	6358329.0
WFA105	410080,6	6358335,5	410077,1	6358329,5
WFA106	410083,1	6358341,9	410076,2	6358330.0
WFA107	410083.0	6358343,6	410074,6	6358329,2

WFA108	410082,1	6358344,1	410073,7	6358329,7
WFA1X1	410079,8	6358328,1	410073,9	6358331,7
WFA1X2	410082,3	6358332,5	410075,7	6358336,5
Also, line WF101, first acquisition				
WF101	410079,8	6358328,1	410089,8	6358341,1

Note: The coordinates above are related to the final length of the line after processing.

A 1.3 Outcrops

		Fig. number	X	Y	
Karoo - Laingsburg	Heuningberg	4.19	482145	6337786	(NW)
			482144	6337768	(SE)
Karoo - Laingsburg	Heuningberg	4.20	482216	6337910	
Karoo - Laingsburg	Heuningberg	4.21a	482285	6338013	
		4.21b	482216	6337910	
		4.21c	482156	6337817	
Karoo - Laingsburg	Heuningberg	4.22	482154	6337712	(NE)
			482144	6337651	(SW)
Karoo - Laingsburg	Heuningberg	4.24	482578	6337330	(NW)
			482621	6337308	(SE)

Karoo - Laingsburg	Heuningberg	4.26	482416	6337508	
Karoo - Laingsburg	Heuningberg	4.28	482273	6337563	
Karoo - Laingsburg	Heuningberg	4.29	482448	6338045	
Karoo - Laingsburg	Heuningberg	4.31	482382	6337975	
Karoo - Laingsburg	Heuningberg	4.33	478890	6333418	(SW)
Karoo - Laingsburg	Heuningberg	4.35d	489534	6334035	
Neuquén	Puesto Seguel	4.41	410806	5664840	
Karoo - Tanqua	Roosterberg	5.1	415490	6360182	

Appendix 2

Data acquisition methodology

The data acquisition of geometric parameters was based on intervals of structures oriented with a high degree of parallelism. The measurement of lateral parameters such as (a) base width, (b) narrowest point and (c) distance to next structure (see Figure 3.14; Appendix 3) was taken orthogonally to flame boundaries, represented by structural and sedimentological changes in case of base width and narrowest point (Figure A2.1a). In the case of distance to next structure, the measurement was taken considering the distance orthogonal to the projected longitudinal axis of the structure (Figure A2.1b). This approach was considered good for sections with close to parallel structures and satisfactory for sections with structures pointing to same quadrants with small (<30°) divergent or convergent angles. In this case an "average" orientation was estimated visually for continuous structures in order to get the measurement orthogonally to that. Particularities for each interval were discussed in the appropriate sections. The problem occurred for structures trend in divergent directions or without clear indication of their orientation (lack of 3D constraint). In the first case the method considered is not applicable and too much error is involved, so the measurements were dropped (Figure A2.1b). This can introduce some bias to the final result but that is inherent to the methodology. The large number of measurements from close-to-parallel structures from different areas and intervals (see Figures 3.15, 3.28, 4.36, 4.37, 4.48) was enough to avoid the influence of omitted examples.

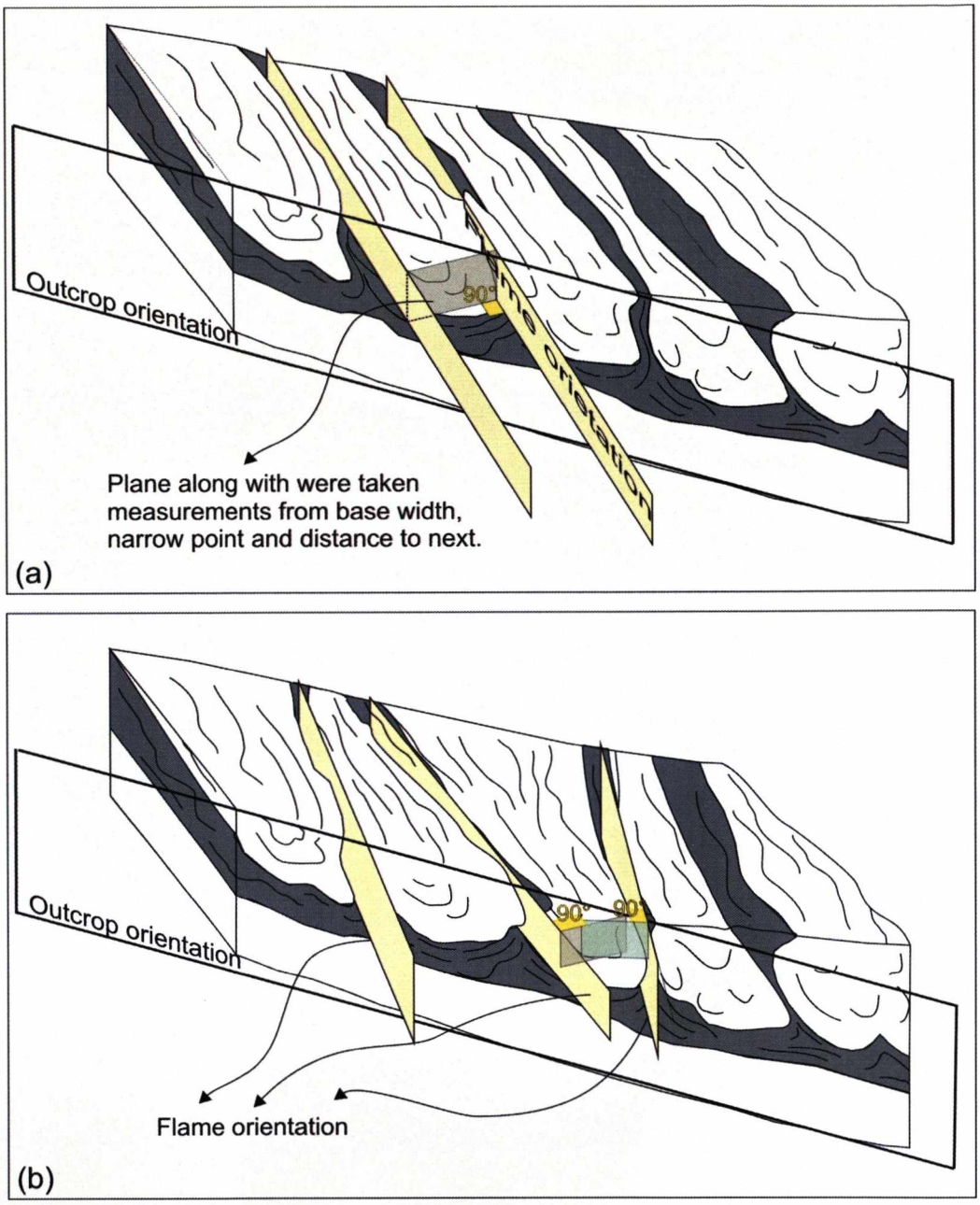

Figure A2.1: Methodology for the measurements of lateral characteristics of flame structures, with emphasis to distance between flames: (a) for parallel flame structures the distance is taken orthogonal to the direction of the oriented flames; (b) in case of flames with distinct orientation (>30° between adjacent structures) it is not possible to obtain the distance to next structure because it will vary along the flame extension. Not scale implied.

Appendix 3 - Raw data of flame structures

Basin	Locality	Bed name	Control Point	Characteristics					
				Unit Thickness	Flame Height	Base Width	Narrow Point	Distance Next	Orientation
Karoo-Tanqua	Waterfall	DA	1	91	52	17	15	50	80
			2	89	21	20	3	75	22
			3	89	50	35	7	60	45
			4	67	42	60	8	63	24
			5	78	27	35	9	75	44
			6	82	48	60	30	85	81
			7	78	40	55	8	60	39
			8	69	43	80	33	65	54
			9	78	48	53	5	45	52
			10	80	50	16	3	70	62
			11	79	35	51	8	76	59
			12	77	40	40	7	80	58
			13	72	28	50	5	69	40
			14	63	25	50	2	125	52
			15	61	36	65	25	65	88
			16	56	30		1	85	99
			17	61	12		3	168	82
			18	53	29	30	3	70	97
			19	46	17	35	2	350?	30
			20	43	23	24	2	100	96
			21		22	35	2	75	94
			22	39	25	12	1	70	36
			23		25	20	2	40	94
			24	34	23	25	2	510?	85
			25		17	15	1	55	80
			26	37	20	15	1	35	86
			27		20		1	38	80
			28		15	30	9	120	96
			29		25	30	4		76
			30	63	13	30	4	35	54
			31		15	20	1		66
Karoo-Tanqua	Waterfall	DB	1	68	26	35	3	50	106
			2	60	30	30	4	130	66
			3	71	45	90	68	100	6
			4	79	35	48	9	50	80
			5	73	34	55	2	60	60
			6	80	30	20		55	60
			7	78	39	70	36	40	68
			8	78	46	25	4	80	67
			9	79	45	55	30	70	77
			10	78	56	35	1	55	76
			11	81	60	50	6	50	70
			12	78	56	30	2	45	92

Karoo-Tanqua	Waterfall	DB	13	75	50	35	2	50	36
			14	77	25	30	9	50	74
			15	81	50	75	48	90	68
			16	74	30	40	12	140	80
			17	76	46	65	5	75	90
			18	75	45	70	22	55	66
			19	83	43	30	3	80	66
			20	73	52	37	3	100	65
			21	75	50	80	2	100	8
			22	73	45	55	10	46	52
			23	74	45	35	3	65	50
			24	74	40	40	2	65	56
			25	74	43	22	14	70	
			26	71	45	35	1	85	98
			27	72	40	40	2	90	70
			28	82	55	50	7	50	58
			29	72	60	50	11	70	92
			30		60	50	5	105	89
			31		55	60	2	105	82
			32		50	65	3	100	89
			33		60	70	3	130	20
			34		45	65	20	125	90
			35		50	65	15	85	95
			36		55	20	1	130	100
			37		55	90	40	60	55
			38		50	40	3	65	90
			39		50	65	7	150	56
			40		39	65	2	55	21
			41	51	46	55	20	67	91
			42	49	44	45	7	80	87
			43		33	25	2		90
Karoo-Tanqua	Waterfall	DC	1	17	8	23	5	40	70
			2	18	9	35	2	50	65
			3	17	12	18	1	60	120
			4	20	14	20	0,5	45	84
			5	25	17	40		115	60
			6	22	4,5	27	1	61	80
			7	24	10,5	17	1	71	89
			8	21	9	18	2	37	89
			9	24	17	31	1	75	82
			10	21	20	30	1,5	75	32
			11	26	12	18	1	70	78
Karoo-Tanqua	Waterfall	DD	1	14	13	30	2	41	172
			2	16	9	7		14	124
			3	17	11	9	8	53	243
			4	14	14	44	12	55	200
			5	15	11	9		33	174
			6	14	5	24	4	57	192
			7	15	12	37	1.5?	37	168, 228
			8	16	10	20		50	244

Karoo-Tanqua	Waterfall	DD	9	15	10	18	4	13	132
			10	15	5	11	2	22	118
			11	15	4	7	2	35	150
			12	15	3,5	26	13		164
			1A	15	9	115	104	130	167
			2A	15	11	40	30	56	198
			3A	15	9	40	35	65	190, 266
			4A	14	8	18		80	192
			5A	15	7	36	28	69	170, 270
			6A	15	5	15	8	90	178
			7A	15	7	30	17	97	250
			8A	15	8	93	72	92	283
			9A	15	9	16	7	45	275
			10A	17	10	9	3	95	275
			11A	16	10	55	45	45	268
			12A	17	10	16	11	25	270
			13A	17	11	15	1	30	275
			14A	15	10	36	2	78	254
			15A	17	9	60	44	97	276
			16A	16	10	15	9	44	240
			17A	17	11	14	4		258
Karoo-Tanqua	Drooge Kloof	DE	1		170		59?	190	70
			2		160	30	40	170	88
			3			120	45	130	88
			4		110	70	50	130	104
			5		100	110	100	130	85
			6		100	100	20	120	104
			8		70	68	30	110	100
			9		80	80	20	65	110
			10		90	60	20		66
			11		100	150	55	270	91?
			12		90	90	36	170	95
			13		120	130	80	140	79
			14		85	100	65	156	56
			15		70	110	50	180	113
			16		90	130	70	155	110
			17		90	130	56	90	98
			18		80	75	35	80	70
			19		80	90	20	100	70
			20		125	110	40		51
			21		125	75	40	110	109
			22		110	90	15	100	90
			23		90	90	30	130	103
			24		110	120	40		108
Karoo-Tanqua	Waterfall	DF	1	12	4	12		33	222
			2	12	5	13		30	248
			3	13,5	6	15	2	30	242
			4	12	5	19		78	224
			5	13	6	20	13	90	208
			6	12	4	8		46	249
			7	13	5	1		50	263

Karoo-Tanqua	Waterfall	DF	8	14	7	6	4	47	243
			9	15	5	6	2	28	237
			10	13	6	10	2	50	228
			11	12	5	5	1	45	240
			12	14	5	12		20	242
			13	13	6	5	1	17	260
			14	14	5			50	250
			15	12	8	29		40	226
			16	14	9	16	6	33	236
			17	13	9	10	5	50	200
			18	14	8	8	2	70	208
			19	14	8	6	2	130	280
			20	11	7	10		35	238
			21	11	7	22		55	222
			22	12	7	35		100	
			23	13	5	5		40	235
			24	12	4	18	10	70	229
			25	12	4	23		35	229
			26	12	6	7	1	35	215
			27	12	3	18		80	
			28	12	10	27	17	40	229
			29	12	5	26	23		261
Karoo-Tanqua	Waterfall	DG	1	130	100	150	10	227	22
			2	127	106	80	5	215	25
			3	130	105	95	5	270	17
			4	140	125	150	5	249	12
			5	120	95	210	30	360	40
			6	160	115	160	35	360	11
			7	180	95	210	95	340	37
			8	187	120	280	85	290	24
			9	175	110	85	20	250	21
			10	150	85	45	9	100	31
			11	170	120	80	5	180	16
			12	175	70	130	5	160	97
			13	175	100	115	5	260	35
Karoo-Tanqua	Roosterberg	DH	A1	10	7	15	1	28	76
			A2	8	6	20	1	15	96
			A3	8,5	6	8	1	20	100
			A4	8	7	20	2	28	
			A5	7	5	17			90
			B1	10	10	60	26	120	137
			B2	10	10	100	70		125
			C1	130	90	100	60		112, 150
			D1	32	32	140		160	
			D2	32	32	60	10		95
			E1	240	200	250	150	300	220
			E2	230	180	75	24	325	
			E3	235	170	275	100	350	90
			E4	240	180	140	35	310	82
			F1	440	440	360	70	470	98

Karoo-Tanqua	Roosterb.	DH	F2	520	430	170	8	470	70
			F3	520	460		40	400	62
			F4	520	460		20	320	59
			G1	420	320	330	60	220	140, 070
Karoo-Laingsburg	Heuningberg	HNCD1	1	95	60	90	20	230	9
			2					180	
			3	95	50	110	16	330	7
			4	65	65	80	3	350	67
			5	100	80	80	3	380	330
			6	105	105	130	38	360	38
			7	130	130	80	6	430	83
			8	130	100	230	10	200	78
			9	120	110	120	20	340	50
			9a	140	70		3	130	282
			9b	150	90		10	90	90
			9c	150	80	110	30	100	82
			9d	150	35	15	15	70	90
			10	150	150	10	10		92
Karoo-Laingsburg	Heuningberg	HNCD2	1	26	14	30	2	100	41
			2	26	20			400	300
			3	30	28	80	30	170	
			4	27	27	100	4	340	24
			5	40	40	110	15	130	71
			6	40	40	80		200	68
			7		45	120	5	200	305
			8	35	35	80	30		310
Karoo-Laingsburg	Heuningberg	HNCD3	1	95	60	140	26	180	39
			2	90	85	160	5	220	52
			3					340	
			4	120	100	200	46	320	330
			5	110	20	60	28	220	345
			6	110	60	160	5	480	50
			7						
			8	130	40	190		310	
			9	110	50	110	12	300	65
			10	110	80	170		300	308
Karoo-Laingsburg	Heuningberg	HN05	1	130	130	200	20	150	93
			2			220	55	180	90
			3				40	170	99
			4			150	50	100	100
			5	110	110	80	25	120	57
			6	115	115	80	20	100	48
			7	115	115	120	20	100	80
			8			120	30		79

Karoo-Laingsburg	Buffels River	WFR01	*1	100	100	80	9		257
			*2	60	60	60	5	70	275
			*3	45	45	5	3	60	244
			*4	35	35	70	3		252
			**5	35	35	60	15	190	261
			**6	50	25	80	2	130	253
			**7	30	15	30	5	220	275
			**8	35	35	60	10	220	234
			**9	50	50	90	18	150	247
Karoo-Laingsburg	Zoutkloof	WFR03	1					600	312
			2	105	70	340		500	319
			3	150	150	650	200	490	310
			4	130	130	200	50	750	324
			5	110	110	510	70	600	357
Neuquén	Puesto Seguel	1	1	102	56	70	32	120	070, 099
			2	100	74	105	40	128	122
			3	100	48	58	28	65	77
			4	90	24	19	5	67	
			5	104	62	97	56	166	
			6	103	73	140	60	190	
			7	90	63	173		180	
			8	95	50	110	48	165	55
			9	90	63	120	50	190	94
			10					382	
			11	75	55	180	70	240	76
			12	84	77	150	108	163?	84
			13	77	38	148	95	360	
			14	90	68		110		
Neuquén	Puesto Seguel	2	1	36	28	90	4	80	12
			2					55	
			3	30	10	20		34	
			4	31	9	15		47	9
			5	32	13	50	4	130	318
			6	33	30	50	6	135	333
			7	40	40	40	3	120	351
			8	40	40	90	40	90	357
			9	35	35	50	17	80	330
			10	30	15	43			
Neuquén	Fortin 1° de Mayo	L1	L1 1	95	25	90		200	
			L1 2	110	100	130	5	190	
			L1 3	70	15	90		87	
			L1 4	60	15	65			
		L2	L2 5		40	400			
		L3	L3 6		150	500			
		L4	L4 7		200	460		1440	
			L4 8		200	600			

Orientation of other flame structures - Laingsburg				
Top Heuningberg	Log HN07 (Heun)	Log HN11 (Heun)	SW Log HN11 (Heun)	BF02 (Buffels River
120	93	56	86	83
144	104	85	90	120
103	107	72	72	57
140	96	48		99
132	89	29		93
158		51		94
113		70		82
114		31		92
120		100		
90		39		
97		14		
		107		
		74		
		64		
		20		
		50		

Appendix 4

Statistical Analysis – Original graphs by interval
Waterfall and Heuningberg areas

A 4.1 – Waterfall area

A 4.1a – Distance next flame x base width

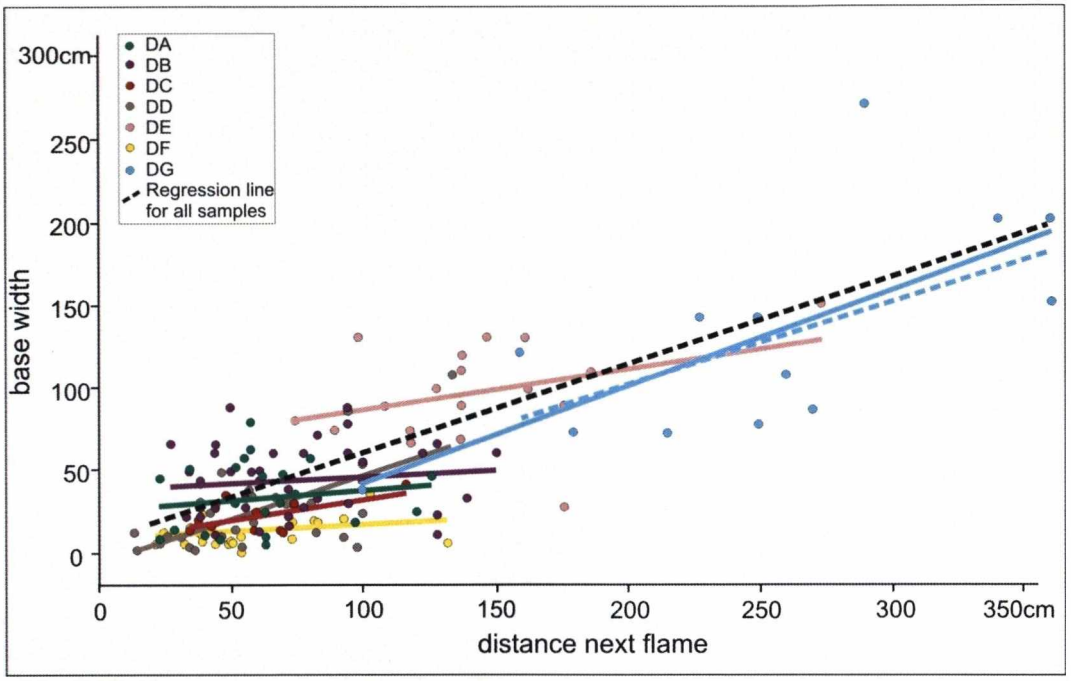

Detailed view:

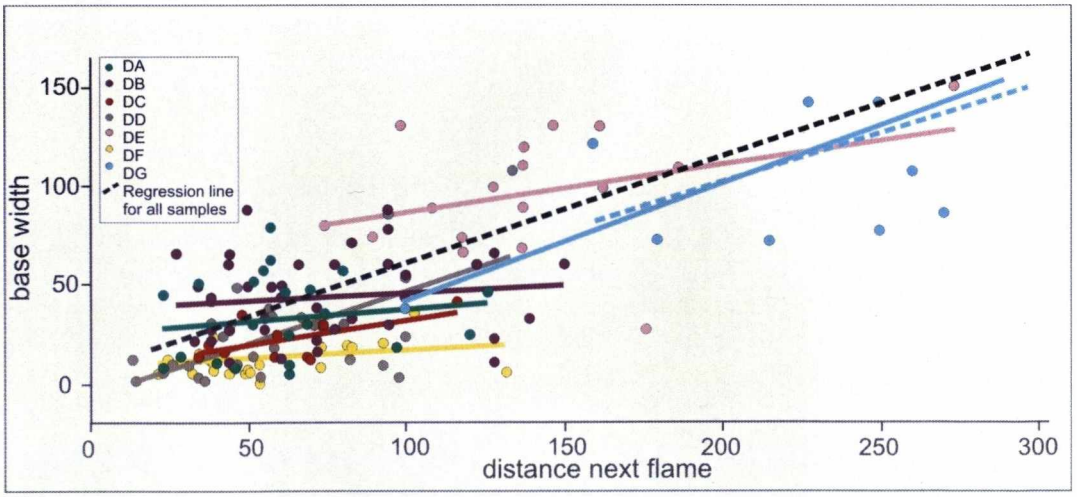

Observations:

a) Values of Pearson correlation and R^2 :

	Correlation	R^2 (%)
DA	0.154	2.4
DB	0.122	1.5
DC	0.576	33.2
DD	0.630	39.6
DE	0.372	13.8
DF	0.241	5.8
DG	0.687	47.2

b) The low correlation values for intervals DA and DB are influenced by anomalous values of distance between structures due to some variability in the orientation of flames (see Appendix 3).

c) The variation in the distance to next flame in each interval is larger compared with the variations in base width.

A 4.1b – Unit thickness x flame height

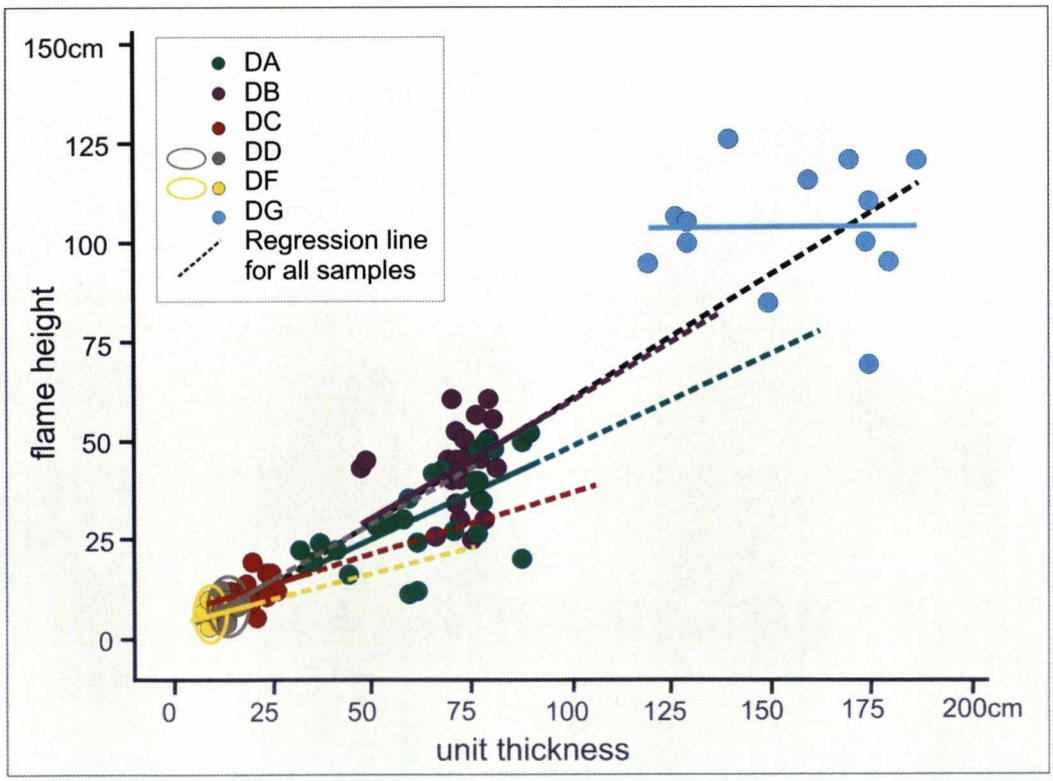

Observations:

a) Values of Pearson correlation and R^2 :

	Correlation	R^2 (%)
DA	0.636	40.4
DB	0.229	5.5
DC	0.347	9.8
DD	0.283	4.3
DE	-	-
DF	0.163	2.6
DG	0.013	0

b) For interval DE it was not possible to measure the bed thickness due to the bad definition of the top of the bed covered by allochthonous material.

c) There is a tendency for constant thickness for some beds (DB, DC, DD and DF). Variations in the flame height were a function of local truncation.

d) Bed DG shows variation in thickness from NE to SW (from flame 1 to flame 13 in Appendix 3) not followed by the flame height that is influenced directly by distinct flame styles and some truncation. The regression line is influenced by the lack of data. The value zero for R^2 indicates that there is a strong possibility that this line is not the best to represent the observed relationship in bed DG.

A 4.1c – Flame height x base width

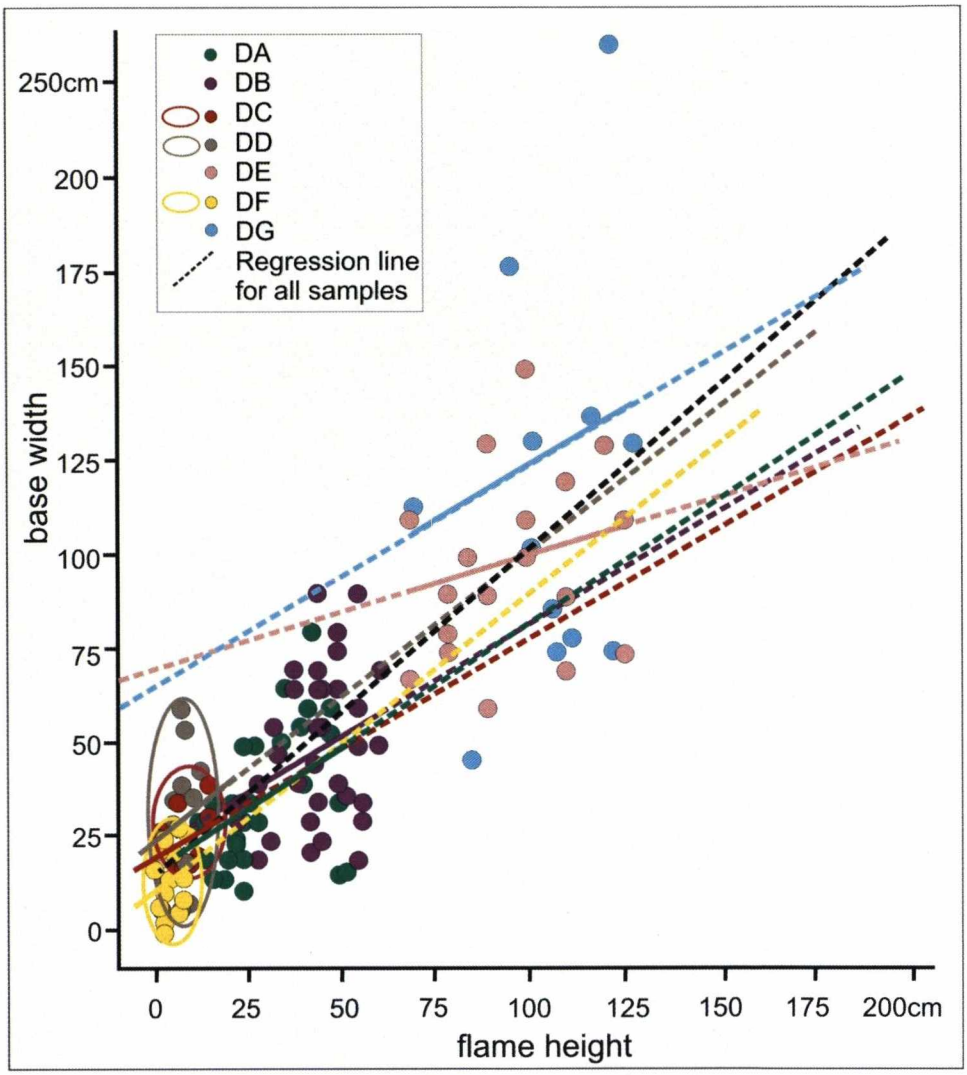

Observations:

a) Values of Pearson correlation and R^2 :

	Correlation	R^2 (%)
DA	0.445	19.8
DB	0.307	9.4
DC	0.359	12.9
DD	0.086	0.7
DE	0.217	4.7
DF	0.396	2.8
DG	0.177	3.1

A 4.1d – Base width x narrow point

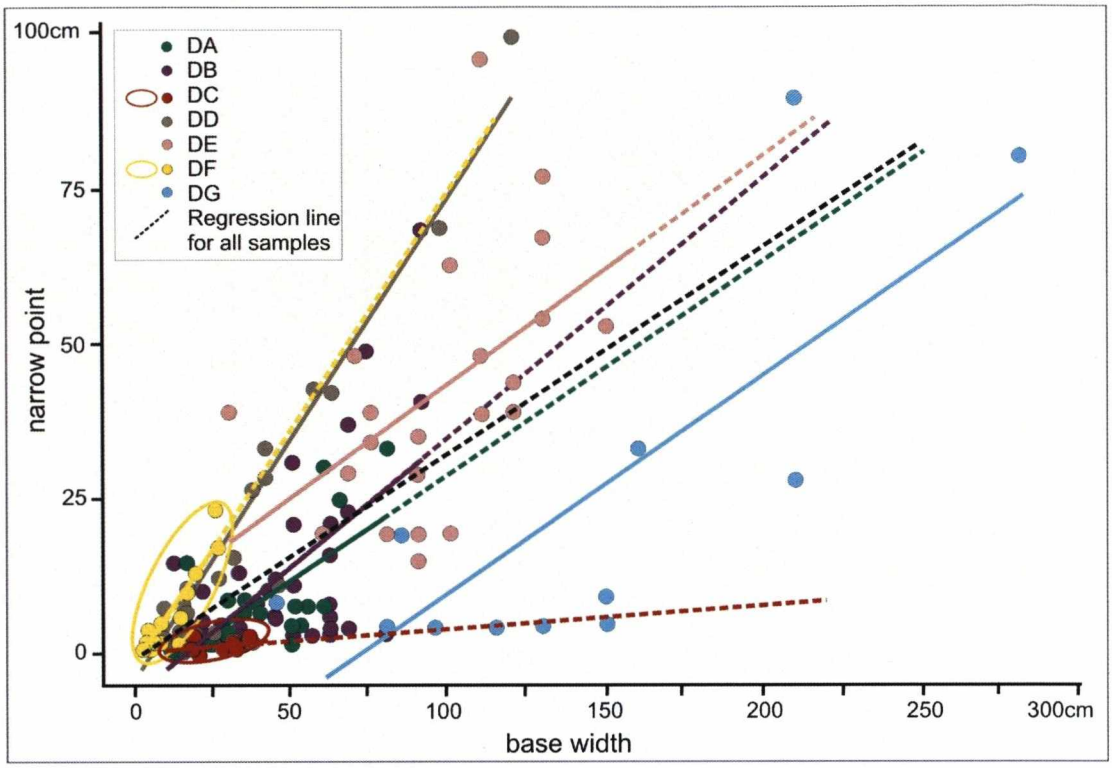

Observations:

a) Values of Pearson correlation and R^2 :

	Correlation	R^2 (%)
DA	0.699	48.8
DB	0.615	37.8
DC	0.370	13.7
DD	0.946	89.6
DE	0.501	25.1
DF	0.915	83.7
DG	0.788	62.1

b) See comparison with distribution of flame style (Figure 3.16).

A 4.2 – Heuningberg area

The interval WFR03 shows a distinct behavior where the structures were formed without liquefaction (see Chapter 4.1.5).

A 4.2a – Distance next flame x base width

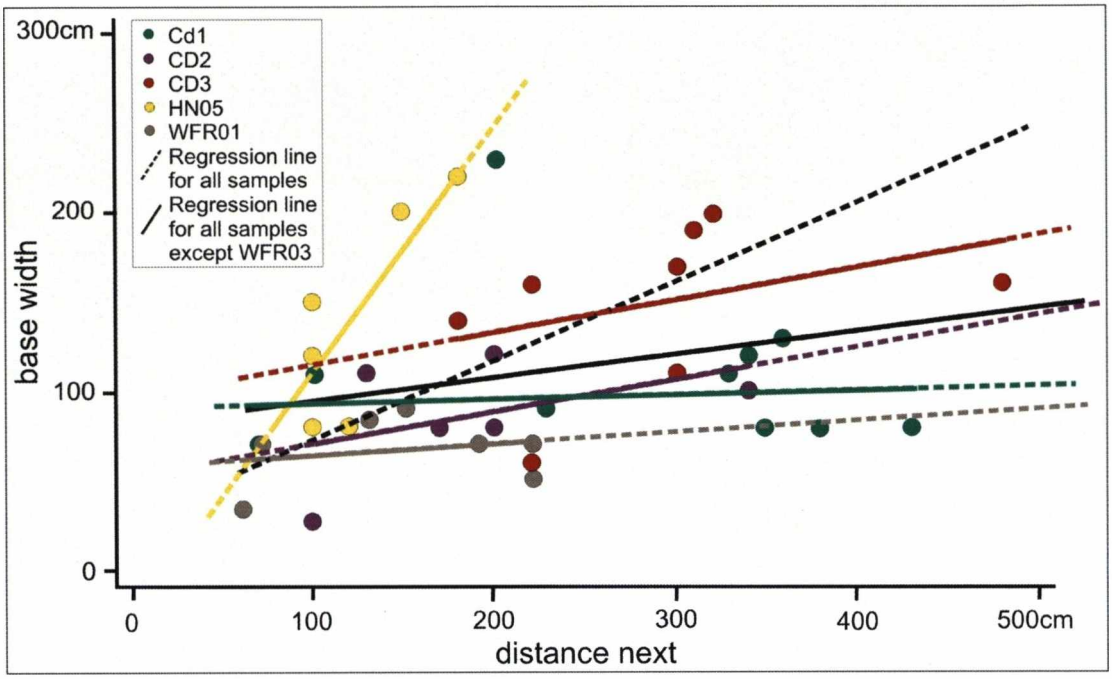

The anomalous interval WFR03:

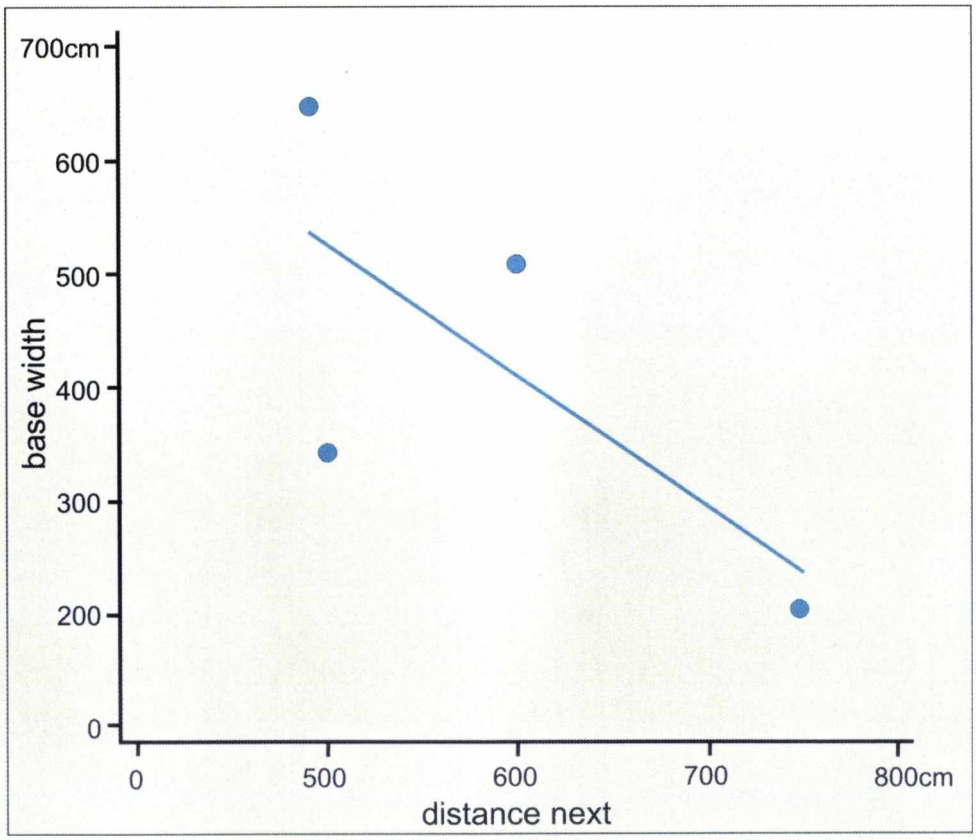

Observations:

a) Values of Pearson correlation and R^2 :

	Correlation	R^2 (%)
CD1	0.136	1.9
CD2	0.456	20.8
CD3	0.365	13.3
HN05	0.802	64.4
WFR01	0.208	4.3
WFR03	-0.703	49.4

b) It is important to emphasize that strong variations in flame orientation for the intervals CD1, CD2 and CD3 (see Figure 4.23) imply difficulties in the measurement of proprieties and influence the final least square regression lines for those beds.

A 4.2b – Unit thickness x flame height

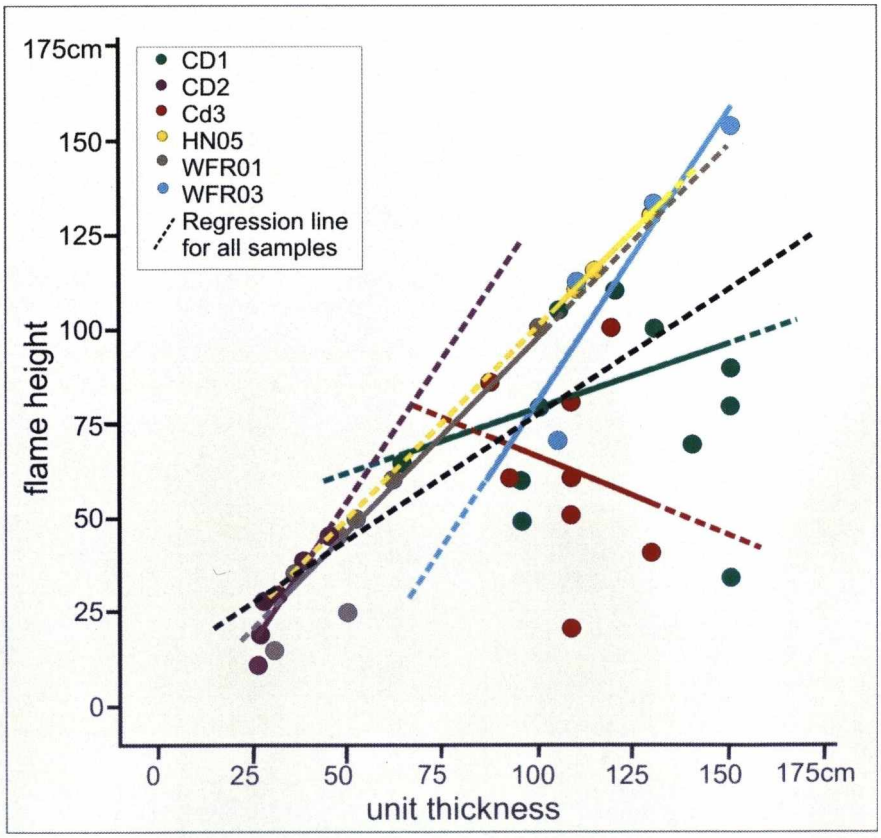

Observations:

a) Values of Pearson correlation and R^2 :

	Correlation	R^2 (%)
CD1	0.293	8.6
CD2	0.935	87.4
CD3	-0.214	4.6
HN05	1.000	100
WFR01	0.930	86.6
WFR03	0.914	83.4

b) The behavior of bed CD3 is a function of anomalous changes in the flame height due to the complexity of the flame styles. Also there are indications (low R^2) that the chosen regression line is not the only possibility for that population.

A 4.2c – Flame height x base width

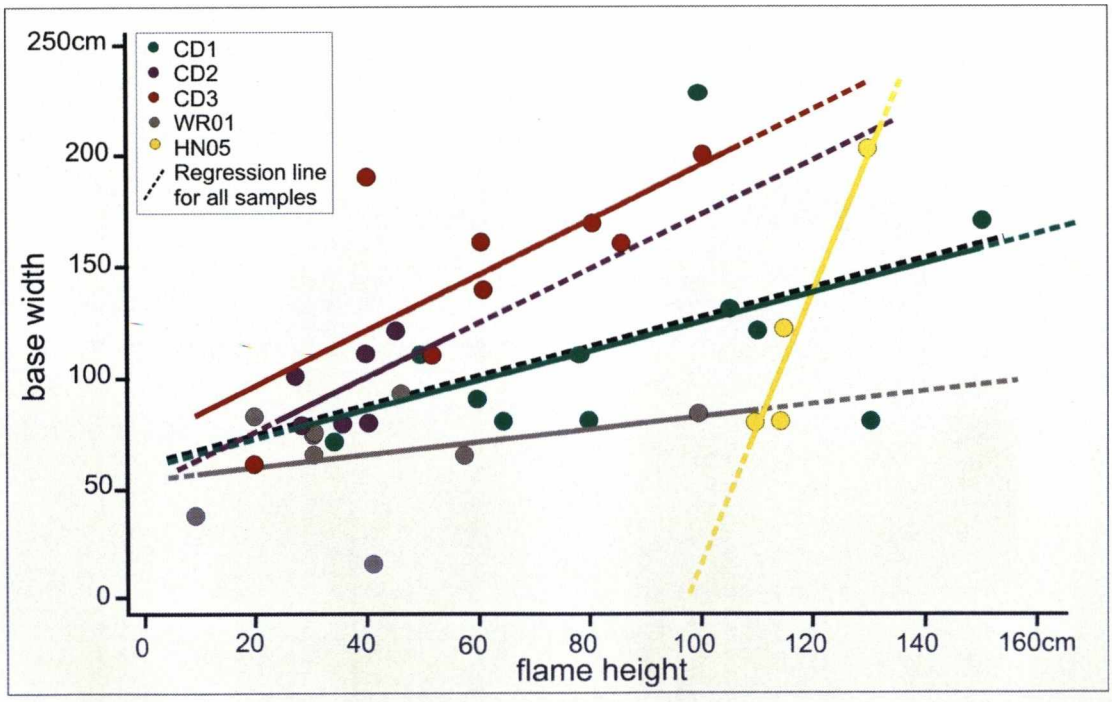

The anomalous interval WFR03:

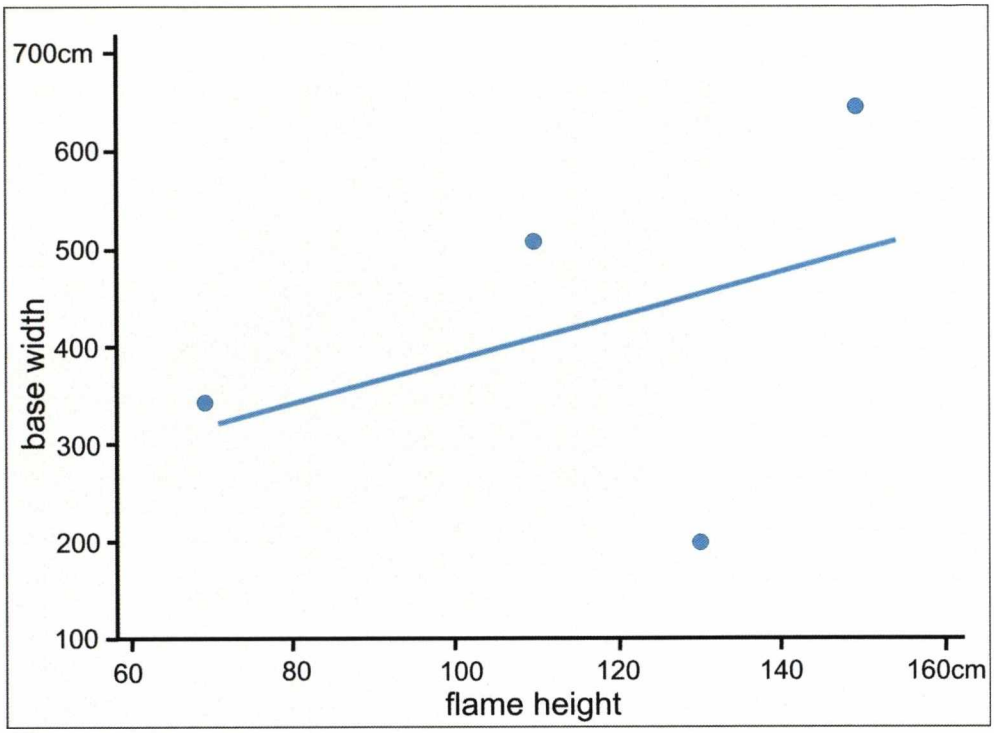

Observations:

a) Values of Pearson correlation and R^2 :

	Correlation	R^2 (%)
CD1	0.484	23.4
CD2	0.494	24.7
CD3	0.711	50.6
HN05	0.953	90.7
WFR01	0.312	9.7
WFR03	0.393	15.4

b) The anomalous behavior for bed HN05 is due to the small number of sample measurements allied to the high influence of pair (130,200).

A 4.2d – Base width x narrow point

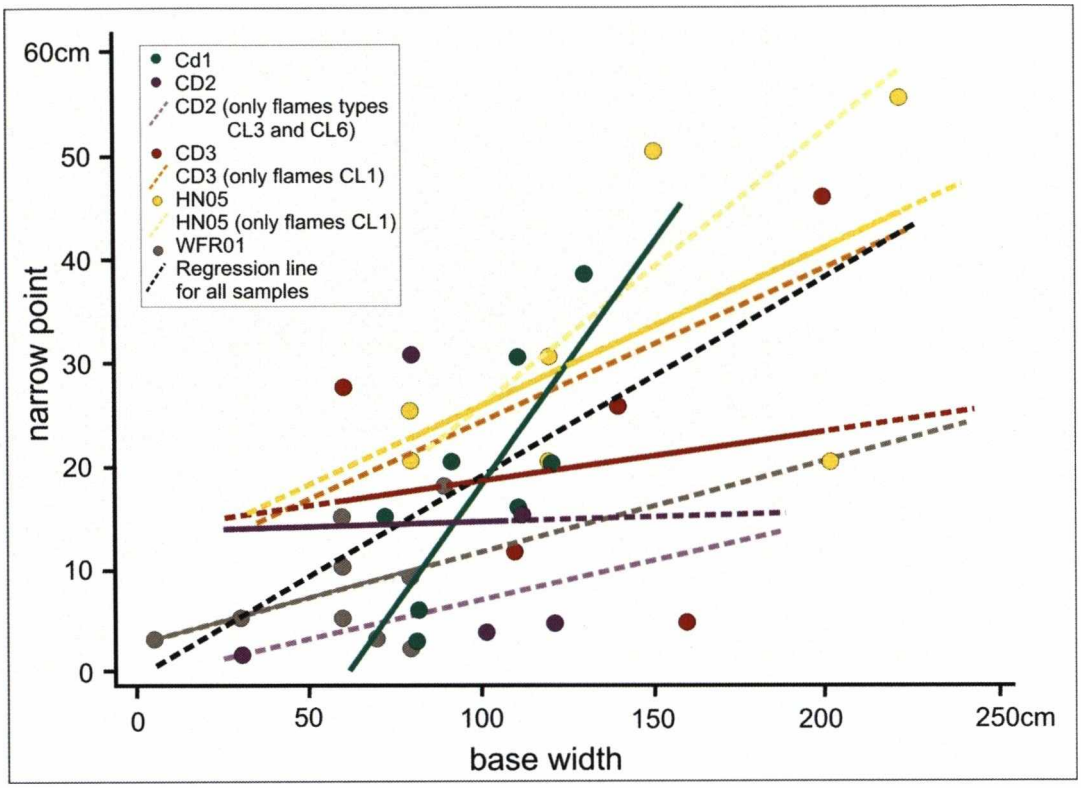

The anomalous interval WFR03:

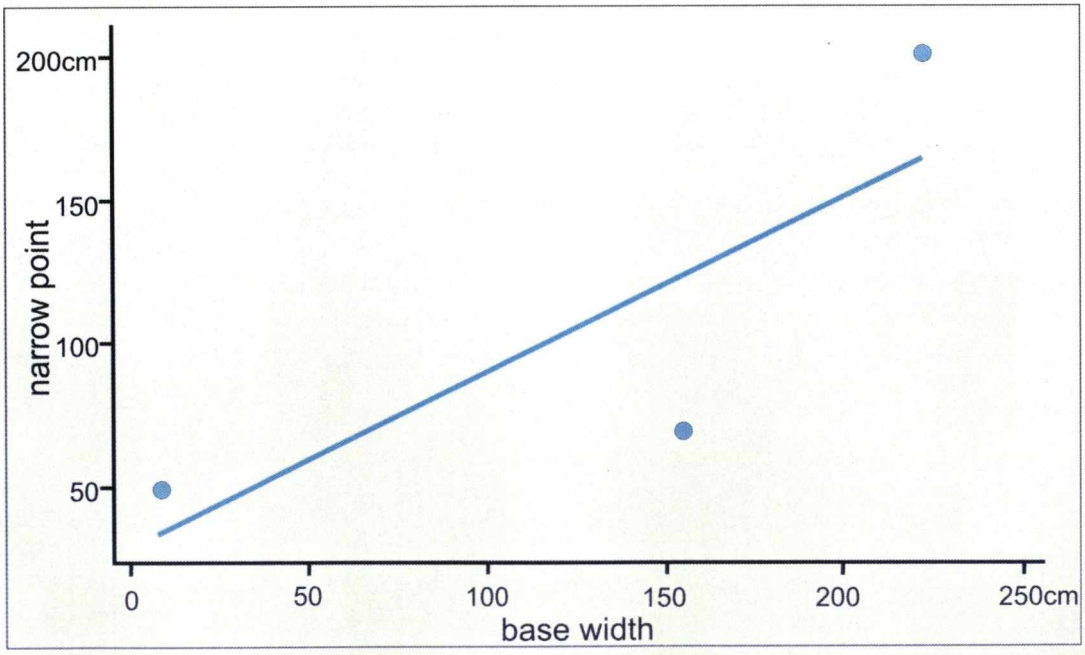

Observations:

a) Values of Pearson correlation and R^2 :

	Correlation	R^2 (%)
CD1	0.794	63.1
CD2	0.027	0.1
CD2 (CL3/CL6)	0.521	27.1
CD3	0.145	2.1
CD3 (CL1)	0.637	40.6
HN05	0.552	30.5
HN05 (CL1)	0.878	77.1
WFR01	0.423	17.9

b) The regression lines for the studied intervals are a response to the effect of distinct types of structures. The degree of correlation increases when each type of flame is considered independently (see above examples from beds CD2, CD3 and HN05).

c) Bed CD1 is dominated by types CL1, CL2 and CL7 (see Figure 3.7) that results in its atypical behavior.